

URSI Commission B School  
for Young Scientists

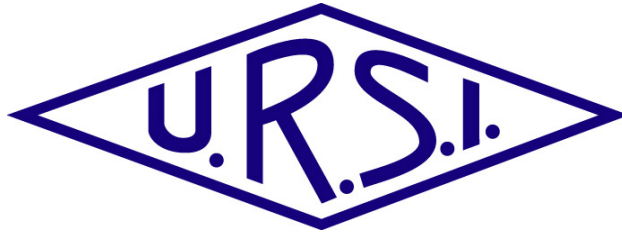
# **Fundamentals of Numerical and Asymptotic Methods**

**Lecture Notes**

**May 20, 2013**

**International Conference Center Hiroshima  
Hiroshima, Japan**





URSI Commission B School  
for Young Scientists

# **Fundamentals of Numerical and Asymptotic Methods<sup>1</sup>**

## **Lecture Notes**

**May 20, 2013**

**International Conference Center Hiroshima  
Hiroshima, Japan**

---

<sup>1</sup> This School is organized during the “2013 URSI Commission B International Symposium on Electromagnetic Theory” (EMTS 2013), May 20-24, 2013, Hiroshima, Japan.



# Table of Contents

<b>Preface</b>		<b>1</b>
<b>Program</b>		<b>3</b>
<b>Lecture Abstracts</b>		<b>5</b>
<b>Biographical Sketches of Course Instructors</b>		<b>7</b>
<b>Lecture 1</b>	<b>The Method of Moments (MoM) Applied to Problems in Electromagnetic Scattering, Radiation, and Guided Waves</b>	
	<i>By Professor Donald R. Wilton, University of Houston, USA</i>	<b>9</b>
Note 1	Linear Operator Equations	11
Note 2	EFIE in 3-D: Rectangular and Triangular Surface Patch Modeling	24
Note 3	The 3-D Magnetic Field Integral Equation (MFIE)	47
Note 4	Combined Field Integral Equation (CFIE)	54
Note 5	Modeling Homogeneous Penetrable Materials - PMCHWT Formulation	61
Note 6	Coupled 3D Finite and Boundary Element Formulation	69
Note 7	Low Frequency Breakdown of Integral and Helmholtz Equations	79
Note 8	Fast Methods	89
Appendix	Computational Methods	108
<b>Lecture 2</b>	<b>A Summary of Asymptotic High Frequency (HF) Methods for Solving Electromagnetic (EM) Wave Problems</b>	
	<i>By Professor Prabhakar Pathak, The Ohio State University, USA</i>	<b>159</b>
Note 1		161
(a)	Introduction to the ray concept and wave localization at high frequencies	
(b)	Geometrical Optics (GO) development	
(c)	Geometrical Theory of Diffraction (GTD) concept	
(d)	Uniform Geometrical Theory of Diffraction (UTD) for edges	
Note 2		206
(a)	The Equivalent Current Method (ECM) for edge diffracted ray caustic regions	
(b)	UTD for smooth convex surfaces and caustics of surface diffracted rays	
Note 3		243
(a)	Applications of UTD for treating antennas on complex platforms	
(b)	Extensions of UTD to wedges with impedance boundary conditions	
Note 4		259
(a)	Wave optical methods (PO and PTD)	
(b)	Complex Source Beams (CSBs) with some applications	
(c)	UTD for analysis of conformal antenna phased arrays	
Appendix	High-Frequency Techniques for Antenna Analysis	290



# Preface

The “URSI Commission B School for Young Scientists” is organized by URSI Commission B and is arranged for the first time on the occasion of the “2013 URSI Commission B International Symposium on Electromagnetic Theory” (EMTS 2013) in Hiroshima, Japan. This School is a one-day event held during EMTS 2013, and is sponsored jointly by URSI Commission B and the EMTS 2013 Local Organizing Committee. The School offers a short, intensive course, where a series of lectures will be delivered by two leading scientists in the Commission B community. Young scientists are encouraged to learn the fundamentals and future directions in the area of electromagnetic theory from these lectures.



# Program

## 1. Course Title

Fundamentals of Numerical and Asymptotic Methods

## 2. Course Program

### Lecture 1

- Date and Time: 9:00-13:00, May 20, 2013
- Venue: International Conference Center Hiroshima (ICCH), Hiroshima, Japan
- Lecture Title: The Method of Moments (MoM) Applied to Problems in Electromagnetic Scattering, Radiation, and Guided Waves
- Instructor: Professor Donald R. Wilton (Dept. of Electrical & Computer Engineering, University of Houston, Houston, Texas, USA)

Lunch: 13:00-14:00

### Lecture 2

- Date and Time: 14:00-18:00, May 20, 2013
- Venue: International Conference Center Hiroshima (ICCH), Hiroshima, Japan
- Lecture Title: A Summary of Asymptotic High Frequency (HF) Methods for Solving Electromagnetic (EM) Wave Problems
- Instructor: Professor Prabhakar H. Pathak (ElectroScience Lab., The Ohio State University, Columbus, Ohio, USA)



# Lecture Abstracts

## The Method of Moments (MoM) Applied to Problems in Electromagnetic Scattering, Radiation, and Guided Waves

**Donald R. Wilton, University of Houston, Dept. of ECE**  
**Houston, Texas 77096, USA**  
**E-mail: [wilton@uh.edu](mailto:wilton@uh.edu)**

The Method of Moments (MoM) is the name given by Harrington to a general procedure for converting linear operator equations (e.g., linear partial differential or integral equations) into approximating systems of linear equations. MoM and the Finite Element Method (FEM) are essentially equivalent, though they have come to have slightly different connotations due to their different origins. Thus, the former is usually associated with integral equations, and the latter with partial differential equations. However, we minimize any distinctions between them, employing similar approaches to discretize both integral and partial differential equations, and to hybrid formulations in which the two are coupled.

Radiation and scattering problems are generally open region problems involving piecewise homogeneous regions. Such problems are often efficiently formulated by introducing surface currents on region boundaries via the equivalence principle. These equivalent currents are then solved for using integral equation approaches, where the Green's functions used ensure that the radiated or scattered fields are outgoing at infinity. Integral equations arise from the imposition of boundary conditions on fields represented in terms of induced or equivalent currents on the boundaries. The equations are converted to matrix form by discretizing both the surface geometry and the equivalent currents. On conducting surfaces, the most common formulations are the electric and the magnetic field integral equations (EFIE and MFIE, respectively). Since one or both of the associated integral operators appear in almost every integral equation, their careful study is warranted. The EFIE is the more restrictive, requiring so-called divergence-conforming current representations (bases) with continuous normal components across element boundaries. However, both operators appear, for example, in the PMCHWT and Müller formulations for scattering by dielectric objects.

For interior problems or those involving extremely inhomogeneous regions, it is often more efficient to seek direct numerical solution of the vector Helmholtz wave equation. In three-dimensions, the solution domain is generally subdivided into a mesh of cubic or tetrahedral cells, with tangential vector components defined at the cell edges. The fields are then expanded in terms of interpolatory bases whose coefficients represent these tangential components; the same bases are also typically used to test the Helmholtz equation, enforcing its equality in some average sense. For the Helmholtz equation, the bases should be curl-conforming, i.e. producing field representations with continuous tangential components, even across material boundaries.

Both integral and Helmholtz equations suffer from low-frequency breakdown problems. In addition, integral equations must deal with the evaluation of singular integrals, interior resonances, and the solution of dense systems of equations. On the other hand, the solution of Helmholtz equations involves issues with preconditioning, and, for open region problems, mesh truncation. Recent advances in dealing with these issues will be discussed briefly.

## **A Summary of Asymptotic High Frequency (HF) Methods for Solving Electromagnetic (EM) Wave Problems**

**Prabhakar H. Pathak, The Ohio State University ElectroScience Lab., Dept. of ECE  
1320 Kinnear Rd., Columbus, Ohio 43212, USA  
E-mail: [pathak.2@osu.edu](mailto:pathak.2@osu.edu)**

The geometrical optics (GO) ray field consists of direct, reflected and refracted rays. GO ray paths obey Fermat's principle, and describe reflection and refraction of HF EM waves, but not the diffraction of waves around edges and smooth objects, etc. Consequently, GO predicts a zero EM field within shadow regions of impenetrable obstacles illuminated by an incident GO ray field. Early attempts by Young to predict edge diffraction via rays, and by Huygen, Fresnel and Kirchhoff to predict diffraction using wave theory will be briefly reviewed. Unlike GO, the wave based physical optics (PO) approach developed later requires an integration of the induced currents on the surface of an impenetrable obstacle illuminated by an external EM source in order to find the scattered field. The induced currents in PO are approximated by those which would exist on a locally flat tangent surface, and are set to zero in the GO shadow region. If the incident field behaves locally as a plane wave at every point on the obstacle, then it can be represented as a GO ray field; the resulting PO calculation constitutes a HF wave optical approach. PO contains diffraction effects due to the truncation of the currents at the GO shadow boundary; these effects may be spurious if there is no physical edge at the GO shadow boundary on the obstacle, whereas it is incomplete even if an edge is present at the GO shadow boundary. In the 1950s, Ufimtsev introduced an asymptotic correction to PO; his formulation is called the physical theory of diffraction (PTD).  $PTD = PO + \Delta$ , where  $\Delta$  is available primarily for edged bodies. In its original form, PTD is not accurate near and in shadow zones of smooth objects without edges, nor in shadow zones for bodies containing edges that are not completely illuminated or visible. At about the same time as PTD, a ray theory of diffraction was introduced by Keller; it is referred to as the geometrical theory of diffraction (GTD). GTD was systematically formulated by generalizing Fermat's principle to include a new class of diffracted rays. Such diffracted rays arise at geometrical and/or electrical discontinuities on the obstacle, and they exist in addition to GO rays.  $GTD = GO + \text{Diffraction}$ . Away from points of diffraction, the diffracted rays propagate like GO rays. Just as the initial values of reflected and refracted rays are characterized by reflection and transmission coefficients, the diffracted rays are characterized by diffraction coefficients. These GTD coefficients may be found from the asymptotic HF solutions to appropriate simpler canonical problems via the local properties of ray fields. Most importantly, the GTD overcomes the failure of GO in the shadow region, it does not require integration over currents, and it provides a vivid physical picture for the mechanisms of radiation and scattering. In its original form, GTD exhibits singularities at GO ray shadow boundaries and ray caustics. Uniform asymptotic methods were developed to patch up GTD in such regions. These uniform theories are referred to as UTD, UAT, spectral synthesis methods, and the equivalent current method (ECM). The pros and cons of wave optical methods (PO, PTD, ECM) and ray optical methods (GO, GTD, UTD, UAT) will be discussed along with some recent advances in PO and UTD. A UTD for edges excited by complex source beams (CSBs) and Gaussian beams (GBs) will also be briefly described; the latter may be viewed as constituting beam optical methods. A hybridization of HF and numerical methods will be briefly discussed as well.

# Biographical Sketches of Course Instructors



**Donald R. Wilton** received the B.S., M.S., and Ph.D. degrees from the University of Illinois, Urbana-Champaign, in 1964, 1966, and 1970, respectively. From 1965 to 1968 he was with Hughes Aircraft Co., Fullerton, CA, engaged in the analysis and design of phased array antennas. From 1970-1983 he was with the Department of Electrical Engineering, University of Mississippi where he attained the rank of Professor. Since 1983 he has been Professor of Electrical Engineering at the University of Houston. From 1978-1979 he was a Visiting Professor at Syracuse University. During 2004-2005 he was a visiting professor at the Polytechnic of Turin, Italy, the Sandia National Laboratories, and the University of Washington. His primary research interest is in computational electromagnetics, and he has published, lectured, and consulted extensively in this area. He is listed at ISIHighlyCited.com as one of the most cited authors in the computer science area.

Dr. Wilton is a Life Fellow of the IEEE and received the IEEE Third Millennium Medal. He has served the IEEE Antennas and Propagation Society as an Associate Editor of the Transactions on Antennas and Propagation, as a Distinguished National Lecturer, and as a member of its Administrative Committee. He is also a member of Commission B of the International Radio Science Union (URSI), in which he has held various offices, including Chair of U. S. Commission B. Dr. Wilton is a member of the Applied Computational Electromagnetics Society (ACES) and recently received the Computational Electromagnetics Award.



**Prabhakar Pathak** received his Ph.D (1973) from the Ohio State Univ (OSU). Currently he is Professor (Emeritus) at OSU. He is regarded as a co-developer of the uniform geometrical theory of diffraction (UTD). Currently his interests are in the development of new UTD solutions, as well as fast Beam and Hybrid methods, for solving large antenna/scattering problems of engineering interest. He was an IEEE (AP-S) Distinguished Lecturer from 1991-1993. He received the 1996 Schelkunoff best paper award from IEEE-AP-S; the ISAP 2009 best paper award; the George Sinclair award (1996) from OSU ElectroScience Laboratory; and, IEEE Third Millennium Medal from AP-S in 2000. He is an IEEE Life Fellow, and a member of URSI-commission B.

**Lecture 1**  
**9:00-13:00, May 20, 2013**

**The Method of Moments (MoM) Applied to  
Problems in Electromagnetic Scattering,  
Radiation, and Guided Waves**

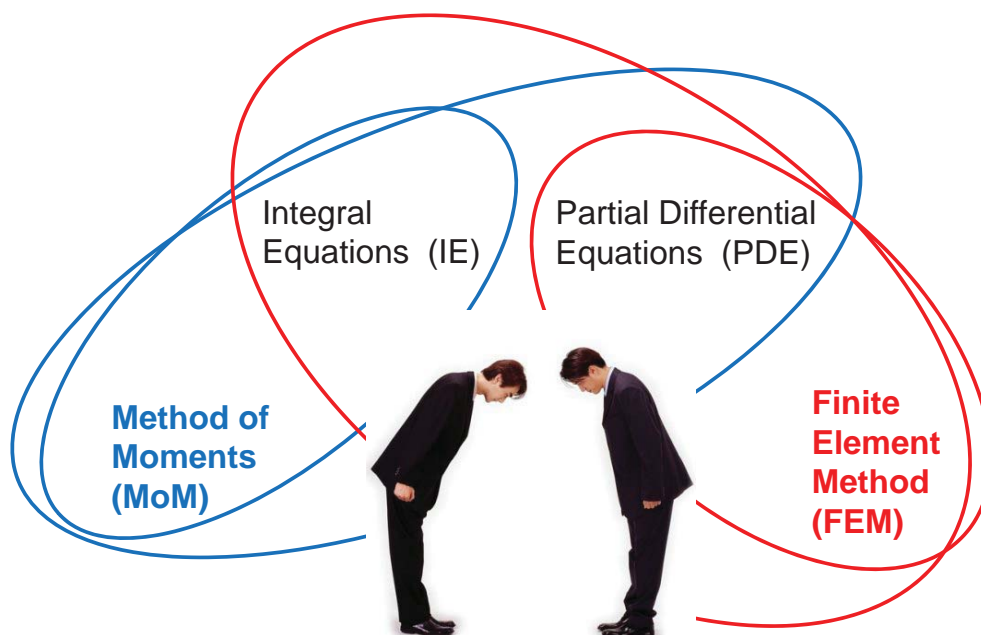
**Professor Donald R. Wilton**  
**Dept. of Electrical & Computer Engineering**  
**University of Houston**  
**Houston, Texas**  
**USA**



# Method of Moments and Finite Element Methods

Donald R. Wilton  
Dept. of Electrical and Computer Engineering  
University of Houston  
Houston, TX 77096 USA  
wilton@uh.edu

## Method of Moments and the Finite Element Method



## Linear Operator Equations

- A linear operator equation is represented symbolically as

$$\mathcal{L}u = f \quad (1)$$

where  $\mathcal{L}$  is a linear operator,

$u = u(\mathbf{r})$  = unknown field or current,  $\mathbf{r} \in \mathcal{D}$

$f = f(\mathbf{r})$  = known source, incident field or other forcing function,  $\mathbf{r} \in \mathcal{D}$

- Operator  $\mathcal{L}$  is linear if it satisfies

$$\mathcal{L}(au_1 + bu_2) = a\mathcal{L}u_1 + b\mathcal{L}u_2$$

- $\mathcal{L}$  is generally a differential, integral, or integro - differential operator on  $\mathcal{D}$  relating sources  $f$  to fields  $u$  in  $\mathcal{D}$  or on its boundary,  $\partial\mathcal{D}$ . Matrices are also linear operators.

## Linear Operators in Computational EM

- $\mathcal{L}V = \frac{d^2V}{dx^2} + k_0^2V + \text{BC's}, x \in (0, L)$
- $\mathcal{L}q_s = \int_s \frac{q_s(\mathbf{r}')}{4\pi\epsilon|\mathbf{r}-\mathbf{r}'|} dS', \mathbf{r} \in \mathcal{S}$
- $\mathcal{L}\mathbf{J} = j\omega\mu \int_s G(\mathbf{r}, \mathbf{r}')\mathbf{J}(\mathbf{r}')dS' - \frac{\nabla}{j\omega\epsilon} \int_s G(\mathbf{r}, \mathbf{r}')\nabla' \cdot \mathbf{J}(\mathbf{r}')dS' + \text{BC's}, \mathbf{r} \in \mathcal{S}$
- $\mathcal{L}\mathbf{J} = \frac{\mathbf{J}(\mathbf{r})}{2} - \hat{\mathbf{n}} \times \text{PV} \int_s \nabla G(\mathbf{r}, \mathbf{r}') \times \mathbf{J}(\mathbf{r}')dS', \mathbf{r} \in \mathcal{S}$
- $\mathcal{L}\Phi = \nabla^2\Phi + k_0^2\epsilon_r\Phi + \text{BC's}, \mathbf{r} \in \mathcal{V}$
- $\mathcal{L}\mathbf{E} = \nabla \times \mu_r^{-1} \nabla \times \mathbf{E} - k_0^2\epsilon_r\mathbf{E} + \text{BC's}, \mathbf{r} \in \mathcal{V}$
- $\mathcal{L}[x_m] = [L_{mn}][x_m]$

Operators are also defined by the characteristics of the functions to which they may be applied.

In statics:

$$G(\mathbf{r}, \mathbf{r}') = \frac{1}{4\pi R}, \quad R = |\mathbf{r} - \mathbf{r}'|, \quad (3D)$$

$$= -\frac{\ln D}{2\pi}, \quad D = |\boldsymbol{\rho} - \boldsymbol{\rho}'|, \quad (2D)$$

In dynamics: ( $e^{j\omega t}$  assumed)

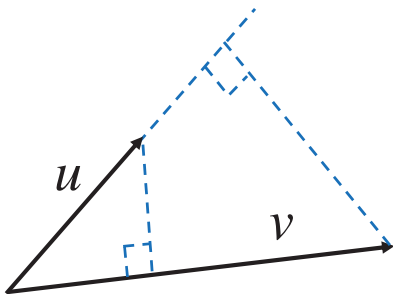
$$G(\mathbf{r}, \mathbf{r}') = \frac{e^{-jkR}}{4\pi R}, \quad (3D)$$

$$= -\frac{H_0^{(2)}(kD)}{4j}, \quad (2D)$$

## Inner Products

- Numerical solution methods are *projection* or *moment methods* involving *inner products*.
- Inner (dot or scalar) product* between pairs of  $N$  - component vectors,  $u = (u_1, u_2, \dots, u_N)$ ,  $v = (v_1, v_2, \dots, v_N)$ :

$$\langle u, v \rangle = u \cdot v = \sum_{n=1}^N u_n v_n = [u_n]^t [v_n] \quad (3)$$



As with ordinary vectors, we may think of the inner product as a projection of “ $u$  on  $v$ ” or “ $v$  on  $u$ .” If the dot product is zero, the vectors are said to be “orthogonal.”

## Inner Products, cont'd

- Inner product between two scalar functions  $u$  and  $v$ :

$$\langle u, v \rangle = \int_D uv \, d\mathcal{D} \quad (4)$$

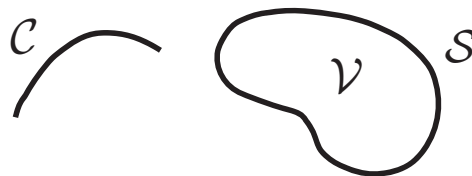
domain  $\mathcal{D} = \mathcal{C}, \mathcal{S}, \mathcal{V}$

(Note : Often  $v$  appears conjugated in inner product definitions!)

$\mathcal{C}$  - line or curve (1-D)

$\mathcal{S}$  - surface (2-D)

$\mathcal{V}$  - volume (3-D)



- (Bi-)linearity of inner product :

$$\begin{aligned} \langle au_1 + bu_2, v \rangle &= a \langle u_1, v \rangle + b \langle u_2, v \rangle, \\ \langle u, cv_1 + dv_2 \rangle &= c \langle u, v_1 \rangle + d \langle u, v_2 \rangle \end{aligned} \quad (5)$$

## Inner Products: Examples

- $u$  and  $v$  vector functions,  $u = \mathbf{u}$  and  $v = \mathbf{v}$  :

$$\langle u; v \rangle = \int_{\mathcal{D}} \mathbf{u}(\mathbf{r}) \cdot \mathbf{v}(\mathbf{r}) d\mathcal{D}, \quad \mathcal{D} = \mathcal{C}, \mathcal{S}, \text{ or } \mathcal{V}. \quad (6)$$

- Scalars  $u$  and  $v$  "convolved" with scalar Green's function  $G(\mathbf{r}, \mathbf{r}')$  ("kernel" of integral equation):

$$\langle u, G, v \rangle \equiv \langle u, \langle G, v \rangle \rangle = \int_{\mathcal{D}} \int_{\mathcal{D}} u(\mathbf{r}) G(\mathbf{r}, \mathbf{r}') v(\mathbf{r}') d\mathcal{D}' d\mathcal{D} \quad (7)$$

- Vectors  $u = \mathbf{u}$  and  $v = \mathbf{v}$  convolved with scalar Green's function  $G(\mathbf{r}, \mathbf{r}')$ :

$$\langle u; G, v \rangle = \int_{\mathcal{D}} \int_{\mathcal{D}} \mathbf{u}(\mathbf{r}) \cdot \mathbf{v}(\mathbf{r}') G(\mathbf{r}, \mathbf{r}') d\mathcal{D}' d\mathcal{D} \quad (8)$$

- Vectors  $u = \mathbf{u}$  and  $v = \mathbf{v}$  convolved with dyadic Green's function  $\mathcal{G}(\mathbf{r}, \mathbf{r}')$ :

$$\langle u; \mathcal{G}; v \rangle = \int_{\mathcal{D}} \int_{\mathcal{D}} \mathbf{u}(\mathbf{r}) \cdot \mathcal{G}(\mathbf{r}, \mathbf{r}') \cdot \mathbf{v}(\mathbf{r}') d\mathcal{D}' d\mathcal{D} \quad (9)$$

- In general,  $\langle u, v \rangle = \langle v, u \rangle$

In EM, an unconjugated inner product is often used because the vector quantities often satisfy the reciprocity theorem.

## Weak and Strong Forms of Operator Equations

- *Strong form* (equality holds at every point in  $\mathcal{D}$ ):

$$\mathcal{L}u = f \quad (10)$$

- *Weak form* (equality holds in a weighted average sense):

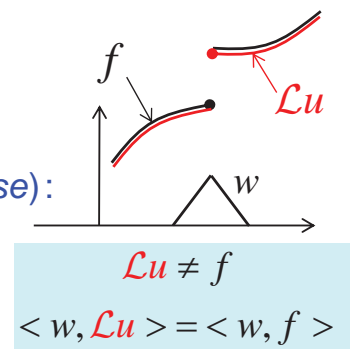
$$\langle w, \mathcal{L}u \rangle = \langle w, f \rangle \quad (11)$$

where  $\{w\}$  is a set of *weighting functions*.

Notes :

- If continuous, solutions  $u$  of (10) and (11) are identical
- For differential operators, integration by parts is often used to transfer differentiability requirements from  $u$  to  $w$ .
- If  $u$  is infinite dimensional, then so is the set of functions  $w$

- In numerical solutions,  $w$ 's are often chosen from a *finite* set of weighting or testing functions  $\{w_m^{(N)}\}$ ,  $m = 1, 2, \dots, N$ .



## Bases and Unknown Representations

- Approximate  $u$  as

$$u \approx u = \sum_{n=1}^N U_n u_n = [U_n]^t [u_n] \quad (12)$$

where coefficients  $U_n$  are unknown and  $u_n, n = 1, \dots, N$  are known *basis functions*.

- $u_n$  must be "independent" and capable of approximating  $u$ .
- Independence of bases is measured by their "projections" onto one another,

$$\langle u_m, u_n \rangle \equiv \text{Gram Matrix} \quad (13)$$

## Independence of Basis Functions

- Ideal are *orthonormal* bases  $u_n$ , for which

$$\langle u_m, u_n \rangle = \int_{\mathcal{D}} u_m u_n d\mathcal{D} = \delta_{mn} = \begin{cases} 1, & m = n, \\ 0, & m \neq n, \end{cases} \quad (14)$$

( $\delta_{mn}$  is the "Kronecker delta") but are difficult to discover for arbitrary  $\mathcal{D}$

- Instead, first approximate  $\mathcal{D}$  by subdividing into *subdomains* or *elements* (e.g., line segments, triangles, rectangles, tetrahedrons)  $\mathcal{D}^e, e = 1, 2, \dots, E$ .

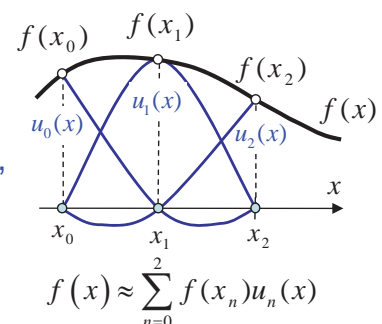
Then  $\mathcal{D} \approx \tilde{\mathcal{D}} = \bigcup_{e=1}^E \mathcal{D}^e$ .

- Then *interpolatory polynomial* bases are usually used.

They satisfy the property  $u_m(\mathbf{r}_j) = \delta_{mj}$  where  $\mathbf{r}_j$ ,

$j = 1, 2, \dots, N$  are interpolation points on  $\tilde{\mathcal{D}}$ . In addition, they also satisfy the following "approximation" to (14):

$$\sum_{j=1}^N u_m(\mathbf{r}_j) u_n(\mathbf{r}_j) = \delta_{mn} \quad (15)$$



## Method of Moments

- Substituting representation for  $u$  into operator equation and testing with  $\{w = w_m, m = 1, 2, \dots, N\}$  yields

$$\sum_{n=1}^N \langle w_m, \mathcal{L}u_n \rangle U_n = \langle w_m, f \rangle, \quad m = 1, 2, \dots, N \quad (16)$$

or in matrix form,

$$[L_{mn}][U_n] = [F_m], \quad (17)$$

$[L_{mn}]$  is a matrix approximate to operator  $\mathcal{L}$ !

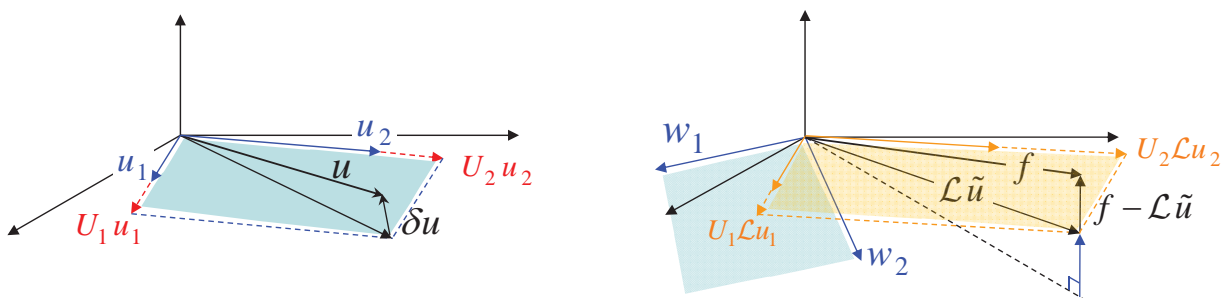
where  $L_{mn} = \langle w_m, \mathcal{L}u_n \rangle$  and  $F_m = \langle w_m, f \rangle$ .

- Solving the linear system yields unknowns  $[U_n]$  that provide an approximation to  $u$  in  $\mathcal{D}$ . The result can also be written as

$$u \approx \tilde{u} = [U_n]^t [u_n] = [u_n]^t [U_n], \quad (18)$$

where  $[u_n]^t$  denotes transpose of  $[u_n]$ .

## Abstract Vector Space Interpretation of the Method of Moments



- The unknown is approximated in the "subspace of basis vectors  $u_n$ " as  $u \approx \tilde{u} = \sum_n U_n u_n$
- Both  $\mathcal{L}\tilde{u} = \sum_n U_n \mathcal{L}u_n$  and  $f$  are *projected* onto the "subspace of testing vectors  $w_m$ "; equating the projections determines  $\{U_n\}$ .
- The projection both "minimizes" the residual error  $f - \sum_n U_n \mathcal{L}u_n$  and makes it orthogonal to the testing vector subspace.

## Linear Functionals

- A *linear functional*  $I[u]$  is a scalar physical parameter or figure of merit that depends linearly on  $u$  (e.g.,  $I[au] = aI[u]$ ).

Examples :

- Capacitance where  $u$  is surface charge
- Input admittance where  $u$  is a surface current
- Vector component of far field where  $u$  is a surface current
- Value of  $u(\mathbf{r})$  at point  $\mathbf{r}$  (may be unbounded at edge or corner!)

- **Riesz representation theorem** : For any *bounded* linear functional, a function  $g$  exists such that  $I[u]$  can be represented as an inner product,

$$I[u] = - \langle u, g \rangle \quad (19)$$

- For  $u \approx \tilde{u}$ ,

$$I[u] \approx I[\tilde{u}] = - \langle \tilde{u}, g \rangle = - \sum_{n=1}^N U_n \langle u_n, g \rangle = - [U_n]^t [\langle u_n, g \rangle] \quad (20)$$

- Note : Sampled values of the unknown involve unbounded functionals :

$$J(\mathbf{r}') = \int_S J(\mathbf{r}) \delta(\mathbf{r} - \mathbf{r}') dS \Rightarrow g(\mathbf{r}) = -\delta(\mathbf{r} - \mathbf{r}') \text{ is unbounded}$$

## Summary of Method of Moments

- Subdivide  $\mathcal{D}$  into  $E$  subdomains or elements  $\mathcal{D}^e$ ; approximate the solution domain as  $\mathcal{D} \approx \tilde{\mathcal{D}} = \bigcup_{e=1}^E \mathcal{D}^e$ .

- Choose (usually interpolating) basis functions  $\{u_n\}$  and approximate  $u$  as

$$u \approx \tilde{u} = \sum_n U_n u_n = [U_n]^t [u_n].$$

- Choose weighting (testing) functions  $\{w_m\}$ . (*Galerkin's method* :  $\{w_m\} \equiv \{u_m\}$ )
- Substitute  $\tilde{u}$  into operator equation and test with  $w_m$ . (For differential or integro-differential operators, integrate by parts to reduce differentiability requirements on  $u_n$  and incorporate boundary conditions.)

## Summary of Method of Moments, Cont'd

- Solve the resulting linear matrix system

$$[L_{mn}][U_n] = [F_m]$$

where

$$L_{mn} = \langle w_m, \mathcal{L}u_n \rangle,$$

$$F_m = \langle w_m, f \rangle$$

for unknown coefficients  $U_n$ . A direct or iterative solution procedure may be used.

- Compute desired figure - of - merit (linear functional)  $I[u]$  as

$$I[u] \approx I[\tilde{u}] = -\langle \tilde{u}, g \rangle = -\sum_{n=1}^N U_n \langle u_n, g \rangle = -[U_n]^t [\langle u_n, g \rangle]. \quad (21)$$

## The Variational Approach

- Variational and MoM approaches appear to be quite different, but really are equivalent, as we'll show.

- As a first step, we define an adjoint operator  $\mathcal{L}^\dagger$  such that

$$\langle w, \mathcal{L}u \rangle = \langle \mathcal{L}^\dagger w, u \rangle \quad (22)$$

for arbitrary  $u$  and  $w$ .

- Adjoints exist and are unique; to find:
  - Differential operators: Successively integrate by parts
  - Integral operators: Interchange source and observation points in the kernel
  - Matrix operator: Simply transpose the original matrix

## The Adjoint Problem

- The variational approach to solving  $\mathcal{L}u = f$  begins by considering the linear functional

$$I[u] = -\langle u, g \rangle$$

- Next define the *adjoint* problem,

$$\mathcal{L}^\dagger w = g. \quad (23)$$

where  $g$  plays role of source or forcing function,  $w$  is solution of adjoint problem.

- Physical significance of  $w$  may not always be clear, but note it does provide an alternative means to compute the functional :

$$\begin{aligned} I[u] &= -\langle u, g \rangle = -\langle u, \mathcal{L}^\dagger w \rangle \\ &= -\langle \mathcal{L}u, w \rangle = -\langle f, w \rangle \end{aligned} \quad (24)$$

In electromagnetics, this dual representation is usually a consequence of *reciprocity*, which also often implies that  $\mathcal{L} = \mathcal{L}^\dagger$  ( $\mathcal{L}$  is *self - adjoint*)

## Adjoint Operator Examples

- $\mathcal{L}^\dagger V = \frac{d^2 V}{dx^2} + k_0^2 V + \text{BC}^\dagger \text{s}$
- $\mathcal{L}^\dagger q_s = \int_s \frac{q_s(\mathbf{r}')}{4\pi\epsilon |\mathbf{r} - \mathbf{r}'|} dS'$
- $\mathcal{L}^\dagger \mathbf{J} = j\omega\mu \int_s G(\mathbf{r}, \mathbf{r}') \mathbf{J}(\mathbf{r}') dS' - \frac{\nabla}{j\omega\epsilon_s} \int_s G(\mathbf{r}, \mathbf{r}') \nabla' \cdot \mathbf{J}(\mathbf{r}') dS' + \text{BC}^\dagger \text{s}$
- $\mathcal{L}^\dagger \mathbf{J} = \frac{\mathbf{J}(\mathbf{r})}{2} - \hat{\mathbf{n}} \times (\hat{\mathbf{n}} \times \nabla \times \text{PV} \int_s G(\mathbf{r}, \mathbf{r}') \hat{\mathbf{n}}' \times \mathbf{J}(\mathbf{r}') dS') + \text{BC}^\dagger$  (see Appendix)
- $\mathcal{L}^\dagger \Phi = \nabla^2 \Phi + k_0^2 \epsilon_r \Phi + \text{BC}^\dagger \text{s}$
- $\mathcal{L}^\dagger \mathbf{E} = \nabla \times \mu_r^{-1} \nabla \times \mathbf{E} - k_0^2 \epsilon_r \mathbf{E} + \text{BC}^\dagger \text{s}$
- $\mathcal{L}^\dagger [x_m] = [L_{mn}]^\dagger [x_m]$

Most of the above operators are "self - adjoint!"

## Bi-Variational Functional

- Define the *bivariational* functional <sup>\*\*</sup>

$$I[\tilde{u}, \tilde{w}] = \langle \mathcal{L}\tilde{u}, \tilde{w} \rangle - \langle \tilde{u}, g \rangle - \langle f, \tilde{w} \rangle \quad (25)$$

Note that  $I[u, w] = \langle \mathcal{L}u, w \rangle - \langle u, g \rangle - \langle f, w \rangle = I[u]$ .

We regard  $\tilde{u}$  and  $\tilde{w}$  as approximate or *trial* solutions to the original and adjoint problems, respectively.

- Define *solution errors* in the original and adjoint problems as

$$\delta u = \tilde{u} - u, \quad \delta w = \tilde{w} - w. \quad (26)$$

Then we can easily show that

$$I[\tilde{u}, \tilde{w}] = -\langle u, g \rangle + \langle \mathcal{L}\delta u, \delta w \rangle \quad (27)$$

or  $\delta I[u, w] = \langle \mathcal{L}\delta u, \delta w \rangle$  with *second order error* in  $\delta u$  and  $\delta w$ .

(Functional is said to be *stationary* or to have only a *second order variation* about the functions  $u$  and  $w$ .)

- <sup>\*\*</sup> Other, less general functionals often restrict the form of the resulting linear system, e.g., to Galerkin's method!

## Rayleigh-Ritz Procedure

- Approximate  $u$  and  $w$  in terms of basis sets  $\{u_n\}$  and  $\{w_m\}$  as

$$\tilde{u} = \sum_n U_n u_n \quad (28)$$

$$\tilde{w} = \sum_m W_m w_m. \quad (29)$$

- Substitute above expansions into the bi-variational functional,

$$I[\tilde{u}, \tilde{w}] = \sum_m \sum_n W_m U_n \langle \mathcal{L}u_n, w_m \rangle - \sum_n U_n \langle u_n, g \rangle - \sum_m W_m \langle f, w_m \rangle \quad (30)$$

and set  $\partial I[\tilde{u}, \tilde{w}] / \partial W_p = \partial I[\tilde{u}, \tilde{w}] / \partial U_p = 0$  (*stationarity condition*).

- Replace dummy index  $p$  by  $m$  in first set,  $p$  by  $n$  in the second.

The surprising result is that ...

## ... One Obtains Independent Moment Equations for Both the Original and the Adjoint Problems!

- (Moment equations for original problem, which are independent of  $g$ )

$$\sum_n \langle w_m, \mathcal{L}u_n \rangle U_n = \langle w_m, f \rangle, \quad m = 1, 2, \dots, N \Rightarrow ([L_{mn}][U_n] = [F_m]) \quad (31)$$

- (Moment equations for original problem, which are independent of  $f$ )

$$\sum_m \langle \mathcal{L}u_n, w_m \rangle W_m = \langle u_n, g \rangle, \quad n = 1, 2, \dots, N. \quad (32)$$

$$(\text{recall } \langle \mathcal{L}u_n, w_m \rangle = \langle u_n, \mathcal{L}^\dagger w_m \rangle) \Rightarrow ([L_{mn}]^\dagger [W_n] = [G_m]) \quad (33)$$

- Note also the independence of equation sets (31) and (32), and the *reversed roles of basis and testing functions* in the adjoint problem.

**Idea :** Why not insert the resulting  $\tilde{u}, \tilde{w}$  into the *variational* form possibly yielding more accurate results than substituting into the *non - variational* form of the functional?

## Evaluation of Functional

Write bivariational functional as

$$\begin{aligned} I(\tilde{u}, \tilde{w}) &= \langle \mathcal{L}\tilde{u}, \tilde{w} \rangle - \langle f, \tilde{w} \rangle - \langle \tilde{u}, g \rangle \\ &= \langle \mathcal{L}\tilde{u} - f, \tilde{w} \rangle - \langle \tilde{u}, g \rangle. \end{aligned} \quad (34)$$

The first term on the right hand side vanishes :

$$\begin{aligned} \langle \mathcal{L}\tilde{u} - f, \tilde{w} \rangle &= \sum_m W_m \left[ \sum_n \langle \mathcal{L}u_n, w_m \rangle U_n - \langle f, w_m \rangle \right] = [W_m]^t ([L_{mn}][U_n] - [F_m]) \\ &= 0. \quad (\text{by (31)}) \end{aligned} \quad (35)$$

Hence

$$I(\tilde{u}, \tilde{w}) = - \langle \tilde{u}, g \rangle = - \sum_n U_n \langle u_n, g \rangle \quad (36)$$

i.e.,

$$I(\tilde{u}) = I(\tilde{u}, \tilde{w}), \quad (37)$$

so we obtain the same result using either the (bi-)variational or non - variational forms of the functional!

## Equivalence of MoM and Variational Approach

- $\tilde{u}$  can be determined from the MoM equations independent of  $w$  and  $g$ . The solution is same as that obtained by the (bi-)variational approach.
- $I[\tilde{u}] = I[\tilde{u}, \tilde{w}]$  independent of  $g$ .
- The variational approach (and adjoint problem) is useful in proving stationarity, but seems otherwise largely superfluous in arriving at a numerical formulation. The moment method yields the same solution but is generally simpler to apply. The variational problem tells us...
  - Moment method solutions are *automatically stationary*.
  - Error in  $I[\tilde{u}, \tilde{w}]$  ( $\delta I[u, w] = \langle \mathcal{L}\delta u, \delta w \rangle$ ) is proportional to that in both  $u, w$ ; so to reduce error, *choose  $w_m$  to well approximate  $w$ , the solution of the adjoint problem.*

**End of Note 1**

## Appendix: Derivation of MFIE Adjoint Operator

$$\bullet \mathcal{L}\mathbf{J} = \frac{\mathbf{J}(\mathbf{r})}{2} - \hat{\mathbf{n}} \times \text{PV} \int_s \nabla G(\mathbf{r}, \mathbf{r}') \times \mathbf{J}(\mathbf{r}') dS' = (\hat{\mathbf{n}} \times \mathbf{H}^{\text{inc}})$$

We first write the MFIE in the non - standard form

$$-\hat{\mathbf{n}} \times \mathcal{L}\mathbf{J} = -\hat{\mathbf{n}} \times \frac{\mathbf{J}(\mathbf{r})}{2} + \hat{\mathbf{n}} \times \left( \hat{\mathbf{n}} \times \nabla \times \text{PV} \int_s G(\mathbf{r}, \mathbf{r}') \mathbf{J}(\mathbf{r}') dS' \right) = -\hat{\mathbf{n}} \times (\hat{\mathbf{n}} \times \mathbf{H}^{\text{inc}})$$

$$\hat{\mathbf{n}} \times (\hat{\mathbf{n}} \times \mathbf{H}^{\text{inc}}) = -\mathbf{H}_{\text{tan}}^{\text{inc}} = -\frac{1}{\mu} \lim_{\mu \uparrow S} \nabla \times \mathbf{A}$$

Then for a tangential surface testing vector  $\mathbf{M}(\mathbf{r})$ , we have that

$$\langle \mathbf{M}, -\hat{\mathbf{n}} \times \frac{\mathbf{J}(\mathbf{r})}{2} + \hat{\mathbf{n}} \times (\hat{\mathbf{n}} \times \nabla \times \text{PV} \int_s G(\mathbf{r}, \mathbf{r}') \mathbf{J}(\mathbf{r}') dS') \rangle$$

which is of the form  $\langle \mathbf{M}, -\lim_{\mathbf{r} \uparrow S} \mathbf{H}[\mathbf{J}] \rangle$  and which can be interpreted as a reaction integral.

Hence, by the reaction theorem, we have

$$\langle \mathbf{M}, -\lim_{\mathbf{r} \uparrow S} \mathbf{H}[\mathbf{J}] \rangle = \langle \mathbf{J}, \lim_{\mathbf{r} \downarrow S} \mathbf{E}[\mathbf{M}] \rangle = \langle \mathbf{J}, \hat{\mathbf{n}} \times \frac{\mathbf{M}(\mathbf{r})}{2} + \hat{\mathbf{n}} \times (\hat{\mathbf{n}} \times \nabla \times \text{PV} \int_s G(\mathbf{r}, \mathbf{r}') \mathbf{M}(\mathbf{r}') dS') \rangle$$

$$-\hat{\mathbf{n}} \times (\hat{\mathbf{n}} \times \mathbf{E}^{\text{sc}}) = \mathbf{E}_{\text{tan}}^{\text{sc}} = -\frac{1}{\epsilon} \lim_{\epsilon \downarrow S} \nabla \times \mathbf{F}$$

## Appendix: Derivation of MFIE Adjoint Operator, cont'd

Thus,

$$\langle \mathbf{M}, -\hat{\mathbf{n}} \times \frac{\mathbf{J}(\mathbf{r})}{2} + \hat{\mathbf{n}} \times (\hat{\mathbf{n}} \times \nabla \times \text{PV} \int_s G(\mathbf{r}, \mathbf{r}') \mathbf{J}(\mathbf{r}') dS') \rangle = \langle \mathbf{J}, \hat{\mathbf{n}} \times \frac{\mathbf{M}(\mathbf{r})}{2} + \hat{\mathbf{n}} \times (\hat{\mathbf{n}} \times \nabla \times \text{PV} \int_s G(\mathbf{r}, \mathbf{r}') \mathbf{M}(\mathbf{r}') dS') \rangle$$

and even though  $\mathbf{M} \cdot \left( -\hat{\mathbf{n}} \times \frac{\mathbf{J}(\mathbf{r})}{2} \right) = \mathbf{J} \cdot \left( \hat{\mathbf{n}} \times \frac{\mathbf{M}(\mathbf{r})}{2} \right)$ , the operator  $-\hat{\mathbf{n}} \times \mathcal{L}$  is non-self-adjoint.

For the original operator, set  $\mathbf{M} = -\hat{\mathbf{n}} \times \mathbf{w}$  and the above becomes

$$\langle \mathbf{w}, \frac{\mathbf{J}(\mathbf{r})}{2} - (\hat{\mathbf{n}} \times \nabla \times \text{PV} \int_s G(\mathbf{r}, \mathbf{r}') \mathbf{J}(\mathbf{r}') dS') \rangle = \langle \mathbf{J}, \frac{\mathbf{w}(\mathbf{r})}{2} - \hat{\mathbf{n}} \times (\hat{\mathbf{n}} \times \nabla \times \text{PV} \int_s G(\mathbf{r}, \mathbf{r}') \hat{\mathbf{n}}' \times \mathbf{w}(\mathbf{r}') dS') \rangle$$

and the adjoint operator is

$$\mathcal{L}^* \mathbf{w} = \frac{\mathbf{w}(\mathbf{r})}{2} - \hat{\mathbf{n}} \times (\hat{\mathbf{n}} \times \nabla \times \text{PV} \int_s G(\mathbf{r}, \mathbf{r}') \hat{\mathbf{n}}' \times \mathbf{w}(\mathbf{r}') dS')$$

# EFIE in 3-D: Rectangular and Triangular Surface Patch Modeling

Donald R. Wilton

Michael A. Khayat

## Features of the 3D Electric Field Integral Equation (EFIE)

- The total electric field vanishes on perfect electric conductors (PEC):

$$-\mathbf{E}_{\text{tan}}^s = \mathbf{E}_{\text{tan}}^{\text{inc}}$$

- Scattered field is produced by the induced surface current,  $\mathbf{J}$ .
- The scattered field is represented in terms of potentials.

$$\mathbf{E}^s = -j\omega\mathbf{A} - \nabla\Phi,$$

$$\mathbf{A} = \mu \int_s G(\mathbf{r}, \mathbf{r}') \mathbf{J}(\mathbf{r}') dS', \quad \Phi = \frac{1}{\epsilon_s} \int_s G(\mathbf{r}, \mathbf{r}') q(\mathbf{r}') dS'$$

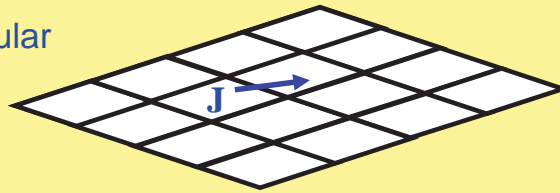
$$\nabla' \cdot \mathbf{J}(\mathbf{r}') = -j\omega q(\mathbf{r}') \quad G(\mathbf{r}, \mathbf{r}') = \frac{e^{-jkR}}{4\pi R}, \quad R = |\mathbf{r} - \mathbf{r}'|$$

## Representing Electric Current on a Conductor

- For simplicity, assume a PEC flat plate at  $z = 0$ ,

$$\mathbf{J}(\mathbf{r}) = J_x \hat{\mathbf{x}} + J_y \hat{\mathbf{y}}$$

- Subdivide plate into rectangular elements or cells.



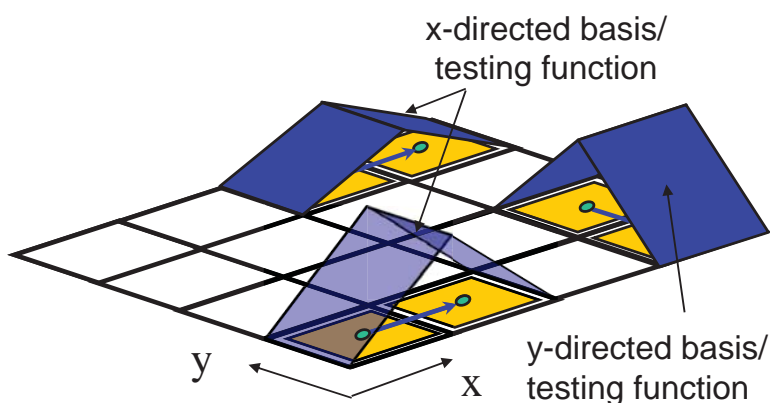
- For the scalar potential, we also need the surface charge density :

$$-j\omega q(\mathbf{r}) = \nabla \cdot \mathbf{J}(\mathbf{r}) = \frac{\partial J_x}{\partial x} + \frac{\partial J_y}{\partial y}$$

⇒  $\mathbf{J}(\mathbf{r})$  must be differentiable along the current direction!

- ⇒
- $J_x$  is piecewise linear in  $x$ , constant in  $y$ ;
  - $J_y$  is piecewise linear in  $y$ , constant in  $x$ ;
  - $q(\mathbf{r})$  is piecewise constant

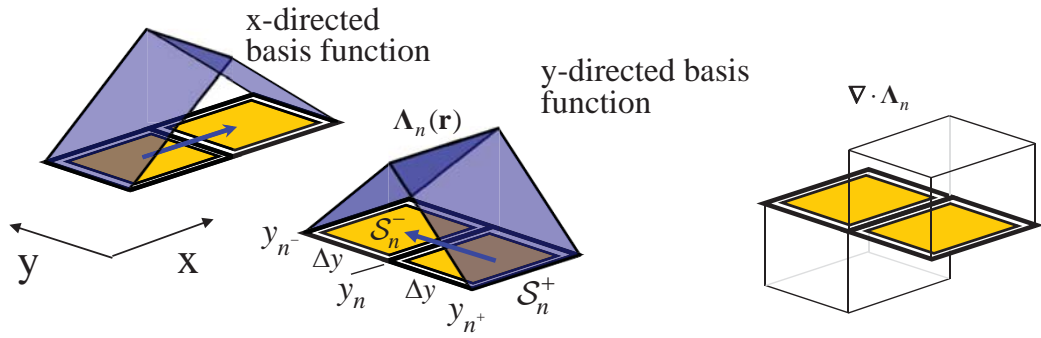
## On Rectangular Elements, Rooftop Bases Provide Good Compromise Between Simplicity and Effectiveness



- Charge, current qualitatively satisfy edge and corner conditions

- Normal current components are continuous, even at bends (*div-conforming*)
- Tangential current components are discontinuous
- Piecewise constant charge representation
- Current vanishes at plate edges

## Rooftop Bases Model Surface Charge Density as Piecewise Constant



For y - directed bases, for instance :

$$\Lambda_n(\mathbf{r}) = \hat{\mathbf{y}} \Lambda_n(y) = \begin{cases} \hat{\mathbf{y}} \frac{|y - y_{n^\pm}|}{\Delta y}, & \mathbf{r} \in S_n^\pm \\ \mathbf{0}, & \text{otherwise} \end{cases}$$

$$\nabla \cdot \Lambda_n = \hat{\mathbf{y}} \cdot \nabla \Lambda_n = \frac{d\Lambda_n}{dy} = \begin{cases} \frac{\pm 1}{\Delta y}, & \mathbf{r} \in S_n^\pm \\ 0, & \text{otherwise} \end{cases}$$

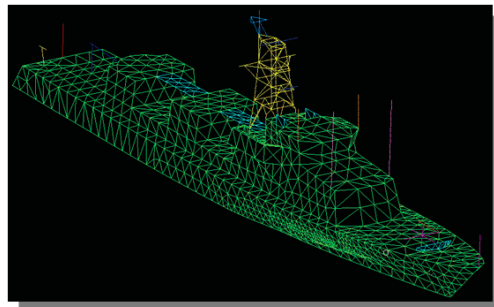
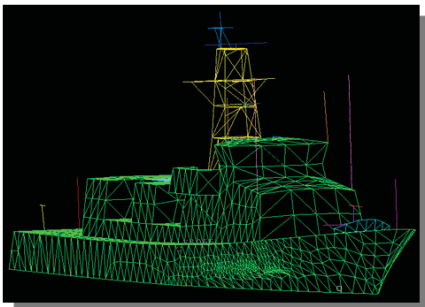
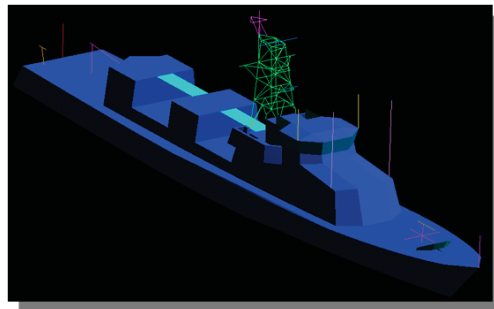
Interpolation properties of y - directed bases :

$$\hat{\mathbf{y}} \cdot \Lambda_n(\mathbf{r}) \Big|_{\substack{x=x_m \\ y=y_m}} = \delta_{mn}$$

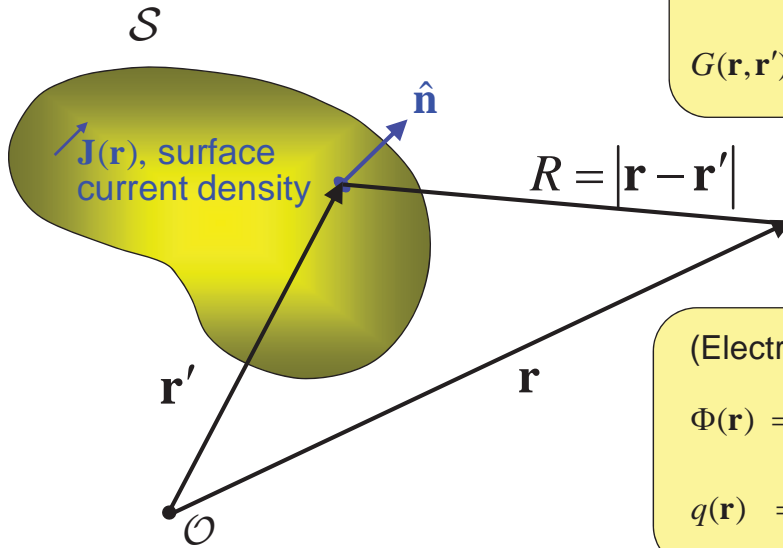
$$\hat{\mathbf{x}} \cdot \Lambda_n(\mathbf{r}) \Big|_{\substack{x=x_n \\ y=y_n}} = 0$$

## But Modern Problems Require the Flexibility of Triangular Surface Patch Modeling

Cyclone Class Patrol Craft, PC-1



# Definitions of Geometrical and Electrical Quantities for Current on a Surface



(Magnetic) Vector Potential :

$$\mathbf{A}(\mathbf{r}) = \mu \int_S G(\mathbf{r}, \mathbf{r}') \mathbf{J}(\mathbf{r}') dS',$$

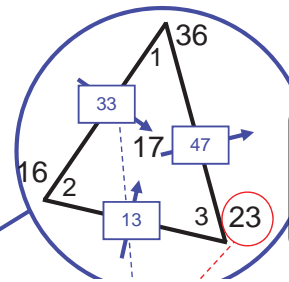
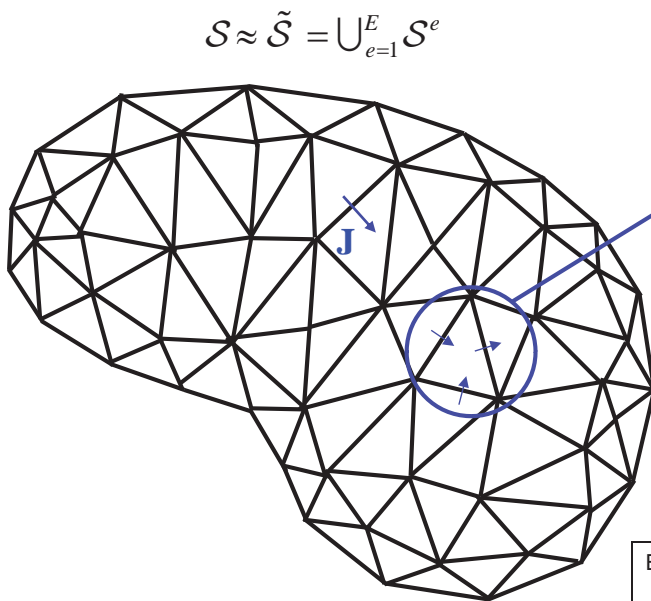
$$G(\mathbf{r}, \mathbf{r}') = \frac{e^{-jkR}}{4\pi R} \quad (\text{Green's function})$$

(Electric) Scalar Potential :

$$\Phi(\mathbf{r}) = \frac{1}{\epsilon} \int_S G(\mathbf{r}, \mathbf{r}') q(\mathbf{r}') dS',$$

$$q(\mathbf{r}) = \frac{1}{-j\omega} \nabla \cdot \mathbf{J}(\mathbf{r}) \quad (\text{continuity eq.})$$

## Surface Discretization



Note :

$$\mathbf{r}_{23}^{\text{global}} = \mathbf{r}_3^{\text{local}}$$

- A **Global Node list** defines vertex locations

Node #	x	y	z
23	$x_{23}$	$y_{23}$	$z_{23}$

- An **element list** contains both global node and DoF numbers

Element e	Global node number/ DoF number		
	local node1	local node 2	local node 3
17	36/ -13	16/ 47	23/ -33

DoF's are current density components normal to triangle edges!

## Area Coordinates Are Used to Represent Bases and Parameterize Element Geometry

$A^e = A_1 + A_2 + A_3$

$$\xi_i = \frac{A_i}{A^e}, \quad i = 1, 2, 3$$

$$\Rightarrow \xi_1 + \xi_2 + \xi_3 = 1$$

$$\mathbf{r} = \xi_1 \mathbf{r}_1^e + \xi_2 \mathbf{r}_2^e + \xi_3 \mathbf{r}_3^e$$

$\mathbf{r}_i^e = \mathbf{r}_n$  for some  $e, i$ , and  $n$

local

global

All elements mapped to "parent element"

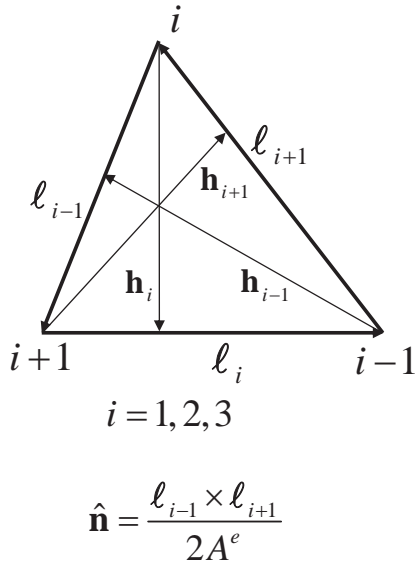
## An Area Coordinate Is Also the Fractional Distance from an Edge to the Opposite Vertex

$$\xi_1 = \frac{\frac{1}{2} l_1 \times \text{height of } A_1}{\frac{1}{2} l_1 h_1} = \frac{\text{height of } A_1}{h_1}$$

$\xi_i$  linearly interpolates node  $i$

It is convenient to define edge vectors associated with each edge and height vectors associated with each vertex.

## Local Geometry Parameter Definitions



<b>Edge vectors</b>	$\mathbf{l}_i = \mathbf{r}_{i-1} - \mathbf{r}_{i+1}, \quad \ell_i =  \mathbf{l}_i ,$ $\hat{\mathbf{l}}_i = \mathbf{l}_i / \ell_i; \quad i = 1, 2, 3$
<b>Area</b>	$A^e = \frac{ \mathbf{l}_{i-1} \times \mathbf{l}_{i+1} }{2}; \quad i = 1, 2, \text{ or } 3$
<b>Height vectors</b>	$h_i = \frac{2A^e}{\ell_i}, \quad \hat{\mathbf{h}}_i = \hat{\mathbf{l}}_i \times \hat{\mathbf{n}},$ $\mathbf{h}_i = h_i \hat{\mathbf{h}}_i; \quad i = 1, 2, 3$
<b>Coordinate gradients</b>	$\nabla_{\xi_i} = -\frac{\hat{\mathbf{h}}_i}{h_i}; \quad i = 1, 2, 3$

## Integration over Triangles Using Area Coordinates

$$\int_{A^e} f(\rho) dS$$

$$= 2A^e \int_0^1 \int_0^{1-\xi_2} f(\xi_1 \rho_1^e + \xi_2 \rho_2^e + \xi_3 \rho_3^e) d\xi_1 d\xi_2$$

$$\approx 2A^e \sum_{k=1}^K w_k f(\xi_1^{(k)} \rho_1^e + \xi_2^{(k)} \rho_2^e + \xi_3^{(k)} \rho_3^e)$$

Numerical integration

Or evaluate analytically using

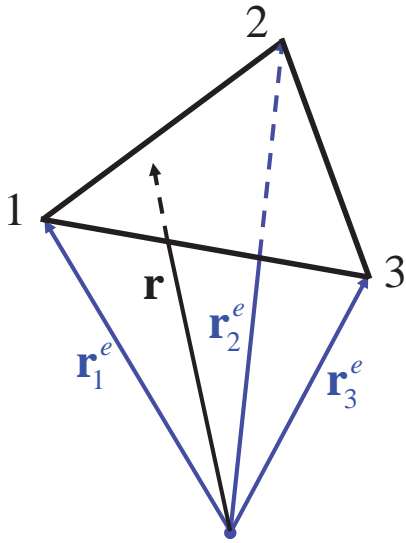
$$\int_0^1 \int_0^{1-\xi_2} \xi_1^\alpha \xi_2^\beta \xi_3^\gamma d\xi_1 d\xi_2$$

$$= \frac{\alpha! \beta! \gamma!}{(\alpha + \beta + \gamma + 2)!}$$

**Table 9** Sample points and weighting coefficients for  $K$ -point quadrature on triangles.

Sample Points, $(\xi_1^{(k)}, \xi_2^{(k)})$ $(\xi_3^{(k)} = 1 - \xi_1^{(k)} - \xi_2^{(k)})$	Weights, $w_k$
<b>K=1, error <math>\mathcal{O}(\xi_i^2)</math>:</b> (0.3333333333333333, 0.3333333333333333)	0.5000000000000000
<b>K=3, error <math>\mathcal{O}(\xi_i^3)</math>:</b> (0.6666666666666667, 0.1666666666666667) (0.1666666666666667, 0.6666666666666667) (0.1666666666666667, 0.1666666666666667)	0.1666666666666667 0.1666666666666667 0.1666666666666667
<b>K=7, error <math>\mathcal{O}(\xi_i^6)</math>:</b> (0.3333333333333333, 0.3333333333333333) (0.79742698535309, 0.10128650732346) (0.10128650732346, 0.79742698535309) (0.10128650732346, 0.10128650732346) (0.47014206410512, 0.47014206410512) (0.47014206410512, 0.05971587178977) (0.05971587178977, 0.47014206410512)	0.1125000000000000 0.06296959027241 0.06296959027241 0.06296959027241 0.06619707639425 0.06619707639425 0.06619707639425

## Triangular Surface Patches



$$\mathbf{r} = \xi_1 \mathbf{r}_1^e + \xi_2 \mathbf{r}_2^e + \xi_3 \mathbf{r}_3^e$$

- EFIE has the form

$$-\mathbf{E}_{\text{tan}}^s(\mathbf{J}) = \mathbf{E}_{\text{tan}}^i$$

- Expand the current in *div - conforming bases*  $\Lambda_n(\mathbf{r})$ ,

$$\mathbf{J}(\mathbf{r}) = \sum_{n=1}^N I_n \Lambda_n(\mathbf{r})$$

- Also use  $\{\Lambda_m(\mathbf{r})\}$  as testing functions,  $m = 1, 2, \dots, N$ .

## 3D EFIE Formulation

$$-\mathbf{E}_{\text{tan}}^s = j\omega \mathbf{A}_{\text{tan}} + \nabla_{\text{tan}} \Phi = \mathbf{E}_{\text{tan}}^i, \quad \mathbf{r} \in \mathcal{S}$$

$$\Rightarrow \left[ j\omega \mu \int_{\mathcal{S}} G(\mathbf{r}, \mathbf{r}') \mathbf{J}(\mathbf{r}') d\mathcal{S}' - \frac{1}{j\omega \epsilon} \nabla \int_{\mathcal{S}} G(\mathbf{r}, \mathbf{r}') \nabla' \cdot \mathbf{J}(\mathbf{r}') d\mathcal{S}' \right]_{\text{tan}} = \mathbf{E}_{\text{tan}}^i,$$

Test with  $\Lambda_m(\mathbf{r})$  (as yet undefined!), to obtain the *weak form*

$$j\omega \langle \Lambda_m; \mathbf{A} \rangle + \langle \Lambda_m; \nabla \Phi \rangle = \langle \Lambda_m; \mathbf{E}^i \rangle$$

where

$$\mathbf{A} = \mu \int_{\mathcal{S}} G(\mathbf{r}, \mathbf{r}') \mathbf{J}(\mathbf{r}') d\mathcal{S}', \quad \Phi = \frac{1}{-j\omega \epsilon} \int_{\mathcal{S}} G(\mathbf{r}, \mathbf{r}') \nabla' \cdot \mathbf{J}(\mathbf{r}') d\mathcal{S}',$$

$$G(\mathbf{r}, \mathbf{r}') = \frac{e^{-jkR}}{4\pi R}, \quad \langle \mathbf{A}; \mathbf{B} \rangle = \int_{\mathcal{S}} \mathbf{A}(\mathbf{r}) \cdot \mathbf{B}(\mathbf{r}) d\mathcal{S}$$

or

$$j\omega \mu \langle \Lambda_m; G, \mathbf{J} \rangle + \frac{1}{-j\omega \epsilon} \langle \Lambda_m; \nabla G, \nabla \cdot \mathbf{J} \rangle = \langle \Lambda_m; \mathbf{E}^i \rangle$$

## Integration by Parts

$$j\omega \langle \Lambda_m; \mathbf{A} \rangle + \langle \Lambda_m; \nabla \Phi \rangle = \langle \Lambda_m; \mathbf{E}^i \rangle$$

Using  $\nabla \cdot (\Lambda_m \Phi) = \Phi \nabla \cdot \Lambda_m + \Lambda_m \cdot \nabla \Phi \Rightarrow$

$$\int_S \nabla \cdot (\Lambda_m \Phi) dS \stackrel{\text{divergence theorem}}{=} \int_{\partial S} \Phi \Lambda_m \cdot \hat{\mathbf{u}} dC = \underbrace{\int_S \Phi \nabla \cdot \Lambda_m dS}_{\langle \nabla \cdot \Lambda_m, \Phi \rangle} + \underbrace{\int_S \Lambda_m \cdot \nabla \Phi dS}_{\langle \Lambda_m, \nabla \Phi \rangle}$$

$$\Rightarrow \langle \Lambda_m; \nabla \Phi \rangle = -\langle \nabla \cdot \Lambda_m, \Phi \rangle + \int_{\partial S} \Phi \underbrace{\Lambda_m \cdot \hat{\mathbf{u}}}_{=0 \text{ on } \partial S \text{ \& cancels on } \partial S^e \text{ if } \Lambda_m \cdot \hat{\mathbf{u}} \text{ is continuous}} dS$$

Hence the weak form becomes

$\Rightarrow \{\Lambda_m\}$  must be *div - conforming*

$$j\omega \langle \Lambda_m; \mathbf{A} \rangle - \langle \nabla \cdot \Lambda_m, \Phi \rangle = \langle \Lambda_m; \mathbf{E}^i \rangle$$

or

$$j\omega \mu \langle \Lambda_m; \mathbf{G}, \mathbf{J} \rangle + \frac{1}{j\omega \epsilon} \langle \nabla \cdot \Lambda_m; \mathbf{G}, \nabla \cdot \mathbf{J} \rangle = \langle \Lambda_m; \mathbf{E}^i \rangle$$

## EFIE MoM Formulation

Setting  $\mathbf{J}(\mathbf{r}') = \sum_n I_n \Lambda_n(\mathbf{r}')$ , and substituting yields

$$[Z_{mn}] [I_n] = [V_m]$$

where  $[Z_{mn}] = j\omega [L_{mn}] + \frac{1}{j\omega} [S_{mn}]$  and

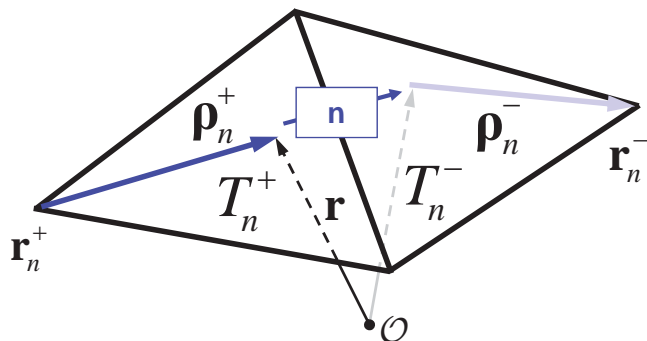
$$L_{mn} = \mu \int_S \int_{S'} G(\mathbf{r}, \mathbf{r}') \Lambda_m(\mathbf{r}) \cdot \Lambda_n(\mathbf{r}') dS' dS \equiv \mu \langle \Lambda_m; \mathbf{G}, \Lambda_n \rangle$$

$$S_{mn} = \frac{1}{\epsilon} \int_S \int_{S'} \nabla \cdot \Lambda_m(\mathbf{r}) G(\mathbf{r}, \mathbf{r}') \nabla' \cdot \Lambda_n(\mathbf{r}') dS' dS \equiv \frac{1}{\epsilon} \langle \nabla \cdot \Lambda_m, \mathbf{G}, \nabla \cdot \Lambda_n \rangle,$$

$$V_m = \langle \Lambda_m; \mathbf{E}^i \rangle, \quad G(\mathbf{r}, \mathbf{r}') = \frac{e^{-jkR}}{4\pi R}, \quad R = |\mathbf{r} - \mathbf{r}'|$$

- divergence of  $\Lambda_n$  must exist
- $\Lambda_n$  must be *div - conforming*

## Basis Functions for Surface Currents on Triangular Elements (Global Representation)



**Global basis definition:**

$$\Lambda_n(\mathbf{r}) = \begin{cases} \frac{\boldsymbol{\rho}_n^\pm}{h_n^\pm}, & \mathbf{r} \in T_n^\pm \\ \mathbf{0}, & \mathbf{r} \notin T_n^\pm \end{cases}$$

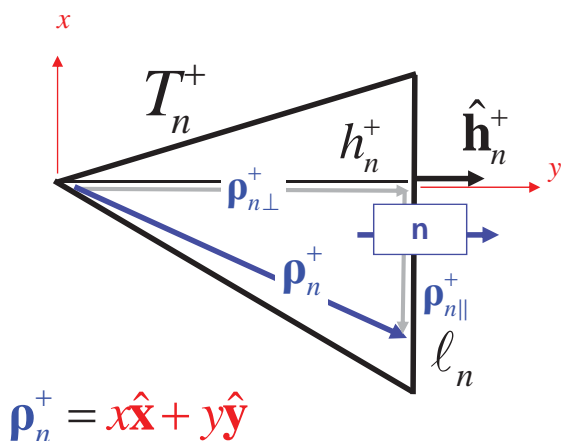
$\Lambda_n$  is linear in the radial direction, constant in the angular direction

$$\boldsymbol{\rho}_n^\pm(\boldsymbol{\xi}) = \pm(\mathbf{r}(\boldsymbol{\xi}) - \mathbf{r}_n^\pm), \quad \mathbf{r} \in T_n^\pm$$

$$\boldsymbol{\xi} = (\xi_1, \xi_2, \xi_3)$$

- Rao, S.M., D.R. Wilton, and A.W. Glisson, "Electromagnetic Scattering by Surfaces of Arbitrary Shape," *IEEE Trans. Antennas and Propagation*, AP-30, No. 3, pp. 409-418, May 1982.

## Interpolation and Divergence Properties



**Interpolation property:**

$$\hat{\mathbf{h}}_n^+ \cdot \Lambda_n \Big|_{\mathbf{r} \in \text{edge } n} = \frac{\hat{\mathbf{h}}_n^+ \cdot \boldsymbol{\rho}_n^+}{h_n^+}$$

$$= \frac{\hat{\mathbf{h}}_n^+ \cdot \boldsymbol{\rho}_{n\perp}^+}{h_n^+} = \frac{h_n^+}{h_n^+} = 1,$$

$$\hat{\mathbf{h}}_m^+ \cdot \Lambda_n \Big|_{\mathbf{r} \in \text{edge } m} = 0, \quad m \neq n$$

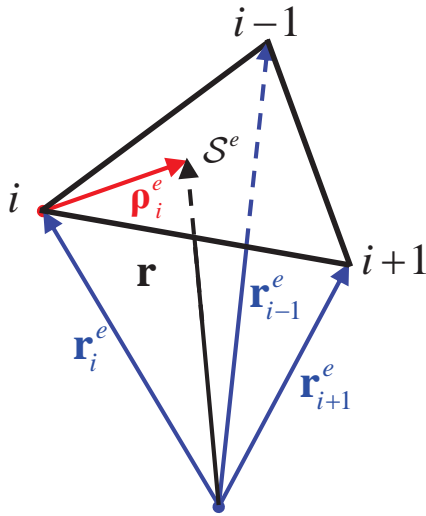
**Divergence property:**

$$\nabla \cdot \Lambda_n = \frac{\nabla \cdot \boldsymbol{\rho}_n^\pm}{h_n^\pm} = \frac{\pm \nabla \cdot (x\hat{\mathbf{x}} + y\hat{\mathbf{y}})}{h_n^\pm} = \pm \frac{2}{h_n^\pm}, \quad \mathbf{r} \in T_n^\pm$$

## Local Representation of Basis Functions for Triangular Elements

Note:

$$\underbrace{\Lambda_n}_{\text{global}} = \pm \underbrace{\Lambda_i^e}_{\text{local}}, \quad \mathbf{r} \in \mathcal{S}^e = T_n^\pm$$



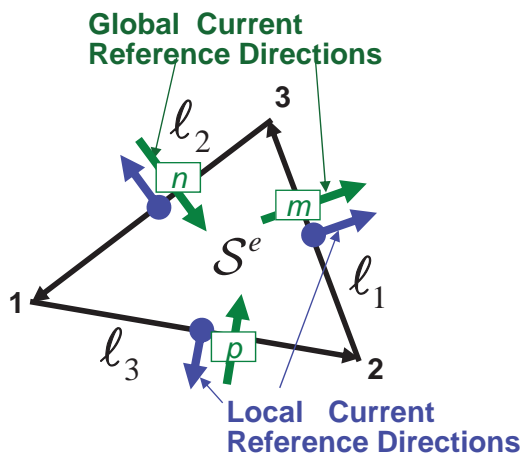
$$\mathbf{r} = \xi_i \mathbf{r}_i^e + \xi_{i+1} \mathbf{r}_{i+1}^e + \xi_{i-1} \mathbf{r}_{i-1}^e$$

Local basis function :

$$\begin{aligned} \Lambda_i^e(\mathbf{r}) &= \frac{\rho_i^e}{h_i} = \frac{\mathbf{r} - \mathbf{r}_i^e}{h_i} \\ &= \frac{\xi_i \mathbf{r}_i^e + \xi_{i+1} \mathbf{r}_{i+1}^e + \xi_{i-1} \mathbf{r}_{i-1}^e - \mathbf{r}_i^e}{h_i} \\ &= \frac{(\cancel{1} - \xi_{i+1} - \xi_{i-1}) \mathbf{r}_i^e + \xi_{i+1} \mathbf{r}_{i+1}^e + \xi_{i-1} \mathbf{r}_{i-1}^e - \cancel{\mathbf{r}_i^e}}{h_i} \\ &= \frac{\xi_{i+1} (\mathbf{r}_{i+1}^e - \mathbf{r}_i^e) - \xi_{i-1} (\mathbf{r}_i^e - \mathbf{r}_{i-1}^e)}{h_i} \end{aligned}$$

$$\Rightarrow \Lambda_i^e(\mathbf{r}) = \frac{\xi_{i+1} l_{i-1} - \xi_{i-1} l_{i+1}}{h_i}, \quad \mathbf{r} \in \mathcal{S}^e, i=1,2,3$$

## Local Basis Functions on Triangular Elements



Local basis functions :

$$\Lambda_i^e(\mathbf{r}) = \frac{\xi_{i+1} l_{i-1} - \xi_{i-1} l_{i+1}}{h_i}, \quad \mathbf{r} \in \mathcal{S}^e$$

$$\nabla \cdot \Lambda_i^e(\mathbf{r}) = \frac{2}{h_i}, \quad \mathbf{r} \in \mathcal{S}^e$$

$$\sigma_i^e = \begin{cases} 1, & \text{Global reference direction} \\ & \text{for } i\text{th DoF is out of element } e \\ -1, & \text{Global reference direction} \\ & \text{for } i\text{th DoF is into element } e \end{cases}$$

## Element Matrix for 3D EFIE

**Element matrix :**

$$\left[ Z_{ij}^{ef} \right] = j\omega \left[ L_{ij}^{ef} \right] + \frac{1}{j\omega} \left[ S_{ij}^{ef} \right],$$

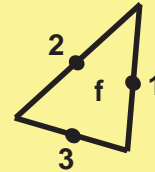
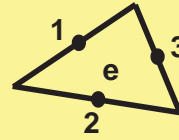
$$L_{ij}^{ef} = \mu \langle \Lambda_i^e; G, \Lambda_j^f \rangle,$$

$$S_{ij}^{ef} = \frac{1}{\epsilon} \langle \nabla \cdot \Lambda_i^e, G, \nabla \cdot \Lambda_j^f \rangle,$$

$i, j = 1, 2, 3$

**Element excitation vector :**

$$V_i^e = \langle \Lambda_i^e; \mathbf{E}^i \rangle, \quad i = 1, 2, 3$$



**Matrix assembly :**

$$\sigma_i^e \sigma_j^f Z_{ij}^{ef} \rightarrow \left[ Z_{mn} \right]$$

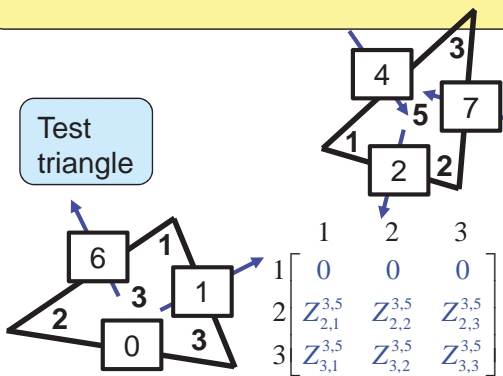
**Excitation vector assembly :**

$$\sigma_i^e V_i^e \rightarrow \left[ V_m \right]$$

## Matrix Assembly

**Matrix Assembly Rule:**

Element  $\sigma_i^e \sigma_j^f Z_{ij}^{ef}$  of the element matrix is added to row  $m$  and column  $n$  of the system matrix if  $m$  is the global DoF corresponding to the  $i$ th local DOF of element  $e$  and  $n$  is the global DoF corresponding to the  $j$ th local DOF of element  $f$ .



**Matrix assembly :**

$$\sigma_i^e \sigma_j^f Z_{ij}^{ef} \rightarrow \left[ Z_{mn} \right]$$

**Excitation vector assembly :**

$$\sigma_i^e V_i^e \rightarrow \left[ V_m \right]$$

$$\sigma_i^e = \begin{cases} 1, & \text{local and global DOFs similarly directed} \\ -1, & \text{otherwise} \end{cases}$$

add (+)(-)  $Z_{2,1}^{3,5}$  to  $Z_{1,7}$ , etc.

**System matrix,  $[Z_{mn}]$**

1	2	3	4	5	6	7	...
1	•	•	•	•	•	•	•
2	•	(+)(+) $Z_{2,3}^{3,5}$	•	(+)(-) $Z_{2,2}^{3,5}$	•	•	(+)(-) $Z_{2,1}^{3,5}$
3	•	•	•	•	•	•	•
4	•	•	•	•	•	•	•
5	•	•	•	•	•	•	•
6	•	•	•	•	•	•	•
7	•	(+)(+) $Z_{3,3}^{3,5}$	•	(+)(-) $Z_{3,2}^{3,5}$	•	•	(+)(-) $Z_{3,1}^{3,5}$
...	•	•	•	•	•	•	•

# The Global Basis Form Can Be Extended to Line Segment, Rectangular and Tetrahedral Elements

$$\Lambda_n(\mathbf{r}) = \begin{cases} \frac{\rho_n^+}{h_n^+}, & \mathbf{r} \in \mathcal{D}_n^+ \\ \frac{\rho_n^-}{h_n^-}, & \mathbf{r} \in \mathcal{D}_n^- \\ \mathbf{0}, & \text{elsewhere} \end{cases} \quad \nabla \cdot \Lambda_n(\mathbf{r}) = \begin{cases} \frac{\dim \rho_n^+}{h_n^+}, & \mathbf{r} \in \mathcal{D}_n^+ \\ -\frac{\dim \rho_n^-}{h_n^-}, & \mathbf{r} \in \mathcal{D}_n^- \\ 0, & \text{elsewhere} \end{cases}$$

$$\dim \rho_n^\pm = \begin{cases} 1, & \rho_n^\pm \text{ varies in 1D} \\ 2, & \rho_n^\pm \text{ varies in 2D} \\ 3, & \rho_n^\pm \text{ varies in 3D} \end{cases}$$

## Numerical Integration to Form Element Matrices

- Typical element matrix has the form
 
$$\langle \Lambda_i^e; G, \Lambda_j^f \rangle$$
- For  $e \neq f$  use the result
 
$$\int_{A^e} f(\mathbf{r}) dS = 2A^e \int_0^1 \int_0^{1-\xi_2} f(\xi_1 \mathbf{r}_1^e + \xi_2 \mathbf{r}_2^e + \xi_3 \mathbf{r}_3^e) d\xi_1 d\xi_2 \approx \mathcal{J}^e \underbrace{\sum_{k=1}^K w_k f(\xi_1^{(k)} \mathbf{r}_1^e + \xi_2^{(k)} \mathbf{r}_2^e + \xi_3^{(k)} \mathbf{r}_3^e)}_{\text{Numerical integration}}, \quad \mathcal{J}^e = 2A^e$$
- For  $e = f$  use a singularity subtraction or cancellation scheme to handle the  $1/R$  singularity

## Singularity Subtraction vs. Singularity Cancellation

Singularity subtraction:

$$\int_S f(\mathbf{r}') \frac{e^{-jkR}}{4\pi R} dS' = \underbrace{\int_S \left( \frac{f(\mathbf{r}') e^{-jkR} - \sum_{n \geq 0, m \geq 0}^{N, M} P^n(\mathbf{r}') R^m}{4\pi R} \right) dS'}_{\text{Integrate numerically}} + \sum_{n \geq 0, m \geq 0}^{N, M} \underbrace{\int_S \frac{P^n(\mathbf{r}') R^m}{4\pi R} dS'}_{\text{Integrate analytically}}$$

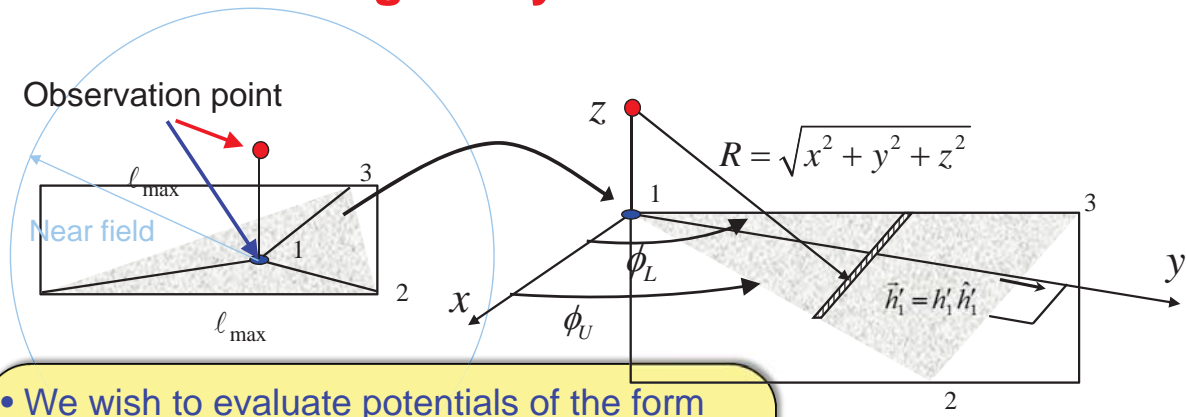
Singularity subtraction has been used very successfully, but has drawbacks:

- Accuracy of numerical integral limited by non-analytic form of difference integrand (i.e.,  $R = \sqrt{x^2 + y^2 + z^2}$  is not "smooth" or "polynomial-like" at  $(x, y, z) = (0, 0, 0)$ ).
- Method is sometimes unsuitable for nearly-singular integrands
- Occasionally a singular expression cannot be analytically integrated
- Analytical integrals are complicated, difficult, and must be performed for every separate combination of basis, element, and Green's function.  
*Hence the approach is poorly-suited to object oriented programming!*

## Singularity Subtraction Methods Appear in the Following References

- S. Järvenpää, M. Taskinen, and P. Ylä-Oijala, "Singularity Subtraction Technique for High-Order Polynomial Vector Basis Functions on Planar Triangles," *IEEE Trans. Antennas and Propagat.*, **54**, 1, pp. 42—49, Jan. 2006.
- R. D. Graglia, "On the numerical integration of the linear shape functions times the 3-D Green's function or its gradient on a plane triangle," *IEEE Trans. Antennas Propag.*, vol. 41, no. 10, pp. 1448–1455, 1993.
- Wilton, D.R., S.M. Rao, A.W. Glisson, D.H. Schaubert, O.M. Al-Bundak, and C.M. Butler, "Potential Integrals for Uniform and Linear Source Distributions on Polygonal and Polyhedral Domains," *IEEE Trans. Antennas and Propagat.*, **32**, 3, pp. 276—281, March 1984.

## Singularity Cancellation



- We wish to evaluate potentials of the form

$$\mathbf{I} = \int_{\mathcal{D}} \underbrace{\Lambda(\mathbf{r}')}_{H(\mathbf{r}')} \frac{e^{-jkR}}{4\pi R} d\mathcal{D}'$$

- Subtriangle integral has the general form

$$\int_0^h \int_{y \cot \phi_L}^{y \cot \phi_U} H(x, y) dx dy = \int_{v_L}^{v_U} \int_{u_L}^{u_U} \underbrace{H[x(u, v), y(u, v)] \mathcal{J}(u, v)}_{\mathcal{J} \text{ cancels singularity of } H} du dv$$

## A Singularity Cancellation Approach

$$\begin{aligned} \int_0^h \int_{y \cot \phi_L}^{y \cot \phi_U} H(x, y) dx dy &= \int_{v_L}^{v_U} \int_{u_L}^{u_U} H[x(u, v), y(u, v)] \mathcal{J}(u, v) du dv \\ &= \int_{u_L}^{u_U} (v_U - v_L) \int_0^1 H[x(u, v(\eta)), y(u, v(\eta))] \mathcal{J}(u, v(\eta)) d\eta du, \\ v &= v_L(1 - \eta) + v_U \eta \end{aligned}$$

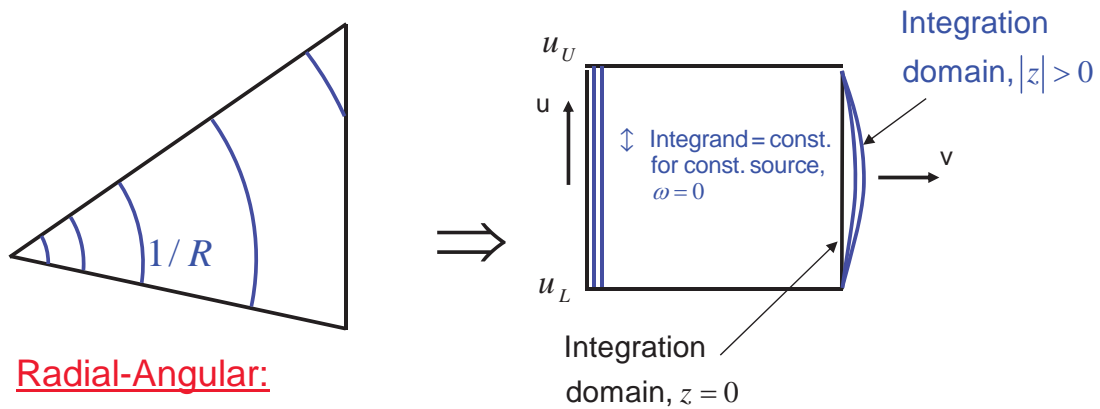
Reverse the order of integration and normalize the interval on the inner integral

$$\begin{aligned} \mathcal{J}(u, v) &\equiv \begin{vmatrix} \frac{\partial x}{\partial u} & \frac{\partial x}{\partial v} \\ \frac{\partial y}{\partial u} & \frac{\partial y}{\partial v} \end{vmatrix} \\ &= \left| \frac{d\mathbf{r}}{du} \times \frac{d\mathbf{r}}{dv} \right| \end{aligned}$$

	TRANSFORMATION	$\mathcal{J}(u, v)$	INTEGRATION LIMITS
Radial-Angular	$u = \ln \tan \frac{\phi}{2} = -\sinh^{-1} \frac{x}{y}$ $v = R$	$\frac{R}{\cosh u}$	$u_{L,U} = \ln \tan \frac{\phi_{L,U}}{2}$ $v_{L,U} =  z , \sqrt{z^2 + (h \cosh u)^2}$

- For more possible transforms, see M. M. Botha, "A family of augmented Duffy Transformations for near-singularity cancellation quadrature," *IEEE Trans. Antennas Propagat.*, 2013.

## Radial-Angular Integration



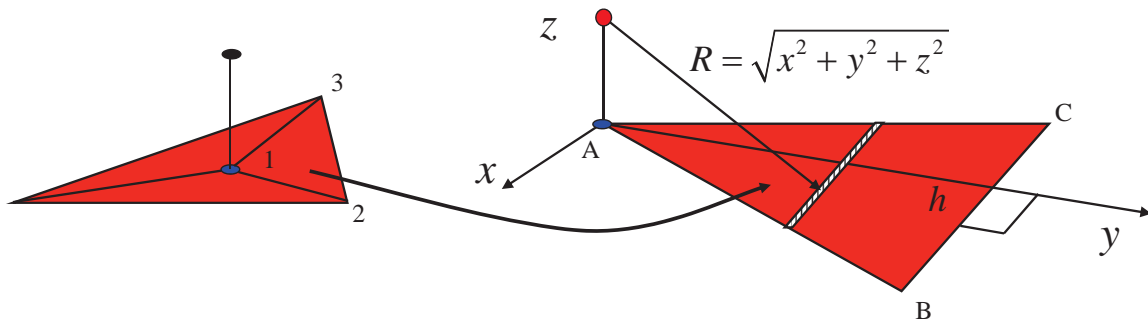
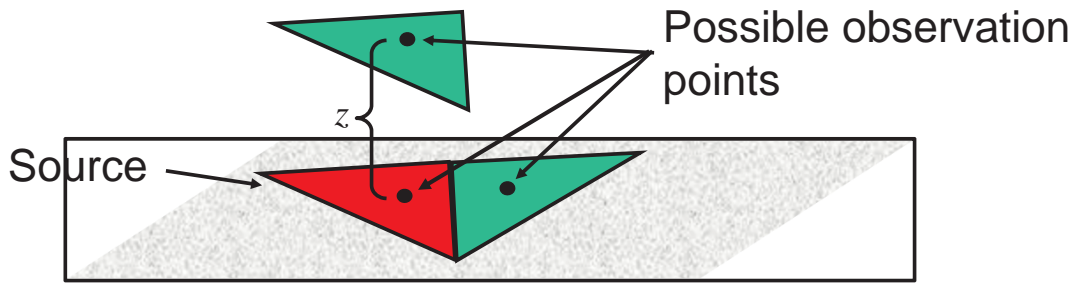
### Radial-Angular:

- Integrates *static* kernel with constant bases exactly (rectangular integration domain needs one sample pt. only; more sample pts. needed to handle variation of bases and exponential phase factor) ☺
- Integration domain insensitive to  $z$  variation of obs. pt. ☺
- Above features suggest this as the method of choice

## Several Singularity Cancellation Schemes Have Been Analyzed in Detail

- Khayat, M. A., D. R. Wilton, and P. W. Fink, "An Improved Transformation and Optimized Sampling Scheme for the Numerical Evaluation of Singular and Near-Singular Potentials," *IEEE Antennas and Wireless Propagation Letters*, Vol. 7, pp. 377 – 380, July 2008.
- M. M. Botha, "A family of augmented Duffy Transformations for near-singularity cancellation quadrature," *IEEE Trans. Antennas Propagat.*, 2013. (Of several schemes tested and compared, the radial-angular scheme was found to be the most effective for both singularities and near-singularities of the form  $1/R$ .)

## Singularity Cancellation Approach for Self and Near Terms

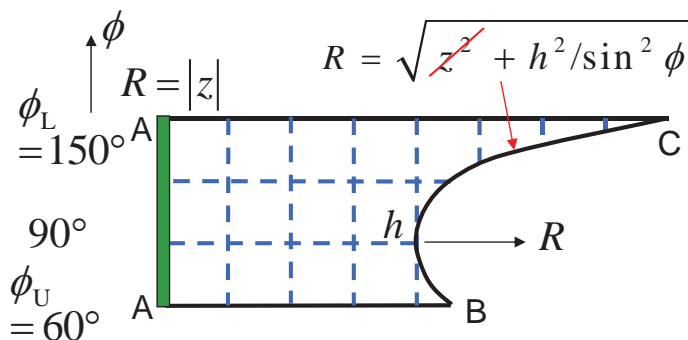
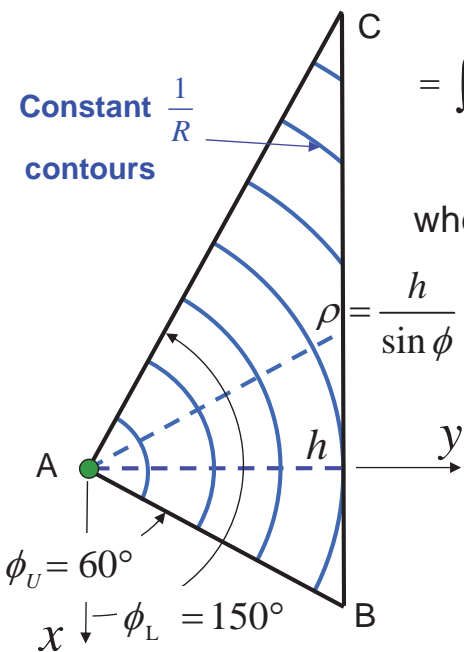


## Radial Transformation Removes Singularity, But Leaves a Non-Rectangular Domain

$$\int_0^h \int_{y \cot \phi_L}^{y \cot \phi_U} \Lambda_j^e(\mathbf{r}') G(\mathbf{r}, \mathbf{r}') dx dy = \int_{\phi_U}^{\phi_L} \int_{|z|}^{\sqrt{z^2 + h^2/\sin^2 \phi}} \Lambda_j^e(\mathbf{r}') G(\mathbf{r}, \mathbf{r}') \frac{\rho d\rho}{R dR d\phi}$$

$$= \int_{\phi_U}^{\phi_L} \left[ \frac{\sqrt{z^2 + h^2/\sin^2 \phi} - |z|}{\underset{z \rightarrow 0}{\rightarrow} h/\sin \phi} \int_0^1 \Lambda_j^e(\mathbf{r}') G(\mathbf{r}, \mathbf{r}') R d\eta \right] d\phi,$$

where  $R^2 = z^2 + \rho^2$ ,  $R = (1-\eta)|z| + \eta\sqrt{z^2 + h^2/\sin^2 \phi}$



## A Second (Angular) Transformation on $\phi$ Regularizes the Domain

$$\int_{\phi_U}^{\phi_L} \left[ \left( \sqrt{z^2 + h^2 / \sin^2 \phi} - |z| \right) \int_0^1 \Lambda_j^e(\mathbf{r}') G(\mathbf{r}, \mathbf{r}') R d\eta \right] d\phi$$

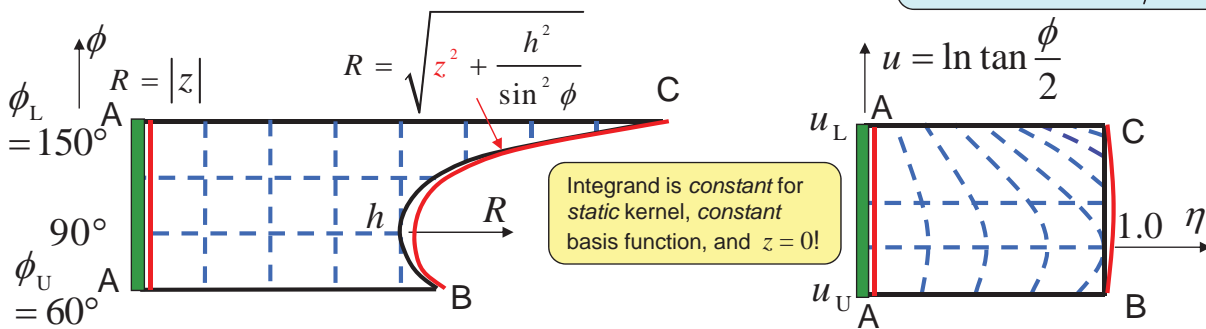
$$\approx \int_{u_U}^{u_L} \left[ \left( \frac{\sqrt{z^2 + h^2 \cosh^2 u} - |z|}{\cosh u} \right) \int_0^1 \Lambda_j^e(\mathbf{r}') G(\mathbf{r}, \mathbf{r}') R d\eta \right] du$$

$$\approx 2A^e \sum_i \sum_j w_i w_j \underbrace{\left( \frac{(u_U - u_L) (\sqrt{z^2 + h^2 \cosh^2 u^{(i)}} - |z|)}{2A^e \cosh u^{(i)}} \right)}_{\tilde{W}_k} R^{(i,j)} \Lambda_j^e(\mathbf{r}^{(i,j)}) G(\mathbf{r}, \mathbf{r}^{(i,j)})$$

Let  $du = \frac{d\phi}{\sin \phi}$

$$\Rightarrow \begin{cases} u = \ln \tan \frac{\phi}{2}, \\ (\sin \phi)^{-1} = \cosh u, \\ R = \sqrt{z^2 + h^2 \cosh^2 u} \end{cases}$$

Domain is insensitive  
to  $z$  for small  $z/h$  !



## The Radial Transformation Introduces Branch Points into the Basis Functions

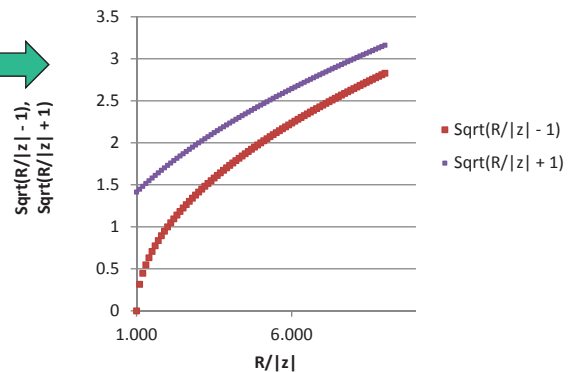
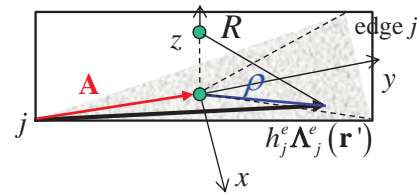
Transformation results in a "branch point" singularity in the basis functions:

$$h_j^e \Lambda_j^e(\mathbf{r}') = \mathbf{A} + \hat{\mathbf{x}} \underbrace{\rho \cos \phi}_x + \hat{\mathbf{y}} \underbrace{\rho \sin \phi}_y$$

$$= \mathbf{A} + \hat{\mathbf{x}} \sqrt{R^2 - z^2} \cos \phi + \hat{\mathbf{y}} \sqrt{R^2 - z^2} \sin \phi,$$

but  $\sqrt{R^2 - z^2} = z^2 \sqrt{R/|z| + 1} \underbrace{\sqrt{R/|z| - 1}}_{\text{non-smooth as } R \rightarrow |z|}$ .

The non-polynomial-like behavior as  $R \rightarrow |z|$  implies that Gauss-Legendre quadrature will be ineffective.



## A Special Quadrature Scheme or an Additional Transformation Handles Branch Points in the Basis Functions

- Branch point singularity in basis functions :

$$h_j^e \Lambda_j^e(\mathbf{r}') = \mathbf{A} + \hat{\mathbf{x}} \sqrt{R^2 - z^2} \cos \phi + \hat{\mathbf{y}} \sqrt{R^2 - z^2} \sin \phi,$$

$$= \mathbf{A} + \sqrt{R - |z|} \left( \hat{\mathbf{x}} \sqrt{R + |z|} \cos \phi + \hat{\mathbf{y}} \sqrt{R + |z|} \sin \phi \right)$$

- Let  $\eta = R - |z| \geq 0$ , and develop special quadrature rules for  $\eta^{\frac{n}{2}}$  (c.f., table at right)

Note  $\sqrt{R + |z|} = \sqrt{\eta + 2|z|} = 2|z| \sqrt{\eta / (2|z|) + 1}$

- Or make the substitution  $\eta^2 = R - |z|$  and use Gauss - Legendre quadrature

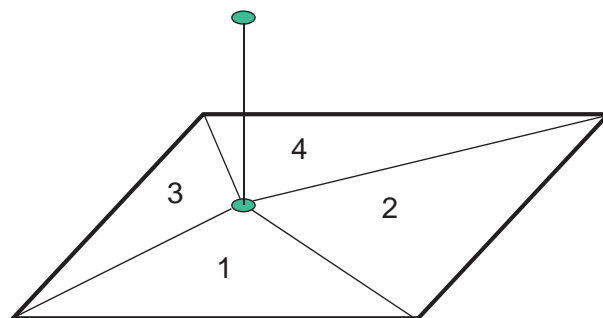
Weights and sample points for integrating the function set

$$\left\{ \eta^n, \eta^n \sqrt{\eta} \right\}, n = 0, 1, 2, \dots, N$$

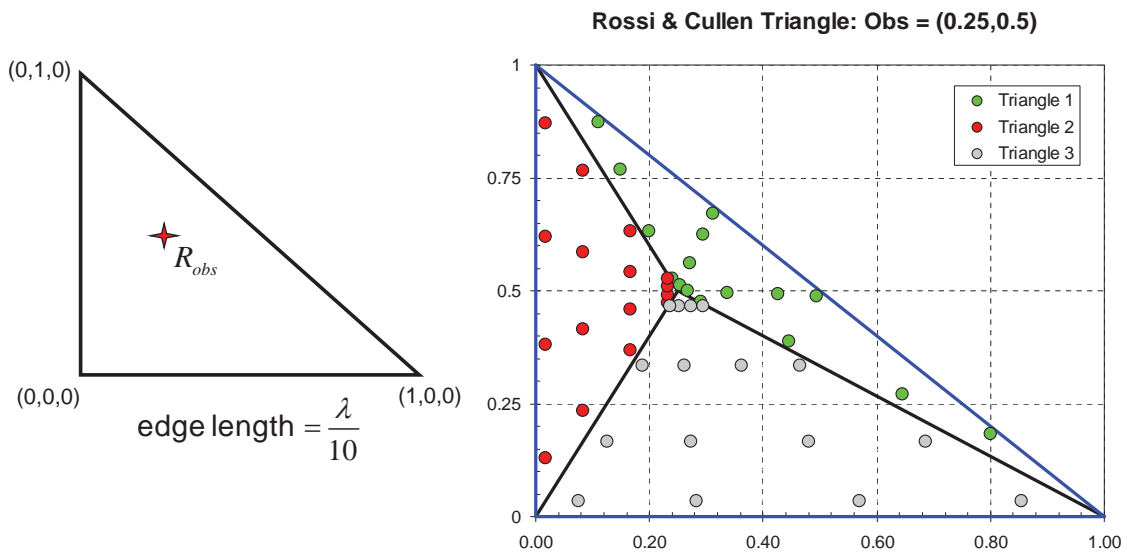
N	Nodes $\eta_i$	Weights $w_i$
2	0.12606123086601956	0.3639172365120473
	0.7139387691339825	0.6360827634879527
3	0.045088504179695364	0.13965395980291434
	0.34872938419346483	0.45848221271917206
	0.8306719075452189	0.4018638274779136
4	0.019532819681463730	0.06236194190019799
	0.17339692801497078	0.25969509521658130
	0.522956026924229700	0.40692913602039693
	0.88905249698491430	0.27101382686282377

## The Same Subtriangle Approach Can Also Be Used to Handle Singular and Near-Singular Integrals on Rectangular Domains

Only the Subtriangle-to-Rectangle Mapping Eqs. Change

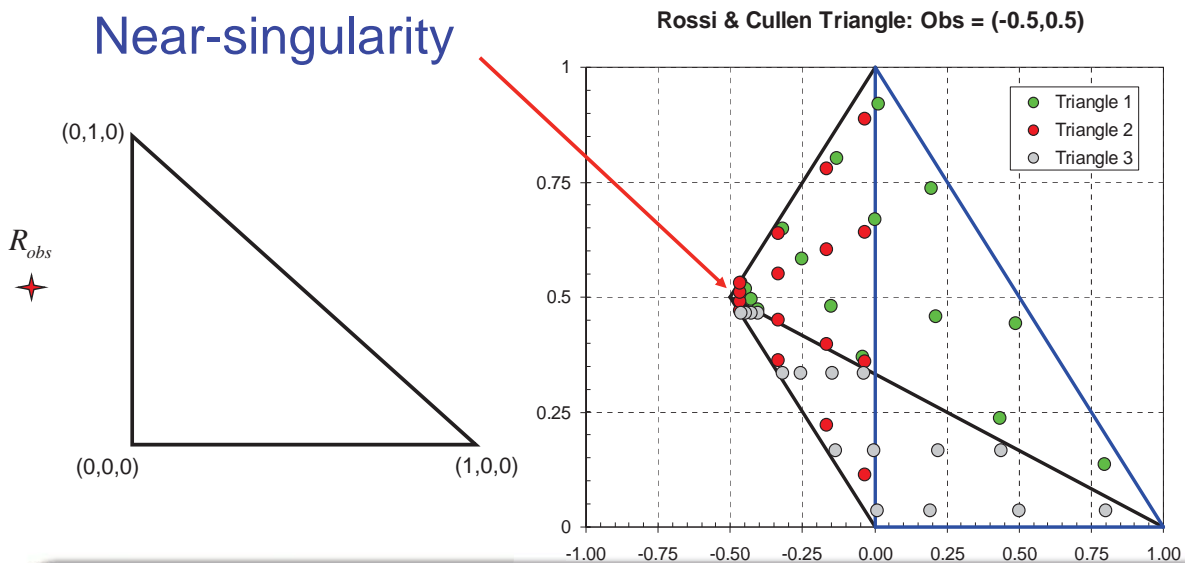


## Distribution of Sampled Points in Example Triangle



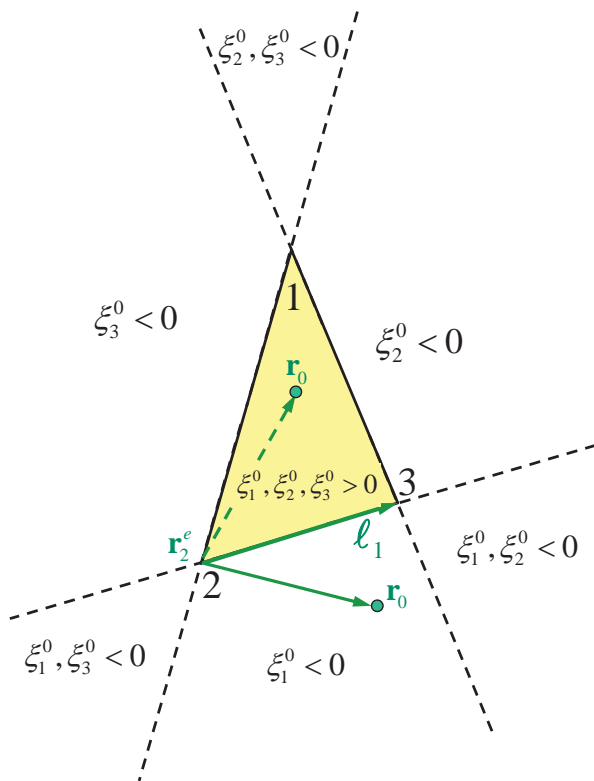
\* L. Rossi and P.J. Cullen, *IEEE Trans. AP-47*, pp. 398-402, April 1999

## Calculation for Near-Singularities with Projected Obs. Pt. Outside Triangle



- Note that the contributions from the integration domains of subtriangles 1 and 3 that lie outside the original triangle are completely canceled by the (negative) contribution of subtriangle 2
- Note also we've introduced a fictitious singularity at the obs. pt. from each of the three subtriangles, but the singularity *cancel*s when contributions are summed

## If the Projected Obs. Pt. Falls Outside a Triangle, at Least One of Its Area Coordinates is Negative



Projected Obs. Pt. :

$$\mathbf{r}_0 = \mathbf{r} - \hat{\mathbf{n}} \cdot (\mathbf{r} - \mathbf{r}_j^e), \quad j = 1, 2, \text{ or } 3$$

Area Coords. of Projected Obs. Pt. :

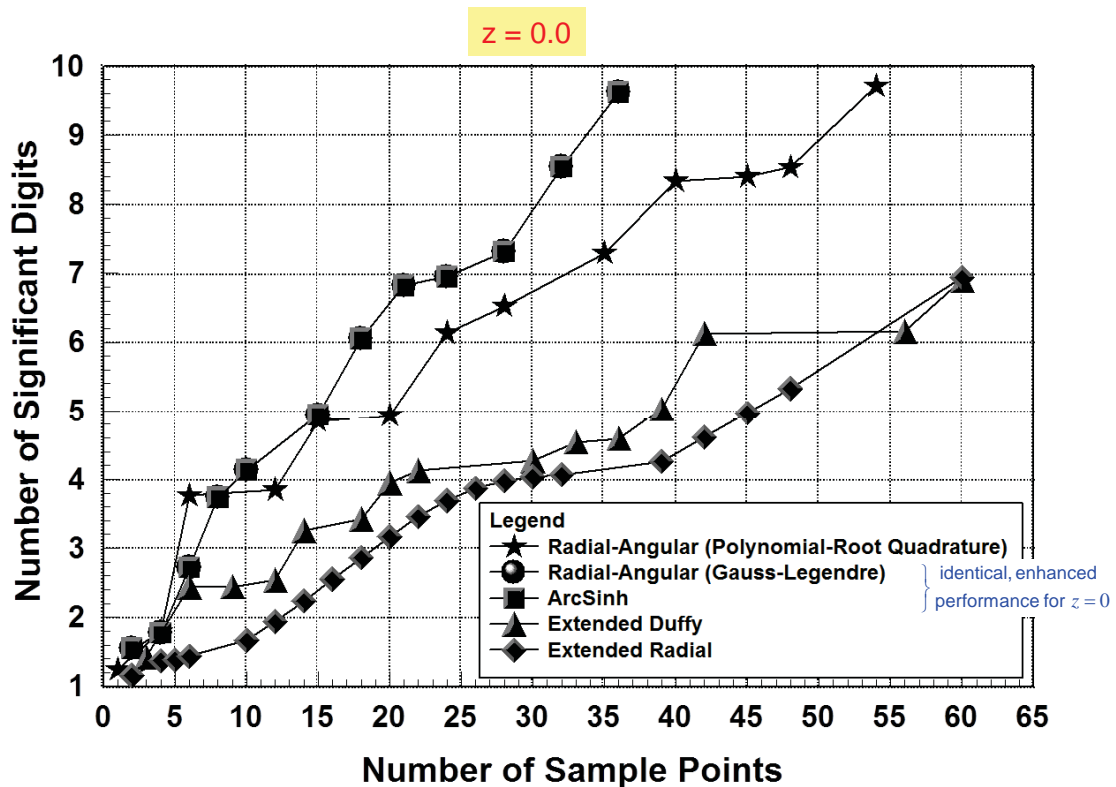
$$\xi_1^0 = \hat{\mathbf{n}} \cdot \frac{\ell_1 \times (\mathbf{r}_0 - \mathbf{r}_2^e)}{2A^e}$$

$$\xi_2^0 = \hat{\mathbf{n}} \cdot \frac{\ell_2 \times (\mathbf{r}_0 - \mathbf{r}_3^e)}{2A^e}$$

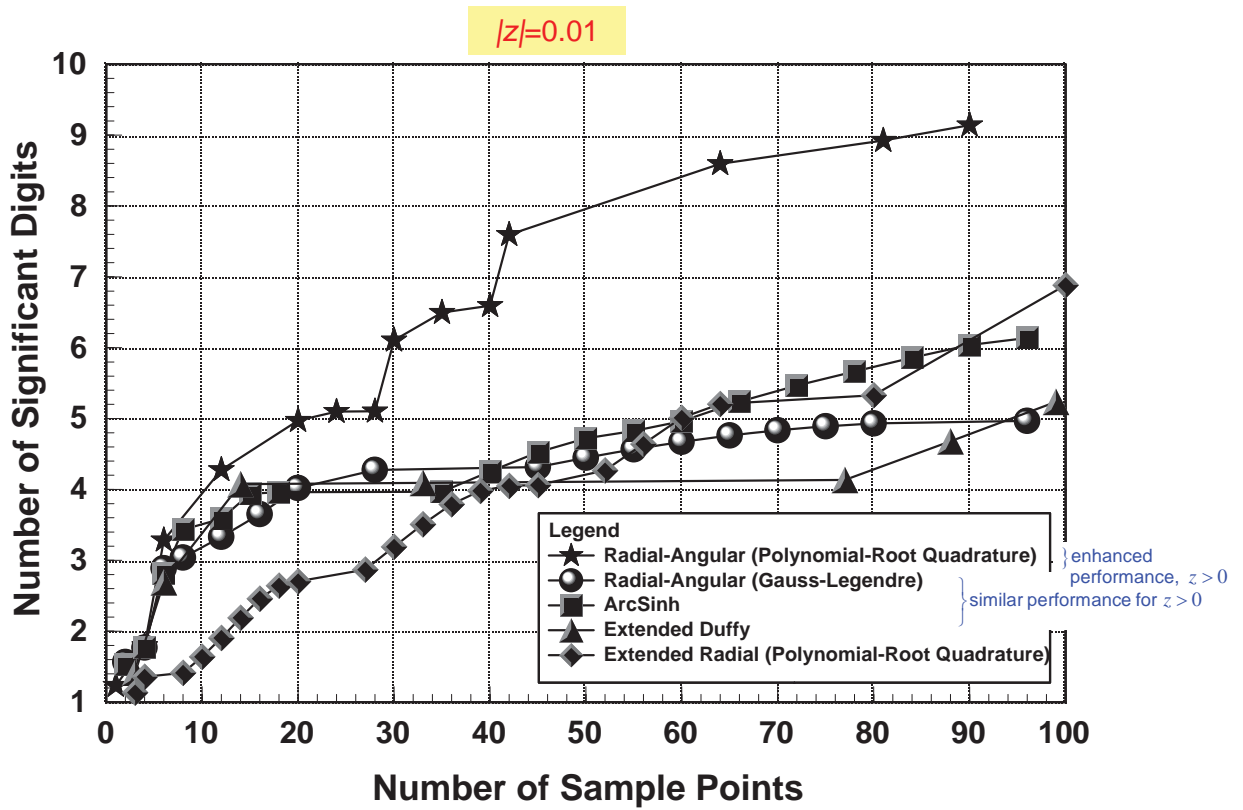
$$\xi_3^0 = 1 - \xi_1^0 - \xi_2^0$$

If area coordinate  $\xi_i^0$  is negative, then the contribution to the integral from subtriangle  $i$  must also be negative.

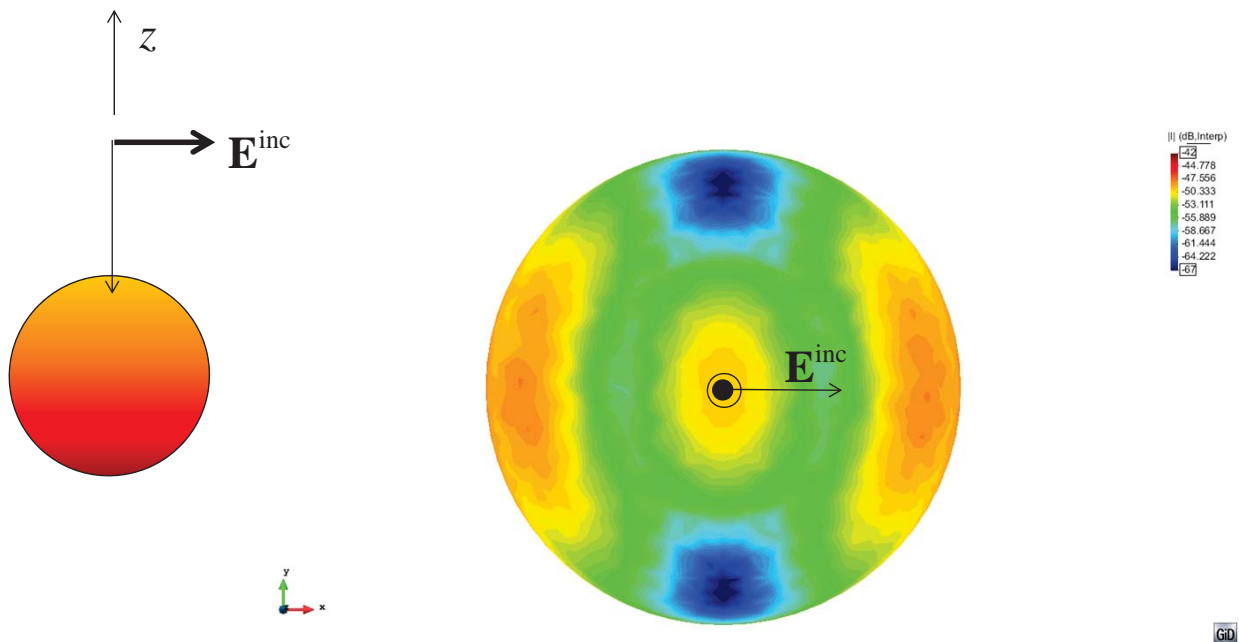
## Scheme is Efficient and Essentially Arbitrary Accuracy Can Be Obtained...



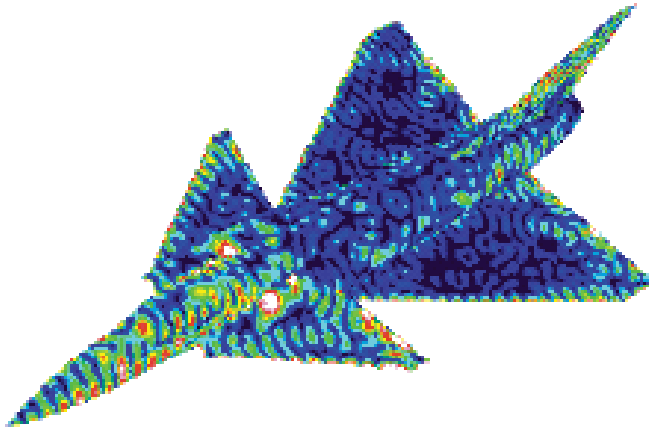
## ... Including the Nearly Singular Case



## Example: Current Induced on Sphere by a Plane Wave Incident along the Negative z-Axis



## Example: Current Induced by Plane Wave Incident on VFY-218



500 MHz  
PC computed with Mercury MOM  
~157,000 unknowns

Courtesy of John Schaeffer

## Voltage Sources

- $\mathbf{E}_{\text{tan}}^i = 0 \Rightarrow \mathbf{E}_{\text{tan}}^s = 0$  except at voltage source
- $\mathbf{J}$  must produce a potential difference between triangles at source terminals :

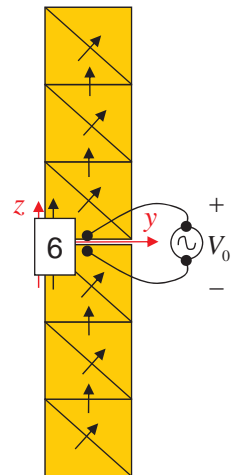
$$\Phi = V_0 \underbrace{u(z)}_{\substack{\text{unit step} \\ \text{function}}} \text{ on } \mathcal{S}$$

$$\Rightarrow \mathbf{E}_{\text{tan}}^s = -\nabla_{\text{tan}} \Phi = -\hat{\mathbf{z}} V_0 \delta(z) \text{ on } \mathcal{S}$$

$$j\omega \mathbf{A}_{\text{tan}}(\mathbf{J}) + \nabla_{\text{tan}} \Phi(\mathbf{J}) = -\mathbf{E}_{\text{tan}}^s$$

$$\Rightarrow -\langle \Lambda_m; \mathbf{E}^s \rangle = V_0 \int_{\mathcal{S}} \underbrace{\Lambda_m \cdot \hat{\mathbf{z}}}_{= \begin{cases} 1 & \text{at } z=0, m=6 \\ 0, & \text{otherwise} \end{cases}} \delta(z) dz dy$$

$$= \begin{cases} V_0 l_6, & m = 6 \\ 0, & \text{otherwise} \end{cases}$$



$$\Rightarrow \langle \Lambda_m, \mathbf{E}^i \rangle = \begin{bmatrix} 0 \\ \vdots \\ V_0 l_6 \\ \vdots \\ 0 \end{bmatrix} \leftarrow \text{row 6}$$

## Impedance Loading

- Load is equivalent to a voltage

source  $V_0 = -Z_L I_6$

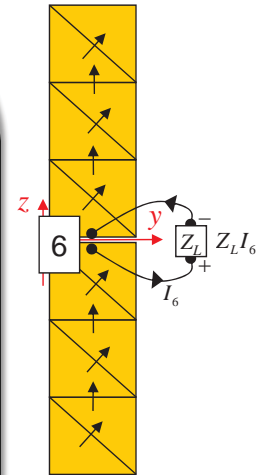
- Replace voltage vector by

$$\langle \Lambda_m, \mathbf{E}^i \rangle = \begin{bmatrix} 0 \\ \vdots \\ -Z_L I_6 \ell_6 \\ \vdots \\ 0 \end{bmatrix} = -I_6 [Z_L \ell_6 \delta_{m,6}]$$

- $\Rightarrow [Z_{mn}][I_n] = I_6 [Z_L \ell_6 \delta_{m,6}] + \text{voltage / and or } \mathbf{E}^i \text{ terms}$

- Transfer load terms to other side of matrix :

$$\left[ \begin{array}{c} Z_{mn} + \underbrace{Z_L \ell_6 \delta_{m,6}}_{\text{add load to matrix diagonal}} \end{array} \right] [I_n] = \text{usual voltage / and or } \mathbf{E}^i \text{ terms}$$

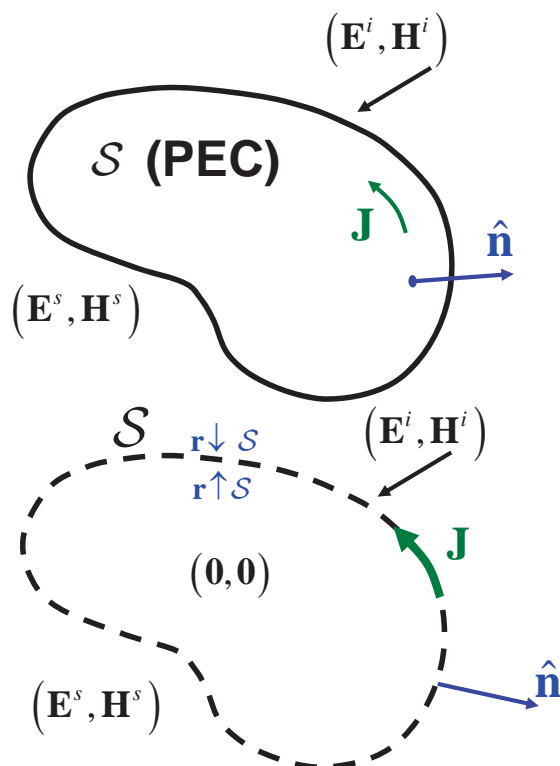


# End of Note 2

# The 3-D Magnetic Field Integral Equation (MFIE)

Donald R. Wilton

## 3D MFIE Formulation



$$\text{EFIE: } -\mathbf{E}_{\text{tan}}^s = \mathbf{E}_{\text{tan}}^i, \quad \mathbf{r} \in S$$

**MFIE (two approaches):**

$$1) \mathbf{J} = \hat{\mathbf{n}} \times \mathbf{H}^i + \lim_{\mathbf{r} \downarrow S} \hat{\mathbf{n}} \times \mathbf{H}^s, \\ \text{(eq. source condition)}$$

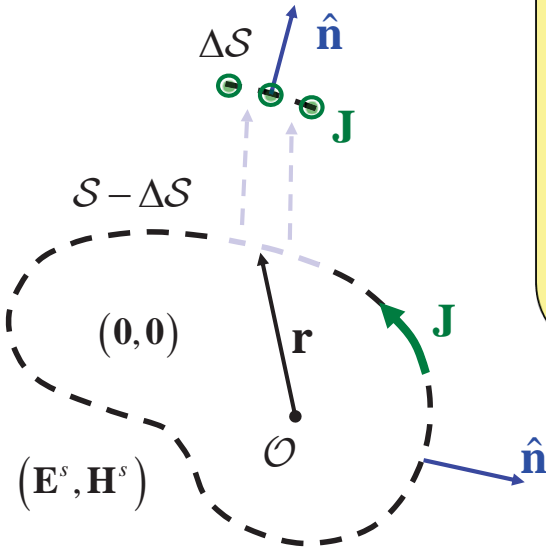
$$2) \hat{\mathbf{n}} \times \mathbf{H}^i + \lim_{\mathbf{r} \uparrow S} \hat{\mathbf{n}} \times \mathbf{H}^s = \mathbf{0}, \\ \text{(null field condition)}$$

Since  $\mathbf{J} = \lim_{\mathbf{r} \downarrow S} \hat{\mathbf{n}} \times \mathbf{H}^s - \lim_{\mathbf{r} \uparrow S} \hat{\mathbf{n}} \times \mathbf{H}^s$   
the approaches are equivalent!

$\dagger \mathbf{r} \downarrow S \Rightarrow \mathbf{r}$  approaches  $S$  from the exterior,  
 $\mathbf{r} \uparrow S \Rightarrow \mathbf{r}$  approaches  $S$  from the interior

## Null Field MFIE Formulation, Limiting Process

$\Delta S$  is a very small, flat circular disk of radius  $a$  removed from  $S$



$$\text{MFIE: } \hat{\mathbf{n}} \times \mathbf{H}^i + \lim_{r \uparrow S} \hat{\mathbf{n}} \times \mathbf{H}^s = \mathbf{0},$$

where

$$\begin{aligned} \lim_{r \uparrow S} \hat{\mathbf{n}} \times \mathbf{H}^s &= \lim_{r \uparrow S} \hat{\mathbf{n}} \times \frac{1}{\mu} \nabla \times \mathbf{A} \\ &= \lim_{r \uparrow S} \hat{\mathbf{n}} \times \nabla \times \int_S \mathcal{G}^A(\mathbf{r}, \mathbf{r}') \cdot \mathbf{J}(\mathbf{r}') dS' \\ &= \lim_{r \uparrow S} \hat{\mathbf{n}} \times \int_S \nabla \times \mathcal{G}^A(\mathbf{r}, \mathbf{r}') \cdot \mathbf{J}(\mathbf{r}') dS' \\ &= \lim_{r \uparrow S} \hat{\mathbf{n}} \times \left( \int_{\Delta S} + \int_{S - \Delta S} \right) \nabla \times \mathcal{G}^A(\mathbf{r}, \mathbf{r}') \cdot \mathbf{J}(\mathbf{r}') dS' \end{aligned}$$

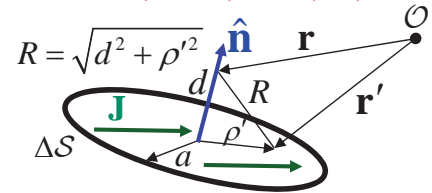
Recall that in homogeneous media,

$$\mathcal{G}^A(\mathbf{r}, \mathbf{r}') = G(\mathbf{r}, \mathbf{r}') \mathcal{I} = \frac{e^{-jkR}}{4\pi R} \mathcal{I} \leftarrow \text{identity dyad}$$

$$\Rightarrow \hat{\mathbf{n}} \times \nabla \times \mathcal{G}^A(\mathbf{r}, \mathbf{r}') \cdot \mathbf{J}(\mathbf{r}') \quad (\text{layered media})$$

$$\begin{array}{l} \text{homogeneous} \\ \text{media} \\ \rightarrow \hat{\mathbf{n}} \times \mathbf{J}(\mathbf{r}') \times \nabla G(\mathbf{r}, \mathbf{r}') \end{array}$$

## Evaluation of $\hat{\mathbf{n}} \times \mathbf{H}_{\Delta}^- \equiv \lim_{r \uparrow S} \hat{\mathbf{n}} \times \int_{\Delta S} \nabla \times \mathcal{G}^A(\mathbf{r}, \mathbf{r}') \cdot \mathbf{J}(\mathbf{r}') dS'$



Dominant integrand behavior for small  $R$ :

$$\hat{\mathbf{n}} \times \nabla \times \mathcal{G}^A(\mathbf{r}, \mathbf{r}') \cdot \mathbf{J}(\mathbf{r}')$$

$$= \hat{\mathbf{n}} \times \nabla \times \left[ G(\mathbf{r}, \mathbf{r}') \mathcal{I} \cdot \mathbf{J}(\mathbf{r}') \right] = \hat{\mathbf{n}} \times \left[ \nabla G \times \mathbf{J}(\mathbf{r}') \right] = -\hat{\mathbf{n}} \times \left[ (1 + jkR) \frac{e^{-jkR}(\mathbf{r} - \mathbf{r}')}{4\pi R^3} \times \mathbf{J}(\mathbf{r}') \right]$$

$$\xrightarrow{kR \rightarrow 0} -\hat{\mathbf{n}} \times \left[ \underbrace{(\mathbf{r} - \mathbf{r}') \times \mathbf{J}(\mathbf{r}')}_{(\mathbf{r} - \mathbf{r}') \hat{\mathbf{n}} \cdot \mathbf{J} - \mathbf{J}(\mathbf{r}') \cdot \hat{\mathbf{n}}} \right] \frac{1}{4\pi R^3} = \mathbf{J}(\mathbf{r}') \frac{\hat{\mathbf{n}} \cdot (\mathbf{r} - \mathbf{r}')}{4\pi R^3} = \mathbf{J}(\mathbf{r}') \frac{d}{4\pi R^3}, \quad R^2 = d^2 + \rho^2$$

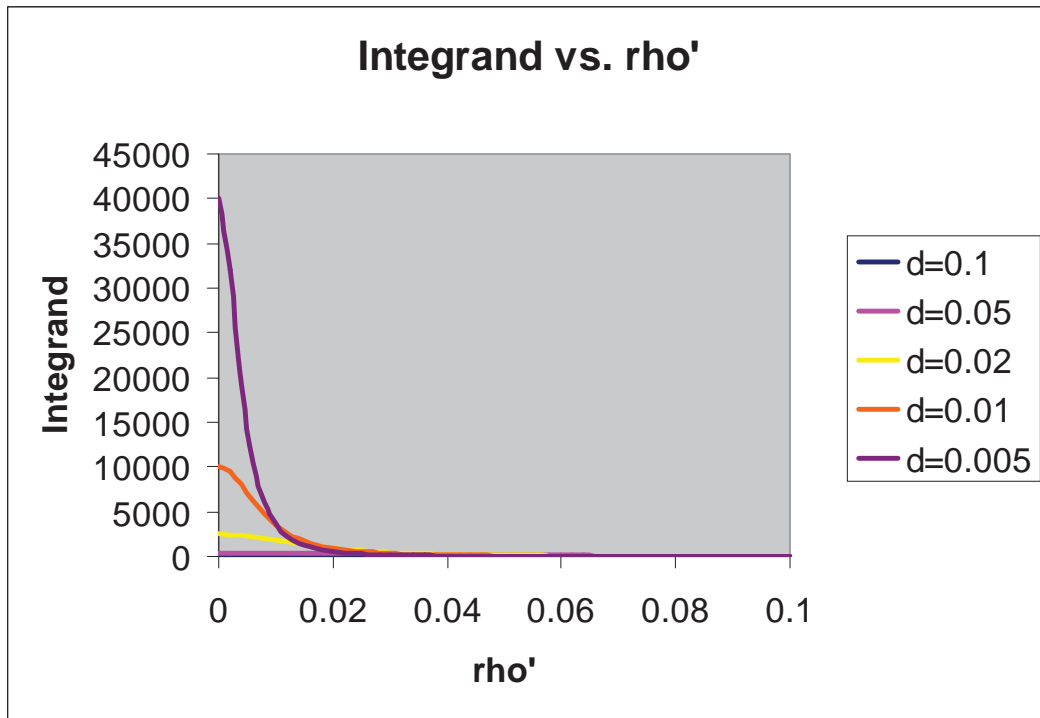
Asymptotic evaluation of integral:

$$\hat{\mathbf{n}} \times \int_{\Delta S} \nabla \times \mathcal{G}^A(\mathbf{r}, \mathbf{r}') \cdot \mathbf{J}(\mathbf{r}') dS' \xrightarrow{kR \rightarrow 0} \mathbf{J}(\mathbf{r}) \int_0^{2\pi} \int_{|d|}^{\sqrt{d^2+a^2}} \frac{d}{4\pi R^3} R dR d\phi' \quad \left( \begin{array}{l} \text{since } \rho' d\rho' = R dR, \\ \text{and } \mathbf{J}(\mathbf{r}') \approx \mathbf{J}(\mathbf{r}) \end{array} \right)$$

$$= \frac{\mathbf{J}(\mathbf{r})}{2} \left[ \frac{-d}{R} \right]_{R=|d|}^{\sqrt{d^2+a^2}} = \frac{\mathbf{J}(\mathbf{r})}{2} \left[ \frac{d}{|d|} - \frac{d}{\sqrt{d^2+a^2}} \right] \xrightarrow{d \rightarrow 0} \frac{\mathbf{J}(\mathbf{r})}{2} \text{sgn}(d)$$

$$\Rightarrow \hat{\mathbf{n}} \times \mathbf{H}_{\Delta}^- \equiv \lim_{r \uparrow S} \hat{\mathbf{n}} \times \int_{\Delta S} \nabla \times \mathcal{G}^A(\mathbf{r}, \mathbf{r}') \cdot \mathbf{J}(\mathbf{r}') dS' = \lim_{d \rightarrow 0} \frac{\mathbf{J}(\mathbf{r})}{2} \text{sgn}(d) = -\frac{\mathbf{J}(\mathbf{r})}{2}$$

## Integrand Approaches a Delta Function in the Limit $d \rightarrow 0$



### Simple Interpretation

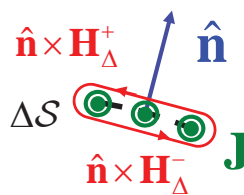
**Current jump condition:**

$$\mathbf{J} = \hat{\mathbf{n}} \times (\mathbf{H}_{\Delta}^+ - \mathbf{H}_{\Delta}^-)$$

By symmetry,

$$\hat{\mathbf{n}} \times \mathbf{H}_{\Delta}^- = -\hat{\mathbf{n}} \times \mathbf{H}_{\Delta}^+$$

$$\Rightarrow \hat{\mathbf{n}} \times \mathbf{H}_{\Delta}^+ = \frac{\pm \mathbf{J}}{2}$$



After removing the singular contribution, the integral is no longer (strongly-)singular and is sometimes written

$$PV \int_S dS' \quad \text{or} \quad \oint_S dS'$$

Hence  $\lim_{r \uparrow S} \hat{\mathbf{n}} \times \mathbf{H}_{\Delta}^- = -\frac{\mathbf{J}(\mathbf{r})}{2}$  and MFIE is

$$\frac{\mathbf{J}(\mathbf{r})}{2} - \hat{\mathbf{n}} \times \int_S \nabla \times \mathcal{G}^A(\mathbf{r}, \mathbf{r}') \cdot \mathbf{J}(\mathbf{r}') dS' = \hat{\mathbf{n}} \times \mathbf{H}^i, \quad \mathbf{r} \in S$$

Recall that in homogeneous media, this reduces to

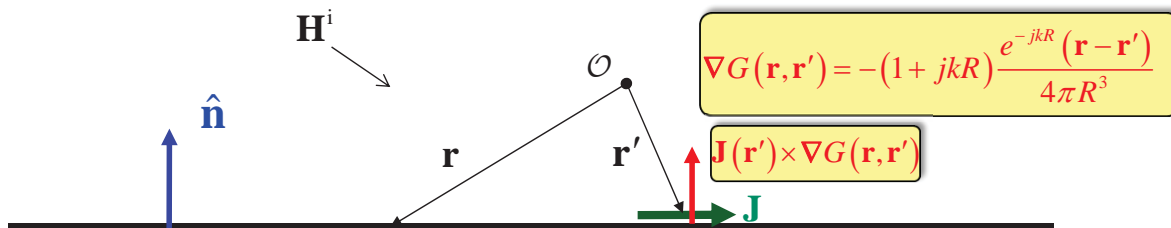
$$\frac{\mathbf{J}(\mathbf{r})}{2} + \hat{\mathbf{n}} \times \int_S \mathbf{J}(\mathbf{r}') \times \nabla G(\mathbf{r}, \mathbf{r}') dS' = \hat{\mathbf{n}} \times \mathbf{H}^i, \quad \mathbf{r} \in S$$

$$\hat{\mathbf{n}} \times \nabla \times \mathcal{G}^A(\mathbf{r}, \mathbf{r}') \cdot \mathbf{J}(\mathbf{r}') \quad \text{(layered media)}$$

homogeneous media

$$\rightarrow \hat{\mathbf{n}} \times \mathbf{J}(\mathbf{r}') \times \nabla G(\mathbf{r}, \mathbf{r}')$$

## Specialization to Infinite Plane



If  $\mathcal{S}$  is an infinite plane, then  $\mathbf{J}$  and  $\nabla G$  are in the plane, and  $\mathbf{J}(\mathbf{r}') \times \nabla G(\mathbf{r}, \mathbf{r}')$  is parallel to  $\hat{\mathbf{n}}$ ; hence

- $\hat{\mathbf{n}} \times \int_{\mathcal{S}} \mathbf{J}(\mathbf{r}') \times \nabla G(\mathbf{r}, \mathbf{r}') d\mathcal{S}' = \mathbf{0}, \mathbf{r}' \neq \mathbf{r} \in \mathcal{S}$ , and

- $\mathbf{J}(\mathbf{r}) = 2\hat{\mathbf{n}} \times \mathbf{H}^i$ , (Physical optics (PO) current)

## Choose Surface Divergence-Conforming Bases for Expanding the Current and Testing the MFIE

$$\frac{\mathbf{J}(\mathbf{r})}{2} - \hat{\mathbf{n}} \times \int_{\mathcal{S}} \nabla \times \mathcal{G}^A(\mathbf{r}, \mathbf{r}') \cdot \mathbf{J}(\mathbf{r}') d\mathcal{S}' = \hat{\mathbf{n}} \times \mathbf{H}^i$$

$$\Rightarrow [\beta_{mn}][I_n] = [I_m^i], \text{ where}$$

$$\beta_{mn} = \frac{1}{2} \langle \Lambda_m; \Lambda_n \rangle - \langle \Lambda_m; \hat{\mathbf{n}} \times \nabla \times \mathcal{G}^A(\mathbf{r}, \mathbf{r}'); \Lambda_n \rangle$$

$$I_m^i = \langle \Lambda_m; \hat{\mathbf{n}} \times \mathbf{H}^i \rangle$$

with corresponding element matrix and element vector

$$\beta_{ij}^{ef} = \begin{cases} \frac{1}{2} \langle \Lambda_i^e; \Lambda_j^f \rangle, & e = f \quad \left( \begin{array}{l} \text{no integral contribution} \\ \text{from flat subdomains!} \end{array} \right) \\ -\langle \Lambda_i^e; \hat{\mathbf{n}} \times \nabla \times \mathcal{G}^A(\mathbf{r}, \mathbf{r}'); \Lambda_j^f \rangle, & e \neq f \end{cases}$$

$$I_i^{ie} = \langle \Lambda_i^e; \hat{\mathbf{n}} \times \mathbf{H}^i \rangle$$

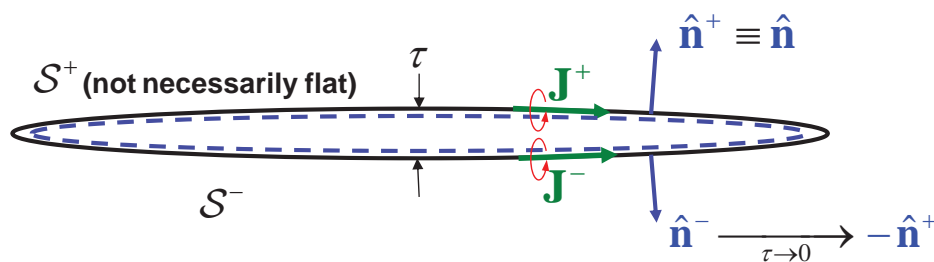
$$\mathbf{J}(\mathbf{r}) \approx \sum_{n=1}^N I_n \Lambda_n(\mathbf{r})$$

Note other basis choices are possible, even desirable!

## Features of the MFIE

- Applies *only* to closed bodies
- The contribution from the integral term *vanishes on flat surfaces*,  $r$  in the surface plane
- MFIE is usually better conditioned than the EFIE (since  $J$  appears outside the integral, it is a *2<sup>nd</sup> kind integral equation*)
- It appears possible to use *either* div- or curl-conforming bases
- MFIE is sometimes slow to converge compared to EFIE
- The MFIE *operator* is important since it appears in both combined field integral equations (CFIE) and in dielectric formulations (PMCHWT)

## Why Does the MFIE Apply to Closed Bodies Only?

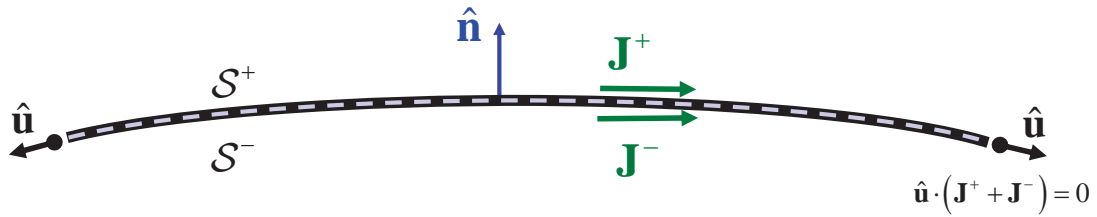


In the limit as  $\tau \rightarrow 0$ , null field surfaces (dashed lines) degenerate to a single surface  $S^- \rightarrow S^+$  with one magnetic field; effect of surface currents  $J^\pm$  at  $r'$  may be *added* in the surface integral for  $r' \neq r$ , however  $r$  is *below*  $J^+(r)$  (as before), but *above*  $J^-(r)$  so there's a sign difference in the singular contributions :

$$\frac{J^+(r)}{2} - \frac{J^-(r)}{2} - \hat{n} \times \int_{S^+} \nabla \times \mathcal{G}^A(r, r') \cdot [J^+(r') + J^-(r')] dS' = \hat{n} \times \mathbf{H}^i, \quad r \in S^+$$

This identity cannot be solved alone for *two* unknowns,  $J^+(r)$ ,  $J^-(r)$ .

## Identity Can be Combined with EFIE to Obtain Opposite Side Currents Independently



**EFIE:**

$$j\omega\mu \int_{S^+} \mathcal{G}^A(\mathbf{r}, \mathbf{r}') \cdot \overbrace{\mathbf{J}^+(\mathbf{r}') + \mathbf{J}^-(\mathbf{r}')}^{\hat{=} \mathbf{J}(\mathbf{r}')} dS' - \frac{\nabla}{j\omega\epsilon} \int_{S^+} K^\Phi(\mathbf{r}, \mathbf{r}') \nabla' \cdot \overbrace{\mathbf{J}^+(\mathbf{r}') + \mathbf{J}^-(\mathbf{r}')}^{\hat{=} \mathbf{J}(\mathbf{r}')} dS' = \mathbf{E}_{\text{tan}}^i$$

**Magnetic field identity:**

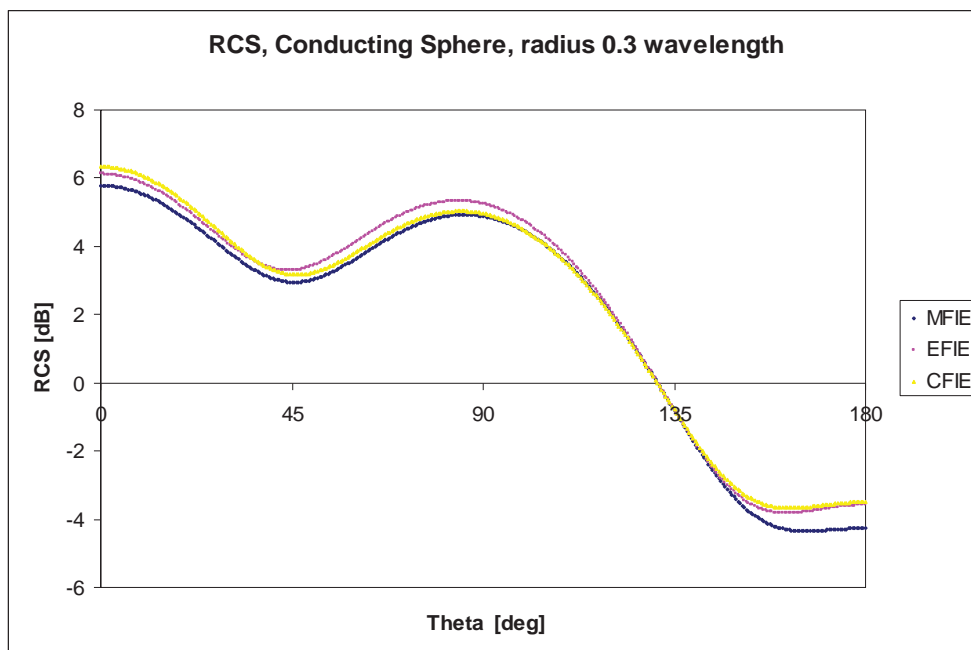
$$\frac{\mathbf{J}^+(\mathbf{r})}{2} - \frac{\mathbf{J}^-(\mathbf{r})}{2} - \hat{\mathbf{n}} \times \int_{S^+} \nabla \times \mathcal{G}^A(\mathbf{r}, \mathbf{r}') \cdot [\mathbf{J}^+(\mathbf{r}') + \mathbf{J}^-(\mathbf{r}')] dS' = \hat{\mathbf{n}} \times \mathbf{H}^i, \quad \mathbf{r} \in S^+$$

- Solve EFIE for  $\mathbf{J} = \mathbf{J}^+ + \mathbf{J}^-$ , use result in identity to obtain  $\mathbf{J}^\pm$ :

$$\mathbf{J}^\pm(\mathbf{r}) = \frac{\mathbf{J}(\mathbf{r})}{2} \pm \hat{\mathbf{n}} \times \mathbf{H}^i \pm \hat{\mathbf{n}} \times \int_{S^+} \nabla \times \mathcal{G}^A(\mathbf{r}, \mathbf{r}') \cdot \mathbf{J}(\mathbf{r}') dS', \quad \mathbf{r} \in S^\pm$$

- Or a) solve eqs. simultaneously or b) add and subtract them to get two equations in two unknowns,  $\mathbf{J}^+(\mathbf{r}')$ ,  $\mathbf{J}^-(\mathbf{r}')$ .

## Scattering by Conducting Sphere Modeled Using 552 Triangles, 828 Unknowns



**End of Note 3**

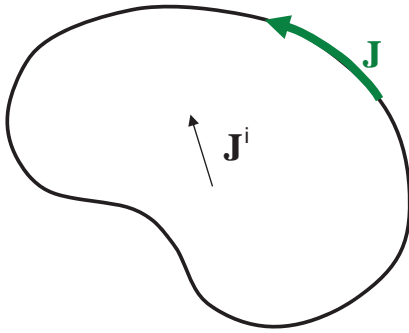
# Combined Field Integral Equation (CFIE)

Donald R. Wilton

## Interior Resonances

- For closed bodies, the EFIE cannot distinguish whether the excitation sources  $J^i$  or  $E^i$  are interior or exterior to the PEC
- At cavity resonant frequencies, *source-free* solutions of the EFIE exist (if an interior source of the same frequency, exists, the resulting fields will generally be infinite).
- The surface currents corresponding to source-free solutions of the EFIE are simply the cavity wall surface currents of the associated resonant cavity mode.

## Interior Resonance Properties of EFIE



@  $\omega = \omega_p, p = 1, 2, \dots$

- At interior resonance freqs., there exist homogeneous solutions  $\mathbf{J}_h$  to the EFIE :

$$\left[ \begin{array}{l} j\omega\mu \int_S G(\mathbf{r}, \mathbf{r}') \mathbf{J}_h(\mathbf{r}') dS' \\ - \frac{\nabla}{j\omega\epsilon} \int_S G(\mathbf{r}, \mathbf{r}') \nabla' \cdot \mathbf{J}_h(\mathbf{r}') dS' \end{array} \right]_{\tan} = \mathbf{0},$$

- In matrix form, this means

$$[Z_{mn}][I_n] = 0 \quad \Rightarrow \quad \det[Z_{mn}] = 0$$

- Unless the Green's function is replaced by a non-radiating form,

e.g.,  $\frac{e^{-jkR}}{4\pi R} \rightarrow \frac{\cos kR}{4\pi R}$ , the determinant doesn't *completely* vanish at real resonant frequencies because discretization errors "leak" radiation.

- The problem becomes ill-conditioned, however, and solutions can be contaminated by homogeneous solutions from nearby complex frequencies.

## The MFIE at Interior Resonances

- Though the physical explanation differs from the EFIE, the MFIE also has homogeneous solutions at interior resonant frequencies

- The MFIE homogeneous form is

$$\frac{\mathbf{J}_h(\mathbf{r})}{2} - \hat{\mathbf{n}} \times \int_S \nabla \times \mathcal{G}^A(\mathbf{r}, \mathbf{r}') \cdot \mathbf{J}_h(\mathbf{r}') dS' = \mathbf{0}$$

- The matrix MFIE homogeneous form is

$$[\beta_{mn}][I_n] = 0 \quad \Rightarrow \quad \det[\beta_{mn}] = 0$$

## Linear Operator Problems and Uniqueness

- $\mathcal{L}$  is a **linear operator** if

$$\mathcal{L}(au_1 + bu_2) = a\mathcal{L}u_1 + b\mathcal{L}u_2$$

for any functions  $u_1, u_2$ , any constants  $a, b$ . (Both the EFIE and MFIE are linear operator eqs. with  $u \equiv J$ .)

- The operator  $\mathcal{L}$  has a non-trivial **homogeneous solution** if there exists a function  $u_h \neq 0$  such that  $\mathcal{L}u_h = 0$  ( $u_h$  is not unique since  $Cu_h$  is also a homogeneous solution:  $\mathcal{L}(Cu_h) = C\mathcal{L}u_h = 0$ )
- If  $\mathcal{L}$  has a non-trivial homogeneous solution, the operator equation  $\mathcal{L}u = f$  has no unique solution, since for every  $u$  a solution,  $u + Cu_h, C \neq 0$ , is also a solution:

$$\mathcal{L}(u + Cu_h) = \mathcal{L}u + C\cancel{\mathcal{L}u_h} = \mathcal{L}u = f$$

- Different solutions  $\mathcal{L}u_1 = f, \mathcal{L}u_2 = f, u_1 \neq u_2$ , may differ only by a homogeneous solution:

$$f - f \equiv 0 = \mathcal{L}u_1 - \mathcal{L}u_2 = \mathcal{L}(u_1 - u_2) \Rightarrow u_1 - u_2 = u_h$$

Uniqueness is proved by assuming  $u_1 - u_2 \equiv u_h \neq 0$  and proving a contradiction!

## Linear Operator Problems and Uniqueness

- $\mathcal{L}u = f$  has a unique solution if and only if the only solution to the homogeneous equation  $\mathcal{L}u_h = 0$  is the trivial solution,  $u_h = 0$

Uniqueness is proved by assuming  $u_1 - u_2 \equiv u_h \neq 0$  and proving a contradiction!

## The Combined Field Integral Equation (CFIE)

- Remarkably, linearly combining the EFIE and MFIE eliminates difficulties with interior resonances!
- Write the EFIE in the abbreviated form

$$-\mathbf{E}_{\text{tan}}(\mathbf{J}) = \mathbf{E}_{\text{tan}}^i \quad \xrightarrow{\text{discretize}} \quad [Z_{mn}][I_n] = [V_m]$$

and the MFIE as

$$-\hat{\mathbf{n}} \times \mathbf{H}(\mathbf{J}) = \hat{\mathbf{n}} \times \mathbf{H}^i, \quad \xrightarrow{\text{discretize}} \quad [\beta_{mn}][I_n] = [I_m^i]$$

with  $\mathbf{r} \uparrow \mathcal{S}$  understood, and combine them as

$$-\frac{\mathbf{E}_{\text{tan}}(\mathbf{J})}{\eta} - \alpha \hat{\mathbf{n}} \times \mathbf{H}(\mathbf{J}) = \frac{\mathbf{E}_{\text{tan}}^i}{\eta} + \alpha \hat{\mathbf{n}} \times \mathbf{H}^i$$

- In discrete form, this is

$$\left[ \frac{Z_{mn}}{\eta} + \alpha \beta_{mn} \right] [I_n] = \left[ \frac{V_m}{\eta} + \alpha I_m^i \right] \quad \text{(CFIE)}$$

## Uniqueness of the CFIE

- To prove CFIE uniqueness, assume  $\exists \mathbf{J}_h \neq \mathbf{0}$  satisfying

$$-\frac{\mathbf{E}_{\text{tan}}(\mathbf{J}_h)}{\eta} - \alpha \hat{\mathbf{n}} \times \mathbf{H}(\mathbf{J}_h) = \mathbf{0}, \quad \mathbf{r} \in \mathcal{S}$$

- Multiply eq. by its conjugate and integrate over  $\mathcal{S}$ :

$$\int_{\mathcal{S}} \left[ \left| \frac{\mathbf{E}_{\text{tan}}(\mathbf{J}_h)}{\eta} \right|^2 + |\alpha|^2 |\mathbf{H}_{\text{tan}}(\mathbf{J}_h)|^2 \right] d\mathcal{S}$$

Power radiated into  $\mathcal{S}$ ,  $\geq 0$

$$+ \frac{2\alpha}{\eta} \text{Re} \int_{\mathcal{S}} [\mathbf{E}(\mathbf{J}_h) \times \mathbf{H}^*(\mathbf{J}_h) \cdot (-\hat{\mathbf{n}})] d\mathcal{S} = 0$$

where  $\frac{\alpha}{\eta}$  is chosen positive and real.

Uniqueness theorem:

- If 1) no sources exterior to  $\mathcal{S}^+$ ,  
2)  $\mathbf{E}_{\text{tan}} = \mathbf{0}$  or  $\mathbf{H}_{\text{tan}} = \mathbf{0}$  on  $\mathcal{S}^+$ ,

$\Rightarrow \mathbf{E} = \mathbf{H} = \mathbf{0}$  exterior to  $\mathcal{S}^+$

- $\Rightarrow \mathbf{H}_{\text{tan}} = \mathbf{0}$  on  $\mathcal{S}^-$ ,  $\mathbf{E}_{\text{tan}} = \mathbf{0}$  on  $\mathcal{S}^{\pm}$ ,  $\xrightarrow{\text{unique thm.}} \mathbf{H}_{\text{tan}} = \mathbf{0}$  on  $\mathcal{S}^+$

$$\Rightarrow \mathbf{J}_h = \hat{\mathbf{n}} \times \mathbf{H}|_{\mathcal{S}^+} - \hat{\mathbf{n}} \times \mathbf{H}|_{\mathcal{S}^-} = \mathbf{0} \quad \text{(contradiction!)}$$

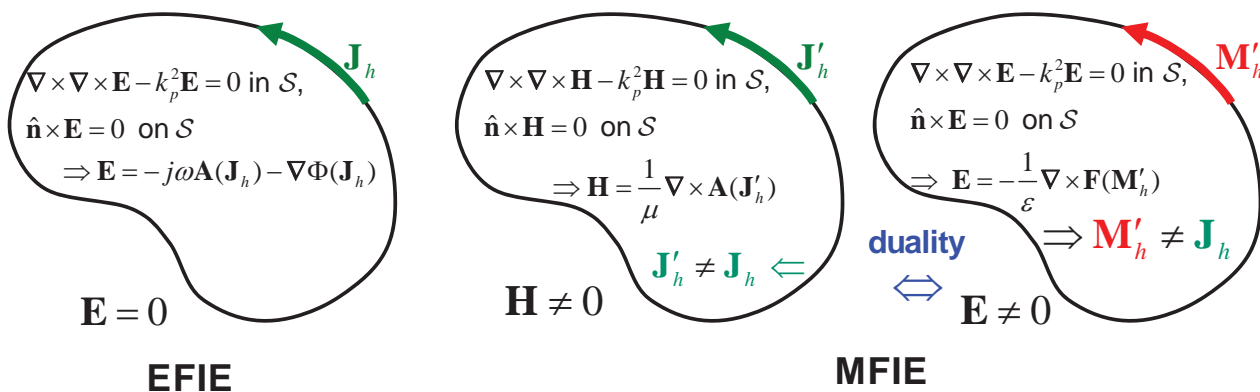
## Uniqueness of the CFIE, cont'd

- If  $\mathcal{L} \mathbf{J}_h = 0$  (EFIE) and  $\mathcal{K} \mathbf{J}_h = 0$  (MFIE) at  $\omega = \omega_p$  then why doesn't the linear combination also have a homogeneous solution :

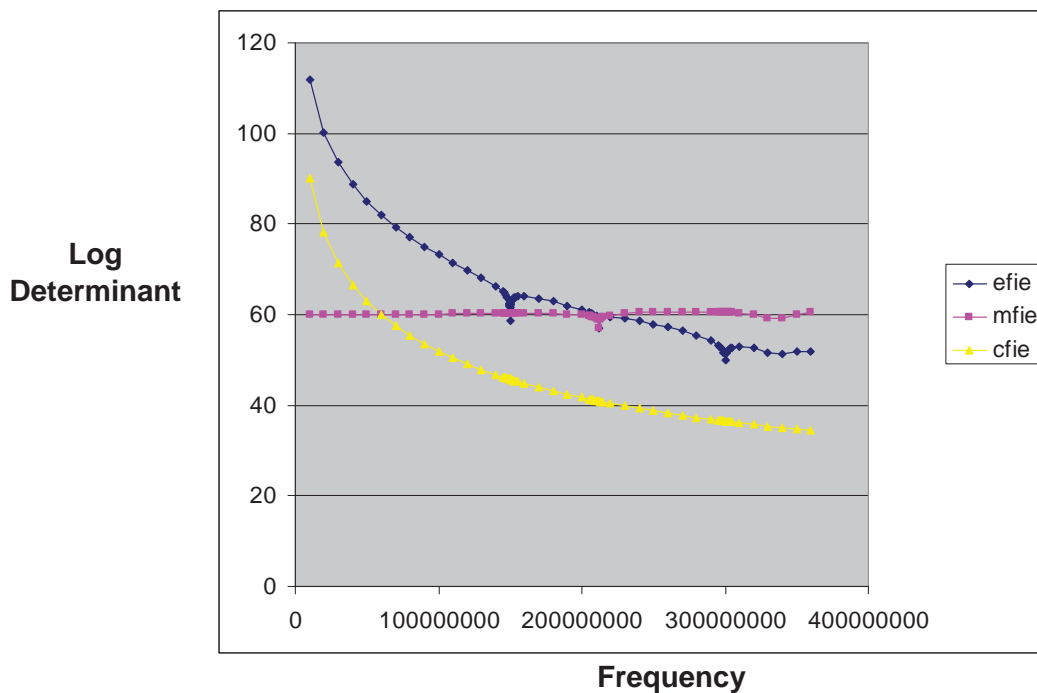
$$\mathcal{L} \mathbf{J}_h + \alpha \mathcal{K} \mathbf{J}_h = (\mathcal{L} + \alpha \mathcal{K}) \mathbf{J}_h \stackrel{?}{=} 0 \text{ (CFIE)}$$

- Ans: The EFIE and MFIE solutions are different!

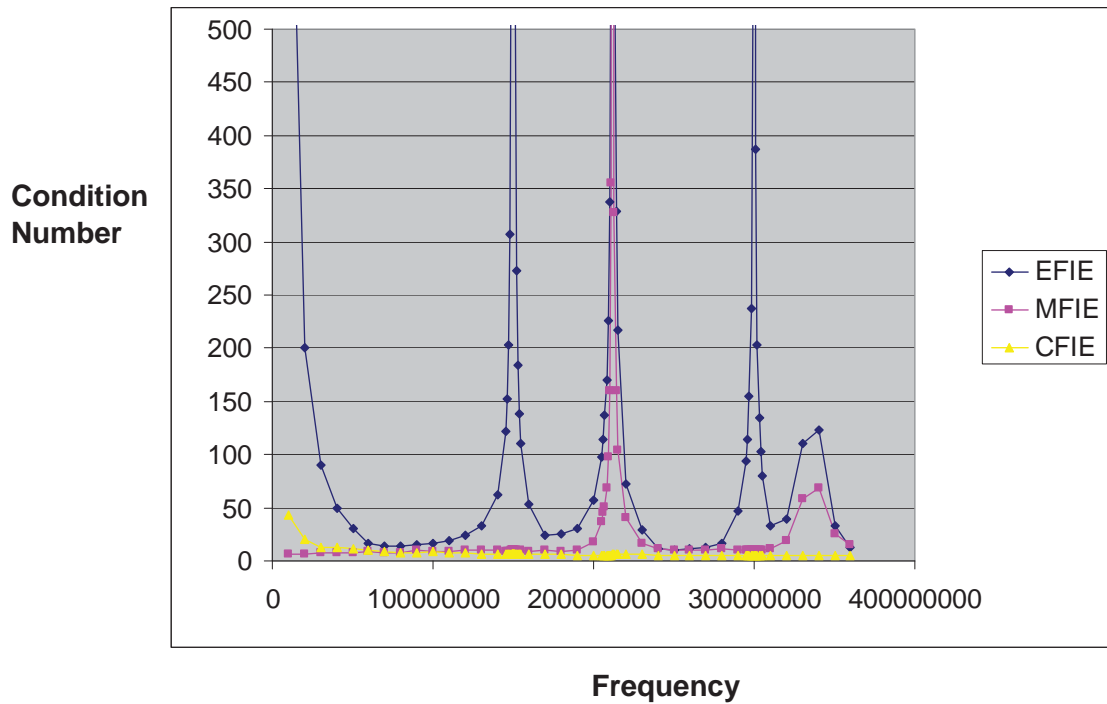
$$\mathcal{L} \mathbf{J}_h = 0 \text{ and } \mathcal{K} \mathbf{J}'_h = 0 \not\Rightarrow \mathcal{L} \mathbf{J}_h + \alpha \mathcal{K} \mathbf{J}_h = 0 \text{ if } \mathbf{J}'_h \neq \mathbf{J}_h$$



## Log<sub>10</sub> of Determinant vs. Frequency, TE Circular Cylinder



## Approx. Condition Number vs. Frequency, TE Circular Cylinder



## Condition Number

If  $Ax = b$

then  $\text{cond } A \equiv \frac{\text{Largest eigenvalue of } A^H A}{\text{Smallest eigenvalue of } A^H A} \geq 1$

and

$$\frac{\|\delta x\|}{\|x\|} \approx \text{cond } A \left[ \frac{\|\delta A\|}{\|A\|} + \frac{\|\delta b\|}{\|b\|} \right]$$

and where

$$(A + \delta A)(x + \delta x) = b + \delta b.$$

**Condition number is the single most important figure of merit in solving linear systems!!**

Roughly,  $\text{cond } A$  measures how much relative errors in  $A$  and  $b$  magnify the relative error of the solution.

Alternatively,  $\log_{10} \text{cond } A$  estimates how many (decimal) digits are lost in solving  $Ax = b$ . I.e., it estimates the worst - case loss of precision.

**End of Note 4**

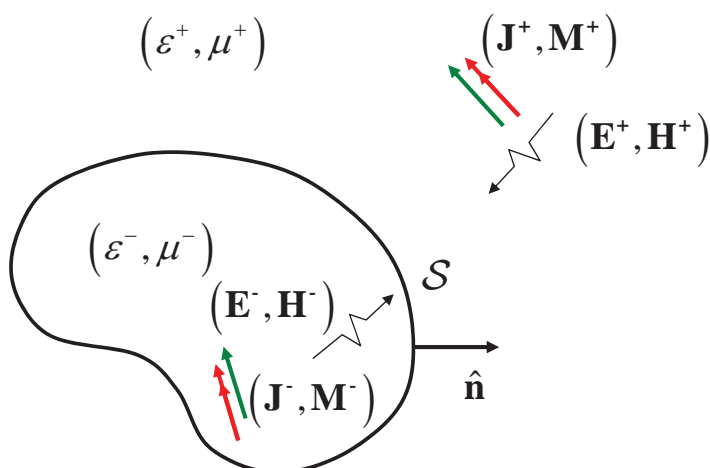
# Modeling Homogeneous Penetrable Materials --- \*PMCHWT Formulation

Donald R. Wilton

Scattering Notes, pp. 37,38

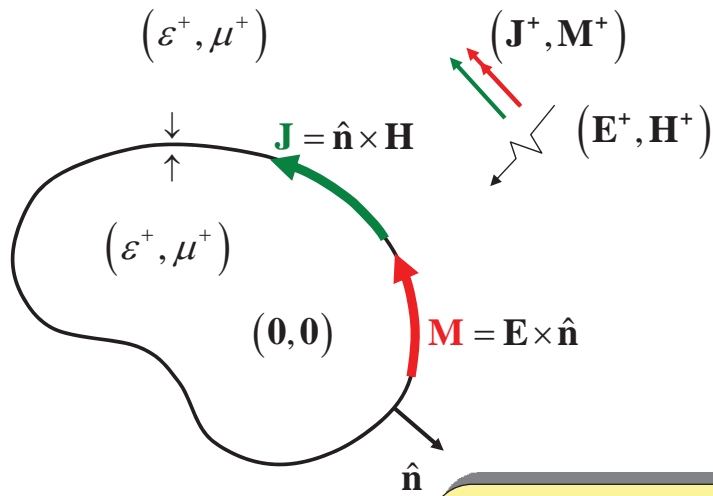
\*Poggio, Miller, Chang, Harrington, Wu, Tsai

## Formulation of Problems Involving Piecewise Homogeneous Media



- $(\mathbf{E}^\pm, \mathbf{H}^\pm)$  are *incident* fields i.e., they are radiated by  $(\mathbf{J}^\pm, \mathbf{M}^\pm)$  in a *homogeneous* medium with parameters  $(\epsilon^\pm, \mu^\pm)$

## Exterior Equivalence, Interior Null Field Conditions



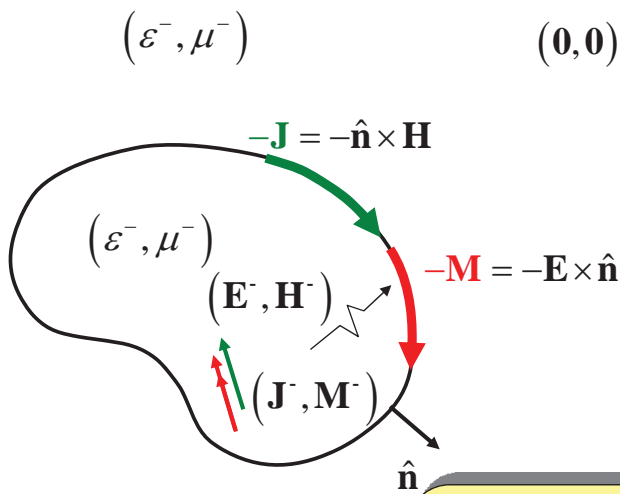
$$k^+ \equiv \omega \sqrt{\mu^+ \epsilon^+},$$

$$\eta^+ \equiv \sqrt{\frac{\mu^+}{\epsilon^+}}$$

**Tested null field conditions:**

- 1)  $\langle \Lambda_m; \mathbf{E}(\mathbf{J}, \mathbf{M}) \rangle + \langle \Lambda_m; \mathbf{E}^+ \rangle = 0, \quad \mathbf{r} \in \lim_{\mathbf{r} \uparrow \mathcal{S}} \mathcal{S}$
- 2)  $\langle \Lambda_m; \mathbf{H}(\mathbf{J}, \mathbf{M}) \rangle + \langle \Lambda_m; \mathbf{H}^+ \rangle = 0, \quad \mathbf{r} \in \lim_{\mathbf{r} \uparrow \mathcal{S}} \mathcal{S}$

## Interior Equivalence, Exterior Null Field Conditions



$$k^- \equiv \omega \sqrt{\mu^- \epsilon^-},$$

$$\eta^- \equiv \sqrt{\frac{\mu^-}{\epsilon^-}}$$

**Tested null field conditions:**

- 3)  $\langle \Lambda_m; \mathbf{E}(-\mathbf{J}, -\mathbf{M}) \rangle + \langle \Lambda_m; \mathbf{E}^- \rangle = 0, \quad \mathbf{r} \in \lim_{\mathbf{r} \downarrow \mathcal{S}} \mathcal{S}$
- 4)  $\langle \Lambda_m; \mathbf{H}(-\mathbf{J}, -\mathbf{M}) \rangle + \langle \Lambda_m; \mathbf{H}^- \rangle = 0, \quad \mathbf{r} \in \lim_{\mathbf{r} \downarrow \mathcal{S}} \mathcal{S}$

## The PMCHWT Equations

**Tested null field conditions :**

$$1) \quad \langle \Lambda_m; \mathbf{E}(\mathbf{J}, \mathbf{M}) \rangle + \langle \Lambda_m; \mathbf{E}^+ \rangle = 0, \quad \mathbf{r} \in \lim_{\mathbf{r} \uparrow S} \mathcal{S}$$

$$2) \quad \langle \Lambda_m; \mathbf{H}(\mathbf{J}, \mathbf{M}) \rangle + \langle \Lambda_m; \mathbf{H}^+ \rangle = 0, \quad \mathbf{r} \in \lim_{\mathbf{r} \uparrow S} \mathcal{S}$$

$$3) \quad \langle \Lambda_m; \mathbf{E}(-\mathbf{J}, -\mathbf{M}) \rangle + \langle \Lambda_m; \mathbf{E}^- \rangle = 0, \quad \mathbf{r} \in \lim_{\mathbf{r} \downarrow S} \mathcal{S}$$

$$4) \quad \langle \Lambda_m; \mathbf{H}(-\mathbf{J}, -\mathbf{M}) \rangle + \langle \Lambda_m; \mathbf{H}^- \rangle = 0, \quad \mathbf{r} \in \lim_{\mathbf{r} \downarrow S} \mathcal{S}$$

**Most common formulation is PMCHWT, obtained by equating 1) to 3) and 2) to 4); it is equivalent to enforcing continuity of tangential  $\mathbf{E}$  and  $\mathbf{H}$  at  $S$ :**

$$\lim_{\mathbf{r} \uparrow S} \langle \Lambda_m; \mathbf{E}(\mathbf{J}, \mathbf{M}) \rangle + \langle \Lambda_m; \mathbf{E}^+ \rangle = \lim_{\mathbf{r} \downarrow S} \langle \Lambda_m; \mathbf{E}(-\mathbf{J}, -\mathbf{M}) \rangle + \langle \Lambda_m; \mathbf{E}^- \rangle$$

$$\lim_{\mathbf{r} \uparrow S} \langle \Lambda_m; \mathbf{H}(\mathbf{J}, \mathbf{M}) \rangle + \langle \Lambda_m; \mathbf{H}^+ \rangle = \lim_{\mathbf{r} \downarrow S} \langle \Lambda_m; \mathbf{H}(-\mathbf{J}, -\mathbf{M}) \rangle + \langle \Lambda_m; \mathbf{H}^- \rangle$$

Any linear combination of 1) and 2) and of 3) and 4) constitutes a valid coupled pair of integral equations for unknowns  $\mathbf{J}$  and  $\mathbf{M}$  ...though their solution may not be unique at all frequencies

PMCHWT is both unique and well-conditioned

## Field and Current Representations

**Represent fields via their potentials :**

$$\begin{aligned} \mathbf{E}(\pm \mathbf{J}, \pm \mathbf{M}) &= \mp j\omega \mathbf{A}^\pm(\mathbf{J}) \mp \nabla \Phi^\pm(\mathbf{J}) \mp \frac{1}{\epsilon^\pm} \nabla \times \mathbf{F}^\pm(\mathbf{M}) \\ &= \mp j\omega \mu^\pm \int_S G^\pm(\mathbf{r}, \mathbf{r}') \mathbf{J}(\mathbf{r}') dS' \pm \frac{\nabla}{j\omega \epsilon^\pm} \int_S G^\pm(\mathbf{r}, \mathbf{r}') \nabla' \cdot \mathbf{J}(\mathbf{r}') dS' \\ &\quad \mp \lim_{\mathbf{r} \uparrow \downarrow S} \nabla \times \int_S G^\pm(\mathbf{r}, \mathbf{r}') \mathbf{M}(\mathbf{r}') dS' \end{aligned}$$

$$G^\pm(\mathbf{r}, \mathbf{r}') = \frac{e^{-jk^\pm R}}{4\pi R}$$

$$\begin{aligned} \mathbf{H}(\pm \mathbf{J}, \pm \mathbf{M}) &= \mp j\omega \mathbf{F}^\pm(\mathbf{M}) \mp \nabla \Psi^\pm(\mathbf{M}) \pm \frac{1}{\mu^\pm} \nabla \times \mathbf{A}^\pm(\mathbf{J}) \\ &= \mp j\omega \epsilon^\pm \int_S G^\pm(\mathbf{r}, \mathbf{r}') \mathbf{M}(\mathbf{r}') dS' \pm \frac{\nabla}{j\omega \mu^\pm} \int_S G^\pm(\mathbf{r}, \mathbf{r}') \nabla' \cdot \mathbf{M}(\mathbf{r}') dS' \\ &\quad \pm \lim_{\mathbf{r} \uparrow \downarrow S} \nabla \times \int_S G^\pm(\mathbf{r}, \mathbf{r}') \mathbf{J}(\mathbf{r}') dS' \end{aligned}$$

## Expansion of Equivalent Currents

Represent currents using div - conforming bases :

$$\mathbf{J}(\mathbf{r}) \approx \sum_{n=1}^N I_n \Lambda_n(\mathbf{r})$$

$$\mathbf{M}(\mathbf{r}) \approx \sum_{n=1}^N V_n \Lambda_n(\mathbf{r})$$

Substitute these into the tested (weak form) of the PMCHWT equations and rearrange.

## Discretized Form of PMCHWT Equations

$$\begin{bmatrix} [Z_{mn}^+ + Z_{mn}^-] & [-\beta_{mn}^+ - \beta_{mn}^-] \\ [\beta_{mn}^+ + \beta_{mn}^-] & [Y_{mn}^+ + Y_{mn}^-] \end{bmatrix} \begin{bmatrix} I_n \\ V_n \end{bmatrix} = \begin{bmatrix} V_m^i \\ I_m^i \end{bmatrix}$$

where

$$Z_{mn}^{\pm} = \eta_{mn}^{\pm 2} Y_{mn}^{\pm} = j\omega L_{mn}^{\pm} + \frac{1}{j\omega} S_{mn}^{\pm} = j\eta_{mn}^{\pm} \left[ k^{\pm} \iint_{S'} \iint_{S} G^{\pm} \left( \Lambda_m \cdot \Lambda_n - \frac{1}{k^{\pm 2}} \nabla \cdot \Lambda_m \nabla \cdot \Lambda_n \right) dS' dS \right]$$

$$L_{mn}^{\pm} = \mu^{\pm} \langle \Lambda_m; G^{\pm}, \Lambda_n \rangle, S_{mn}^{\pm} = \frac{1}{\epsilon^{\pm}} \langle \nabla \cdot \Lambda_m, G^{\pm}, \nabla \cdot \Lambda_n \rangle$$

$$\beta_{mn}^{\pm} = -\langle \Lambda_m; \nabla G^{\pm} \times, \Lambda_n \rangle = -\iint_{S'} \iint_{S} \Lambda_m \cdot \nabla G^{\pm} \times \Lambda_n dS' dS, G^{\pm} = \frac{e^{-jk^{\pm}R}}{4\pi R},$$

$$V_m^i = \langle \Lambda_m; \mathbf{E}^+ - \mathbf{E}^- \rangle, I_m^i = \langle \Lambda_m; \mathbf{H}^+ - \mathbf{H}^- \rangle,$$

Note that  $\pm \frac{\mathbf{J}}{2}, \pm \frac{\mathbf{M}}{2}$  terms *cancel* both in formulation and in matrix element "self" terms (i.e.,  $\frac{1}{2} \langle \Lambda_m; \Lambda_n \rangle$  terms).

## Row Scaling

Consider

$$[a_{mn}][x_n] = [b_m] \Rightarrow \begin{bmatrix} a_{11} & \cdots & a_{1N} \\ \vdots & & \vdots \\ a_{N1} & \cdots & a_{NN} \end{bmatrix} \begin{bmatrix} x_1 \\ \vdots \\ x_N \end{bmatrix} = \begin{bmatrix} b_1 \\ \vdots \\ b_N \end{bmatrix}$$

To scale row  $p$  by  $C_R$ ,

- Multiply all elements of  $p$ th row of  $[a_{mn}]$  by  $C_R$
- Multiply  $p$ th row of  $[b_m]$  by  $C_R$

$$\text{row } p \rightarrow \begin{bmatrix} a_{11} & \cdots & a_{1N} \\ \vdots & & \vdots \\ C_R a_{pq} & \cdots & C_R a_{pN} \\ \vdots & & \vdots \\ a_{N1} & \cdots & a_{NN} \end{bmatrix} \begin{bmatrix} x_1 \\ \vdots \\ x_N \end{bmatrix} = \begin{bmatrix} b_1 \\ \vdots \\ C_R b_p \\ \vdots \\ b_N \end{bmatrix}$$

## Column Scaling

Consider

$$[a_{mn}][x_n] = [b_m] \Rightarrow \begin{bmatrix} a_{11} & \cdots & a_{1N} \\ \vdots & & \vdots \\ a_{N1} & \cdots & a_{NN} \end{bmatrix} \begin{bmatrix} x_1 \\ \vdots \\ x_N \end{bmatrix} = \begin{bmatrix} b_1 \\ \vdots \\ b_N \end{bmatrix}$$

To scale column  $q$  by  $C_C$ ,

- Multiply all elements of  $q$ th column of  $[a_{mn}]$  by  $C_C$
- Divide  $q$ th row of  $[x_n]$  by  $C_C$

$$\begin{matrix} & \text{column } q & & & \\ \begin{bmatrix} a_{11} & \cdots & C_C a_{1q} & \cdots & a_{1N} \\ \vdots & & \vdots & & \vdots \\ a_{N1} & \cdots & C_C a_{Nq} & \cdots & a_{NN} \end{bmatrix} & \begin{bmatrix} x_1 \\ \vdots \\ x_q / C_C \\ \vdots \\ x_N \end{bmatrix} & = & \begin{bmatrix} b_1 \\ \vdots \\ b_N \end{bmatrix} \end{matrix}$$

- Note that column scaling scales the solution vector,  $[x_n]$ , which must be "unscaled" after the system is solved!

## Normalization and Symmetrization of PMCHWT Equations

Normalize and symmetrize the system matrix by

- multiplying first column block by  $1 / \eta_0$ , renormalizing the current vector  $I_n$
- multiplying the second row block by  $-j\eta_0$
- multiplying the second column block by  $j$ :

$$\begin{bmatrix} \left[ \frac{Z_{mn}^+ + Z_{mn}^-}{\eta_0} \right] & -j \left[ \beta_{mn}^+ + \beta_{mn}^- \right] \\ -j \frac{\eta_0}{\eta_0} \left[ \beta_{mn}^+ + \beta_{mn}^- \right] & \left[ \eta_0 (Y_{mn}^+ + Y_{mn}^-) \right] \end{bmatrix} \begin{bmatrix} \eta_0 I_n \\ -j V_n \end{bmatrix} = \begin{bmatrix} V_m^i \\ -j \eta_0 I_m^i \end{bmatrix}$$

Note that, unfortunately,

$$\eta_0 (Y_{mn}^+ + Y_{mn}^-) = \eta_0 \left( \frac{Z_{mn}^+}{\eta^{+2}} + \frac{Z_{mn}^-}{\eta^{-2}} \right) \neq \frac{Z_{mn}^+ + Z_{mn}^-}{\eta_0}$$

## Far Field Computation

$$\mathbf{E} \xrightarrow{r \rightarrow \infty} -j\omega(\hat{\theta}\hat{\theta} + \hat{\phi}\hat{\phi}) \cdot \mathbf{A} + j\omega\eta(\hat{\phi}\hat{\theta} - \hat{\theta}\hat{\phi}) \cdot \mathbf{F} \quad (\text{Note } \nabla\Phi \xrightarrow{r \rightarrow \infty} -j\omega\hat{\mathbf{r}}\hat{\mathbf{r}} \cdot \mathbf{A})$$

$$\mathbf{H} \xrightarrow{r \rightarrow \infty} -j\omega(\hat{\theta}\hat{\theta} + \hat{\phi}\hat{\phi}) \cdot \mathbf{F} + \frac{j\omega}{\eta}(\hat{\theta}\hat{\phi} - \hat{\phi}\hat{\theta}) \cdot \mathbf{A} \quad (\text{Note } \nabla\Psi \xrightarrow{r \rightarrow \infty} -j\omega\hat{\mathbf{r}}\hat{\mathbf{r}} \cdot \mathbf{F})$$

where

$$\mathbf{A} = \frac{\mu^+ e^{-jk^+r}}{4\pi r} \int_S \mathbf{J}(\mathbf{r}') e^{jk^+\hat{\mathbf{r}}\cdot\mathbf{r}'} dS' \approx \frac{\mu^+ e^{-jk^+r}}{4\pi r} [\tilde{\Lambda}_n]^t [I_n]$$

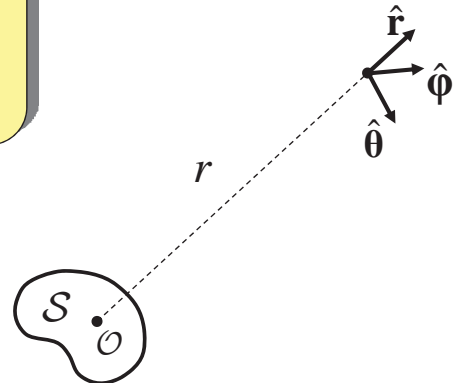
$$\mathbf{F} = \frac{\varepsilon^+ e^{-jk^+r}}{4\pi r} \int_S \mathbf{M}(\mathbf{r}') e^{jk^+\hat{\mathbf{r}}\cdot\mathbf{r}'} dS' \approx \frac{\varepsilon^+ e^{-jk^+r}}{4\pi r} [\tilde{\Lambda}_n]^t [V_n]$$

$$\hat{\mathbf{r}} = \hat{\mathbf{x}} \cos \phi \sin \theta + \hat{\mathbf{y}} \sin \phi \sin \theta + \hat{\mathbf{z}} \cos \theta$$

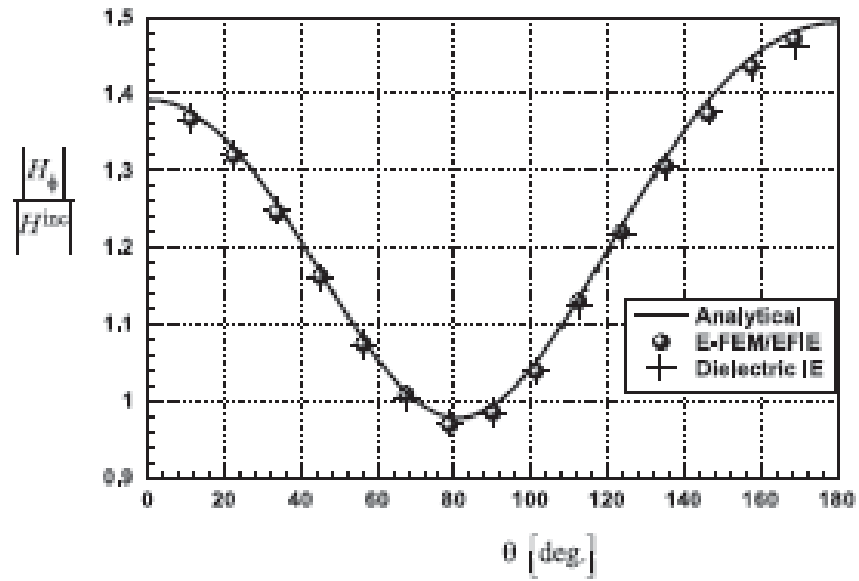
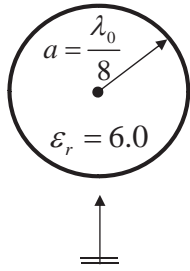
$$\hat{\theta} = \hat{\mathbf{x}} \cos \phi \cos \theta + \hat{\mathbf{y}} \sin \phi \cos \theta - \hat{\mathbf{z}} \sin \theta$$

$$\hat{\phi} = -\hat{\mathbf{x}} \sin \phi + \hat{\mathbf{y}} \cos \phi$$

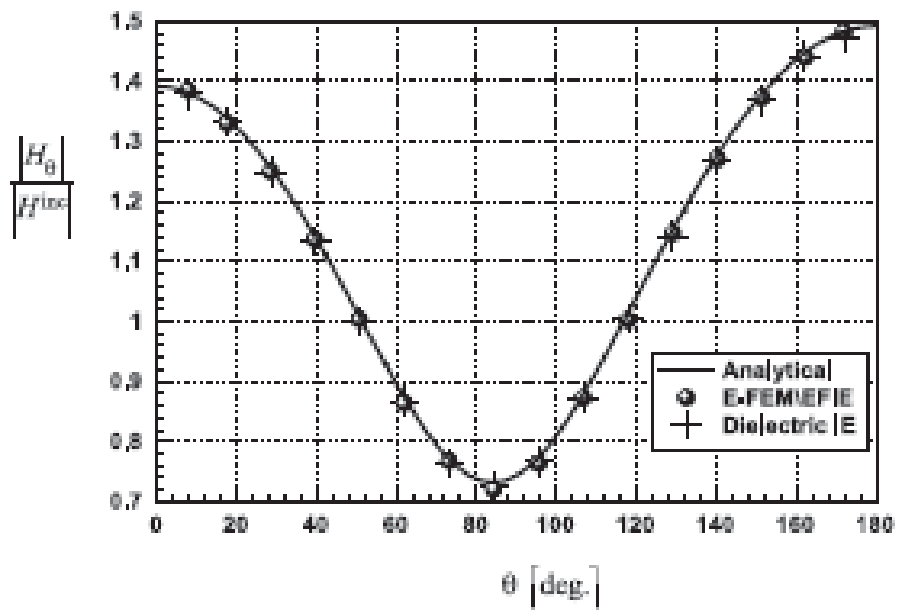
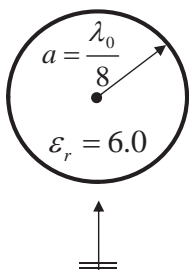
$$[\tilde{\Lambda}_n] \equiv \left[ \int_S \Lambda_n(\mathbf{r}') e^{jk^+\hat{\mathbf{r}}\cdot\mathbf{r}'} dS' \right]$$



## Surface Magnetic Field, $H_\phi$ Dielectric Sphere

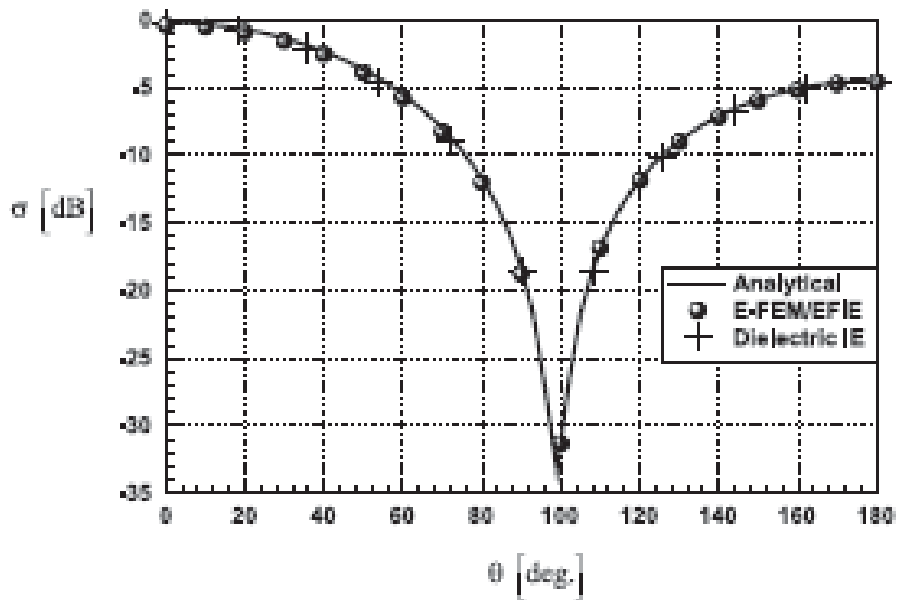


## Surface Magnetic Field, $H_\theta$ Dielectric Sphere



## Radar Cross Section, Dielectric Sphere

$$\sigma(\hat{r}, \hat{k}) = \lim_{r \rightarrow \infty} 4\pi r^2 \frac{|E|^2}{|E^{inc}|^2}$$



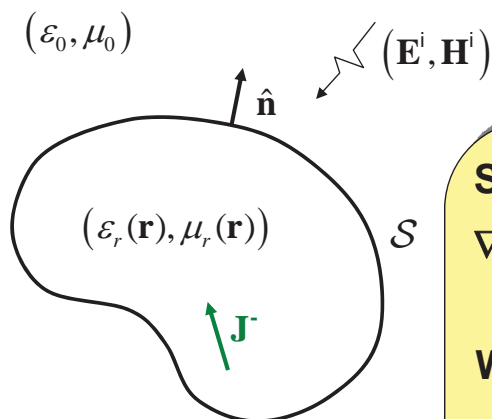
**End of Note 5**

# Coupled 3D Finite and Boundary Element Formulation

Donald R. Wilton

Scattering notes, pp. 39-41 3D-FEM  
pp. 41-43, hybrid FEM/BEM

## Strong and Weak Forms of the 3-D Helmholtz Equation



**Strong form :**

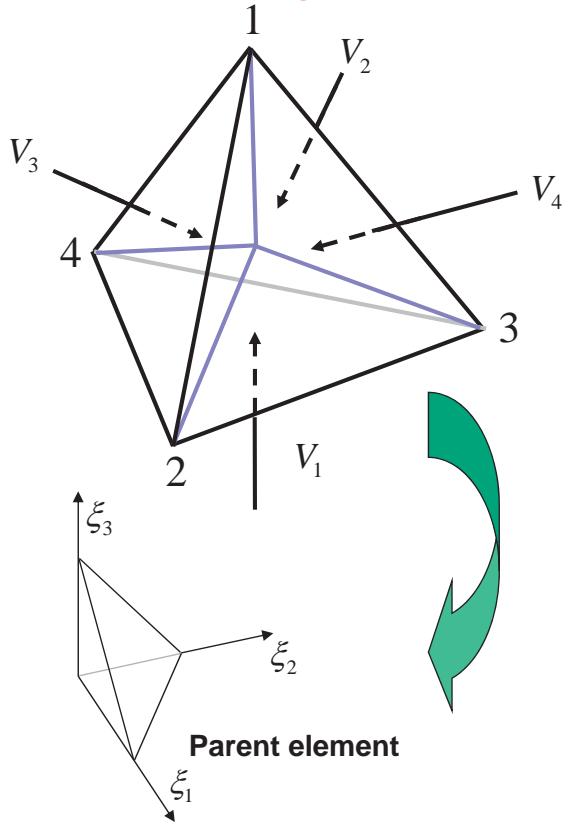
$$\nabla \times \mu_r^{-1} \nabla \times \mathbf{E} - k_0^2 \epsilon_r \mathbf{E} = -j\omega\mu_0 \mathbf{J}^-, \quad \mathbf{r} \in \mathcal{V}$$

**Weak form :**

$$\frac{1}{j\omega\mu_0} \langle \nabla \times \Omega_m, \mu_r^{-1} \nabla \times \mathbf{E} \rangle + j\omega\epsilon_0 \langle \Omega_m, \epsilon_r \mathbf{E} \rangle - \oint_S \Omega_m \cdot \hat{\mathbf{n}} \times \mathbf{H} dS = -\langle \Omega_m, \mathbf{J}^- \rangle, \quad \mathbf{r} \in \mathcal{V}$$

Vanishes if either  $\Omega_m$  or  $\hat{\mathbf{n}} \times \mathbf{H}$  vanishes on  $S$

## Volume Coordinates for Tetrahedral Meshes



### Volume Coordinates :

$$\xi_i = \frac{V_i}{V^e}, \quad i = 1, 2, 3, 4$$

$$\Rightarrow \xi_1 + \xi_2 + \xi_3 + \xi_4 = 1$$

### Geometry Parametrization :

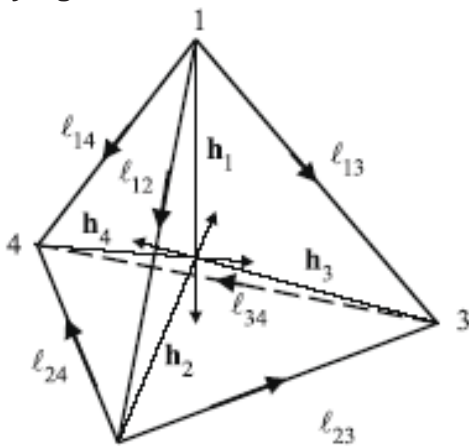
$$\mathbf{r} = \mathbf{r}_1^e \xi_1 + \mathbf{r}_2^e \xi_2 + \mathbf{r}_3^e \xi_3 + \mathbf{r}_4^e \xi_4,$$

$\mathbf{r}_i^e$  = vector from global origin to  $i$ th vertex of element  $e$

Traversing the path from vertices 1-2-3 should determine outward normal  $\hat{n}$  according to the right hand rule.

## Geometrical Parameters Associated with a Tetrahedron

Our convention: Choose vertices 1,2,3, such that traversing them in order produces an outward normal by right hand rule



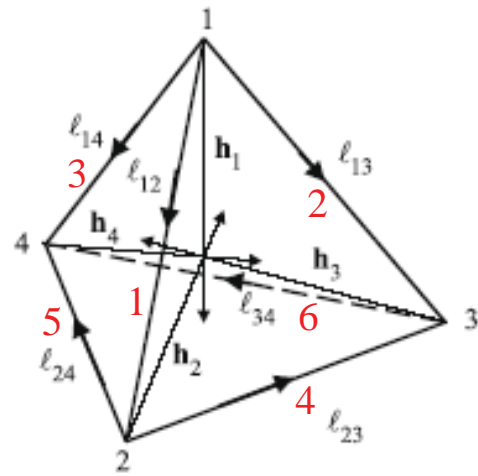
Edge vectors	$l_{ij} = \mathbf{r}_j^e - \mathbf{r}_i^e; \quad l_{ij} =  l_{ij} ;$ $\hat{l}_{ij} = \frac{l_{ij}}{l_{ij}}, \quad i \neq j \in \{1, 2, 3, 4\}$
Volume	$V^e = \frac{ l_{14} \cdot (l_{24} \times l_{34}) }{6}$ $= \frac{A_i h_i}{3},$ $A_i = \text{area of face } i,$ $h_i = \text{height of vertex } i$
Coordinate gradients,	$\nabla \xi_1 = \frac{l_{24} \times l_{34}}{6V^e},$ $\nabla \xi_2 = \frac{l_{34} \times l_{14}}{6V^e},$ $\nabla \xi_3 = \frac{l_{14} \times l_{24}}{6V^e},$ $\nabla \xi_4 = -\nabla \xi_1 - \nabla \xi_2 - \nabla \xi_3$

- Gradient *direction* is from face  $i$  to vertex  $i = -\hat{h}_i$
- Gradient *magnitude* = change in  $\xi_i$  from face  $i$  to vertex  $i \div \text{distance} (= 1/h_i \Rightarrow |\nabla \xi_i| = 1/h_i)$   
 $\Rightarrow \nabla \xi_i = -\hat{h}_i / h_i$

## Local Edge Numbering and Reference Directions

- Note  $l_{ii} = 0$ .
- Also  $l_{ij} = -l_{ji}$ , so for independent edge vectors, use only  $l_{ij}$ ,  $j > i$ .

Local edge number	Edge reference direction
1	$l_{12}$
2	$l_{13}$
3	$l_{14}$
4	$l_{23}$
5	$l_{24}$
6	$l_{34}$



## Parameterization of Integrals and Numerical Integration over Tetrahedrons

$$\int_{V^e} f(\mathbf{r}) dV = 6V^e \int_0^1 \int_0^{1-\xi_k} \int_0^{1-\xi_j-\xi_k} f(\mathbf{r}) d\xi_i d\xi_j d\xi_k, \quad i \neq j \neq k$$

$$\approx \frac{6V^e}{\mathcal{J}_e} \sum_{k=1}^K w_k f(\mathbf{r}_1^e \xi_1^{(k)} + \mathbf{r}_2^e \xi_2^{(k)} + \mathbf{r}_3^e \xi_3^{(k)} + \mathbf{r}_4^e \xi_4^{(k)})$$

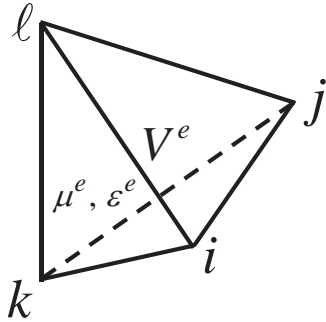
Table 13 Sample points and weighting coefficients for  $K$ -point quadrature on tetrahedrons.

Sample Points, $(\xi_1^{(k)}, \xi_2^{(k)}, \xi_3^{(k)})$ $(\xi_4^{(k)} = 1 - \xi_1^{(k)} - \xi_2^{(k)} - \xi_3^{(k)})$	Weights, $w_k$
<b>K=1, error <math>\mathcal{O}(\xi_i^2)</math>:</b> (0.25000000, 0.25000000, 0.25000000)	0.16666667
<b>K=4, error <math>\mathcal{O}(\xi_i^3)</math>:</b> (0.58541020, 0.13819660, 0.13819660)	0.041666667
(0.13819660, 0.58541020, 0.13819660)	0.041666667
(0.13819660, 0.13819660, 0.58541020)	0.041666667
(0.13819660, 0.13819660, 0.13819660)	0.041666667

...or use the exact result

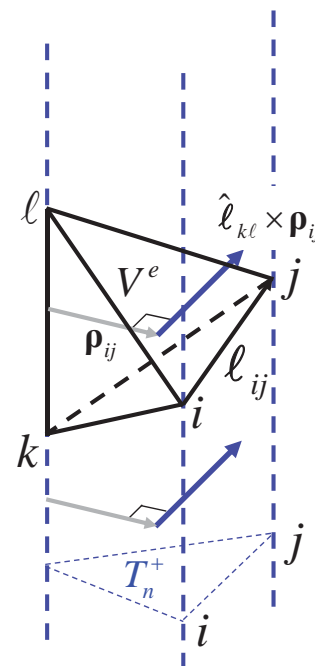
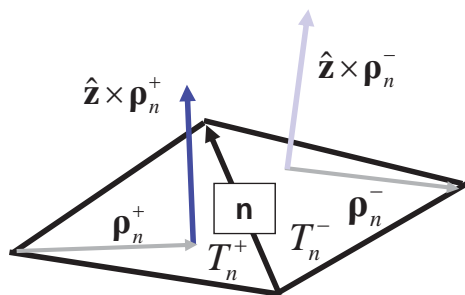
$$\int_{V^e} \xi_1^\alpha \xi_2^\beta \xi_3^\gamma \xi_4^\delta dV = \frac{6V^e \alpha! \beta! \gamma! \delta!}{(\alpha + \beta + \gamma + \delta + 3)!}$$

## Properties of Curl-Conforming Bases Needed on Tetrahedral Meshes



- Assume medium parameters constant within a tetrahedron
- Make tangential electric field continuous across medium boundaries by defining DOFs at edges
- Make interpolatory by allowing *only* the basis associated with the DOF at an edge to have a unit tangential component there

## Planar Triangle Curl-Conforming Bases May Be Extended to Tetrahedrons by Viewing Them as Embedded in Infinite Cylinders



$$\Omega_{ij}^e(\mathbf{r}) \propto \hat{l}_{kl} \times \boldsymbol{\rho}_{ij} \Rightarrow$$

$$\Omega_{ij}^e(\mathbf{r}) = l_{ij} (\xi_i \nabla \xi_j - \xi_j \nabla \xi_i),$$

$$\nabla \times \Omega_{ij}^e(\mathbf{r}) = 2l_{ij} (\nabla \xi_i \times \nabla \xi_j),$$

$$j > i, \mathbf{r} \in V^e$$

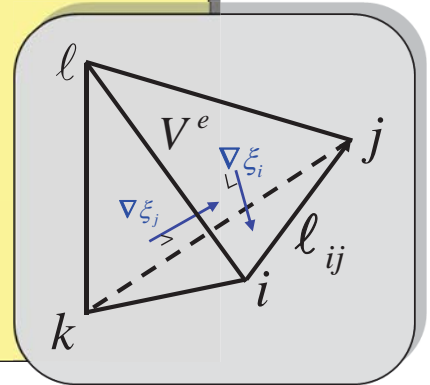
## Demonstration of Interpolatory Properties of Curl-Conforming Bases

$$\Omega_{ij}^e(\mathbf{r}) = l_{ij} (\xi_i \nabla \xi_j - \xi_j \nabla \xi_i)$$

- $\nabla \xi_i$  is  $\perp$  to face  $i$  and hence to edges  $jk, kl, lj$   
 $\Rightarrow \Omega_{ij}^e(\mathbf{r})|_{\xi_i=0} \cdot \hat{\ell}_{jk} = \Omega_{ij}^e(\mathbf{r})|_{\xi_i=0} \cdot \hat{\ell}_{kl} = \Omega_{ij}^e(\mathbf{r})|_{\xi_i=0} \cdot \hat{\ell}_{lj} = 0$
- $\nabla \xi_j$  is  $\perp$  to face  $j$  and hence to edges  $il, lk, ki$   
 $\Rightarrow \Omega_{ij}^e(\mathbf{r})|_{\xi_j=0} \cdot \hat{\ell}_{il} = \Omega_{ij}^e(\mathbf{r})|_{\xi_j=0} \cdot \hat{\ell}_{lk} = \Omega_{ij}^e(\mathbf{r})|_{\xi_j=0} \cdot \hat{\ell}_{ki} = 0$

• Finally,

$$\begin{aligned} \Omega_{ij}^e(\mathbf{r})|_{\xi_k=\xi_l=0} \cdot \hat{\ell}_{ij} &= l_{ij} \hat{\ell}_{ij} \cdot (\xi_i \nabla \xi_j - \xi_j \nabla \xi_i) \\ &= -l_{ij} \cdot \left( \xi_i \frac{\mathbf{h}_j}{h_j} - \xi_j \frac{\mathbf{h}_i}{h_i} \right) \Big|_{\xi_k=\xi_l=0} = \xi_i \frac{h_j}{h_j} + \xi_j \frac{h_i}{h_i} \\ &= \xi_i + \xi_j = 1 \end{aligned}$$



## Discretized Equations Obtained by Substituting Representations for Electric and Surface Magnetic Fields

$$\mathbf{E} \approx \sum_{n=1}^{N_V} \underbrace{V_n^V}_{\text{volume DoFs}} \Omega_n(\mathbf{r}) + \sum_{n=1}^{N_S} \underbrace{V_n^S}_{\text{surface DoFs}} \Omega_{N_V+n}(\mathbf{r})$$

$$\mathbf{J} \equiv \hat{\mathbf{n}} \times \mathbf{H} \approx \sum_{n=1}^{N_S} I_n^S \Omega_n^S(\mathbf{r})$$

$\Rightarrow$

$$\begin{aligned} \begin{bmatrix} Y_{mn}^{VV} \end{bmatrix} \begin{bmatrix} V_n^V \end{bmatrix} + \begin{bmatrix} Y_{mn}^{VS} \end{bmatrix} \begin{bmatrix} V_n^S \end{bmatrix} &= \begin{bmatrix} I_m^{-V} \end{bmatrix} \\ \begin{bmatrix} Y_{mn}^{SV} \end{bmatrix} \begin{bmatrix} V_n^V \end{bmatrix} + \begin{bmatrix} Y_{mn}^{SS} \end{bmatrix} \begin{bmatrix} V_n^S \end{bmatrix} + \begin{bmatrix} \gamma_{mn}^{SS} \end{bmatrix} \begin{bmatrix} I_n^S \end{bmatrix} &= \begin{bmatrix} I_m^{-S} \end{bmatrix} \end{aligned}$$

• 2 equation blocks,  
3 vector unknown blocks  
• If  $S$  is not PEC or PMC, need another block of equations to determine  $I_n^S$  and supply radiation conditions

$S$  is PEC

$S$  is PMC

PEC:  $\hat{\mathbf{n}} \times \mathbf{E}|_S = 0 \Rightarrow [V_n^S] = 0$

PMC:  $\hat{\mathbf{n}} \times \mathbf{H}|_S = 0 \Rightarrow [I_n^S] = 0$

## Matrix Block Definitions

$$Y_{mn}^{VV} = \frac{1}{j\omega\mu_0} \langle \nabla \times \Omega_m, \mu_r^{-1} \nabla \times \Omega_n \rangle + j\omega\epsilon_0 \langle \Omega_m, \epsilon_r \Omega_n \rangle$$

$$Y_{mn}^{VS} = \frac{1}{j\omega\mu_0} \langle \nabla \times \Omega_m, \mu_r^{-1} \nabla \times \Omega_{N_V+n} \rangle + j\omega\epsilon_0 \langle \Omega_m, \epsilon_r \Omega_{N_V+n} \rangle$$

$$Y_{mn}^{SV} = \frac{1}{j\omega\mu_0} \langle \nabla \times \Omega_{N_V+m}, \mu_r^{-1} \nabla \times \Omega_n \rangle + j\omega\epsilon_0 \langle \Omega_{N_V+m}, \epsilon_r \Omega_n \rangle$$

$$Y_{mn}^{SS} = \frac{1}{j\omega\mu_0} \langle \nabla \times \Omega_{N_V+m}, \mu_r^{-1} \nabla \times \Omega_{N_V+n} \rangle + j\omega\epsilon_0 \langle \Omega_{N_V+m}, \epsilon_r \Omega_{N_V+n} \rangle$$

$$\gamma_{mn}^{SS} = -\langle \Omega_{N_V+m}, \Omega_n^S \rangle = -\langle \Omega_m^S, \Omega_n^S \rangle = -\langle \Lambda_m^S, \Lambda_n^S \rangle$$

Volume integrals!

Surface integral!

**Index ranges:**

$$V_p \Rightarrow p = 1, 2, \dots, N_V$$

$$S_p \Rightarrow p = 1, 2, \dots, N_S$$

$$\Lambda_m^S = \Omega_m^S \times \hat{\mathbf{n}}$$

$$-\hat{\mathbf{n}} \times \hat{\mathbf{n}} \times \Omega_{N_V+m} \Big|_{\mathbf{r} \in \mathcal{S}} = \Omega_m^S$$

$$I_m^{-V} = -\langle \Omega_m, \mathbf{J}^- \rangle$$

$$I_m^{-S} = -\langle \Omega_{N_V+m}, \mathbf{J}^- \rangle$$

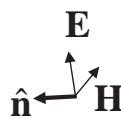
## In Far Field, We Also Know the *Ratio* of Tangential Surface Electric and Magnetic Fields ...

In the far field,

$$\hat{\mathbf{r}} \times \mathbf{H} = \hat{\mathbf{n}} \times \mathbf{H} = -\frac{\mathbf{E}_{\text{tan}}}{\eta_0} \Rightarrow [I_n^S] = -\frac{1}{\eta_0} [V_n^S],$$

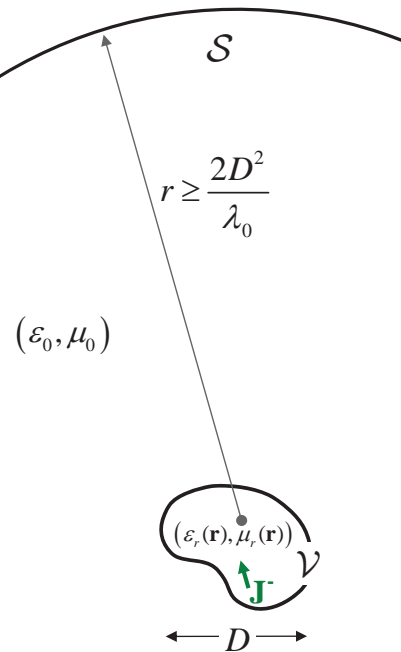
$$\mathbf{J} \Big|_{\mathcal{S}} = 0 \Rightarrow [I_m^{-S}] = 0:$$

$$\Rightarrow \begin{bmatrix} [Y_{mn}^{VV}] & [Y_{mn}^{VS}] \\ [Y_{mn}^{SV}] & [Y_{mn}^{SS} - \frac{\gamma_{mn}^{SS}}{\eta_0}] \end{bmatrix} \begin{bmatrix} [V_n^V] \\ [V_n^S] \end{bmatrix} = \begin{bmatrix} [I_m^{-V}] \\ [0] \end{bmatrix}$$



Note we also know their ratio for surface impedances:

$$\hat{\mathbf{n}} \times \mathbf{H} = -\frac{\mathbf{E}_{\text{tan}}}{Z_s} \Rightarrow [I_n^S] = -\frac{1}{Z_s} [V_n^S]$$



Mesh fills scatterer and surrounding region out to the far field!

## ...Or Null Field Condition Provides Add'l Eq. at Boundary

Expressing the magnetic null field condition (see PMCHWT formulation) using equivalent currents and potentials provides the missing equation :

$$-\hat{\mathbf{n}} \times \mathbf{H}^{\text{sc}}[\mathbf{J}, \mathbf{M}] = \hat{\mathbf{n}} \times \mathbf{H}^{\text{inc}}, \quad \mathbf{r} \uparrow S$$

$$\Rightarrow \frac{\mathbf{J}}{2} - \frac{1}{\mu_0} \hat{\mathbf{n}} \times \int_S \nabla \times \mathcal{G}^A(\mathbf{r}, \mathbf{r}') \cdot \mathbf{J}(\mathbf{r}') dS' + j\omega\epsilon_0 \hat{\mathbf{n}} \times \int_S G(\mathbf{r}, \mathbf{r}') \mathbf{M}(\mathbf{r}') dS' - \frac{1}{j\omega\mu_0} \hat{\mathbf{n}} \times \nabla \int_S G(\mathbf{r}, \mathbf{r}') \nabla' \cdot \mathbf{M}(\mathbf{r}') dS' = \hat{\mathbf{n}} \times \mathbf{H}^{\text{inc}}$$

Relate equivalent currents to fields of the Helmholtz eq. :

$$\mathbf{J} \equiv \hat{\mathbf{n}} \times \mathbf{H} = \sum_{n=1}^{N_S} I_n^S \boldsymbol{\Omega}_n^S(\mathbf{r}), \quad \mathbf{M} \equiv \mathbf{E} \times \hat{\mathbf{n}} = \sum_{n=1}^{N_S} V_n^S \boldsymbol{\Lambda}_n^S(\mathbf{r})$$

Substituting into above and testing with  $\boldsymbol{\Omega}_n^S$  yields final matrix equation :

$$\Rightarrow \left[ \hat{\beta}_{mn}^{SS} \right] \left[ I_n^S \right] + \left[ \frac{Z_{mn}^{SS}}{\eta_0^2} \right] \left[ V_n^S \right] = \left[ I_m^{\text{inc}} \right]$$

Homogeneous background medium is assumed to be free space

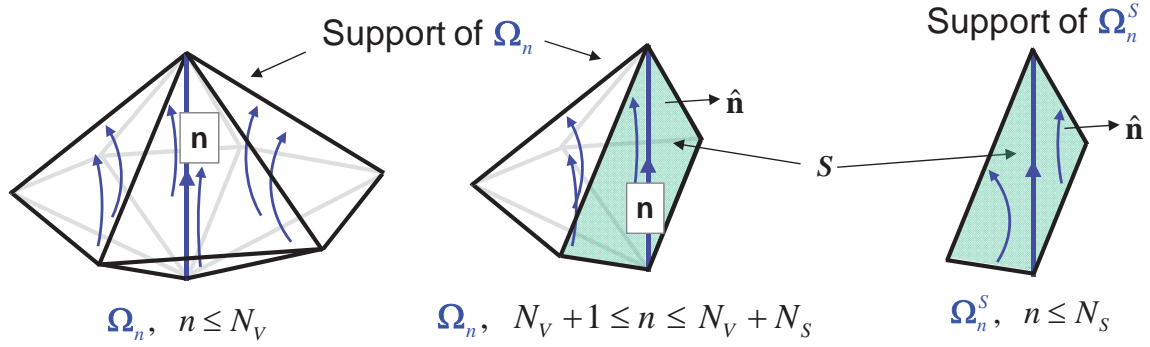
## Integral Equation Matrix Block Definitions

$$\frac{Z_{mn}^{SS}}{\eta_0^2} = j\omega\epsilon_0 \langle \boldsymbol{\Lambda}_m^S; G, \boldsymbol{\Lambda}_n^S \rangle + \frac{1}{j\omega\mu_0} \langle \nabla \cdot \boldsymbol{\Lambda}_m^S, G, \nabla \cdot \boldsymbol{\Lambda}_n^S \rangle, \quad m, n = 1, \dots, N_S$$

$$\begin{aligned} \hat{\beta}_{mn}^{SS} &= \frac{1}{2} \langle \boldsymbol{\Omega}_m^S, \boldsymbol{\Omega}_n^S \rangle - \frac{1}{\mu_0} \langle \boldsymbol{\Omega}_m^S; \hat{\mathbf{n}} \times \nabla \times \mathcal{G}^A; \boldsymbol{\Omega}_n^S \rangle \\ &= -\frac{1}{2} \gamma_{mn}^{SS} - \frac{1}{\mu_0} \langle \boldsymbol{\Omega}_m^S; \hat{\mathbf{n}} \times \nabla \times \mathcal{G}^A; \boldsymbol{\Omega}_n^S \rangle, \quad m, n = 1, \dots, N_S, \end{aligned}$$

$$I_m^{\text{inc}} = \langle \boldsymbol{\Lambda}_m^S, \mathbf{H}^{\text{inc}} \rangle$$

## Pictorial Representation of Surface Bases, Interior and Surface Volume Bases



$$\mathbf{E} \approx = \sum_{n=1}^{N_V} \underbrace{V_n^V}_{\text{volume DoFs}} \Omega_n(\mathbf{r}) + \sum_{n=1}^{N_S} \underbrace{V_n^S}_{\text{surface DoFs}} \Omega_{N_V+n}(\mathbf{r})$$

$$\mathbf{J} \equiv \hat{\mathbf{n}} \times \mathbf{H} \approx \sum_{n=1}^{N_S} I_n^S \Omega_n^S(\mathbf{r})$$

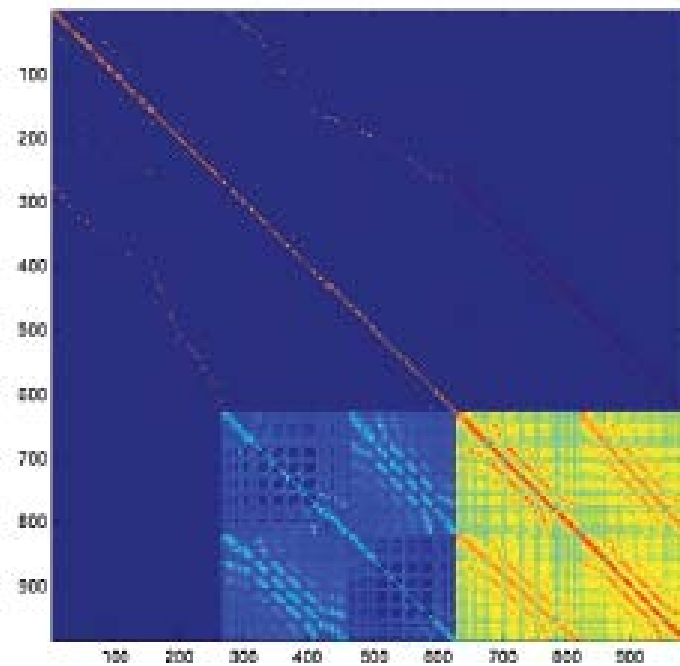
$$\Lambda_m^S = \Omega_m^S \times \hat{\mathbf{n}}$$

$$-\hat{\mathbf{n}} \times \hat{\mathbf{n}} \times \Omega_{N_V+m} \Big|_{\mathbf{r} \in S} = \Omega_m^S$$

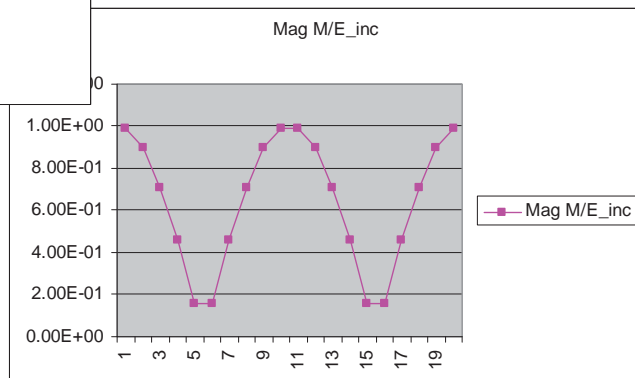
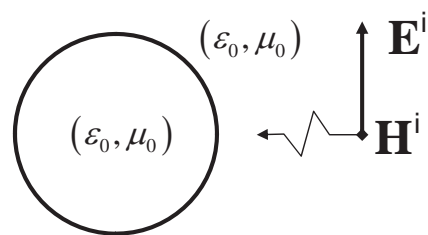
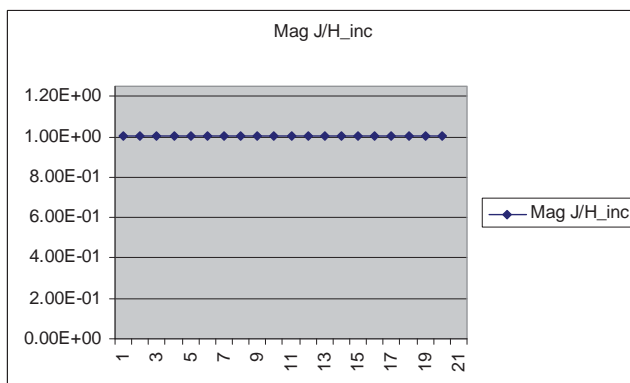
## Complete System of Coupled FEM and Integral (Hybrid) Equations

$$\begin{bmatrix} \left[ Y_{mn}^{VV} \right] & \left[ Y_{mn}^{VS} \right] & [0] \\ \left[ Y_{mn}^{SV} \right] & \left[ Y_{mn}^{SS} \right] & \left[ \gamma_{mn}^{SS} \right] \\ [0] & \left[ Z_{mn}^{SS} / \eta_0^2 \right] & \left[ \hat{\beta}_{mn}^{SS} \right] \end{bmatrix} \begin{bmatrix} \left[ V_n^V \right] \\ \left[ V_n^S \right] \\ \left[ I_n^S \right] \end{bmatrix} = \begin{bmatrix} \left[ I_m^{-,V} \right] \\ \left[ I_m^{-,S} \right] \\ \left[ I_m^{\text{inc}} \right] \end{bmatrix}$$

## Typical Matrix Structure for Hybrid Problems



## Check: Reduce Medium to Free Space



**End of Note 6**

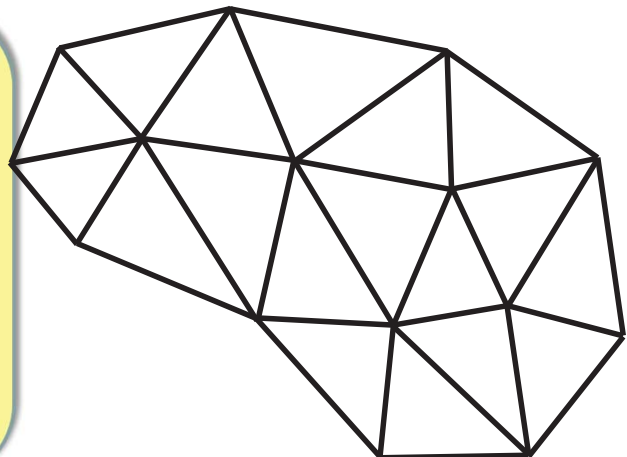
# Low Frequency Breakdown of Integral and Helmholtz Equations

Donald R. Wilton  
Dept. of Electrical and Computer Engineering  
University of Houston  
Houston, TX 77096 USA  
wilton@uh.edu

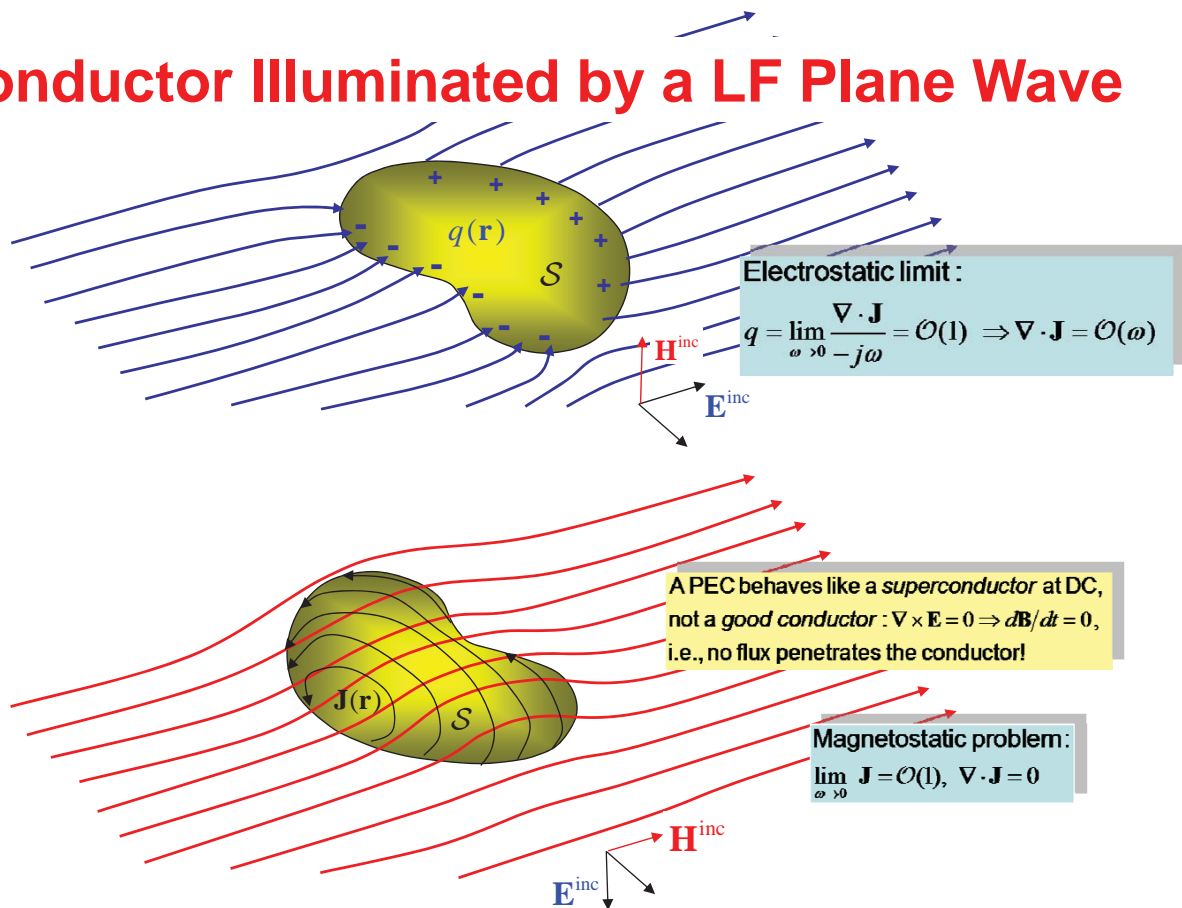
## Mesh Index Notation

- V - Number of mesh nodes or vertices
- E - Number of mesh edges
- F - Number of mesh faces
- B - Number of boundary edges and vertices

	test	source
vertex indices	$u$	$v$
global edge indices	$m$	$n$
local edge indices	$i$	$j$
face indices	$e$	$f$



## Conductor Illuminated by a LF Plane Wave



## EFIE and Vector Helmholtz Equations at Low Frequencies

- EFIE (strong form) :**

$$\mathcal{L}\mathbf{J} \equiv \left[ j\omega\mu \int_S G(\mathbf{r}, \mathbf{r}') \mathbf{J}(\mathbf{r}') dS' - \frac{\nabla}{j\omega\epsilon} \int_S G(\mathbf{r}, \mathbf{r}') \nabla \cdot \mathbf{J}(\mathbf{r}') dS' \right]_{\text{tan}} = \mathbf{E}_{\text{tan}}^{\text{inc}}, \mathbf{r} \in S$$

$$\xrightarrow{\omega \rightarrow 0} \mathcal{L}_{\text{LF}}\mathbf{J} \equiv \left[ -\frac{\nabla}{j\omega\epsilon} \int_S G(\mathbf{r}, \mathbf{r}') \nabla \cdot \mathbf{J}(\mathbf{r}') dS' \right]_{\text{tan}} = \mathbf{E}_{\text{tan}}^{\text{inc}}$$

$\Rightarrow$  Any divergenceless current ( $\nabla \cdot \mathbf{J}_h(\mathbf{r}') = 0$ ) distribution on  $S$  is a homogeneous solution,  $\mathcal{L}_{\text{LF}}\mathbf{J}_h = 0$ , implying *non-uniqueness of solutions at low frequencies*.

- Helmholtz Eq. (strong form) :**

$$\mathcal{L}\mathbf{E} \equiv \nabla \times \mu_r^{-1} \nabla \times \mathbf{E} - \omega^2 \mu_0 \epsilon_0 \epsilon_r \mathbf{E} = -j\omega\mu_0 \mathbf{J}, \mathbf{r} \in \mathcal{D} = S \text{ (2-D) or } \mathcal{V} \text{ (3-D)}$$

$$\xrightarrow{\omega \rightarrow 0} \mathcal{L}_{\text{LF}}\mathbf{E} \equiv \nabla \times \mu_r^{-1} \nabla \times \mathbf{E} = -j\omega\mu_0 \mathbf{J}$$

$\Rightarrow$  Any curl-free field ( $\nabla \times \mathbf{E}_h = 0$ ) in  $\mathcal{D}$  is a homogeneous solution,  $\mathcal{L}_{\text{LF}}\mathbf{E}_h = 0$ , implying *non-uniqueness of solutions at low frequencies*.

## Helmholtz Decomposition of EFIE Current

- **EFIE current splitting :**

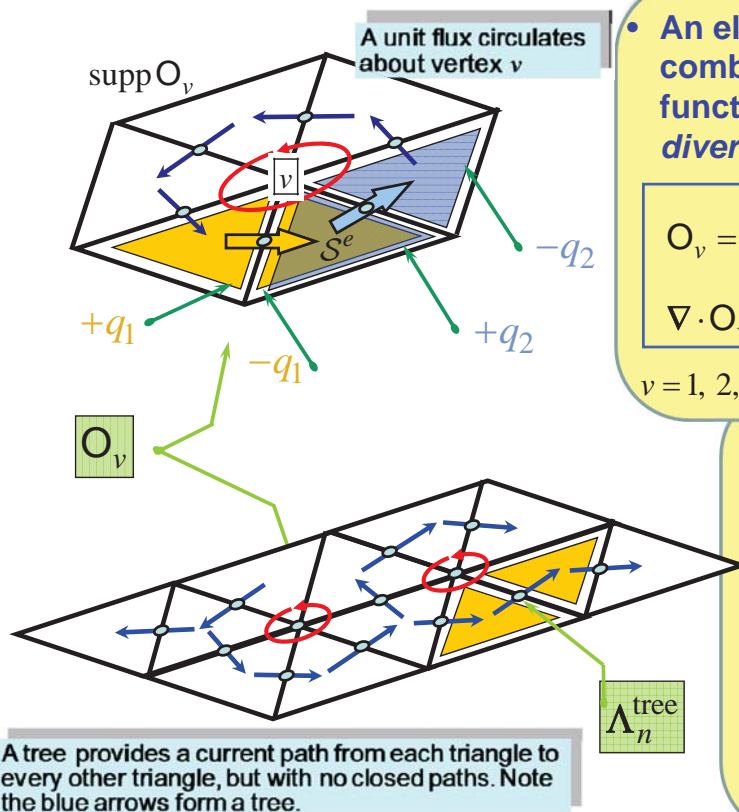
$$\mathbf{J} = \underbrace{\mathbf{J}^0}_{\substack{\text{divergenceless,} \\ \text{magnetostatic}}} + \underbrace{\mathbf{J}^\star}_{\substack{\text{non-divergenceless,} \\ \text{electrostatic}}}$$

- **Low frequency behavior :**

$$\mathbf{J} \xrightarrow{\omega \rightarrow 0} \mathbf{J}^0 \Rightarrow \mathbf{J}^0 = \mathcal{O}(1) \text{ (real)}$$

$$q = \frac{\nabla \cdot \mathbf{J}^\star}{-j\omega} = \mathcal{O}(1) \text{ (real)} \Rightarrow \mathbf{J}^\star = \mathcal{O}(\omega) \text{ (imaginary)}$$

## Loop-Tree Basis Decomposition



- An elemental “loop” is a linear combination of patch basis functions to produce a *divergence-free* basis function

$$\mathbf{O}_v = \frac{\Lambda_{i+1}^e}{l_{i+1}} - \frac{\Lambda_{i-1}^e}{l_{i-1}}, \quad \mathbf{r} \in \mathcal{S}^e \subset \text{supp } \mathbf{O}_v$$

$$\nabla \cdot \mathbf{O}_v = 0 \Rightarrow q_1 = q_2$$

$$v = 1, 2, \dots, \# \text{ interior vertices} = V - B$$

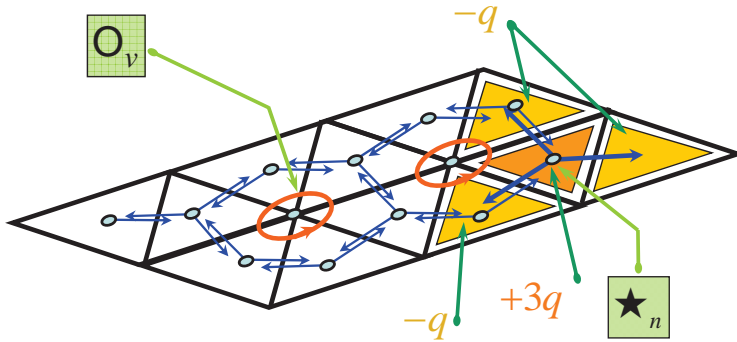
**At low frequencies:**

- $\mathbf{O}_v$  forms a magnetostatic source (current loop)
- $\Lambda_n^{\text{tree}}$  forms an electrostatic source (charge dipole)

$$n = 1, 2, \dots, \# \text{ triangles} - 1 = F - 1,$$

$$V - B + F - 1 = E - B = N$$

## Loop-Star Basis Decomposition



At low frequencies:

- $O_v$  becomes a magnetostatic source (current loop)
- $\star_e$  becomes an electrostatic source (charge multipole)

- $O_v$  is a vertex-based source
- $\star_e$  is an element-based source
- $\star_e$  bases are linear combinations of  $\Lambda_n^{\text{tree}}$  bases and vice versa

In principle, the loop-star decomposition eliminates the necessity of identifying a “tree” on triangularly meshed surfaces

## Loop Basis Representation

- We can write a loop basis  $O_v$  about interior vertex  $v$  containing triangle  $S^e$  in its support,  $\text{supp} O_v$ , and with the  $i$ -th local vertex of  $S^e$  corresponding to vertex  $v$ , in various ways :

$$O_v = \frac{\Lambda_{i+1}^e}{l_{i+1}} - \frac{\Lambda_{i-1}^e}{l_{i-1}} = \frac{l_i}{2A^e} = \frac{\hat{l}_i}{h_i} = \frac{\hat{\mathbf{n}} \times \hat{\mathbf{h}}_i}{h_i}, \quad \mathbf{r} \in S^e \subset \text{supp} O_v,$$

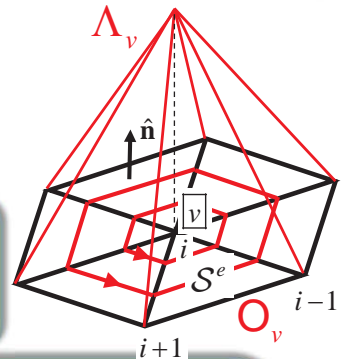
but perhaps most useful is

$$O_v = \nabla \xi_i \times \hat{\mathbf{n}}, \quad \mathbf{r} \in S^e \subset \text{supp} O_v$$

- For an arbitrary, continuous vector  $\mathbf{A}$  on  $S^e$ , we have

$$\int_{S^e} (\nabla \xi_i \times \hat{\mathbf{n}}) \cdot \mathbf{A} dS = - \int_{S^e} (\nabla \xi_i \times \mathbf{A}) \cdot \hat{\mathbf{n}} dS = \int_{S^e} (\xi_i \hat{\mathbf{n}} \cdot \nabla \times \mathbf{A}) dS - \oint_{\partial S^e} \xi_i \mathbf{A} \cdot d\mathcal{C}$$

(Van Bladel, A3.57)



where the contour integral vanishes when contributions from all adjacent triangles with a common vertex are added, so that

$$\langle O_v; \mathbf{A} \rangle = \int_S O_v \cdot \mathbf{A} dS = \int_S (\Lambda_v \hat{\mathbf{n}} \cdot \nabla \times \mathbf{A}) dS = \langle \Lambda_v \hat{\mathbf{n}}; \nabla \times \mathbf{A} \rangle,$$

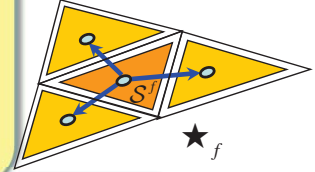
where  $\Lambda_v = \xi_i$ ,  $\mathbf{r} \in S^e \subset \text{supp} O_v$  is the scalar rooftop function with peak at node  $v$ .

Hence, testing a continuous vector with a loop function is equivalent to averaging the rooftop-weighted normal component of the vector's curl over the loop's support.

# Tree, Star Basis Representations

- *Tree bases* are usual basis set but with any tree links forming closed loops removed from the set :  $\{\Lambda_n^{\text{tree}}\} \subset \{\Lambda_n\}$
- *Star bases* are not uniquely defined; two possible definitions are

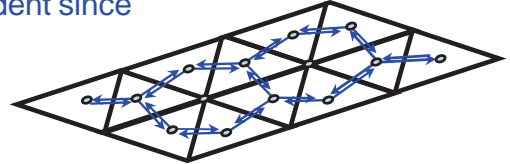
$$\star_f = \sum_n \sigma_{fn}^* \Lambda_n, \quad \sigma_{fn}^* = \pm 1 \quad \text{or} \quad \sigma_{fn}^* = \pm \frac{1}{\ell_n}$$



where the sum is over edge DoFs for edges of element  $f$  ( $S^f$ ) and the signs are chosen so current flows out of triangular face  $f$  and into adjacent faces.

- We note that only  $F - 1$  of the star bases are independent since

$$\sum_{f=1}^F \star_f = 0.$$



- The divergence of star bases is simply

$$\nabla \cdot \star_f = \sum_n \sigma_{fn}^* \nabla \cdot \Lambda_n$$

- The star and loop bases form a quasi-Helmholtz decomposition of  $\mathbf{J}$  :

$$\mathbf{J}(\mathbf{r}') \approx \underbrace{\sum_{v=1}^{V-B} I_v^O \mathbf{O}_v}_{\text{divergenceless}} + j\omega \underbrace{\sum_{f=1}^{F-1} P_f^* \star_f}_{\text{non-divergenceless}}$$

## Loop- and Star-Tested EFIE

- Testing EFIE with a loop basis  $\mathbf{O}_u$  :

$$\cancel{j\omega\mu} \langle \mathbf{O}_u; G(\mathbf{r}, \mathbf{r}'), \mathbf{J}(\mathbf{r}') \rangle + \frac{1}{j\omega\epsilon} \langle \nabla \cdot \mathbf{O}_u, G(\mathbf{r}, \mathbf{r}'), \nabla \cdot \mathbf{J} \rangle$$

$$= \langle \mathbf{O}_u; \mathbf{E}^{\text{inc}} \rangle = \langle \Lambda_u \hat{\mathbf{n}}; \nabla \times \mathbf{E}^{\text{inc}} \rangle = -\cancel{j\omega\mu} \langle \Lambda_u \hat{\mathbf{n}}; \mathbf{H}^{\text{inc}} \rangle$$

$$\Rightarrow \langle \mathbf{O}_u; G(\mathbf{r}, \mathbf{r}'), \mathbf{J}(\mathbf{r}') \rangle = -\langle \Lambda_u \hat{\mathbf{n}}; \mathbf{H}^{\text{inc}} \rangle, \quad u = 1, 2, \dots, V - B,$$

$$\left( \text{weak form of magnetostatic integral eq., } \hat{\mathbf{n}} \cdot \mathbf{H}^{\text{sc}}[\mathbf{J}^0] = \hat{\mathbf{n}} \cdot \frac{1}{\mu} \nabla \times \mathbf{A}[\mathbf{J}^0] = -\hat{\mathbf{n}} \cdot \mathbf{H}^{\text{inc}} \right)$$

- Now expand the surface current in terms of loops and star (or tree) bases :

$$\mathbf{J}(\mathbf{r}') \approx \sum_{v=1}^{V-B} I_v^O \mathbf{O}_v + j\omega \sum_{f=1}^{F-1} P_f^* \star_f \quad \left( \mathbf{J}(\mathbf{r}') \approx \sum_{v=1}^{V-B} I_v^O \mathbf{O}_v + j\omega \sum_{n=1}^{F-1} P_n^{\text{tree}} \Lambda_n^{\text{tree}} \right)$$

Substitute into the EFIE and the boxed eq. above; test with star (or tree) bases  $\star_e$ , yielding

$$\begin{bmatrix} \langle \mathbf{O}_u; G, \mathbf{O}_v \rangle & j\omega \langle \mathbf{O}_u; G, \star_f \rangle \\ j\omega\mu \langle \star_e; G, \mathbf{O}_v \rangle & \left[ \frac{1}{\epsilon} \langle \nabla \cdot \star_e, G, \nabla \cdot \star_f \rangle - \omega^2 \mu \langle \star_e; G, \star_f \rangle \right] \end{bmatrix} \begin{bmatrix} I_v^O \\ P_f^* \end{bmatrix} = \begin{bmatrix} -\langle \Lambda_u \hat{\mathbf{n}}; \mathbf{H}^{\text{inc}} \rangle \\ \langle \star_e; \mathbf{E}^{\text{inc}} \rangle \end{bmatrix}$$

$$\xrightarrow{\omega \rightarrow 0} \begin{bmatrix} \langle \mathbf{O}_u; \frac{1}{4\pi R}, \mathbf{O}_v \rangle & 0 \\ 0 & \left[ \frac{1}{\epsilon} \langle \nabla \cdot \star_e, \frac{1}{4\pi R}, \nabla \cdot \star_f \rangle \right] \end{bmatrix} \begin{bmatrix} I_v^O \\ P_f^* \end{bmatrix} = \begin{bmatrix} -\langle \Lambda_u \hat{\mathbf{n}}; \mathbf{H}^{\text{inc}} \rangle \\ \langle \star_e; \mathbf{E}^{\text{inc}} \rangle \end{bmatrix} \quad (\text{or } \star_{e,f} \rightarrow \Lambda_{m,n}^{\text{tree}})$$

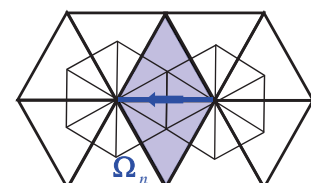
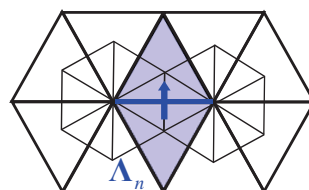
## Summary of EFIE Low Frequency Treatment

- Split surface current  $\mathbf{J}$  into a divergenceless and non - divergenceless part using loop and star (or tree) bases, respectively.
- Equate the EFIE's surface curl and quasi - divergence parts by testing with loop and star (or tree) bases, respectively.
- The separated parts require appropriate frequency scaling to reduce to static limits.
- The electrostatic limit approximates the integral equation  $-\nabla\Phi[q]=\mathbf{E}^{\text{inc}}$ , with constraint  $\int_S q dS = 0$ , by the matrix equation  $\left[ \langle \nabla \cdot \star_m, \frac{1}{4\pi\epsilon R} \nabla \cdot \star_n \rangle \right] [P_n^\star] = \langle \star_m; \mathbf{E}^{\text{inc}} \rangle$ , where  $\Phi[q]$  is the electrostatic scalar potential in terms of surface charge  $q$ , expanded as a superposition of charge dipoles to satisfy the constraint. Testing the equation with stars (or tree) ensures no closed path integrals over the conservative electrostatic field are formed.
- The magneostatic limit approximates the integral equation  $-(1/\mu)\hat{\mathbf{n}} \cdot \nabla \times \mathbf{A}[\mathbf{J}] = \hat{\mathbf{n}} \cdot \mathbf{H}^{\text{inc}}$  with constraint  $\nabla \cdot \mathbf{J} = 0$ , by the matrix equation  $\left[ -\langle \mathbf{O}_u; \frac{1}{4\pi R} \mathbf{O}_v \rangle \right] [I_v^O] = \langle \Lambda_v \hat{\mathbf{n}}; \mathbf{H}^{\text{inc}} \rangle$ , where  $\mathbf{A}[\mathbf{J}]$  is the magnetostatic vector potential due to the surface current  $\mathbf{J}$  expanded in divergence - less loop bases to satisfy the constraint.

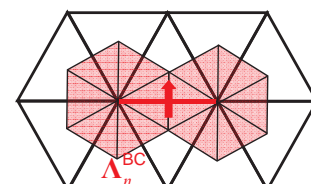
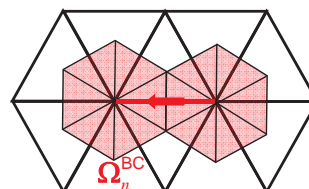
## Further Considerations and Comments

- In practice, using tree rather than star basis and testing functions yields better conditioned systems.
- Recently, so - called Buffa - Christiansen bases,  $\Lambda_n^{\text{BC}}$  and  $\Omega_n^{\text{BC}}$ , have proved useful as testing functions, improving both low frequency behavior and the discretization of various operators. They are also especially useful in discretizing so - called Calderon preconditioners. "BC" loop and star bases can also be defined. All BC and related bases are defined on the "barycentric mesh," and are a superposition of the usual  $\Lambda$  functions defined on that mesh.

**RWG div- and curl-conforming bases**



**BC div- and curl-conforming bases are also quasi-div and quasi-curl conforming, rsp.**



## Helmholtz Decomposition of Electric Field

- E - field splitting :**

$$\mathbf{E} = -j\omega\mathbf{A} - \overbrace{\nabla\Phi}^{\text{curl-free}}$$

$$\xrightarrow{\omega \rightarrow 0} \underbrace{\mathbf{E}^0}_{\substack{\text{divergenceless,} \\ \text{magnetostatic}}} + \underbrace{\mathbf{E}^\star}_{\substack{\text{curl-free,} \\ \text{electrostatic}}}$$

- Low frequency behavior :**

$$q = \nabla \cdot (\epsilon \mathbf{E}^\star) = \mathcal{O}(1) \text{ (real)} \Rightarrow \boxed{\mathbf{E}^\star = \mathcal{O}(1) \text{ (real)}}$$

$$\mathbf{E}^0 \xrightarrow{\omega \rightarrow 0} -j\omega\mathbf{A}, \nabla \cdot \mathbf{A} = 0 \Rightarrow \boxed{\mathbf{E}^0 = \mathcal{O}(\omega) \text{ (imaginary)}}$$

## Dual Loop- and Star-Tested Helmholtz Eq.

- Consider the vector Helmholtz equation,

$$\nabla \times \mu_r^{-1} \nabla \times \mathbf{E} - \omega^2 \mu_0 \epsilon_0 \epsilon_r \mathbf{E} = -j\omega \mu_0 \mathbf{J},$$

- We expand the field in the following quasi-Helmholtz decomposition :

$$\mathbf{E}(\mathbf{r}') \approx \overbrace{\sum_{v=1}^{V-B} V_v^\star \star_v}^{\text{curl-free}} + j\omega \overbrace{\sum_{f=1}^{F-1} A_f^0 \mathbf{O}_f}^{\text{non-curl free}}$$

where in this case,

- $\nabla \times \star_v = 0$
- $\langle \star_v; \mathbf{A} \rangle = \int \star_v \cdot \mathbf{A} d\mathcal{D} = \int (\Lambda_v \nabla \cdot \mathbf{A}) d\mathcal{D} = \langle \Lambda_v, \nabla \cdot \mathbf{A} \rangle$  for  $\mathbf{A}$  arbitrary, continuous  
hence  $\langle \star_v; \mathbf{J} \rangle = \langle \Lambda_v, \nabla \cdot \mathbf{J} \rangle = -j\omega \langle \Lambda_v, q \rangle$
- $\langle \mathbf{A}; \nabla \times \mu_r^{-1} \nabla \times \mathbf{E} \rangle = \langle \nabla \times \mathbf{A}; \mu_r^{-1} \nabla \times \mathbf{E} \rangle - \oint_{\partial \mathcal{D}} (\mathbf{A} \times \mu_r^{-1} \nabla \times \mathbf{E}) \cdot \hat{\mathbf{u}} d\mathcal{B}$ , if  $\mathbf{A}, \mathbf{E}$  continuous

Substituting the E - field expansion into the Helmholtz eq. and testing with loops and stars yields

$$\begin{bmatrix} \left[ \begin{array}{cc} \epsilon_0 \epsilon_r \langle \star_u; \star_v \rangle & j\omega \epsilon_0 \epsilon_r \langle \star_u; \mathbf{O}_f \rangle \\ j\omega \mu_0 \epsilon_0 \epsilon_r \langle \mathbf{O}_e; \star_v \rangle & \langle \nabla \times \mathbf{O}_e; \mu_r^{-1} \nabla \times \mathbf{O}_f \rangle - \omega^2 \mu_0 \epsilon_0 \epsilon_r \langle \mathbf{O}_e; \mathbf{O}_f \rangle \end{array} \right] \begin{bmatrix} V_v^\star \\ A_f^0 \end{bmatrix} = \begin{bmatrix} \langle \Lambda_u, q \rangle \\ -\mu_0 \langle \mathbf{O}_e; \mathbf{J} \rangle \end{bmatrix} \\ \xrightarrow{\omega \rightarrow 0} \begin{bmatrix} \left[ \begin{array}{cc} \epsilon_0 \epsilon_r \langle \star_u; \star_v \rangle & [0] \\ [0] & \langle \nabla \times \mathbf{O}_e; \mu_r^{-1} \nabla \times \mathbf{O}_f \rangle \end{array} \right] \begin{bmatrix} V_v^\star \\ A_f^0 \end{bmatrix} = \begin{bmatrix} \langle \Lambda_u, q \rangle \\ -\mu_0 \langle \mathbf{O}_e; \mathbf{J} \rangle \end{bmatrix} \end{bmatrix}$$

# Dual Star Basis Representation

- We define a *dual* star basis  $\star_v$  about an interior vertex  $v$  containing  $\mathcal{D}^e$  in its support,  $\text{supp } \star_v$ , and with the  $i$ -th local vertex of  $\mathcal{D}^e$  corresponding to vertex  $v$ :

$$\star_v = \mathbf{O}_v \times \hat{\mathbf{n}} = \frac{\boldsymbol{\Omega}_{i-1}^e}{\ell_{i-1}} - \frac{\boldsymbol{\Omega}_{i+1}^e}{\ell_{i+1}} = \frac{\hat{\mathbf{h}}_i}{h_{i,i}}, \quad \mathbf{r} \in \mathcal{D}^e \subset \text{supp } \star_v$$

or more usefully,

$$\star_v = -\nabla \xi, \quad \mathbf{r} \in \mathcal{D}^e \subset \text{supp } \star_v$$

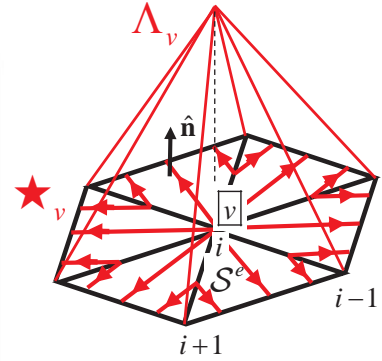
- Note  $\nabla \times \star_v = -\nabla \times \nabla \xi = 0$ , i.e.  $\star_v$  is curl-free.
- For an arbitrary, continuous vector  $\mathbf{A}$  on  $\mathcal{D}^e$ , we have

$$-\int_{\mathcal{D}^e} \nabla \xi \cdot \mathbf{A} d\mathcal{D} = \int_{\mathcal{D}^e} (\xi_i \nabla \cdot \mathbf{A}) d\mathcal{D} - \oint_{\partial \mathcal{D}^e} \xi_i \mathbf{A} \cdot \hat{\mathbf{n}} dB$$

where the contour integral vanishes when contributions from all adjacent elements with a common vertex are added, so that

$$\langle \star_v; \mathbf{A} \rangle = \int_{\mathcal{D}} \star_v \cdot \mathbf{A} d\mathcal{D} = \int_{\mathcal{D}} (\Lambda_v \nabla \cdot \mathbf{A}) d\mathcal{D} = \langle \Lambda_v, \nabla \cdot \mathbf{A} \rangle,$$

where  $\Lambda_v = \xi_i, \mathbf{r} \in \mathcal{D}^e \subset \text{supp } \star_v$  is the scalar rooftop function with peak at node  $v$ . Hence, testing a continuous vector with a star function is equivalent to averaging its rooftop-weighted divergence over the star's support.



# Dual Loop Basis Representations

- Dual loop bases are not uniquely defined; two possible definitions are

$$\mathbf{O}_f = \sum_n \sigma_{fn}^* \boldsymbol{\Omega}_n, \quad \sigma_{fn}^* = \pm 1 \quad \text{or} \quad \sigma_{fn}^* = \pm \frac{1}{\ell_n}$$

where the sum is over edge DoFs for edges of face  $f$  ( $\mathcal{S}^f$ ) and the signs are chosen so flux is parallel to edges of  $f$  and defined on adjacent elements.

- We note that only  $F - 1$  of the star bases are independent since

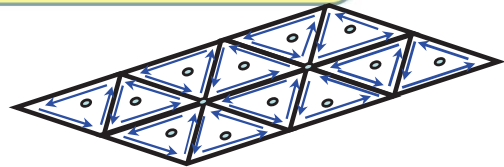
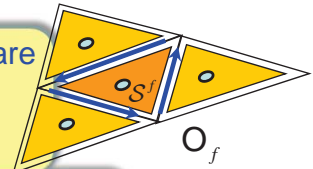
$$\sum_{n=1}^F \mathbf{O}_n = 0.$$

- The curl of loop bases may be simply defined by

$$\nabla \times \mathbf{O}_f = \sum_n \sigma_{fn}^* \nabla \times \boldsymbol{\Omega}_n$$

- The star and loop bases form a quasi-Helmholtz decomposition of  $\mathbf{E}$ :

$$\mathbf{E}(\mathbf{r}) \approx \underbrace{\sum_{v=1}^{V-B} V_v^* \star_v}_{\text{curl-free}} + j\omega \underbrace{\sum_{f=1}^{F-1} A_f^0 \mathbf{O}_f}_{\text{non-curl free}}$$



## Summary of Helmholtz Equation Low Frequency Treatment

- Split field  $\mathbf{E}$  into a divergenceless and non - divergenceless part using loop and star (or tree) bases, respectively.
- Equate the Helmholtz equations curl and quasi - divergence parts by testing with loop and star (or tree) bases, respectively. For simplicity, we illustrated only for the 2-D case.
- The separated parts require appropriate frequency scaling to reduce to static limits.
- The electrostatic limit approximates the PDE  $\nabla \cdot (\epsilon \mathbf{E}) = q$  with constraint  $\nabla \times \mathbf{E} = 0$  by the matrix equation  $[\epsilon_0 \epsilon_r \langle \star_u, \star_v \rangle][V_v^\star] = \langle \Lambda_u; q \rangle$ , where  $q$  is the volume charge density. Star (or tree) testing the equation ensures no closed path integrals over the conservative electrostatic field are formed.
- The magneostatic limit approximates the PDE  $\nabla \times \nabla \times \mathbf{A} = -\mu \mathbf{J}$  with constraint  $\nabla \cdot \mathbf{A} = 0$ , by the matrix equation  $[\langle \nabla \times \mathbf{O}_e; \mu_r^{-1} \nabla \times \mathbf{O}_f \rangle][A_v^0] = [-\mu_0 \langle \mathbf{O}_e; \mathbf{J} \rangle]$ , where  $\mathbf{A}$  is the magnetostatic vector potential expanded in loop bases to satisfy the constraint.

## References

- Wilton, D.R., and A.W. Glisson, "On Improving the Stability of the Electric Field Integral Equation at Low Frequencies," 1981 AP-S/URSI International Symposium, Los Angeles, California, June 1981.
- Wilton, D.R., "Topological Considerations in Surface Patch and Volume Cell Modeling of Electromagnetic Scatterers," 1983 URSI International Symposium on Electromagnetic Theory, Santiago de Compostela, Spain, August, 1983.
- M. B. Stephanson and J.-F. Lee, "Preconditioner electric field integral equation using Calderon identities and dual loop/star basis functions," IEEE Trans. Antennas Propag., vol. 57, no. 4, pp. 1274–1279, Apr. 2009.
- S. Yuan, J.-M. Jin, and Z. Nie, "EFIE analysis of low-frequency problems with loop-star decomposition and Calderon multiplicative preconditioner," IEEE Trans. Antennas Propag., vol. 58, no. 3, pp. 857–867, 2010.

**End of Note 7**

IML

ACA

MLMA

# Fast Methods

MLFMA

Donald R. Wilton  
Vikram Jandhyala

SVD

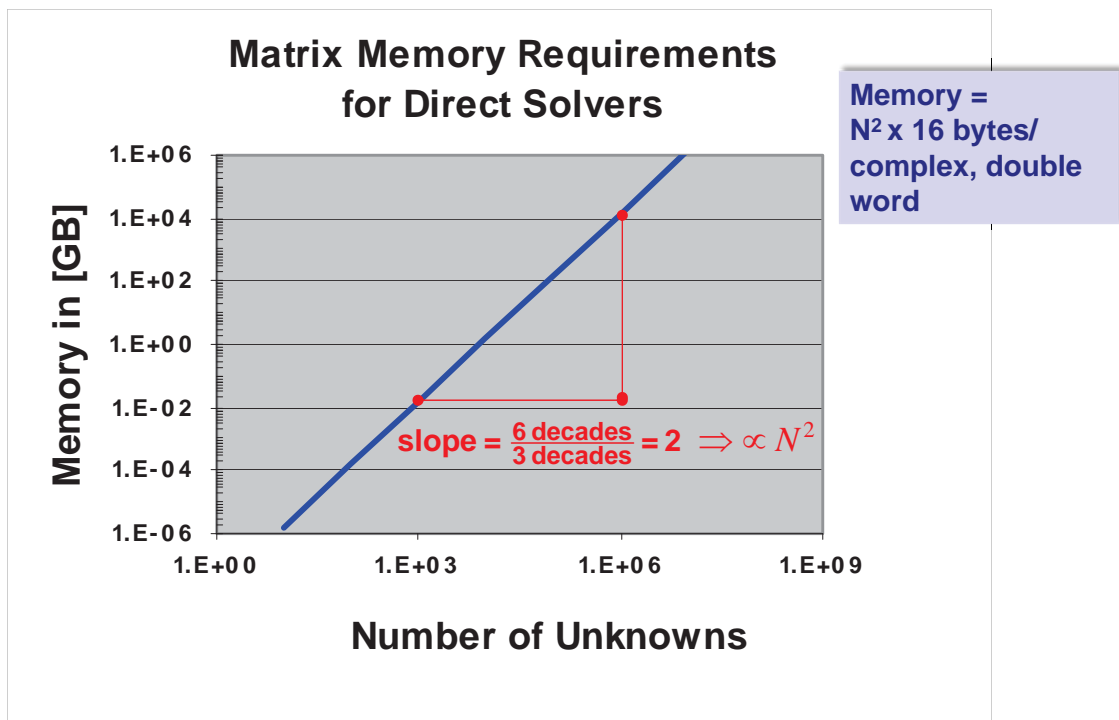
CGFFT

GIFFT

Precorrected FFT

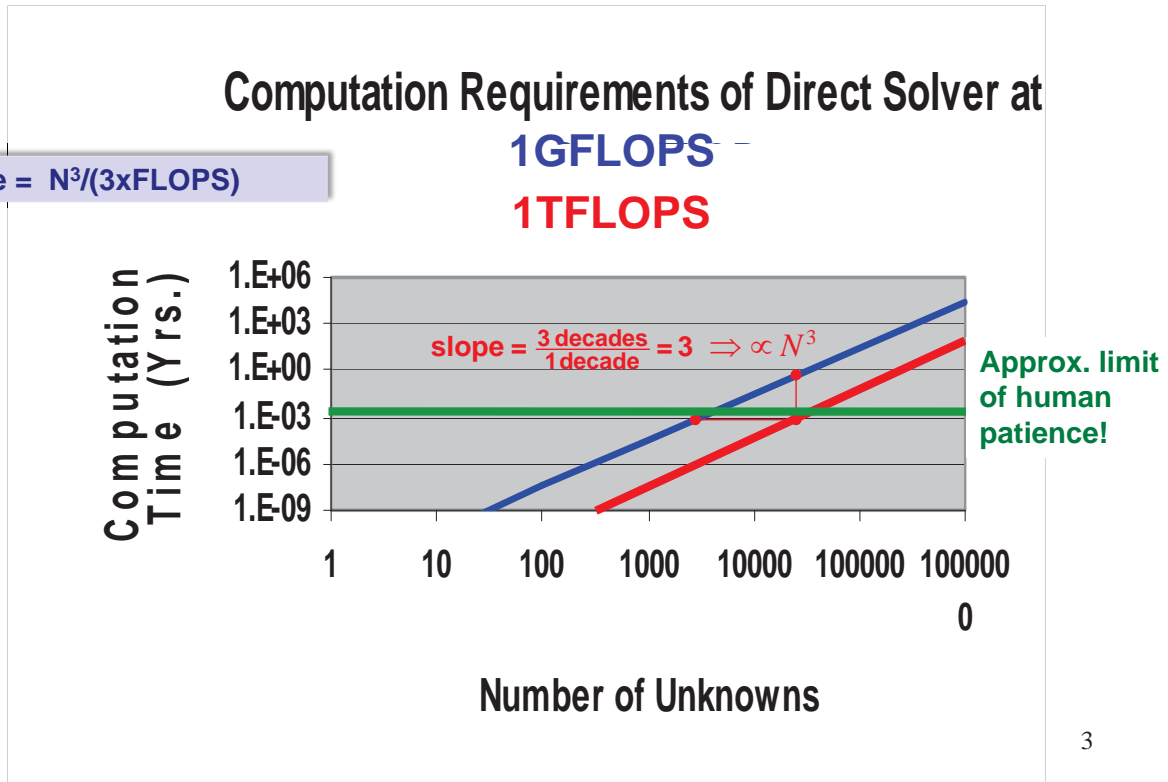
1

## Why Are Fast Methods Needed for Large MoM Problems?



2

# Approximate Computation Times for Large Problems



## Main Features of Fast Methods

- We assume solution uses an *iterative*, not a *direct* method
- Use *redundant information* in MoM matrix and/or Green's function to reduce storage requirements ("compress" the matrix) and speed up the solution process

## Iterative Methods

- Instead of directly solving

$$Ax = b$$

by, e.g. Gaussian elimination, we iterate on an equation of the form

$$x_n = B_n x_{n-1} + c_n, \quad n = 1, 2, \dots, \quad B_n = B_n(A, x_{n-1}, x_{n-2}, \dots, r_{n-1})$$

where  $x_0$  is an initial guess, until we achieve

convergence, say  $\|x_n - x_{n-1}\| < \varepsilon_1$ , and/or  $\| \overbrace{Ax_n - b}^{r_n} \| < \varepsilon_2$ .

- The process must usually be sped up by *preconditioning* the system, i.e., premultiplying by a matrix  $P$  and solving the modified system

$$PAx = Pb$$

5

## Iterating the Preconditioned System

- The preconditioner should in some sense approximate the inverse of the system matrix,  $P \approx A^{-1}$ , or equivalently  $PA \sim I$
- When this is the case, we may view the term  $(I - PA)$  in the *identity*

$$x = \underbrace{(I - PA)}_{\text{"small"}} x + \underbrace{Pb}_{\approx A^{-1}b}$$

← add:

$$0 = -PAx + Pb$$

$$x = Ix$$

as a "small" correction to the RHS, leading to the simple iterative procedure

$$x_n = (I - PA)x_{n-1} + Pb \quad \Leftrightarrow \quad x_n = B_n x_{n-1} + c_n, \quad n = 1, 2, \dots$$

6

## Iterative Convergence of the Preconditioned System

- Beginning with  $\mathbf{x}_0 \equiv \mathbf{0}$ , successive iterations of the simple iterative procedure yield

$$\mathbf{x}_0 = \mathbf{0}$$

$$\mathbf{x}_1 = \mathbf{Pb}$$

$$\mathbf{x}_2 = (\mathbf{I} - \mathbf{PA})\mathbf{Pb} + \mathbf{Pb}$$

$$\mathbf{x}_3 = (\mathbf{I} - \mathbf{PA})^2 \mathbf{Pb} + (\mathbf{I} - \mathbf{PA})\mathbf{Pb} + \mathbf{Pb}$$

$$\vdots$$

$$\mathbf{x}_{n+1} = \left[ \sum_{i=0}^n (\mathbf{I} - \mathbf{PA})^i \right] \mathbf{Pb}$$

$$\mathbf{x}_n = (\mathbf{I} - \mathbf{PA})\mathbf{x}_{n-1} + \mathbf{Pb}$$

- Identifying  $(\mathbf{I} - \mathbf{PA}) \equiv \mathbf{R}$  in the identity, and noting

$$\sum_{i=0}^{\infty} \mathbf{R}^i = (\mathbf{I} - \mathbf{R})^{-1}, \quad \|\mathbf{R}\| < 1 \quad (\Rightarrow \sum_{i=0}^{\infty} (\mathbf{I} - \mathbf{PA})^i = (\mathbf{PA})^{-1})$$

we see that the solution converges to

$$\mathbf{x} = (\mathbf{PA})^{-1} \mathbf{Pb} = \mathbf{A}^{-1} \mathbf{P}^{-1} \mathbf{Pb} = \mathbf{A}^{-1} \mathbf{b}$$

if  $\|\mathbf{I} - \mathbf{PA}\| < 1$ .

7

## Observations on the Iterative Procedure

- Our *simple* procedure *may* not converge at all (i.e., if  $\|\mathbf{I} - \mathbf{PA}\| > 1$ ) though in principle, that is not the case with more sophisticated iterative algorithms. Commonly used algorithms include BiCGSTAB, GMRES, QMR, etc.
- Convergence is sped up if  $\mathbf{P}$  is close to  $\mathbf{A}^{-1}$ .
- The main computational bottleneck is the repeated calculation of the matrix/vector ("*matvec*") products  $(\mathbf{I} - \mathbf{PA})\mathbf{x}_{n-1}$ . All fast methods attempt to speed up the matrix/vector product ("*matvec*") computation.
- Modern iterative solvers require that the *user* implement the *matvec* computations to allow use of the most appropriate speedup method.

8

## Matrix/Vector Products

- The *inner product* between two vectors generates a *scalar* given by

$$\langle \mathbf{u}, \mathbf{v} \rangle = \mathbf{u}^t \mathbf{v} = [u_1, u_2, \dots, u_N] \begin{bmatrix} v_1 \\ v_2 \\ \vdots \\ v_N \end{bmatrix} = u_1 v_1 + u_2 v_2 + \dots + u_N v_N$$

The product requires approximately  $N$  operations.

- The *outer product* between two vectors generates a *matrix* given by

$$\mathbf{u} \mathbf{v}^t = \begin{bmatrix} u_1 \\ u_2 \\ \vdots \\ u_M \end{bmatrix} [v_1, v_2, \dots, v_N] = \begin{bmatrix} u_1 v_1 & u_1 v_2 & \dots & u_1 v_N \\ u_2 v_1 & u_2 v_2 & \dots & u_2 v_N \\ \vdots & \vdots & \ddots & \vdots \\ u_M v_1 & u_M v_2 & \dots & u_M v_N \end{bmatrix}$$

Matrix rank = number of rows (columns) of largest submatrix with non-vanishing determinant

Since all rows and columns are proportional, the matrix is only rank 1.

The product requires approximately  $MN$  operations.

9

## Matrix/Vector Products with Low Rank Matrices

- The sum of  $r$  *outer products* of independent vectors,

$$\sum_{p=1}^r \mathbf{u}_p \mathbf{v}_p^t \equiv \mathbf{U} \mathbf{V}^t \text{ where } \mathbf{U} \equiv [\mathbf{u}_1 \ \mathbf{u}_2 \ \dots \ \mathbf{u}_r], \mathbf{V}^t \equiv [\mathbf{v}_1 \ \mathbf{v}_2 \ \dots \ \mathbf{v}_r]^t = \begin{bmatrix} \mathbf{v}_1^t \\ \mathbf{v}_2^t \\ \vdots \\ \mathbf{v}_r^t \end{bmatrix}$$

is a matrix of rank  $r$ ; conversely, such matrices can be so factorized.

- The matrix / vector product  $\mathbf{A} \mathbf{b} (= \mathbf{A}_{M \times N} \mathbf{b}_{N \times 1})$  generally requires

$MN$  multiplies, but the product

$$\left( \sum_{p=1}^r \mathbf{u}_p \mathbf{v}_p^t \right) \mathbf{b} = \sum_{p=1}^r \mathbf{u}_p (\mathbf{v}_p^t \mathbf{b}) = \mathbf{U} (\mathbf{V}^t \mathbf{b})$$

Storage of  $\mathbf{A}$ :  $MN$

Storage of  $\mathbf{u}_p, \mathbf{v}_p$ :  $r(M + N)$

requires only about  $r(N + M)$  multiplies when performed using the

RHS grouping. If  $r \ll \min(M, N)$ ,  $\Rightarrow$  significant speedup.

- But  $r < M, N \Rightarrow \left( \sum_{p=1}^r \mathbf{u}_p \mathbf{v}_p^t \right)$  is singular; hence it must be that only *subblocks* of  $\mathbf{A}$ , *not* the entire system matrix, can be represented in this form. Such matrices are said to be *rank deficient*.

10

## Obtaining Low Rank Matrices

- Fast methods approximate *off-diagonal blocks* of the system matrix as low rank matrices that can be represented in product form,  $UV^t$ . Such blocks typically represent *far interactions* between closely grouped observation and source element *clusters*.
- There are two approaches to obtaining reduced rank blocks :
  - 1) Represent the Green's function in *separable* or *degenerate* form over the block's observer and source domains.
  - 2) Use matrix algebraic methods to directly find reduced-rank block representations

11

## Matrix-Vector Product for Sums of Separable Matrices

- Separable kernels lead to separable matrix blocks:

E.g., for simple integral eq.  $\int_{\mathcal{D}} G(\mathbf{r}, \mathbf{r}') x(\mathbf{r}') d\mathcal{D} = f(\mathbf{r}), \mathbf{r} \in \mathcal{D}$   
 with kernel expansion  $G(\mathbf{r}, \mathbf{r}') \approx \sum_{p=1}^r u_p(\mathbf{r}) v_p(\mathbf{r}'), \mathbf{r}, \mathbf{r}' \in \text{subregion of } \mathcal{D}$   
 and basis representation  $x(\mathbf{r}) \approx \sum_n x_n b_n(\mathbf{r}) = [b_n(\mathbf{r})]^t [x_n]$   
 contributions to a block of the Galerkin system matrix are

$$UV^t \mathbf{x},$$

where

$$\mathbf{U} = \left[ \langle b_m, u_p \rangle \right]_{M \times r} \quad \mathbf{x} = [x_n]_{N \times 1}$$

$$\mathbf{V} = \left[ \langle b_n, v_p \rangle \right]_{N \times r}$$

**Matrix-Vector Product for Separable Matrix:**

$$UV^t \mathbf{x} \equiv \left[ \sum_{p=1}^r \mathbf{u}_p \mathbf{v}_p^t \right] \mathbf{x} = [\mathbf{u}_1 \mathbf{u}_2 \cdots \mathbf{u}_r] [\mathbf{v}_1 \mathbf{v}_2 \cdots \mathbf{v}_r]^t \mathbf{x}$$

- $r(M+N)$  operations if performed right-to-left
- $MN(r+1)$  operations if performed left-to-right

## Approach Generalizes to More Complex Operators

- A block of an EFIE matrix becomes

$$\begin{aligned} \mathbf{Z}_{M \times N} &= j\omega\mu \sum_{p=1}^r [\langle \Lambda_m, u_p \rangle]_{M \times r} \cdot [\langle \Lambda_n, v_p \rangle]_{N \times r}^t \\ &\quad + \frac{1}{j\omega\epsilon} \sum_{p=1}^r [\langle \nabla \cdot \Lambda_m, u_p \rangle]_{M \times r} [\langle \nabla \cdot \Lambda_n, v_p \rangle]_{N \times r}^t \\ &= j\omega\mu \mathbf{U} \cdot \mathbf{V}^t + \frac{1}{j\omega\epsilon} \mathbf{U}' \mathbf{V}'^t \end{aligned}$$

where

$$\begin{aligned} \mathbf{U} &= [\langle \Lambda_m, u_p \rangle]_{M \times r}, & \mathbf{V} &= [\langle \Lambda_n, v_p \rangle]_{N \times r} \\ \mathbf{U}' &= [\langle \nabla \cdot \Lambda_m, u_p \rangle]_{M \times r}, & \mathbf{V}' &= [\langle \nabla \cdot \Lambda_n, v_p \rangle]_{N \times r} \end{aligned}$$

13

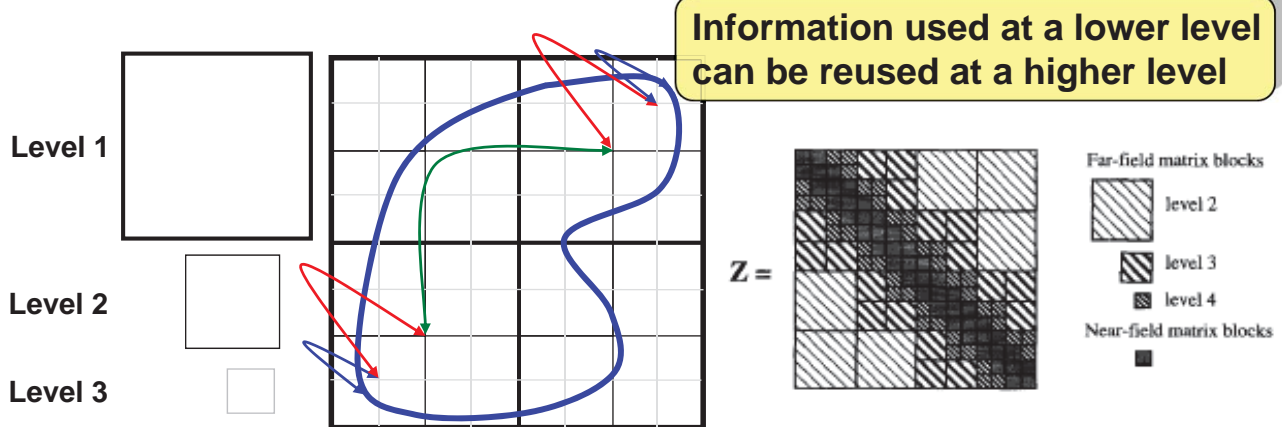
## Fast Methods Often Combine Separable Matrix Approximation with Hierarchical Methods

- Separable matrices reduce both storage and matrix vector multiplication counts from  $MN$  to  $r(M + N)$
- Unfortunately it is not possible to approximate the *entire* system matrix by a separable matrix---it will be *rank deficient* and hence have no inverse (i.e., no solution)
- Nevertheless, nearly all fast methods in computational electromagnetics are based on approximating *blocks* of the system matrix by separable matrices
- For additional speed, some hierarchical scheme must be used to transfer information at one discretization level to another

14

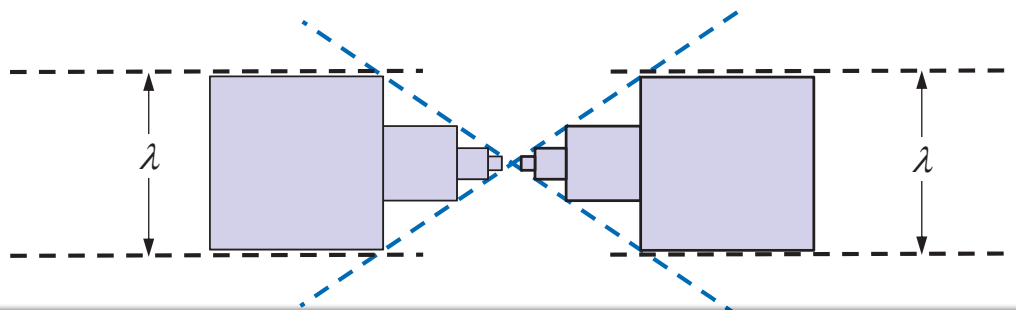
## Central Fast Method Ideas

- *Fast* methods all employ a form of matrix or Green's function rank-reduced separability
- *Multi-level* schemes gain additional efficiency by a *hierarchical* grouping scheme.



15

## Ability to Group Scales with Distance Until Wavelength Scale Enters



- Most methods apply in the quasi-static region, but performance begins to degrade when block sizes reach the wavelength scale.
- MLFMA, however scales beyond the wavelength limit.

16

## Examples of Separable Expansions of Green's Function

- Taylor Series (elegant but difficult to apply):

$$G(\mathbf{r}, \mathbf{r}') \approx \sum_{p=0}^P \sum_{q=0}^Q \frac{1}{p!q!} [(\mathbf{r} - \mathbf{r}_0) \cdot \nabla]^p [(\mathbf{r}' - \mathbf{r}_s) \cdot \nabla']^q G(\mathbf{r}, \mathbf{r}') \Big|_{\mathbf{r}=\mathbf{r}_0, \mathbf{r}'=\mathbf{r}_s}$$

- Products of terms like  $(\mathbf{r} - \mathbf{r}_0)^p (\mathbf{r}' - \mathbf{r}_s)^q$ , where  $\mathbf{r}_0, \mathbf{r}_s$  are centered in an obs. & source group, rsp.
- Works best for asymptotically smooth Green's functions, e.g. quasi-statics
- Dynamic case limited by wavelength

17

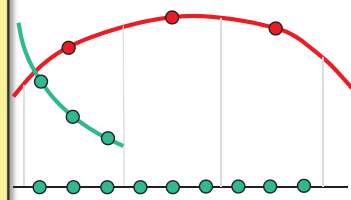
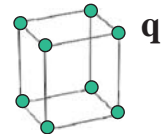
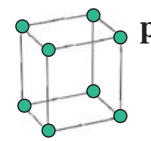
## Separable Expansions of Green's Fn, Cont'd

**Polynomial Interpolation:**

$$G(\mathbf{r}, \mathbf{r}') \approx \sum_{\mathbf{p}} \sum_{\mathbf{q}} \overbrace{G(\mathbf{r}^{(\mathbf{p})}, \mathbf{r}'^{(\mathbf{q})})}^{G_{\mathbf{p}, \mathbf{q}}} L_{\mathbf{p}}(\mathbf{r}) L_{\mathbf{q}}(\mathbf{r}'),$$

$$\mathbf{p} = (p_x, p_y, p_z), \quad \mathbf{q} = (q_x, q_y, q_z)$$

- More accuracy simply implies using high order interpolation
- Wavelength limited
- Hierarchical principle: Lagrange polynomials  $L_{\mathbf{p}}(\mathbf{r}) = L_{p_1}(x) L_{p_2}(y) L_{p_3}(z)$  at low levels (coarse discretization) are represented in terms of those at higher levels (fine discretization).



18

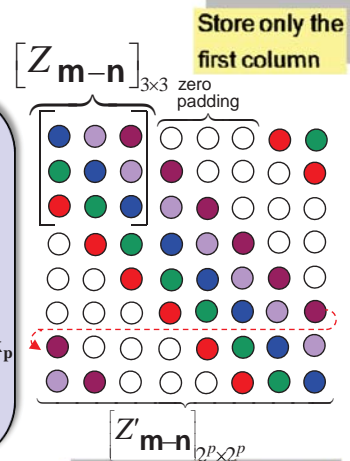
## Separable Expansions of Green's Fn, Cont'd

### CGFFT, AIM, Pre-Corrected FFT:

$$\sum_n \langle \Lambda_m, G(\mathbf{r}-\mathbf{r}'), \Lambda_n \rangle I_n \xRightarrow{\text{CGFFT}}$$

$$\sum_n \underbrace{\langle \Lambda_m, L_p \rangle}_{\text{precompute}} G_{p-q} \langle L_q, \Lambda_n \rangle I_n \xRightarrow{\text{AIM}} \underbrace{[Z'_{m-n}][I'_n]}_{\text{extended to circulant form}}$$

$$\underbrace{Z'_m}_{\text{1st col. of } Z'} = \sum_p \tilde{Z}'_p e^{-jm \cdot \mathbf{k}_p} = \text{DFT}(\tilde{Z}'_p) \Rightarrow Z'_{m-n} = \sum_p \tilde{Z}'_p e^{-jm \cdot \mathbf{k}_p} e^{jn \cdot \mathbf{k}_p}$$



$$\mathbf{m} = (m_x \hat{\mathbf{x}} + m_y \hat{\mathbf{y}} + m_z \hat{\mathbf{z}}), \quad \mathbf{k}_p = \frac{2\pi p_x}{N_x} \hat{\mathbf{x}} + \frac{2\pi p_y}{N_y} \hat{\mathbf{y}} + \frac{2\pi p_z}{N_z} \hat{\mathbf{z}}$$

For efficient FFT, the augmented array  $Z'_{m-n}$  should be dim  $2^p \times 2^p$

- Separability follows from DFT representation; FFT automatically provides hierarchical scheme
- Green's function must be convolutional
- Requires space-filling, regular grid

## Separable Expansions of Green's Fn, Cont'd

### FMM, MLFMA:

$$G(\mathbf{r}, \mathbf{r}') \approx \oint_{\hat{\mathbf{k}}} e^{j\mathbf{k} \cdot (\mathbf{r}-\mathbf{r}')} T(\hat{\mathbf{k}} \cdot \mathbf{R}_{l,l'}) e^{j\mathbf{k} \cdot (\mathbf{r}'-\mathbf{r}_r)} d\hat{\mathbf{k}}^2$$

$$\approx \sum_p \sum_q e^{j\mathbf{k}_{pq} \cdot (\mathbf{r}-\mathbf{r}_r)} T(\hat{\mathbf{k}}_{pq} \cdot \mathbf{R}_{l,l'}) e^{j\mathbf{k}_{pq} \cdot (\mathbf{r}'-\mathbf{r}_r)} \sin \theta_p \Delta \theta \Delta \phi$$

### Translation operator :

$$T(\hat{\mathbf{k}}_{pq} \cdot \mathbf{R}_{l,l'}) \equiv [T_{pq}]_{l,l'} = \sum_p \sum_q \sum_{\ell=0}^L (-j)^\ell (2\ell+1) P_\ell(\hat{\mathbf{k}}_{pq} \cdot \mathbf{R}_{l,l'})$$

- Hierarchy provided by successive translation between (multi)-levels with interpolation ( $[I_{pq}]_{l'-1}$ ) and anterpolation ( $[I_{pq}]_{l-1}$ ) of translation operator:

← increasing levels, decreasing interpolation density

$$[T_{pq}]_{l,l'} = [T_{pq}]_{l,l-1} [I_{pq}]_{l-1}^t [T_{pq}]_{l-1,l-2} [I_{pq}]_{l-2}^t$$

$$\dots \times [T_{pq}]_{3,2} [I_{pq}]_2^t [T_{pq}]_{2,2} [I_{pq}]_2 [T_{pq}]_{2,3}$$

$$\dots \times [I_{pq}]_{l'-2} [T_{pq}]_{l'-2,l'-1} [I_{pq}]_{l'-1} [T_{pq}]_{l'-1,l'}$$

increasing levels, decreasing interpolation density →

$$[I_{pq}]_{l'-1} = \hat{\mathbf{k}} \text{- space interpolation operator at level } l$$

## Examples of Direct (“Kernel-Free”) Methods

### SVD:

- Singular value decomposition can be used to directly obtain

$$\mathbf{A} \approx \mathbf{U}\mathbf{\Sigma}\mathbf{V}^\dagger$$

where

$$\mathbf{V} = [\mathbf{v}_1, \mathbf{v}_2, \dots, \mathbf{v}_r]$$

$$\mathbf{U} = [\mathbf{u}_1, \mathbf{u}_2, \dots, \mathbf{u}_r]$$

$\mathbf{\Sigma}_r = \text{diag}(\sigma_1, \sigma_2, \dots, \sigma_r)$  are the singular values

- Method needs all of the original matrix block  $\mathbf{A}$  and is inefficient

21

## Direct Methods, Cont'd

### ACA:

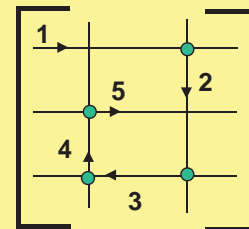
- Adaptive Cross Approximation builds a block by adding products  $\mathbf{u}_{r+1}\mathbf{v}_{r+1}^t$  that are essentially rows and columns of the residual matrix, resp.:

$$\mathbf{A} \approx \mathbf{U}_r \mathbf{V}_r^\dagger$$

where

$$\mathbf{U}_r = [\mathbf{u}_1, \mathbf{u}_2, \dots, \mathbf{u}_r]$$

$$\mathbf{V}_r = [\mathbf{v}_1, \mathbf{v}_2, \dots, \mathbf{v}_r]$$



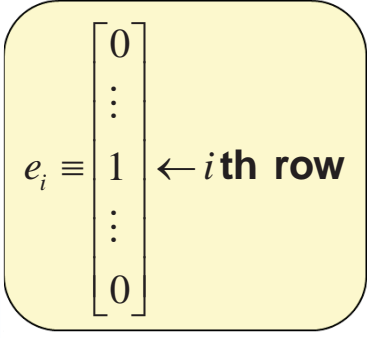
- Simple to apply
- Only necessary to compute rows and cols of  $\mathbf{A}$  needed to form  $\mathbf{U}_r, \mathbf{V}_r$
- Appears to work best for statics, moderate freqs.

22

## ACA Method, Cont'd

**ACA Algorithm:** (S.Kurz,O. Rain, and S. Rjasanow, "The Adaptive Cross-Approximation Technique for the 3-D Boundary-Element Method" IEEE TRANS. MAG., **38**, MAR. 2002.

- 1)  $e_{i_{k+1}}^T R_k = e_{i_{k+1}}^T A - \sum_{l=1}^k (u_l)_{i_{k+1}} v_l^T$
- 2)  $j_{k+1}: |(R_k)_{i_{k+1}, j_{k+1}}| = \max_j |(R_k)_{i_{k+1}, j}|$
- 3)  $v_{k+1} = e_{i_{k+1}}^T R_k / (R_k)_{i_{k+1}, j_{k+1}}$
- 4)  $u_{k+1} = A e_{j_{k+1}} - \sum_{l=1}^k (v_l)_{j_{k+1}} u_l$
- 5)  $i_{k+2}: |(u_{k+1})_{i_{k+2}}| = \max_{i \neq i_{k+1}} |(u_{k+1})_i|$
- 6)  $S_{k+1} = S_k + u_{k+1} v_{k+1}^T$ .



**Stopping criterion:**  $\|u_k\|_F \|v_k\|_F \leq \epsilon \|S_k\|_F$ .

**with recursive norm computation,**

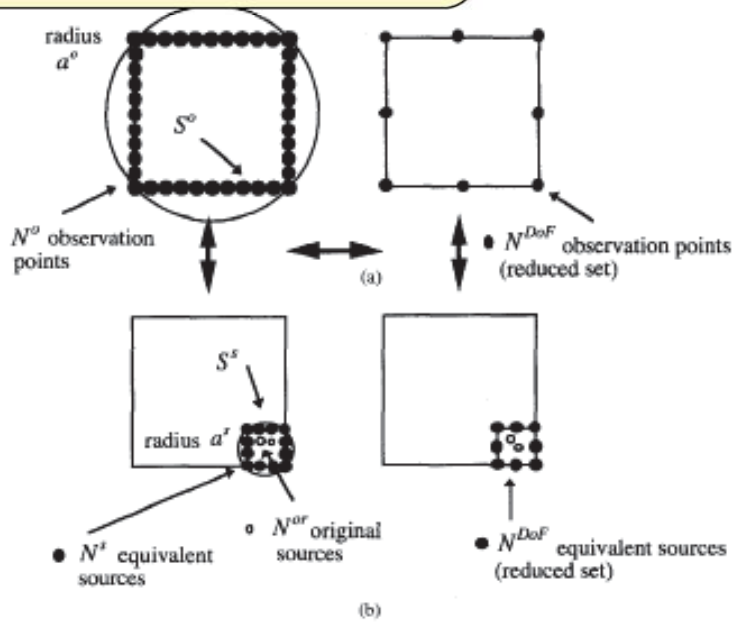
$$\|S_k\|_F^2 = \|S_{k-1}\|_F^2 + 2 \sum_{j=1}^{k-1} (u_j, u_k) (v_j, v_k) + \|u_k\|_F^2 \|v_k\|_F^2$$

## Direct Methods, Cont'd

**MLMDA**

- **Multilevel Matrix Decomposition Algorithm (Michielssen, Boag)**

- **Uses equivalence principle and far-field DoF concepts for hierarchical representation**



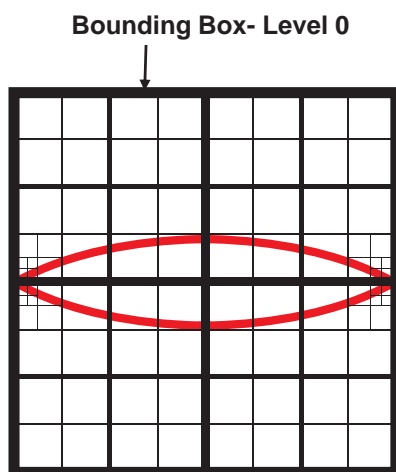
## Direct Methods, Cont'd

### Rank-Revealing QR Decomposition

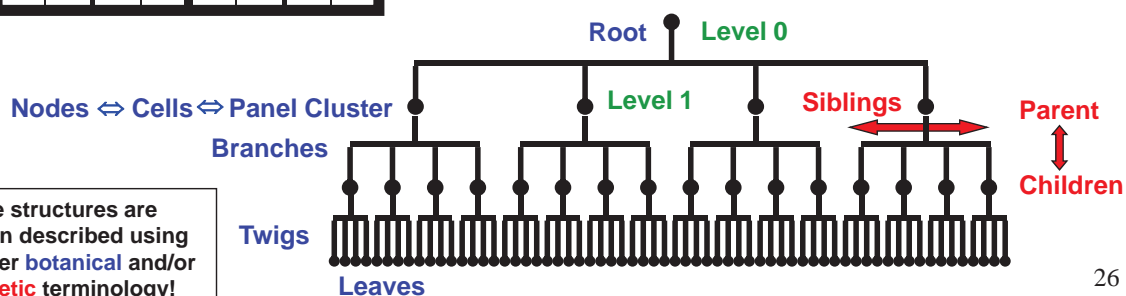
- Columns of block are taken as bases for representing matrix through modified Gram-Schmidt orthogonalization to produce Q;  $R=Q^tA$  (since  $QQ^t = I$  implies  $A=QR$ )
- In principle, a low frequency method, but has been successfully applied to objects about 20 wavelengths in size
- Very efficient when combined with PILOT algorithm (Jandhyala)

25

## Problem Domains Are Generally Partitioned to Find Compressible Matrix Blocks



- Object bounding box is recursively subdivided into cells to form quad-tree (2D) or oct-tree (3D)
- No information stored for empty cells (panels)
- Roughly equal number of DoFs per cell
- Interactions between elements are now between groups of elements in different cells



Tree structures are often described using either **botanical** and/or **genetic** terminology!

26

## Definitions of Sibling, Nearest Neighbor Shell, and Interaction Shell Sets

**Define :**  
 $C_i^\ell$  -  $i$ th cell at  $\ell$ th level  
 $P_{C_i^\ell}$  - parent cell of cell  $C_i^\ell$

$S_{C_j^{\ell+1}}$  - **Sibling Set :**  

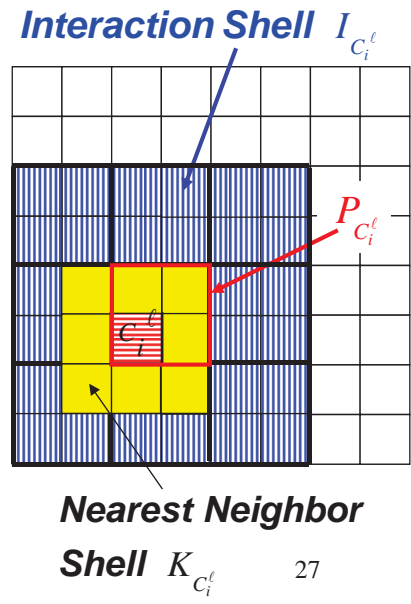
$$S_{C_j^{\ell+1}} = \left\{ C_k^{\ell+1} \mid \forall k \mid P_{C_k^{\ell+1}} = P_{C_j^{\ell+1}} \right\}$$
 = set of cells with the same parent

$K_{C_i^\ell}$  - **Nearest Neighbor Shell :**  

$$K_{C_i^\ell} = \left\{ C_j^\ell \mid C_j^\ell \text{ is in the same level as } C_i^\ell \text{ and has at least one point of contact with } C_i^\ell \right\}$$

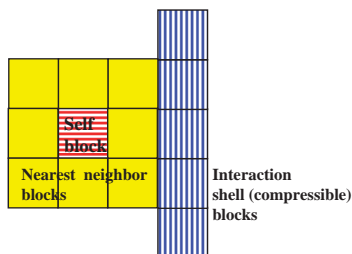
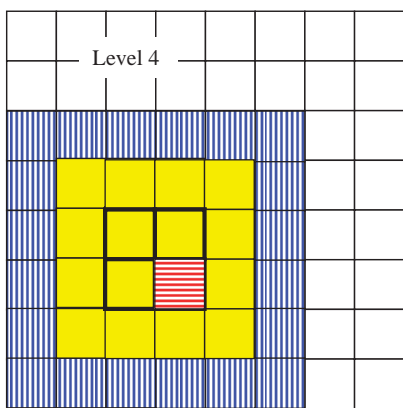
$I_{C_i^\ell}$  - **Interaction Shell :**  

$$I_{C_i^\ell} = \left\{ C_j^\ell \mid P_{C_j^\ell} \in K_{P_{C_i^\ell}} ; C_j^\ell \notin K_{C_i^\ell} \right\}$$
 = set of cells  $C_j^\ell$  at the same level as  $C_i^\ell$  whose parents are in the nearest neighbor shell of  $C_i^\ell$ 's parent, but are not a nearest neighbor cell of  $C_i^\ell$



27

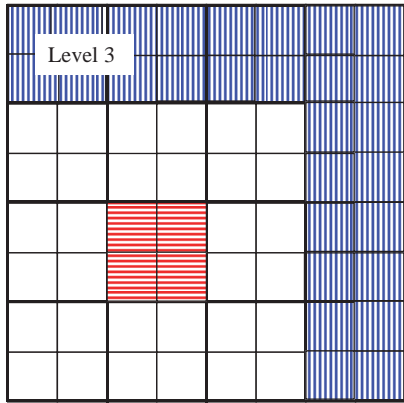
### Begin at the Deepest Level and Fill System Matrix with Interactions between Elements in each Cell and Those of its Near Neighbors



- Find interactions between elements in each cell and elements in its near neighbor cells:
  - Self-blocks and nearest neighbor shell blocks are filled by usual MoM procedure
  - Interaction shell blocks are compressible, so fill using ACA, QR, SVD, FMM, etc.
- Treat all siblings as a group

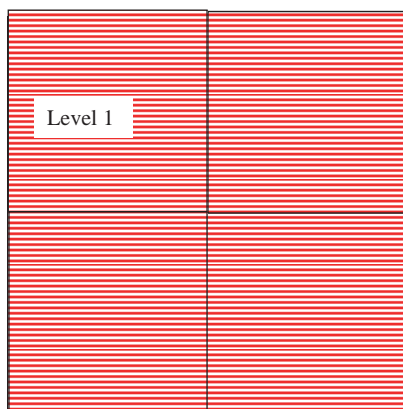
28

**Successively Move to Higher Levels (Larger Cell Sizes) and Fill (Compressed) Blocks Representing Coupling Between Elements in a Cell and Those of Same Level in its Interaction Shell**



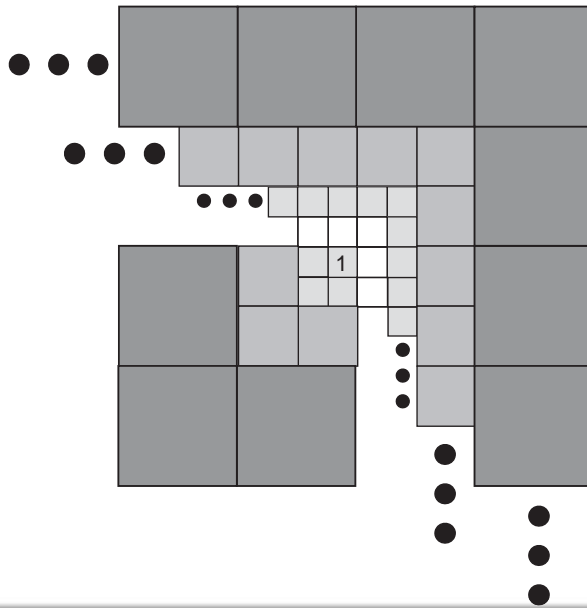
- Moving up a level, we next consider cells that are parents of the cells at the previous level
- Note that the nearest neighbor interactions at this level were treated at the previous level
- Hence, find interactions between each cell at this level and the cells of its interaction shell; the resulting interaction blocks are all compressible
- Repeat this procedure at each level until we reach level 2

**The Filling Procedure is Finished When Level 2 Is Reached**



- Level 1 has no nearest neighbor or interaction shells
- Level 2 has only previously-filled nearest neighbors

## Note That We Tile All Interaction Domains Using Blocks of Ever-Increasing Size

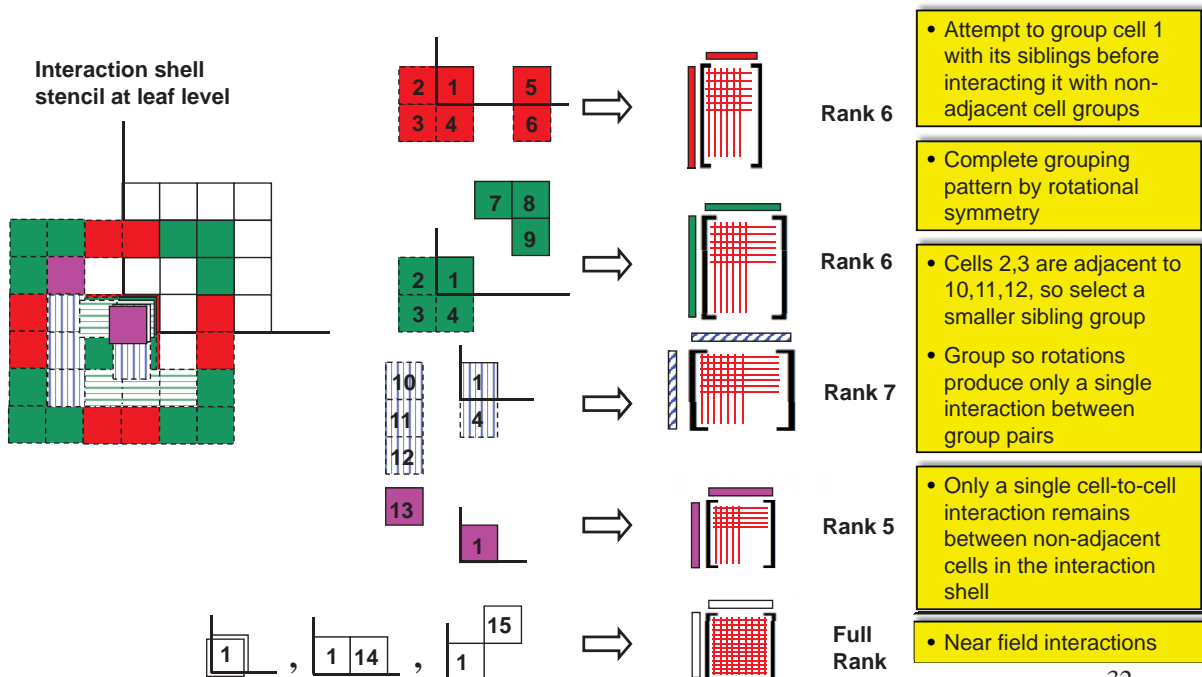


- As levels are added, all interaction groups are “tiled” by the increasingly larger groups
- Maximum rank pattern remains same at each level up to scales of almost a wavelength
- FMM or similar algorithms can be used beginning at scale levels on the order of a wavelength or larger

The PILOT algorithm attempts to further compress the system matrix by combining neighboring groups of cells at each stage

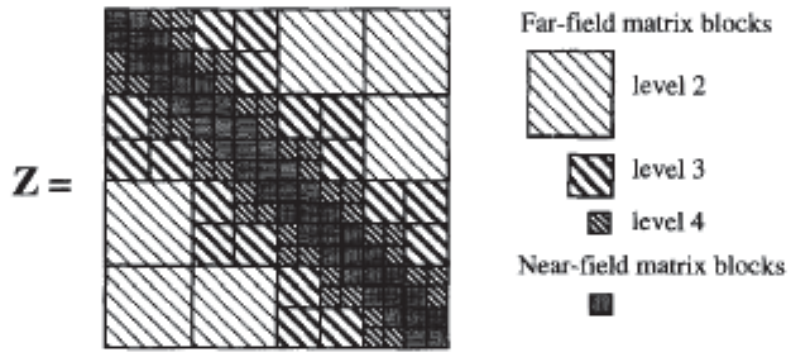
31

## Predetermined Interaction List Oct-Tree (PILOT) Algorithm for Domain Decomposition



32

## Typical Matrix Block Decomposition



33

## PILOT Performance: Cone Problem

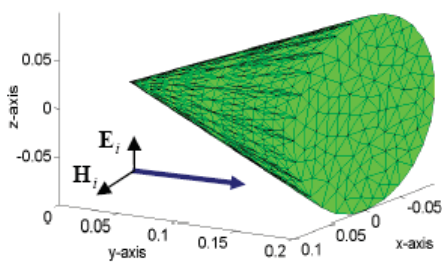


Figure 6a: Conducting cone and incident plane wave.

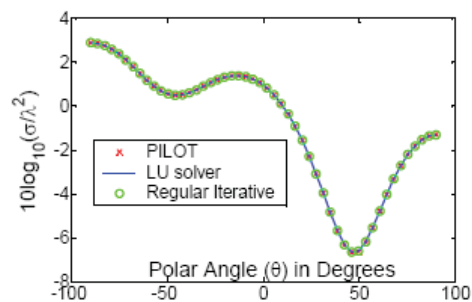


Figure 6b: The bi-static E-plane RCS

34

## PILOT Performance : Cone Problem

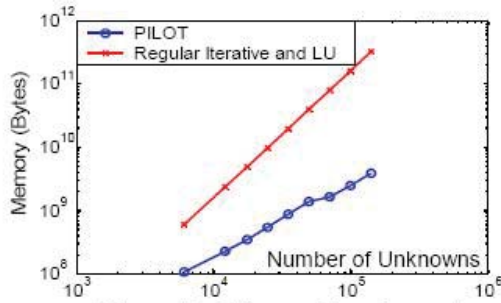


Figure 7a: Memory Requirement

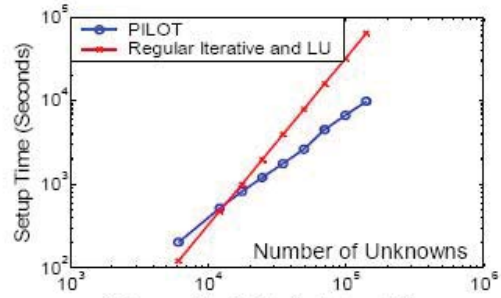


Figure 7b: Matrix Setup Time

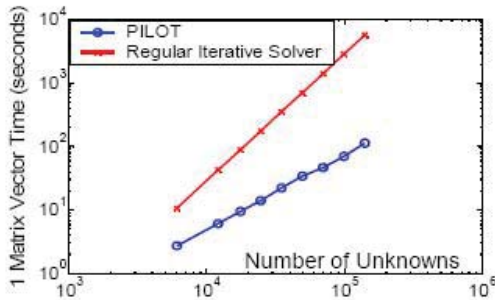


Figure 7c: Matrix Vector Product Time

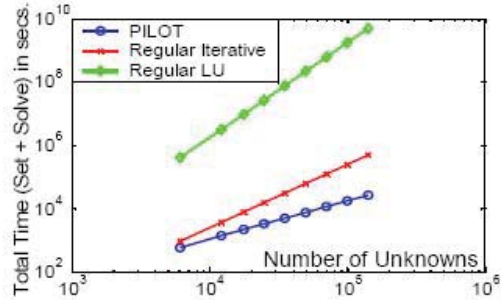


Figure 7d: Total Time Required

## PILOT Performance : Drone Problem

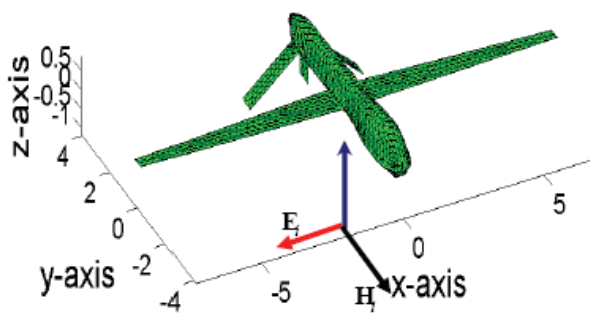


Figure 8a: Surface mesh for airborne drone

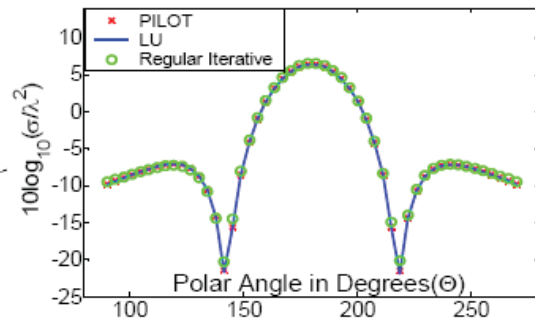


Figure 8b: The bi-static RCS of the drone

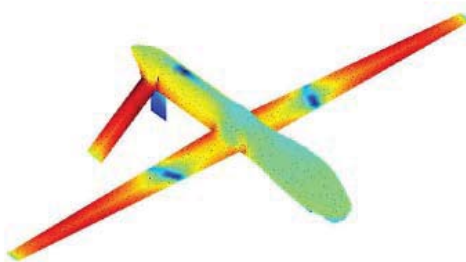


Figure 9a: The current density with LU

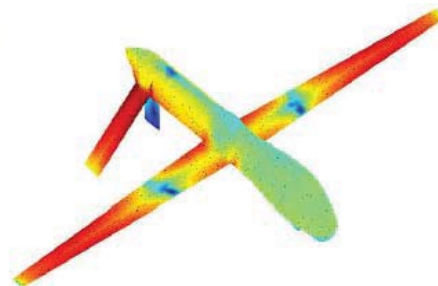
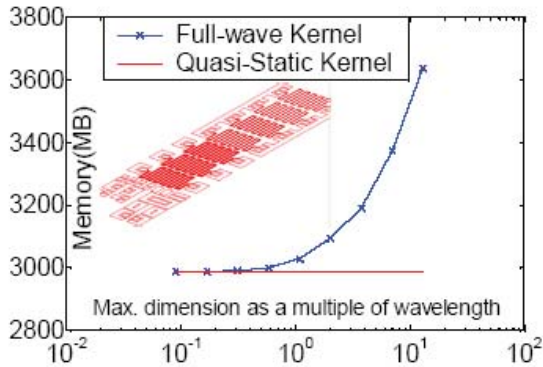
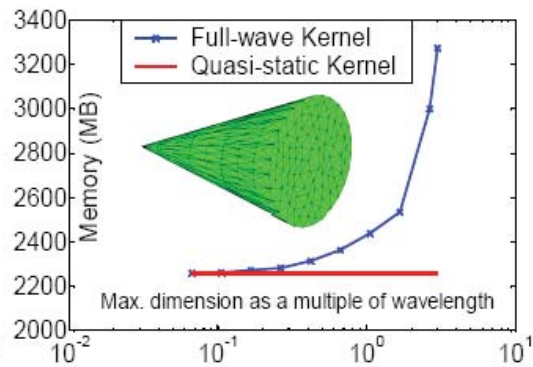


Figure 9b: The current density with PILOT

## PILOT Performance vs. Frequency



**Figure 10a:** Memory required by PILOT for a 2D structure. The corresponding MoM memory requirement is 540 GB.



**Figure 10b:** Memory required by PILOT for a 3D structure. The corresponding MoM memory requirement is 150 GB.

**Results can be improved by switching to an FMM or similar scheme when block sizes are on the order of a wavelength or larger.**

37

# End of Note 8

38

## Chapter 1.5.5

# COMPUTATIONAL METHODS

**D. R. Wilton**

Department of Electrical and Computer Engineering,  
 University of Houston,  
 Houston, TX 77204,  
 USA

### PART 1 SCATTERING OF WAVES BY MACROSCOPIC TARGETS

#### Topic 1.5 Electromagnetic Wave Scattering: Approximate and Numerical Methods

#### Contents

<b>§1</b> Fundamental Concepts	317	<b>§11</b> Conducting Bodies: MFIE, 3D	348
Maxwell's Equations	317	Evaluation of Element Matrices	349
Vector Wave Equation	317	<b>§12</b> Dielectric Bodies: PMCHW Formulation, 3D	349
Potential Representations	317	Evaluation of Far Fields	350
Far Fields, Radiation Conditions and Radar		Numerical Results	350
Cross Sections	318	<b>§13</b> Inhomogeneous Bodies: Electric Field Wave	
Equivalent Current Representations	318	Equation, 3D	351
Field Discontinuities at Surface Sources	319	Volume Coordinates	351
<b>§2</b> Conducting Cylinders: EFIE, TM Polarisation	320	Basis Functions	352
Evaluation of Impedance Matrix Entries	321	Evaluation of Element Matrices	353
Evaluation of Voltage Excitation Vector for		<b>§14</b> Inhomogeneous Bodies in Open Regions:	
Incident Plane Waves	322	Hybrid FEM/IE, 3D	353
Computation of Far Scattered Field	323	<b>§15</b> Extending the Methods	355
Numerical Results	323	Composite Geometries	355
<b>§3</b> Inhomogeneous Cylinders: Electric Field Wave		Apertures	355
Equation, TM Polarisation	323	Wires	357
The Element Matrix and Matrix Assembly	326	Point and Surface Loading, Thin Materials	358
Evaluation of the Element Matrices	327	Green's Functions and Geometrical	
Evaluation of Element Excitation Vector	329	Symmetries	359
Numerical Results	329	Higher-Order Modelling	360
<b>§4</b> Moment and Finite Element Methods	330	Solvers and Fast Methods	361
The Variational Approach and the Moment		<b>§16</b> Other Methods	361
Method	332	Frequency Domain Methods	361
<b>§5</b> Conducting Cylinders: MFIE, TM Polarisation	334	Time Domain Methods	362
<b>§6</b> Conducting Cylinders: CFIE, TM Polarisation	334	<b>§17</b> Mesh Truncation: Absorbing Boundary	
<b>§7</b> Conducting Cylinders: EFIE, TE Polarisation	336	Conditions	363
Evaluation of Element Matrices	338		
Evaluation of Far Fields	339		
Numerical Results	340		
<b>§8</b> Conducting Cylinders: MFIE, TE Polarisation	340		
Far Fields	340		
<b>§9</b> Inhomogeneous Cylinders: Electric Field Wave			
Equation, TE Polarisation	341		
Development of Basis Functions	343		
Evaluation of Element Matrices	343		
Numerical Results	344		
<b>§10</b> Conducting Bodies: EFIE, 3D	344		
Construction of Bases	345		
Evaluation of Element Matrices	346		
Evaluation of Far Fields	348		
Numerical Results	348		

Numerical techniques are becoming increasingly important in determining electromagnetic scattering properties. In this chapter we emphasise frequency domain methods because they have such wide applicability. Both integral and partial differential equation formulations are treated, as are hybrid approaches that combine features of each. The following section summarises fundamental concepts; two sections illustrating the formulation of simple integral and partial differential equations appear next. These are but special cases of linear operator equations, and this abstract point of view is taken in the next section where general methods for their discretisation are considered. Also the variational point of view commonly used in the finite element approach is introduced, and its equivalence to the method of moments

approach of Harrington (1993) is demonstrated. The resulting unification allows us to borrow freely from the most useful concepts and terminology of each approach. The succeeding sections concentrate on formulations that summarise the discretisation of two- and three-dimensional operators that commonly appear in computational electromagnetics. The remaining sections summarise extensions to the techniques introduced, consider associated computational issues and summarise alternative approaches.

## §1. Fundamental Concepts

### Maxwell's Equations

If the electromagnetic fields are assumed to be time harmonic with an  $e^{j\omega t}$  time variation, Faraday's and Ampere's laws become

$$\nabla \times \mathbf{E} = -j\omega \boldsymbol{\mu} \cdot \mathbf{H} - \mathbf{M}_V, \quad (1)$$

$$\nabla \times \mathbf{H} = j\omega \boldsymbol{\epsilon} \cdot \mathbf{E} + \mathbf{J}_V, \quad (2)$$

respectively, where  $\mathbf{E}$  and  $\mathbf{H}$  are the electric and magnetic fields, and  $\mathbf{J}_V$  and  $\mathbf{M}_V$  are electric and magnetic volume current densities, respectively. Here we assume that the permittivity  $\boldsymbol{\epsilon} = \boldsymbol{\epsilon}_r \boldsymbol{\epsilon}_0$  and permeability  $\boldsymbol{\mu} = \boldsymbol{\mu}_r \boldsymbol{\mu}_0$  are dyadic functions of position so that the medium parameters may be both inhomogeneous and anisotropic. The permittivity of free space is  $\epsilon_0 \approx 8.85419 \times 10^{-12}$  and permeability of free space is  $\mu_0 = 4\pi \times 10^{-7}$ . The electric and magnetic forms of Gauss's laws are

$$\nabla \cdot \mathbf{D} = q_V \quad (3)$$

$$\nabla \cdot \mathbf{B} = m_V, \quad (4)$$

where  $q_V$  and  $m_V$  are electric and magnetic volume charge densities, respectively. The electric and magnetic currents are related to the corresponding charge quantities by the equations of continuity,

$$\nabla \cdot \mathbf{J}_D = -j\omega q_D \quad (5)$$

$$\nabla \cdot \mathbf{M}_D = -j\omega m_D, \quad (6)$$

where  $D = C, S, \mathcal{V}$  are line, surface and volume current or charge densities, respectively, and the appropriate dimensionality of the divergence is assumed.

### Vector Wave Equation

Taking the divergence of both sides of (1) and (2) and employing the identity  $\nabla \cdot (\nabla \times \mathbf{A}) = 0$ , we find that, together with the equations of continuity, (1) and (2) automatically incorporate Gauss's laws, (3) and (4), if  $\omega \neq 0$ . Eliminating  $\mathbf{H}$  or  $\mathbf{E}$  from (1) and (2) yields the vector wave equations

$$\nabla \times (\boldsymbol{\mu}_r^{-1} \cdot \nabla \times \mathbf{E}) - k_0^2 \boldsymbol{\epsilon}_r \cdot \mathbf{E} = -j\omega \mu_0 \mathbf{J}_V - \nabla \times (\boldsymbol{\mu}_r^{-1} \cdot \mathbf{M}_V) \quad (7)$$

or

$$\nabla \times (\boldsymbol{\epsilon}_r^{-1} \cdot \nabla \times \mathbf{H}) - k_0^2 \boldsymbol{\mu}_r \cdot \mathbf{H} = -j\omega \epsilon_0 \mathbf{M}_V + \nabla \times (\boldsymbol{\epsilon}_r^{-1} \cdot \mathbf{J}_V) \quad (8)$$

for electric or magnetic fields, respectively.

### Potential Representations

The electric and magnetic fields can be represented in terms of potentials as

$$\begin{aligned} \mathbf{E} &= -j\omega \mathbf{A} - \nabla \Phi - \frac{1}{\boldsymbol{\epsilon}} \nabla \times \mathbf{F}, \\ \mathbf{H} &= -j\omega \mathbf{F} - \nabla \Psi + \frac{1}{\boldsymbol{\mu}} \nabla \times \mathbf{A}, \end{aligned} \quad (9)$$

where, in homogeneous, isotropic media, the potentials

$$\mathbf{A} = \mu \int_D \mathbf{J}_D(\mathbf{r}') G(\mathbf{r}, \mathbf{r}') dD', \quad (10)$$

$$\mathbf{F} = \epsilon \int_D \mathbf{M}_D(\mathbf{r}') G(\mathbf{r}, \mathbf{r}') dD', \quad (11)$$

$$\Phi = \frac{1}{\epsilon} \int_D q_D(\mathbf{r}') G(\mathbf{r}, \mathbf{r}') dD', \quad (12)$$

$$\Psi = \frac{1}{\mu} \int_D m_D(\mathbf{r}') G(\mathbf{r}, \mathbf{r}') dD' \quad (13)$$

are the magnetic and electric vector potentials and the scalar electric and magnetic potentials, respectively. The domain  $D$  may be a volume  $\mathcal{V}$ , a surface  $S$ , or a curve  $C$ . In a medium with wavenumber  $k = \omega \sqrt{\boldsymbol{\mu} \boldsymbol{\epsilon}}$ , the three-dimensional scalar Green's function  $G(\mathbf{r}, \mathbf{r}')$  is the potential function

$$G(\mathbf{r}, \mathbf{r}') = \frac{e^{-jkR}}{4\pi R}, \quad (14)$$

where  $R = |\mathbf{r} - \mathbf{r}'|$  is the distance between a unit strength point source located at  $\mathbf{r}'$  and an observation point at  $\mathbf{r} = x\hat{\mathbf{x}} + y\hat{\mathbf{y}} + z\hat{\mathbf{z}}$ . If the problem domain, sources and fields are invariant with respect to the  $z$  coordinate, the problem is two-dimensional and the potential integrals can be written as

$$\begin{aligned} \int_D (\cdot) G(\mathbf{r}, \mathbf{r}') dD' &= \int_{D_z} \int_{-\infty}^{\infty} (\cdot) G(\mathbf{r}, \mathbf{r}') dz' dD_z' \\ &= \int_{D_z} (\cdot) G(\boldsymbol{\rho}, \boldsymbol{\rho}') dD_z', \end{aligned} \quad (15)$$

where integrals over  $D = \mathcal{V}$  or  $S$  become integrals over the domain's cross section in the  $x$ - $y$  plane,  $D_z = S$  or  $C$ , respectively. The identity

$$\begin{aligned} G(\boldsymbol{\rho}, \boldsymbol{\rho}') &= \frac{H_0^{(2)}(kD)}{4j} = \int_{-\infty}^{\infty} \frac{e^{-jkR}}{4\pi R} dz' \\ &= \int_{-\infty}^{\infty} G(\mathbf{r}, \mathbf{r}') dz' \end{aligned} \quad (16)$$

permits replacement of the three-dimensional, homogeneous medium Green's function  $G(\mathbf{r}, \mathbf{r}')$  by its two-dimensional counterpart,  $G(\boldsymbol{\rho}, \boldsymbol{\rho}')$ . In (16),  $D = |\boldsymbol{\rho} - \boldsymbol{\rho}'|$  is the distance in the  $x$ - $y$  plane between a unit line source located at  $\boldsymbol{\rho}'$  and an observation point at  $\boldsymbol{\rho} = x\hat{\mathbf{x}} + y\hat{\mathbf{y}}$ , and  $H_0^{(2)}(x)$  is the Hankel function of the second kind, order zero.

## Far Fields, Radiation Conditions and Radar Cross Sections

In three dimensions, the vector potentials in the far field become

$$\mathbf{A} \xrightarrow{r \rightarrow \infty} \frac{\mu}{4\pi r} e^{-jkr} \int_D \mathbf{J}_D(\mathbf{r}') e^{jk\hat{\mathbf{r}} \cdot \mathbf{r}'} dD' \quad (17)$$

and

$$\mathbf{F} \xrightarrow{r \rightarrow \infty} \frac{\epsilon}{4\pi r} e^{-jkr} \int_D \mathbf{M}_D(\mathbf{r}') e^{jk\hat{\mathbf{r}} \cdot \mathbf{r}'} dD', \quad (18)$$

where

$$\hat{\mathbf{r}} = \hat{\mathbf{x}} \cos \phi \sin \theta + \hat{\mathbf{y}} \sin \phi \sin \theta + \hat{\mathbf{z}} \cos \theta \quad (19)$$

is the radial unit vector in the observation direction  $(\theta, \phi)$  in spherical coordinates. In terms of potentials, the far electric and magnetic fields are

$$\begin{aligned} \mathbf{E} &= j\omega \hat{\mathbf{r}} \times (\hat{\mathbf{r}} \times \mathbf{A}) + j\omega \eta (\hat{\mathbf{r}} \times \mathbf{F}) \\ &= -j\omega (\hat{\boldsymbol{\theta}} \hat{\boldsymbol{\theta}} + \hat{\boldsymbol{\phi}} \hat{\boldsymbol{\phi}}) \cdot \mathbf{A} + j\omega \eta (\hat{\boldsymbol{\phi}} \hat{\boldsymbol{\theta}} - \hat{\boldsymbol{\theta}} \hat{\boldsymbol{\phi}}) \cdot \mathbf{F}, \end{aligned} \quad (20)$$

and

$$\begin{aligned} \mathbf{H} &= \frac{1}{\eta} \hat{\mathbf{r}} \times \mathbf{E} = \frac{-j\omega}{\eta} (\hat{\mathbf{r}} \times \mathbf{A}) + j\omega \hat{\mathbf{r}} \times (\hat{\mathbf{r}} \times \mathbf{F}) \\ &= -j\omega (\hat{\boldsymbol{\theta}} \hat{\boldsymbol{\theta}} + \hat{\boldsymbol{\phi}} \hat{\boldsymbol{\phi}}) \cdot \mathbf{F} + j\frac{\omega}{\eta} (\hat{\boldsymbol{\theta}} \hat{\boldsymbol{\phi}} - \hat{\boldsymbol{\phi}} \hat{\boldsymbol{\theta}}) \cdot \mathbf{A}, \end{aligned} \quad (21)$$

respectively, where

$$\hat{\boldsymbol{\theta}} = \hat{\mathbf{x}} \cos \phi \cos \theta + \hat{\mathbf{y}} \sin \phi \cos \theta - \hat{\mathbf{z}} \sin \theta \quad (22)$$

$$\hat{\boldsymbol{\phi}} = -\hat{\mathbf{x}} \sin \phi + \hat{\mathbf{y}} \cos \phi, \quad (23)$$

and  $\eta = \sqrt{\mu/\epsilon}$  is the intrinsic impedance of the medium. Note that the fields satisfy *vector radiation conditions*

$$\lim_{r \rightarrow \infty} r \left[ \hat{\mathbf{r}} \times \mathbf{H} + \frac{\mathbf{E}}{\eta} \right] = 0, \quad \lim_{r \rightarrow \infty} r [\hat{\mathbf{r}} \times \mathbf{E} - \eta \mathbf{H}] = 0 \quad (24)$$

that are needed to obtain unique solutions of (7) and (8) in unbounded regions. The Green's function appearing in the potential field representations satisfies the *scalar radiation condition*  $\lim_{r \rightarrow \infty} r \left[ \frac{\partial G}{\partial r} + jkG \right] = 0$ , which in turn ensures that fields obtained from potentials automatically satisfy radiation conditions.

If  $\mathbf{E}$  and  $\mathbf{H}$  represent fields scattered by an object illuminated by an incident plane wave  $\mathbf{E}^{\text{inc}}$  travelling in the direction of the unit vector  $\hat{\mathbf{k}}$ , the *bistatic radar cross section* in the observation direction  $\hat{\mathbf{r}}$  is

$$\sigma(\hat{\mathbf{r}}, \hat{\mathbf{k}}) = \lim_{r \rightarrow \infty} 4\pi r^2 \frac{|\mathbf{E}|^2}{|\mathbf{E}^{\text{inc}}|^2}. \quad (25)$$

This cross section is defined as the area through which an incident plane wave carries sufficient power to produce, by omnidirectional radiation, the same scattered power density as that observed in a given far field direction. The *monostatic radar cross section* is defined as the radar cross section observed in the backscattering direction,  $\sigma(-\hat{\mathbf{k}}, \hat{\mathbf{k}})$ . Another quantity of interest is the *total scattering cross section*,

$$\sigma_t(\hat{\mathbf{k}}) = \frac{\eta \operatorname{Re} \int_D \mathbf{E}^{\text{inc}} \cdot \mathbf{J}_D^* dD}{|\mathbf{E}^{\text{inc}}|^2}, \quad (26)$$

where the asterisk denotes the complex conjugate. This cross section is defined as the ratio of the total scattered power to the power density of the incident wave.

In two dimensions, the far vector potentials have the form

$$\mathbf{A} \xrightarrow{\rho \rightarrow \infty} \frac{\mu}{\sqrt{8\pi k \rho}} e^{-j(k\rho + \frac{\pi}{4})} \int_{D_z} \mathbf{J}_D(\boldsymbol{\rho}') e^{jk\hat{\boldsymbol{\rho}} \cdot \boldsymbol{\rho}'} dD_z', \quad (27)$$

$$\mathbf{F} \xrightarrow{\rho \rightarrow \infty} \frac{\epsilon}{\sqrt{8\pi k \rho}} e^{-j(k\rho + \frac{\pi}{4})} \int_{D_z} \mathbf{M}_D(\boldsymbol{\rho}') e^{jk\hat{\boldsymbol{\rho}} \cdot \boldsymbol{\rho}'} dD_z', \quad (28)$$

and the fields are given by

$$\begin{aligned} \mathbf{E} &= j\omega \hat{\boldsymbol{\rho}} \times (\hat{\boldsymbol{\rho}} \times \mathbf{A}) + j\omega \eta (\hat{\boldsymbol{\rho}} \times \mathbf{F}) \\ &= -j\omega (\hat{\boldsymbol{\phi}} \hat{\boldsymbol{\phi}} + \hat{\mathbf{z}} \hat{\mathbf{z}}) \cdot \mathbf{A} + j\omega \eta (\hat{\mathbf{z}} \hat{\boldsymbol{\phi}} - \hat{\boldsymbol{\phi}} \hat{\mathbf{z}}) \cdot \mathbf{F}, \end{aligned} \quad (29)$$

and

$$\begin{aligned} \mathbf{H} &= \frac{1}{\eta} \hat{\boldsymbol{\rho}} \times \mathbf{E} = \frac{-j\omega}{\eta} (\hat{\boldsymbol{\rho}} \times \mathbf{A}) + j\omega \hat{\boldsymbol{\rho}} \times (\hat{\boldsymbol{\rho}} \times \mathbf{F}) \\ &= -j\omega (\hat{\boldsymbol{\phi}} \hat{\boldsymbol{\phi}} + \hat{\mathbf{z}} \hat{\mathbf{z}}) \cdot \mathbf{F} + j\frac{\omega}{\eta} (\hat{\boldsymbol{\phi}} \hat{\mathbf{z}} - \hat{\mathbf{z}} \hat{\boldsymbol{\phi}}) \cdot \mathbf{A}, \end{aligned} \quad (30)$$

where

$$\hat{\boldsymbol{\rho}} = \hat{\boldsymbol{\phi}} \times \hat{\mathbf{z}} = \hat{\mathbf{x}} \cos \phi + \hat{\mathbf{y}} \sin \phi \quad (31)$$

is the radial unit vector in cylindrical coordinates in the direction of the observation angle  $\phi$  measured from the  $x$  axis. The radiation conditions are

$$\lim_{\rho \rightarrow \infty} \sqrt{\rho} \left[ \hat{\mathbf{r}} \times \mathbf{H} + \frac{\mathbf{E}}{\eta} \right] = 0, \quad \lim_{\rho \rightarrow \infty} \sqrt{\rho} [\hat{\mathbf{r}} \times \mathbf{E} - \eta \mathbf{H}] = 0. \quad (32)$$

In two dimensions, the bistatic radar cross section for scattering by a cylindrical object illuminated by an incident plane wave  $\mathbf{E}^{\text{inc}}$  travelling in the direction of the unit vector  $\hat{\mathbf{k}}$  normal to the cylinder axis is

$$\sigma(\hat{\boldsymbol{\rho}}, \hat{\mathbf{k}}) = \lim_{\rho \rightarrow \infty} 2\pi \rho \frac{|\mathbf{E}|^2}{|\mathbf{E}^{\text{inc}}|^2}. \quad (33)$$

This cross section is the equivalent width across which an incident plane wave carries sufficient power to produce, by omnidirectional radiation, the same scattered power density as that observed in a given far field direction. The monostatic radar cross section is  $\sigma(-\hat{\mathbf{k}}, \hat{\mathbf{k}})$ . The total scattering cross section is

$$\sigma_t(\hat{\mathbf{k}}) = \frac{\eta \operatorname{Re} \int_{D_z} \mathbf{E}^{\text{inc}} \cdot \mathbf{J}_D^* dD_z}{|\mathbf{E}^{\text{inc}}|^2}, \quad (34)$$

defined for cylinders as the ratio of the total scattered power per unit length to the power density of the incident wave.

## Equivalent Current Representations

The *surface equivalence principle* is usually used to formulate an integral equation at a surface  $S$  separating two regions. A Green's function must usually

be known for at least one of the regions, or at least for the region formed by appropriately extending the region's material parameters into the complementary region. Surface  $S$  might be chosen arbitrarily or for some convenient property it possesses—often it is the boundary of a scatterer or of a homogeneous material region. We assume that  $S$  is closed, of bounded extent, and has an outward unit normal  $\hat{\mathbf{n}}$ . The region interior to  $S$  is designated  $\mathcal{V}^-$ , while the exterior region is  $\mathcal{V}^+$ . Let  $(\mathbf{E}^+, \mathbf{H}^+)$  be fields in  $\mathcal{V}^+$ ; we need only know their tangential values on  $S$  and their sources  $\mathbf{J}_D^+$  in  $\mathcal{V}^+$ . We place so-called equivalent electric and magnetic surface currents,

$$\mathbf{J}_S^+ = \hat{\mathbf{n}} \times \mathbf{H}^+, \quad \mathbf{M}_S^+ = \mathbf{E}^+ \times \hat{\mathbf{n}}, \quad (35)$$

respectively, on  $S$ . The equivalence principle (Harrington, 1961) then asserts that the fields radiated by the equivalent surface currents  $\mathbf{J}_S^+, \mathbf{M}_S^+$  on  $S$  and the sources  $\mathbf{J}_D^+$  in  $\mathcal{V}^+$  are the original fields  $(\mathbf{E}^+, \mathbf{H}^+)$  throughout  $\mathcal{V}^+$ . Further, the fields radiated by the equivalent and exterior region sources together vanish in  $\mathcal{V}^-$ . This *exterior equivalence* is illustrated in Fig. 1a.

An *interior equivalence* dual to the exterior equivalence may also be set up. We consider a second set of fields  $(\mathbf{E}^-, \mathbf{H}^-)$ , possibly unrelated to the first, for which we need only know the tangential values on  $S$

and its sources  $\mathbf{J}_D^-$  in  $\mathcal{V}^-$ . Equivalent electric and magnetic surface currents,

$$\mathbf{J}_S^- = -\hat{\mathbf{n}} \times \mathbf{H}^-, \quad \mathbf{M}_S^- = -\mathbf{E}^- \times \hat{\mathbf{n}}, \quad (36)$$

respectively, are placed on  $S$ . The equivalent surface currents  $\mathbf{J}_S^-, \mathbf{M}_S^-$  on  $S$  and the interior sources  $\mathbf{J}_D^-$  in  $\mathcal{V}^-$  then produce the original fields  $(\mathbf{E}^-, \mathbf{H}^-)$  everywhere in  $\mathcal{V}^-$ ; together the sources produce null fields in  $\mathcal{V}^+$ . The interior equivalence is illustrated in Fig. 1b.

Since in both equivalences the fields vanish in the region complementary to that for which the equivalence is valid, the medium parameters may be changed in the complementary region as convenient. Often the equivalence region medium parameters are suitably extended into the null field region such that a Green's function exists for the resulting composite medium.

### Field Discontinuities at Surface Sources

Integral equations are generally obtained by applying boundary conditions at material interfaces where equivalent surface currents are used for field representations. In formulating the equations, one must pay particular attention to discontinuities of the surface fields at boundaries. In potential integral representations, these discontinuities arise from terms involving derivatives of Green's functions that behave like three-dimensional Dirac delta distributions,  $\delta(\mathbf{r} - \mathbf{r}')$ , as an observation point  $\mathbf{r}$  approaches a source point  $\mathbf{r}'$ . The integrand sampling properties of the Dirac delta distributions thus allow terms involving the source at the observation point to be explicitly removed from the integral. Thus, if  $\mathbf{E}$  and  $\mathbf{H}$  are the fields radiated by surface equivalent sources  $\mathbf{J}_S$  and  $\mathbf{M}_S$  on a surface  $S$ , then the fields have the following limits as a point  $\mathbf{r}$  approaches a *smooth* point on  $S$ :

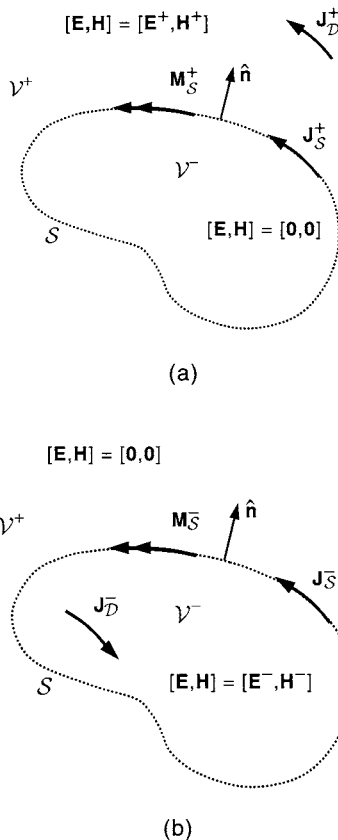
$$\begin{aligned} \lim_{\mathbf{r} \downarrow S} \mathbf{E} &= \pm \hat{\mathbf{n}} \times \frac{\mathbf{M}_S(\mathbf{r})}{2} \pm \hat{\mathbf{n}} \frac{q_s(\mathbf{r})}{2\epsilon} - j\omega \mathbf{A} - \langle \nabla \Phi \rangle - \frac{1}{\epsilon} \langle \nabla \times \mathbf{F} \rangle \\ \lim_{\mathbf{r} \uparrow S} \mathbf{H} &= \mp \hat{\mathbf{n}} \times \frac{\mathbf{J}_S(\mathbf{r})}{2} \pm \hat{\mathbf{n}} \frac{m_s(\mathbf{r})}{2\mu} - j\omega \mathbf{F} - \langle \nabla \Psi \rangle + \frac{1}{\mu} \langle \nabla \times \mathbf{A} \rangle, \end{aligned} \quad (37)$$

where “ $\downarrow$ ” indicates the surface is approached from the side into which the surface normal  $\hat{\mathbf{n}}$  points, and “ $\uparrow$ ” indicates the surface is approached from the opposite side. The potential derivative quantities enclosed in brackets in (37) are discontinuous at  $S$ , the brackets signifying the *average* value of a discontinuous quantity as  $S$  is approached from opposite sides. It is seen that the source terms appearing outside the potential integrals completely account for the well-known discontinuities in fields (potential derivatives) at surface sources:

$$\begin{aligned} \lim_{\mathbf{r} \downarrow S} \mathbf{E} - \lim_{\mathbf{r} \uparrow S} \mathbf{E} &= \hat{\mathbf{n}} \times \mathbf{M}_S + \hat{\mathbf{n}} \frac{q_s}{\epsilon} \\ \lim_{\mathbf{r} \downarrow S} \mathbf{H} - \lim_{\mathbf{r} \uparrow S} \mathbf{H} &= -\hat{\mathbf{n}} \times \mathbf{J}_S + \hat{\mathbf{n}} \frac{m_s}{\mu}. \end{aligned} \quad (38)$$

The bracketed potential integrals may be written as

**Figure 1** Equivalent currents for (a) exterior region and (b) interior region.



$$\langle \nabla \times \mathbf{A} \rangle = -\mu \int_S \mathbf{J}_s(\mathbf{r}') \times \nabla G(\mathbf{r}, \mathbf{r}') dS' \quad (39)$$

$$\langle \nabla \times \mathbf{F} \rangle = -\epsilon \int_S \mathbf{M}_s(\mathbf{r}') \times \nabla G(\mathbf{r}, \mathbf{r}') dS' \quad (40)$$

$$\langle \nabla \Phi \rangle = -\frac{1}{j\omega\epsilon} \int_S \nabla' \cdot \mathbf{J}_s(\mathbf{r}') \nabla G(\mathbf{r}, \mathbf{r}') dS' \quad (41)$$

$$\langle \nabla \Psi \rangle = -\frac{1}{j\omega\mu} \int_S \nabla' \cdot \mathbf{M}_s(\mathbf{r}') \nabla G(\mathbf{r}, \mathbf{r}') dS', \quad (42)$$

but one must keep in mind that they no longer include singular contributions of the potential integrals from the source point  $\mathbf{r}' = \mathbf{r}$  on the surface. Thus the integrals represent contributions from all points of  $S$ , *excluding* the isolated point  $\mathbf{r}$ .

## §2. Conducting Cylinders: EFIE, TM Polarisation

In this section we introduce a simple two-dimensional scattering problem formulated as an integral equation, and solved by a numerical solution procedure known as the method of moments (MoM) (Harrington, 1993). We consider a conducting cylinder of infinite extent with its axis parallel to the  $z$  axis. The cross section of the cylinder is described by the curve  $C$ . If an electric field with only a  $z$  component  $E_z^{\text{inc}}$  is incident normal to the cylinder axis, then the induced surface current and scattered fields also have only  $z$  components,  $J_z$  and  $E_z^{\text{sc}}$ , respectively. Since the resulting magnetic field is directed transverse to the cylinder axis, this polarisation is termed the *transverse magnetic* (TM) polarisation. For an open curve  $C$ , the conductor is generally modelled as having only infinitesimal thickness. Though independent surface currents exist on opposite sides of the conductor, they become coincident in this model, and hence we can take  $J_z$  as the *sum* of the surface currents on opposite sides of  $C$ . In view of the problem's translational symmetry with respect to the  $z$  axis, the fields and induced currents are independent of the  $z$  coordinate. This implies that there is no charge density associated with the current and that the scattered electric field may be represented in terms of a vector potential alone. Thus, combining (9), (10) and (16), we have

$$\begin{aligned} E_z^{\text{sc}} &= -j\omega A_z = -j\omega\mu \int_C J_z(\boldsymbol{\rho}') G(\boldsymbol{\rho}, \boldsymbol{\rho}') dC' \\ &= -\frac{\omega\mu}{4} \int_C J_z(\boldsymbol{\rho}') H_0^{(2)}(kD) dC', \end{aligned} \quad (43)$$

where  $D = |\boldsymbol{\rho} - \boldsymbol{\rho}'|$ .

An integral equation for determining the induced current is obtained by requiring the total tangential electric field,  $E_z^{\text{sc}} + E_z^{\text{inc}}$ , to vanish on the cylinder surface:

$$\frac{\omega\mu}{4} \int_C J_z(\boldsymbol{\rho}') H_0^{(2)}(kD) dC' = E_z^{\text{inc}}(\boldsymbol{\rho}), \quad \boldsymbol{\rho} \in C. \quad (44)$$

For a numerical solution of (44), known as an electric field integral equation (EFIE), we first approxi-

mate the curve  $C$  by means of  $N$  straight *line segments*,  $C^n$ , as illustrated for the hemicylindrical geometry with fin whose cross section is shown in Fig. 2. The line segments are also called *elements* or *subdomains*, and provide a piecewise linear approximation  $\tilde{C} = \cup_{n=1}^N C^n$  to  $C$ . As the figure depicts, curved structures incur geometry modelling errors in this approach. These errors can only be reduced by decreasing the segment lengths, i.e., by increasing the number of segments  $N$ . Note that the integral equation (44) applies even when there is a junction between conducting surfaces, as the junction between the hemicylinder and fin shown in the figure. Furthermore, (44) is not limited to single scatterers, but also applies to multiple, disjoint scatterers so long as the geometry remains cylindrical and the excitation is  $z$  invariant.

The geometry of Fig. 2 also serves to illustrate the geometry data structure required for a typical problem. Tables 1 and 2, for instance, tabulate the node

**Figure 2** Piecewise linear model of cross section  $C$  of hemicylinder with fin.

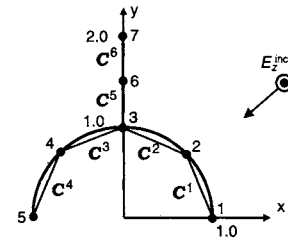


**Table 1** Global Nodes and Coordinates

Global node number	Coordinates	
	x	y
1	1.0000	0.0000
2	0.7071	0.7071
3	0.0000	1.0000
4	-0.7071	0.7071
5	-1.0000	0.0000
6	0.0000	1.5000
7	0.0000	2.0000

**Table 2** Element and Node Associations

Element number	Global node numbers	
	Local node 1	Local node 2
1	1	2
2	2	3
3	3	4
4	4	5
5	3	6
6	6	7

locations and list the nodes that make up each element of the geometry, respectively.

To approximate the current distribution, we assume that every subdomain  $C^n$  is sufficiently small, both electrically ( $k\ell^n \ll 1$ , where  $\ell^n$  is the subdomain length) and with respect to any geometrically distinct features of  $C$ , that the current density within an element may be assumed constant,  $J_z \approx I_n$ . This piecewise constant approximation of the current distribution is depicted in Fig. 3. The current distribution on  $\tilde{C}$  is thus approximated as

$$J_z(\boldsymbol{\rho}) \approx \sum_{n=1}^N I_n \Pi_n(\boldsymbol{\rho}), \quad (45)$$

where  $\Pi_n(\boldsymbol{\rho})$  is the unit pulse function defined as

$$\Pi_n(\boldsymbol{\rho}) = \begin{cases} 1, & \boldsymbol{\rho} \in C^n, \\ 0, & \boldsymbol{\rho} \notin C^n \end{cases} \quad (46)$$

and illustrated in Fig. 4.

We substitute this representation for the current into the left-hand side of the integral equation (44), noting that, since the current is approximate, it is not possible to satisfy the equality there at *every* point of  $C$ . To obtain  $N$  equations in the  $N$  unknowns  $I_n$ , therefore, we elect to enforce the equality at the midpoint of element  $m$ . That is, we set  $\boldsymbol{\rho} = \boldsymbol{\rho}^m$  on both sides of (44), where  $\boldsymbol{\rho}^m \equiv (\boldsymbol{\rho}_1^m + \boldsymbol{\rho}_2^m)/2$  is the midpoint of element  $m$

$$\sum_{n=1}^N I_n \frac{\omega\mu}{4} \int_{C^n} H_0^{(2)}(kD^m) dC' = E_z^{\text{inc}}(\boldsymbol{\rho}^m), \quad m = 1, 2, \dots, N, \quad (47)$$

with  $D^m = |\boldsymbol{\rho}^m - \boldsymbol{\rho}'|$ . Note that the pulse function property (46) limits the domain of the integral in (47).

**Figure 3** Piecewise constant approximation of  $J_z$  on  $C$ .

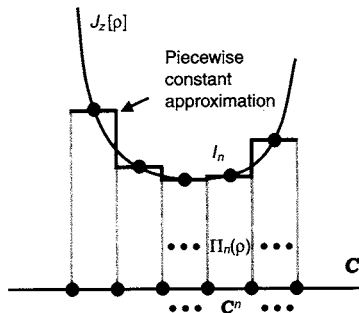
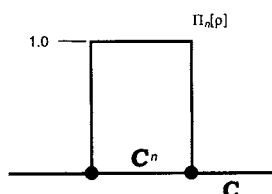


**Figure 4** Unit pulse function on  $C$ .



This system of linear equations can also be conveniently written in matrix form as

$$[Z_{mn}][I_n] = [V_m], \quad (48)$$

where  $[I_n]$  is a column vector containing the unknown current coefficients, and  $[Z_{mn}]$  is the *impedance matrix* with elements

$$Z_{mn} = \frac{\omega\mu}{4} \int_{C^n} H_0^{(2)}(kD^m) dC'. \quad (49)$$

The excitation column vector  $[V_m]$  on the right-hand side of (48) is termed the *voltage vector*, and its elements are sampled values of the incident field,

$$V_m = E_z^{\text{inc}}(\boldsymbol{\rho}^m). \quad (50)$$

The solution of the matrix equation (48) yields the current column vector  $[I_n]$ , and (45) provides a global representation of the current distribution.

### Evaluation of Impedance Matrix Entries

Further processing is required to accurately evaluate the elements  $Z_{mn}$  of (49). First, we must parameterise each of the line segments  $C^n$  for numerical integration. Referring to Table 2, let the coordinate vector to the first node associated with element  $n$  be denoted  $\boldsymbol{\rho}_1^n$ , and the second,  $\boldsymbol{\rho}_2^n$ .

Then, as illustrated in Fig. 5, if  $\ell$  is arc length measured from node 1, the position vector  $\boldsymbol{\rho}$  in  $C^n$  may be parameterised as

$$\boldsymbol{\rho} = \boldsymbol{\rho}_1^n + \frac{\boldsymbol{\rho}_2^n - \boldsymbol{\rho}_1^n}{\ell^n} \ell, \quad (51)$$

where  $\ell^n = |\boldsymbol{\rho}_2^n - \boldsymbol{\rho}_1^n|$  is the segment length. To express this result in a convenient general form, we define *normalised coordinates*  $\xi_1 = 1 - \ell/\ell^n$  and  $\xi_2 = \ell/\ell^n$ , which allow (51) to be replaced by

$$\boldsymbol{\rho} = \boldsymbol{\rho}_1^n \xi_1 + \boldsymbol{\rho}_2^n \xi_2 \quad (52)$$

in  $C^n$ . The normalised coordinate terms in (52) are merely linear interpolation functions on the interval  $(0,1)$ , as shown in Fig. 6. In effect, every line segment element of  $\tilde{C}$  is mapped onto this unit *parent* line segment.

**Figure 5** Parameterisation of line segment  $C^n$ .

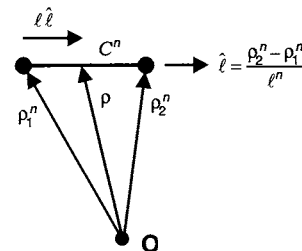
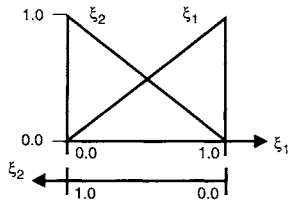


**Figure 6** Normalised coordinates on a line segment and piecewise linear interpolation functions.



An integral on  $C^n$  may now be parameterised and approximated as

$$\int_{C^n} f(\mathbf{p}) dC = \varrho^n \int_0^1 f(\mathbf{p}_1^n \xi_1 + \mathbf{p}_2^n \xi_2) d\xi_i, \quad i = 1 \text{ or } 2$$

$$\approx \varrho^n \sum_{k=1}^K w_k f(\mathbf{p}_1^n \xi_1^{(k)} + \mathbf{p}_2^n \xi_2^{(k)}), \quad (53)$$

where the last line assumes a numerical quadrature rule on the interval (0,1) with weights  $w_k$  and sample points  $\xi_1^{(k)} = 1 - \xi_2^{(k)}$ ,  $k = 1, 2, \dots, K$ . If  $f(\mathbf{p})$  is smooth on  $C^n$ , Gauss–Legendre rules are well suited to this task. Sampling points and corresponding weights for  $K = 1, 2$ , and 4 point Gauss–Legendre quadrature are listed in Table 3.

For  $m \neq n$ , the integrals (49) in the impedance matrix have smooth integrands and may be evaluated straightforwardly using the Gauss–Legendre rules of Table 3. For these impedance matrix elements,

$$Z_{mn} = \frac{\omega \mu \varrho^n}{4} \sum_{k=1}^K w_k H_0^{(2)}(kD_m^{(k)}), \quad m \neq n, \quad (54)$$

where, using (52),

$$D_m^{(k)} = |\mathbf{p}^m - \mathbf{p}_1^n \xi_1^{(k)} - \mathbf{p}_2^n \xi_2^{(k)}|. \quad (55)$$

For  $m = n$ , the integrand in (49) is singular at the observation point  $\mathbf{p}^m$ , i.e., for small arguments  $D$ ,  $H_0^{(2)}(kD) \approx 1 - j \frac{2}{\pi} \ln(kD)$  and thus the integrand

**Table 3** Sample Points and Weighting Coefficients for  $K$ -Point Gauss–Legendre Quadrature

Sample points, $\xi_1^{(k)}$	Weights, $w_k$
<b>K=1</b>	
0.5000000000000000	1.0000000000000000
<b>K=2</b>	
0.211324865405187	0.5000000000000000
0.788675134594813	0.5000000000000000
<b>K=4</b>	
0.069431844202974	0.173927422568727
0.330009478207572	0.326072577431273
0.669990521792428	0.326072577431273
0.930568155797027	0.173927422568727

is logarithmically singular at  $D = 0$ . The Gauss–Legendre quadrature scheme is poorly suited for this case; to handle it, we first note that the observation point divides the line segment in half. Each half contributes equally to the integral so that we may write these so-called *self-terms* of the impedance matrix as

$$Z_{mm} = \frac{\omega \mu \varrho^m}{4} \int_0^1 H_0^{(2)}\left(\frac{k \varrho^m \xi_1}{2}\right) d\xi_1. \quad (56)$$

This integral may be handled by the quadrature scheme of Ma *et al.* (1996) that exactly evaluates integrals of the form  $\int_0^1 f(\xi) d\xi$ , when  $f(\xi)$  is a linear combination of powers of  $\xi$  and products of powers of  $\xi$  and  $\ln \xi$ . Thus,

$$Z_{mm} = \frac{\omega \mu \varrho^m}{4} \sum_{k=1}^K w_k H_0^{(2)}\left(\frac{k \varrho^m \xi_1^{(k)}}{2}\right), \quad (57)$$

where now the weights  $w_k$  and sample points  $\xi_1^{(k)}$  are taken from Table 4.

**Evaluation of Voltage Excitation Vector for Incident Plane Waves**

For a plane wave incident from an angle  $\phi^{\text{inc}}$  with respect to the  $x$  axis,

$$E_z^{\text{inc}} = E_0 e^{-jk \hat{\mathbf{k}}^{\text{inc}} \cdot \mathbf{p}}, \quad (58)$$

where the unit incidence vector is

$$\hat{\mathbf{k}}^{\text{inc}} = -\hat{\mathbf{x}} \cos \phi^{\text{inc}} - \hat{\mathbf{y}} \sin \phi^{\text{inc}} \quad (59)$$

**Table 4** Sample Points and Weighting Coefficients for  $K$ -Point Quadratures of Form  $\int_0^1 f(\xi_1) d\xi_1 \approx \sum_{k=1}^K w_k f(\xi_1^{(k)})$  where  $f(\xi_1)$  has a Logarithmic Singularity at  $\xi_1 = 0$

Sample points, $\xi_1^{(k)}$	Weights, $w_k$
<b>K=1</b>	
0.367879441171442	1.0000000000000000
<b>K=2</b>	
$0.882968651376531 \times 10^{-1}$	0.298499893705525
0.675186490909887	0.701500106294475
<b>K=3</b>	
$0.288116625309523 \times 10^{-1}$	0.103330707964930
0.304063729612140	0.454636525970100
0.811669225344079	0.442032766064970
<b>K=5</b>	
$0.565222820508010 \times 10^{-2}$	$0.210469457918546 \times 10^{-1}$
$0.734303717426523 \times 10^{-1}$	0.130705540744447
0.284957404462558	0.289702301671314
0.619482264084778	0.350220370120399
0.915758083004698	0.208324841671986

and  $E_0$  is the amplitude of the incident field. Hence the excitation voltage column vector (50) is given by

$$[V_m] = E_0 \left[ e^{-jk \hat{\mathbf{k}}^{\text{inc}} \cdot \boldsymbol{\rho}^m} \right]. \quad (60)$$

### Computation of Far Scattered Field

The scattered electric field is given by

$$E_z^{\text{sc}} = -j\omega A_z = -\frac{\omega\mu}{4} \int_C J_z(\boldsymbol{\rho}') H_0^{(2)}(k|\boldsymbol{\rho} - \boldsymbol{\rho}'|) dC'. \quad (61)$$

If  $\boldsymbol{\rho}$  is assumed to be in the far field,  $|\boldsymbol{\rho}| = \rho \gg |\boldsymbol{\rho}'|$ , we may employ the asymptotic form of the Hankel function for large argument, given by

$$H_0^{(2)}(k|\boldsymbol{\rho} - \boldsymbol{\rho}'|) \xrightarrow{\rho \rightarrow \infty} \sqrt{\frac{2}{\pi k \rho}} e^{-j(k\rho - \frac{\pi}{4})} e^{jk\hat{\boldsymbol{\rho}} \cdot \boldsymbol{\rho}'}, \quad (62)$$

where  $\hat{\boldsymbol{\rho}}$  is the unit vector in the direction of the observation point making an angle  $\phi$  with respect to the  $x$  axis,

$$\hat{\boldsymbol{\rho}} = \hat{\mathbf{x}} \cos \phi + \hat{\mathbf{y}} \sin \phi. \quad (63)$$

Employing (62) and (63) in (61), we obtain

$$E_z^{\text{sc}} = \frac{\omega\mu}{\sqrt{8\pi k \rho}} e^{-j(k\rho + \frac{3\pi}{4})} \int_C J_z(\boldsymbol{\rho}') e^{jk\hat{\boldsymbol{\rho}} \cdot \boldsymbol{\rho}'} dC'. \quad (64)$$

Alternatively, we obtain (64) directly from (27) and (29). With our approximation (45) for  $J_z$  on  $C$ , this becomes

$$\begin{aligned} E_z^{\text{sc}} &= \frac{\omega\mu}{\sqrt{8\pi k \rho}} e^{-j(k\rho + \frac{3\pi}{4})} \sum_{n=1}^N I_n \varrho^n \int_0^1 e^{jk\hat{\boldsymbol{\rho}} \cdot \boldsymbol{\rho}'} d\xi_1 \\ &= \frac{\omega\mu}{\sqrt{8\pi k \rho}} e^{-j(k\rho + \frac{3\pi}{4})} \sum_{n=1}^N I_n \varrho^n e^{jk\hat{\boldsymbol{\rho}} \cdot \boldsymbol{\rho}^n} \text{sinc} \psi^n, \end{aligned} \quad (65)$$

where  $\boldsymbol{\rho}'$  is given by (52), and the ‘‘sinc’’ function is defined as  $\text{sinc} x = \frac{\sin(\pi x)}{\pi x}$  with argument

$$\psi^n = \frac{k\hat{\boldsymbol{\rho}} \cdot (\boldsymbol{\rho}_2^n - \boldsymbol{\rho}_1^n)}{2\pi}. \quad (66)$$

The integral in (65) alternatively may be evaluated numerically using a Gauss–Legendre rule from Table 3. If the subdomains are sufficiently small, even a one-point approximation may be used, leading to the approximation

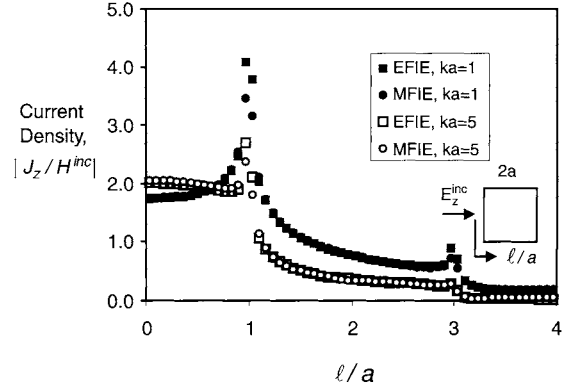
$$\begin{aligned} E_z^{\text{sc}} &= \frac{\omega\mu}{\sqrt{8\pi k \rho}} e^{-j(k\rho + \frac{3\pi}{4})} \sum_{n=1}^N I_n \varrho^n e^{jk\hat{\boldsymbol{\rho}} \cdot \boldsymbol{\rho}^n} \\ &= \frac{\omega\mu}{\sqrt{8\pi k \rho}} e^{-j(k\rho + \frac{3\pi}{4})} [I_n \varrho^n]^t \left[ e^{jk\hat{\boldsymbol{\rho}} \cdot \boldsymbol{\rho}^n} \right], \end{aligned} \quad (67)$$

where the superscript  $t$  denotes the transpose. An important observation is that the same algorithm may be used to evaluate both (60) and the last column vector in (67).

### Numerical Results

Figure 7 shows the current distribution on a square cylinder illuminated by a TM plane wave. Each side of the cylinder is of width  $2a$ , and the current distribu-

**Figure 7** Current distribution on a square cylinder illuminated by TM plane wave.



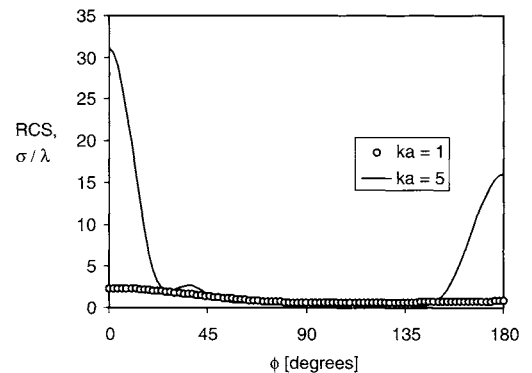
tion is plotted beginning from the middle of the illuminated side. The singular nature of the current parallel to the edges is evident in the figure. As the frequency increases, the current on the illuminated side should approach the physical optics result  $2H^{\text{inc}}$ , and this behaviour is evident in the figure. For these computations, the cylinder cross section was subdivided into 40 subdomains. Also shown in the figure for comparison are results from the magnetic field integral equation (MFIE) approach to be considered in §5.

In Fig. 8, the bistatic radar cross section of the cylinder for the same illumination is given. The observation angle  $\phi = 0^\circ$  corresponds to the cylinder’s backscattering direction.

### §3. Inhomogeneous Cylinders: Electric Field Wave Equation, TM Polarisation

In this section, we specialise the vector wave equation to a scalar wave equation and solve it as an interior problem using the *finite element method* (FEM). In reality, the variational formulation of FEM is

**Figure 8** Bistatic radar cross section of square cylinder illuminated by TM plane wave.



equivalent to the MoM, but historically the former has been usually applied to partial differential equations while the latter has typically been applied to integral equations. In recent years, it has become more common to formulate the FEM from the weak form of the underlying partial differential equation, and this approach is even closer to the spirit of the MoM approach. Because it is simpler to apply, we also present the FEM from this point of view; we establish the equivalence of the variational FEM and MoM approaches in the following section.

The vector wave equation for the electric field, (7), reduces to a scalar form when only a single component of  $\mathbf{E}$  is present. For example, we assume that all field quantities and material parameters are independent of  $z$  and there exists only a  $z$  component of the electric field—the so-called *transverse magnetic* polarisation. The problem is thus two-dimensional, and hence we restrict consideration to the domain  $S$ , the cross section of the cylindrical geometry in the  $z = 0$  plane. We assume that  $C$  is the boundary of  $S$ , and is a (closed) curve of finite length in the plane  $z = 0$ . With these assumptions, we write  $\mathbf{E} = E_z(\boldsymbol{\rho})\hat{\mathbf{z}}$ ,  $\mathbf{J} = J_z(\boldsymbol{\rho})\hat{\mathbf{z}}$ , where  $\boldsymbol{\rho} = x\hat{\mathbf{x}} + y\hat{\mathbf{y}}$  is the two-dimensional position vector. For simplicity, we also consider isotropic media,  $\boldsymbol{\mu}_r^{-1}(\boldsymbol{\rho}) = \mu_r^{-1}(\boldsymbol{\rho})\mathbf{I}$ ,  $\boldsymbol{\epsilon}_r(\boldsymbol{\rho}) = \epsilon_r(\boldsymbol{\rho})\mathbf{I}$ , where  $\mathbf{I}$  is the identity dyad. Thus the wave equation (7) reduces to the scalar, two-dimensional form

$$\nabla \cdot (\mu_r^{-1} \nabla E_z) + k_0^2 \epsilon_r E_z = j\omega\mu_0 J_z, \quad \boldsymbol{\rho} \in S, \quad (68)$$

where  $\nabla = \hat{\mathbf{x}} \frac{\partial}{\partial x} + \hat{\mathbf{y}} \frac{\partial}{\partial y}$  is the two-dimensional nabla operator. Equation (68) is an elliptic partial differential equation, for which boundary conditions on  $C$  must be specified to uniquely determine a solution.

The equality (68) is termed the *strong form* of the scalar wave equation; it must hold at every point in the domain. In a numerical solution, however, we must necessarily approximate  $E_z$  in (68), and hence it will not be possible to satisfy the equality everywhere in the solution domain. Instead, we enforce the equality in a weighted average sense. This is done by requiring the equality of an inner product of both sides of (68) with a set of *weighting* or *testing functions*. The inner product used is defined as

$$\langle A, B \rangle = \int_S A(\boldsymbol{\rho})B(\boldsymbol{\rho})dS. \quad (69)$$

Usually one of the terms in an inner product is conjugated, but without the conjugate the product often gains important properties stemming from the reciprocity of fields. To distinguish it from the usual form, this type of inner product is called a *symmetric* or *pseudo-inner product*.

Thus, we assume the availability of a suitable set of weighting functions  $\Lambda_m$ , multiply both sides of Eq. (68) by  $\Lambda_m$  and integrate over  $S$ . We further apply an integration by parts to the first resulting

term using the identity  $\nabla \cdot (\psi \mathbf{a}) = \psi \nabla \cdot \mathbf{a} + \mathbf{a} \cdot \nabla \psi$ , the divergence theorem and Faraday's law specialised to the TM case,  $\frac{1}{\mu_r} \nabla E_z \times \hat{\mathbf{z}} = -j\omega\mu_0 \mathbf{H}$ . This results in the following so-called *weak form* of the scalar wave equation

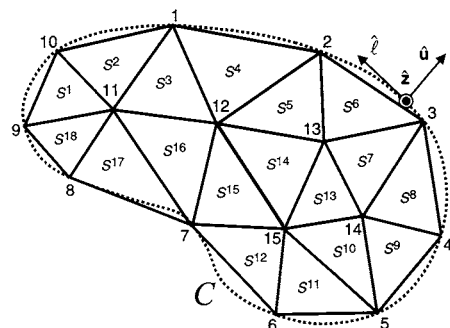
$$-\langle \nabla \Lambda_m; \mu_r^{-1} \nabla E_z \rangle + k_0^2 \langle \Lambda_m, \epsilon_r E_z \rangle + j\omega\mu_0 \int_C \Lambda_m \mathbf{H} \cdot \hat{\boldsymbol{\ell}} dC = j\omega\mu_0 \langle \Lambda_m, J_z \rangle, \quad (70)$$

where  $\hat{\boldsymbol{\ell}} = \hat{\mathbf{z}} \times \hat{\mathbf{u}}$  is a unit vector tangent to  $C$ , and  $\hat{\mathbf{u}}$  is the outward unit normal to  $C$  in the plane  $z = 0$  (cf. Fig. 9). From the method of moments point of view, instead of enforcing equality (68) directly, (70) enforces equality of its generalised moments with respect to the testing functions. The symmetric product between the two vector quantities appearing in (70) is defined as

$$\langle \mathbf{A}; \mathbf{B} \rangle = \int_S \mathbf{A}(\boldsymbol{\rho}) \cdot \mathbf{B}(\boldsymbol{\rho}) dS. \quad (71)$$

An advantage of the weak form is that the boundary conditions of the problem can be incorporated in the integral term involving  $\mathbf{H}$ ; values for  $\mathbf{E}$ ,  $\mathbf{H}$ , or a relationship between them can be inserted into this term. If the boundary  $C$  of  $S$  is a conductor, i.e., it is the boundary of a two-dimensional cavity (waveguide at cutoff), then the tangential electric field vanishes on the boundary:  $E_z = 0$  on  $C$ . To enforce this so-called *Dirichlet boundary condition*, we must choose a basis representation for  $E_z$  that vanishes on  $C$ . As we will see, the testing functions  $\Lambda_m$  will also serve as basis functions for representing  $E_z$ , and hence they must vanish on  $C$ . Consequently, the integral term over  $C$  in (70) also vanishes. Since it must be enforced explicitly, the Dirichlet boundary condition is called an *essential boundary condition*. By contrast, if the tangential magnetic field vanishes on the boundary, i.e.,  $\hat{\boldsymbol{\ell}} \cdot \mathbf{H} = \frac{1}{j\omega\mu} \frac{\partial E_z}{\partial n} = 0$  on  $C$ , then we need only substitute this condition into (70), which also eliminates the integral over  $C$ . This so-called *Neumann boundary condition* places no requirements on the bases, and hence is known as a *natural boundary condition*.

**Figure 9** Surface  $S$  with boundary  $C$  subdivided into triangles  $S^e$ .



In the following we assume that  $C$  is a conducting boundary with  $E_z = 0$  in order to illustrate application of essential boundary conditions.

We can approximate the solution domain  $S$  by subdividing it into a set of  $E$  triangular elements  $S^e$ ,  $e = 1, 2, \dots, E$  as shown in Fig. 9. The resulting approximation to the original domain is denoted  $\tilde{S} = \cup_{e=1}^E S^e$  and constitutes the problem's geometry model. The data structure for describing the model consists of two tables of data. As Table 5 illustrates, one table contains *node data* locating the coordinates of the model's nodes or vertices,  $\mathbf{p}_v = x_v \hat{\mathbf{x}} + y_v \hat{\mathbf{y}}$ ,  $v = 1, 2, \dots, V$ . A second table, illustrated by Table 6, contains the *connection data*, which lists from Fig. 9 the nodes making up each triangular element. These are listed as global node indices in the table.

The remaining entries in the table are concerned with the approximation of  $E_z$ , to which we turn next. First we note that in converting the scalar wave equation from the strong form (68) to the weak form (70),  $E_z$  must no longer be twice differentiable but merely

differentiable. This reduced requirement is accomplished at the expense, however, of requiring differentiability of the testing functions. Since now both basis and testing functions must be differentiable, this suggests using the same set of functions  $\Lambda_n$  for both basis and testing. This choice, known as *Galerkin's method*, is assumed here, although it is by no means necessary. We further note that  $E_z$  is everywhere continuous in  $S$ , since, in the two-dimensional problem, it is tangent to any material boundaries. Both continuity and the differentiability requirement of our field model may be simultaneously realised if we choose a piecewise linear representation for  $E_z$  on  $\tilde{S}$ , as depicted in Fig. 10. The figure illustrates a perspective view of the geometry of Fig. 9 with the piecewise linear approximation of  $E_z$  plotted in the vertical dimension.

As the figure shows, the piecewise linear representation also easily accommodates the boundary condition  $E_z = 0$  on  $C$ . The representation is completely specified if we know only the values of  $E_z$  at the interior (nonboundary) nodes of  $\tilde{S}$ , the so-called *degrees of freedom* (DoF) of  $E_z$ ; field values at all other points are merely determined from these by linear interpolation. Each interior node is assigned a DoF index,  $n = 1, 2, \dots, N$ , where  $N$  is the total number of unknowns or degrees of freedom. The required associations between DoF, local and global indices are illustrated in Table 6 for the geometry of Fig. 10. Note that in the table, boundary nodes are easily identified by their null DoF index.

The piecewise linear approximation of the field  $E_z$  may be represented as a linear combination of a set of pyramidal interpolation functions  $\Lambda_n$ , as shown in Fig. 11. Each internal node with DoF index  $n$  has an associated basis function,  $\Lambda_n$ , where  $\Lambda_n$  is a linear

**Table 5** Partial Listing of Global Node Coordinates

Global node index $v$	Coordinates	
	$x_v$	$y_v$
1	-0.500	1.100
2	1.100	0.700
⋮	⋮	⋮
12	0.000	0.000
⋮	⋮	⋮
15	0.700	-1.100

**Table 6** Partial Listing of Element Connection Data Corresponding to Figs. 9 and 10

$e$	Local node 1		Local node 2		Local node 3	
	Global node no.		Global node no.		Global node no.	
	No. DoF's	DoF index	No. DoF's	DoF index	No. DoF's	DoF index
1	9		11		10	
	0	0	1	1	0	0
2	11		1		10	
	1	1	0	0	0	0
⋮	⋮		⋮		⋮	
14	15		13		12	
	1	5	1	3	1	2
⋮	⋮		⋮		⋮	
18	8		11		9	
	0	0	1	1	0	0

**Figure 10** Piecewise linear representation of  $E_z$  and DoF labelling on  $\tilde{S}$ , the approximation to  $S$  of Fig. 9.

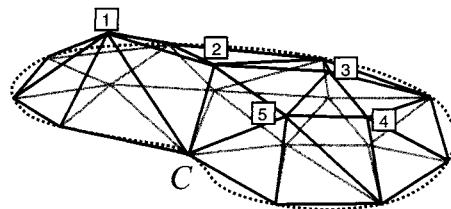
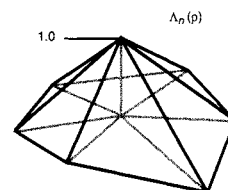


**Figure 11** Linear interpolating basis function  $\Lambda_n$  and its support.



function with a unit value at node  $n$  and zero value at the remaining nodes of the triangles surrounding and sharing node  $n$ . The basis function vanishes everywhere except on these triangles, known collectively as the *support* of the basis function.

One should keep in mind that basis function  $\Lambda_n$  is associated with an *interior* node with DoF index  $n$ . This is generally not the same as the  $n$ th node of the geometry representation because the latter also includes boundary nodes. In terms of these bases, the field is represented as

$$E_z(\boldsymbol{\rho}) \approx \sum_{n=1}^N V_n \Lambda_n(\boldsymbol{\rho}) = [\Lambda_n(\boldsymbol{\rho})]^t [V_n], \quad (72)$$

where the superscript  $t$  denotes the transpose and the coefficient  $V_n$  represents a single DoF, the approximate value of  $E_z$  at the node with DoF index  $n$ . Note in particular that no degrees of freedom are associated with boundary nodes where  $E_z$  vanishes; if bases for these nodes were included, their coefficients would vanish.

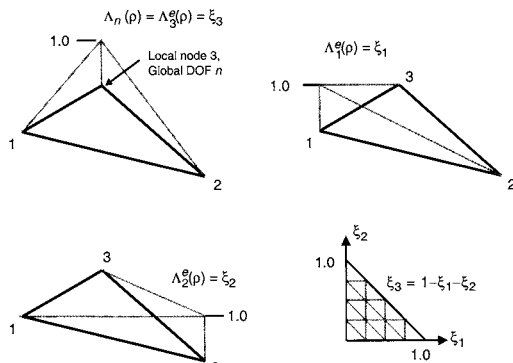
Up to three bases have supports overlapping a single element; clearly, they are the bases whose DoF nodes are vertices of the element. On an element  $e$ , a local indexing scheme is used to label the restrictions of these bases to the element. That is, we write

$$\Lambda_n(\boldsymbol{\rho}) = \Lambda_i^e(\boldsymbol{\rho}), \quad \boldsymbol{\rho} \in S^e \quad (73)$$

if the  $i$ th local node index,  $i = 1, 2$  or  $3$ , of element  $e$  corresponds to the node with DoF index  $n$ . The restrictions of the bases to an element are illustrated in Fig. 12. As will be seen, this local representation and indexing scheme is also convenient for other quantities defined on the element.

It should be kept in mind that a node may be referred to in up to three different ways. As seen in Table 6, an interior node of element  $e$  may have a global node index  $\nu$ , a global DoF index  $n$  and a local node index  $i$ . Also note that a local index  $i$  for an

**Figure 12** Local bases on element  $e$ ; local node  $i = 3$  is assumed to be associated with global basis with DoF index  $n$ . All elements and bases are mapped to the parent triangle shown.



interior node of element  $e$  corresponds to a single DoF index, but not vice versa.

Substitution of the representation (72) for  $E_z$  into the weak form of the wave equation, Eq. (70), yields the matrix system

$$[Y_{mn}][V_n] = [I_m], \quad (74)$$

where  $[V_n]$  is a column vector of unknown voltage coefficients,

$$[Y_{mn}] = \frac{1}{j\omega} [\Gamma_{mn}] + j\omega [C_{mn}] \quad (75)$$

is the system admittance matrix and

$$\Gamma_{mn} = \mu_0^{-1} \langle \nabla \Lambda_m; \mu_r^{-1} \nabla \Lambda_n \rangle, \quad (76)$$

$$C_{mn} = \epsilon_0 \langle \Lambda_m, \epsilon_r \Lambda_n \rangle \quad (77)$$

are the reciprocal inductance and the capacitance matrices, respectively. The source is represented by the excitation column vector

$$[I_m] = -[\langle \Lambda_m, J_z \rangle]. \quad (78)$$

Note that the units of  $V_n$ ,  $Y_{mn}$ ,  $\Gamma_{mn}$ ,  $C_{mn}$  and  $I_m$  are V/m, S·m, H<sup>-1</sup>·m, F·m and A, respectively. Once (75) and the excitation column vector are obtained, the coefficient column vector  $[V_n]$  may be found by algebraic methods. We turn our attention next to the evaluation of the elements of the matrix  $[Y_{mn}]$  and column vector  $[I_m]$ .

### The Element Matrix and Matrix Assembly

Consider first the evaluation of a capacitance matrix element,  $C_{mn}$ . Note in (77) that there will be no contribution to  $C_{mn}$  from bases  $\Lambda_m$  and  $\Lambda_n$  if their supports do not overlap. Hence, many of the off-diagonal elements of  $C_{mn}$  are zero; i.e., the matrix  $[C_{mn}]$  is *sparse*. If one attempts to fill the matrix  $[C_{mn}]$  by naively advancing through its row and column indices, one must constantly search through the element connection data to determine which elements are in the support of  $\Lambda_m$  and  $\Lambda_n$ , and then determine whether their supports overlap. To avoid this time-consuming process, a more efficient approach is usually taken. Note that the symmetric product integral involved in a capacitance matrix element can be written as a sum over contributions from individual triangle elements  $S^e$  as

$$\begin{aligned} C_{mn} &= \epsilon_0 \langle \Lambda_m, \epsilon_r \Lambda_n \rangle = \epsilon_0 \int_S \epsilon_r \Lambda_m(\boldsymbol{\rho}) \Lambda_n(\boldsymbol{\rho}) dS \\ &= \sum_{e=1}^E \epsilon^e \int_{S^e} \Lambda_m(\boldsymbol{\rho}) \Lambda_n(\boldsymbol{\rho}) dS, \end{aligned} \quad (79)$$

where, for simplicity, we have assumed that the permittivity is constant in each element; i.e.,  $\epsilon_0 \epsilon_r = \epsilon^e$  in element  $e$ . Of the  $N \times N$  basis pair combinations that may appear in the last integral, only up to nine combinations will make any contribution to the integral—those pairs whose associated DoF nodes

are also nodes of  $S^e$ . The interactions between these contributing basis pairs on  $S^e$  are equivalent to those between the three local bases depicted in Fig. 12. Indeed, the latter are just the restrictions on  $S^e$  of the global bases contributing to element  $S^e$ . Thus, using (73) in (79), we find that the interactions between the global bases on  $S^e$  may be completely determined from the contributions of *element matrices*

$$[C_{ij}^e] = \left[ \epsilon^e \int_{S^e} \Lambda_i^e(\mathbf{p}) \Lambda_j^e(\mathbf{p}) dS \right], \quad (80)$$

in which  $C_{ij}^e$  represents the interaction between bases  $\Lambda_i^e$  and  $\Lambda_j^e$  associated with local node pairs  $i$  and  $j$ ,  $i, j = 1, 2, 3$ , of element  $e$ ,  $e = 1, 2, \dots, E$ .

The same arguments apply to the reciprocal inductance matrix (76), so that we may define a reciprocal inductance element matrix,

$$[\Gamma_{ij}^e] = \frac{1}{\mu^e} \left[ \int_{S^e} \nabla \Lambda_i^e \cdot \nabla \Lambda_j^e dS \right], \quad (81)$$

where  $\mu_0 = \mu_r = \mu^e$  is assumed constant in an element. The capacitance and reciprocal inductance matrices for an element may be combined to form an element admittance matrix corresponding to the system admittance matrix (75),

$$[Y_{ij}^e] = j\omega [C_{ij}^e] + \frac{1}{j\omega} [\Gamma_{ij}^e]. \quad (82)$$

In the *matrix assembly* process, the elements of the element admittance matrix  $[Y_{ij}^e]$  are then assembled as contributions to the global admittance matrix  $Y_{mn}$  according to the following *Matrix Assembly Rule*:

#### MATRIX ASSEMBLY RULE

$Y_{ij}^e$  is added to  $Y_{mn}$  if  $m, n$  are nodal degree of freedom indices associated with local nodes  $i$  and  $j$ , respectively, of element  $e$ .

The assembly process completes the connection between locally and globally defined quantities. Clearly, the correspondence needed to carry out the process for a given element  $e$  is simply that between the local node indices at the top of Table 6 and the global degree of freedom indices listed for element  $e$  in the table. The resulting assembly process for the meshing scheme of Figs. 9 and 10 is partially summarised in Table 7.

#### Evaluation of the Element Matrices

We consider next the detailed evaluation of the element capacitance matrix. To parameterise the integral over a triangle, we introduce a set of *normalised area coordinates*. Let a point in the triangle be designated by the position vector  $\mathbf{p}$ . As Fig. 13 shows, the point defines a subdivision of the triangle into three subtriangles. The area of the subtriangle opposite vertex  $i$  has area  $A_i$ . Normalised area

**Figure 13** Subdivision of a triangle into three subareas defining normalised area coordinates.

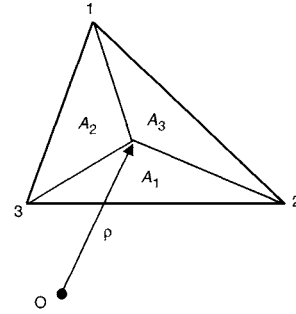


**Table 7** Assembly of Element Matrix Contributions to System Matrix Elements

Contributing elements of element matrix	Elements added to in system matrix
$Y_{22}^1$	$Y_{11}$
$Y_{11}^2$	$Y_{11}$
$\vdots$	$\vdots$
$Y_{11}^{14}$	$Y_{55}$
$Y_{12}^{14}, Y_{21}^{14}$	$Y_{53}, Y_{35}$ (respectively)
$Y_{13}^{14}, Y_{31}^{14}$	$Y_{52}, Y_{25}$ (respectively)
$Y_{22}^{14}$	$Y_{33}$
$Y_{23}^{14}, Y_{32}^{14}$	$Y_{32}, Y_{23}$ (respectively)
$Y_{33}^{14}$	$Y_{22}$
$\vdots$	$\vdots$
$Y_{22}^{18}$	$Y_{11}$

coordinates are then defined as

$$\xi_i = \frac{A_i}{A^e}, \quad i = 1, 2, 3, \quad (83)$$

where  $A^e$  is the area of element  $e$ . Since the areas of the subtriangles sum to  $A^e$ , the coordinates satisfy

$$\xi_1 + \xi_2 + \xi_3 = 1, \quad (84)$$

so that only two of the coordinates are independent. From (83), clearly  $\xi_i = 0$  at edge  $i$  and is unity at vertex  $i$  of a triangle. In effect, every triangle, as well as the scalar bases defined on them, is mapped onto a standard *parent* triangle, as depicted in Fig. 12.

Table 8 summarises the computation of an element triangle's area  $A^e$ , edge vectors  $\mathbf{e}_i$ , height vectors  $\mathbf{h}_i$  and coordinate gradients  $\nabla \xi_i$ . For our triangles in the  $x$ - $y$  plane, the triangle's unit normal  $\hat{\mathbf{n}}$  is  $\hat{\mathbf{z}}$ . These quantities are also depicted in Fig. 14 and are used in evaluating element matrices for triangular elements.

**Figure 14** Edge and height vectors defined on a triangle.

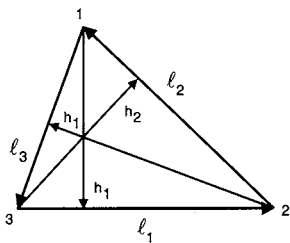


**Table 8** Geometrical Quantities Defined on Triangular Elements

Edge vectors	$l_i = \mathbf{p}_{i-1}^e - \mathbf{p}_{i+1}^e$ ; $l_i =  l_i $ ; $\hat{l}_i = \frac{l_i}{l_i}$ , $i = 1, 2, 3$
Area	$A^e = \frac{ l_{i-1} \times l_{i+1} }{2}$ , $i = 1, 2$ , or $3$
Height vectors	$h_i = \frac{2A^e}{l_i}$ ; $\hat{h}_i = -\hat{n} \times \hat{l}_i$ ; $\mathbf{h}_i = h_i \hat{h}_i$ , $i = 1, 2, 3$
Coordinate gradients	$\nabla \xi_i = -\frac{\hat{h}_i}{h_i}$ , $i = 1, 2, 3$

Since the coordinates  $\xi_i$  vary linearly from zero along edge  $i$  to unity at vertex  $i$ , they are also the local linear interpolation functions depicted in Fig. 12. In terms of area coordinates then, points in a triangle may be represented by linearly interpolating its vertex

coordinates

$$\mathbf{p} = \mathbf{p}_1^e \xi_1 + \mathbf{p}_2^e \xi_2 + \mathbf{p}_3^e \xi_3, \quad (85)$$

where  $\mathbf{p}_i^e$  is the position vector of the  $i$ th vertex of element  $e$ . As shown in Fig. 12, the local bases are also linear interpolating functions that in area coordinates are simply

$$\Lambda_i^e = \xi_i. \quad (86)$$

Furthermore, since

$$\begin{aligned} dS &= \left| \frac{\partial \mathbf{p}}{\partial \xi_{i-1}} \times \frac{\partial \mathbf{p}}{\partial \xi_{i+1}} \right| d\xi_{i-1} d\xi_{i+1} \\ &= |l_{i+1} \times l_{i-1}| d\xi_{i-1} d\xi_{i+1} \\ &= 2A^e d\xi_{i-1} d\xi_{i+1}, \end{aligned} \quad (87)$$

where the index arithmetic is performed modulo 3, any integral over an element triangle may be expressed in terms of an integral over the parent triangle as

$$\begin{aligned} \int_{S^e} f(\mathbf{p}) dS &= 2A^e \int_0^1 \int_0^{1-\xi_{i+1}} f(\mathbf{p}_1^e \xi_1 + \mathbf{p}_2^e \xi_2 + \mathbf{p}_3^e \xi_3) d\xi_{i-1} d\xi_{i+1} \\ &\approx 2A^e \sum_{k=1}^K w_k f(\mathbf{p}_1^e \xi_1^{(k)} + \mathbf{p}_2^e \xi_2^{(k)} + \mathbf{p}_3^e \xi_3^{(k)}), \end{aligned} \quad (88)$$

where the last line is a  $K$ -point rule for numerical integration over a triangle. Sample points and weighting coefficients for  $K = 1, 3, 7$  are given in Table 9 (Hammer *et al.*, 1956; Zienkiewicz, 1971). Combining (86)–(88) and the results of Table 8, (80) and (81)

**Table 9** Sample Points and Weighting Coefficients for  $K$ -Point Quadrature on Triangles

Sample points, $(\xi_1^{(k)}, \xi_2^{(k)})$ $(\xi_3^{(k)} = 1 - \xi_1^{(k)} - \xi_2^{(k)})$	Weights, $w_k$
<b>K=1, error <math>\mathcal{O}(\xi_i^2)</math></b>	
(0.33333333333333, 0.33333333333333)	0.50000000000000
<b>K=3, error <math>\mathcal{O}(\xi_i^3)</math></b>	
(0.66666666666667, 0.16666666666667)	0.16666666666667
(0.16666666666667, 0.66666666666667)	0.16666666666667
(0.16666666666667, 0.16666666666667)	0.16666666666667
<b>K=7, error <math>\mathcal{O}(\xi_i^6)</math></b>	
(0.33333333333333, 0.33333333333333)	0.11250000000000
(0.79742698535309, 0.10128650732346)	0.06296959027241
(0.10128650732346, 0.79742698535309)	0.06296959027241
(0.10128650732346, 0.10128650732346)	0.06296959027241
(0.47014206410512, 0.47014206410512)	0.06619707639425
(0.47014206410512, 0.05971587178977)	0.06619707639425
(0.05971587178977, 0.47014206410512)	0.06619707639425

may be evaluated numerically. To obtain numerically exact results for such integrals, one should choose quadrature schemes from Table 9 whose error order is higher than the highest order of coordinate products appearing in the integrand. In (80), the integrand is of quadratic order, and hence  $K \geq 3$ .

In this case, however, the integrals may be evaluated analytically. For example, the element capacitance matrix is easily determined as

$$\begin{aligned} [C_{ij}^e] &= \left[ \epsilon^e \int_{S^e} \Lambda_i^e \Lambda_j^e dS \right] \\ &= \left[ 2A^e \epsilon^e \int_0^1 \int_0^{1-\xi_2} \xi_i \xi_j d\xi_1 d\xi_2 \right] \\ &= \frac{A^e \epsilon^e}{12} \begin{bmatrix} 2 & 1 & 1 \\ 1 & 2 & 1 \\ 1 & 1 & 2 \end{bmatrix}, \end{aligned} \quad (89)$$

the evaluation of which is facilitated by the identity

$$\int_{S^e} \xi_1^{\alpha} \xi_2^{\beta} \xi_3^{\gamma} dS = \frac{2A^e \alpha! \beta! \gamma!}{(\alpha + \beta + \gamma + 2)!}. \quad (90)$$

The elements of the reciprocal inductance matrix  $[\Gamma_{ij}^e]$  are given by

$$\Gamma_{ij}^e = \frac{1}{\mu^e} \int_{S^e} \nabla \xi_i \cdot \nabla \xi_j dS. \quad (91)$$

Since  $\xi_i$  varies linearly from zero to unity from a triangle's  $i$ th edge to its  $i$ th vertex over a distance equal to its height  $h_i$ , the gradient  $\nabla \xi_i$  is the (constant) vector (cf. Table 8 and Fig. 14)

$$\nabla \xi_i = -\frac{\hat{h}_i}{h_i} = \frac{\hat{z} \times \ell_i}{2A^e}, \quad (92)$$

where  $\hat{h}_i$  is the unit outward normal vector in the plane of the triangle at edge  $i$ . With (92), we find that the integrand of (91) is constant, and immediately obtain

$$\Gamma_{ij}^e = \frac{1}{\mu^e} \frac{\ell_i \cdot \ell_j}{4A^e}. \quad (93)$$

For  $i \neq j$  this can be written as

$$\begin{aligned} \Gamma_{ij}^e &= \frac{1}{\mu^e} \frac{\ell_i \cdot \ell_j}{2|\ell_i \times \ell_j|} = \frac{1}{2\mu^e} \cot \theta_{ij} \\ &= -\frac{1}{2\mu^e} \cot \theta_k, \quad i \neq j \neq k, \end{aligned} \quad (94)$$

where  $\theta_{ij}$  is the (exterior) angle between edge vectors  $\ell_i$  and  $\ell_j$ , while  $\theta_k$  is the (interior) angle of  $S^e$  between edges  $i$  and  $j$  at node  $k$ . When  $i = j$ , we note that

$$\begin{aligned} \Gamma_{ii}^e &= \frac{1}{\mu^e} \frac{\ell_i \cdot \ell_i}{4A^e} \\ &= \frac{1}{\mu^e} \frac{\ell_i \cdot (-\ell_j - \ell_k)}{4A^e} \\ &= \frac{1}{2\mu^e} [\cot \theta_j + \cot \theta_k], \quad i \neq j \neq k. \end{aligned} \quad (95)$$

Thus, we can construct all the matrix elements  $\Gamma_{ij}^e$  from the three values

$$\cot \theta_i = -\frac{\ell_j \cdot \ell_k}{2A^e}, \quad i = 1, 2, 3, \quad i \neq j \neq k. \quad (96)$$

For computational efficiency, Silvester and Ferrari (1996) suggest computing the element matrix  $[\Gamma_{ij}^e]$  by expressing the result as a linear combination of terms associated with the vertices of the triangular element:

$$\begin{aligned} [\Gamma_{ij}^e] &= \frac{1}{2\mu^e} \begin{bmatrix} \cot \theta_2 + \cot \theta_3 & -\cot \theta_3 & -\cot \theta_2 \\ -\cot \theta_3 & \cot \theta_1 + \cot \theta_3 & -\cot \theta_1 \\ -\cot \theta_2 & -\cot \theta_1 & \cot \theta_1 + \cot \theta_2 \end{bmatrix} \\ &= \frac{1}{\mu^e} \cot \theta_1 [Q_1] + \frac{1}{\mu^e} \cot \theta_2 [Q_2] + \frac{1}{\mu^e} \cot \theta_3 [Q_3], \end{aligned} \quad (97)$$

where

$$[Q_1] = \begin{bmatrix} 0 & 0 & 0 \\ 0 & \frac{1}{2} & -\frac{1}{2} \\ 0 & -\frac{1}{2} & \frac{1}{2} \end{bmatrix}, \quad (98)$$

$$[Q_2] = \text{rot} [Q_1] = \begin{bmatrix} \frac{1}{2} & 0 & -\frac{1}{2} \\ 0 & 0 & 0 \\ -\frac{1}{2} & 0 & \frac{1}{2} \end{bmatrix}, \quad (99)$$

$$[Q_3] = \text{rot} [Q_2] = \begin{bmatrix} \frac{1}{2} & -\frac{1}{2} & 0 \\ -\frac{1}{2} & \frac{1}{2} & 0 \\ 0 & 0 & 0 \end{bmatrix}. \quad (100)$$

The rotation operator, "rot", is defined as the operator that cyclically permutes row and column indices, i.e.,  $1 \rightarrow 2 \rightarrow 3 \rightarrow 1$ .

### Evaluation of Element Excitation Vector

Contributions to the system excitation column vector,

$$[I_m] = -\langle \Lambda_m, J_z \rangle, \quad (101)$$

may also be assembled from an element column vector. For simplicity, we assume that the excitation current density is constant,  $J_z = J_z^e$ , in element  $S^e$ . Then the element column vector is simply

$$[I_i^e] = -J_z^e \langle \Lambda_i^e, 1 \rangle = -\frac{J_z^e A^e}{3}, \quad i = 1, 2, 3. \quad (102)$$

The Matrix Assembly Rule following (82) may also be used to accumulate these element contributions into the system excitation column vector  $[I_m]$ .

### Numerical Results

Because we have so far considered only the Dirichlet boundary condition  $E_z = 0$ , we cannot yet consider scattering problems using the finite element method.

Scattering problems must somehow incorporate radiation conditions at the mesh boundaries. To illustrate the method for interior regions, however, we determine the TM eigenfrequencies of an air-filled square waveguide. Since these are source-free solutions of the wave equation, we set  $[I_m] = 0$  in (74) and, using (75), we find the eigenvalues  $\omega_{pq}^2$  of the generalised eigenvalue problem

$$[\Gamma_{mn}][V_n] = \omega_{pq}^2 [C_{mn}][V_n]. \quad (103)$$

The eigenvalues of the waveguide are known to be  $\omega_{pq}^2 = \left[\frac{c_0\pi}{a}\right]^2 (p^2 + q^2)$  where  $c_0$  is the speed of light in air,  $a$  is the dimension of a side, and  $p, q = 1, 2, \dots$ . The error in the first five distinct eigenvalues is plotted versus  $N$ , the number of subdivisions per side, in Fig. 15. By plotting the error on a logarithmic scale, one immediately establishes that, as the mesh density increases, the error in the eigenvalues decreases as  $(1/N)^2$ .

### §4. Moment and Finite Element Methods

In this section we look at numerical solution procedures for scattering problems from the abstract point of view of numerical solution methods for linear operator equations; familiarity with the material of the previous two sections is assumed. The abstract point of view not only provides a deeper understanding of the methods, but also illuminates the essential equivalence between moment, finite element, variational and other approaches that, for historical reasons, go by different names.

An electromagnetic scattering problem is usually formulated as a problem in determining an unknown field or equivalent source  $u$  due to a given source or excitation  $f$ . This linear problem (or its linearised approximant) can be stated in equation form as

$$\mathcal{L}u = f, \quad (104)$$

where  $\mathcal{L}$  is a linear operator, i.e., one satisfying the linearity condition

$$\mathcal{L}(au_1 + bu_2) = a\mathcal{L}u_1 + b\mathcal{L}u_2 \quad (105)$$

for arbitrary constants  $a$  and  $b$ . In scattering problems,  $\mathcal{L}$  is usually a differential, integral or integro-differential operator relating a field within a domain  $D$  to its sources in the region or its values on the domain boundary  $\partial D$ .

Most methods for obtaining numerical solutions of (104) can be viewed as *projection* or *moment methods*. Having presented some specific examples in previous sections, it is now useful to summarise the approach from this abstract point of view. The first step in the process is to introduce a *symmetric product* between two scalar functions  $u$  and  $v$  of the form

$$\langle u, v \rangle = \int_D uv dD, \quad D = C, S, \text{ or } \mathcal{V}, \quad (106)$$

on the domain  $D$  with differential element  $dD$ . Domain  $D$  may be a line or (one-dimensional) curve  $C$ , a (two-dimensional) surface  $S$  or a (three-dimensional) volume  $\mathcal{V}$ . Clearly, the symmetric product satisfies the linearity conditions

$$\begin{aligned} \langle au_1 + bu_2, v \rangle &= a \langle u_1, v \rangle + b \langle u_2, v \rangle, \\ \langle u, cv_1 + dv_2 \rangle &= c \langle u, v_1 \rangle + d \langle u, v_2 \rangle. \end{aligned} \quad (107)$$

The symmetric product is easily extended to the case in which  $u$  and  $v$  are vector functions,  $u = \mathbf{u}$  and  $v = \mathbf{v}$ , and, if necessary, this case can be distinguished explicitly by writing

$$\langle \mathbf{u}; \mathbf{v} \rangle = \int_D \mathbf{u} \cdot \mathbf{v} dD. \quad (108)$$

In integral equation formulations, convolutional integrals between  $v$  and a Green's function  $G(\mathbf{r}, \mathbf{r}')$  (the *kernel* of the integral equation) appear in symmetric products with  $u$ . When necessary, the various cases that arise can be distinguished explicitly via the compact notation

$$\langle u, G, v \rangle \equiv \int_D \int_D u(\mathbf{r}) G(\mathbf{r}, \mathbf{r}') v(\mathbf{r}') dD' dD \quad (109)$$

when  $u$  and  $v$  and the Green's function are scalars,

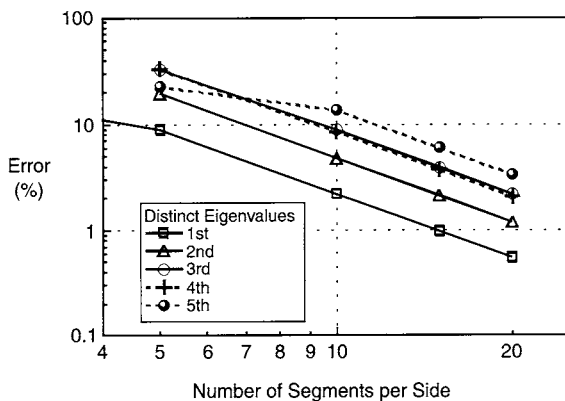
$$\langle \mathbf{u}; G, \mathbf{v} \rangle \equiv \int_D \int_D \mathbf{u}(\mathbf{r}) \cdot \mathbf{v}(\mathbf{r}') G(\mathbf{r}, \mathbf{r}') dD' dD \quad (110)$$

when  $u$  and  $v$  are vectors and the Green's function is a scalar and

$$\langle \mathbf{u}; \mathcal{G}; \mathbf{v} \rangle \equiv \int_D \int_D \mathbf{u}(\mathbf{r}) \cdot \mathcal{G}(\mathbf{r}, \mathbf{r}') \cdot \mathbf{v}(\mathbf{r}') dD' dD \quad (111)$$

when the Green's function is a dyad,  $\mathcal{G}$ . As in (106), the domain  $D$  in any of these symmetric products may be a curve  $C$ , a surface  $S$  or a volume  $\mathcal{V}$ . We observe that the symmetric product merely generalises to function pairs the dot (inner) product between pairs of  $N$ -dimensional vectors  $u = (u_1, u_2, \dots, u_N)$  and

**Figure 15** Convergence of first five distinct TM eigenvalues of a square waveguide.



$v = (v_1, v_2, \dots, v_N)$  given by  $\sum_{n=1}^N u_n v_n$ . Further borrowing from the language of vector analysis, we say that the symmetric product (106) represents a *projection of  $u$  onto  $v$*  or vice versa. By projecting Eq. (104) onto a space of so-called *weighting* or *testing functions*  $w$ , (104) is reformulated in the so-called *weak form*:

$$\langle w, \mathcal{L}u \rangle = \langle w, f \rangle. \quad (112)$$

In contrast to the *strong form* (104) for which equality holds at each point in  $\mathcal{D}$ , (112) requires only that equality hold in a (weighted) average sense for various choices  $w$  selected from the space of weighting functions. If the space of  $w$  for which (112) holds is sufficiently large (infinite, in general), it may be shown that (112) implies that (104) holds *almost everywhere*—that is, at all but a denumerable set of discrete points in  $\mathcal{D}$ . In a numerical solution, we can only choose a finite number of these weighting or testing functions, i.e., a set  $\{w_m^{(N)}\}, m = 1, 2, \dots, N$ . Ideally, this set should have the property that as  $N \rightarrow \infty$ , the equality (104) holds almost everywhere. Such a set of testing functions is said to be *complete*, and guarantees that if  $N$  is chosen sufficiently large, the error in the equality can be made arbitrarily small.

For a numerical solution, not only the equality, but also the unknown  $u$  must be approximated. We choose the approximation

$$u \approx \tilde{u} = \sum_{n=1}^N U_n u_n, \quad (113)$$

where  $U_n$  is a set of unknown coefficients and  $u_n, n = 1, 2, \dots, N$ , is a set of known *basis functions* capable of providing a good approximation for  $u$ . The representation (113) reduces the infinite-dimensional problem of determining  $u$  at all points within its domain  $\mathcal{D}$  to the more manageable problem of determining a finite set of unknown coefficients  $U_n$ , a task more suited for computation. To obtain a unique solution, the  $u_n$  must merely be independent; to obtain a *numerically stable* solution, we should also ensure that the bases have a high *degree* of independence, as measured by their projections on one another. *Orthonormal* bases  $u_n$ , whose projections satisfy

$$\langle u_m, u_n \rangle = \int_{\mathcal{D}} u_m u_n dD = \delta_{mn} = \begin{cases} 1, & m = n, \\ 0, & m \neq n, \end{cases} \quad (114)$$

where  $\delta_{mn}$  is the Kronecker delta, are ideal, but such bases are difficult to define for arbitrarily shaped domains  $\mathcal{D}$ . As an alternative, we first approximate  $\mathcal{D}$  by subdividing it into a finite set of canonical *subdomains* or *elements* (e.g., line segments, triangles, rectangles, or tetrahedrons)  $\mathcal{D}^e, e = 1, 2, \dots, E$ . Taken together, the elements provide an approximation  $\tilde{\mathcal{D}}$  to  $\mathcal{D}$ , i.e.,  $\mathcal{D} \approx \tilde{\mathcal{D}} = \cup_{e=1}^E \mathcal{D}^e$ . It is convenient to define a set of *interpolatory polynomial* bases  $u_n$  on

$\tilde{\mathcal{D}}$  with the property  $u_m(\mathbf{r}_n) = \delta_{mn}$ , where  $\mathbf{r}_n, n = 1, 2, \dots, N$  is a set of interpolation points on  $\tilde{\mathcal{D}}$ . These bases clearly have the property that

$$\sum_{j=1}^N u_m(\mathbf{r}_j) u_n(\mathbf{r}_j) = \delta_{mn}. \quad (115)$$

The similarity between (114) and (115) is clear, and indeed it is found that interpolatory bases are generally highly independent and that calculations involving them are usually stable. Thus it is no accident that interpolatory bases are at the foundation of most numerical methods for solving (104).

Substituting the representation (113) for  $u$  into the weak form (112) and choosing a set of testing functions  $\{w = w_m, m = 1, 2, \dots, N\}$ , we obtain

$$\sum_{n=1}^N \langle w_m, \mathcal{L}u_n \rangle U_n = \langle w_m, f \rangle, \quad m = 1, 2, \dots, N, \quad (116)$$

which may be put into matrix form as

$$[L_{mn}][U_n] = [F_m], \quad (117)$$

where  $L_{mn} = \langle w_m, \mathcal{L}u_n \rangle$  and  $F_m = \langle w_m, f \rangle$ . Solution of the linear system (116) or (117) yields the column vector of unknowns,  $[U_n]$ , which in turn provides an approximation to  $u$  throughout  $\mathcal{D}$  by (113). This result may also be written as a symmetric product of column vectors as

$$u \approx \tilde{u} = [U_n]^t [u_n] = [u_n]^t [U_n], \quad (118)$$

where “t” denotes transpose, i.e.,  $[u_n]^t$  is the row vector formed by transposing the basis function column vector  $[u_n]$ .

Once an approximate value for  $u$  is obtained, one is often interested in determining a scalar physical parameter or figure of merit that depends linearly on  $u$ , i.e., a *linear functional* of  $u$ ,  $I[u]$ . For example,  $I[u]$  might be the capacitance of a conducting structure with surface charge density  $u$  or  $I[u]$  might be a vector component of the far field scattered by a conductor with surface current density  $u$ . Even the value of  $u$  at a point  $\mathbf{r}$  in the solution domain,  $u(\mathbf{r})$ , is a linear functional, although it may become unbounded at points where the field is singular. The Riesz representation theorem (Stakgold, 1967) guarantees that for any *bounded* linear functional there exists a function  $g$  such that the functional can be represented as the symmetric product of  $u$  and  $g$  as

$$I[u] = - \langle u, g \rangle, \quad (119)$$

where the minus sign is introduced merely for convenience.<sup>1</sup> Once an approximate solution  $\tilde{u}$  has been obtained, functionals on  $u$  may be approximated as

$$\begin{aligned} I[u] \approx I[\tilde{u}] &= - \langle \tilde{u}, g \rangle = - \sum_{n=1}^N U_n \langle u_n, g \rangle \\ &= - [U_n]^t [ \langle u_n, g \rangle ]. \end{aligned} \quad (120)$$

The procedure outlined above constitutes the MoM approach (Harrington, 1993) for solving the linear operator equation (104). The steps employed in the approach may be summarised as follows:

- Subdivide the problem domain  $D$  into  $E$  sub-domains or elements  $D^e$ , approximating  $D$  as  $\tilde{D} = \bigcup_{e=1}^E D^e$ .

- Choose a set of interpolating or other appropriate basis functions  $\{u_n\}$  defined on  $\tilde{D}$  and approximate  $u$  in terms of a set of unknown coefficients  $U_n$  as

$$u \approx \tilde{u} = \sum_n U_n u_n = [U_n]^t [u_n].$$

- Choose a set of weighting or testing functions  $\{w_m\}$ . When the basis functions  $\{u_m\}$  are also chosen as testing functions, the approach is known as *Galerkin's method*.

- Substitute the approximation  $\tilde{u}$  into (104) and test the resulting equation with the  $w_m$  to enforce the equality in a weighted average sense. Since testing amounts to forming a symmetric product or projecting the equality onto the set of testing functions. Hence the method of moments is also called the *method of projections*. If  $\mathcal{L}$  is a differential or integro-differential operator, integration by parts is often used to transfer differentiation onto the testing function, thereby reducing differentiability requirements on the bases  $u_n$ . Boundary terms resulting from integration by parts often can be eliminated or evaluated using boundary conditions of the problem.

- Solve the resulting matrix system

$$[ \langle w_m, \mathcal{L}u_n \rangle ] [U_n] = [ \langle w_m, f \rangle ]$$

for the unknown coefficients  $U_n$ . In principle, the system may be solved using any classical direct or iterative solution method; in practice, properties of the matrix  $\langle w_m, \mathcal{L}u_n \rangle$  may determine which of these or other special purpose approaches should be used for efficiency.

- Use (119) to approximate  $u$  or to determine desired figures of merit according to

$$\begin{aligned} I[u] &\approx I[\tilde{u}] = - \langle \tilde{u}, g \rangle \\ &= - \sum_{n=1}^N U_n \langle u_n, g \rangle \\ &= - [U_n]^t [ \langle u_n, g \rangle ]. \end{aligned} \quad (121)$$

### The Variational Approach and the Moment Method

A linear operator equation may also be formulated as a *variational* problem, and an approximating linear system of equations can be obtained via the Rayleigh-Ritz procedure. When the variational approach is formulated in the most general way, it is found to be equivalent to the moment method in the sense that both approaches yield the same system of equations

when the sets of underlying approximating functions are identical. Hence the variational and moment approaches yield the same approximate solution  $\tilde{u}$ . To see this, we require the notion of an *adjoint operator*. The operator  $\mathcal{L}^\dagger$  adjoint to  $\mathcal{L}$  is defined as the operator for which

$$\langle w, \mathcal{L}u \rangle = \langle \mathcal{L}^\dagger w, u \rangle \quad (122)$$

for arbitrary  $u$  and  $w$ . For most practical problems of interest the adjoint operator exists and is unique, as we assume in the following. It often happens that  $\mathcal{L} = \mathcal{L}^\dagger$ , in which case the operator is said to be *self-adjoint*. For differential operators, for example, the adjoint is usually found by integration by parts; for integral operators, the adjoint operator is an integral operator with the same kernel as the original integral equation, but with the dependence on the observation and source point variables reversed. For a matrix operator, the adjoint is the transpose of the original matrix.

The variational formulation begins by considering some linear functional that we wish to compute, say  $I[u] = - \langle u, g \rangle$  as in (119). The function  $g$  appearing in the functional is used to define an auxiliary *adjoint problem*,

$$\mathcal{L}^\dagger w = g. \quad (123)$$

Note that in the adjoint problem,  $g$  plays the role of the source or forcing function of the problem having  $w$  as its solution. While  $w$  may not always have a clear physical significance, it plays an important role in deriving the desired variational property. Although we may have no direct interest in the adjoint problem, we see that the solution to the adjoint problem at least provides an alternative way to represent the functional (119) since

$$\begin{aligned} I[u] &= - \langle u, g \rangle = - \langle u, \mathcal{L}^\dagger w \rangle \\ &= - \langle \mathcal{L}u, w \rangle = - \langle f, w \rangle, \end{aligned} \quad (124)$$

where (104), (122) and (123) are used. In electromagnetics, this dual representation of the functional is usually a consequence of the *reciprocity* (Harrington, 1961) between sources and fields.

A generalisation of the functional  $I[u]$  is the so-called *bivariational* functional given by

$$I[\tilde{u}, \tilde{w}] = \langle \mathcal{L}\tilde{u}, \tilde{w} \rangle - \langle \tilde{u}, g \rangle - \langle f, \tilde{w} \rangle, \quad (125)$$

which is easily seen to reduce to  $I[u]$  when  $\tilde{u} = u$  and  $\tilde{w} = w$ . In Eq. (125) we regard the two functions  $\tilde{u}$  and  $\tilde{w}$  as approximate or *trial solutions* to the original and adjoint problems, respectively. If we define the error in  $u$  and  $w$  as

$$\delta u = \tilde{u} - u, \quad \delta w = \tilde{w} - w, \quad (126)$$

respectively, then, using (122), (123) and the linearity properties of the symmetric products, Eq. (125) can also be written as

$$I[\tilde{u}, \tilde{w}] = - \langle u, g \rangle + \langle \mathcal{L}\delta u, \delta w \rangle. \quad (127)$$

In this form, it is not only clear that  $I[\tilde{u}, \tilde{w}]$  reduces to  $I[u]$  when  $\tilde{u} = u$  and  $\tilde{w} = w$ , but also since the last symmetric product in (127) involves the product of two first-order error terms, the error in the functional is seen to be of second order in  $\delta u$  and  $\delta w$ . That is, the functional is *stationary* for variations  $\delta u$  and  $\delta w$  in  $\tilde{u}$  and  $\tilde{w}$  about  $u$  and  $w$ , respectively. This is the key feature of  $I[u, w]$  in (125) that makes it a variational quantity.

In the so-called Rayleigh–Ritz procedure,  $u$  and  $w$  are both approximated in terms of basis function sets  $\{u_n\}$  and  $\{w_m\}$ , respectively, as

$$\tilde{u} = \sum_n U_n u_n \quad (128)$$

and

$$\tilde{w} = \sum_m W_m w_m, \quad (129)$$

where the bases are chosen to yield good approximations to  $u$  and  $w$ . Substituting (128) and (129) into (125) yields

$$I[\tilde{u}, \tilde{w}] = \sum_m \sum_n W_m U_n \langle \mathcal{L}u_n, w_m \rangle - \sum_n U_n \langle u_n, g \rangle - \sum_m W_m \langle f, w_m \rangle. \quad (130)$$

A pair of linear equation systems for determining the coefficients  $U_n$  and  $W_m$  are then obtained by requiring that the first-order variations of  $I[\tilde{u}, \tilde{w}]$  with respect to the coefficients  $U_n$  and  $W_m$  vanish, that is, by enforcing the stationary property of approximations to  $u$  and  $w$ . Thus we require that (130) be invariant with respect to first-order variations in the  $p$ th coefficients,  $U_p$  and  $W_p$ , by setting  $\partial I[\tilde{u}, \tilde{w}] / \partial W_p = \partial I[\tilde{u}, \tilde{w}] / \partial U_p = 0$ . On replacing the dummy index  $p$  by  $m$  in the resulting equations, we obtain again the moment method equations (116) for determining  $U_n$ ,

$$\sum_n U_n \langle w_m, \mathcal{L}u_n \rangle = \langle w_m, f \rangle, \quad m = 1, 2, \dots, N \quad (131)$$

and a second set of moment equations for determining  $W_m$ ,

$$\sum_m W_m \langle \mathcal{L}u_n, w_m \rangle = \langle u_n, g \rangle, \quad n = 1, 2, \dots, N. \quad (132)$$

We also see that Eq. (132) for determining the adjoint solution may also be obtained by applying the moment method directly to the adjoint problem (123) with the roles of basis and testing functions interchanged.

Assuming that the moment equations (131) and (132) can be solved to obtain the coefficients  $U_n$  and  $W_m$  for approximating  $u$  and  $w$ , we return to the initial problem of evaluating the desired functional. Apparently, we now have a choice of substituting our solutions into either  $I[u]$  or  $I[u, w]$ . Although more work is required since both  $u$  and  $w$  are needed, we try the latter since we know it to be stationary and hence

possibly more accurate. Thus the approximations of  $u$  and  $w$  are substituted into (125), which we now write as

$$I[\tilde{u}, \tilde{w}] = \langle \mathcal{L}\tilde{u} - f, \tilde{w} \rangle - \langle \tilde{u}, g \rangle. \quad (133)$$

In this form, it is easily seen that, in view of (131), the quantity represented by the first term on the right-hand side of (133) vanishes:

$$\begin{aligned} & \langle \mathcal{L}\tilde{u} - f, \tilde{w} \rangle \\ &= \sum_m W_m \left[ \sum_n U_n \langle \mathcal{L}u_n, w_m \rangle - \langle f, w_m \rangle \right] = 0. \end{aligned} \quad (134)$$

Hence for  $\tilde{u}$  and  $\tilde{w}$  satisfying (131) and (132), we have

$$I[\tilde{u}, \tilde{w}] = - \langle \tilde{u}, g \rangle = - \sum_n U_n \langle u_n, g \rangle. \quad (135)$$

We now see that the same result could have been obtained merely by substituting  $u \approx \tilde{u}$  into  $I[u]$  directly; i.e.,  $I[\tilde{u}] = I[\tilde{u}, \tilde{w}]$  if  $\tilde{u}$  and  $\tilde{w}$  satisfy the moment equations (131) independent of  $\tilde{w}$ , and, as seen,  $I[\tilde{u}]$  yields the same stationary value as  $I[\tilde{u}, \tilde{w}]$ , solving the adjoint problem becomes superfluous. Furthermore, we note that the moment equations (131) for determining  $\tilde{u}$  are *independent of  $g$*  and hence of the linear functional we wish to compute. Thus any bounded linear functional  $I[u]$  we compute using  $u \approx \tilde{u}$  from the moment equations is automatically stationary. Since the moment formulation is more direct than the variational procedure, we can always choose to use the moment approach, taking comfort in the knowledge that any bounded linear functional computed from its solution is automatically stationary.

Here we emphasise that the variational property of the moment method in its general form depends on use of the bivariational functional (125). For self-adjoint problems, for example, and with  $g = f$ , the adjoint problem becomes identical to the original problem,  $\mathcal{L}u = f$ , and the bilinear functional reduces to  $I[\tilde{u}] = \langle \mathcal{L}\tilde{u}, \tilde{u} \rangle - 2 \langle f, \tilde{u} \rangle$ . If one begins with this latter functional, however, the moment equations obtained by the Rayleigh–Ritz procedure produce only Galerkin’s method, and may lead one to the erroneous conclusion that the general moment equations are not variational.

Although we have shown that the discretised adjoint and original problems are relatively independent, we point out one connection between them evident from Eq. (127). Since the error in  $I[\tilde{u}, \tilde{w}]$  is clearly reduced by making *both*  $\delta u$  and  $\delta w$  small, we see that the accuracy of functional evaluations can be improved by choosing the testing functions  $w_m$  so as to provide good approximations to the solution  $w$  of the adjoint problem.

In the following sections, formulations for a number of scattering problems of interest in two and three

dimensions are presented. Initially, only perfect conducting scatterers are treated, but the discrete approximations to the operators developed are used later in more general scattering problems.

## §5. Conducting Cylinders: MFIE, TM Polarisation

An alternative to the EFIE formulation discussed in §2 for TM illumination of a conducting cylinder may be used if the curve  $C$  describing the cylinder cross section is closed. Let  $\hat{\mathbf{n}}$  and  $\hat{\boldsymbol{\ell}} = \hat{\mathbf{z}} \times \hat{\mathbf{n}}$  be unit vectors normal and tangent to  $C$ , respectively. If the cylinder is replaced by its induced current  $\mathbf{J} = J_z \hat{\mathbf{z}}$ , then, by the equivalence principle, the total magnetic field, consisting of the incident field  $\mathbf{H}^{\text{inc}}$  and the scattered field  $\mathbf{H}^{\text{sc}}$  radiated by the induced current, must vanish just inside  $C$ ,

$$\hat{\boldsymbol{\ell}} \cdot (\mathbf{H}^{\text{sc}} + \mathbf{H}^{\text{inc}}) = 0, \quad \boldsymbol{\rho} \in \lim_{\rho \uparrow C} C, \quad (136)$$

where  $\boldsymbol{\rho} \uparrow C$  indicates that  $C$  is approached from the interior. Employing (37) and rearranging (136) leads to

$$\frac{J_z(\boldsymbol{\rho})}{2} - \frac{\hat{\boldsymbol{\ell}}}{\mu} \cdot (\nabla \times \mathbf{A}) = H_\varrho^{\text{inc}}(\boldsymbol{\rho}), \quad \boldsymbol{\rho} \in C, \quad (137)$$

where  $H_\varrho^{\text{inc}} = \hat{\boldsymbol{\ell}} \cdot \mathbf{H}^{\text{inc}}$  is the tangential component of  $\mathbf{H}^{\text{inc}}$  and the simplification  $\hat{\boldsymbol{\ell}} \cdot (\hat{\mathbf{n}} \times \mathbf{J}) = (\hat{\boldsymbol{\ell}} \times \hat{\mathbf{n}}) \cdot \mathbf{J} = -\hat{\mathbf{z}} \cdot \mathbf{J}$  has been used. Also making use of (39) and  $\hat{\boldsymbol{\ell}} \cdot (\hat{\mathbf{z}} \times \nabla G) = (\hat{\boldsymbol{\ell}} \times \hat{\mathbf{z}}) \cdot \nabla G = \hat{\mathbf{n}} \cdot \nabla G = \frac{\partial}{\partial n} G$ , we finally obtain the *magnetic field integral equation* for TM polarisation,

$$\frac{J_z(\boldsymbol{\rho})}{2} + \int_C J_z(\boldsymbol{\rho}') \frac{\partial G(\boldsymbol{\rho}, \boldsymbol{\rho}')}{\partial n} dC' = H_\varrho^{\text{inc}}(\boldsymbol{\rho}), \quad \boldsymbol{\rho} \in C, \quad (138)$$

where the normal derivative of the two-dimensional Green's function appearing in the integral may be written in several equivalent forms:

$$\begin{aligned} \frac{\partial}{\partial n} G(\boldsymbol{\rho}, \boldsymbol{\rho}') &= \hat{\mathbf{n}} \cdot \nabla G(\boldsymbol{\rho}, \boldsymbol{\rho}') = \hat{\mathbf{n}} \cdot \hat{\mathbf{u}} \frac{-k}{4j} H_1^{(2)}(kD) \\ &= \frac{-k}{4j} \cos \theta H_1^{(2)}(kD), \end{aligned} \quad (139)$$

with  $D = |\boldsymbol{\rho} - \boldsymbol{\rho}'|$ ,  $\hat{\mathbf{u}} = \nabla D = \frac{\boldsymbol{\rho} - \boldsymbol{\rho}'}{D}$  and  $\cos \theta = \hat{\mathbf{n}} \cdot \hat{\mathbf{u}}$ .

To discretise (138), we employ a piecewise linear model of  $C$  as in Fig. 2 except that  $C$  must now be a closed curve.<sup>2</sup> To model the current, the pulse approximation of Eqs. (45) and (46) is used. Also we use point matching to enforce the equation by setting  $\boldsymbol{\rho} = \boldsymbol{\rho}^m$  on both sides of (138), where  $\boldsymbol{\rho}^m \equiv \boldsymbol{\rho}_1^m + \boldsymbol{\rho}_2^m/2$  is the midpoint of element  $m$ . This leads to the matrix equation

$$[\beta_{mn}] [[I_n]] = [I_m^{\text{inc}}], \quad (140)$$

where

$$\beta_{mn} = \begin{cases} \frac{1}{2} & , \quad m = n \\ -\frac{k}{4j} \int_{C^n} \frac{\hat{\mathbf{n}}^m \cdot (\boldsymbol{\rho}^m - \boldsymbol{\rho}')}{D^m} H_1^{(2)}(kD^m) dC', & m \neq n, \end{cases} \quad (141)$$

and where  $D^m = |\boldsymbol{\rho}^m - \boldsymbol{\rho}'|$ . The normal to segment  $m$  at the observation point,  $\hat{\mathbf{n}}^m$ , may be computed as the cross product of  $\hat{\mathbf{z}}$  and the unit segment tangent vector at the observation point,  $\hat{\boldsymbol{\ell}}^m$ :

$$\hat{\boldsymbol{\ell}}^m = \frac{\boldsymbol{\rho}_2^m - \boldsymbol{\rho}_1^m}{|\boldsymbol{\rho}_2^m - \boldsymbol{\rho}_1^m|}, \quad \hat{\mathbf{n}}^m = \hat{\boldsymbol{\ell}}^m \times \hat{\mathbf{z}}. \quad (142)$$

Note that to ensure the segment normal is in the outward direction, it is necessary that the local geometry nodes be numbered such that one proceeds counterclockwise around  $C$  in going from  $\boldsymbol{\rho}_1^m$  to  $\boldsymbol{\rho}_2^m$  on element  $m$ . The integral in (141) may be parameterised using (52) and (53) and numerically integrated using the Gauss–Legendre quadrature scheme of Table 3.

The right-hand side excitation vector in (140) has elements

$$I_m^{\text{inc}} = \hat{\boldsymbol{\ell}}^m \cdot \mathbf{H}^{\text{inc}}(\boldsymbol{\rho}_m), \quad (143)$$

which for plane wave excitation may be represented in a form similar to (58)–(60), yielding

$$[I_m^{\text{inc}}] = \frac{E_0}{\eta} \left[ \hat{\boldsymbol{\ell}}^m \times \hat{\mathbf{k}}^{\text{inc}} e^{-jk \hat{\mathbf{k}}^{\text{inc}} \cdot \boldsymbol{\rho}^m} \right]. \quad (144)$$

The far fields may be determined from (61) and the discussion that follows. Numerical results comparing the MFIE and EFIE solutions for currents induced by TM scattering from a conducting square cylinder are in Fig. 7.

## §6. Conducting Cylinders: CFIE, TM Polarisation

For conducting bodies enclosing a domain  $D = \mathcal{V}$  or  $S$  with boundary  $\partial D = S$  or  $C$  in two or three dimensions, respectively, the electric field integral equation enforces the condition that the electric field vanish on the boundary,

$$\mathbf{E}_{\text{tan}}(\mathbf{J}) + \mathbf{E}_{\text{tan}}^{\text{inc}} = 0, \quad \boldsymbol{\rho} \in \partial D. \quad (145)$$

The magnetic field integral equation, on the other hand, enforces the condition that the tangential magnetic field vanish on the surface just inside the boundary,

$$\hat{\mathbf{n}} \times \mathbf{H}(\mathbf{J}) + \hat{\mathbf{n}} \times \mathbf{H}^{\text{inc}} = 0, \quad \boldsymbol{\rho} \in \lim_{\rho \uparrow \partial D} \partial D. \quad (146)$$

In (145) and (146),  $\mathbf{E}(\mathbf{J})$  and  $\mathbf{H}(\mathbf{J})$  represent the scattered electric and magnetic fields radiated by the equivalent surface current  $\mathbf{J}$ . It is found that solutions of these two formulations are not unique at all frequencies. To examine the question of uniqueness, we note that solutions of (145) or (146) are not unique if there exist nontrivial solutions  $\mathbf{J}_h$  to the corresponding homogeneous (excitation-free) equations,

$$\mathbf{E}_{\text{tan}}(\mathbf{J}_h) = 0, \quad \boldsymbol{\rho} \in \partial D \quad (147)$$

or

$$\hat{\mathbf{n}} \times \mathbf{H}(\mathbf{J}_h) = 0, \quad \boldsymbol{\rho} \in \lim_{\boldsymbol{\rho} \uparrow \partial D} \partial D, \quad (148)$$

respectively.

At such frequencies, a multiple of the current distribution  $\mathbf{J}_h$  from (147) or (148), respectively, may be added to any solution  $\mathbf{J}$  of (145) or (146) and the result will also satisfy (145) or (146); i.e., the solution is not unique.

Since the field in (147) is determined from potential quantities relating  $\mathbf{J}_h$  to  $\mathbf{E}$ , the resulting field satisfies both Maxwell's equations and the boundary condition implied by the integral equation. That is, the field radiated by  $\mathbf{J}_h$  satisfies

$$\begin{aligned} \nabla \times \nabla \times \mathbf{E} - k^2 \mathbf{E} &= 0, \quad \boldsymbol{\rho} \in D, \\ \hat{\mathbf{n}} \times \mathbf{E} &= 0, \quad \boldsymbol{\rho} \in \lim_{\boldsymbol{\rho} \uparrow \partial D} \partial D, \end{aligned} \quad (149)$$

but these are just the conditions for determining the interior resonant frequencies  $k = k_i = \omega_i \sqrt{\mu\epsilon}$  of a conducting cavity with  $\partial D$  as its boundary. It is well known that such cavity resonances exist in both the two- and three-dimensional cases; in the former case, the frequencies may alternatively be interpreted as the cutoff frequencies of the various modes that the waveguide with boundary  $\partial D = C$  can support. Furthermore, the homogeneous solutions  $\mathbf{J}_h$  are just the wall currents associated with the corresponding cavity or cutoff waveguide modes. For the TM polarisation to be considered in this section, these frequencies are the waveguide cutoff frequencies for the TM modes of the waveguide with closed boundary  $\partial D = C$ . The existence of these frequencies is well known, and hence we conclude that the EFIE for the TM polarisation does not have unique solutions at frequencies corresponding to the cutoff frequencies for the TM modes of the waveguide with boundary  $\partial D = C$ .

By similar arguments, we conclude that the magnetic fields radiated by solutions  $\mathbf{J}_h$  of the excitation-free magnetic field integral equation (148) must satisfy

$$\begin{aligned} \nabla \times \nabla \times \mathbf{H} - k^2 \mathbf{H} &= 0, \quad \boldsymbol{\rho} \in D, \\ \hat{\mathbf{n}} \times \mathbf{H} &= 0, \quad \boldsymbol{\rho} \in \lim_{\boldsymbol{\rho} \uparrow \partial D} \partial D. \end{aligned} \quad (150)$$

Exchanging the symbol  $\mathbf{H}$  for  $\mathbf{E}$ , we find the above equation is identical to (149), and hence the same argument for the existence of homogeneous solutions follows. For the TM polarisation, however, the magnetic field in (150) is transverse to the cylinder axis and when  $\mathbf{E}$  is substituted for  $\mathbf{H}$ , the resulting equation now involves transverse *electric* fields. Hence, in contrast to the EFIE, the MFIE equation in the TM polarisation has resonant frequencies corresponding to the transverse electric (TE) modes rather than the TM modes.

For the discretised form of the integral equations at a resonant frequency  $k = k_i$ , the condition that a

homogeneous solution exists implies that the determinant of the system matrix approximating the integral equation should vanish:

$$\det[Z_{mn}]|_{k=k_i} = 0, \quad \det[\beta_{mn}]|_{k=k_i} = 0. \quad (151)$$

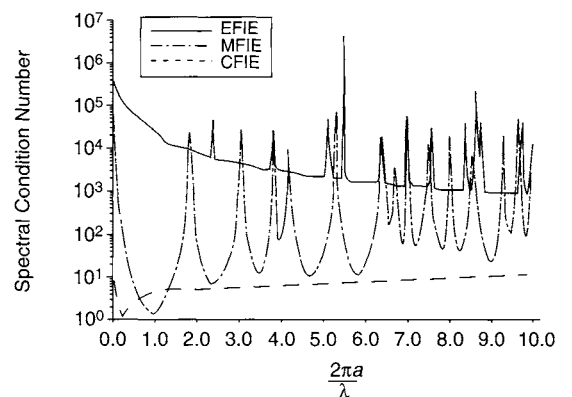
Due to approximations made, in practice the system determinant does not vanish identically, but does have sharp minima at frequencies near the true resonant frequencies. As these approximate resonant frequencies are approached, the solution often becomes *ill-conditioned*; i.e., it becomes unstable and contains a large error component arising from contributions of the homogeneous solution  $\mathbf{J}_h$ . In principle, one could monitor the system determinant to avoid these frequencies. However, the magnitude of the determinant not only depends strongly on the scaling of matrix elements, but it also varies over an extremely wide dynamic range. For this reason, other quantities are more conveniently monitored instead. For example, the *spectral condition number* of a matrix  $[A_{mn}]$ , defined as

$$\text{cond}[A_{mn}] = \frac{|\lambda_{\max}|}{|\lambda_{\min}|}, \quad (152)$$

where  $\lambda_{\max}$  and  $\lambda_{\min}$  are the maximum and minimum magnitudes of the eigenvalues of  $[A_{mn}]$ , respectively, has better numerical characteristics and is often monitored to indicate potential problems near resonant frequencies. If the condition number  $\text{cond}[A_{mn}]$  of the matrix is much larger than unity, or equivalently, if the reciprocal condition number  $1/(\text{cond}[A_{mn}])$  is small compared to unity, then ill-conditioning may be expected. While the spectral condition number can be expensive to compute, it is often reliably estimated by many linear equation-solving algorithms. Figure 16 shows the spectral condition number vs frequency for a circular cylinder.

The alternating positions of the maxima of the EFIE and MFIE condition numbers illustrate the fact that the EFIE resonances occur at the cutoff

**Figure 16** Spectral condition number for a circular cylinder vs circumference in wavelengths for EFIE, MFIE and CFIE, TM illumination.



frequencies of the TM modes, while those of the MFIE occur at the cutoff frequencies of the TE modes. At high frequencies, as Fig. 16 shows, the density of resonant frequencies increases so that it becomes increasingly difficult to avoid these internal resonances. Thus one would prefer a formulation that would work well at all frequencies. Such a formulation is provided by the *combined field integral equation* (CFIE) (Mautz and Harrington, 1978), obtained by forming the following linear combination of (145) and (146):

$$-\frac{\mathbf{E}_{\tan}(\mathbf{J})}{\eta} - \alpha \hat{\mathbf{n}} \times \mathbf{H}(\mathbf{J}) = \frac{\mathbf{E}_{\tan}^{\text{inc}}}{\eta} + \alpha \hat{\mathbf{n}} \times \mathbf{H}^{\text{inc}}, \quad \rho \in \lim_{\rho \uparrow \partial D} \partial D. \quad (153)$$

The intrinsic impedance  $\eta$  is introduced to normalise the fields so that the quantities added have like dimensions and similar magnitudes. The parameter  $\alpha$  is a dimensionless constant that may be chosen to balance emphases on contributions from the EFIE or the MFIE.

As with the EFIE and MFIE, the uniqueness characteristics of CFIE solutions are deduced by examination of the homogeneous form of the equation,

$$\frac{\mathbf{E}_{\tan}(\mathbf{J}_h)}{\eta} + \alpha \hat{\mathbf{n}} \times \mathbf{H}(\mathbf{J}_h) = 0, \quad \rho \in \lim_{\rho \uparrow \partial D} \partial D, \quad (154)$$

where the right-hand side of (153) has been set to 0. We first assume that solutions are not unique, i.e., that there exist nontrivial currents,  $\mathbf{J}_h \neq 0$ , satisfying (154). Multiplying (154) by its complex conjugate and integrating over  $\partial D$ , we then obtain

$$\int_{\partial D} \left( \left| \frac{\mathbf{E}_{\tan}(\mathbf{J}_h)}{\eta} \right|^2 + |\alpha|^2 \left| \mathbf{H}_{\tan}(\mathbf{J}_h) \right|^2 \right) dD + 2 \frac{\alpha}{\eta} \left[ \text{Re} \int_{\partial D} \mathbf{E}(\mathbf{J}_h) \times \mathbf{H}^*(\mathbf{J}_h) \cdot (-\hat{\mathbf{n}}) dD \right] = 0, \quad \rho \in \lim_{\rho \uparrow \partial D} \partial D, \quad (155)$$

where  $\alpha$  is assumed to be chosen such that  $\frac{\alpha}{\eta}$  is real. The term in square brackets is proportional to the net power radiated by the current  $\mathbf{J}_h$  into the region  $D$  bounded by  $\partial D$ . It must be positive if the region is lossy and vanish otherwise. This result implies that the first integral in (155) must vanish and hence that  $\mathbf{E}_{\tan}(\mathbf{J}_h) = \mathbf{H}_{\tan}(\mathbf{J}_h) = 0$  on  $\partial D^-$ , the limit as  $\partial D$  is approached from the interior, but since  $\mathbf{E}_{\tan}$  is continuous across an electric surface current, it is also zero on  $\partial D^+$ , the limit as  $\partial D$  is approached from the exterior. Thus the region outside  $\partial D$  has a vanishing electric field on its boundary and is source-free. By the uniqueness theorem for exterior problems (Harrington, 1961), the magnetic field exterior to  $D$  must then vanish also. Hence  $\mathbf{J}_h$  vanishes since  $\mathbf{J}_h = \hat{\mathbf{n}} \times (\mathbf{H}|_{\partial D^+} - \mathbf{H}|_{\partial D^-}) = 0$ , but  $\mathbf{J}_h$  was initially assumed nonvanishing, and the resulting contradiction proves the uniqueness of solutions of (153).

The discretised form of the CFIE for the TM polarisation is obtained by forming the linear combination (153) specialised to this polarisation. If a piecewise constant current representation and point matching is chosen in a moment solution of (153), the corresponding linear combination of the EFIE and MFIE system matrices for the TM polarisation arises, resulting in the system equation

$$\left[ \frac{Z_{mn}}{\eta} + \alpha \beta_{mn} \right] [I_n] = \left[ \frac{V_m}{\eta} + \alpha J_m^{\text{inc}} \right], \quad (156)$$

where the corresponding matrices and column vectors are defined in (49), (50), (141) and (144).

As Fig. 16 shows, this combination eliminates ill-conditioning problems inherent in the original formulations. Once (156) is solved for the current coefficients, other quantities, e.g., the far fields given in Eqs. (61)–(67), may be determined from them.

In principle, the parameter  $\alpha$  need only be chosen such that  $\frac{\alpha}{\eta}$  is real, or  $\arg \alpha = -\arg \eta$ . As might be expected due to the normalisation of the impedance operator by the intrinsic impedance, values of  $\alpha$  with magnitudes near unity generally result in well-conditioned systems, although it is found in practice that quite a wide range of values of  $\alpha$  near unity may also be used.

## §7. Conducting Cylinders: EFIE, TE Polarisation

In §2, we considered the EFIE formulation for scattering by a conducting cylinder with a TM polarised field incident normal to the cylinder axis. Here we consider the corresponding TE case; that is, the incident and scattered magnetic fields have only a  $z$  component. The fields as well as the induced current are also independent of the  $z$  coordinate in this case, but the surface current is directed in the  $x$ – $y$  plane, tangential to the contour  $C$  representing the cylinder cross section. From (9), (10), (12) and (16), the scattered electric field can be represented in terms of the induced currents as

$$\mathbf{E}^{\text{sc}} = -j\omega \mathbf{A} - \nabla \Phi, \quad (157)$$

where the magnetic vector and electric scalar potentials are

$$\mathbf{A} = \mu \int_C \mathbf{J}(\boldsymbol{\rho}') G(\boldsymbol{\rho}, \boldsymbol{\rho}') dC' \quad (158)$$

and

$$\Phi = -\frac{1}{j\omega \epsilon} \int_C \nabla' \cdot \mathbf{J}(\boldsymbol{\rho}') G(\boldsymbol{\rho}, \boldsymbol{\rho}') dC', \quad (159)$$

respectively, and the two-dimensional Green's function is

$$G(\boldsymbol{\rho}, \boldsymbol{\rho}') = \frac{1}{4j} H_0^{(2)}(kD). \quad (160)$$

An integro-differential equation for the induced current is obtained by requiring the total tangential electric field to vanish on the cylinder:

$$[j\omega\mathbf{A} + \nabla\Phi]_{\text{tan}} = \mathbf{E}_{\text{tan}}^{\text{inc}}(\boldsymbol{\rho}), \quad \boldsymbol{\rho} \in C. \quad (161)$$

A weak form of the equation is obtained by testing it with a vector-valued weighting function  $\mathbf{w}_m(\boldsymbol{\rho})$  defined on and tangent to the cylinder. Using the identity  $\nabla \cdot (\mathbf{w}_m \Phi) = \Phi \nabla \cdot \mathbf{w}_m + \nabla \Phi \cdot \mathbf{w}_m$  and the divergence theorem, the term involving the scalar potential may be integrated by parts to obtain the weak form

$$j\omega \langle \mathbf{w}_m; \mathbf{A} \rangle - \langle \nabla \cdot \mathbf{w}_m, \Phi \rangle = \langle \mathbf{w}_m; \mathbf{E}_{\text{tan}}^{\text{inc}} \rangle. \quad (162)$$

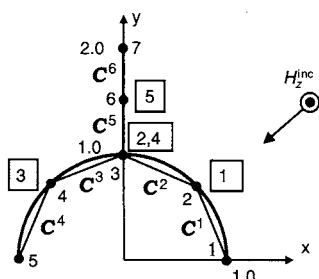
To eliminate the boundary terms arising from integration by parts in (162), it is assumed that the weighting functions are continuous and vanish at any endpoints of  $C$ . With (158) and (159), we may finally write the weak form of the integro-differential equation as

$$\begin{aligned} j\omega\mu \langle \mathbf{w}_m; \mathbf{G}, \mathbf{J} \rangle + \frac{1}{j\omega\epsilon} \langle \nabla \cdot \mathbf{w}_m, \mathbf{G}, \nabla' \cdot \mathbf{J} \rangle \\ = \langle \mathbf{w}_m; \mathbf{E}^{\text{inc}} \rangle. \end{aligned} \quad (163)$$

The contour cross section  $C$  may be approximated by a piecewise linear approximation  $\tilde{C} = \cup_{e=1}^E C^e$ , as illustrated for the hemicylindrical geometry with attached fin in Fig. 17. The node location data are the same as that of Table 1; the node connection data are listed in Table 10, which not only includes the data of Table 2, but also lists the degree of freedom indices associated with each node as labelled in Fig. 17.

Note that the current in the integral equation is the net sum of currents on both sides of the conductor surface  $\tilde{C}$ . At an endpoint of  $\tilde{C}$ , the charge flows continuously from one side of the conducting surface to the other, reversing direction in the process. Hence the net current vanishes at endpoints of  $\tilde{C}$  and, as the figure illustrates, no degrees of freedom are associated with these points. On the other hand, at a junction between conductor surfaces, such as at node 3 of the figure, more than one degree of freedom must exist. In general, if  $J$  surfaces meet, there are  $J$  surface currents into the junction from the various branches. Since

**Figure 17** Piecewise linear model of cross section of hemicylinder with fin. The segment and vertex numbering are the same as in Fig. 2 but DoF labels (in boxes) are added.



there can be no line charge buildup at the junction, the continuity equation requires that the surface current densities into the junction sum to 0; that is, they must satisfy Kirchhoff's current law. Thus Kirchhoff's law provides a constraint condition on the  $J$  surface currents so that there are only  $J - 1$  independent degrees of freedom. For example, the junction at node 3 in Fig. 17 is formed by three surfaces, but only two independent current degrees of freedom (labelled 2 and 4) exist. The data structure illustrated in Table 10 reflects both the element connections and the DoF labelling of Fig. 17. Note that the DoF index for a current whose reference direction is assumed to be out of the associated segment has a positive index; the index is negative if the reference direction is assumed into the segment. The reference direction for each DoF may be chosen either arbitrarily or by any convenient scheme; for example, in Fig. 17 the positive reference direction is assumed to be from lower to higher numbered elements.

Since the divergences appearing in (163) require that the current be differentiable, we choose a piecewise linear representation and write

$$\mathbf{J}(\boldsymbol{\rho}) \approx \sum_{n=1}^N I_n \boldsymbol{\Lambda}_n(\boldsymbol{\rho}), \quad (164)$$

where  $\boldsymbol{\Lambda}_n$  is a *vector-valued* basis function,

$$\boldsymbol{\Lambda}_n(\boldsymbol{\rho}) = \hat{\ell}_n \Lambda_n(\boldsymbol{\rho}), \quad (165)$$

with the unit vector  $\hat{\ell}_n$  giving the direction and  $\Lambda_n$  giving the magnitude of the basis function. The support

**Table 10** Listing of Element Connection Data Corresponding to Fig. 17

e	Local nodes, element e					
	1		2			
	Global node no.		Global node no.			
No. DoF's		DoF index	No. DoF's		DoF index	
1	1		2			
	0		0	1	+1	
2	2		3			
	1		-1	2	+2, +4	
3	3		4			
	1		-2	1	+3	
4	4		5			
	1		-3	0	0	
5	3		6			
	1		-4	1	+5	
6	6		7			
	1		-5	0	0	

of the basis function  $\Lambda_n$  is the pair of line segments associated with DoF index  $n$  and sharing a common node. The unit vector  $\hat{\ell}_n$  is assumed tangent to these line segments and directed along the positive reference direction, i.e., towards the common node on the element with positive DoF index and away from the node on the element with negative DoF index.  $\Lambda_n = |\Lambda_n|$  is the *scalar* linear interpolation or triangle function associated with the node with DoF  $n$ . A single basis function is associated with each node that is not an endpoint or a junction of  $\tilde{C}$ , and  $J-1$  bases are associated with a junction having  $J$  arms. The support of a junction basis may be any pair of elements attached to the junction so long as no bases have precisely the same pair of elements as their support. In the model of Fig. 17, it is assumed that all bases defined at the junction share the lowest numbered element ( $C^2$  in the figure) as one arm of their support, while one of the  $J-1$  remaining junction arms is assigned as the second arm of their support. The magnitudes of the two basis functions spanning the junction arms of Fig. 17 are illustrated in Fig. 18.

With the Galerkin approach, the testing functions are chosen as  $\mathbf{w}_m = \Lambda_m$ . Substituting this choice and the piecewise linear representation (164) into (163) yields the matrix system

$$[Z_{mn}][I_n] = [V_m], \quad (166)$$

where the system impedance matrix is

$$[Z_{mn}] = j\omega[L_{mn}] + \frac{1}{j\omega}[S_{mn}], \quad (167)$$

defined in terms of an *inductance matrix*,

$$[L_{mn}] = \mu \langle \Lambda_m; G(\boldsymbol{\rho}, \boldsymbol{\rho}'), \Lambda_n \rangle, \quad (168)$$

and an *elastance matrix*,

$$[S_{mn}] = \frac{1}{\epsilon} \langle \nabla \cdot \Lambda_m, G(\boldsymbol{\rho}, \boldsymbol{\rho}'), \nabla' \cdot \Lambda_n \rangle. \quad (169)$$

The excitation column vector in (166) is

$$V_m = \langle \Lambda_m; \mathbf{E}^{\text{inc}} \rangle. \quad (170)$$

The system matrix (167) can be most efficiently assembled by evaluating contributions to the matrix arising from interactions between local restrictions of the global bases to a single pair of elements. The process is

similar to the matrix assembly process associated with the wave equation (§3), but with one important difference: In the wave equation, only the interactions between local bases sharing an element are needed and the resulting matrix is sparse; for the integro-differential equation (163), the Green's function serves to propagate interactions between local bases on one element to all other elements. In general then, all pairs of elements interact, and the resulting system matrix is not sparse, but instead is said to be *full*.

The bases whose supports overlap on a common element  $e$  may be written in terms of the locally defined index scheme as

$$\Lambda_n(\boldsymbol{\rho}) = \sigma_i^e \Lambda_i^e(\boldsymbol{\rho}), \quad \boldsymbol{\rho} \in C^e, \quad (171)$$

where the basis associated with node  $i$  ( $= 1, 2$ ) of element  $e$  has DoF index  $n$ . The factor  $\sigma_i^e$  is a sign accounting for the reference direction associated with the node and is defined as

$$\sigma_i^e = \begin{cases} 1, & \text{ith node reference direction out of element } e, \\ -1, & \text{ith node reference direction into element } e. \end{cases} \quad (172)$$

Note that the reference direction for each of the *local* bases  $\Lambda_i^e$  is always assumed to be out of node  $i$  of element  $e$ .

Thus the element matrix corresponding to (167) is defined as

$$[Z_{ij}^{ef}] = j\omega \sigma_i^e \sigma_j^f [L_{ij}^{ef}] + \frac{\sigma_i^e \sigma_j^f}{j\omega} [S_{ij}^{ef}], \quad (173)$$

with each matrix element representing the interaction between the  $i$ th basis of element  $e$  and the  $j$ th basis of element  $f$ . The associated element inductance and elastance matrices are

$$[L_{ij}^{ef}] = \mu \left[ \int_{C^e} \int_{C^f} \Lambda_i^e(\boldsymbol{\rho}) \cdot \Lambda_j^f(\boldsymbol{\rho}') G(\boldsymbol{\rho}, \boldsymbol{\rho}') dC' dC \right] \quad (174)$$

and

$$[S_{ij}^{ef}] = \frac{1}{\epsilon} \left[ \int_{C^e} \int_{C^f} \nabla \cdot \Lambda_i^e(\boldsymbol{\rho}) G(\boldsymbol{\rho}, \boldsymbol{\rho}') \nabla' \cdot \Lambda_j^f(\boldsymbol{\rho}') dC' dC \right], \quad (175)$$

respectively. The element excitation column vector corresponding to (170) is given by

$$[V_i^e] = \left[ \sigma_i^e \int_{C^e} \Lambda_i^e \cdot \mathbf{E}^{\text{inc}} dC \right]. \quad (176)$$

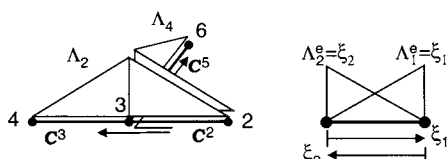
### Evaluation of Element Matrices

To evaluate the element matrices, we first note that the locally indexed bases are simply linear interpolation functions that may be expressed in terms of local normalised coordinates as

$$\Lambda_i^e = \hat{\ell}_i^e \xi_i, \quad i = 1, 2, \quad (177)$$

where  $\hat{\ell}_i^e = \ell_i^e / \varrho^e$ ,  $\ell_1^e = -\ell_2^e = \boldsymbol{\rho}_1^e - \boldsymbol{\rho}_2^e$  is the vector between segment nodes and  $\varrho^e = |\ell_1^e| = |\ell_2^e|$  is the segment

**Figure 18** Bases wrapping around cross section of a junction of surfaces and their mapping onto a parent element.



length. Since the basis function is linear, its surface divergence is constant and given by

$$\nabla_s \cdot \Lambda_i^e = \frac{1}{\varrho^e}. \quad (178)$$

Thus the element inductance matrix is given by

$$\left[ L_{ij}^{ef} \right] = \mu \left[ \hat{\ell}_i^e \cdot \hat{\ell}_j^f \psi_{ij}^{ef} \right], \quad (179)$$

where  $\psi_{ij}^{ef}$  is the potential integral

$$\psi_{ij}^{ef} = \frac{\varrho^e \varrho^f}{4j} \int_0^1 \int_0^1 \xi_i H_0^{(2)}(kD) \xi_j' d\xi_1' d\xi_2' \quad (180)$$

and

$$D = \left| \boldsymbol{\rho}_1^e \xi_1 + \boldsymbol{\rho}_2^e \xi_2 - \boldsymbol{\rho}_1^f \xi_1' - \boldsymbol{\rho}_2^f \xi_2' \right|. \quad (181)$$

Turning to the evaluation of  $S_{ij}^{ef}$ , Eq. (175), we use (178) and recall that  $\xi_1 + \xi_2 = \xi_1' + \xi_2' = 1$  to obtain

$$S_{ij}^{ef} = \frac{1}{\epsilon \varrho^e \varrho^f} \sum_{k=1}^2 \sum_{\ell=1}^2 \Psi_{k\ell}^{ef}. \quad (182)$$

The evaluation of all the element matrices therefore reduces to the problem of evaluating the potential integrals (180). For  $e \neq f$ , the Gauss–Legendre rule may be applied successively to evaluate each integral in (180). Sampling points and corresponding weights for one-, two- and four-point Gauss–Legendre quadrature rules for this purpose are listed in Table 3.

For  $e = f$ , the potential becomes

$$\psi_{ij}^{ee} = \frac{(\varrho^e)^2}{4j} \int_0^1 \int_0^1 \xi_i H_0^{(2)}(kD) \xi_j' d\xi_1' d\xi_2', \quad (183)$$

with

$$D = \left| \boldsymbol{\rho}_1^e (\xi_1 - \xi_1') + \boldsymbol{\rho}_2^e (\xi_2 - \xi_2') \right|. \quad (184)$$

The Gauss–Legendre rules may be used to evaluate the outer integral in (183). However, the inner integral is singular at  $D = 0$  because, for small arguments,

$$H_0^{(2)}(kD) \approx 1 - j \frac{2}{\pi} \left( \ln \frac{kD}{2} + \gamma \right), \quad (185)$$

where  $\gamma = 0.5772\dots$  is Euler's constant, and  $D$  vanishes when  $\xi_1 = \xi_1'$  (i.e., when observation and source points become equal) in (183). Gauss–Legendre quadrature cannot be used effectively in such cases. However, the singularity in the inner integral is easily handled via the quadrature scheme developed by Ma *et al.* (1996) that exactly evaluates  $\int_0^1 f(\xi'') d\xi''$  when  $f(\xi'')$  is a finite linear combination of powers of  $\xi''$  and products of powers of  $\xi''$  and  $\ln \xi''$ . To apply the scheme, however, for each sample point of the outer integral of (183), the interval of integration of the inner integral must be decomposed into two parts, the first from  $\boldsymbol{\rho}_1^e$  to the sample point  $\xi_1^{(k)} = 1 - \xi_2^{(k)}$  and the second from the sample point to  $\boldsymbol{\rho}_2^e$ . The superscript

$k$  in parentheses denotes the operation of evaluating at the  $k$ th sampling point. In both instances, the interval must be reparameterised to  $0 \leq \xi_1'' \leq 1$  with the singularity at  $\xi_1'' = 0$ . Thus the inner integral becomes

$$\begin{aligned} \varrho^e \int_0^1 H_0^{(2)}(kD) \xi_j' d\xi_1' &= \varrho^e \xi_2^{(k)} \int_0^1 H_0^{(2)}(kD_i^k) \xi_j' d\xi_1'' \\ &+ \varrho^e \xi_1^{(k)} \int_0^1 H_0^{(2)}(kD_i^k) \xi_j' d\xi_1'', \end{aligned} \quad (186)$$

where  $D_i^k = \left| \boldsymbol{\rho}_1^e \xi_1^{(k)} + \boldsymbol{\rho}_2^e \xi_2^{(k)} - \boldsymbol{\rho}_i^e \right| \xi_1''$ ,  $i = 1, 2$ , and

$$\xi_j' = \begin{cases} \xi_1^{(k)} \xi_2'' + \xi_1'', & j = 1, \\ \xi_2^{(k)} \xi_2'' & , \quad j = 2, \end{cases} \quad (187)$$

parameterises  $\xi_j'$  in terms of  $\xi_1'' = 1 - \xi_2''$  in the first integral of (186), while

$$\xi_j' = \begin{cases} \xi_1^{(k)} \xi_2'' & , \quad j = 1, \\ \xi_1'' + \xi_2^{(k)} \xi_2'' & , \quad j = 2 \end{cases} \quad (188)$$

does so in the second.

To evaluate the excitation element vector (176), consider a plane wave incident from an angle  $\phi^{\text{inc}}$  with respect to the  $x$  axis, and which we write as

$$\mathbf{E}^{\text{inc}} = \mathbf{E}_0 e^{-jk\hat{\mathbf{k}}^{\text{inc}} \cdot \boldsymbol{\rho}}, \quad (189)$$

where  $\mathbf{E}_0 = E_0(\hat{\mathbf{z}} \times \hat{\mathbf{k}}^{\text{inc}})$  and

$$\hat{\mathbf{k}}^{\text{inc}} = -\hat{\mathbf{x}} \cos \phi^{\text{inc}} - \hat{\mathbf{y}} \sin \phi^{\text{inc}}. \quad (190)$$

The global excitation vector is thus

$$[V_m] = [ \langle \Lambda_m; \mathbf{E}^{\text{inc}} \rangle ] = \mathbf{E}_0 \cdot [ \tilde{\Lambda}_m(-\hat{\mathbf{k}}^{\text{inc}}) ], \quad (191)$$

where

$$\tilde{\Lambda}_m(\hat{\mathbf{k}}) = \int_C \Lambda_m(\boldsymbol{\rho}) e^{jk\hat{\mathbf{k}} \cdot \boldsymbol{\rho}} dC \quad (192)$$

is the Fourier transform of the global basis function. Thus the corresponding element excitation vector is

$$[\sigma_i \langle \Lambda_i^e; \mathbf{E}^{\text{inc}} \rangle] = \sigma_i \mathbf{E}_0 \cdot [ \tilde{\Lambda}_i^e(-\hat{\mathbf{k}}^{\text{inc}}) ], \quad (193)$$

where

$$\tilde{\Lambda}_i^e(\hat{\mathbf{k}}) = \int_{C^e} \Lambda_i^e(\boldsymbol{\rho}) e^{jk\hat{\mathbf{k}} \cdot \boldsymbol{\rho}} dC \quad (194)$$

is the Fourier transform of the  $i$ th local basis on element  $e$ . Elements of the column vector may be evaluated either analytically or by using Gauss–Legendre quadrature, and then assembled into the system transform vector. Factoring the incident field amplitude from the system excitation matrix as in (191) enables us to use the Fourier transform algorithm both in the construction of the excitation vector and in the computation of far fields, as shown below.

### Evaluation of Far Fields

The scattered far electric field at a radius  $\rho$  and angle  $\phi$  from the  $x$  axis has only a  $\phi$  component and, using

(27), (29) and (164), is given by

$$\begin{aligned} E_{\phi}^{\text{sc}} &= -\frac{j\omega\mu}{\sqrt{8\pi\rho}} e^{-j(k\rho+\pi/4)} \sum_{n=1}^N I_n(\hat{z} \times \hat{\rho}) \cdot \int_C \Lambda_n e^{jk\hat{\rho} \cdot \rho'} dC' \\ &= -\frac{j\omega\mu}{\sqrt{8\pi\rho}} e^{-j(k\rho+\pi/4)} (\hat{z} \times \hat{\rho}) \cdot \left[ \tilde{\Lambda}_n(\hat{\rho}) \right]^{\text{t}} [I_n], \end{aligned} \quad (195)$$

where the superscript t denotes transpose and  $\hat{\rho} = \hat{x} \cos \phi + \hat{y} \sin \phi$ . Note that the far field computation makes use of the transform of the bases (192).

### Numerical Results

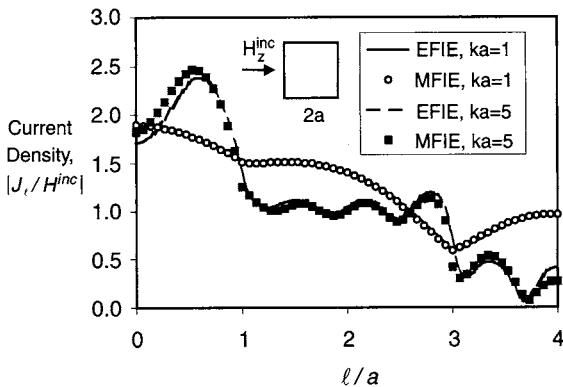
Figure 19 shows the current distribution on a square cylinder illuminated by a TE plane wave. Each side of the cylinder is of width  $2a$ , and the current distribution is plotted vs (normalised) arc length  $\ell$  beginning at the centre of the illuminated side. Note that as the frequency increases, the current on the cylinder oscillates about the physical optics approximation:  $2\hat{n} \times \mathbf{H}^{\text{inc}}$  on the illuminated side and zero on the shadow side of the cylinder. For the computations, the cylinder cross section was subdivided into 40 subdomains. Also shown in the figure for comparison are results from the MFIE approach to be considered in the following section.

## §8. Conducting Cylinders: MFIE, TE Polarisation

As in the TM case, a TE form of the MFIE may be used as an alternative to the EFIE if the curve  $C$  describing the cylinder cross section is closed. With unit vectors  $\hat{n}$  and  $\hat{\ell}$  defined as in §5, and with the cylinder replaced by its induced current  $\mathbf{J} = J_{\ell} \hat{\ell}$ , the sum of the incident field  $H_z^{\text{inc}}$  and the scattered field  $H_z^{\text{sc}}$  radiated by the induced current must vanish just inside  $C$ ,

$$(H_z^{\text{sc}} + H_z^{\text{inc}}) = 0, \quad \rho \in \lim_{\rho \uparrow C} C, \quad (196)$$

**Figure 19** Current distribution on a square cylinder illuminated by TE plane wave.



where  $\rho \uparrow C$  indicates that  $C$  is approached from the interior. Employing (37) and rearranging (196) leads to

$$\frac{J_{\ell}(\rho)}{2} + \frac{\hat{z}}{\mu} \cdot (\nabla \times \mathbf{A}) = -H_z^{\text{inc}}(\rho), \quad \rho \in C, \quad (197)$$

where  $H_z^{\text{inc}}$  is the tangential magnetic field and  $\hat{n} \times \hat{\ell} = \hat{z}$  has been used. Making use of (39) and  $\hat{z} \cdot (\hat{\ell} \times \nabla G) = (\hat{z} \times \hat{\ell}) \cdot \nabla G = -\hat{n}' \cdot \nabla G = \hat{n}' \cdot \nabla' G = \frac{\partial}{\partial n'} G$ , we finally obtain the MFIE for TE polarisation,

$$\frac{J_{\ell}(\rho)}{2} - \int_C J_{\ell}(\rho') \frac{\partial G(\rho, \rho')}{\partial n'} dC' = -H_z^{\text{inc}}(\rho), \quad \rho \in C, \quad (198)$$

where the normal derivative of the two-dimensional Green's function with respect to the source point may be written in various equivalent forms

$$\begin{aligned} \frac{\partial}{\partial n'} G(\rho, \rho') &= \hat{n}' \cdot \nabla' G(\rho, \rho') = \hat{n}' \cdot \hat{u} \frac{k}{4j} H_1^{(2)}(kD) \\ &= \frac{k}{4j} \cos \theta' H_1^{(2)}(kD), \end{aligned} \quad (199)$$

with  $D = |\rho - \rho'|$ ,  $\hat{u} = \nabla D = \frac{\rho - \rho'}{D}$ , and  $\cos \theta' = \hat{n}' \cdot \hat{u}$ .

We approximate the curve  $C$  by means of  $N$  straight line segments,  $C^n$ , as illustrated in Fig. 2, but here  $C$  must be closed. Since there are no derivatives on the current in (198), we may employ a pulse representation

$$J_{\ell}(\rho) \approx \sum_{n=1}^N I_n \Pi_n(\rho), \quad (200)$$

where the unit pulse function  $\Pi_n$  is defined in (46).

Point matching may be used to enforce the equation by setting  $\rho = \rho^m$  on both sides of (198), where  $\rho^m \equiv (\rho_1^m + \rho_2^m)/2$  is the midpoint of element  $m$ . With (198)–(200), this leads to the matrix equation

$$[\beta_{mn}] [[I_n]] = [I_m^{\text{inc}}], \quad (201)$$

where

$$\beta_{mn} = \begin{cases} \frac{1}{2} & , \quad m = n \\ -\frac{k}{4j} \int_{C^n} \frac{\hat{n}^n \cdot (\rho^m - \rho')}{D^m} H_1^{(2)}(kD^m) dC', & m \neq n, \end{cases} \quad (202)$$

and where  $D^m = |\rho^m - \rho'|$ . The integral in (201) may be parameterised using (52) and (53) and integrated using the Gauss–Legendre quadrature scheme of Table 3.

The right-hand side excitation vector in (201) has elements

$$I_m^{\text{inc}} = -H_z^{\text{inc}}(\rho^m). \quad (203)$$

### Far Fields

The vector potential in the far field is, from (27) and (200),

$$\begin{aligned} \mathbf{A} &= \frac{\mu}{\sqrt{8\pi k\rho}} e^{-j(k\rho+\pi/4)} \sum_{n=1}^N I_n \hat{\ell}^n \int_{C^n} \Pi_n(\rho') e^{jk\hat{\rho} \cdot \rho'} dC' \\ &= \frac{\mu}{\sqrt{8\pi k\rho}} e^{-j(k\rho+\pi/4)} \left[ \hat{\ell}^n \tilde{\Pi}_n(\hat{\rho}) \right]^{\text{t}} [I_n], \end{aligned} \quad (204)$$

where

$$\tilde{\Pi}_n(\hat{\rho}) = \int_{C^n} \Pi_n(\hat{\rho}') e^{jk\hat{\rho}\cdot\hat{\rho}'} dC' = \varrho^n \text{sinc} \psi^n \quad (205)$$

is the Fourier transform of the unit pulse function, evaluated as in (65) and (66). From (29), the far electric field is

$$E_\phi = -j\omega A_\phi = -j\omega \hat{\phi} \cdot \mathbf{A}. \quad (206)$$

Numerical results comparing the MFIE and EFIE solutions for currents induced by TE scattering from a conducting square cylinder are found in Fig. 19.

## §9. Inhomogeneous Cylinders: Electric Field Wave Equation, TE Polarisation

With no magnetic currents present, the vector wave equation (7) becomes

$$\nabla \times (\mu_r^{-1} \cdot \nabla \times \mathbf{E}) - k_0^2 \epsilon_r \cdot \mathbf{E} = -j\omega \mu_0 \mathbf{J}_V \quad (207)$$

in a volume  $\mathcal{V}$ , where  $k_0 = \omega\sqrt{\mu_0\epsilon_0}$ . In the two-dimensional TM polarisation problem of §3, the equation reduced to a scalar equation; for the TE polarisation considered in this section, the equation retains its vector character. Initially we deal with the three-dimensional form of the equation and specialise to two dimensions when appropriate. Furthermore, we assume that  $\mathcal{V}$  is a cavity with perfect conducting walls satisfying the vector Dirichlet condition  $\hat{\mathbf{n}} \times \mathbf{E} = \mathbf{0}$  on the boundary  $S$  of  $\mathcal{V}$ .

As in the scalar problem of §3, the finite element procedure for vector problems assumes that the solution domain is subdivided into a mesh of elements such as triangles in two dimensions or tetrahedrons in three dimensions. In modelling vector fields, however, it is undesirable to interpolate the unknown fields at the element vertices. There are two principal reasons for this:

- For ease in modelling, element boundaries should be chosen to coincide with material boundaries. Hence, in general, adjacent elements sharing a common mesh vertex may have different material parameters, but boundary conditions and numerical considerations require that tangential components of  $\mathbf{E}$  be continuous across element boundaries. To implement this condition at a vertex generally requires one unknown per element interface. Since, on average, six triangles (two dimensions) or 12 tetrahedrons (three dimensions) intersect at a vertex, an excessive number of degrees of freedom results.

- By taking the divergence of (207) and applying the continuity equation (5), one obtains Gauss's Law,

$$k_0^2 \nabla \cdot (\epsilon_0 \epsilon_r \cdot \mathbf{E}) = k_0^2 q_V,$$

which is thus automatically satisfied by solutions of (207)—*unless*, as we see above,  $k_0 = \omega\sqrt{\mu_0\epsilon_0} = 0$ . In the latter case, we find directly from (207) that any curl-free vector, i.e., a solution of the form  $\mathbf{E} = -\nabla\Phi$ , that satisfies appropriate conditions on the boundary of  $\mathcal{V}$  is a source-free (homogeneous) solution of (207). Since our interest is in solving (207) for  $k_0 \neq 0$ , the existence of such nonphysical solutions should not concern us. However, in a numerical solution, if the basis functions chosen cannot *exactly* model curl-free electric fields, then the eigenfrequencies of these homogeneous solutions are not confined precisely to  $k_0 = 0$ , but instead are perturbed to nonzero eigenfrequencies  $k_0$ , often within the frequency range of the problem of interest. These so-called *spurious resonances* can result in the addition of strong homogeneous field error contributions to the correct fields, severely affecting a problem's solution. To eliminate these contributions, it is thus necessary to ensure that the basis functions chosen can model curl-free vector fields, i.e., that they can model the *null space* of the curl operator. This further requires that basis functions have continuous tangential components across element boundaries, since discontinuous tangential components are equivalent to concentrated vortex sources along the discontinuities.

The above considerations argue strongly for the use of so-called *curl-conforming* bases with continuous tangential components at element edges. In fact, we choose bases for which the unknowns are simply the tangential component of the field at the midpoints of edges of the mesh. In the following, we assume the existence of curl-conforming bases,  $\Omega_m(\mathbf{r})$ , that have continuous tangential components throughout  $\mathcal{V}$ . Before developing an expansion of the electric field in terms of these bases, we use them first to test (207). Assuming that  $m$  is an index for the degrees of freedom associated with *edges* of a mesh in  $\mathcal{V}$ , testing (207) with  $\Omega_m(\mathbf{r})$  leads to

$$\begin{aligned} \langle \Omega_m; \nabla \times (\mu_r^{-1} \cdot \nabla \times \mathbf{E}) \rangle - k_0^2 \langle \Omega_m; \epsilon_r \cdot \mathbf{E} \rangle \\ = -j\omega \mu_0 \langle \Omega_m; \mathbf{J}_V \rangle. \end{aligned} \quad (208)$$

The integral involved in the first symmetric product in (208) may be integrated by parts using the identity  $\nabla \cdot (\mathbf{A} \times \mathbf{B}) = \mathbf{B} \cdot \nabla \times \mathbf{A} - \mathbf{A} \cdot \nabla \times \mathbf{B}$  and the divergence theorem, and (1) may be used to obtain

$$\begin{aligned} \langle \Omega_m; \nabla \times (\mu_r^{-1} \cdot \nabla \times \mathbf{E}) \rangle = \langle \nabla \times \Omega_m; \mu_r^{-1} \cdot \nabla \times \mathbf{E} \rangle \\ - j\omega \mu_0 \int_S \mathbf{H} \cdot (\Omega_m \times \hat{\mathbf{n}}) dS, \end{aligned} \quad (209)$$

where  $S$  is the boundary of  $\mathcal{V}$ . The last integral vanishes if either  $\hat{\mathbf{n}} \times \mathbf{H} = \mathbf{0}$  (vector Neumann condition) or  $\hat{\mathbf{n}} \times \Omega_m = \mathbf{0}$  on  $S$ .<sup>3</sup> Since we are assuming the vector Dirichlet condition  $\hat{\mathbf{n}} \times \mathbf{E} = \mathbf{0}$  on  $S$  and our intent is to use the testing functions  $\Omega_m$  as basis functions representing  $\mathbf{E}$ , we require the tangential components of

$\mathbf{\Omega}_m$  to vanish on  $S$ , thus eliminating the last integral in (209). Note that the vector Dirichlet condition is explicitly enforced through the choice of basis functions; hence, it is an essential boundary condition. Because the degree of freedom associated with basis functions at boundary edges must vanish, we discard these bases by assuming that the index  $m$  runs over only the  $N$  interior edges of the mesh. Combining the above results, we obtain the weak form of the vector wave equation,

$$\begin{aligned} & \langle \nabla \times \mathbf{\Omega}_m; \boldsymbol{\mu}_r^{-1} \cdot \nabla \times \mathbf{E} \rangle - k_0^2 \langle \mathbf{\Omega}_m; \boldsymbol{\epsilon}_r \cdot \mathbf{E} \rangle \\ & = -j\omega\mu_0 \langle \mathbf{\Omega}_m; \mathbf{J}_V \rangle, \end{aligned} \quad (210)$$

with  $m = 1, 2, \dots, N$ .

Next we expand the electric field  $\mathbf{E}$  in the same set of curl-conforming bases  $\mathbf{\Omega}_n$  as used in testing the wave equation,

$$\mathbf{E}(\mathbf{r}) \approx \sum_{n=1}^N V_n \mathbf{\Omega}_n(\mathbf{r}), \quad (211)$$

and substitute the result into (210), obtaining the matrix equation

$$[Y_{mn}][V_n] = [I_m], \quad (212)$$

where

$$I_m = - \langle \mathbf{\Omega}_m; \mathbf{J}_V \rangle, \quad (213)$$

$$Y_{mn} = \frac{1}{j\omega} \Gamma_{mn} + j\omega C_{mn}, \quad (214)$$

with reciprocal inductance matrix

$$\Gamma_{mn} = \frac{1}{\mu_0} \langle \nabla \times \mathbf{\Omega}_m; \boldsymbol{\mu}_r^{-1} \cdot \nabla \times \mathbf{\Omega}_n \rangle \quad (215)$$

and capacitance matrix

$$C_{mn} = \epsilon_0 \langle \mathbf{\Omega}_m; \boldsymbol{\epsilon}_r \cdot \mathbf{\Omega}_n \rangle. \quad (216)$$

We now simplify and specialise the problem in the following ways:

- We assume that the media filling the cavity is isotropic and can be modelled as piecewise homogeneous (i.e., medium parameters are assumed constant within each element).

- We specialise the formulation from three to two dimensions. Thus the region of interest changes from  $\mathcal{V}$  with boundary  $S$  to the cross section  $S$  bounded by the curve  $C$ .

With these specialisations, the global reciprocal inductance and capacitance matrices (215) and (216) become, respectively,

$$\Gamma_{mn} = \frac{1}{\mu_0} \langle \nabla \times \mathbf{\Omega}_m; \boldsymbol{\mu}_r^{-1} \nabla \times \mathbf{\Omega}_n \rangle \quad (217)$$

and

$$C_{mn} = \epsilon_0 \langle \mathbf{\Omega}_m; \boldsymbol{\epsilon}_r \mathbf{\Omega}_n \rangle, \quad (218)$$

where the integration implied by the symmetric product is now over the cavity cross section  $S$  bounded by  $C$ . We assume that  $C$  and  $S$  lie in the  $x$ - $y$  plane and that there is no variation of the fields with respect to  $z$ . The problem further decomposes into two independent polarisations: a TM part, with  $E_z$  as the only (scalar) unknown, and which we treated in §3, and a TE part, with the transverse field  $\mathbf{E}$  as the unknown, and which is the case of interest here. Hence we assume that the electric field  $\mathbf{E}$  and current source  $\mathbf{J}_V$  are entirely transverse (TE) to the  $z$  axis.

Next we assume that the cross section  $S$  is subdivided into a mesh of  $E$  triangular elements  $S^e$ ,  $e = 1, 2, \dots, E$ , as in the meshing scheme of Fig. 9. The cavity field is represented in terms of the bases by (211), where  $N$  is the number of interior edges of the triangular mesh and  $V_n$  is a tangential component of  $\mathbf{E}$  at the midpoint of an interior edge with global DoF index  $n$ . The degree of freedom indices associated with the mesh of Fig. 9 are illustrated in Fig. 20. In the latter figure, the vertex indices are the same as in Fig. 9, but have been removed for clarity. Table 11 gives a partial listing of the data structure needed to implement the mapping implied by Figs. 9 and 20 between local and global degree of freedom indices associated with interior edges. Note that the local index of an edge in a triangular element is assumed to be the same as that of its opposite vertex.

A positive reference direction must also be chosen for the component of  $\mathbf{E}$  along each edge. For convenience, we assume that the reference direction for the  $i$ th local basis function is always in the direction of the corresponding edge vector  $\boldsymbol{\ell}_i$ , i.e., directed in a counterclockwise direction along the triangle's boundary, but to ensure continuity of tangential components at an edge common to two triangles, the corresponding global reference direction must be reversed for one of the two triangles that share a degree of freedom. Hence we relate the local basis to the global basis on element  $S^e$  as

$$\mathbf{\Omega}_n(\boldsymbol{\rho}) = \sigma_i \boldsymbol{\Omega}_i^e(\boldsymbol{\rho}), \quad \boldsymbol{\rho} \in S^e, \quad (219)$$

where  $\sigma_i^e$  incorporates the sign accounting for the reference choice and is defined by

$$\sigma_i^e = \begin{cases} 1, & \text{reference direction for edge } i, \\ & \text{element } e, \text{ is parallel to } \boldsymbol{\ell}_i, \\ -1, & \text{reference direction for edge } i, \\ & \text{element } e \text{ is antiparallel to } \boldsymbol{\ell}_i. \end{cases} \quad (220)$$

Note that this sign is incorporated into the index that maps local to global indices in Table 11. The global reference direction for an edge may be chosen arbitrarily or for convenience. As in Table 11, a common scheme is to choose it in the direction of increasing global indices of an edge's bounding vertices.

**Figure 20** Edge degree of freedom indices corresponding to mesh of Fig. 9.

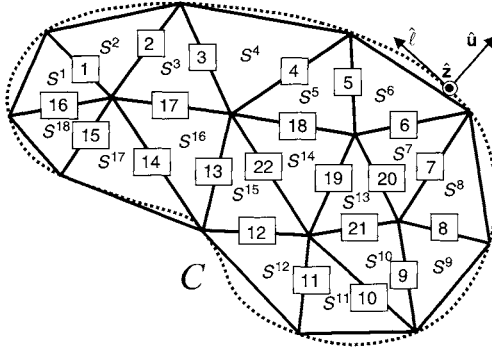


**Table 11** Partial Listing of Element Connection Data Corresponding to Figs. 9 and 20

Local nodes, element $e$						
1		2		3		
Global node no.		Global node no.		Global node no.		
$e$	No. DoF's	DoF index	No. DoF's	DoF index	No. DoF's	DoF index
1	9		11		10	
	1	-1	0	0	1	16
2	11		1		10	
	0	0	1	1	1	-2
⋮	⋮		⋮		⋮	
14	15		13		12	
	1	-18	1	22	1	-19
⋮	⋮		⋮		⋮	
18	8		11		9	
	1	-16	0	0	1	-15

With our assumption that the medium parameters are constant in element  $e$  ( $\mu_r = \mu_r^e$ ,  $\epsilon_r = \epsilon_r^e$ ), we find that element matrices corresponding to (214), (217) and (218) are

$$Y_{ij}^e = \frac{\sigma_i^e \sigma_j^e}{j\omega} \Gamma_{ij}^e + j\omega \sigma_i^e \sigma_j^e C_{ij}^e, \quad (221)$$

$$\Gamma_{ij}^e = \frac{1}{\mu^e} \langle \nabla \times \Omega_i^e; \nabla \times \Omega_j^e \rangle \quad (222)$$

and

$$C_{ij}^e = \epsilon^e \langle \Omega_i^e; \Omega_j^e \rangle, \quad (223)$$

respectively. The element excitation vector corresponding to (213) is

$$I_i^e = -\sigma_i^e \langle \Omega_i^e; \mathbf{J}_v \rangle. \quad (224)$$

In the next section, we develop local curl-conforming basis functions  $\Omega_i^e$  defined on element  $e$ .

## Development of Basis Functions

To construct basis functions on an element, we note that an interpolatory basis appearing in (222) and (223) should satisfy the following conditions:

- To model the curl to lowest order,  $\nabla \times \Omega_i^e$  must be a constant vector; hence  $\Omega_i^e$  must vary linearly within an element.
- $\Omega_i^e$  should have a tangential component along edge  $i$  of element  $e$ , but a vanishing tangential component along the two remaining edges.

The second condition may be satisfied if we assume that  $\Omega_i^e$  has the form

$$\Omega_i^e = f(\rho_i) \hat{\phi}_i, \quad (225)$$

where  $(\rho_i, \phi_i)$  are polar coordinates in the plane of the element centred at vertex  $i$  and with associated unit basis vectors  $(\hat{\rho}_i, \hat{\phi}_i)$ . We note that if

$$f(\rho_i) = C\rho_i, \quad (226)$$

where  $C$  is a constant, the first condition will also be satisfied since

$$\nabla \times \Omega_i^e = \frac{1}{\rho_i} \frac{d}{d\rho_i} [\rho_i f(\rho_i)] \hat{z} = 2C\hat{z}. \quad (227)$$

Hence,

$$\Omega_i^e = C\rho_i \hat{\phi}_i = C(\hat{z} \times \hat{\rho}_i) \rho_i = C\hat{z} \times \mathbf{p}_i, \quad (228)$$

where  $\mathbf{p}_i$  is the vector from vertex  $i$  to the point  $(\rho_i, \phi_i)$  in the element. Finally, we note that along local edge  $i$ , the magnitude of the component of  $\mathbf{p}_i$  normal to the edge is the height of the triangle  $h_i$  from edge  $i$ ; hence

$$\Omega_i^e = \frac{\hat{z} \times \mathbf{p}_i}{h_i} \quad (229)$$

has a unit tangential component along edge  $i$ . Noting that  $\mathbf{p}_i$  can be written in terms of normalised coordinates and element edge vectors as  $\mathbf{p}_i = \xi_{i+1} \ell_{i-1} - \xi_{i-1} \ell_{i+1}$ , we also have, using results from Table 8,

$$\begin{aligned} \Omega_i^e &= \hat{z} \times \frac{(\xi_{i+1} \ell_{i-1} - \xi_{i-1} \ell_{i+1})}{h_i} \\ &= \varrho_i (\xi_{i+1} \nabla \xi_{i-1} - \xi_{i-1} \nabla \xi_{i+1}), \end{aligned} \quad (230)$$

with curl given by

$$\nabla \times \Omega_i^e = \frac{2}{h_i} \hat{z} = \frac{\varrho_i}{A^e} \hat{z}. \quad (231)$$

Using (230) and (231), we may now evaluate the element matrices.

## Evaluation of Element Matrices

From (231), the element matrix  $[\Gamma_{ij}^e]$  (222) is easily evaluated as

$$[\Gamma_{ij}^e] = \frac{1}{\mu^e A^e} \begin{bmatrix} \varrho_1^2 & \varrho_1 \varrho_2 & \varrho_1 \varrho_3 \\ \varrho_2 \varrho_1 & \varrho_2^2 & \varrho_2 \varrho_3 \\ \varrho_3 \varrho_1 & \varrho_3 \varrho_2 & \varrho_3^2 \end{bmatrix}. \quad (232)$$

Similarly, we evaluate  $C_{ij}^e$  of (223) by noting that

$$\begin{aligned} C_{ii}^e &= \frac{\epsilon^e}{h_i^2} \int_{S^e} \left[ \xi_{i+1}^2 |\ell_{i-1}|^2 - 2\xi_{i+1}\xi_{i-1}\ell_{i-1} \cdot \ell_{i+1} + \xi_{i-1}^2 |\ell_{i+1}|^2 \right] dS \\ &= \frac{\epsilon^e \varrho_i^2}{6} \left( \frac{|\ell_{i-1}|^2 - \ell_{i-1} \cdot \ell_{i+1} + |\ell_{i+1}|^2}{4A^e} \right) \\ &= \frac{\epsilon^e \varrho_i^2}{12} [3 \cot \theta_i + \cot \theta_{i+1} + \cot \theta_{i-1}], \end{aligned} \quad (233)$$

and that

$$\begin{aligned} C_{i+1,i-1}^e &= \frac{\epsilon^e}{h_{i+1}h_{i-1}} \int_{S^e} \left[ \xi_{i-1}\xi_i \ell_i \cdot \ell_{i+1} - \xi_{i-1}\xi_{i+1} |\ell_i|^2 \right. \\ &\quad \left. + \xi_i \xi_{i+1} \ell_{i-1} \cdot \ell_i - \xi_i^2 \ell_{i+1} \cdot \ell_{i-1} \right] dS \\ &= \frac{\epsilon^e \varrho_{i+1} \varrho_{i-1}}{12} \left( \frac{\ell_i \cdot \ell_{i+1} - |\ell_i|^2 + \ell_{i-1} \cdot \ell_i - 2\ell_{i+1} \cdot \ell_{i-1}}{4A^e} \right) \\ &= \frac{\epsilon^e \varrho_{i+1} \varrho_{i-1}}{12} (\cot \theta_i - \cot \theta_{i+1} - \cot \theta_{i-1}), \end{aligned} \quad (234)$$

evaluated with the aid of (88), (90) and (96). Hence the element matrix  $[C_{ij}^e]$  is

$$[C_{ij}^e] = \frac{\epsilon^e}{12} (\cot \theta_1 [R_1] + \cot \theta_2 [R_2] + \cot \theta_3 [R_3]), \quad (235)$$

where

$$[R_1] = \begin{bmatrix} 3\varrho_1^2 & -\varrho_1\varrho_2 & -\varrho_1\varrho_3 \\ -\varrho_2\varrho_1 & \varrho_2^2 & \varrho_2\varrho_3 \\ -\varrho_3\varrho_1 & \varrho_3\varrho_2 & \varrho_3^2 \end{bmatrix}, \quad (236)$$

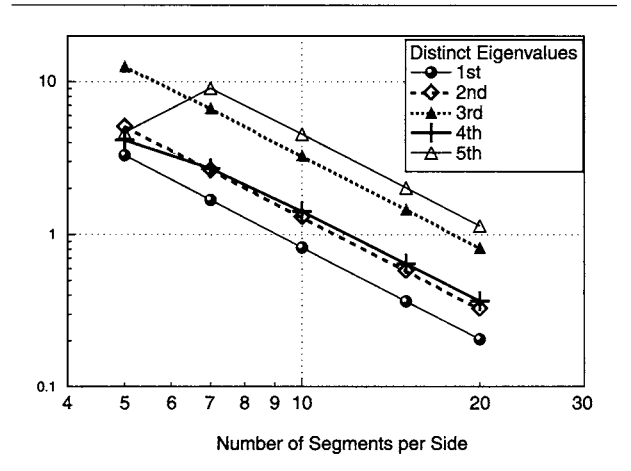
$$[R_2] = \begin{bmatrix} \varrho_1^2 & -\varrho_1\varrho_2 & \varrho_1\varrho_3 \\ -\varrho_2\varrho_1 & 3\varrho_2^2 & -\varrho_2\varrho_3 \\ \varrho_3\varrho_1 & -\varrho_3\varrho_2 & \varrho_3^2 \end{bmatrix}, \quad (237)$$

$$[R_3] = \begin{bmatrix} \varrho_1^2 & \varrho_1\varrho_2 & -\varrho_1\varrho_3 \\ \varrho_2\varrho_1 & \varrho_2^2 & -\varrho_2\varrho_3 \\ -\varrho_3\varrho_1 & -\varrho_3\varrho_2 & 3\varrho_3^2 \end{bmatrix}. \quad (238)$$

## Numerical Results

Without means to incorporate radiation conditions, we cannot yet solve TE scattering problems. Nevertheless we can easily illustrate the methods of this section by determining the eigenfrequencies for which there exist source-free solutions for a closed TE conducting cylinder. Thus, following the approach leading to (103), we determine the TE eigenfrequencies of an air-filled square waveguide. These eigenfrequencies are given by  $\omega_{pq}^2 = \left[ \frac{c_0 \pi}{a} \right]^2 (p^2 + q^2)$  where  $c_0$  is the speed of light in air,  $a$  is the dimension of a side and  $p, q = 0, 1, 2, \dots$  with  $p$  and  $q$  not both zero. The error in the first five distinct eigenvalues is plotted versus the number of subdivisions per side in Fig. 21.

**Figure 21** Convergence of first five distinct TE eigenvalues of a square waveguide.



## §10. Conducting Bodies: EFIE, 3D

In §2 and §7, we considered scattering by a conducting cylinder illuminated by TM and TE polarised incident fields, respectively. Here we treat the corresponding three-dimensional problem using the electric field integral equation (EFIE) (Rao *et al.*, 1982). The scatterer is assumed to be a perfectly conducting body of arbitrary shape with boundary  $S$  and illuminated by an incident field  $E^{\text{inc}}$ . If  $S$  is an open surface, then it also has a boundary  $C$ . For open surfaces, the induced surface current density  $\mathbf{J}$  is assumed to be a sum of current densities on opposite sides of the surface. Furthermore, following the discussion of §7, the normal component of the total current must vanish at  $C$ . Expressed in terms of potentials, (9)–(14), the scattered electric field is

$$E^{\text{sc}} = -j\omega\mathbf{A} - \nabla\Phi, \quad (239)$$

where the magnetic vector and electric scalar potentials are

$$\mathbf{A} = \mu \int_S \mathbf{J}(\mathbf{r}') G(\mathbf{r}, \mathbf{r}') dS' \quad (240)$$

and

$$\Phi = -\frac{1}{j\omega\epsilon} \int_S \nabla' \cdot \mathbf{J}(\mathbf{r}') G(\mathbf{r}, \mathbf{r}') dS', \quad (241)$$

respectively, and the three-dimensional Green's function is

$$G(\mathbf{r}, \mathbf{r}') = \frac{e^{-jkR}}{4\pi R}, \quad (242)$$

where  $R = |\mathbf{r} - \mathbf{r}'|$ . The electric field integro-differential equation for the induced current is obtained by requiring that the total tangential electric field,  $E^{\text{sc}} + E^{\text{inc}}$ , vanish on the conductor surface:

$$[j\omega\mathbf{A} + \nabla\Phi]_{\text{tan}} = \mathbf{E}_{\text{tan}}^{\text{inc}}(\mathbf{r}), \quad \mathbf{r} \in S. \quad (243)$$

The corresponding weak form of the equation is obtained by testing it with a vector-valued weighting

function  $\Lambda_m(\mathbf{r})$  defined on and tangent to  $S$ . Using the identity  $\nabla \cdot (\Lambda_m \Phi) = \Phi \nabla \cdot \Lambda_m + \nabla \Phi \cdot \Lambda_m$  and the divergence theorem, the term involving the scalar potential is integrated by parts to obtain the weak form

$$j\omega \langle \Lambda_m; \mathbf{A} \rangle - \langle \nabla \cdot \Lambda_m, \Phi \rangle = \langle \Lambda_m; \mathbf{E}_{\tan}^{\text{inc}} \rangle, \quad \mathbf{r} \in S. \quad (244)$$

The boundary terms arising from integration by parts in (244) vanish because the components of weighting functions normal to  $C$  are assumed to vanish. This assumption is consistent with our intention to use the testing functions as basis functions that interpolate the normal components of total surface current at triangle edges; these components vanish at surface boundaries. With (240) and (241), we thus write the integro-differential equation as

$$\begin{aligned} j\omega \mu \langle \Lambda_m; \mathbf{G}, \mathbf{J} \rangle + \frac{1}{j\omega \epsilon} \langle \nabla \cdot \Lambda_m, \mathbf{G}, \nabla' \cdot \mathbf{J} \rangle \\ = \langle \Lambda_m; \mathbf{E}^{\text{inc}} \rangle, \quad \mathbf{r} \in S. \end{aligned} \quad (245)$$

We approximate the conductor surface  $S$  by a mesh of planar triangles, with the  $e$ th triangle denoted  $S^e$ . The resulting approximate surface  $\tilde{S}$  is continuous and forms a piecewise linear approximation to the surface  $S \approx \tilde{S} = \cup_{e=1}^E S^e$ .

Since (245) requires the divergence of the current, we choose *divergence-conforming* bases  $\Lambda_n$  to represent the current, i.e., bases with continuous normal components across element boundaries. Otherwise nonphysical line charges will appear at the element boundaries. In fact, we choose the degrees of freedom for the current to be the normal component of current at the midpoint of each nonboundary edge of the mesh. Thus the surface current representation is given by

$$\mathbf{J}(\mathbf{r}) \approx \sum_{n=1}^N I_n \Lambda_n(\mathbf{r}), \quad (246)$$

where  $I_n$  represents the component of current normal to an edge. The support of each basis is the pair of triangles sharing the edge at which its interpolation point is defined. Since the component of current normal to boundary edges vanishes, we simply do not associate basis functions with such edges. On the other hand, where two or more conducting surfaces intersect, at least three triangles share a common edge along the intersection. To prevent a line charge buildup at the edge, these surface current densities must satisfy Kirchhoff's current law; hence if  $J$  surfaces intersect, there can only be  $J - 1$  degrees of freedom. The situation simply generalises to three dimensions the discussion of §7, and the basis overlapping scheme described there is directly adapted to this case.

Substituting (246) into (245), we obtain the matrix system

$$[\mathbf{Z}_{mn}][I_n] = [\mathbf{V}_m], \quad (247)$$

where the system impedance matrix is

$$[\mathbf{Z}_{mn}] = j\omega [L_{mn}] + \frac{1}{j\omega} [S_{mn}], \quad (248)$$

with *inductance* and *elastance matrices*

$$[L_{mn}] = \mu [\langle \Lambda_m; \mathbf{G}(\mathbf{r}, \mathbf{r}'); \Lambda_n \rangle] \quad (249)$$

and

$$[S_{mn}] = \frac{1}{\epsilon} [\langle \nabla \cdot \Lambda_m, \mathbf{G}(\mathbf{r}, \mathbf{r}'), \nabla' \cdot \Lambda_n \rangle], \quad (250)$$

respectively. The excitation column vector is defined as

$$\mathbf{V}_m = [\langle \Lambda_m; \mathbf{E}^{\text{inc}} \rangle]. \quad (251)$$

### Construction of Bases

We express the global basis  $\Lambda_n$ , associated with DoF index  $n$ , in terms of a local basis  $\Lambda_i^e$ , the  $i$ th edge of element  $S^e$ , as

$$\Lambda_n(\mathbf{r}) = \sigma_i^e \Lambda_i^e(\mathbf{r}), \quad \mathbf{r} \in S^e, \quad (252)$$

where  $\sigma_i^e$  determines the global reference direction for surface current crossing the  $i$ th edge of  $S^e$ , generalising to triangles the definition (172) of §7. For the local bases,  $\Lambda_i^e$ , the positive reference direction is always assumed to be out of the element.

Divergence-conforming bases must have continuous normal components across element boundaries so that nonphysical line charges do not appear there. The additional requirement that the bases be interpolatory at element edges thus imposes the following conditions on their construction:

- To model surface charge to lowest order,  $\nabla \cdot \Lambda_i^e$  must be constant; hence  $\Lambda_i^e$  must vary linearly within an element.
- $\Lambda_i^e$  should have a normal component along edge  $i$  of element  $e$ , but a vanishing normal component along the two remaining edges.

Note that these requirements are essentially dual to those used in constructing curl-conforming bases in §9. In fact, the required local bases in a triangle are easily constructed as the cross product of local curl-conforming bases and the triangle's unit normal vector

$$\Lambda_i^e(\mathbf{r}) = \mathbf{\Omega}_i^e(\mathbf{r}) \times \hat{\mathbf{n}} = \frac{(\xi_{i+1} \ell_{i-1} - \xi_{i-1} \ell_{i+1})}{h_i}, \quad (253)$$

with divergence

$$\nabla \cdot \Lambda_i^e(\mathbf{r}) = \frac{2}{h_i}. \quad (254)$$

The definitions of the edge vectors and heights appearing in these equations are given in Table 8.

The data structures of Tables 5 and 11 are readily adapted to this problem. Since the problem is three-

dimensional, an extra column is needed in Table 5 to hold the  $z$  coordinates of the nodes. The element connection data of Table 11 remain the same, except that the sign on the DoF indices now refers to the reference direction for the *normal* component of current at an edge, with a positive or negative sign implying a reference direction out of or into the triangle, respectively.

### Evaluation of Element Matrices

The element matrix accounts for all interactions between those bases whose support includes a given pair of interacting triangles. Thus the element impedance matrix associated with the global impedance matrix (248) is defined as

$$[Z_{ij}^{ef}] = j\omega\sigma_i^e\sigma_j^f[L_{ij}^{ef}] + \frac{\sigma_i^e\sigma_j^f}{j\omega}[S_{ij}^{ef}], \quad (255)$$

where each matrix element represents the interaction between the  $i$ th basis of element  $e$  and the  $j$ th basis of element  $f$ . The element inductance and elastance matrices are given by

$$[L_{ij}^{ef}] = \mu \left[ \int_{S^e} \int_{S^f} \Lambda_i^e(\mathbf{r}) \cdot \Lambda_j^f(\mathbf{r}') G(\mathbf{r}, \mathbf{r}') dS' dS \right] \quad (256)$$

and

$$[S_{ij}^{ef}] = \frac{1}{\epsilon} \left[ \int_{S^e} \int_{S^f} \nabla \cdot \Lambda_i^e(\mathbf{r}) G(\mathbf{r}, \mathbf{r}') \nabla' \cdot \Lambda_j^f(\mathbf{r}') dS' dS \right], \quad (257)$$

respectively. The element excitation column vector associated with the corresponding global vector (251) is given by

$$[V_i^e] = \left[ \sigma_i^e \int_{S^e} \Lambda_i^e \cdot \mathbf{E}^{\text{inc}} dS \right]. \quad (258)$$

Making use of (253), the element inductance matrix is given by

$$[L_{ij}^{ef}] = \frac{\mu}{h_i h_j} \left[ \ell_{i-1}^e \cdot \ell_{j-1}^f \Psi_{i+1, j+1}^{ef} - \ell_{i-1}^e \cdot \ell_{j+1}^f \Psi_{i+1, j-1}^{ef} \right. \\ \left. - \ell_{i+1}^e \cdot \ell_{j-1}^f \Psi_{i-1, j+1}^{ef} + \ell_{i+1}^e \cdot \ell_{j+1}^f \Psi_{i-1, j-1}^{ef} \right], \quad (259)$$

where  $\Psi_{ij}^{ef}$  is the potential integral

$$\Psi_{ij}^{ef} = 4A^e A^f \int_0^1 \int_0^{1-\xi_2} \int_0^1 \int_0^{1-\xi_2'} \xi_i \frac{e^{-jkR}}{4\pi R} \\ \times \xi_j' d\xi_1' d\xi_2' d\xi_1 d\xi_2 \quad (260)$$

and

$$R = \left| \mathbf{r}_1^e \xi_1 + \mathbf{r}_2^e \xi_2 + \mathbf{r}_3^e \xi_3 - \mathbf{r}_1^f \xi_1' - \mathbf{r}_2^f \xi_2' - \mathbf{r}_3^f \xi_3' \right|. \quad (261)$$

Turning to the evaluation of  $S_{ij}^{ef}$ , Eq. (257), we use (254) and recall that  $\xi_1 + \xi_2 + \xi_3 = \xi_1' + \xi_2' + \xi_3' = 1$  to obtain the element elastance matrix

$$S_{ij}^{ef} = \frac{4}{\epsilon h_i h_j} \sum_{k=1}^3 \sum_{\ell=1}^3 \Psi_{k\ell}^{ef}. \quad (262)$$

The evaluation of element matrices thus reduces to the problem of evaluating the scalar potential integrals (260). For  $e \neq f$ , the Gaussian quadrature rules of Table 9 may be used to evaluate both the inner pair of integrals over the source triangle and the outer pair of integrals over the observation triangle. Since triangles must be electrically small for good accuracy—typically no larger than an eighth of a wavelength on a side—the potential is slowly varying over a triangle and hence a one-point rule for the outer surface integral is often both efficient and sufficiently accurate. The quadrature order needed for good accuracy in evaluating the inner integral generally depends on the relative distance between source and observation points. If an observation point is very close to the source triangle, however, it may be necessary to appropriately adapt the scheme below for the source point integration.

For  $e = f$ , the observation points are on the source triangle and the potential integral (260) becomes

$$\Psi_{ij}^{ee} = 4(A^e)^2 \int_0^1 \int_0^{1-\xi_2} \int_0^1 \int_0^{1-\xi_2'} \xi_i \frac{e^{-jkR}}{4\pi R} \xi_j' d\xi_1' d\xi_2' d\xi_1 d\xi_2 \\ = 4(A^e)^2 \sum_{k=1}^K w_k \xi_i^{(k)} I_j^{(k)}, \quad (263)$$

where the Gaussian quadrature rules of Table 9 are used to evaluate the outer pair of integrals over observation coordinates, and the remaining inner integral is

$$I_j^{(k)} = \int_0^1 \int_0^{1-\xi_2'} G(\mathbf{r}^{(k)}, \mathbf{r}') \xi_j' d\xi_1' d\xi_2', \quad (264)$$

with

$$G(\mathbf{r}^{(k)}, \mathbf{r}') = \frac{e^{-jk|\mathbf{r}^{(k)} - \mathbf{r}'|}}{4\pi|\mathbf{r}^{(k)} - \mathbf{r}'|} \quad (265)$$

and

$$\mathbf{r}^{(k)} = \mathbf{r}_1^e \xi_1^{(k)} + \mathbf{r}_2^e \xi_2^{(k)} + \mathbf{r}_3^e \xi_3^{(k)}. \quad (266)$$

The remaining integral, (264), contains a singularity since  $R$  vanishes when observation and source points coincide. Two separate approaches may be used to treat this case, one a *singularity subtraction* method and the other a *singularity cancellation* method. In the subtraction approach, we note that the integrand approaches  $\xi_j'/(4\pi|\mathbf{r}^{(k)} - \mathbf{r}'|)$  as  $\mathbf{r}'$  approaches  $\mathbf{r}^{(k)}$ . We merely subtract this factor from the integrand of (264) and add it back as a separate integral, yielding

$$I_j^{(k)} = \int_0^1 \int_0^{1-\xi_2'} \frac{e^{-jk|\mathbf{r}^{(k)} - \mathbf{r}'|} - 1}{4\pi|\mathbf{r}^{(k)} - \mathbf{r}'|} \xi_j' d\xi_1' d\xi_2' \\ + \int_0^1 \int_0^{1-\xi_2'} \frac{1}{4\pi|\mathbf{r}^{(k)} - \mathbf{r}'|} \xi_j' d\xi_1' d\xi_2'. \quad (267)$$

The integrand of the first integral in (267) is bounded and may now be integrated by the rules of Table 9, while the last integral can be integrated in closed form

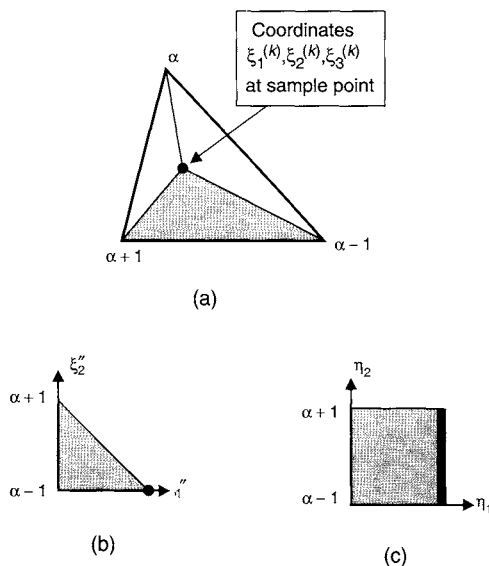
(Wilton *et al.*, 1984). Although quite widely used and simple to apply, this approach does have drawbacks. Although the integrand of the first term of (267) is bounded, there remain singularities in its derivatives at the observation point, violating the underlying assumption of the Gaussian scheme that the integrand is well modelled by a polynomial. Consequently, a high-order quadrature—at least the seven-point scheme of Table 9—is required for only moderate accuracy; high accuracy is often difficult to obtain. Fortunately, this term is usually dominated by the analytically exact contribution of the second integral, but one must take care in evaluating expressions for the latter for very narrow triangles or for observation points near the edges. Finally, there also exist Green's functions for which the asymptotic form of the singularity in the integrand cannot be integrated in closed form.

The singularity cancellation method suffers none of these deficiencies, although high accuracy may also require many sampling points. In this method, we introduce a transformation of coordinates such that the Jacobian of the transformation cancels the singularity. Figure 22 shows a source triangle with an interior observation point at one of the Gaussian points of (263).

The sample point subdivides the triangle into subtriangles, one of which is shown opposite vertex  $\alpha$ . The area coordinates within this subtriangle are mapped into an intermediate triangle with unit vertex coordinates and then to a unit square by the successive transformations

$$\begin{aligned}\xi'_\alpha &= \xi_\alpha^{(k)} \xi''_1 \\ \xi'_{\alpha+1} &= \xi_{\alpha+1}^{(k)} \xi''_1 + \xi''_2 \\ \xi'_{\alpha-1} &= \xi_{\alpha-1}^{(k)} \xi''_1 + \xi''_3,\end{aligned}\quad (268)$$

**Figure 22** Subtriangle mapped to intermediate triangle and to unit square.



and

$$\begin{aligned}\xi''_1 &= \eta'_1 \\ \xi''_2 &= (1 - \eta'_1) \eta'_2 \\ \xi''_3 &= (1 - \eta'_1) (1 - \eta'_2),\end{aligned}\quad (269)$$

for which we find that

$$d\xi'_1 d\xi'_2 = \xi_\alpha^{(k)} d\xi''_1 d\xi''_2 = \xi_\alpha^{(k)} (1 - \eta'_1) d\eta'_1 d\eta'_2. \quad (270)$$

Note that the interior vertex of the original subtriangle, where the singularity in the integrand occurs, is mapped onto the line  $\eta'_1 = 1$ , where the vanishing factor  $(1 - \eta'_1)$  in (270) cancels the singularity. The integral (264) may now be evaluated as a sum over the transformed subtriangles,

$$I_j^{(k)} = \sum_{\alpha=1}^3 \xi_\alpha^{(k)} \int_0^1 \int_0^1 G(\mathbf{r}^{(k)}, \mathbf{r}') \xi'_j (1 - \eta'_1) d\eta'_1 d\eta'_2, \quad (271)$$

where in each subtriangle integral,

$$\begin{aligned}\mathbf{r}' &= \mathbf{r}_\alpha^e \xi_\alpha^{(k)} \eta'_1 + \mathbf{r}_{\alpha+1}^e \left[ \xi_{\alpha+1}^{(k)} \eta'_1 + (1 - \eta'_1) \eta'_2 \right] \\ &+ \mathbf{r}_{\alpha-1}^e \left[ \xi_{\alpha-1}^{(k)} \eta'_1 + (1 - \eta'_1) (1 - \eta'_2) \right]\end{aligned}\quad (272)$$

and

$$\xi'_j = \xi_j^{(k)} \eta'_1 + \delta_{j, \alpha+1} (1 - \eta'_1) \eta'_2 + \delta_{j, \alpha-1} (1 - \eta'_1) (1 - \eta'_2). \quad (273)$$

In (273), we have used the Kronecker delta,

$$\delta_{ij} = \begin{cases} 1, & i = j, \\ 0, & i \neq j. \end{cases}\quad (274)$$

The double integral of (271) may be evaluated by successively applying the one-dimensional Gauss-Legendre rules of Table 3 to each integral.

For the excitation element vector (251), consider a plane wave incident from spherical coordinate angles  $(\theta^{\text{inc}}, \phi^{\text{inc}})$ ,

$$\mathbf{E}^{\text{inc}} = \mathbf{E}_0 e^{-jk \hat{\mathbf{k}}^{\text{inc}} \cdot \mathbf{r}}, \quad (275)$$

where

$$\hat{\mathbf{k}}^{\text{inc}} = -\hat{\mathbf{x}} \cos \phi^{\text{inc}} \sin \theta^{\text{inc}} - \hat{\mathbf{y}} \sin \phi^{\text{inc}} \sin \theta^{\text{inc}} - \hat{\mathbf{z}} \cos \theta^{\text{inc}} \quad (276)$$

and  $\mathbf{E}_0$  is a complex constant vector with components only along the spherical coordinate unit vectors  $\hat{\theta}^{\text{inc}}$  and  $\hat{\phi}^{\text{inc}}$ . The global system excitation vector is thus

$$\langle \Lambda_m; \mathbf{E}^{\text{inc}} \rangle = \mathbf{E}_0 \cdot \left[ \tilde{\Lambda}_m(-\hat{\mathbf{k}}^{\text{inc}}) \right], \quad (277)$$

where

$$\left[ \tilde{\Lambda}_m(\hat{\mathbf{k}}) \right] = \left[ \int_S \Lambda_m(\mathbf{r}) e^{jk \hat{\mathbf{k}} \cdot \mathbf{r}} dS \right] \quad (278)$$

is a vector-valued column vector of Fourier transforms of the bases. Thus the element excitation vector corresponding to (258) is

$$\left[ \sigma_i^e \langle \Lambda_i^e; \mathbf{E}^{\text{inc}} \rangle \right] = \sigma_i^e \mathbf{E}_0 \cdot \left[ \tilde{\Lambda}_i^e(-\hat{\mathbf{k}}^{\text{inc}}) \right], \quad (279)$$

where

$$\left[ \tilde{\Lambda}_i^e(\hat{\mathbf{k}}) \right] = \left[ \int_{S^e} \Lambda_i^e(\mathbf{r}) e^{j\hat{\mathbf{k}} \cdot \mathbf{r}} dS \right] \quad (280)$$

is a column vector of Fourier transforms of the local bases on element  $e$ . Elements of the column vector may be evaluated either analytically (Lee and Mittra, 1983) or by numerical quadrature, and assembled into the system transform column vector. Note that factoring the incident field amplitude from the system excitation vector in (277) enables us to use the Fourier transform algorithm both in the construction of the excitation vector and in the computation of far fields below.

### Evaluation of Far Fields

The scattered far electric field at a distance  $r$  and angle  $(\theta, \phi)$  is given by (17) and (20):

$$\mathbf{E}^{\text{sc}} = -\frac{j\omega\mu}{4\pi r} e^{-jkr} \left( \hat{\theta}\hat{\theta} + \hat{\phi}\hat{\phi} \right) \cdot \int_S \mathbf{J}(\mathbf{r}') e^{jk\hat{\mathbf{r}} \cdot \mathbf{r}'} dS'. \quad (281)$$

Substituting in the approximation (246) for the surface current  $\mathbf{J}$  yields

$$\begin{aligned} \mathbf{E}^{\text{sc}} &= -\frac{j\omega\mu}{4\pi r} e^{-jkr} \left( \hat{\theta}\hat{\theta} + \hat{\phi}\hat{\phi} \right) \cdot \sum_{n=1}^N I_n \int_S \Lambda_n(\mathbf{r}') e^{jk\hat{\mathbf{r}} \cdot \mathbf{r}'} dS' \\ &= -\frac{j\omega\mu}{4\pi r} e^{-jkr} \left( \hat{\theta}\hat{\theta} + \hat{\phi}\hat{\phi} \right) \cdot \left[ \tilde{\Lambda}_n(\hat{\mathbf{r}}) \right]^t [I_n], \end{aligned} \quad (282)$$

where the unit vector in the observation direction is

$$\hat{\mathbf{r}} = \hat{\mathbf{x}} \cos\phi \sin\theta + \hat{\mathbf{y}} \sin\phi \sin\theta + \hat{\mathbf{z}} \cos\theta \quad (283)$$

and the superscript  $t$  denotes the transpose. Note that we use the column vector of Fourier transforms of the bases defined in (278), but with the transform variable now as the observation angle rather than the incident angle.

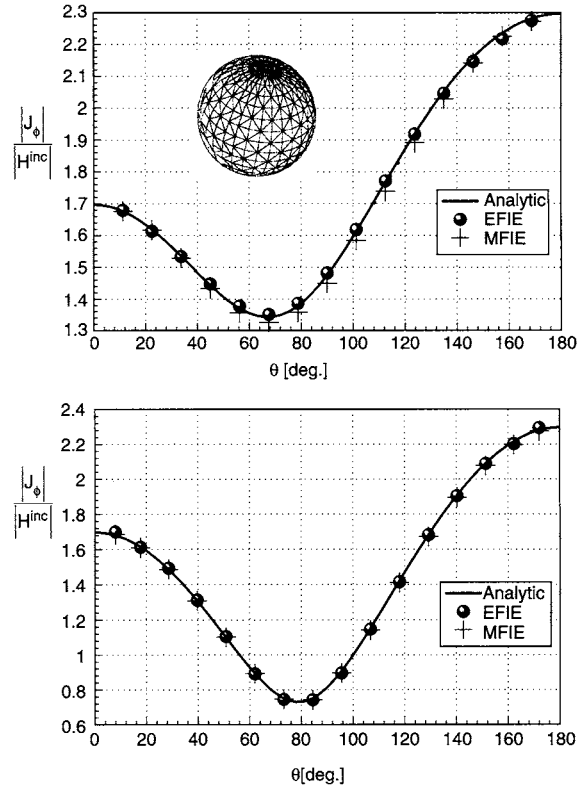
### Numerical Results

Figure 23 shows the current induced on a conducting sphere illuminated by a linearly polarised plane wave incident from  $\theta^{\text{inc}} = 180^\circ$ . The cut for  $J_\theta$  is taken in the plane containing the incident electric field vector; that for  $J_\phi$  is in the plane containing the incident magnetic field. Note that the mesh density at low frequencies must be sufficient to adequately model the curvature and surface area; at higher frequencies, it must also provide sufficient sampling density per wavelength. Also shown in the figure for comparison are results from the MFIE approach of the following section.

## §11. Conducting Bodies: MFIE, 3D

An alternative to the electric field integral equation for three-dimensional problems is the MFIE. In the case

**Figure 23** Current (a) in  $x$ - $z$  plane and (b) in the  $y$ - $z$  plane on conducting sphere illuminated by a plane wave.



of the MFIE, the surface  $S$  of the conducting scatterer must be closed. The scattered magnetic field is related to the induced surface current  $\mathbf{J}$  via

$$\mathbf{H}^{\text{sc}} = \frac{1}{\mu} \nabla \times \mathbf{A}, \quad (284)$$

where the magnetic vector potential is given by (240) and (242). The total magnetic field must vanish just inside the conductor surface:

$$\hat{\mathbf{n}} \times \mathbf{H}^{\text{sc}}(\mathbf{J}) + \hat{\mathbf{n}} \times \mathbf{H}^{\text{inc}} = 0, \quad \mathbf{r} \in \lim_{r \uparrow S} S. \quad (285)$$

Using (37) and (39), this becomes

$$\frac{\mathbf{J}(\mathbf{r})}{2} + \hat{\mathbf{n}} \times \int_S \mathbf{J}(\mathbf{r}') \times \nabla G(\mathbf{r}, \mathbf{r}') dS' = \hat{\mathbf{n}} \times \mathbf{H}^{\text{inc}}, \quad \mathbf{r} \in S, \quad (286)$$

where  $G(\mathbf{r}, \mathbf{r}')$  is given by (242).

We may use the same triangular element representation and data structure for  $S$  as in §10, except that  $S$  must now be a closed surface. We also approximate  $\mathbf{J}$  using (246), substitute it into (286) and test the resulting equation with  $\Lambda_m$ , yielding

$$[\beta_{mn}][I_n] = [I^{\text{inc}}], \quad (287)$$

where

$$\begin{aligned} \beta_{mn} &= \frac{1}{2} \langle \Lambda_m; \Lambda_n \rangle + \int_S \int_S (\Lambda_m(\mathbf{r}) \times \hat{\mathbf{n}}) \\ &\quad \cdot (\Lambda_n(\mathbf{r}') \times \nabla G(\mathbf{r}, \mathbf{r}')) dS' dS. \end{aligned} \quad (288)$$

Elements of the excitation column vector in (287) are given by

$$I_m^{\text{inc}} = \langle \Lambda_m; \hat{\mathbf{n}} \times \mathbf{H}^{\text{inc}} \rangle. \quad (289)$$

Solving (287) yields the current coefficients, and hence, from (246), the surface current density  $\mathbf{J}$ .

### Evaluation of Element Matrices

The element matrix corresponding to (288) is given by

$$\beta_{ij}^{ef} = \begin{cases} \frac{\sigma_i^e \sigma_j^e}{2} \langle \Lambda_i^e; \Lambda_j^e \rangle, & e = f \\ \sigma_i^e \sigma_j^f \int_{S^e} \int_{S^f} (\Lambda_i^e(\mathbf{r}) \times \hat{\mathbf{n}}) \cdot (\Lambda_j^f(\mathbf{r}') \times \nabla G(\mathbf{r}, \mathbf{r}')) dS' dS, & e \neq f, \end{cases} \quad (290)$$

where the reference direction factors  $\sigma_i^e$  merely generalise to triangles the definition (172).

From (253), which relates divergence- and curl-conforming bases on a surface, and the similarity of the symmetric product in (290) to that of (223), one easily verifies that the case  $e = f$  in (290) reduces to

$$\beta_{ij}^{ee} = \frac{\sigma_i^e \sigma_j^e C_{ij}^e}{2\epsilon^e}, \quad (291)$$

where  $C_{ij}^e$  is given in (235) and following. We note that in the double surface integral (290),

$$\nabla G(\mathbf{r}, \mathbf{r}') = -\frac{(1 + kR)e^{-jkR}}{R^2} \hat{\mathbf{R}}, \quad (292)$$

where  $\hat{\mathbf{R}} = \frac{\mathbf{r} - \mathbf{r}'}{R}$ . The element excitation column vector corresponding to (289) is given by

$$I_i^{e, \text{inc}} = \sigma_i \langle \Lambda_i^e; \hat{\mathbf{n}} \times \mathbf{H}^{\text{inc}} \rangle. \quad (293)$$

Both (290) and (293) may be evaluated by numerical quadrature methods described in §10. Since the geometry and current representations are the same as in §10, we can evaluate the far field using (282).

Numerical results comparing the MFIE and EFIE solutions for scattering by a conducting sphere are presented in Fig. 23.

## §12. Dielectric Bodies: PMCHW Formulation, 3D

In this section, we consider a homogeneous dielectric scatterer with closed boundary  $S$ . The region exterior to  $S$  is denoted  $\mathcal{V}^+$  and its interior is  $\mathcal{V}^-$ . The medium parameters in  $\mathcal{V}^\pm$  are  $\mu^\pm, \epsilon^\pm$ , respectively, and may be complex-valued with negative imaginary parts for lossy media. A triangular surface patch model of  $S$  is assumed using the data structure described in §10. To represent the exterior region fields using the equivalence principle, the scatterer is replaced by equivalent electric and magnetic surface currents  $\mathbf{J} = \hat{\mathbf{n}} \times \mathbf{H}$

and  $\mathbf{M} = \mathbf{E} \times \hat{\mathbf{n}}$ , respectively, where  $\hat{\mathbf{n}}$  is the outward unit surface normal. The total fields, i.e., the sum of fields  $\mathbf{E}^{\text{inc}}, \mathbf{H}^{\text{inc}}$  incident from the exterior and the corresponding scattered electric and magnetic fields radiated by the equivalent currents, vanish in  $\mathcal{V}^-$ . Hence, in the exterior region field representation, the exterior medium parameters may be extended into the interior without disturbing the fields. Similarly, a representation of the fields in  $\mathcal{V}^-$  is obtained by placing currents  $-\mathbf{J}$  and  $-\mathbf{M}$  on  $S$ ; since the incident field is assumed incident from the exterior, its sources and corresponding fields are not included in the interior representation. The currents  $-\mathbf{J}$  and  $-\mathbf{M}$  radiate a null field in  $\mathcal{V}^+$ , and hence the interior medium parameters may be extended to the exterior. With the extension of medium parameters into the complementary null field regions, the equivalent currents of both interior and exterior representations reside finally in homogeneous media, and hence the homogeneous medium Green's function (14) may be employed in potential representations for the corresponding fields.

The null field conditions described above can be written in terms of the incident fields and scattered fields produced by the equivalent currents as (Mautz and Harrington, 1979)

$$\mathbf{E}^{\text{sc}}(\mathbf{J}, \mathbf{M}) + \mathbf{E}^{\text{inc}} = 0, \quad \mathbf{r} \in \mathcal{V}^-, \quad (294)$$

$$\mathbf{H}^{\text{sc}}(\mathbf{J}, \mathbf{M}) + \mathbf{H}^{\text{inc}} = 0, \quad \mathbf{r} \in \mathcal{V}^-, \quad (295)$$

and

$$\mathbf{E}^{\text{sc}}(-\mathbf{J}, -\mathbf{M}) = 0, \quad \mathbf{r} \in \mathcal{V}^+, \quad (296)$$

$$\mathbf{H}^{\text{sc}}(-\mathbf{J}, -\mathbf{M}) = 0, \quad \mathbf{r} \in \mathcal{V}^+, \quad (297)$$

or in equivalent weak forms using tangential vector testing functions  $\Lambda_m$ ,

$$\langle \Lambda_m; \mathbf{E}^{\text{sc}}(\mathbf{J}, \mathbf{M}) \rangle + \langle \Lambda_m; \mathbf{E}^{\text{inc}} \rangle = 0, \quad \mathbf{r} \in \lim_{r \downarrow S} S, \quad (298)$$

$$\langle \Lambda_m; \mathbf{H}^{\text{sc}}(\mathbf{J}, \mathbf{M}) \rangle + \langle \Lambda_m; \mathbf{H}^{\text{inc}} \rangle = 0, \quad \mathbf{r} \in \lim_{r \downarrow S} S, \quad (299)$$

and

$$\langle \Lambda_m; \mathbf{E}^{\text{sc}}(-\mathbf{J}, -\mathbf{M}) \rangle = 0, \quad \mathbf{r} \in \lim_{r \downarrow S} S, \quad (300)$$

$$\langle \Lambda_m; \mathbf{H}^{\text{sc}}(-\mathbf{J}, -\mathbf{M}) \rangle = 0, \quad \mathbf{r} \in \lim_{r \downarrow S} S. \quad (301)$$

Equations (294)–(301) implicitly assume potential representations for the scattered fields employing the medium parameters of the region complementary to that for which the null field condition holds.

Any pair of equations formed as linearly independent combinations of (298)–(301) constitutes a possible formulation for a coupled system of integral equations for the unknown surface currents  $\mathbf{J}$  and  $\mathbf{M}$ . Not all formulations have unique solutions, however. One choice that does is the PMCHW formulation, named from the initials of the five researchers who, in three separate articles, first applied it (Mautz and Harrington, 1979). It is obtained by equating (298) to (300) and (299) to (301), and is equivalent to requiring

that both electric and magnetic fields be continuous across  $S$ . With this choice, we expand both the electric and magnetic currents in the basis functions of §10,

$$\mathbf{J} = \hat{\mathbf{n}} \times \mathbf{H} = \sum_{n=1}^N I_n \mathbf{\Lambda}_n(\mathbf{r}), \quad (302)$$

$$\mathbf{M} = \mathbf{E} \times \hat{\mathbf{n}} = \sum_{n=1}^N V_n \mathbf{\Lambda}_n(\mathbf{r}), \quad (303)$$

and substitute the result into the PMCHW equations, using (37)–(42) to obtain the coupled system of equations (Umashankar *et al.*, 1986)

$$\begin{bmatrix} [Z_{mn}^+ + Z_{mn}^-] & [-\beta_{mn}^+ - \beta_{mn}^-] \\ [\beta_{mn}^+ + \beta_{mn}^-] & [Y_{mn}^+ + Y_{mn}^-] \end{bmatrix} \begin{bmatrix} I_n \\ V_n \end{bmatrix} = \begin{bmatrix} V_m^{\text{inc}} \\ I_m^{\text{inc}} \end{bmatrix}. \quad (304)$$

Elements of the impedance submatrices in (304) are defined as

$$Z_{mn}^\pm = j\omega L_{mn}^\pm + \frac{1}{j\omega} S_{mn}^\pm, \quad (305)$$

where

$$L_{mn}^\pm = \mu^\pm \langle \mathbf{\Lambda}_m; \mathbf{G}^\pm; \mathbf{\Lambda}_n \rangle, \quad (306)$$

$$S_{mn}^\pm = \frac{1}{\epsilon^\pm} \langle \nabla \cdot \mathbf{\Lambda}_m, \mathbf{G}^\pm, \nabla \cdot \mathbf{\Lambda}_n \rangle, \quad (307)$$

and the media Green's functions are

$$G^\pm(\mathbf{r}, \mathbf{r}') = \frac{e^{-jk^\pm R}}{4\pi R}, \quad R = |\mathbf{r} - \mathbf{r}'|, \quad (308)$$

with  $k^+$  and  $k^-$  the wavenumbers of the exterior and interior media, respectively. The corresponding element impedance matrices are given by (255), (256) and (257) with the Green's function  $G$  replaced by  $G^+$  or  $G^-$ , as appropriate.

The admittance matrices in (304) are dual to the impedance matrices, and are simply related to one another as

$$Y_{mn}^\pm = \frac{Z_{mn}^\pm}{(\eta^\pm)^2}, \quad (309)$$

where  $\eta^+$  and  $\eta^-$  are the intrinsic impedances of the exterior and interior media, respectively.

The matrix elements  $\beta_{mn}^\pm$  in (304) are given by

$$\beta_{mn}^\pm = \int_S \int_S \mathbf{\Lambda}_m(\mathbf{r}) \cdot (\mathbf{\Lambda}_n(\mathbf{r}') \times \nabla G^\pm(\mathbf{r}, \mathbf{r}')) dS' dS, \quad (310)$$

for which the corresponding element matrices can be evaluated by the methods of §10, and where  $\nabla G^\pm$  is the same as (292) with  $G$  replaced by  $G^+$  or  $G^-$ , as appropriate.

### Evaluation of Far Fields

The vector potentials in the far field are, from (17), (18), (302) and (303),

$$\begin{aligned} \mathbf{A} &= \frac{\mu^+}{4\pi r} e^{-jk^+ r} \int_S \mathbf{J}(\mathbf{r}') e^{jk^+ \hat{\mathbf{r}} \cdot \mathbf{r}'} dS' \\ &= \frac{\mu^+}{4\pi r} e^{-jk^+ r} [\tilde{\mathbf{\Lambda}}_n(\hat{\mathbf{r}})]^t [I_n] \end{aligned} \quad (311)$$

and

$$\begin{aligned} \mathbf{F} &= \frac{\epsilon^+}{4\pi r} e^{-jk^+ r} \int_S \mathbf{M}(\mathbf{r}') e^{jk^+ \hat{\mathbf{r}} \cdot \mathbf{r}'} dS' \\ &= \frac{\epsilon^+}{4\pi r} e^{-jk^+ r} [\tilde{\mathbf{\Lambda}}_n(\hat{\mathbf{r}})]^t [V_n], \end{aligned} \quad (312)$$

where

$$\hat{\mathbf{r}} = \hat{\mathbf{x}} \cos \phi \sin \theta + \hat{\mathbf{y}} \sin \phi \sin \theta + \hat{\mathbf{z}} \cos \theta \quad (313)$$

is the radial unit vector in the observation direction  $(\theta, \phi)$  in spherical coordinates, and

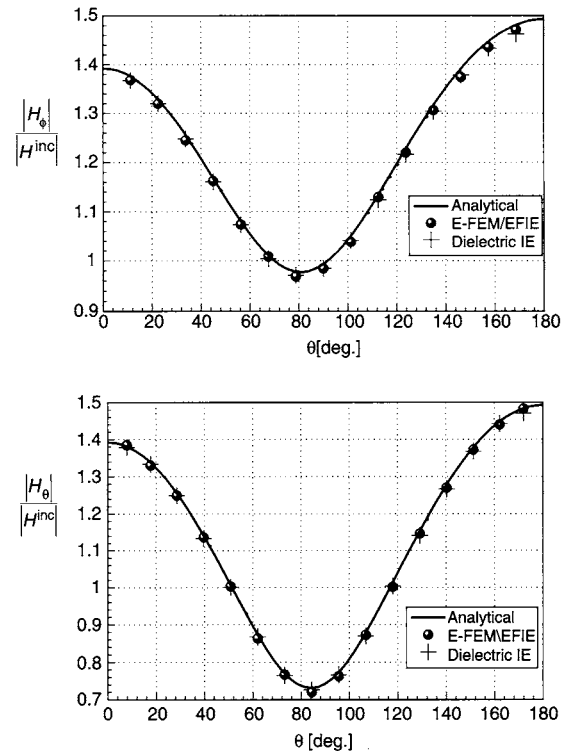
$$\tilde{\mathbf{\Lambda}}_n(\hat{\mathbf{r}}) = \int_S \mathbf{\Lambda}_n(\mathbf{r}) e^{jk^+ \hat{\mathbf{r}} \cdot \mathbf{r}} dS' \quad (314)$$

is the Fourier transform of the vector basis functions. Equation (314) can either be integrated numerically or in closed form (Lee and Mittra, 1983). In terms of the potentials, the far fields are given by (20) and (21).

### Numerical Results

Figure 24 shows the two components of the total magnetic field on the surface of a dielectric sphere. The illumination is by a plane wave incident from  $\theta = 180^\circ$ ; the relative permittivity of the sphere is  $\epsilon_r = 6.0$  and its radius is  $a = 0.125\lambda_0$ , where  $\lambda_0$  is the wavelength in free space. The fields along the two cuts are in good agreement with those of an analytical solution for sphere scattering. The results are also compared with those obtained from a hybrid approach using

**Figure 24** Total magnetic fields on the surface of a dielectric sphere.



both integral and wave equations and which is discussed in §14. The radar cross section of the sphere is shown in Fig. 25.

### §13. Inhomogeneous Bodies: Electric Field Wave Equation, 3D

The finite element approach in three dimensions follows closely that of two dimensions for the TE polarisation (§9). We assume a volumetric region  $\mathcal{V}$  with a closed, conducting boundary  $S$  forming a cavity. We also assume that  $\mathcal{V}$  is subdivided into a number of tetrahedrons chosen to provide an approximation  $\tilde{\mathcal{V}}$  to the region. That is, if the  $e$ th tetrahedron is  $\mathcal{V}^e$ , then  $\mathcal{V} \approx \tilde{\mathcal{V}} = \cup_{e=1}^E \mathcal{V}^e$ . A tetrahedral mesh is defined by the position vectors of the vertices of the tetrahedrons plus a description of the connectivity between vertices to form tetrahedrons. Each vertex of a tetrahedron has both a global index and local index  $i = 1, 2, 3$  or 4. Each face has the same local index as its vertex opposite. As in Fig. 26, local vertices are assumed numbered such that the orientation induced for face 4 when its vertices are traversed in the order 1, 2, 3 produces, using the right-hand rule, an outward normal to the face.

**Figure 25** Radar cross section of a dielectric sphere.

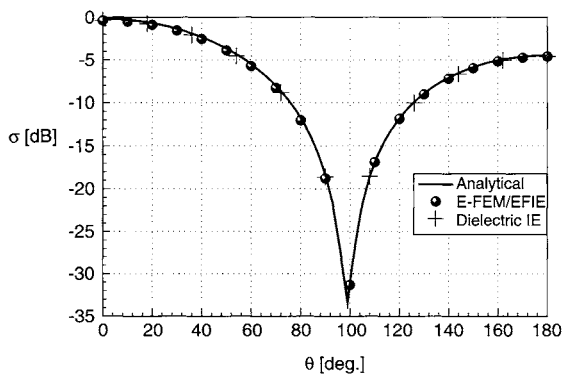
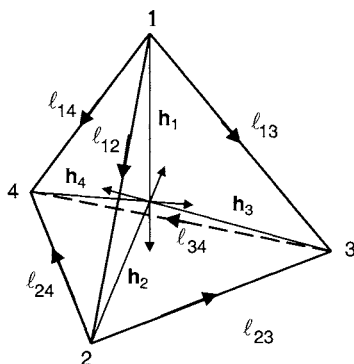


**Figure 26** Local vertex indices and reference directions for a tetrahedron.



To label edges it is convenient to employ a double-indexing scheme in which the index merely lists the two vertices bounding the edge. Thus the edges of the tetrahedron of Fig. 26 are locally indexed 12, 13, 14, 23, 24 and 34. As in §9, the unknowns are taken as the tangential components of  $E$  at the edge midpoints, with a local reference direction assumed from the lowest to the highest local vertex index, as shown in the figure. The complete meshing data structure thus comprises the following tables:

- A table similar to Table 5 listing the coordinates corresponding to each of the global indices.
- A table similar to Table 6 giving the global vertex index corresponding to each of the four local vertices, and listing the number of degrees of freedom and the global degree of freedom index for each of the six edges of the tetrahedron in the order 12, 13, 14, 23, 24, 34.

If there is no degree of freedom associated with an edge (e.g., it corresponds to an edge lying on the conducting boundary  $S$  where the tangential electric field is zero), then the latter table lists both the number of degrees of freedom and the index as zero. Otherwise, a sign is included with the degree of freedom index to indicate if the local reference direction is the same as (positive sign) or opposite (negative sign) that of a global reference direction chosen for the edge.

The initial development for obtaining the system matrices is identical to that described in §9 and is given by Eqs. (207)–(218), without the specialisation to two dimensions. Modifications needed to accommodate a tetrahedral mesh and bases are given in the following.

#### Volume Coordinates

Similar to the use of normalised area coordinates on triangles, we introduce a set of *normalised volume coordinates* for parameterising integrals over tetrahedrons. Let the position vector  $\mathbf{r}$  designate a point within a tetrahedron.

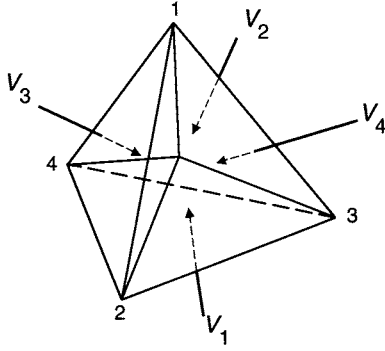
As Fig. 27 shows, the point defines a subdivision of the tetrahedron into four tetrahedral subvolumes. If the volume of the subvolume opposite vertex  $i$  is  $V_i$ , then normalised volume coordinates are defined as

$$\xi_i = \frac{V_i}{V^e}, \quad i = 1, 2, 3, 4, \quad (315)$$

where  $V^e$  is the volume of the original tetrahedral element  $e$ . The volumes of the subregions must sum to  $V^e$ , and hence the coordinates satisfy

$$\xi_1 + \xi_2 + \xi_3 + \xi_4 = 1; \quad (316)$$

i.e., only three of the coordinates are independent. Clearly,  $\xi_i = 0$  at face  $i$  and is unity at vertex  $i$  of the tetrahedron. Constant coordinate surfaces of

**Figure 27** Subdivision of a tetrahedron into four tetrahedrons.


a normalised coordinate are parallel to the face representing its zero coordinate. This parameterisation defines a mapping from each tetrahedron onto a standard parent tetrahedron. Since the coordinate  $\xi_i$  varies linearly from zero at face  $i$  to unity at vertex  $i$ , it is also a local linear interpolation function. Points within a tetrahedron thus may be parameterised as a linear interpolation of its vertex coordinates as

$$\mathbf{r} = r_1^e \xi_1 + r_2^e \xi_2 + r_3^e \xi_3 + r_4^e \xi_4, \quad (317)$$

where  $r_i^e$  is the position vector of the  $i$ th vertex of element  $e$ .

Table 12 summarises the computation of an element tetrahedron's volume  $V^e$ , edge vectors  $\ell_i$ , height vectors  $h_i$  and coordinate gradients  $\nabla \xi_i$ . These quantities are also depicted in Fig. 26, and are used in evaluating elements matrices for tetrahedral elements.

The differential element of volume in volume coordinates is given by

$$\begin{aligned} dV &= \left| \frac{\partial \mathbf{r}}{\partial \xi_1} \cdot \left( \frac{\partial \mathbf{r}}{\partial \xi_2} \times \frac{\partial \mathbf{r}}{\partial \xi_3} \right) \right| d\xi_1 d\xi_2 d\xi_3 \\ &= |\ell_{14} \cdot (\ell_{24} \times \ell_{34})| d\xi_1 d\xi_2 d\xi_3 \\ &= 6V^e d\xi_1 d\xi_2 d\xi_3, \quad \mathcal{J}^e d\xi_i d\xi_j d\xi_k, \quad i \neq j \neq k, \quad (318) \end{aligned}$$

**Table 12** Geometrical Quantities Defined on Tetrahedral Elements

Edge vectors	$\ell_{ij} = \mathbf{r}_j^e - \mathbf{r}_i^e$ ; $\ell_{ij} =  \ell_{ij} $ ; $\hat{\ell}_{ij} = \frac{\ell_{ij}}{\ell_{ij}}, \quad i \neq j \in \{1, 2, 3, 4\}$
Volume	$V^e = \frac{ \ell_{14} \cdot (\ell_{24} \times \ell_{34}) }{6}$ $= \frac{A_i h_i}{3}$ , $A_i = \text{area of face } i$ , $h_i = \text{height of vertex } i$
Coordinate gradients,	$\nabla \xi_1 = \frac{\ell_{24} \times \ell_{34}}{6V^e}$ , $\nabla \xi_2 = \frac{\ell_{34} \times \ell_{14}}{6V^e}$ , $\nabla \xi_3 = \frac{\ell_{14} \times \ell_{24}}{6V^e}$ , $\nabla \xi_4 = -\nabla \xi_1 - \nabla \xi_2 - \nabla \xi_3$
$\nabla \xi_i = -\frac{\hat{h}_i}{h_i}$	

and hence an integral over a tetrahedral element may be expressed in terms of an integral over a parent element as

$$\begin{aligned} \int_{V^e} f(\mathbf{r}) dV &= 6V^e \int_0^1 \int_0^{1-\xi_k} \int_0^{1-\xi_j-\xi_k} f(\mathbf{r}) d\xi_i d\xi_j d\xi_k, \quad i \neq j \neq k \\ &\approx 6V^e \sum_{k=1}^K w_k f(\mathbf{r}_1^e \xi_1^{(k)} + \mathbf{r}_2^e \xi_2^{(k)} + \mathbf{r}_3^e \xi_3^{(k)} + \mathbf{r}_4^e \xi_4^{(k)}), \quad (319) \end{aligned}$$

where the last line is a  $K$ -point rule for numerical integration over a tetrahedron. Sample points and weighting coefficients for  $K = 1, 4$  are given in Table 13 (Hammer *et al.*, 1956). Note that to obtain numerically exact results for such integrals, one should choose quadrature schemes whose error order is higher than the highest order of the coordinate products appearing in the integrand.

### Basis Functions

An edge-based basis function associated with edge  $ij$  of the  $e$ th tetrahedron is given by

$$\Omega_{ij}^e = \ell_{ij} (\xi_i \nabla \xi_j - \xi_j \nabla \xi_i), \quad (320)$$

with curl given by

$$\nabla \Omega_{ij}^e = 2\ell_{ij} \nabla \xi_i \times \nabla \xi_j = \frac{2\ell_{ij}}{\mathcal{J}^e} \ell_{ij} = \frac{\ell_{ij}}{3V^e} \ell_{ij}. \quad (321)$$

Equation (320) follows directly from (230) if the following geometrical identification is made. First we note that a tetrahedron may be embedded in an infinite cylinder of triangular cross section such that faces  $i$  and  $j$  of the tetrahedron lie in two sides of the cylinder. The edge formed by the intersection of faces  $i$  and  $j$  lies along an edge of the cylinder, and edge  $\ell_{ij}$  connecting vertices  $i$  and  $j$  lies in the third side of the cylinder. The right-hand side of (230) is a basis function defined on the cylinder cross section that may be restricted to the tetrahedron and renormalised such that its tangential component along edge  $\ell_{ij}$  is unity. This construction leads directly to (320).

**Table 13** Sample Points and Weighting Coefficients for  $K$ -Point Quadrature on Tetrahedrons

Sample points, $(\xi_1^{(k)}, \xi_2^{(k)}, \xi_3^{(k)})$	Weights, $w_k$
$(\xi_4^{(k)} = 1 - \xi_1^{(k)} - \xi_2^{(k)} - \xi_3^{(k)})$	
<b><math>K=1</math>, error <math>\mathcal{O}(\xi_i^2)</math></b>	
(0.25000000, 0.25000000, 0.25000000)	0.16666667
<b><math>K=4</math>, error <math>\mathcal{O}(\xi_i^3)</math></b>	
(0.58541020, 0.13819660, 0.13819660)	0.041666667
(0.13819660, 0.58541020, 0.13819660)	0.041666667
(0.13819660, 0.13819660, 0.58541020)	0.041666667
(0.13819660, 0.13819660, 0.13819660)	0.041666667

With bases now defined, the element matrices corresponding to (214), (217) and (218) are

$$Y_{ij,k\ell}^e = \frac{\sigma_{ij}^e \sigma_{k\ell}^e}{j\omega} \Gamma_{ij,k\ell}^e + j\omega \sigma_{ij}^e \sigma_{k\ell}^e C_{ij,k\ell}^e, \quad (322)$$

with element reciprocal inductance matrix

$$\Gamma_{ij,k\ell}^e = \frac{1}{\mu_0 \mu_r^e} \langle \nabla \times \Omega_{ij}^e; \nabla \times \Omega_{k\ell}^e \rangle, \quad (323)$$

and element capacitance matrix

$$C_{ij,k\ell}^e = \epsilon_0 \epsilon_r^e \langle \Omega_{ij}^e; \Omega_{k\ell}^e \rangle. \quad (324)$$

The term  $\sigma_{ij}^e$  incorporates a sign accounting for the reference direction associated with the edge  $ij$  and is defined as

$$\sigma_{ij}^e = \begin{cases} 1, & \text{reference direction for edge } ij, \\ & \text{element } e, \text{ is parallel to } \ell_{ij}, \\ -1, & \text{reference direction for edge } ij, \\ & \text{element } e, \text{ is antiparallel to } \ell_{ij}. \end{cases} \quad (325)$$

The volume integrals implied by the symmetric products in (323) and (324) can be evaluated numerically using the four-point formula of Table 13 or analytically as follows.

### Evaluation of Element Matrices

From (321) and (323), the elements of the matrix  $[\Gamma_{ij,k\ell}^e]$  are easily evaluated as

$$\Gamma_{ij,k\ell}^e = \frac{\ell_{ij} \ell_{k\ell}}{9V^e} \ell_{ij} \cdot \ell_{k\ell}. \quad (326)$$

By repeated use of the identity

$$\int_{V^e} \xi_1^{\alpha} \xi_2^{\beta} \xi_3^{\gamma} \xi_4^{\delta} dV = \frac{6V^e \alpha! \beta! \gamma! \delta!}{(\alpha + \beta + \gamma + \delta + 3)!}, \quad (327)$$

we may similarly evaluate  $C_{ij,k\ell}^e$  as

$$\begin{aligned} C_{ij,k\ell}^e &= \epsilon^e \ell_{ij} \ell_{k\ell} \int_{V^e} (\xi_i \nabla \xi_j - \xi_j \nabla \xi_i) \cdot (\xi_k \nabla \xi_\ell - \xi_\ell \nabla \xi_k) dV \\ &= \frac{\epsilon^e \ell_{ij} \ell_{k\ell} V^e}{20} [(1 + \delta_{ik}) \nabla \xi_j \cdot \nabla \xi_\ell - (1 + \delta_{i\ell}) \nabla \xi_j \cdot \nabla \xi_k \\ &\quad - (1 + \delta_{jk}) \nabla \xi_i \cdot \nabla \xi_\ell + (1 + \delta_{j\ell}) \nabla \xi_i \cdot \nabla \xi_k], \end{aligned} \quad (328)$$

where  $\delta_{ij}$  is the Kronecker delta defined in (274).

The determination of interior eigenvalues of a three-dimensional conducting cavity follows the same procedure discussed in §3 and §9. In the following section, we combine the wave equation of this section with an integral equation on the boundary to obtain a hybrid approach to scattering problems.

## § 14. Inhomogeneous Bodies in Open Regions: Hybrid FEM/IE, 3D

The principal difficulty in applying the finite element method to the wave equation in unbounded regions is that the mesh must somehow be terminated and

radiation conditions applied at the termination. When a bounded, inhomogeneous scatterer is embedded in an unbounded homogeneous region, a hybrid finite element method/integral equation (FEM/IE) approach may be used to terminate the mesh. The equivalence theorem (§1) can be used to formulate the approach by setting up equivalent electric and magnetic currents on a surface containing the inhomogeneity and separating the bounded and unbounded regions. The equivalent currents may be used with potentials to represent the fields exterior to the inhomogeneity, and serve to isolate the exterior and interior regions. An integral equation involving the equivalent currents is set up at the boundary between the regions. The integral equation then couples the interior and exterior regions by relating the equivalent currents to boundary fields that appear in the wave equation describing the interior fields. The radiation condition is thus implicitly enforced through the use of Green's functions in the potential representations of the exterior fields.

We assume that the inhomogeneous region is contained inside a bounded volume  $\mathcal{V}$  with boundary  $S$  and unit outward normal  $\hat{\mathbf{n}}$ . The region exterior to  $\mathcal{V}$  is assumed to be free space.

Inside  $\mathcal{V}$ , we combine (208) and (209) to obtain the weak form of the wave equation,

$$\begin{aligned} \langle \nabla \times \Omega_m; \mu_r^{-1} \cdot \nabla \times \mathbf{E} \rangle - k_0^2 \langle \Omega_m; \epsilon_r \cdot \mathbf{E} \rangle \\ - j\omega \mu_0 \int_S \Omega_m \cdot (\hat{\mathbf{n}} \times \mathbf{H}) dS = -j\omega \mu_0 \langle \Omega_m; \mathbf{J}_v \rangle. \end{aligned} \quad (329)$$

Note the appearance of the tangential magnetic field  $\hat{\mathbf{n}} \times \mathbf{H}$  at the surface. In the hybrid formulation, this field is not known *a priori*. Furthermore, we cannot assume that  $\hat{\mathbf{n}} \times \Omega_m$  vanishes there since the electric field does not and therefore, its basis functions  $\Omega_m$  do not. An integral equation provides the missing information for relating the unknown electric and magnetic fields on  $S$ .

To represent the total fields in the region outside  $S$ , we set up equivalent electric and magnetic surface currents,

$$\mathbf{J} = \hat{\mathbf{n}} \times \mathbf{H}, \quad \mathbf{M} = \mathbf{E} \times \hat{\mathbf{n}}, \quad (330)$$

where  $\mathbf{E}$  and  $\mathbf{H}$  are the electric and magnetic fields on  $S$ , respectively. We obtain the required integral equation by recognising that the total fields inside  $\mathcal{V}$  must vanish. Thus, in particular,  $\mathbf{E} = \mathbf{E}^{\text{sc}} + \mathbf{E}^{\text{inc}} = \mathbf{0}$  just inside  $S$ , where  $\mathbf{E}^{\text{inc}}$  is the incident field and  $\mathbf{E}^{\text{sc}}$  is the field scattered by the inhomogeneity. Testing this equation with tangential basis functions  $\Lambda_m$  on  $S$ , we obtain a weak form of the equality,

$$\langle \Lambda_m; \mathbf{E}^{\text{sc}}(\mathbf{J}, \mathbf{M}) \rangle + \langle \Lambda_m; \mathbf{E}^{\text{inc}} \rangle = 0, \quad \mathbf{r} \in \lim_{\text{rf}} S. \quad (331)$$

When  $\mathbf{E}^{\text{sc}}$  is expressed in terms of potential integrals using (9) and (12), Eq. (331) yields the desired

integral equation. With the definitions (330), we wish to solve the coupled pair of equations (329) and (331).

We now assume that  $\mathcal{V}$  is approximated as a mesh of tetrahedral elements  $\mathcal{V}^e$ . The boundary  $S$  of the mesh is the set of triangular faces of tetrahedrons making up the boundary of  $\mathcal{V}$ . A data structure for representing the mesh combines that for triangular meshes in §9 with that for tetrahedral meshes in §13.

Curl-conforming basis/testing functions  $\mathbf{\Omega}_n(\mathbf{r})$  are used to represent the electric field,

$$\mathbf{E} = \sum_{n=1}^N V_n \mathbf{\Omega}_n(\mathbf{r}), \quad (332)$$

in  $\mathcal{V}$  and on  $S$ . As in §13,  $\mathbf{\Omega}_n$  has a unit tangential component at the centre of the edge with DoF index  $n$  of the mesh; the tangential component of  $\mathbf{E}$  there is  $V_n$ . However in contrast to the cavity problem of §13,  $\mathbf{E}$  does not generally vanish on  $S$ . Nevertheless it is convenient to partition the degrees of freedom  $V_n$  into a list with the first  $N_{\mathcal{V}}$  unknowns  $V_n^{\mathcal{V}}$  all interior to  $\mathcal{V}$  and the remaining  $N_S$  unknowns  $V_n^S$  on the boundary  $S$ , so that we write the total field interior to  $\mathcal{V}$  and on  $S$  as

$$\mathbf{E} = \sum_{n=1}^{N_{\mathcal{V}}} V_n^{\mathcal{V}} \mathbf{\Omega}_n(\mathbf{r}) + \sum_{n=1}^{N_S} V_n^S \mathbf{\Omega}_{N_{\mathcal{V}}+n}(\mathbf{r}), \quad \mathbf{r} \in \mathcal{V}, S. \quad (333)$$

In view of (330) and (333), we thus have

$$\mathbf{M} = \sum_{n=1}^{N_S} V_n^S [\mathbf{\Omega}_{N_{\mathcal{V}}+n}(\mathbf{r}) \times \hat{\mathbf{n}}] = \sum_{n=1}^{N_S} V_n^S \mathbf{\Lambda}_n(\mathbf{r}), \quad \mathbf{r} \in S, \quad (334)$$

where the easily verified identity  $\mathbf{\Omega}_{N_{\mathcal{V}}+n} \times \hat{\mathbf{n}} = \mathbf{\Lambda}_n$  on  $S$  has been used.

Finally, we express the equivalent electric current in terms of divergence-conforming bases  $\mathbf{\Lambda}_n$  defined on the set of triangles (i.e., the boundary faces of the tetrahedrons) comprising the boundary  $S$  of  $\mathcal{V}$  as

$$\mathbf{J} = \sum_{n=1}^{N_S} I_n^S \mathbf{\Lambda}_n(\mathbf{r}), \quad \mathbf{r} \in S. \quad (335)$$

Substituting (333), (334) and (335) into (329) and (331), and assuming the source current  $\mathbf{J}_{\mathcal{V}}$  is zero in  $\mathcal{V}$  for scattering problems, we thus obtain the partitioned matrix system

$$\begin{bmatrix} [Y_{mn}^{\mathcal{V}\mathcal{V}}] & [Y_{mn}^{\mathcal{V}S}] & [0] \\ [Y_{mn}^S] & [Y_{mn}^{SS}] & [\gamma_{mn}^{SS}] \\ [0] & [-\beta_{mn}^{SS}] & [Z_{mn}^{SS}] \end{bmatrix} \begin{bmatrix} [V_n^{\mathcal{V}}] \\ [V_n^S] \\ [I_n^S] \end{bmatrix} = \begin{bmatrix} [0] \\ [0] \\ [V_m^{\text{inc}}] \end{bmatrix}, \quad (336)$$

which must be solved for the unknowns  $V_n^{\mathcal{V}}$ ,  $V_n^S$  and  $I_n^S$ .

The admittance matrices in (336) arise from the wave equation; they are sparse matrices whose elements, assuming an isotropic medium, are defined as

$$Y_{mn}^{\mathcal{V}\mathcal{V}} = \frac{1}{j\omega} \langle \nabla \times \mathbf{\Omega}_m; \mu^{-1} \nabla \times \mathbf{\Omega}_n \rangle + j\omega \langle \mathbf{\Omega}_m; \epsilon \mathbf{\Omega}_n \rangle, \quad (337)$$

$$Y_{mn}^{\mathcal{V}S} = \frac{1}{j\omega} \langle \nabla \times \mathbf{\Omega}_m; \mu^{-1} \nabla \times \mathbf{\Omega}_{N_{\mathcal{V}}+n} \rangle + j\omega \langle \mathbf{\Omega}_m; \epsilon \mathbf{\Omega}_{N_{\mathcal{V}}+n} \rangle, \quad (338)$$

$$Y_{mn}^{S\mathcal{V}} = \frac{1}{j\omega} \langle \nabla \times \mathbf{\Omega}_{N_{\mathcal{V}}+m}; \mu^{-1} \nabla \times \mathbf{\Omega}_n \rangle + j\omega \langle \mathbf{\Omega}_{N_{\mathcal{V}}+m}; \epsilon \mathbf{\Omega}_n \rangle, \quad (339)$$

and

$$Y_{mn}^{SS} = \frac{1}{j\omega} \langle \nabla \times \mathbf{\Omega}_{N_{\mathcal{V}}+m}; \mu^{-1} \nabla \times \mathbf{\Omega}_{N_{\mathcal{V}}+n} \rangle + j\omega \langle \mathbf{\Omega}_{N_{\mathcal{V}}+m}; \epsilon \mathbf{\Omega}_{N_{\mathcal{V}}+n} \rangle. \quad (340)$$

Equations (337)–(340) all give rise to element admittance matrices of the same form. Assuming constant medium parameters within each element, these matrices are given by (322)–(324).

The impedance matrix  $[Z_{mn}^{SS}]$  in (336) represents the electric field produced by the equivalent electric surface current. Assuming the external medium is free space, the impedance matrix is a full matrix with elements

$$Z_{mn}^{SS} = j\omega\mu_0 \langle \mathbf{\Lambda}_m; G, \mathbf{\Lambda}_n \rangle + \frac{1}{j\omega\epsilon_0} \langle \nabla \cdot \mathbf{\Omega}_m, G, \mathbf{\Lambda}_n \rangle, \quad (341)$$

for which the corresponding element matrices are given by (255)–(257) with  $\mu = \mu_0$  and  $\epsilon = \epsilon_0$ .

The matrix  $[\beta_{mn}^{SS}]$  is the same as that relating electric currents to magnetic fields and is given in §11, Eq. (288), as

$$\beta_{mn}^{SS} = -\frac{1}{2} \langle \mathbf{\Lambda}_m; \hat{\mathbf{n}} \times \mathbf{\Lambda}_n \rangle + \int_S \int_S \mathbf{\Lambda}_m(\mathbf{r}) \cdot (\mathbf{\Lambda}_n(\mathbf{r}') \times \nabla G(\mathbf{r}, \mathbf{r}')) dS' dS. \quad (342)$$

However, here we want the dual operator that relates source magnetic currents to electric fields; these operators differ only by a sign, which accounts for the negative sign appearing with  $\beta_{mn}^{SS}$  in (336). The element matrix corresponding to (342) is defined in (290).

Finally, we have

$$\begin{aligned} \gamma_{mn}^{S\mathcal{V}} &= - \langle \mathbf{\Omega}_{N_{\mathcal{V}}+m}; \mathbf{\Lambda}_n \rangle \\ &= - \langle \hat{\mathbf{n}} \times \mathbf{\Lambda}_m; \mathbf{\Lambda}_n \rangle, \end{aligned} \quad (343)$$

for which the associated element matrix,

$$\gamma_{ij}^e = -\sigma_i^e \sigma_j^e \langle \hat{\mathbf{n}} \times \mathbf{\Lambda}_i^e; \mathbf{\Lambda}_j^e \rangle, \quad (344)$$

may be evaluated either numerically or analytically following the procedure used for (223). The excitation matrix  $[V_m^{\text{inc}}]$  is given by the right-hand side of (251) and has the corresponding element matrix (258).

As an alternative formulation, we can enforce the condition that the *magnetic* field vanish just inside the surface  $S$  containing the equivalent currents:

$$\langle \mathbf{\Lambda}_m; \mathbf{H}^{\text{sc}}(\mathbf{J}, \mathbf{M}) \rangle + \langle \mathbf{\Lambda}_m; \mathbf{H}^{\text{inc}} \rangle = 0, \quad \mathbf{r} \in \lim_{\uparrow} S. \quad (345)$$

Replacing (331) with (345) and (333) with

$$\mathbf{H} = \sum_{n=1}^{N_V} I_n^V \boldsymbol{\Omega}_n(\mathbf{r}) + \sum_{n=1}^{N_S} I_n^S \boldsymbol{\Omega}_{N_V+n}(\mathbf{r}), \quad \mathbf{r} \in \mathcal{V}, \mathcal{S}, \quad (346)$$

respectively, and again carrying out the above procedure yields

$$\begin{bmatrix} [Y^{VV}] & [Y^{VS}] & [0] \\ [Y^{SV}] & [Y^{SS}] & [\gamma_{mn}^{SS}] \\ [0] & [\frac{Z_{mn}^{SS}}{\eta_0^2}] & [\beta_{mn}^{SS}] \end{bmatrix} \begin{bmatrix} [V_n^V] \\ [V_n^S] \\ [I_n^S] \end{bmatrix} = \begin{bmatrix} [0] \\ [0] \\ [I_m^{inc}] \end{bmatrix}, \quad (347)$$

with

$$I_m^{inc} = \langle \mathbf{A}_m; \mathbf{H}^{inc} \rangle. \quad (348)$$

There exist resonant frequencies for which these formulations do not have unique solutions (Pearson *et al.*, 1992), and a number of remedies for this nonuniqueness problem have been proposed (Silvester and Pelosi, 1994). The far fields are those radiated by the equivalent currents  $\mathbf{J}$  and  $\mathbf{M}$ , and are given by (311)–(314). Total magnetic fields computed on the surface of a sphere by the hybrid method are compared to those obtained from the integral equation formulation and analytical solution in Fig. 24.

## §15. Extending the Methods

### Composite Geometries

By employing them as basic building blocks, we may extend the numerical techniques discussed so far to more complex situations. To illustrate, consider a composite scatterer comprising a collection of different homogeneous materials and conductors (Medgyesi-Mitschang and Putnam, 1984). A key concept in setting up these problems is use of the equivalence principle to replace each bounded homogeneous region by an unbounded homogeneous region with equivalent sources on the original boundary. That is, the (closed) boundary of a homogeneous material region is taken as the support for equivalent surface currents  $\mathbf{J}$  and  $\mathbf{M}$  that, together with the independent sources in the region, reproduce the original fields within the region and produce null fields outside. The homogeneous material parameters within the region may thus be extended into the null field region without disturbing the original fields, and hence potential integrals with homogeneous media Green's functions may be used to represent fields in the region. This field equivalence may be constructed for each separate homogeneous region. The equivalent currents on opposite sides of the region boundaries are simply negatives of one another wherever the original tangential fields were continuous. Thus an unknown

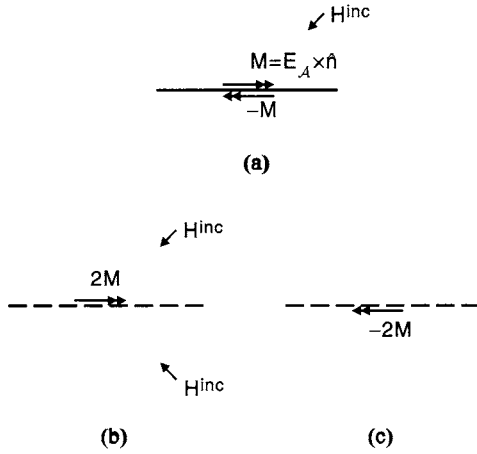
pair of equivalent electric and magnetic currents exists at every material interface. Conductors, on the other hand, are replaced by their surface equivalent electric currents, with separate electric currents on opposite sides for conductors at an interface between different homogeneous media. For conductors lying entirely within a homogeneous region, the net sum of these currents may be taken as the equivalent current. Coupled integral equations are obtained for the equivalent surface current(s) at each boundary by (1) enforcing the continuity of tangential fields across each material interface and (2) forcing the electric field to vanish on conductors. Inhomogeneous or composite groups of piecewise homogeneous regions may also be included in this scheme if one requires that fields in such regions satisfy the vector wave equation. The wave equation relates interior fields throughout a volume to its boundary fields, which in turn couples to an integral equation at the boundary (Volakis *et al.*, 1997, 1998). Other useful but less straightforward representations for these composite problems also exist (Glisson, 1984; Yeung, 1999), but they are not described here.

### Apertures

**Planar Screens** Apertures in planar ground screens may be treated by slightly extending the methods of earlier sections. Consider an aperture  $\mathcal{A}$  located in an infinite conducting ground plane at  $z = 0$ . The homogeneous half-spaces above and below the ground plane may be filled with different materials. An incident magnetic field  $\mathbf{H}^{inc}$ , defined as the field that would exist without the screen and with the upper medium filling all space, is incident from above the aperture. The tangential components of the unknown aperture electric and magnetic fields are  $(\mathbf{E}_{\mathcal{A}}, \mathbf{H}_{\mathcal{A}})$ . We form an equivalent problem by first shorting the aperture and placing on the shorted conductor a magnetic current  $\mathbf{M} = \mathbf{E}_{\mathcal{A}} \times \hat{\mathbf{z}}$  just above the ground screen ( $z = 0^+$ ), as illustrated in Fig. 28a. A magnetic current  $-\mathbf{M}$  is placed just below the ground screen ( $z = 0^-$ ).

Note that the shorted ground screen isolates the upper and lower half-spaces,  $\mathcal{V}^+$  and  $\mathcal{V}^-$ , respectively. The ground plane also shorts the electric field in the aperture, but the magnetic currents at  $z = 0^+$  and  $z = 0^-$  are chosen to restore the original electric field just above and below the currents, respectively. For determining fields in the upper half-space, all quantities—the upper magnetic current, the material media and the sources of the incident field—are imaged in the ground screen. This results in the equivalent system shown in Fig. 28b whose sources reside in an unbounded homogeneous medium. Thus potentials employing homogeneous medium Green's functions can be used to represent the fields in the upper half-space.

**Figure 28** Aperture (a) replaced by equivalent magnetic currents; images in ground plane form (b) upper half-space and (c) lower half-space equivalences.



Similarly, imaging the lower half-space problem results in the equivalent system of Fig. 28c.

Although  $\mathbf{M}$  is unknown, the use of equal but oppositely directed magnetic currents on opposing sides of the screen guarantees that the electric field is continuous through the aperture; an integral equation for  $\mathbf{M}$  is obtained by weak enforcement of continuity of the tangential magnetic field through the aperture,

$$\langle \Lambda_m, \mathbf{H}_{\mathcal{A}}^+ \rangle = \langle \Lambda_m, \mathbf{H}_{\mathcal{A}}^- \rangle, \quad (349)$$

where the tangential magnetic field in the aperture in the upper half-space is

$$\mathbf{H}_{\mathcal{A}}^+ = -2[j\omega\mathbf{F}^+(\mathbf{M}) + \nabla\Psi^+(\mathbf{M})]_{\tan} + 2\mathbf{H}_{\tan}^{inc}, \quad (350)$$

and in the lower half-space is

$$\mathbf{H}_{\mathcal{A}}^- = 2[j\omega\mathbf{F}^-(\mathbf{M}) + \nabla\Psi^-(\mathbf{M})]_{\tan}. \quad (351)$$

The potentials in (350) and (351) are

$$\mathbf{F}^{\pm}(\mathbf{M}) = \epsilon \int_{\mathcal{A}} \mathbf{M}(\mathbf{r}') G^{\pm}(\mathbf{r}, \mathbf{r}') dS', \quad (352)$$

$$\Psi^{\pm}(\mathbf{M}) = -\frac{1}{j\omega\mu} \int_{\mathcal{A}} \nabla \cdot \mathbf{M}(\mathbf{r}') G^{\pm}(\mathbf{r}, \mathbf{r}') dS', \quad (353)$$

and the Green's function is

$$G^{\pm}(\mathbf{r}, \mathbf{r}') = \frac{e^{-jk^{\pm}R}}{4\pi R}, \quad (354)$$

where  $k^+$  and  $k^-$  are wavenumbers in the original upper and lower half-spaces, respectively. Note the various factors of 2 arising from imaging (1) the magnetic current and (2) the magnetic incident field in the ground plane. Also note the negative sign in the relation between fields and potentials in (351) that arises because  $-\mathbf{M}$  is the source in the lower half-space equivalence. If the aperture is triangulated and magnetic surface current is represented as

$$\mathbf{M}(\mathbf{r}) = \sum_{n=1}^N V_n \Lambda_n(\mathbf{r}), \quad \mathbf{r} \in \mathcal{A}, \quad (355)$$

where  $\Lambda_n$  is defined as in §10, Eqs. (349)–(355) can be combined to yield the system matrix equation

$$[Y_{mn}^+ + Y_{mn}^-][V_n] = [I_m]. \quad (356)$$

One readily determines the element matrices corresponding to system matrix (356) to be

$$Y_{ij}^{\pm ef} = j\omega\sigma_i^e \sigma_j^f C_{ij}^{\pm ef} + \frac{\sigma_i^e \sigma_j^f}{j\omega} \Gamma_{ij}^{\pm ef}, \quad (357)$$

where

$$C_{ij}^{\pm ef} = \epsilon^{\pm} \langle \Lambda_i^e; G^{\pm}, \Lambda_j^f \rangle, \quad (358)$$

$$\Gamma_{ij}^{\pm ef} = \frac{1}{\mu^{\pm}} \langle \nabla \cdot \Lambda_i^e, G^{\pm}, \nabla \cdot \Lambda_j^f \rangle. \quad (359)$$

The element excitation column vector is

$$I_i^{\pm e} = \frac{\sigma_i^e}{2} \langle \Lambda_i^e, \mathbf{H}^{inc} \rangle. \quad (360)$$

In the special case of half-spaces with the same material parameters, the problem is the electromagnetic dual of the problem of scattering by a planar conductor of cross section  $\mathcal{A}$  embedded in the same medium (Butler *et al.*, 1970).

**Nonplanar Screens** If a conductor containing an aperture is nonplanar, then imaging cannot be used to replace the conductor; one must also model the conductor numerically. One approach is to model the entire conductor by the methods of §10, the aperture boundary becoming simply the conductor's boundary, but if the aperture is small so that the conductor is almost a closed cavity, field penetration into the cavity region may be weak. The low field levels result from near-cancellation of incident and scattered fields, and the computation of the small differences between these field quantities may result in partial or complete loss of significant figures. This difficulty is circumvented by using a modified form of the magnetic current formulation above. First, the aperture  $\mathcal{A}$  is replaced by a conducting surface so as to form a closed conductor  $S$ . Separate equivalent electric surface currents  $\mathbf{J}^{\pm}$  are then placed on the exterior and interior walls, respectively, of  $S$ , and, as in the planar screen case above, magnetic currents of opposite signs are placed on opposite sides of  $\mathcal{A}$  to reproduce the original electric field in the aperture. These equivalent currents are determined by requiring continuity of the tangential magnetic field across  $\mathcal{A}$  and vanishing of the electric field on both sides of  $S$ . The weak form of the resulting coupled system of equations is

$$\langle \Lambda_m, \mathbf{H}_{\mathcal{A}}^+(\mathbf{J}^+, \mathbf{M}^+) \rangle + \langle \Lambda_m, \mathbf{H}^{inc} \rangle = \langle \Lambda_m, \mathbf{H}_{\mathcal{A}}^-(\mathbf{J}^-, \mathbf{M}^-) \rangle, \quad \mathbf{r} \in \mathcal{A}, \quad (361)$$

$$\langle \Lambda_m, \mathbf{E}_{\mathcal{A}}(\mathbf{M}^+, \mathbf{J}^+) \rangle + \langle \Lambda_m, \mathbf{E}^{inc} \rangle = 0, \quad \mathbf{r} \in S, \quad (362)$$

$$\langle \Lambda_m, \mathbf{E}_{\mathcal{A}}(\mathbf{M}^-, \mathbf{J}^-) \rangle = 0, \quad \mathbf{r} \in S. \quad (363)$$

In (361)–(363), the dependence of the fields on the currents producing them is shown explicitly. The  $\pm$

superscripts on the magnetic field indicate that the quantity is evaluated just exterior or interior to  $\mathcal{A}$ , respectively, and  $\pm$  superscripts on the current quantities indicate that the surface current  $\mathbf{M}^\pm = \pm \mathbf{M}$  on the exterior or interior of  $S$  is used, respectively. The potential representations (9)–(16) play the role of operators relating current and field quantities.

## Wires

**Piecewise Linear Wire Segment Modelling** Wire scatterers may be treated using the electric field integral equation. We assume that a wire's radius is small compared to the wavelength, and its length is large compared to its radius. Under these conditions, a number of further assumptions are justified:

- The surface current has only a component parallel to the wire axis, and is invariant about the circumference of the wire. This implies that if  $\mathbf{r}$  is a point on the wire axis, the wire surface current at that cross section is modelled as  $\mathbf{J}(\mathbf{r}) = \frac{I(\mathbf{r})}{2\pi a(\mathbf{r})} \hat{\ell}$ , where  $I(\mathbf{r})$  is the total current,  $a(\mathbf{r})$  is the cross-sectional radius, and  $\hat{\ell}$  is the unit vector parallel to the wire axis at  $\mathbf{r}$ .

- Both the scattered and incident electric field components do not vary significantly about the wire circumference.

- The surface area and hence the charge contained on any wire ends or junction surfaces are negligible. We loosely define a junction surface as wire surfaces inside a spherical ball of radius no more than a few wire radii and containing two or more intersecting wires (possibly with dissimilar radii). From the continuity equation, neglecting charge accumulation at wire junctions and end surfaces implies, respectively, that (1) Kirchhoff's current law applies to total currents at junctions and that (2) the total current vanishes at wire ends.

The numerical modelling of wires via the EFIE under these assumptions incorporates features of both the three-dimensional EFIE and its two-dimensional TE counterpart. We model the wire geometry as a piecewise linear approximation to a three-dimensional curve representing the wire axis, with a (constant) wire radius associated with each segment. The data structure for the model segment coordinates is thus identical to that of Table 1, except that a third column is added to store the  $z$  coordinates of segment endpoints. The data structure of Table 10 may be used to store the element, node connection, DoF and current reference data; an additional entry containing the radius of the segment (element) completes the table. Wire segments and currents are parameterised by generalising to three dimensions the nodal coordinates, the edge vector definitions and the bases of §7. The

changes are effected in expressions there by merely replacing the local two-dimensional node vectors  $\boldsymbol{\rho}_i^e$  by three-dimensional vectors  $\mathbf{r}_i^e$ . With these generalisations, the surface current density at a wire segment cross section with axis at  $\mathbf{r}$  is modelled as

$$\mathbf{J}(\mathbf{r}) = \frac{1}{2\pi a(\mathbf{r})} \sum_{n=1}^N I_n \boldsymbol{\Lambda}_n(\mathbf{r}), \quad (364)$$

where  $\boldsymbol{\Lambda}_n$  is defined in (165), (171) and (177), and  $I_n$  is the *total* current at the cross section of a segment end node with degree of freedom index  $n$ . Wire-to-wire junctions are handled by overlapping bases at a junction just as described for strip junctions in §7.

System matrices are obtained by using  $\frac{\boldsymbol{\Lambda}_m}{2\pi a(\mathbf{r})}$  as testing functions and substituting (364) into (245). The corresponding element matrices have the same form as (173), (179) and (182), but with potential integrals now given by

$$\Psi_{ij}^{ef} = \varrho^e \varrho^f \int_0^1 \int_0^1 K(\mathbf{r}, \mathbf{r}') d\xi_1' d\xi_1, \quad (365)$$

where, for  $e \neq f$ ,

$$K(\mathbf{r}, \mathbf{r}') = \frac{e^{-jkR}}{4\pi R} \quad (366)$$

with

$$R^2 = |\mathbf{r}_1^e \xi_1 + \mathbf{r}_2^e \xi_2 - \mathbf{r}_1^f \xi_1' - \mathbf{r}_2^f \xi_2'|^2 + (a^e)^2. \quad (367)$$

In the above, we have approximated  $R = |\mathbf{r} - \mathbf{r}'|$  by restricting  $\mathbf{r}$  and  $\mathbf{r}'$  to the axes of tube segments representing source and observation elements, thereby reducing the surface integration to an integration along the wire axes; the correction term involving the radius of the observation segment added in (367) improves the accuracy of this potential calculation when source and observation segments are close and the assumption of circumferential invariance of fields and currents no longer strictly holds. The integrals in (365) may be performed using Gauss–Legendre rules, Table 3.

For  $e = f$ , we have

$$K(\mathbf{r}, \mathbf{r}') = \frac{1}{2\pi} \int_0^{2\pi} \frac{e^{-jkR} - 1}{4\pi R} d\phi + \frac{\beta}{\pi a^f} \mathcal{K}(\beta), \quad (368)$$

with

$$R = \sqrt{[\varrho^e(\xi_1 - \xi_1')]^2 + 4(a^f)^2 \sin^2 \frac{\phi}{2}},$$

$$\frac{1}{\beta} = \sqrt{1 + \left(\frac{\varrho^e}{2a^f}\right)^2 (\xi_1 - \xi_1')^2}. \quad (369)$$

The integration on  $\phi$  in the first term of (368) can be performed using Gauss–Legendre rules, as can its successive integration along the wire axis in (365). The singularity originally at  $R = 0$  in the integral has been removed and added back in the second term (Wilton and Butler, 1981), which is expressed in terms of  $\mathcal{K}(\beta)$ , a complete elliptic integral of the first kind, defined as

$$\mathcal{K}(\beta) = \int_0^{\frac{\pi}{2}} \frac{d\theta}{\sqrt{1 - \beta^2 \sin^2 \theta}}. \quad (370)$$

The elliptic integral has a logarithmic singularity at  $\beta = 1$ , i.e., when  $\xi_1 = \xi'_1$ . Hence the inner integral in (365) on this term should be performed using the quadrature rules of Table 4; Gauss–Legendre rules may be used on the outer integral. In obtaining (368), we observed that the field on the segment produced by a circumferentially invariant basis is also circumferentially invariant, and hence the observation point integral over the circumference becomes trivial. The longitudinal integrals are performed using normalised coordinates to parameterise points along the tube axes of both the source and observation segments.

**Wire-to-Surface Junctions** Special basis functions must be used to attach wires to surfaces. Without loss of generality, we assume that a wire is attached to a surface at the vertex of a triangle(s). For the wire model segment that attaches to the surface, a DoF exists at the attachment point to account for the current from the surface into the wire. The same DoF index also applies to the common vertex of the triangles surrounding the attachment point. Let one of these triangles be element  $e$  with the wire attached at its  $i$ th vertex. Then a junction basis on element  $e$  has the form

$$\Lambda^J(\mathbf{r}) = \frac{1}{\varrho_i} \left[ 1 - \frac{b_i^2}{(\hat{\mathbf{h}}_i \cdot \boldsymbol{\rho}_i)^2} \right] \Lambda_i^e(\mathbf{r}), \quad (371)$$

where  $\varrho_i$ ,  $b_i$  and  $\hat{\mathbf{h}}_i$  are the triangle parameters defined in Table 8,  $\boldsymbol{\rho}_i$  is the vector to  $\mathbf{r}$  from vertex  $i$  of the triangle and  $\Lambda_i^e$  is the usual surface basis function associated with edge  $i$  (opposite vertex  $i$ ) of triangular element  $e$  and defined in §10. Several properties make the basis function in (371) useful for modelling the surface current associated with the wire junction:

- The total flux of current into the attachment vertex is unity.
- The current density has the correct  $1/|\boldsymbol{\rho}_i|$  dependence near the vertex.
- The normal component of current vanishes along the three edges of the triangle where DoFs for the usual surface bases are defined.

pt It should be assumed that the wire surface current distributes itself uniformly on the surface at the base of its attachment point; any angular nonuniformities in the surface current distribution near the base of the junction are modelled by the usual surface bases. The first of the above properties allows us to assign to each triangle a fraction of the total current entering the wire proportional to the triangle's vertex interior angle at the attachment point. Thus, if the interior angle of vertex  $i$  of triangle  $n$  at the attachment point is  $\alpha^n$ , the junction basis function on triangle  $e$  is

$$\frac{\alpha^e}{\sum_{n=1}^{N_j} \alpha^n} \Lambda^J(\mathbf{r}), \quad (372)$$

where the sum is over the angles of all the  $N_j$  triangles attached to the junction. When used in the EFIE, we also need the divergence of the basis function,

$$\nabla \cdot \Lambda^J(\mathbf{r}) = \frac{1}{\varrho_i} \nabla \cdot \Lambda_i^e(\mathbf{r}) = \frac{1}{A^e}. \quad (373)$$

In the magnetic vector potential, the junction basis produces an integrand singularity at the junction vertex for *every* observation point; the integral may be handled by the singularity analyses of §10.

### Point and Surface Loading, Thin Materials

Using coatings of special materials or placing lumped loads at strategic points on conducting scatterers are often used to control scattering characteristics. Also the materials of some scatterers are composed of thin, anisotropic dielectrics, or have surface roughness, corrugations or other surface modifications.

Point or lumped loads on conductors are easily modelled using the EFIE. Suppose a point load with terminal impedance  $Z_L$  is connected between two elements sharing a node with global degree of freedom index  $p$ . This is equivalent to placing a (dependent) point voltage source  $V_p = -I_p Z_L$  between elements at the node, where  $I_p$  is the *total* current associated with the DoF. The equivalent voltage source adds a term  $-Z_L I_p \int_{C_p} \Lambda_p(\mathbf{r}) \cdot \hat{\mathbf{u}} dC$  to the  $p$ th row of the excitation vector, where  $C_p$  is the element's edge and the integral is the basis function's flux across the edge. When taken to the left-hand side of the equation, the load impedance and flux integral product is merely added to the  $p$ th diagonal element of the system matrix. If the coefficient  $I_p$  represents a surface density rather than a total current quantity, then a multiplicative edge length factor also appears.

Good conductors, even when very thin, can be modelled as satisfying a surface impedance boundary condition,

$$[\mathbf{E}^{\text{sc}}(\mathbf{J}) + \mathbf{E}^{\text{inc}}]_{\text{tan}} = Z_S \mathbf{J}, \quad (374)$$

where the left-hand side represents the total field. This equation is simply a modified form of the EFIE in which the net effect of expanding the current and testing the right-hand side is to add terms  $\langle \Lambda_m; Z_S \Lambda_n \rangle$  to the EFIE system matrix.

Although most problems can, in principle, be modelled via the methods presented to this point, some would require excessive computational resources or become unnecessarily complex. A number of approximate boundary conditions have therefore been developed to reduce the complexity of such problems (Richmond and Newman, 1976; Volakis *et al.*, 1998). Thin material sheets, conductor-backed dielectrics,

corrugations and rough surfaces, for example, can often be modelled using the Leontovitch boundary condition (Senior and Volakis, 1995),

$$\hat{\mathbf{n}} \times \mathbf{E} = Z \hat{\mathbf{n}} \times (\hat{\mathbf{n}} \times \mathbf{H}), \quad (375)$$

for which an efficient three-dimensional numerical treatment is available (Bendali *et al.*, 1999). Leontovitch boundary conditions are approximate relations between field quantities at a point. More accurate, higher-order boundary conditions involve not only the fields, but also their derivatives at a point. Higher-order boundary conditions have been used, for example, to model curvature in dielectrics and coated conductors, multilayered materials and tapered dielectric-filled grooves (Hoppe and Rahmat-Samii, 1995; Senior and Volakis, 1995).

### Green's Functions and Geometrical Symmetries

**Layered Media Green's Functions** The integral equation approach becomes particularly powerful when combined with Green's functions to represent fields or potentials of point sources radiating in a complex medium. The principal advantage of the approach is that the required number of degrees of freedom can be much less than that of the wave equation and finite element approach (Newman, 1988). One commonly appearing three-dimensional Green's function is that for a layered medium. A mixed potential formulation due to Michalski and Zheng (1990) is particularly well suited for problems involving scatterers near, penetrating or immersed in a layered medium. The scatterer is replaced by a set of boundary equivalent currents; the equivalence theorem then guarantees that the interior fields vanish, and that the layered medium may be extended into the region occupied by the scatterer so as to complete a region of uniform layers. Fields radiated by the equivalent currents can then be calculated using the Green's function for the layered medium. If the interior of the scatterer is homogeneous, the interior fields may be represented using equivalent currents and an integral equation can be used as in §12. If, instead, the scatterer interior is inhomogeneous, a finite element formulation can be used as in §14. The exterior region integral equation is formulated as in §10, §12 and §14. The needed potential integrals generalise the forms of (10)–(13), respectively, as (Michalski and Zheng, 1990)

$$\begin{aligned} \mathbf{A} &= \int_D \mathcal{G}^A(\mathbf{r}, \mathbf{r}') \cdot \mathbf{J}_D(\mathbf{r}') dD', \\ \mathbf{F} &= \int_D \mathcal{G}^F(\mathbf{r}, \mathbf{r}') \cdot \mathbf{M}_D(\mathbf{r}') dD', \\ \Phi &= \int_D q_D(\mathbf{r}') K^\Phi(\mathbf{r}, \mathbf{r}') dD' + \int_D \hat{\mathbf{z}} \cdot \mathbf{J}_D(\mathbf{r}') P_z(\mathbf{r}, \mathbf{r}') dD', \\ \Psi &= \int_D m_D(\mathbf{r}') K^\Psi(\mathbf{r}, \mathbf{r}') dD' + \int_D \hat{\mathbf{z}} \cdot \mathbf{M}_D(\mathbf{r}') Q_z(\mathbf{r}, \mathbf{r}') dD', \end{aligned} \quad (376)$$

where  $\mathcal{G}^A, \mathcal{G}^F$  are dyadic vector potentials and  $K^\Phi, K^\Psi, P_z, Q_z$  are scalar partial potentials for a medium with layer axis  $\hat{\mathbf{z}}$ . These Green's potentials are, in turn, expressed as spectral integrals over transmission line Green's functions representing the layers. Asymptotic spectral forms of the latter are simply contributions of direct and first-bounce plane wave reflections from adjacent layers, and their spectral integrals represent direct and quasi-static image point source contributions, respectively, in the spatial domain (Michalski and Mosig, 1997). Explicit removal of these terms from spectral representations significantly improves their convergence. Reinstating the removed terms in spatial domain form allows their contributions, which include singularities, to be treated by the methods developed in earlier sections (Bunger and Arendt, 1997).

**Periodic Structures** The Green's functions of the previous section can also be adapted to treat periodic structures involving layered media. Periodic media Green's functions are doubly infinite series whose terms are simply sampled values of the spectral integrands for nonperiodic layered media. The sampling period in the spectral domain controls the periodicity properties of the Green's function in the spatial domain. As in the nonperiodic case, asymptotic forms of the spectral Green's function can be identified, but they now comprise infinite *arrays* of point sources representing direct and quasi-image contributions in homogeneous media. The direct summation of contributions from these infinite arrays is slowly converging, but may be greatly accelerated by means of the Ewald method (Jordan *et al.*, 1986). By isolating the individual point sources that represent direct and quasi-image contributions from the array, singular integrals may be treated by the methods discussed for homogeneous media.

A rectangular waveguide with longitudinal inhomogeneities may be treated as a special case of a layered periodic structure obtained by alternately imaging the guide geometry in the waveguide walls (Harrington, 1961).

**Reflection Symmetries** Green's functions may usually be found only for regions whose boundaries have certain symmetries. Conversely, problems with geometrical symmetries can be efficiently modelled using appropriate transformations of the background medium Green's function. As a simple example, consider *reflection* symmetries. Unfortunately, vector fields and sources do not have the familiar “even” and “odd” reflection symmetries of scalar fields and sources. The appropriate generalisation, however, is obtained by considering images in perfect electric or perfect magnetic ground planes (Harrington, 1961) (PEC or PMC, respectively), assumed to be in the

plane  $z = 0$ . We also assume the primary currents of interest are in a homogeneous region  $z > 0$  and the image currents are in  $z < 0$ . Taking into account the sign changes of the various image components associated with electric and magnetic currents and charge, the Green's potentials, in the notation of (376), are found to be

$$\begin{aligned} G^A(\mathbf{r}, \mathbf{r}') &= (\hat{x}\hat{x} + \hat{y}\hat{y} + \hat{z}\hat{z})\mu G(\mathbf{r}, \mathbf{r}') \\ &\mp (\hat{x}\hat{x} + \hat{y}\hat{y} - \hat{z}\hat{z})\mu G(\mathbf{r}, \mathbf{r}' - 2z'\hat{z}) \\ G^F(\mathbf{r}, \mathbf{r}') &= (\hat{x}\hat{x} + \hat{y}\hat{y} + \hat{z}\hat{z})\epsilon G(\mathbf{r}, \mathbf{r}') \\ &\pm (\hat{x}\hat{x} + \hat{y}\hat{y} - \hat{z}\hat{z})\epsilon G(\mathbf{r}, \mathbf{r}' - 2z'\hat{z}) \\ K^\Phi(\mathbf{r}, \mathbf{r}') &= \frac{1}{\epsilon} [G(\mathbf{r}, \mathbf{r}') \mp G(\mathbf{r}, \mathbf{r}' - 2z'\hat{z})], \quad P_z(\mathbf{r}, \mathbf{r}') = 0 \\ K^\Psi(\mathbf{r}, \mathbf{r}') &= \frac{1}{\mu} [G(\mathbf{r}, \mathbf{r}') \pm G(\mathbf{r}, \mathbf{r}' - 2z'\hat{z})], \quad Q_z(\mathbf{r}, \mathbf{r}') = 0, \quad (377) \end{aligned}$$

where  $G(\mathbf{r}, \mathbf{r}')$  is the homogeneous medium Green's function. The upper sign in (377) applies to reflection in a PEC plane, the lower, to a PMC plane. The form of symmetry used depends on whether a PEC or PMC ground plane is actually present, or, if modelling a body with a geometrical reflection symmetry plane, what boundary conditions are satisfied by the total fields on the symmetry plane with the body symmetrically illuminated. For objects having a symmetry plane, the excitation must be decomposed into *symmetrical components*, each of which excites currents with the same symmetries as those imaged in PEC or PMC ground screens. Because almost half the surface currents (i.e., all those not touching or passing through the ground plane) are related by symmetry, the number of unknowns can be reduced by nearly a factor of 2 for every plane of symmetry present in a problem's geometry. The approach can be applied successively for up to three orthogonal object symmetry planes (Tsai *et al.*, 1974).

**Bodies of Revolution** A *body of revolution* (BOR) is an object with continuous rotational symmetry; i.e., it is formed by rotating a curve in the  $x$ - $z$  plane—the so-called *generating curve*—about the  $z$  axis. If the original curve is modelled by piecewise linear segments, a model made up of conical annular segments results from the rotation. A point on the BOR surface may be parameterised by its position along the generating curve and its rotation angle  $\phi$  measured from the  $x$ - $z$  plane. A key feature of the BOR is that the fields and equivalent currents are periodic in  $\phi$  and hence can be expanded in Fourier series in  $\phi$ . For example, the electric surface current has the form

$$\mathbf{J} = \sum_{p=-\infty}^{\infty} \sum_{n=1}^N \left[ I_n^{p,\theta} \frac{\Lambda_n(\mathbf{r})}{\rho} + I_n^{p,\phi} \Pi_n(\mathbf{r}) \right] e^{jp\phi}, \quad (378)$$

where  $\Lambda_n$  and  $\Pi_n$  are triangle and pulse functions modelling, respectively, current components parallel to and perpendicular to the generating curve. The quantity  $\rho$  is the distance from a point on the surface

of the BOR to its axis. Each Fourier angular harmonic couples only to a like harmonic of the incident field. Thus the associated EFIE, for example, reduces to the system

$$\begin{bmatrix} [Z_{mn}^{p,\theta\theta}] & [Z_{mn}^{p,\theta\phi}] \\ [Z_{mn}^{p,\phi\theta}] & [Z_{mn}^{p,\phi\phi}] \end{bmatrix} \begin{bmatrix} [I_n^{p,\theta}] \\ [I_n^{p,\phi}] \end{bmatrix} = \begin{bmatrix} [V_n^{p,\theta}] \\ [V_n^{p,\phi}] \end{bmatrix}, \quad (379)$$

which may be solved for the  $p$ th harmonic current distribution independently of the other harmonics (Govind *et al.*, 1984). In practice, one obtains sufficient accuracy with approximately  $P \approx k\rho_{\max}$  harmonics, where  $\rho_{\max}$  is the largest value of  $\rho$  on the BOR. For each of the  $P$  problems, current coefficients associated with just the two orthogonal current components along the generating arc are determined, in contrast to the usual approach in which current over the entire scatterer surface must be found.

A related problem is one in which a body has  $P$ -fold rotational symmetry. A body is said to be a *discrete body of revolution* (DBOR) if it reproduces itself when rotated through a *slice angle* of  $\frac{2\pi}{P}$  radians or any multiple thereof. In this case, a *generating slice* exists such that, when it is rotated through the slice angle  $P$  times, it generates the entire geometry. The generating slice may be subdivided into a triangular mesh with  $N$  degrees of freedom per slice. If the degree of freedom index within a slice is  $n$  and the slice index is  $k$ , the current is represented as the discrete Fourier series

$$\mathbf{J} = \sum_{p=0}^{P-1} \sum_{n=1}^N I_n^p \left( \sum_{k=0}^{P-1} \Lambda_n^k(\mathbf{r}) e^{j\frac{2pk\pi}{P}} \right), \quad (380)$$

where  $\Lambda_n^k$  is a basis function associated with the  $n$ th DoF on the  $k$ th slice. The currents in (380) have been decomposed via the discrete Fourier transform into symmetrical components with harmonic index  $p$  such that components at corresponding element locations in adjacent slices differ only by a common progressive phase factor,  $e^{j\frac{2pk\pi}{P}}$ . When the excitation is similarly decomposed, it is found that only the Fourier components of like harmonics are coupled. The equivalent current may then be separately determined for each harmonic, using as unknowns only the currents within a single slice. As  $P \rightarrow \infty$ , the DBOR becomes a BOR, and one may readily identify terms of (380) that approach those of (378).

### Higher-Order Modelling

**Higher-Order Geometrical Modelling** Piecewise linear models have been used to model all the problems considered up to this point. For problems involving curves or curved surfaces, higher-order models that include curvature can be applied to obtain improved accuracy due to the improved geometrical

fidelity. Models of almost any order are possible, but quadratic curve and surface approximations (Champagne *et al.*, 1992; Brown and Wilton, 1999) are found to be relatively simple to apply and sufficiently accurate for many purposes.

**Higher-Order Field and Source Modelling** Higher-order bases can be used to improve surface current and field representations in both integral and differential equation formulations. Usually the required bases must be divergence- or curl-conforming, respectively (Graglia *et al.*, 1997). It is also desirable that they be defined on curved surfaces so that they may be used in higher-order geometry modelling schemes, and interpolatory so they yield well-conditioned system matrices. In dealing with higher-order bases it is important to maintain accuracy in the evaluation of element matrices; otherwise, the potential for higher-order bases to reduce the error may not be realised.

### Solvers and Fast Methods

For very large systems of equations, the matrix solution time can dominate the overall computation time. For such problems, it may be necessary to give careful consideration to the solution procedure. So-called “direct solvers”, which use classical Gaussian elimination methods, are often used for solving the full matrices that arise from integral equation formulations, but they become expensive to use for large problems. One then turns to “iterative methods” in which an updated solution column vector at a given stage is estimated from previous trial solution vectors and a *residual error*—the difference between right- and left-hand sides of the matrix equation when the most recent trial solution is substituted for the unknown vector. The methods terminate when the residual or other error measure falls below a specified tolerance; the most recent trial vector is then taken as the approximate solution. The stabilised biconjugate gradient (BICGSTAB) and generalised minimum residual (GMRES) algorithms (Gutknecht, 1993; Saad, 1996) are found to be among the most effective iterative methods when applied to the complex-valued, non-Hermitian matrices that typically arise in electromagnetic scattering calculations.

The more iterations a method requires to reach convergence, the poorer the method’s efficiency, but slow convergence is likely due to use of a poorly conditioned equation set. To improve the convergence of iterative methods, one can look for a more well-conditioned formulation or for a good *preconditioner*. The latter is equivalent to a matrix that, when it multiplies both sides of the system equation, improves the conditioning of the resulting system (Saad, 1996). Good preconditioners—even if only crudely—

approximate the inverse of the system matrix, and finding them is often an ad hoc exercise that relies on physical knowledge of the behaviour of or approximations to the solution of the particular problem.

In using iterative procedures, one may save matrix storage by generating matrix elements only as needed during an iteration. The matrix–vector product required of the iterative scheme can be computed as they are generated, and after being used to update the solution, the elements may be discarded and regenerated on the next iteration. Differential equation approaches have an inherent advantage in storage reduction schemes because their system matrix is sparse; it may not even be necessary to discard matrix elements after each iteration, although they are relatively inexpensive to regenerate. To take advantage of matrix sparsities that arise, a number of sparse matrix storage schemes have been devised.

Matrix sparsity not only reduces storage requirements, but also speeds up the most time-consuming task in iterative solution processes—the formation of matrix–vector products involving the system matrix and the trial solution vector. One merely skips the product calculation when a zero element from the system matrix is one of the factors (or, equivalently, the element is not present in a sparse storage scheme). Accelerating the computation of matrix–vector products in iterative approaches is at the heart of all so-called *fast* methods (Chew *et al.*, 1997). A number of such schemes have been developed, among which are the following:

- Basis functions are used that produce directed beams interacting with only small portions of a structure (Canning, 1990)
- Basis functions are projected onto a regular grid such that the moments to a certain order are preserved; the matrix–vector product on a rectangular grid is convolutional in form and can be performed quickly using discrete Fourier transforms.
- A block of the matrix representing interactions between a group of spatially adjacent sources and a group of spatially adjacent testing functions can be diagonalised for fast multiplication by means of plane wave expansions. Multilevel (Chew *et al.*, 1997) versions of this scheme appear to yield the fastest schemes currently available.

## § 16. Other Methods

### Frequency Domain Methods

There exist a number of frequency domain approaches that we have not considered, but which are closely related to the methods of this chapter. The simplest of these is the finite difference method, in

which the rectangular coordinate derivatives in the wave equation are replaced by finite differences. In principle, this approach could always be used instead of the finite element method, but in practice it works best when the boundaries of the region to be modelled are parallel to the coordinate axes.

The generalised multipole techniques (GMT) may be used to model closed conductors and homogeneous material regions that are not too thin. They employ modified forms of the equivalence principle in which the equivalent surface sources are moved slightly off the surface and into the null field region, i.e., the region complementary to the equivalence region. Instead of surface density sources, the sources are point sources or collections of multipole sources. While the testing procedure for fields is similar to that for moment and finite element methods, the field contributions of equivalent surface sources are replaced by sums over point or multipole sources that are located just off the surface. An advantage of the approach is that no singularities arise in enforcing boundary conditions (Hafner, 1991). As might be expected, some care must be exercised in selecting the number and locations of sources and in the treatment of geometrical singularities, such as corners. The method fails when the null field region is thin.

The T-matrix method (Waterman, 1969) is also a very efficient method when used to treat homogeneous materials with smooth boundaries. The surface equivalent currents are expanded in terms of tangential vector components of spherical multipole sources about a common origin within the scatterer. The fields radiated by the surface sources must vanish in the null field regions—the regions complementary to the equivalence region—and this condition is enforced by testing with spherical harmonics on a spherical surface in the null field region to obtain a system of equations for the current expansion coefficients. The system matrix approaches an identity matrix as the boundary approaches a sphere, but becomes quite ill-conditioned as the boundary approaches flat or narrow shapes. Hence the method is most widely used in modelling nearly spherical scatterers such as aerosols and hydrometers.

### Time Domain Methods

Our concentration here has been on frequency domain methods, not only because many problems of interest are posed in the frequency domain, but also because linear dispersive materials are easier to treat, and most parameters and figures of merit (e.g., surface impedances, radar cross sections) are defined only in the frequency domain. Nevertheless, much fruitful insight can be obtained by modelling problems directly in the time domain, and considerable progress has

been made in this area. Time domain formulations are often more efficient than corresponding frequency domain formulations. For example, frequency domain parameters can often be determined over a wide band from a single simulation by Fourier transforming the time domain response to a narrow pulse simulating an impulse. To obtain the same result, a frequency domain computation would require solution at many different frequencies. It is also often necessary to solve nonlinear problems directly in the time domain. Most frequency domain integral and partial differential formulations have time domain counterparts that may be found by inverse Fourier transforming the corresponding frequency domain equations. The process simply employs the frequency multiplication–time derivative correspondence,  $j\omega \rightarrow \frac{\partial}{\partial t}$ , and the exponential shift theorem,  $\mathbf{J}(\mathbf{r}, \omega)e^{-jkR} \rightarrow \mathbf{J}(\mathbf{r}, t - R/c)$ . Usually a finite difference or linear interpolation scheme is used for discretising the time variable.

The finite difference time domain (FDTD) approach is quite widely used (Kunz and Luebbers, 1993; Taflove, 1995), both to simulate time domain excitations directly and to obtain wideband responses by Fourier transforming the time domain response. It employs a pair of separate, staggered rectangular grids for modelling the electric and magnetic fields, respectively, which enables all derivatives with respect to rectangular coordinate quantities in Maxwell's equations to be replaced by central finite difference approximations. When the time derivatives are also replaced by central differences, one obtains a very simple yet efficient explicit scheme for alternately updating the electric and magnetic fields at successive time steps.

For geometries that do not conform well to a rectangular mesh, some efficiency is lost in finite difference methods due to the need for a fine mesh to avoid so-called *stair-stepping error* in approximating object and material boundaries. Also, if the time interval of interest is sufficiently long that the scattered field can reach the outer mesh boundary, reflect and return to corrupt the field at the point of interest, then some scheme must be employed to absorb the scattered fields incident to the mesh boundary. This consideration is not confined to the FDTD approach, but is common to all partial differential equations approaches and is discussed in §17.

Closely related to the finite difference approach is the transmission line modelling (TLM) approach (Hafner, 1990; Trenkic *et al.*, 1997), in which points in space represent junctions between short transmission line sections whose parameters depend on the local material properties. The transmission lines communicate propagation and polarisation information between adjacent nodes, and scattering matrices

describe the interactions of the lines with one another at the junctions.

To enable the use of unstructured grids for modelling object boundaries, a time domain finite element formulation of the wave equation can, in principle, be developed. This approach has the potential to eliminate the stair-stepping errors associated with rectangular meshes, but is still in the early stages of development for three-dimensional problems (Lee *et al.*, 1997). In two dimensions, hybrid methods using time-domain integral equations to truncate a finite element mesh have been developed (Rao, 1999).

As in the frequency domain, time domain integral equations offer the potential for modelling just the fields on the boundaries of piecewise homogeneous objects. Stabilised methods for treating time domain integral equations usually employ so-called implicit schemes, for which at least a banded matrix must be inverted (Rao, 1999). Often the banded matrix can be solved efficiently using iterative methods at each time step, or can be inverted once at the initial time step and the result used for all subsequent time steps. Time domain integral equations are likely to begin to see increased usage as mesh terminators for time domain partial differential equation approaches such as FDTD or FEM methods. Fast methods for time domain integral equations are also under development.

## § 17. Mesh Truncation: Absorbing Boundary Conditions

When discrete methods are used to solve time or frequency domain wave equations in open regions, we must consider mesh truncation conditions. Scattered fields must satisfy the radiation conditions (24) at infinity, but one cannot generally afford to extend a mesh to regions where these conditions hold even approximately. Hence conditions that apply on mesh boundaries of finite extent are needed. One rigorous approach is to use the hybrid integral equation approach of § 14 to provide a radiation condition via a boundary integral equation, but the hybrid integral approach couples all boundary elements together, leading to a full matrix in the frequency domain. Often one would prefer an approximate but simpler approach, with local coupling only, that preserves the sparsity of the finite element or finite difference equations. Consequently, considerable effort has gone towards the development of local so-called *absorbing boundary conditions* (ABC) (Silvester and Pelosi, 1994). Early approaches focussed primarily on obtaining conditions that reproduced the leading asymptotic terms of various outgoing wave expansions. More recent methods have concentrated on synthesising lossy artificial materials and profiles that, when

discretised by finite techniques, absorb incident fields over wide incidence angles and bandwidths (Berenger, 1994; Kuzuoglu and Mittra, 1997). A number of such ABCs with very good performance have been developed for both frequency and time domain applications.

## Notes

1. Though the representation theorem applies only to bounded functionals, some unbounded functionals may also be similarly represented if  $g$  is suitably extended to distributional functions. For example, if  $g = -\delta(x-x')\delta(y-y')\delta(z-z')$ , we have  $[u] = u(\mathbf{r}')$ , the value of the field at  $\mathbf{r}'$ , but  $u(\mathbf{r}')$  may be unbounded, for example, at geometrical singularities.
2. If one attempts to apply the MFIE to an open curve  $C$  with normal  $\hat{\mathbf{n}}$ , one must treat the currents on opposite sides as existing on two limiting surfaces:  $J_z^+$  on  $C^+$ , the side with normal  $\hat{\mathbf{n}}$ , and  $J_z^-$  on  $C^-$ , the opposite side. With observation points on  $C$  between the two limiting surfaces, the resulting MFIE for the TM case, for example, is

$$\frac{J_z^+(\boldsymbol{\rho}) - J_z^-(\boldsymbol{\rho})}{2} - \int_C [J_z^+(\boldsymbol{\rho}') + J_z^-(\boldsymbol{\rho}')] \frac{\partial G(\boldsymbol{\rho}, \boldsymbol{\rho}')}{\partial n} dC' = H_\theta^{\text{inc}}(\boldsymbol{\rho}).$$

- In the EFIE case we combined the net equivalent current  $J_z = J_z^+ + J_z^-$  into a single unknown. In the MFIE case, however, the appearance of both a sum and difference current in the above equation does not allow this. The equation above, while a valid identity, does not contain sufficient information to determine either the sum or the individual currents  $J_z^+$  and  $J_z^-$ .
3. Since bases are generally defined only piecewise over the mesh, strictly speaking the integration by parts can only be performed over individual elements, with boundary terms like that in (209) arising from the element boundaries. Adding results for adjacent elements, however, one finds that the element boundary terms cancel since tangential components of both the magnetic field and the basis functions are continuous across element boundaries.

## References

- Bendali, A., Fares, M'B. and Gay, J. 1999, A boundary-element solution of the Leontovitch problem. *IEEE Trans. Ant. Prop.* **47**, 1597–1605.
- Berenger, J.-P. 1994, A perfectly matched layer for the absorption of electromagnetic waves. *J. Comput. Phys.* **114**, 185–200.
- Brown, W. J. and Wilton, D. R. 1999, Singular basis functions and curvilinear triangles in the solution of the electric field integral equation. *IEEE Trans. Ant. Prop.* **47**, 347–353.
- Bunger, R. and Arndt, F. 1997, Efficient MPIE approach for the analysis of three-dimensional microstrip structures in layered media. *IEEE Trans. Microwave Theory Tech.* **45**, 1141–1153.
- Butler, C. M., Rahmat-Samii, Y. and Mittra, R. 1970, Electromagnetic penetration through apertures in conducting surfaces. *IEEE Trans. Ant. Prop.* **26**, 82–93.

- Canning, F. X. 1990, Transformations that produce a sparse moment matrix. *J. Electromag. Waves Appl.* 4, 983–993.
- Champagne, N. J., Williams, J. T. and Wilton, D. R. 1992, The use of curved segments for numerically modeling thin wire antennas and scatterers. *IEEE Trans. Ant. Prop.* 40, 682–689.
- Chew, W. C., Jin, J.-M., Lu, C.-C., Michielssen, E. and Song, J. M. 1997, Fast solution methods in electromagnetics. *IEEE Trans. Ant. Prop.* 45, 533–543.
- Glisson, A. W. 1984, An integral equation for electromagnetic scattering from homogeneous dielectric bodies. *IEEE Trans. Ant. Prop.* 32, 173–175.
- Govind, S., Wilton, D. R. and Glisson, A. W. 1984, Scattering from inhomogeneous penetrable bodies of revolution. *IEEE Trans. Ant. Prop.* 32, 1163–1173.
- Graglia, R. D., Wilton, D. R. and Peterson, A. F. 1997, Higher order interpolatory basis functions for computational electromagnetics. *IEEE Trans. Ant. Prop.* 45, 329–342.
- Gutknecht, M. H. 1993, Variants of BiCGStab for matrices with complex spectrum. *SIAM J. Sci. Comput.* 14, 1020–1033.
- Hafner, C. 1990, *Generalized Multipole Techniques for Computational Electromagnetics*. Artech House, London.
- Hammer, P. C., Marlowe, O. P. and Stroud, A. H. 1956, Numerical integration over simplexes and cones. *Math. Tables Aids Comp.* 10, 130–137.
- Harrington, R. F. 1961, *Time-Harmonic Electromagnetic Fields*. McGraw-Hill, New York.
- Harrington, R. F. 1993, *Field Computation by Moment Methods*. IEEE Press, New York.
- Hoppe, D. J. and Rahmat-Samii, Y. 1995, *Impedance Boundary Conditions in Electromagnetics*. Taylor and Francis, Washington, DC.
- Jordan, K. E., Richter, G. R. and Sheng, P. 1986, An efficient numerical evaluation of the Greens function for the Helmholtz operator on periodic structures. *J. Comp. Phys.* 63, 222–235.
- Kunz, K. S. and Luebbers, R. J. 1993, *The Finite Difference Time Domain Method for Electromagnetics*. CRC Press, Boca Raton, FL.
- Kuzuoglu, M. and Mittra, R. 1997, Investigation of nonplanar perfectly matched absorbers for finite-element mesh truncation. *IEEE Trans. Ant. Prop.* 45, 474–486.
- Lee, J.-F., Lee, R. and Cangellaris, A. 1997, Time-domain finite-element methods. *IEEE Trans. Ant. Prop.* 45, 430–442.
- Lee, S. W. and Mittra, R. 1983, Fourier transform of a polygonal shape function and its application in electromagnetics. *IEEE Trans. Ant. Prop.* 31, 99–103.
- Ma, J., Rokhlin, V. and Wandzura, S. 1996, Generalized Gaussian quadrature rules for systems of arbitrary functions. *SIAM J. Numer. Anal.* 33, 971–996.
- Mautz, J. R. and Harrington, R. F. 1978, H-field E-field, and combined field solutions for conducting bodies of revolution. *Arch. Electron. Übertragungstech* 32, 159–164.
- Mautz, J. R. and Harrington, R. F. 1979, Electromagnetic scattering from a homogeneous material body of revolution. *Arch. Electron. Übertragungstech* 33, 71–80.
- Medgyesi-Mitschang, L. N. and Putnam, J. M. 1984, Electromagnetic scattering from axially inhomogeneous bodies of revolution. *IEEE Trans. Ant. Prop.* 32, 797–806.
- Michalski, K. A. and Mosig, J. R. 1997, Multilayered media Green's functions in integral equation formulations. *IEEE Trans. Ant. Prop.* 45, 508–520.
- Michalski, K. A. and Zheng, D. 1990, Electromagnetic scattering and radiation by surfaces of arbitrary shape in layered media, part I: Theory. *IEEE Trans. Ant. Prop.* 38, 335–344.
- Newman, E. H. 1988, An overview of the hybrid MM/Green's function method in electromagnetics. *Proc. IEEE* 76, 270–282.
- Pearson, L. W., Peterson, A. F., Bahrmassel, L. J. and Whittaker, R. A. 1992, Inward-looking and outward-looking formulations for scattering from penetrable objects. *IEEE Trans. Ant. Prop.* 40, 714–720.
- Rao, S. M. (Ed.) 1999, *Time Domain Electromagnetics*. Academic Press, New York.
- Rao, S. S. M., Wilton, D. R. and Glisson, A. W. 1982, Electromagnetic scattering by surfaces of arbitrary shape. *IEEE Trans. Ant. Prop.* 30, 409–418.
- Richmond, J. H. and Newman, E. H. 1976, Dielectric coated wire antennas. *Radio Sci.* 11, 13–20.
- Saad, Y. 1996, *Iterative Methods for Sparse Linear Systems*. PWS, New York.
- Senior, T. B. A. and Volakis, J. L. 1995, *Approximate Boundary Conditions in Electromagnetics*. IEE, Bath, UK.
- Silvester, P. P. and Ferrari, R. L. 1996, *Finite Elements for Electrical Engineers*. Cambridge, Univ. Press, New York.
- Silvester, P. P. and Pelosi, G. 1994, *Finite Elements for Wave Electromagnetics*. IEEE Press, New York.
- Stakgold, I. 1967, *Boundary Value Problems of Mathematical Physics, Vols. I, II*. Macmillan, New York. (Reprinted 2000, Society for Industrial and Applied Mathematics.)
- Taflove, A. 1995, *Computational Electrodynamics: The Finite-Difference Time-Domain Method*. Artech House, Norwood, MA.
- Trenkic, V., Christopoulos, C. and Benson, T. M. 1997, Optimization of TLM schemes based on the general symmetrical condensed node. *IEEE Trans. Ant. Prop.* 45, 457–465.
- Tsai, L. L., Dudley, D. G. and Wilton, D. R. 1974, Electromagnetic scattering by a three-dimensional conducting rectangular box. *J. Appl. Phys.* 45, 4393–4400.

- Umashankar, K. R., Taflove, A. and Rao, S. M. 1986, Electromagnetic scattering by arbitrary shaped three-dimensional homogeneous lossy dielectric objects. *IEEE Trans. Ant. Prop.* **34**, 758–766.
- Volakis, J. L., Özdemir, T. and Gong, J. 1997, Hybrid finite-element methodologies for antennas and scattering. *IEEE Trans. Ant. Prop.* **45**, 493–507.
- Volakis, J. L., Chatterjee, A. and Kempel, L. C. 1998, *Finite Element Method for Electromagnetics*. IEEE Press, New York.
- Waterman, P. C. 1969, Scattering by dielectric obstacles. *Alta Frequenza* **38**, 348.
- Wilton, D. R. and Butler, C. M. 1981, Effective methods for solving integral and integro-differential equations. *Electromagnetics* **1**, 289–308.
- Wilton, D. R., Rao, S. M., Glisson, A. W., Schaubert, D. H., Al-Bundak, O. M. and Butler, C. M. 1984, Potential integrals for uniform and linear source distributions on polygonal and polyhedral domains. *IEEE Trans. Ant. Prop.* **32**, 276–281.
- Yeung, M. S. 1999, Single integral equation for electromagnetic scattering by three-dimensional homogeneous dielectric objects. *IEEE Trans. Ant. Prop.* **47**, 1615–1622.
- Zienkiewicz, O. D. 1971, *The Finite Element Method in Engineering Science*. McGraw-Hill, New York.



**Lecture 2**  
**14:00-18:00, May 20, 2013**

**A Summary of Asymptotic High Frequency  
(HF) Methods for Solving Electromagnetic  
(EM) Wave Problems**

**Professor Prabhakar Pathak**  
**ElectroScience Lab.**  
**The Ohio State University**  
**Columbus, Ohio**  
**USA**



## A Summary of Asymptotic High Frequency (HF) Methods for Solving Electromagnetic (EM) Wave Problems

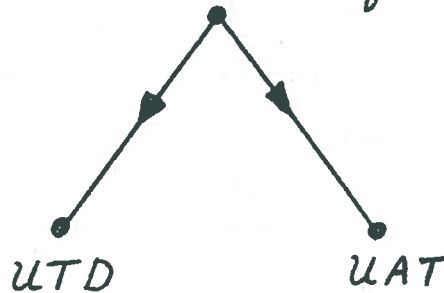
Prabhakar H. Pathak, The Ohio State University ElectroScience Lab., Dept. of ECE,  
1320 Kinnear Rd., Columbus, Ohio 43212  
E-mail: [pathak.2@osu.edu](mailto:pathak.2@osu.edu)

The geometrical optics (GO) ray field consists of direct, reflected and refracted rays. GO ray paths obey Fermat's principle, and describe reflection and refraction of HF EM waves, but not the diffraction of waves around edges and smooth objects, etc. Consequently, GO predicts a zero EM field within shadow regions of impenetrable obstacles illuminated by an incident GO ray field. Early attempts by Young to predict edge diffraction via rays, and by Huygen, Fresnel and Kirchhoff to predict diffraction using wave theory will be briefly reviewed. Unlike GO, the wave based physical optics (PO) approach developed later requires an integration of the induced currents on the surface of an impenetrable obstacle illuminated by an external EM source in order to find the scattered field. The induced currents in PO are approximated by those which would exist on a locally flat tangent surface, and are set to zero in the GO shadow region. If the incident field behaves locally as a plane wave at every point on the obstacle, then it can be represented as a GO ray field; the resulting PO calculation constitutes a HF wave optical approach. PO contains diffraction effects due to the truncation of the currents at the GO shadow boundary; these effects may be spurious if there is no physical edge at the GO shadow boundary on the obstacle, whereas it is incomplete even if an edge is present at the GO shadow boundary. In the 1950s, Ufimtsev introduced an asymptotic correction to PO; his formulation is called the physical theory of diffraction (PTD).  $PTD = PO + \dots$ , where  $\dots$  is available primarily for edged bodies. In its original form, PTD is not accurate near and in shadow zones of smooth objects without edges, nor in shadow zones for bodies containing edges that are not completely illuminated or visible. At about the same time as PTD, a ray theory of diffraction was introduced by Keller; it is referred to as the geometrical theory of diffraction (GTD). GTD was systematically formulated by generalizing Fermat's principle to include a new class of diffracted rays. Such diffracted rays arise at geometrical and/or electrical discontinuities on the obstacle, and they exist in addition to GO rays.  $GTD = GO + \text{Diffraction}$ . Away from points of diffraction, the diffracted rays propagate like GO rays. Just as the initial values of reflected and refracted rays are characterized by reflection and transmission coefficients, the diffracted rays are characterized by diffraction coefficients. These GTD coefficients may be found from the asymptotic HF solutions to appropriate simpler canonical problems via the local properties of ray fields. Most importantly, the GTD overcomes the failure of GO in the shadow region, it does not require integration over currents, and it provides a vivid physical picture for the mechanisms of radiation and scattering. In its original form, GTD exhibits singularities at GO ray shadow boundaries and ray caustics. Uniform asymptotic methods were developed to patch up GTD in such regions. These uniform theories are referred to as UTD, UAT, spectral synthesis methods, and the equivalent current method (ECM). The pros and cons of *wave optical* methods (PO, PTD, ECM) and *ray optical* methods (GO, GTD, UTD, UAT) will be discussed along with some recent advances in PO and UTD. A UTD for edges excited by complex source beams (CSBs) and Gaussian beams (GBs) will also be briefly described; the latter may be viewed as constituting *beam optical* methods. A hybridization of HF and numerical methods will be briefly discussed as well.

- Two Basic Asymptotic High Frequency (HF) Methodologies can be Categorized as follows:

### 1. RAY OPTICAL METHODS

- Geometrical Optics (GO)
- Geometrical Theory of Diffraction (GTD)  
[GTD = GO + Diffraction]
- Uniform version of the GTD



### 2. WAVE OPTICAL METHODS

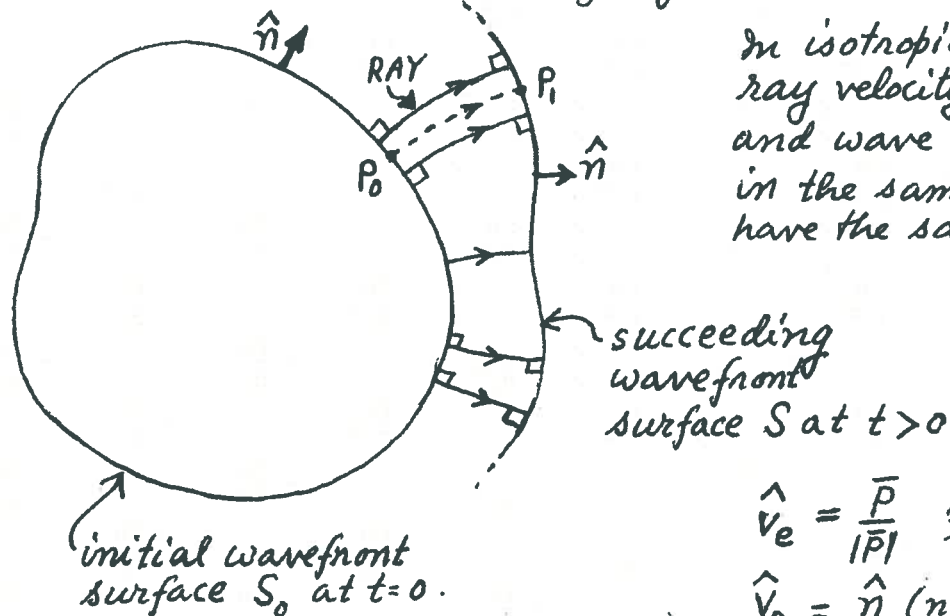
- Physical Optics (PO)
- Physical Theory of Diffraction (PTD)  
[PTD = PO + Diffraction Correction]

## GENERAL COMMENTS ON ASYMPTOTIC HF METHODS

- Asymptotic HF methods are powerful for analyzing a wide variety of electrically large EM problems.
- Conventional numerical computational EM (NCEM) methods based on self consistent wave formulations become rapidly inefficient, or even intractable, for solving large EM problems.
- UTD is more developed, especially for handling smooth convex boundary diffraction, than wave optical methods.
- Ray optical methods require ray tracing. Wave optical methods require numerical integration on the large object.
- Ray optical methods are generally more efficient. Wave optical methods are generally more robust.
-  Most importantly, unlike all other methods, ray methods provide a simple picture for the mechanisms of wave radiation, propagation, scattering and diffraction.

## DEVELOPMENT OF THE RAY CONCEPT

- In the high frequency regime, EM waves exhibit highly local properties. Local wave propagation phenomena is physically described in terms of RAY paths.
- The RAY concept is introduced to describe the propagation of wavefronts or phasefronts, at high frequencies, in a simple but approximate fashion.
- The classical ray concept of GO is applicable to isotropic, loss-free media which in general may be inhomogeneous.
- In the classical GO framework, any point  $P_0$  on a given wavefront  $S_0$  at time  $t=0$  (say) transforms to a corresponding point  $P$  onto the succeeding wavefront  $S$  at a slightly later time  $t=t' > 0$ .



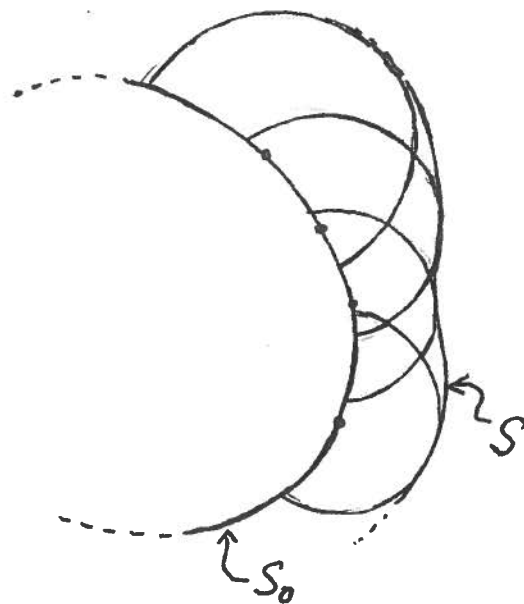
In isotropic media, the ray velocity (energy velocity) and wave velocity are in the same direction and have the same value.

$$\hat{v}_e = \frac{\bar{P}}{|\bar{P}|} \quad ; \quad \bar{P} = \text{Poynting vector}$$

$$\hat{v}_p = \hat{n} \quad (\text{normal to } S)$$

The point to point transformation from  $S_0$  to  $S$  takes place along curved paths called RAYS; these rays are normal to their associated wavefronts.

- In a homogeneous medium, ray paths are straight lines.
- In the rigorous wave representation (or equivalence) theorems for wave propagation, the field at  $P$  is an integration over the equivalent sources defined at every point on the initial wavefront surface  $S_0$ . Thus, there is no point to point transformation in this case.
- In the Huygen's wave optical (or wavelet) construction, each point on  $S_0$  generates a spherical wavelet. Then, a superposition of all these spherical secondary wavelets originating from the initial wavefront surface  $S_0$  now form the new wavefront surface  $S$  as the ENVELOPE of the secondary spherical wavelets.



$S$  is the same as that based on GO point-point transf. only for isotropic case.

- For anisotropic media, the wavelets in Huygen's construction generally become ellipsoidal. GO point to point transformation thus becomes inapplicable for the anisotropic case where the  $\hat{v}_e$  and  $\hat{v}_p$  are generally not in the same direction. ( $\hat{v}_p = \hat{k} \cdot \hat{v}_e$ ).

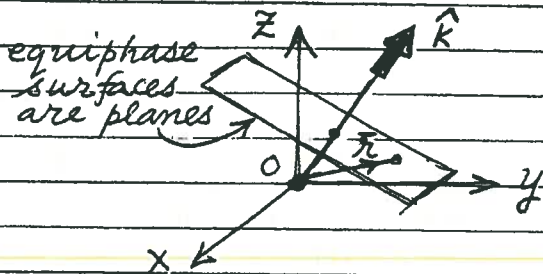
(isotropic, homogeneous medium)

PLANE WAVE CONCEPT

The electric and magnetic fields  $\vec{E}$  and  $\vec{H}$ , resp. of the plane wave propagating in the  $\hat{k}$ -direction, are given as usual by:

$$\vec{E}(\vec{r}) = \hat{u} A_0 e^{-j\vec{k} \cdot \vec{r}}$$

$$\vec{H}(\vec{r}) = Y_0 \hat{k} \times \vec{E}(\vec{r}) \quad ; \quad Y_0 = Z_0^{-1} \quad (Z_0 = \text{impedance of the plane wave in the medium})$$



EQUIPHASE SURFACE  
IS GIVEN BY:  $\hat{k} \cdot \vec{r} = \text{CONSTANT}$

Thus, equiphase surfaces are PLANES; hence these waves are referred to as PLANE WAVE.

The corresponding time dependent field  $\vec{E}(\vec{r}, t)$  which pertains to the phasor domain field  $\vec{E}(\vec{r}, \omega)$  is given by

$$\vec{E}(\vec{r}, t) = \text{Re } \vec{E} e^{j\omega t} = \text{Re } \hat{u} A_0 e^{j(\omega t - \vec{k} \cdot \vec{r})}$$

Therefore, the plane wave propagates in the direction  $\hat{k}$  with a phase velocity  $v_p = c = \text{speed of light (EM field) in the medium}$ . This is seen as usual by requiring the argument of  $E$  to be constant to move with the wave:

$$\omega t - \vec{k} \cdot \vec{r} = [\text{constant} \triangleq \Gamma_0]$$

Then differentiating the above with respect to time ( $t$ ) one obtains:

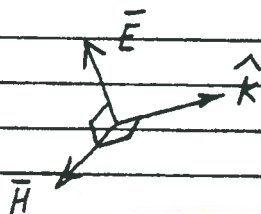
$$\omega - \vec{k} \cdot \frac{d\vec{r}}{dt} = 0$$

$$\text{ie. } \hat{k} \cdot \frac{d\vec{r}}{dt} = \frac{\omega}{k} > 0 \Rightarrow v_p = \frac{\hat{k} \cdot d\vec{r}}{dt} = \frac{\omega}{k} = c$$

( $\because k = \omega \sqrt{\mu \epsilon}$ )  
=  $\omega/c$ )

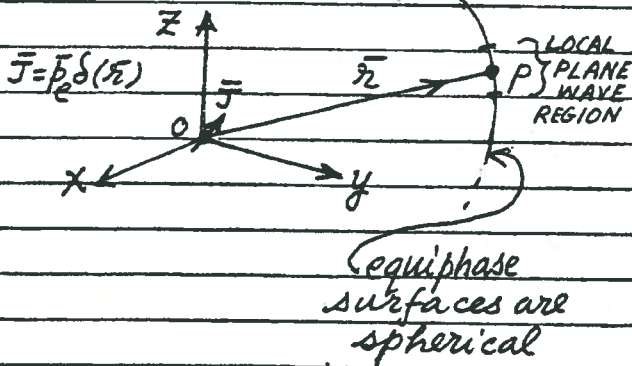
$v_p = \text{velocity of phasefront in the } \hat{k} \text{ direction.}$

Thus, the plane wave field propagates in the direction  $\hat{k}$  which is  $\perp$  planes of constant phase and the condition  $\nabla \cdot \vec{E} = 0 \Rightarrow \hat{k} \cdot \vec{E} = 0$  requires that  $\hat{k} \cdot \hat{u} = 0$  which in turn makes  $\vec{E} \perp \hat{k}$  (or  $\hat{u} \perp \hat{k}$ ) furthermore,  $\vec{H} = \frac{\nabla \times \vec{E}}{-jkz_0}$  requires  $\vec{H} = \gamma_0 \hat{k} \times \vec{E}$  or  $\vec{H} \perp \vec{E}$ .



Next, consider the field  $\vec{E}_e$  generated by a point electric current source of strength  $\vec{p}_e$ :

$$\vec{E}(\vec{r}) \approx \frac{+jkz_0}{4\pi} \hat{r} \times \hat{r} \times \vec{p}_e \frac{e^{-jk r}}{r} \quad (kr \gg 1)$$



EQUIPHASE SURFACE

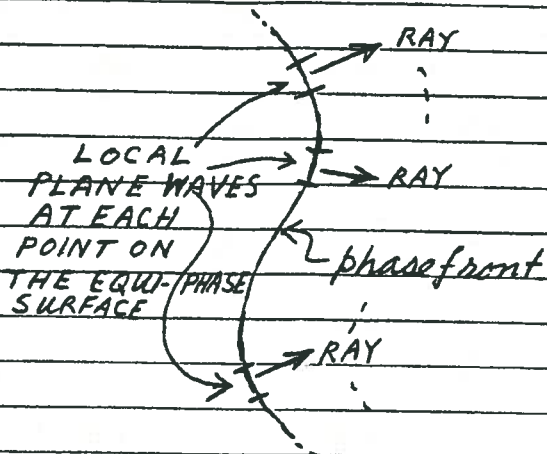
IS GIVEN BY:  $kr = \text{constant}$

Thus, the equiphase surfaces are SPHERICAL; hence, a point current source generates SPHERICAL WAVES (centered at the point source).

$$\vec{H}(\vec{r}) \approx \gamma_0 \hat{r} \times \vec{E}(\vec{r}) \quad (kr \gg 1)$$

Therefore, if  $kr$  is sufficiently large, i.e., when the frequency is sufficiently high, the field of a point source behaves locally like a PLANE WAVE at and near P; i.e.,  $\vec{k} \cdot \vec{r} = kr \rightarrow \hat{k} = \hat{r}$  and  $\vec{E} \perp \vec{H} \perp \hat{r} (= \hat{k})$  at and near P where P is arbitrary.

The local plane wave concept can be generalized to an arbitrary but slowly varying phasefront at high frequencies as shown below:

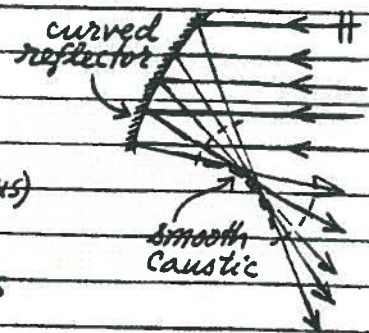
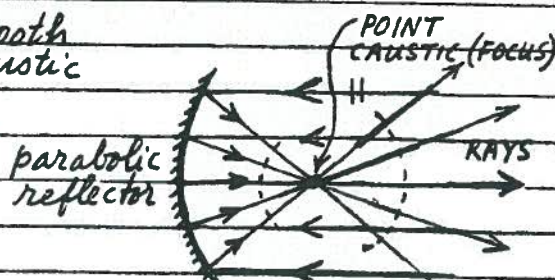
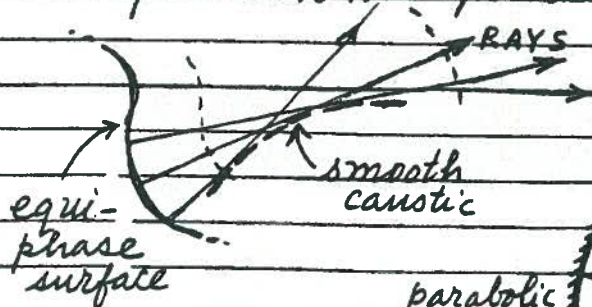


⇒ This picture at left leads to local plane wave propagation paths; such paths are called RAYS, FAMILY OF RAYS ⊥ ASSOCIATED phasefront.

⇒ The concept of RAYS is based on LOCAL PLANE WAVE TRACKING of the phasefront.

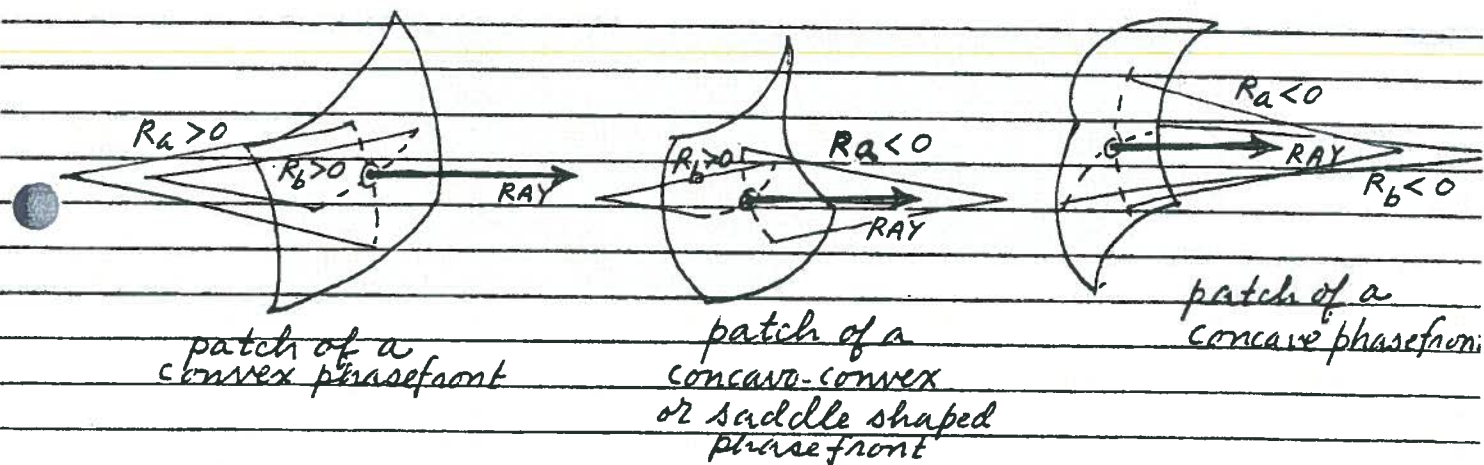
The ray concept of wave propagation is in contrast to the Huygen's principle of wave propagation which considers each point on the equiphase surface as a source of spherical waves. For the ray concept to be valid it is necessary that the surface radii of curvature of the equiphase surface are sufficiently large in terms of the wavelength. i.e., the ray concept is valid at high frequencies. In summary,

EACH POINT on the electrically large phasefront behaves LOCALLY like a PLANE WAVE, so that the LOCAL direction of PROPAGATION ⊥ phasefront at EACH POINT on the phasefront; furthermore, the FIELD is POLARIZED ⊥ the local direction of propagation or to the RAY. Also, the electric and magnetic field satisfy the plane wave relationships locally at each point on the phasefront.

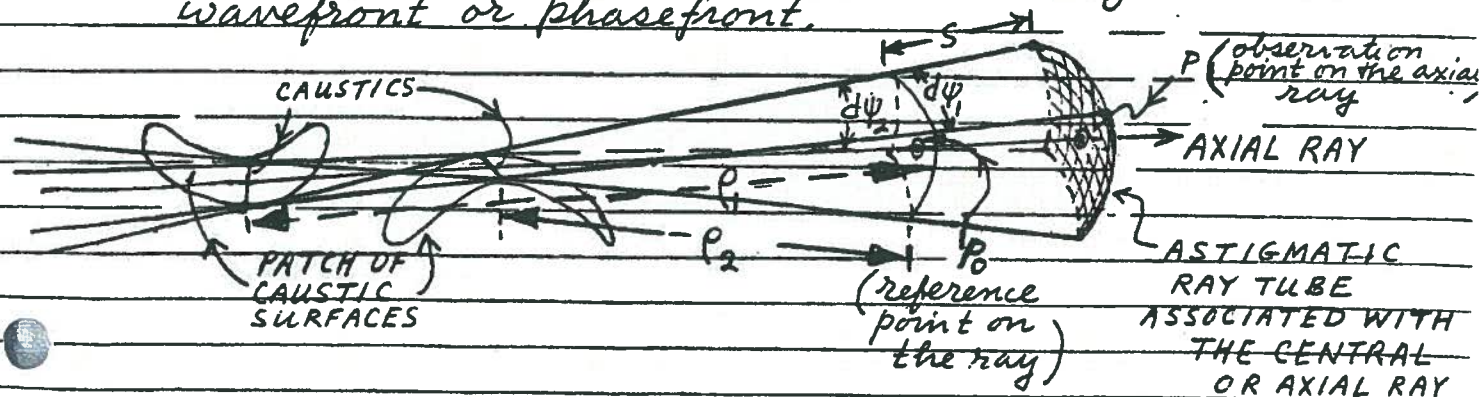


## GO TRANSPORT SINGULARITIES

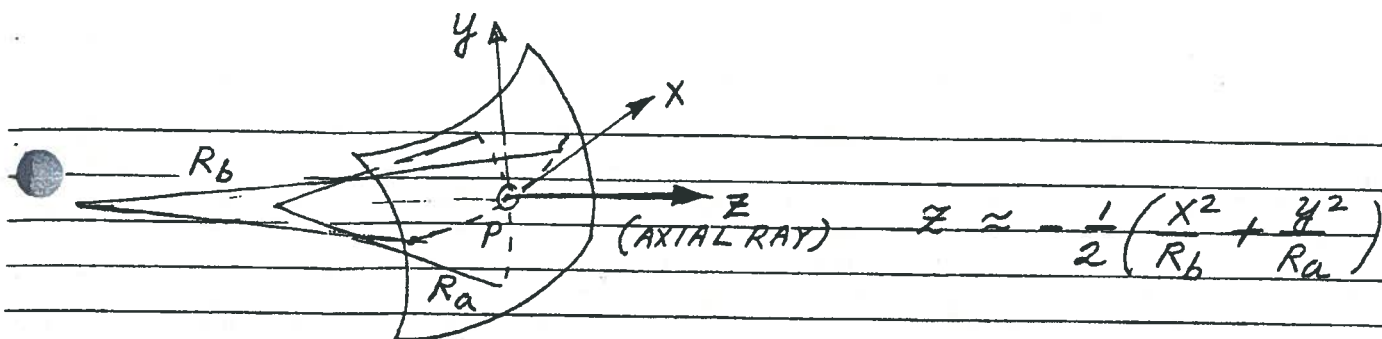
Caustics are formed by an intersection of the same family of rays (i.e. by the intersection of rays from the same wavefront or phasefront). Caustics are the loci of the centers of curvature of the phasefront, thus, if the caustic surface is smooth then rays are tangent to this caustic surface and the phasefront is everywhere perpendicular (orthogonal) to these family of rays. In the case of two-dimensions, the caustic surfaces reduce to caustic curves. In some instances, the caustic surface collapses to a single point or point focus. In the two-dimensional case, a point caustic becomes a line caustic (- focal line).



An arbitrary quadratic phasefront which accommodates the above cases is referred to as a general ASTIGMATIC wavefront or phasefront.



ASTIGMATIC RAY TUBE



The astigmatic phasefront can be locally approximated by a quadratic surface as shown above. Thus the astigmatic ray tube, which is an infinitesimal tube of rays around a central (AXIAL) RAY is often referred to as a quadratic ray pencil. This quadratic surface approximation at and near P on the phasefront is given by a LOCAL PARABOLOID with two DISTINCT PRINCIPAL RADII OF CURVATURES  $R_a$  and  $R_b$  at P.

It is noted that the astigmatic phasefront, when sufficiently far (in terms of  $\lambda$ ) from the caustics, is LOCALLY PLANE at P. The EM field of the axial ray at P can be found by postulating that it satisfies the local plane wave behaviour at P and that power is conserved in the ray tube at P. The EM RAY FIELD is found as follows:

It is assumed that the field at  $P_0$  (reference point) is known. Then  $|\vec{E}(P)|$  can be found by invoking conservation of power:

$$\text{complex power crossing } \Delta S_0 = \frac{1}{2} \frac{|\vec{E}(P_0)|^2}{Z_0} \Delta S_0$$

where  $\Delta S_0$  = area of the ray tube at  $P_0$

$$\text{complex power crossing } \Delta S = \frac{1}{2} \frac{|\vec{E}(P)|^2}{Z_0} \Delta S$$

where  $\Delta S$  = area of the ray tube at P.

It is assumed when computing the complex power density that the field is locally plane at  $P_0$  and P.

It is clear that

$$\Delta S_0 \approx |e_1 d\psi_1 \cdot e_2 d\psi_2|$$

and

$$\Delta S \approx |(e_1 + s) d\psi_1 \cdot (e_2 + s) d\psi_2|$$

∴ conservation of power in the ray tube requires:

$$\frac{1}{2} \frac{|E(P_0)|^2}{Z_0} |e_1 d\psi_1 \cdot e_2 d\psi_2| = \frac{1}{2} \frac{|E(P)|^2}{Z_0} |(e_1 + s) d\psi_1 \cdot (e_2 + s) d\psi_2|$$

i.e.  $|E(P)| = |E(P_0)| \sqrt{\frac{e_1 e_2}{e_1 + s e_2 + s}}$

Next, introducing polarization and phase associated with the LOCAL PLANE WAVE it follows that the above result can be modified to yield:

$$\vec{E}(P) \approx \vec{E}(P_0) \sqrt{\frac{e_1 e_2}{e_1 + s e_2 + s}} e^{-jks}$$

← PHASE DELAY ALONG THE RAY

← RAY SPREADING

← INITIAL VALUE

where  $\sqrt{\frac{e_i}{e_i + s}} = \begin{cases} \left| \sqrt{\frac{e_i}{e_i + s}} \right|, & \frac{e_i}{e_i + s} > 0 \\ j \left| \sqrt{\frac{e_i}{e_i + s}} \right|, & \frac{e_i}{e_i + s} < 0 \end{cases}$

(i=1,2)

for  $e^{+j\omega t}$

The polarization at P = polarization at P<sub>0</sub> in a homogeneous isotropic medium. Also the field  $\vec{E}$  is polarized  $\perp \hat{s} \Rightarrow \vec{E} \cdot \hat{s} = 0$

NOTE: The phase jump of (j) for  $e_i$  occurs  $\frac{e_i}{e_i + s}$

whenever a caustic is crossed between P<sub>0</sub> and P. One can choose P<sub>0</sub> arbitrarily

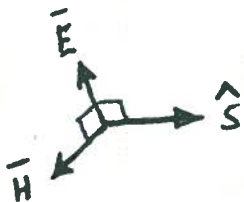
NOTE:  $e_i > 0$  if caustic  $\frac{z}{2}$  lies behind P<sub>0</sub> as the ray propagates along  $\hat{s}$ ; otherwise,  $e_i < 0$ .

$$\bar{E}(P) = \bar{E}(0) \sqrt{\frac{\rho_1}{\rho_1 + s}} \sqrt{\frac{\rho_2}{\rho_2 + s}} e^{-jks}$$

	as measured along $\hat{s}$	as measured along $-\hat{s}$
$\rho_i$	$< 0$	$> 0$
$s$	$> 0$	$< 0$

⇒ All distances ( $\rho_i, s$ ) are measured from the REFERENCE point at 0.

$$\bar{H}(P) \sim Y_0 \hat{s} \times \bar{E}(P)$$



NOTE :  $\bar{E}(P) \rightarrow \infty$  if  $\rho_1 + s = 0$  ; i.e, RAY FIELD IS SINGULAR AT A CAUSTIC.

NOTE :  $s \geq 0$  if  $\bar{P}_0 P = \pm |\bar{P}_0 P| \hat{s}$ , where  $\hat{s}$  is the direction of RAY PROPAGATION.

NOTE : (a) If  $\rho_1 \rightarrow \infty$  &  $\rho_2 \rightarrow \infty$ , then the wave is PLANE  
 (b) If  $\rho_1 \rightarrow \infty$  &  $\rho_2$  is FINITE, then the wave is CYLINDRICAL  
 (c) If  $\rho_1 = \rho_2$ , then the wave is SPHERICAL.

PLANE WAVE : Let  $\rho_1 \rightarrow \infty$  &  $\rho_2 \rightarrow \infty$ , then

$$\bar{E}(P) = \bar{E}(P_0) e^{-jks} \Rightarrow \text{PLANE WAVE}$$

with  $\bar{E} \cdot \hat{s} = 0$

CYLINDRICAL WAVE : Let  $\rho_1 \rightarrow \infty$  & let  $\rho_2$  be finite, then

$$\bar{E}(P) = \bar{E}(P_0) \sqrt{\frac{\rho_2}{\rho_2 + s}} e^{-jks}$$

It is convenient to move the reference point  $P_0$  to the caustic (center of curvature), whose distance  $\rho_2$  must now be set equal to zero. Thus

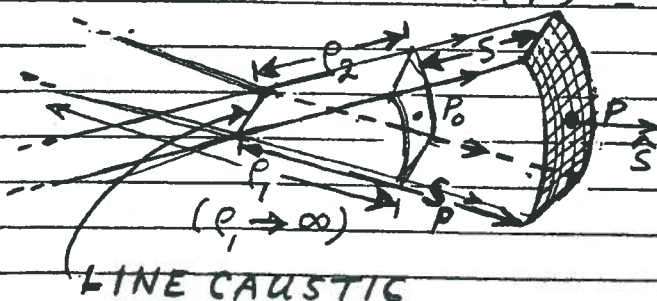
$$\bar{E}(P) = \lim_{\rho_2 \rightarrow 0} \bar{E}(P_0) \sqrt{\rho_2} \frac{e^{-jks_p}}{\sqrt{s_p}} ; \begin{matrix} s \rightarrow s_p \\ \text{as } \rho_2 \rightarrow 0 \end{matrix}$$

Since  $\bar{E}(P_0) \rightarrow \infty$  as  $\rho_2 \rightarrow 0$ ; and since  $\bar{E}(P)$  should be independent of the choice of  $P_0$  as long as  $P$  is not near a caustic, it follows that

$$\lim_{\rho_2 \rightarrow 0} \bar{E}(P_0) \sqrt{\rho_2} \text{ exists } \& \equiv \bar{A}_0$$

$$\therefore \bar{E}(P) = \bar{A}_0 \frac{e^{-jks_p}}{\sqrt{s_p}} \Rightarrow \text{CYLINDRICAL WAVE}$$

$\bar{E} \cdot \hat{s} = 0$



The field of a line source

$$\text{is } \propto \hat{u} \left( \frac{-j}{4} \right) H_0^{(2)}(ks_p)$$

$$\approx \hat{u} \left( \frac{-j}{4} \right) \sqrt{\frac{2j}{\pi k}} \frac{e^{-jks_p}}{\sqrt{s_p}} \text{ CYL. WAVE}$$

SPHERICAL WAVE: If  $\rho_1 = \rho_2 \equiv \rho$ , then

$$\bar{E}(P) = \bar{E}(P_0) \frac{\rho}{\rho + s} e^{-jk s}$$

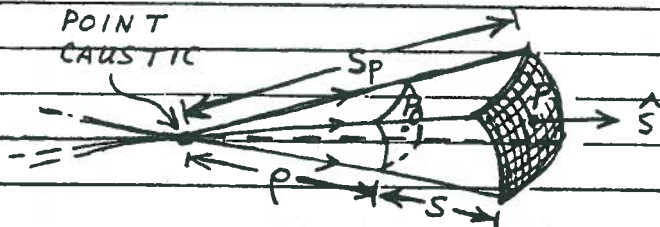
It is convenient to move the reference point  $P_0$  to the caustic (center of curvature), whose distance  $\rho$  must now be set equal to zero. Thus,

$$E(P) = \lim_{\rho \rightarrow 0} \bar{E}(P_0) \cdot \rho \cdot \frac{e^{-jk s}}{s_p} ; \begin{matrix} s \rightarrow s_p \\ \text{as } \rho \rightarrow 0 \end{matrix}$$

Since  $\bar{E}(P_0) \rightarrow \infty$  if  $\rho \rightarrow 0$ , and since  $\bar{E}(P)$  should be independent of the choice of  $P_0$  as long as  $P$  is not at or near a caustic, it follows that

$$\lim_{\rho \rightarrow 0} \bar{E}(P_0) \cdot \rho \text{ exists } \& \equiv \bar{B}_0$$

$$\therefore \left. \begin{aligned} \bar{E}(P) &= \bar{B}_0 \frac{e^{-jk s}}{s_p} \\ \bar{E} \cdot \hat{s} &= 0 \end{aligned} \right\} \Rightarrow \text{SPHERICAL WAVE}$$



The field of a point source is  $\propto \frac{\bar{C}_0}{s_p} e^{-jk s} + O\left(\frac{1}{s_p^2}\right)$

$$\sim \frac{\bar{C}_0}{s_p} e^{-jk s} \quad (ks_p \gg 1) \quad \leftarrow \text{SPHERICAL WAVE}$$

It is clear from the above limiting cases that plane, cylindrical (& also conical) & spherical waves are special cases of the more general ASTIGMATIC RAY OPTICAL FIELD:

$$\bar{E}(P) \sim \bar{E}(P_0) \sqrt{\frac{\rho_1 \rho_2}{(\rho_1 + s)(\rho_2 + s)}} e^{-jk s}$$

GO for inhomogeneous media:

$$(\nabla^2 + k^2) u = 0 \quad ; \quad k^2 = n^2 k_0^2 \quad ; \quad n = \frac{c}{v} \quad \text{REFRACTIVE INDEX}$$

$$u = \begin{cases} E_i \\ H_i \end{cases} \quad ; \quad i \Rightarrow x, y \text{ or } z.$$

$v =$  velocity of wave in the medium

$$k_0^2 = \omega^2 \mu_0 \epsilon_0 = \frac{\omega^2}{c^2} \quad ; \quad (\mu_0, \epsilon_0) \Rightarrow \text{free space parameters}$$

Let  $u(\vec{r}) \sim A e^{-jk_0 \psi}$  in the wave eqn.

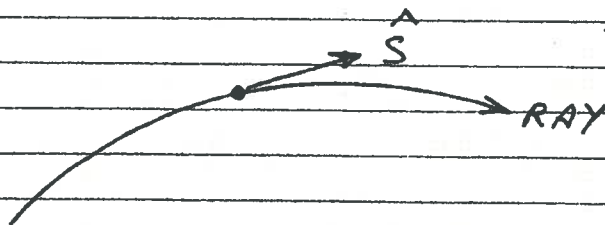
$$k_0^2 (n^2 - |\nabla \psi|^2) - j k_0 (\nabla^2 \psi + 2 \nabla \psi \cdot \frac{\nabla A}{A}) + \frac{\nabla^2 A}{A} = 0$$

$\rightarrow$  neglect (lower order in  $k_0$ ).

$$\therefore \left. \begin{aligned} |\nabla \psi|^2 &= n^2 \\ \nabla \psi \cdot \frac{\nabla A}{A} + \frac{1}{2} \nabla^2 \psi &= 0 \end{aligned} \right\} \begin{array}{l} \text{EIKONAL} \\ \text{TRANSPORT EQNS.} \end{array}$$

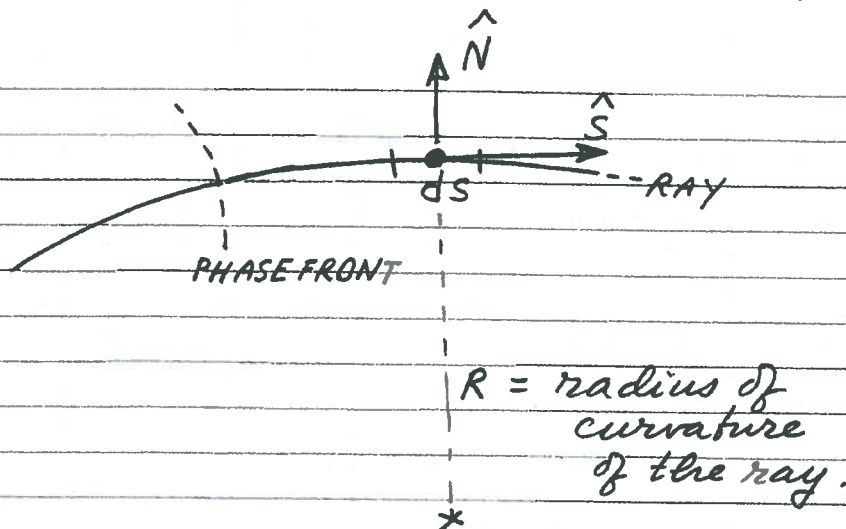
NOTE:  $v$  and  $n$  depend on  $\vec{r}$ .

$$|\nabla \psi| = n \quad \rightarrow \quad \nabla \psi = n \hat{s}$$



(Inhomogeneous, isotropic medium)

60-11



$$\frac{d\hat{S}}{ds} = \frac{\hat{N}}{R} \quad ; \quad \text{ie, } (\hat{S} \cdot \nabla) \hat{S} = \frac{\hat{N}}{R}$$

$$\text{or} \quad -\hat{S} \times \nabla \times \hat{S} = \frac{\hat{N}}{R}$$

$$-\hat{N} \cdot (\hat{S} \times \nabla \times \hat{S}) = \frac{1}{R}$$

$$-(\hat{N} \times \hat{S}) \cdot (\nabla \times \hat{S}) = \frac{1}{R}$$

$$-(\hat{N} \times \hat{S}) \cdot (\nabla \times \left[ \frac{\nabla \psi}{n} \right]) = \frac{1}{R}$$

$$-(\hat{N} \times \hat{S}) \cdot \left( \nabla \frac{1}{n} \times \nabla \psi \right) = \frac{1}{R}$$

$$-(\hat{N} \times \hat{S}) \cdot \left( -\frac{1}{n} \nabla [\ln n] \times n \hat{S} \right) = \frac{1}{R}$$

$$\hat{N} \cdot \nabla (\ln n) = \frac{1}{R}$$

$\therefore$  RAY bends toward regions of higher refractive index

Alternatively:

For a linearly polarized wave, let the electric field be

$$\bar{E}(\bar{r}) \sim \underbrace{\bar{A}(\bar{r})}_{\text{slowly varying}} e^{-j \underbrace{k_0 S}_{\text{fast varying}}} \quad (S \text{ is like } \psi \text{ of page GO-11}).$$

(for large  $k_0 \equiv \frac{\omega}{c}$ ).

Thus,  $\bar{E}(\bar{r}, t) = \text{Re } \bar{A}(\bar{r}) e^{-j \frac{\omega}{c} (S - ct)}$

To move with the propagating wavefront surface  $S$ , the time-phase must be kept constant relative to the motion. Thus,

Let  $\Phi(\bar{r}, t) \equiv S(\bar{r}) - ct = \text{constant}$

At  $t = 0$  (initial time);  $\Phi = S - 0 \equiv S_0$  (constant)  
 Hence

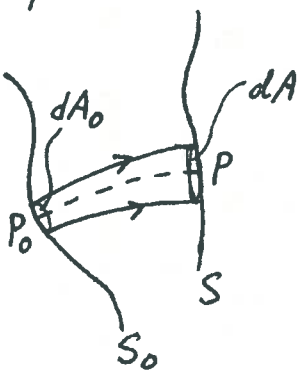
$$\frac{d\Phi}{dt} = 0, \text{ or } \frac{d\Phi}{dt} = \nabla S \cdot \frac{d\bar{r}}{dt} + \frac{\partial \Phi}{\partial t} = \nabla S \cdot \bar{v} - c$$

Note:  $\frac{d\bar{r}}{dt} \equiv \bar{v}$ ;  $\nabla S = |\nabla S| \hat{n}$

Based on the GO postulate, rays  $\perp S$  and ray velocity is  $\bar{v}$ ; hence  $\bar{v} = \hat{n} v$  ( $\because \hat{n} \perp \text{wavefront}$ ). Finally

$$0 = |\nabla S| \hat{n} \cdot \bar{v} - c \rightarrow |\nabla S| = \frac{c}{v} \quad (\text{EIKONAL equation})$$

$$\left. \begin{array}{l} \text{Plane wave} \Rightarrow S = \frac{1}{k_0} [k_x x + k_y y + k_z z] = \frac{\bar{k}_0 \cdot \bar{r}}{k_0} \\ \text{Spherical wave} \Rightarrow S = \frac{k}{k_0} [\sqrt{x^2 + y^2 + z^2}] = \frac{k r}{k_0} \end{array} \right\}$$



$\Rightarrow$  CONSERVATION OF POWER IN GO RAY TUBE:

$$\sqrt{\epsilon_r(P_0)} |\bar{E}(P_0)|^2 dA_0 = \sqrt{\epsilon_r(P)} |\bar{E}(P)|^2 dA$$

if  $p = p_0$

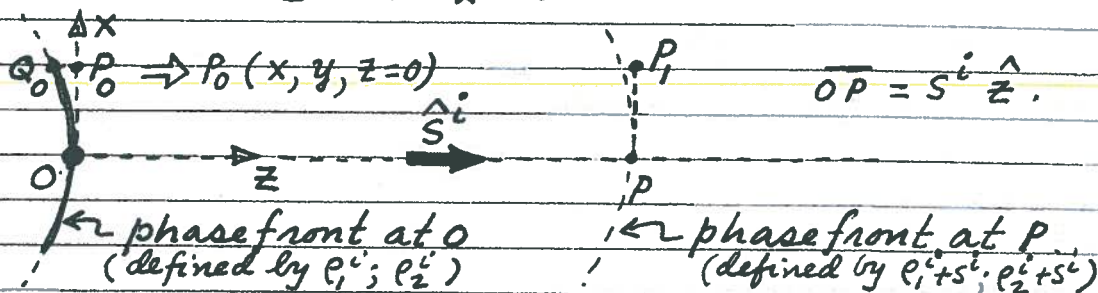
(Note:  $\frac{1}{2Z(P_0)} |\bar{E}(P_0)|^2 dA_0 = \frac{1}{2Z(P)} |\bar{E}(P)|^2 dA$ ).

# Geometrical Optics (GO) Fields.

## 1. Incident Field :

The incident GO electric field  $\vec{E}^i(P)$  is given in terms of its initial value at  $O$  by the expression :

$$\vec{E}^i(P) \sim \vec{E}^i(O) \sqrt{\frac{\rho_1^i \rho_2^i}{(\rho_1^i + s^i)(\rho_2^i + s^i)}} e^{-jks^i}$$



The phase of the field at  $P_0 =$  phase at  $O$  + phase delay from  $Q_0$  to  $P_0$ .

$$= 0 + \underbrace{(\text{delay})}_{\text{delay}} = 0 + k \left[ -\frac{1}{2} \left( \frac{x^2}{\rho_1^i} + \frac{y^2}{\rho_2^i} \right) \right] = + \frac{k}{2} \left[ \frac{x^2}{\rho_1^i} + \frac{y^2}{\rho_2^i} \right]$$

The phase at any point  $(x, y, z = s^i)$  where  $x$  &  $y$  are small is likewise given by  $k\psi^i$  where

$$k\psi^i \approx \underbrace{(ks^i)}_{\text{phase at } s^i} + \frac{k}{2} \left[ \frac{x^2}{\rho_1^i + s^i} + \frac{y^2}{\rho_2^i + s^i} \right] \underbrace{(\text{additional delay})}_{\text{additional delay}}$$

Let  $[t_i] \equiv \begin{bmatrix} x \\ y \end{bmatrix}$  ;  $Q^i(0) \equiv \begin{bmatrix} \frac{1}{\rho_1^i} & 0 \\ 0 & \frac{1}{\rho_2^i} \end{bmatrix}$  ;  $Q^i(s^i) = \begin{bmatrix} \frac{1}{\rho_1^i + s^i} & 0 \\ 0 & \frac{1}{\rho_2^i + s^i} \end{bmatrix}$

Then

$$\vec{E}^i(P_i) \sim \vec{E}^i(0) \sqrt{\frac{\det \dot{Q}^i(s^i)}{\det \dot{Q}^i(0)}} e^{-jk\psi^i}$$

or

$$\vec{E}^i(P_i) \sim \vec{E}^i(0) \sqrt{\frac{\det \dot{Q}^i(s^i)}{\det \dot{Q}^i(0)}} e^{-jk\left(s^i + [t_i]^T \frac{\dot{Q}^i(s^i)}{2} [t_i]\right)}$$

where  $\det \dot{Q}^i(0) = \frac{1}{\rho_1^i \rho_2^i}$ ,  $\det \dot{Q}^i(s^i) = \frac{1}{\rho_1^i + s^i} \cdot \frac{1}{\rho_2^i + s^i}$

in which  $\det \Rightarrow$  determinant.

$$\text{Tr } \dot{Q}^i(0) \equiv \text{Trace of } \dot{Q}^i(0) = \frac{1}{\rho_1^i} + \frac{1}{\rho_2^i}$$

Note that:  $\dot{Q}^i(s^i) = \dot{Q}^i(0) + s^i I$ ;  $I \equiv \begin{bmatrix} 1 & 0 \\ 0 & 1 \end{bmatrix}$ .

Clearly  $Z = -\frac{1}{2} \left( \frac{x^2}{\rho_1^i} + \frac{y^2}{\rho_2^i} \right)$ , which describes

the equiphase (phasefront) surface at and near

0 is such that  $x$  and  $y$  are the principal

surface directions at 0. It is for this reason

that there are no cross terms (i.e.  $xy$  terms)

in this surface description. If one were to

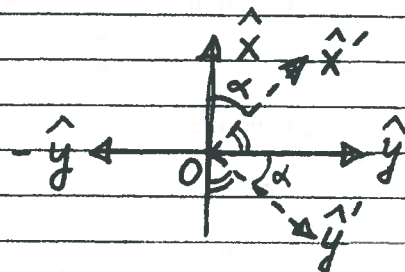
use a different coordinate system  $(x', y', z)$

at 0 where

$$[t_i] \equiv \begin{bmatrix} x' \\ y' \end{bmatrix}$$

and

$$[t_i] = T [t_i]$$



$$\text{ie } \begin{bmatrix} x \\ y \end{bmatrix} = \begin{bmatrix} T_{11} & T_{12} \\ T_{21} & T_{22} \end{bmatrix} \begin{bmatrix} x' \\ y' \end{bmatrix}$$

$$\text{then: } \begin{cases} x = x' \cos \alpha - y' \sin \alpha \\ y = x' \sin \alpha + y' \cos \alpha \end{cases} \Rightarrow \begin{bmatrix} x \\ y \end{bmatrix} = \begin{bmatrix} \cos \alpha & -\sin \alpha \\ \sin \alpha & \cos \alpha \end{bmatrix} \begin{bmatrix} x' \\ y' \end{bmatrix}$$

$$\text{Thus, } T = \begin{bmatrix} T_{11} & T_{12} \\ T_{21} & T_{22} \end{bmatrix} = \begin{bmatrix} \cos \alpha & -\sin \alpha \\ \sin \alpha & \cos \alpha \end{bmatrix} = \begin{bmatrix} \hat{x} \cdot \hat{x}' & \hat{x} \cdot \hat{y}' \\ \hat{y} \cdot \hat{x}' & \hat{y} \cdot \hat{y}' \end{bmatrix}$$

Also,  $T^{-1} = T^T$ , where  $T \Rightarrow$  TRANSPOSE.

Therefore,  $\bar{E}^i(P_1)$  in the  $(x', y', z)$  system is:

$$\bar{E}^i(P_1) \sim \bar{E}^i(O) \sqrt{\frac{\rho_1^i \rho_2^i}{(\rho_1^i + s^i)(\rho_2^i + s^i)}} e^{-jk(s^i + \{T[\tilde{t}_i]\}^T Q(s^i) \{T[\tilde{t}_i]\})}$$

$$\text{ie } \bar{E}^i(P_1) \sim \bar{E}^i(O) \sqrt{\frac{\rho_1^i \rho_2^i}{(\rho_1^i + s^i)(\rho_2^i + s^i)}} e^{-jk(s^i + [\tilde{t}_i]^T T^T Q(s^i) T [\tilde{t}_i])}$$

$\therefore [AB]^T = B^T A^T$ . Also, let

$$\tilde{Q}^i(s^i) \equiv T^T Q^i(s^i) T = \begin{bmatrix} \tilde{Q}_{11}^i(s^i) & \tilde{Q}_{12}^i(s^i) \\ \tilde{Q}_{21}^i(s^i) & \tilde{Q}_{22}^i(s^i) \end{bmatrix}$$

Note that  $\tilde{Q}_{12}^i(s^i)$  and  $\tilde{Q}_{21}^i(s^i)$  are non-zero, so  $\tilde{Q}^i(s^i)$  is NOT a diagonal matrix, implying that  $(\hat{x}', \hat{y}')$  are NOT principal directions of the phasefront at O. Since

$Q^i(s^i) = Q^i(0) + s^i I$   
it follows that:

$$\tilde{Q}^i(s^i) = \tilde{Q}^i(0) + s^i I$$

Since  $\tilde{Q}^i = T^T Q^i T \Rightarrow \tilde{Q}^{i-1} = (T^T Q^i T)^{-1} = T^{-1} (T^T Q^i)^{-1}$

and because  $T^T = T^{-1}$ ,  $\tilde{Q}^{i-1} = T^{-1} Q^{i-1} (T^T)^{-1}$   
 $\tilde{Q}^{-1} = T^T Q^{-1} T$

$$\therefore T^T \tilde{Q}^{i-1}(s^i) T = T^T \tilde{Q}^{i-1}(0) T + s^i T^T I T$$

or  $\tilde{Q}^{i-1}(s^i) = \tilde{Q}^{i-1}(0) + s^i I$

Furthermore,  $\det \tilde{Q}^i = \det T^T \cdot \det Q^i \cdot \det T$

$$= \det Q^i \cdot \det T^T \cdot \det T$$

$$= \det Q^i \cdot \det (T^T T) = \det Q^i$$

ie,  $\det \tilde{Q}^i = \det Q^i$

As a result of the above development:

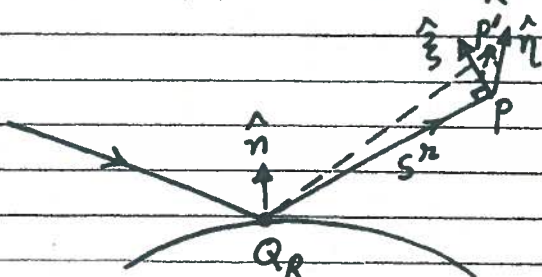
$$\vec{E}^i(P_i) \sim \vec{E}^i(0) \sqrt{\frac{\det \tilde{Q}^i(s^i)}{\det \tilde{Q}^i(0)}} e^{-jk[s^i + [\hat{t}_i]^T \tilde{Q}^i(s^i) \hat{t}_i]}$$

Note:  $\frac{1}{\rho_i} = \frac{1}{2} [T_{xx} \tilde{Q}^i(0) \pm \sqrt{\{T_{xx} \tilde{Q}^i(0)\}^2 - 4 \det \tilde{Q}^i(0)}]$

## 2. Reflected Field:

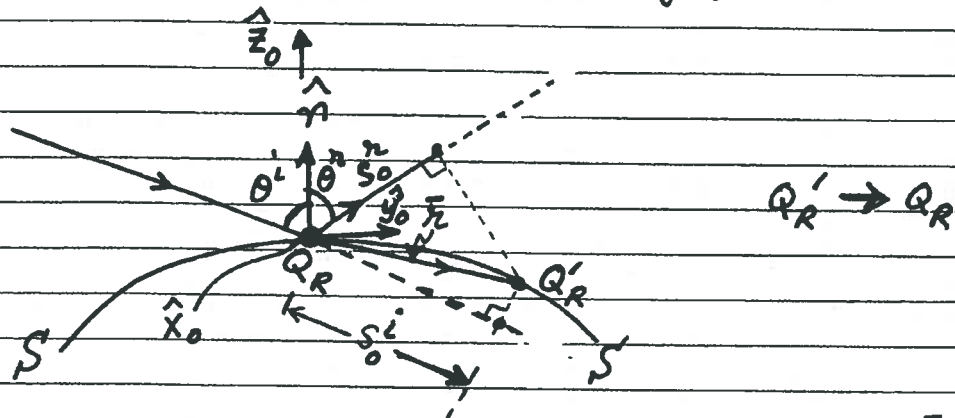
The reflected GO electric field  $\vec{E}^r(P)$  can be expressed like the incident GO field as

$$\vec{E}^r(P) \sim \vec{E}^r(Q_R) \cdot \sqrt{\frac{\det \tilde{Q}^r(s^r)}{\det \tilde{Q}^r(Q_R)}} e^{-jk[s^r + [\hat{t}_r]^T \tilde{Q}^r(s^r) \hat{t}_r]}$$



$$[\tilde{t}_r] = \begin{bmatrix} \xi \\ \eta \end{bmatrix}$$

### Reflection of a GO ray pencil :



$$\bar{E}^i(Q_R') \sim \bar{E}^i(Q_R) \cdot \sqrt{\frac{\det \tilde{Q}^i(s_0^i)}{\det \tilde{Q}^i(Q_R)}} e^{-jk(s_0^i + [\hat{t}_i]^T \tilde{Q}^i(s_0^i) [\hat{t}_i]) / 2}$$

$$\bar{E}^r(Q_R') \sim \bar{E}^r(Q_R) \cdot \sqrt{\frac{\det \tilde{Q}^r(s_0^r)}{\det \tilde{Q}^r(Q_R)}} e^{-jk(s_0^r + [\hat{t}_r]^T \tilde{Q}^r(s_0^r) [\hat{t}_r]) / 2}$$

$\hat{n} \times (\bar{E}^i + \bar{E}^r) \Big|_{Q_R}$  is given. Enforcing this boundary condition yields as  $Q_R' \rightarrow Q_R$  :

$$\bar{E}^r(Q_R) = \bar{R}(Q_R) \cdot \bar{E}^i(Q_R)$$

$$\bar{r} \Big|_S \text{ (at } Q_R') = x_0 \hat{x}_0 + y_0 \hat{y}_0 + z_0 \hat{z}_0 \approx x_0 \hat{x}_0 + y_0 \hat{y}_0 + \frac{\hat{z}_0}{2} [t_0]^T Q_S(Q_R) [t_0]$$

where  $[t_0] = \begin{bmatrix} x_0 \\ y_0 \end{bmatrix}$  ;  $Q_S(Q_R) = \begin{bmatrix} Q_{11} & Q_{12} \\ Q_{21} & Q_{22} \end{bmatrix}$

Note :  $s_0^i = \hat{n} \cdot \hat{s}_0^i$  ;  $s_0^r = \hat{n} \cdot \hat{s}_0^r$

A consequence of Snell's law is that the phase of the incident ray must be matched to the phase of the reflected ray at  $Q'_R$  (i.e.  $Q'_R$  as  $Q'_R \rightarrow Q_R$ ) on  $S$ . Thus,

$$\hat{S}_0^i \cdot (x_0 \hat{x}_0 + y_0 \hat{y}_0 + \hat{z}_0 \left\{ \frac{-1}{2} \right\} [t_0]^T Q_S(Q'_R) [t_0]) + \frac{1}{2} [\tilde{t}_i]^T \tilde{Q}^i(s_0^i) [\tilde{t}_i] \\ \approx \hat{S}_0^r \cdot (x_0 \hat{x}_0 + y_0 \hat{y}_0 + \hat{z}_0 \left\{ \frac{-1}{2} \right\} [t_0]^T Q_S(Q'_R) [t_0]) + \frac{1}{2} [\tilde{t}_r]^T \tilde{Q}^r(s_0^r) [\tilde{t}_r]$$

Matching first only the linear phase terms yields:

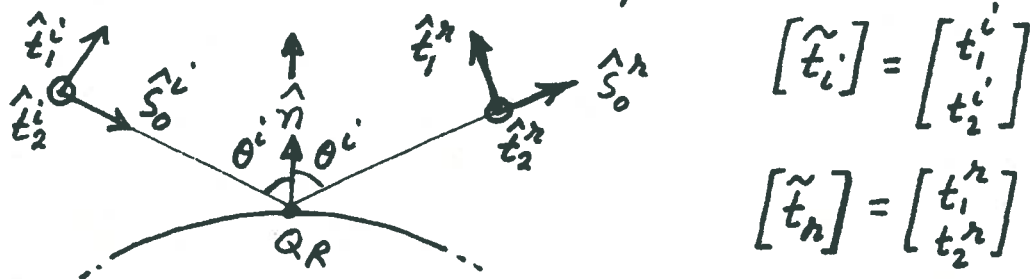
$$\hat{S}_0^i \cdot \hat{x}_0 = \hat{S}_0^r \cdot \hat{x}_0 \quad ; \quad \hat{S}_0^i \cdot \hat{y}_0 = \hat{S}_0^r \cdot \hat{y}_0 \quad ; \quad Q'_R \rightarrow Q_R$$

$$\text{det } \hat{S}_0^i = -\cos \theta^i \hat{z}_0 + \sin \theta^i \hat{y}_0$$

$$\{ \hat{S}_0^r = +\cos \theta^r \hat{z}_0 + \sin \theta^r \hat{y}_0$$

$$\therefore \sin \theta^i = \sin \theta^r \quad \rightarrow \quad \theta^i = \theta^r \quad ; \quad Q'_R \rightarrow Q_R$$

Let  $[\tilde{t}_i]$  and  $[\tilde{t}_r]$  be expressed in terms of  $[t_0]$



$$\therefore [\tilde{t}_i] = T_i [t_0] \quad ; \quad [\tilde{t}_r] = T_r [t_0] \quad \hat{n} = \hat{z}_0$$

$$T_i = \begin{bmatrix} 0 & \cos \theta^i \\ 1 & 0 \end{bmatrix} \quad ; \quad T_r = \begin{bmatrix} 0 & -\cos \theta^r \\ 1 & 0 \end{bmatrix}$$

Next, matching the quadratic phase terms yield

$$-\frac{\cos\theta^i}{2} [t_0]^T Q_S(Q_R) [t_0] + \frac{1}{2} [t_0]^T T_i^T \tilde{Q}^i(Q_R) T_i [t_0]$$

$$\approx -\frac{+\cos\theta^i}{2} [t_0]^T Q_S(Q_R) [t_0] + \frac{1}{2} [t_0]^T T_R^T \tilde{Q}^R(Q_R) T_R [t_0]; Q_R^i \rightarrow Q_R.$$

$$\text{i.e. } 2\cos\theta^i Q_S(Q_R) + T_i^T \tilde{Q}^i(Q_R) T_i = T_R^T \tilde{Q}^R(Q_R) T_R.$$

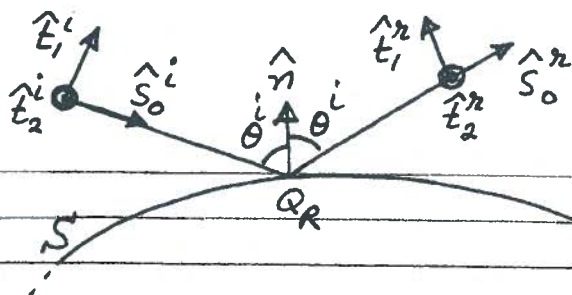
Clearly, one can now find  $\rho_{1,2}^R$  from  $\tilde{Q}^R(Q_R)$  which is now known in terms of  $Q_S(Q_R)$  &  $\tilde{Q}^i(Q_R)$ ; this can be achieved by diagonalizing  $\tilde{Q}^R(Q_R)$ .

Also, one may view  $\frac{1}{\rho_{1,2}^R}$  as the eigenvalues of  $\tilde{Q}^R(Q_R)$  and the principal directions of the reflected wavefront at  $Q_R$  then correspond to the eigenvectors.

Note:

$$\frac{1}{\rho_{1,2}^R} = \frac{1}{2} \left[ \text{Tr} \tilde{Q}^R(Q_R) \pm \sqrt{\{\text{Tr} \tilde{Q}^R(Q_R)\}^2 - 4 \det \tilde{Q}^R(Q_R)} \right]$$

- \* Exercise: Find  $(\rho_{1,2}^R)^{-1}$  explicitly in terms of,  $\theta^i$ ,  $(\rho_{1,2}^i)^{-1}$  and the principal surface curvatures  $\frac{1}{R_{1,2}}$ .
- \* Find the principal directions of the reflected wave.



In the transformations at the bottom of pg GO-6 it is important to note that  $(\hat{t}_1^i; \hat{t}_1^r)$  lie in the plane of incidence defined by  $(\hat{s}_0^i; \hat{n})$  whereas  $(\hat{t}_2^i; \hat{t}_2^r)$  lie  $\perp$  the plane of incidence. This choice is convenient because it provides relatively simple  $T_i$  and  $T_r$ , and it provides a diagonal form of  $\bar{R}$  for a given surface impedance at  $Q_R$ :

$$\bar{R}(Q_R) = \hat{t}_1^i \hat{t}_1^r R_{||} + \hat{t}_2^i \hat{t}_2^r R_{\perp}$$

Note that:  $Z_0 \vec{H}^{i,r} \sim \hat{s}_0^{i,r} \times \vec{E}^{i,r}$  along the incident/reflected ray.

3-D  $\Rightarrow$  2-D: The 2-D solution can be

obtained from 3-D by letting  $\rho_2^{i,r} \rightarrow \infty$  and  $\rho_1^{i,r} \triangleq \rho^{i,r}$ . Thus:

$$\left. \begin{aligned} \vec{E}^i(P) &\sim \vec{E}^i(Q_R) \sqrt{\frac{\rho^i}{\rho^i + s^i}} e^{-jks^i} \\ \vec{E}^r(P_R) &\sim \vec{E}^r(Q_R) \cdot \bar{R} \sqrt{\frac{\rho^r}{\rho^r + s^r}} e^{-jks^r} \end{aligned} \right\} \text{2-D}$$

## RAY METHODS & SOME APPLICATIONS (cont.)

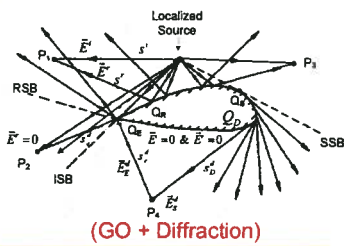
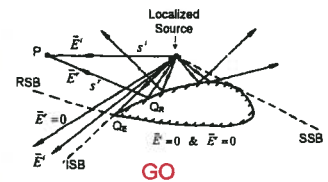
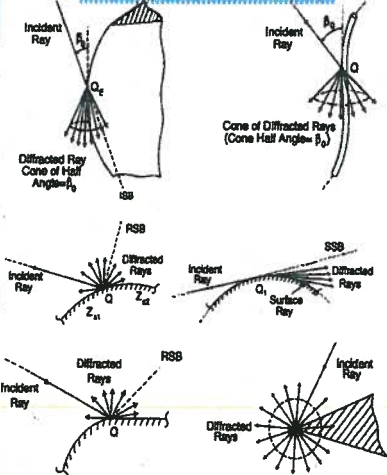
- Keller and coworkers (1958; 1962) introduced a **new** class of rays, i.e. diffracted rays, to describe diffraction in his geometrical theory of diffraction (GTD).
- Diffracted rays exist in addition to geometrical optics (GO) rays.
- Diffracted rays are produced at structural and material discontinuities, as well as at grazing incidence on a smooth convex surface.



ElectroScience LABORATORY

3

### Examples of diffraction



$$\vec{E}_c^d(P_2, P_4) \sim \vec{E}^i(Q_E) \cdot D_E f(s_c^d) e^{-jk s_c^d}$$

$$\vec{E}_s^d(P_4) \sim \vec{E}^i(Q_S) \cdot T(Q_S, Q_D) f(s_D^d) e^{-jk s_D^d}$$

## RAY METHODS & SOME APPLICATIONS (cont.)



ElectroScience LABORATORY

4

- To find  $\bar{D}$  and  $\bar{T}$ , etc, in diffraction problems, one may:
  - (a) Solve appropriate, simpler canonical problems which model the LOCAL geometrical and electrical properties of the original surface in the neighborhood of diffraction points.
  - (b) An exact (or sometimes approximate) solution to a canonical problem is first expressed as an integral containing an exponent  $\kappa D$ 

$$\kappa = \text{wave number} = \frac{2\pi}{\lambda}$$

$$D = \text{characteristic dimension}$$
  - (c) Canonical integral is then evaluated asymptotically, generally in closed form, as parameter  $\kappa D$  becomes large (i.e. at HF).
  - (d)  $\bar{D}$  and  $\bar{T}$  are then typically found from (c) by inspection.
  - (e) Canonical  $\bar{D}$  and  $\bar{T}$  generalized to arbitrary shapes by invoking principle of locality of HF waves.
- Keller's original GTD is not valid at and near ISB, RSB, SSB (i.e. in SB transition regions).
  - UTD developed to patch Keller's original theory within the SB transition regions.
  - GTD corrects GO, and GTD = GO + diffraction
- UTD corrects GTD, but usually UTD  $\rightarrow$  GTD outside SB transition regions.

## RAY METHODS & SOME APPLICATIONS (cont.)

• **Additional Comments :**



ElectroScience  
LABORATORY

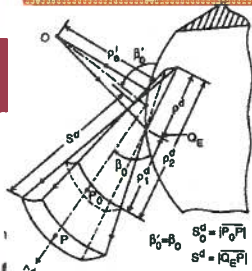
- (a) Ufimtsev's Physical Theory of Diffraction (PTD) (1950s) corrects Physical Optics (PO). PO contains incomplete diffraction.
- (b) PTD generally requires numerical integration on the radiating/scattering objects, hence, loses efficiency as frequency increases.
- (c) PTD does not describe creeping/surface wave diffraction on smooth convex objects; hence, does not accurately predict patterns in shadow zone of antennas on such complex objects.
- (d) Conventional numerical CEM methods become rapidly inefficient with increase in frequency.
- (e) In contrast, UTD ray paths remain independent of frequency.
- (f) UTD offers an analytical (generally closed form) solution to many complex problems that can not otherwise be solved in an analytical fashion.

5

## RAY METHODS & SOME APPLICATIONS (cont.)

• In many practical applications of UTD, the following diffraction ray mechanisms dominate

**(a) PEC Wedge Diffraction**



[1] R. G. Kouyoumjian and P. H. Pathak, "A uniform geometrical theory of diffraction for an edge in a perfectly conducting surface," *Proc. IEEE*, vol. 62, pp. 1448-1461, Nov. 1974.

**Alternative ray solutions (UAT)**

- [2] S. W. Lee and G. A. Deschamps, "A Uniform Asymptotic theory of EM diffraction by a curved wedge," *IEEE Trans. Antennas Propagat.*, vol. AP-24, pp. 25-34, Jan. 1976.
- [3] Borovikov, V.A. and Kimber B. Ye, "Some problems in the asymptotic theory of diffraction", *IEEE Proceedings*, volume 62, pp. 1416-1437, Nov. 1974.

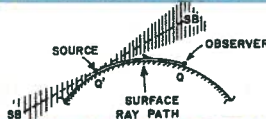
**(b) PEC Convex Surface Diffraction**



- [1] P.H Pathak, "An asymptotic analysis of the scattering of plane waves by a smooth convex cylinder," *Radio Science*, Vol 14 pp419-435, 1979
- [2] P.H Pathak et al., "A uniform GTD analysis of the diffraction of EM waves by a smooth convex surface," *IEEE Trans Ant and Prop.* Vol 8 Sept 1980.



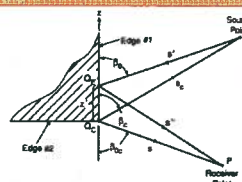
- [1] P.H Pathak et al., "A uniform GTD solution for the radiation from sources on a convex surface," *IEEE Trans Ant and Prop.* Vol 29 July 1981.



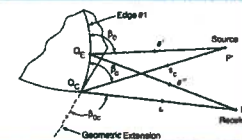
- [1] P.H Pathak and N. Wang, "Ray analysis of mutual coupling between antennas on a convex surface," *IEEE Trans Ant and Prop.* Vol 29 Nov 1981.

(Alt. Soln. by S.W. Lee in IEEE AP-S)

**(c) PEC Corner Diffraction**



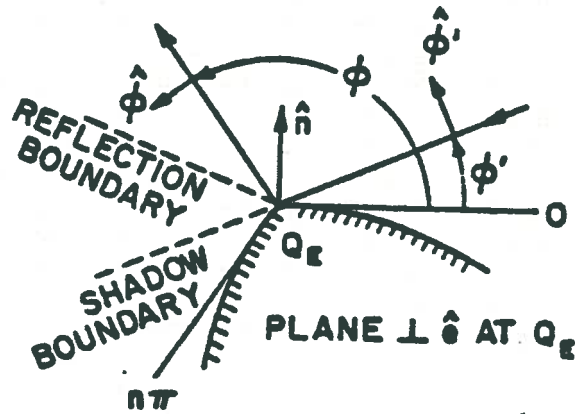
- [1] K.C Hill and P.H Pathak, "A UTD solution for EM diffraction by a corner in a plane angular sector," *IEEE Ant. Prop. Symp.* June 1991.
- [2] K. C. Hill, "A UTD solution to the EM scattering by the vertex of a perfectly conducting plane angular sector," Ph.D dissertation, The Ohio State University, 1990.



- [1] G. Carluccio, "A UTD Diffraction Coefficient for a Corner Formed by Truncation of Edges in an Otherwise Smooth Curved Surface," *IEEE Ant. Prop. Symp.* June 2008.

6



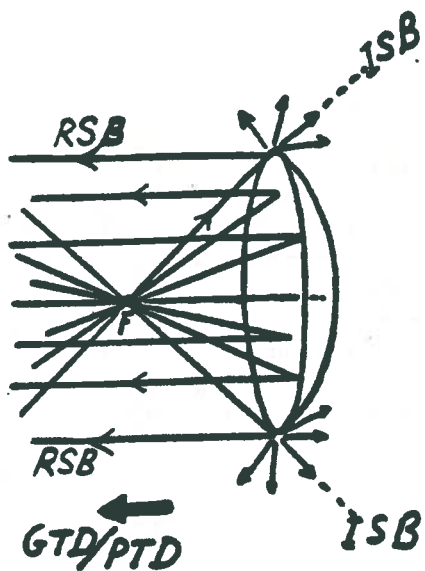


$$D_{es}^k = \frac{-e^{-j\frac{\pi}{4}}}{2n\sqrt{2\pi k} \sin\beta_0} \left[ \left\{ \cot\left(\frac{\pi+\beta^-}{2n}\right) + \cot\left(\frac{\pi-\beta^-}{2n}\right) \right\} \right. \\ \left. + \left\{ \cot\left(\frac{\pi+\beta^+}{2n}\right) + \cot\left(\frac{\pi-\beta^+}{2n}\right) \right\} \right]$$

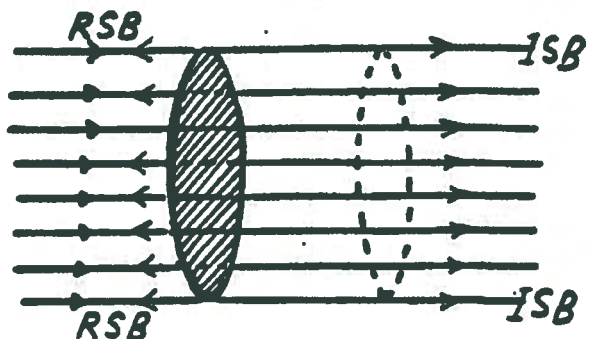
$$\beta^\mp = \phi \mp \phi'$$



SINGULARITIES OF GTD FIELDS.

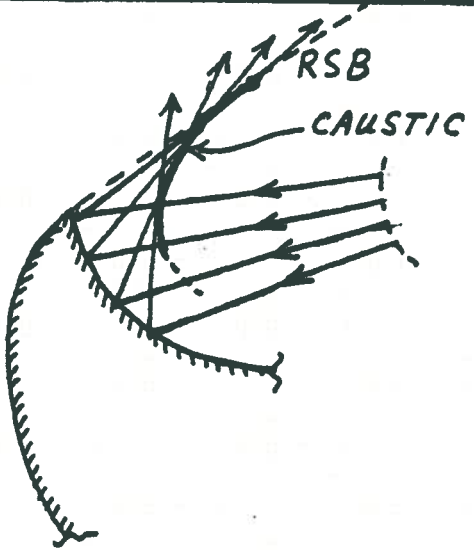
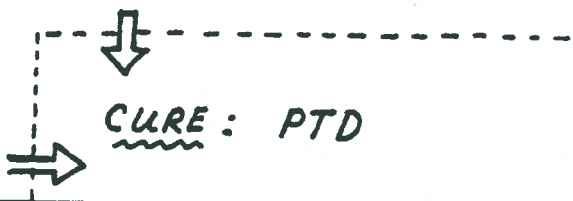


parabolic reflector



← GO REFLECTOR RAY CAUSTIC COINCIDES WITH DIFFRACTED RAY CAUSTIC AND RSB  
 → FORWARD SCATTER ALONG ISB.

← GO ray caustic coincides with diffracted ray caustic and RSB



Overlap of the CAUSTIC & RSB transition regions

CURE : UTD or UAT if observation point crosses RSB away from the caustic.

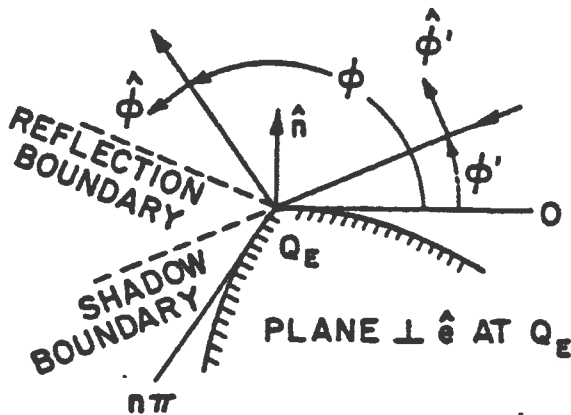
Across GO ray caustic one must use (incomplete) AIRY type transition functions.

## UNIFORM RAY THEORIES OF EDGE DIFFRACTION

- GTD fails within transition regions adjacent to shadow boundaries (SB's) of G.O. rays.
- To obtain a H.F. total field which is continuous across the ISB & RSB, one must depart from a ray-optical description of the GTD in the ISB, RSB transition zones.
- The above requirement (of departure from ray optic behaviour in transition regions) can be achieved by introducing special functions (or transition functions) in the manner of Sommerfelds  $\frac{1}{2}$  plane soln.
- Outside the SB transition regions one must recover back the GTD solution.
- A uniform solution which remains valid uniformly across SB transition regions where GTD fails, & which uniformly recovers the GTD outside these SB trans. regions is therefore important.

( Kouyoumjian & Pathak )

PROC. IEEE, Nov. '74, pp. 1448-1461.



$$D_{\substack{es \\ eh}} = \frac{-e^{-j\frac{\pi}{4}}}{2n\sqrt{2\pi k} \sin\beta_0} \cdot \left[ \cot\left(\frac{\pi+(\phi-\phi')}{2n}\right) F[kL^i a^+(\phi-\phi')] \right. \\ \left. + \cot\left(\frac{\pi-(\phi-\phi')}{2n}\right) F[kL^i a^-(\phi-\phi')] \right] \\ \mp \left\{ \cot\left(\frac{\pi+(\phi+\phi')}{2n}\right) F[kL^{rn} a^+(\phi+\phi')] + \cot\left(\frac{\pi-(\phi+\phi')}{2n}\right) F[kL^{ro} a^-(\phi+\phi')] \right\}$$

$$a^\pm(\beta) = 2 \cos^2\left(\frac{2n\pi N^\pm - \beta}{2}\right)$$

The  $N^\pm$  are integers which most nearly satisfy :

$$2\pi n N^\pm - \beta = \pm \pi$$

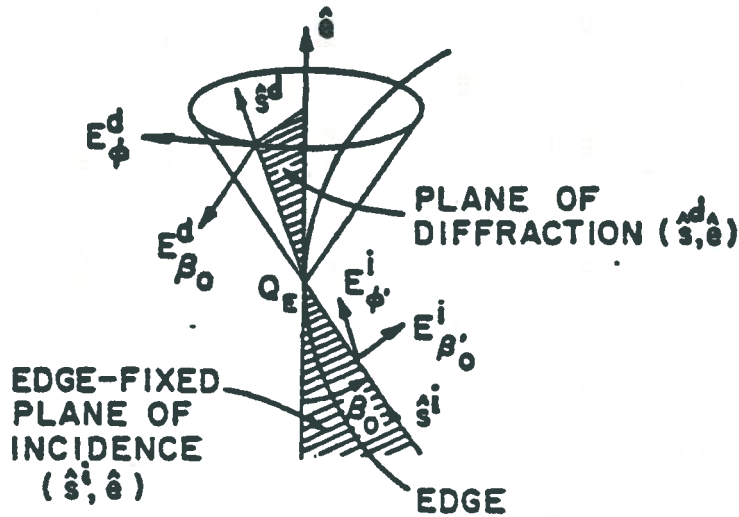
with

$$\beta = \phi \pm \phi'$$

(  $kL^i, rn, ro$  is the large parameter )

GTD  $\rightarrow$  edge diffraction

$$\bar{E}^d(P) \sim \bar{E}^i(Q) \cdot \bar{D}_e^k \sqrt{\frac{\rho_e}{s^d(\rho_e + s^d)}} e^{-jk s^d}$$



$$\hat{\beta}_0^i = \hat{s}^i \times \hat{\phi}^i \quad ; \quad \hat{\beta}_0^d = \hat{s}^d \times \hat{\phi}^d$$

$$\bar{E}^i(Q_E) = \hat{\beta}_0^i E_{\beta_0}^i + \hat{\phi}^i E_{\phi}^i$$

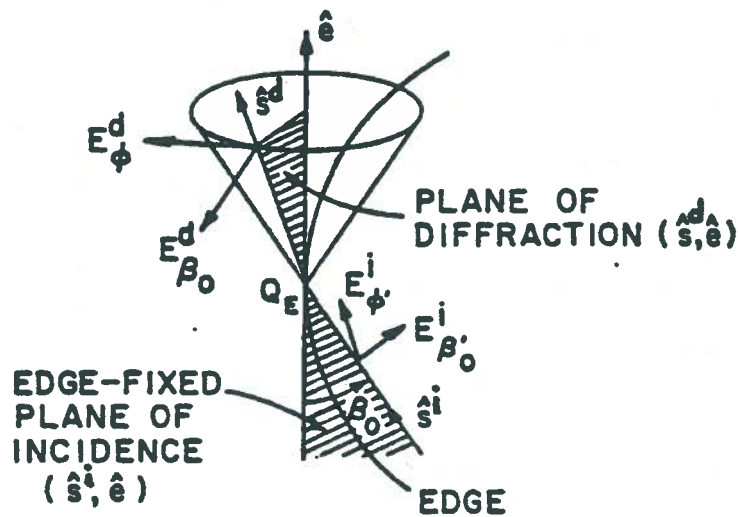
$$\bar{E}^d(P) = \hat{\beta}_0^d E_{\beta_0}^d + \hat{\phi}^d E_{\phi}^d$$

$$\bar{D}_e^k = -\hat{\beta}_0^i \hat{\beta}_0^d D_{es}^k - \hat{\phi}^i \hat{\phi}^d D_{eh}^k \quad (\text{PEC wedge})$$

$$\begin{bmatrix} E_{\beta_0}^d \\ E_{\phi}^d \end{bmatrix} = \begin{bmatrix} -D_{es}^k & 0 \\ 0 & -D_{eh}^k \end{bmatrix} \begin{bmatrix} E_{\beta_0}^i \\ E_{\phi}^i \end{bmatrix} \sqrt{\frac{\rho_e}{s^d(\rho_e + s^d)}} e^{-jk s^d}$$

UTD  $\rightarrow$  edge diffraction

$$\bar{E}^d(P) \sim \bar{E}^i(Q) \cdot \bar{D}_e \sqrt{\frac{\rho_e}{s^d(\rho_e + s^d)}} e^{-jk s^d}$$



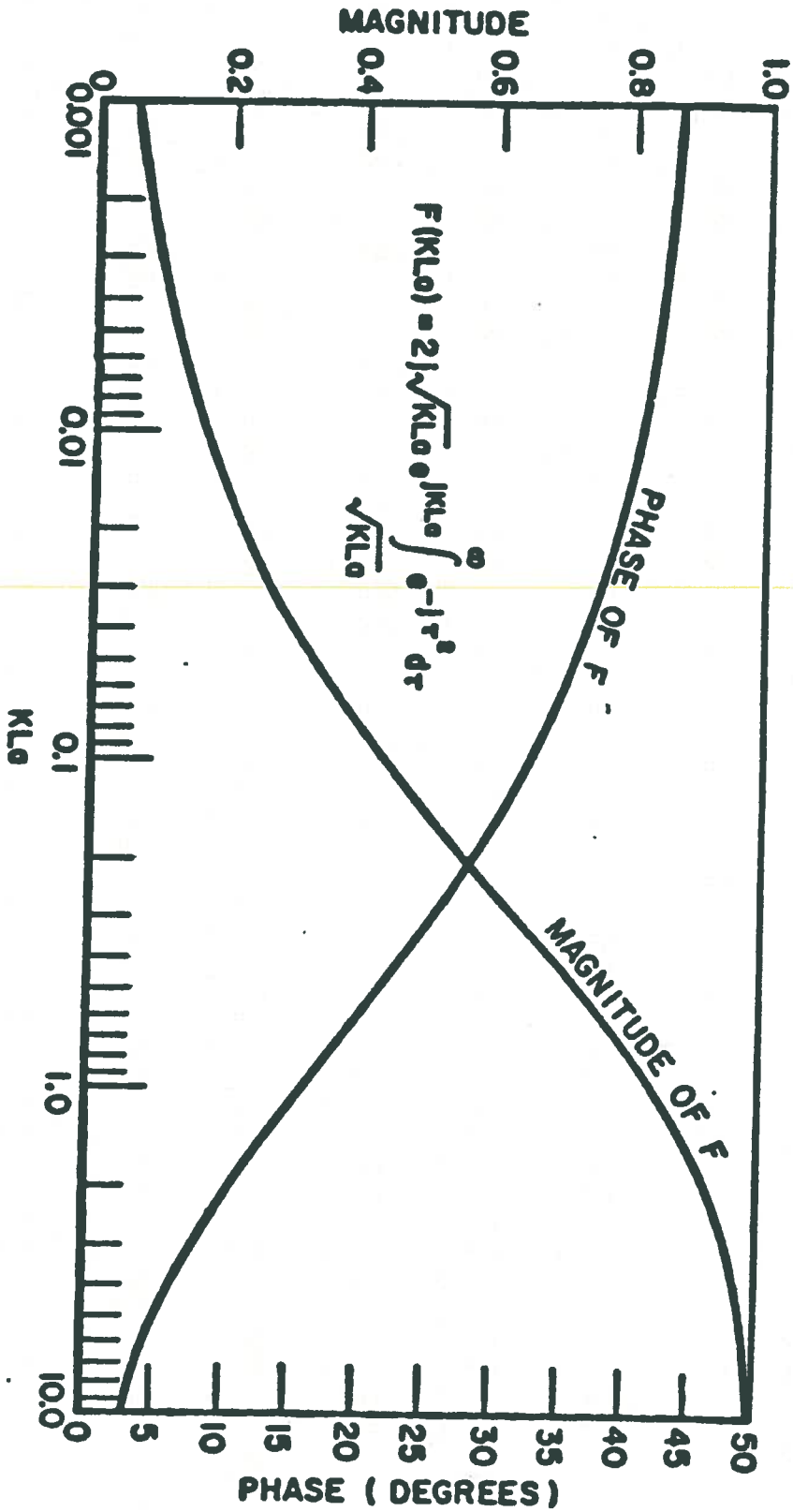
$$\hat{\beta}_0' = \hat{s}^i \times \hat{\phi}' \quad ; \quad \hat{\beta}_0 = \hat{s}^d \times \hat{\phi}$$

$$\bar{E}^i(Q_E) = \hat{\beta}_0' E_{\beta_0'}^i + \hat{\phi}' E_{\phi'}^i$$

$$\bar{E}^d(P) = \hat{\beta}_0 E_{\beta_0}^d + \hat{\phi} E_{\phi}^d$$

$$\bar{D}_e = -\hat{\beta}_0' \hat{\beta}_0 D_{es} - \hat{\phi}' \hat{\phi} D_{eh} \quad (\text{PEC wedge})$$

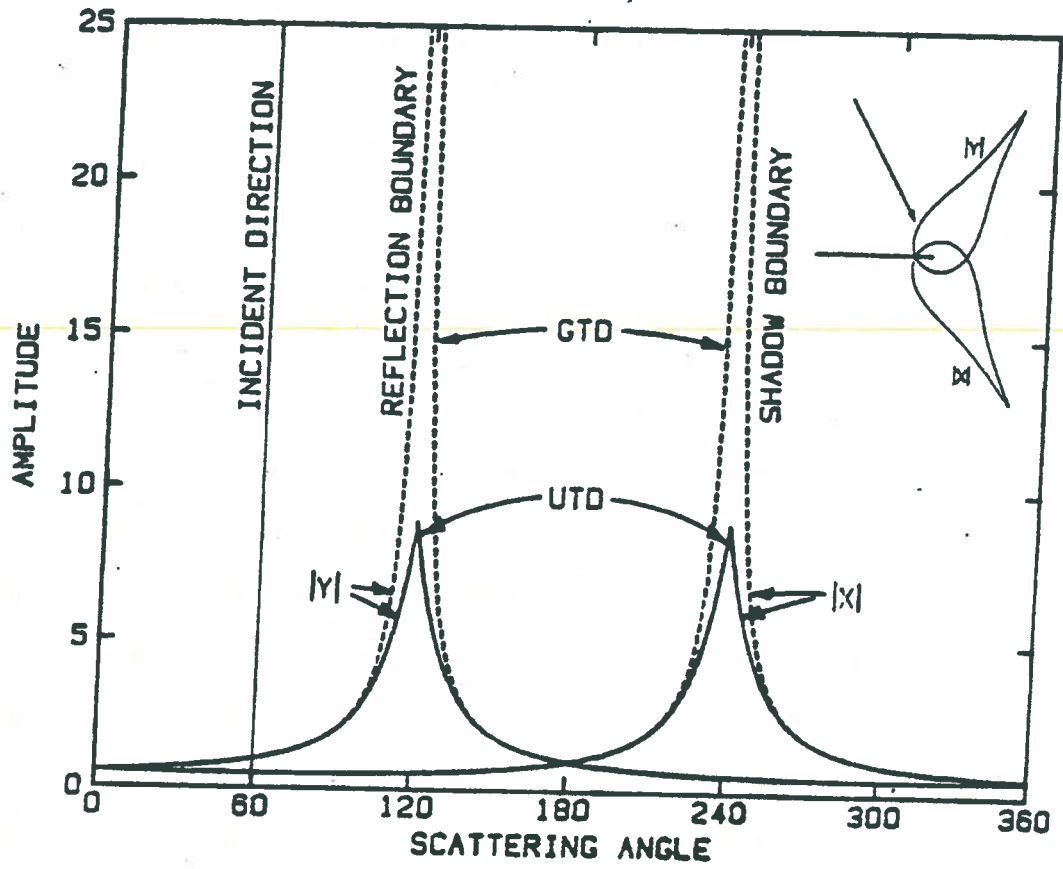
$$\begin{bmatrix} E_{\beta_0}^d \\ E_{\phi}^d \end{bmatrix} = \begin{bmatrix} -D_{es} & 0 \\ 0 & -D_{eh} \end{bmatrix} \begin{bmatrix} E_{\beta_0'}^i \\ E_{\phi'}^i \end{bmatrix} \sqrt{\frac{\rho_e}{s^d(\rho_e + s^d)}} e^{-jk s^d}$$

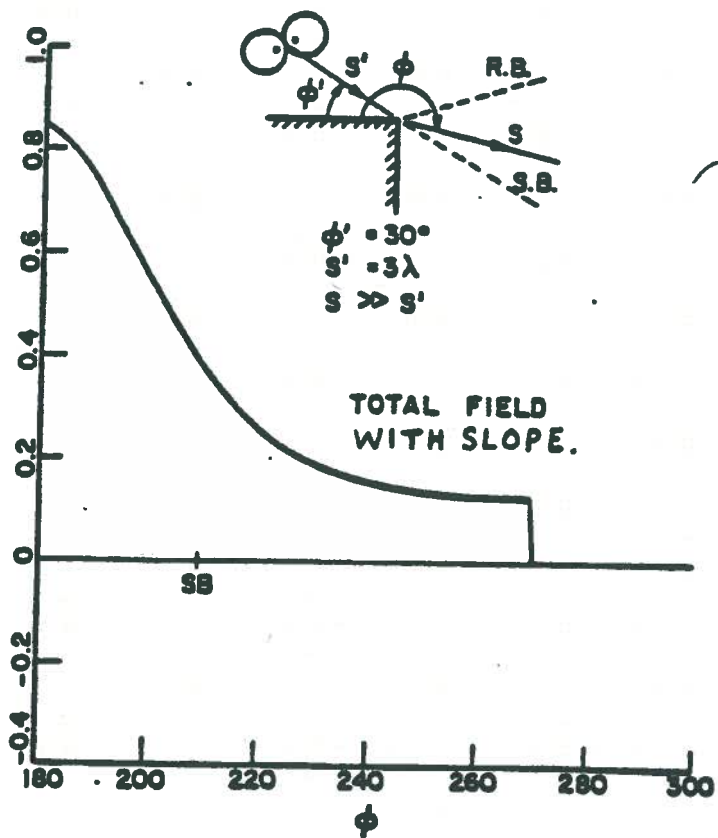
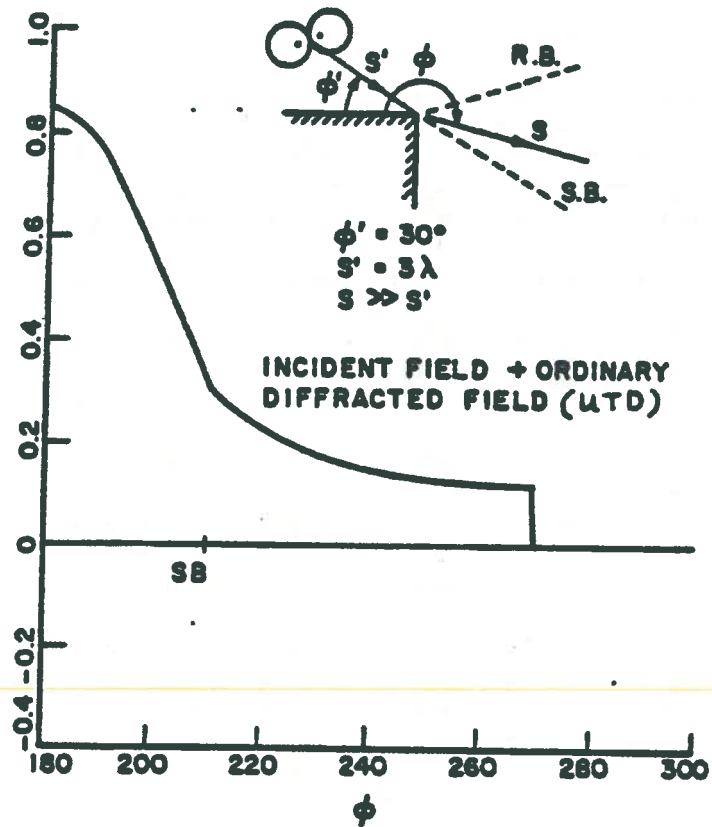


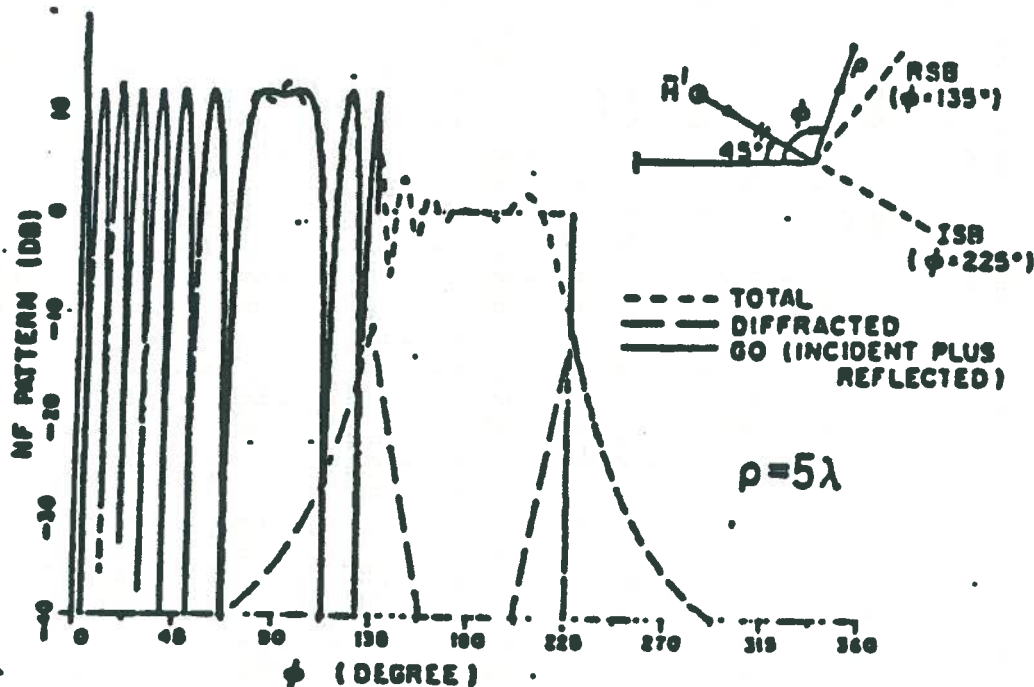
Transition function.

$F(KLa) \approx 1$  ;  $KLa > 10$ .

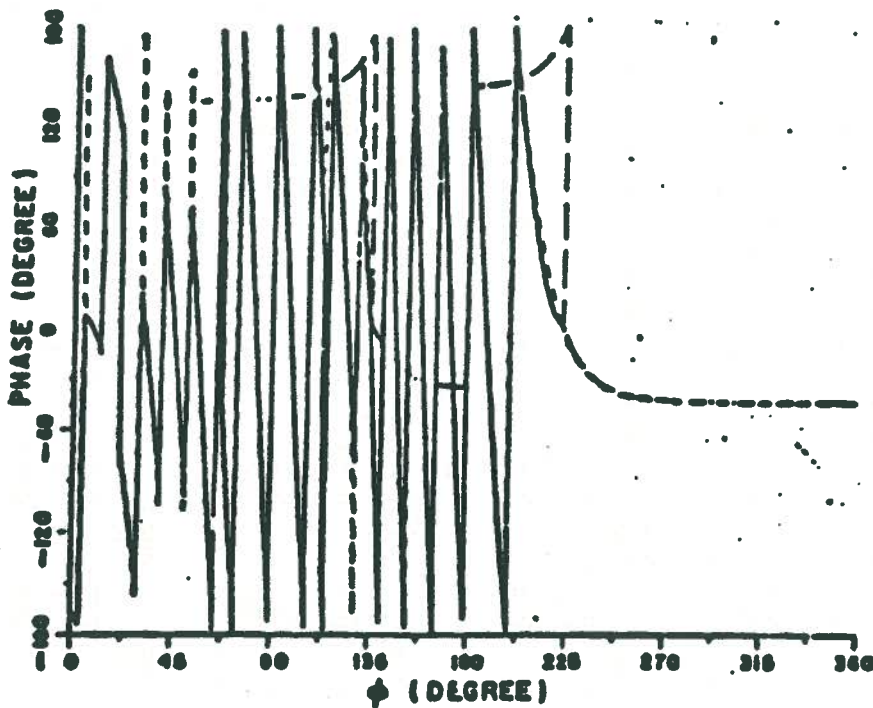
$F(KLa) \approx \frac{j\pi}{4} \sqrt{KLa}$  ;  $KLa \ll 1$ .





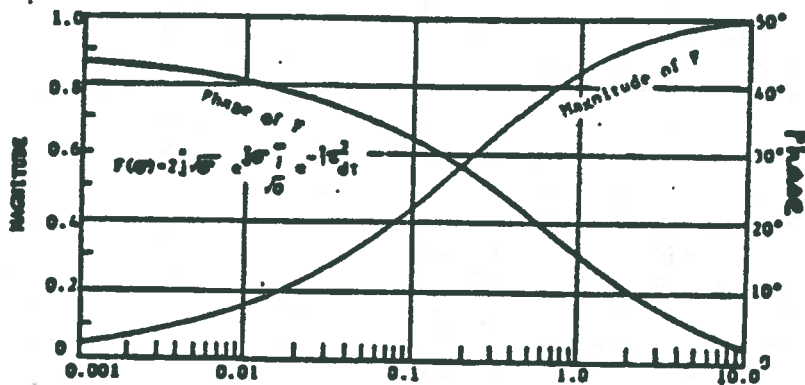


(a) magnitude



(b) phase

Continuity of the total UTD field surrounding a perfectly-conducting half plane excited by a plane wave



Plot of  $F(\sigma)$  versus  $\sigma$

$$F(x) = 2j\sqrt{x} e^{jx} \int_{\sqrt{x}}^{\infty} dz e^{-jz^2} ;$$

$$\sqrt{x} = \begin{cases} |\sqrt{x}|, & \text{if } x > 0 \\ -j|\sqrt{x}|, & \text{if } x < 0 \end{cases}$$

$$F(x) \Big|_{x < 0} = F^*(|x|) .$$

➡ Near the ISB or RSB,  $x \rightarrow 0$

$$F(x) \xrightarrow{x \rightarrow 0} \sqrt{\pi x} e^{j(\frac{\pi}{4} + x)}$$

➡ Far from ISB or RSB,  $x$  is large

$$F(x) \sim 1 + \frac{1}{2jx}, \quad x > 10 .$$

---


$$\bar{E}^d \Big|_{\text{rec. rec.}} \sim \mp \frac{1}{2} \bar{E}^i e^{j\tau} + \Delta, \quad \begin{cases} \text{lit side of ISB; RSB} \\ \text{shadow side of rec. rec.} \end{cases}$$

① Incident Spherical Wave :

$$L^i = \frac{s^i s^d}{s^i + s^d} \sin^2 \beta_0$$

$$L^{r0} = L^{rn} = L^i$$

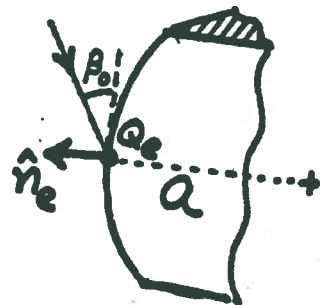
② Arbitrary Ray Optical Illumination :

$$L^i = \left[ \left( \frac{e_e^i}{s^d(e_e^i + s^d)} \right)^{-1} \cdot \frac{(e_1^i e_2^i)}{(e_1^i + s^d)(e_2^i + s^d)} \sin^2 \beta_0 \right] \text{ at ISB}$$

$$L^r = \left[ \left( \frac{e_e^r}{s^d(e_e^r + s^d)} \right)^{-1} \cdot \frac{(e_1^r e_2^r)}{(e_1^r + s^d)(e_2^r + s^d)} \sin^2 \beta_0 \right] \text{ at RSB}$$

$$\frac{1}{e_e^r} = \frac{1}{e_e^i} - \frac{2(\hat{n} \cdot \hat{n}_e)(\hat{s}^i \cdot \hat{n})}{a \sin^2 \beta_0}$$

$$\frac{1}{e_e} = \frac{1}{e_e^i} - \frac{\hat{n}_e \cdot (\hat{s}^i - \hat{s}^d)}{a \sin^2 \beta_0}$$



At the ISB ,  $kL^i a^\pm(\phi - \phi') = 0$

At an RSB ,  $kL^{rn} a^+(\phi + \phi') = 0$

... or  $kL^{r0} a^+(\phi + \phi') = 0$ .

→ It is easily verified that the total high frequency field is continuous at ISB and RSB.

→ Far from ISB and RSB ,  $F \rightarrow 1$  and  $\bar{D}_e \rightarrow \bar{D}_e^k$  , where

$$\bar{D}_e^k = -\hat{\beta}'_0 \hat{\beta}_0 D_{es}^k - \hat{\phi}' \hat{\phi} D_{eh}^k \quad \leftarrow \left\{ \text{KELLER'S WEDGE DIFFRACTION COEFFS. } D_{es,eh}^k \right\}$$

$$D_{es,eh}^k = e^{-j\frac{\pi}{4}} \frac{1}{\sqrt{2\pi k \sin\beta_0}} \frac{\sin\frac{\pi}{n}}{n} \cdot \left[ \frac{1}{\cos\frac{\pi}{n} - \cos(\frac{\beta^-}{n})} \mp \frac{1}{\cos\frac{\pi}{n} - \cos(\frac{\beta^+}{n})} \right]$$

with  $\beta^\mp = \phi \mp \phi'$ .

→ For the special case of a half plane ( $n=2$ ) or curved screen:

$$D_{es,eh}^k = \frac{-e^{-j\frac{\pi}{4}}}{2\sqrt{2\pi k \sin\beta_0}} \left[ (\sec\frac{\beta^-}{2}) F(kL^i a(\beta^-)) \mp (\sec\frac{\beta^+}{2}) F(kL^i a(\beta^+)) \right]$$

with  $a(\beta) = 2 \cos^2 \beta/2$ .

2-D Case :

$$\underline{\text{3-D}}: \bar{E}^d(P) \sim \bar{E}^i(Q_E) \cdot \bar{D}_e \sqrt{\frac{\rho_e}{s^d(\rho_e + s^d)}} e^{-jks^d}$$

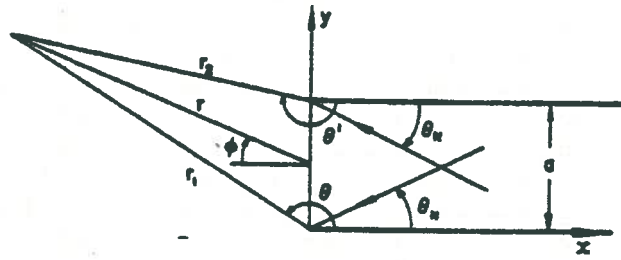
2-D: Let  $\rho_e \rightarrow \infty$

$$\therefore \bar{E}^d(P) \sim \bar{E}^i(Q_E) \cdot \bar{D}_e \frac{e^{-jks^d}}{\sqrt{s^d}}$$

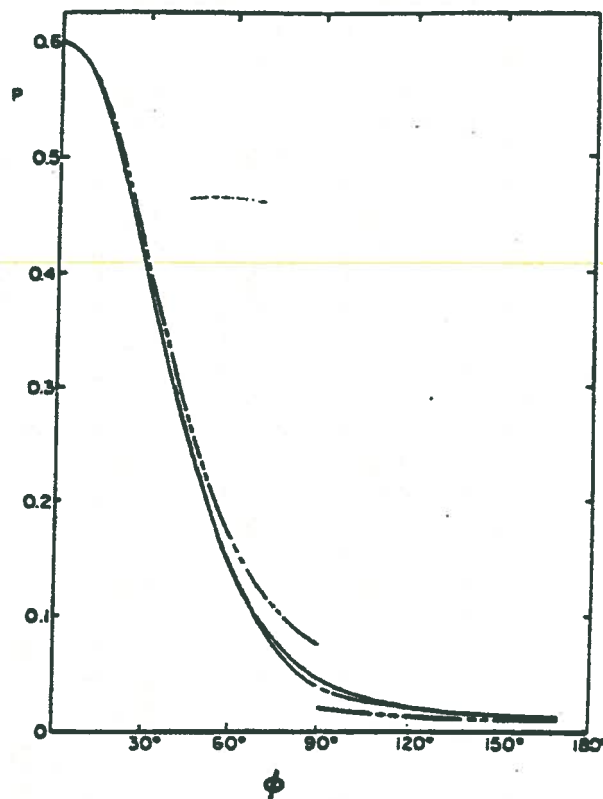
Note also that if  $s^d \ll \rho_e$  but  $ks^d \gg 1$   
 then:  $\bar{E}^d(P) \sim \bar{E}^i(Q_E) \cdot \bar{D}_e \frac{e^{-jks^d}}{\sqrt{s^d}}$

This limit is of interest to the  
 Equivalent Current Method (ECM).

If  $s^d \gg \rho_e$ , then:  $\bar{E}^d(P) \sim \bar{E}^i(Q_E) \cdot \bar{D}_e \sqrt{\rho_e} \frac{e^{-jks^d}}{s^d}$



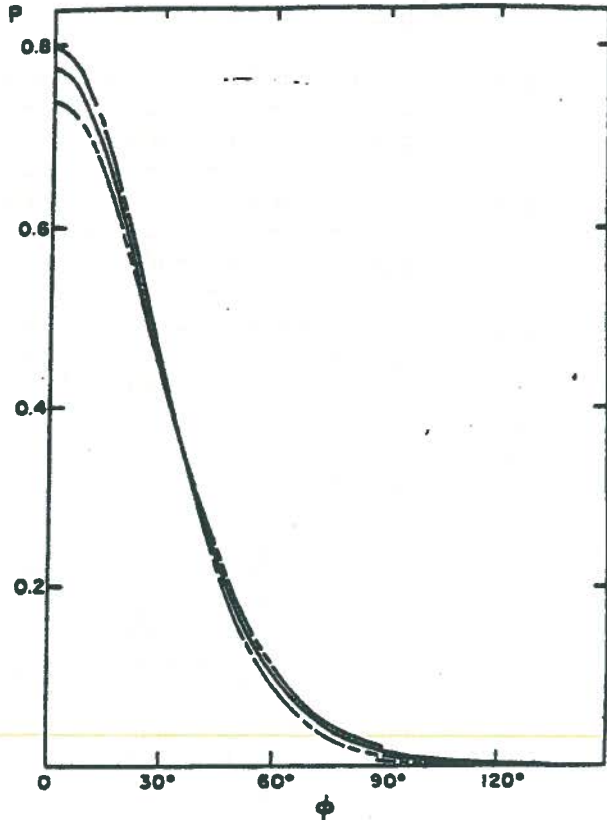
Coordinates for radiation from an open-ended parallel-plate waveguide



Radiated power patterns for TEM mode incidence on the open end of a parallel-plate waveguide of width  $a = 0.6\lambda$ .

- - - single diffraction, from eqns. 9.27, 9.28
- - - single and multiple diffraction
- exact, eqn. 9.29

(Reprinted from Yee and Felsen, 1968)



Radiated power patterns for  $TE_1$  mode incidence on the open end of a parallel-plate waveguide of width  $a = 0.8\lambda$

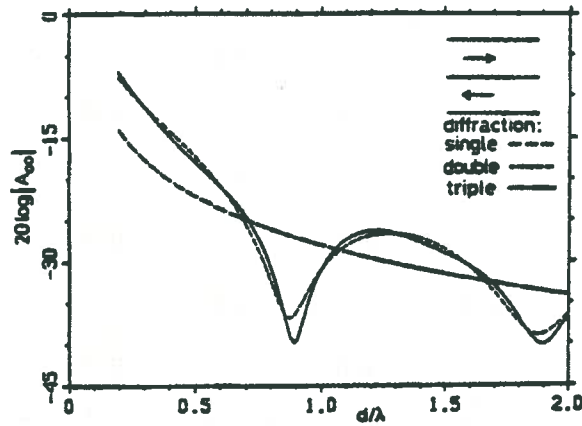
--- single diffraction, from eqns. 9.33, 9.34

- · - single and multiple diffraction

— exact, eqn. 9.35

(The three results agree for  $\phi = \theta_1 = \sin^{-1}(\lambda/2a) = 38.7^\circ$ )

(Reprinted from Yee and Felsen, 1968)



Amplitude of TEM coupling between adjacent parallel-plate waveguides of equal width  $d$

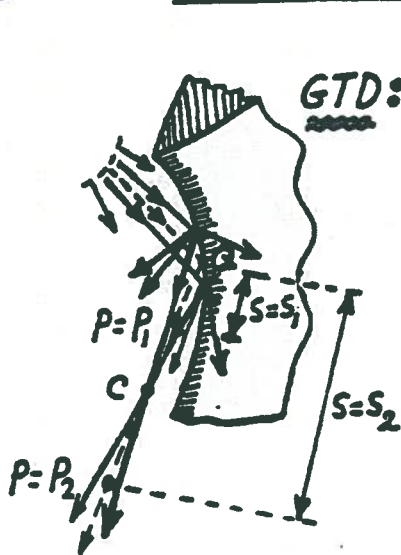
--- single diffraction only

..... single and double diffraction

— single, double and triple diffraction

(Reprinted from Driessen, 1979)

## EQUIVALENT CURRENT METHOD (ECM)



$$\text{GTD: } \bar{E}^d(P) \sim \bar{E}^i(Q) \cdot \bar{D}_e^k \sqrt{\frac{\rho}{s(\rho+s)}} e^{-jks}$$

$$|\bar{Q}C| = |\rho| \quad ; \quad \rho < 0$$

$\bar{E}^d(P) \rightarrow \infty$  if  $P \rightarrow C$  (i.e.  $s = -|\rho|$ )  
 i.e. the diffracted field becomes singular at the diffracted ray caustic

Remedy: if  $ks \gg 1$  and if  $s \ll |\rho|$ , then:

$$\left. \bar{E}^d(P) \right|_{\substack{ks \gg 1 \\ s \ll |\rho|}} \sim \bar{E}^i \cdot \bar{D}_e^k \frac{e^{-jks}}{\sqrt{s}}$$



line current tangent to Q with a traveling wave propagation constant =  $k \cos \beta_0$

This result is like the field of a traveling wave line source with a complex amplitude  $\{ I_0 \} e^{-jkl \cos \beta_0}$  if the diffracted ray caustic direction is far from the incident & reflection shadow boundary directions so that  $F \rightarrow 1$  &  $\bar{D}_e \rightarrow \bar{D}_e^k$ . If  $F \neq 1$  then the field behaviour is more complex than the one above for  $ks \gg 1$  &  $s \ll |\rho|$ .



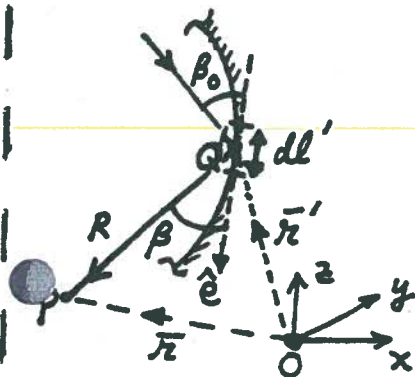
EQUIVALENT CURRENTS (IN ABSENCE OF EDGE) THAT GENERATE THE SAME  $\bar{E}^d(P)$ .

$$I = \frac{-e^{-j\pi/4}}{Z_0} \sqrt{\frac{8\pi}{k}} \left[ \hat{e} \cdot \bar{E}^i(Q) \right] \frac{D_{es}^k}{\sin \beta_0} \quad ; \quad M = \frac{-e^{-j\pi/4}}{Y_0} \sqrt{\frac{8\pi}{k}} \left[ \hat{e} \cdot \bar{H}^i(Q) \right] \frac{D_{eh}^k}{\sin \beta_0}$$

ECM

The strength of  $\begin{Bmatrix} I \\ M \end{Bmatrix} = \begin{Bmatrix} I_0 \\ M_0 \end{Bmatrix} e^{-jk l' \cos \beta_0}$  depends on  $\bar{D}$  which is defined only over the Keller cone of edge diffracted rays.

$$\therefore \vec{E}^d(P) \Rightarrow \vec{E}_c^d(P) \sim \frac{jkZ_0}{4\pi} \oint_{\substack{L \\ \text{(edge)}}} [\hat{R} \times \hat{R} \times I \hat{e} + Y_0 \hat{R} \times M \hat{e}] \frac{e^{-jkR}}{R} dl'$$



$I \rightarrow I(Q') = I(l')$   
 $M \rightarrow M(Q') = M(l')$  }  $Q'$  is any point on edge.  
 (NOTE: The above  $I$  &  $M$  change with the observer location !!)

$$R = |\vec{r} - \vec{r}'|$$

$\vec{E}_c^d(P)$  is well behaved if  $P \rightarrow C$ .

The above concept is an outgrowth of work by:  
 → R. F. Millar (PROC. IEE; Mar.'56; Mar.'57; Sept.'57).

→ Ryan, C.E & L. Peters independently (of Millar) arrived at the above postulate. For  $P$  not on Keller cone (i.e.  $\beta \neq \beta_0$ ), they set  $I$  &  $M$  fixed to their values on the Keller cone.  
 (IEEE TRANS. AP-7, pp. 292-299, 1969)

→ Knott, E.F. & T.B.A. Senior allowed  $I$  &  $M$  to be defined for  $P$  even outside the Keller cone by heuristically allowing  $\sin \beta_0$  in  $\bar{D}$  (contained in  $I$  &  $M$ ) to be replaced by  $\sqrt{\sin \beta_0 \sin \beta}$ . (PROC. IEEE, Nov.'74)

The following new  $\tilde{I}(\hat{Q})$  and  $\tilde{M}(\hat{Q})$  which contain  $\sqrt{\sin\beta_0 \sin\beta}$  are thus defined as follows:

$$\tilde{I}(\hat{Q}) = -e^{-j\frac{\pi}{4}} \frac{\sqrt{8\pi}}{Z_0} \frac{[\hat{e} \cdot \vec{E}^i(\hat{Q})]}{\sqrt{\sin\beta_0 \sin\beta}} \tilde{D}_{es}^k$$

$$\tilde{M}(\hat{Q}) = -e^{-j\frac{\pi}{4}} \frac{\sqrt{8\pi}}{Y_0} \frac{[\hat{e} \cdot \vec{H}^i(\hat{Q})]}{\sqrt{\sin\beta_0 \sin\beta}} \tilde{D}_{eh}^k$$

with  $\tilde{D}_{es,eh}^k$  being related to the  $D_{es,eh}^k$  as shown below:

$$\tilde{D}_{es,eh}^k = \frac{\sin\beta_0}{\sqrt{\sin\beta_0 \sin\beta}} D_{es,eh}^k$$

Note that  $D_{es,eh}^k$  depends only on  $\sin\beta_0$ , whereas  $\tilde{D}_{es,eh}^k$  depends on both  $\sin\beta_0$  and  $\sin\beta$ . The radiation integrals now become

$$\vec{E}^d(P) \sim \frac{j k Z_0}{4\pi} \oint_{\mathcal{L}} [\hat{R} \times \hat{R} \times \tilde{I}(\hat{Q}) \hat{e} + Y_0 \hat{R} \times \tilde{M}(\hat{Q}) \hat{e}] e^{-j k R} dl'$$

and

$$\vec{H}^d(P) \sim \frac{-j k}{4\pi} \oint_{\mathcal{L}} [\hat{R} \times \tilde{I}(\hat{Q}) \hat{e} - Y_0 \hat{R} \times \hat{R} \times \tilde{M}(\hat{Q}) \hat{e}] e^{-j k R} dl'$$

The  $\mathcal{L}$  is a closed path formed by a line of discontinuity or edge from where the diffracted rays are produced. If  $\mathcal{L}$  is not a ring type edge discontinuity, then  $\mathcal{L}$  may not be closed in which case the end points of  $\mathcal{L}$  will contribute. If part of  $\mathcal{L}$  is shadowed then spurious end point contributions may result from an incorrect truncation of the currents at the onset of the shadow on  $\mathcal{L}$ .

ECM (contd.).

It is important to note that the integral over  $L$  in the ECM cannot in general be evaluated in closed form except in a few special cases. Therefore, the ECM integral must in general be evaluated numerically. On the other hand one also notes that away from the diffracted ray caustic direction (and away from LSB/RSB) the ECM integral reduces via a stationary phase approximation to a closed form GTD solution. The latter result is based on the fact that the stationary points on  $L$  satisfy Keller's law of edge diffraction; thus:

$$E^d(P) \Big|_{\substack{P \text{ not} \\ \text{close to} \\ \text{edge diffracted} \\ \text{ray caustic}}} \sim \frac{j k Z_0 \phi}{4\pi} \int_L [\dots] \frac{e^{j k R}}{R} dl' \sim \sum_{p=1}^N E^d(Q'_p) \frac{D(Q'_p)}{e} \sqrt{\frac{e_p}{e_p + s_p}} e^{j k R_p}$$

$N =$  number of points of edge diffraction on  $L$  which satisfy the Keller cone condition  $\beta = \beta_0$ .

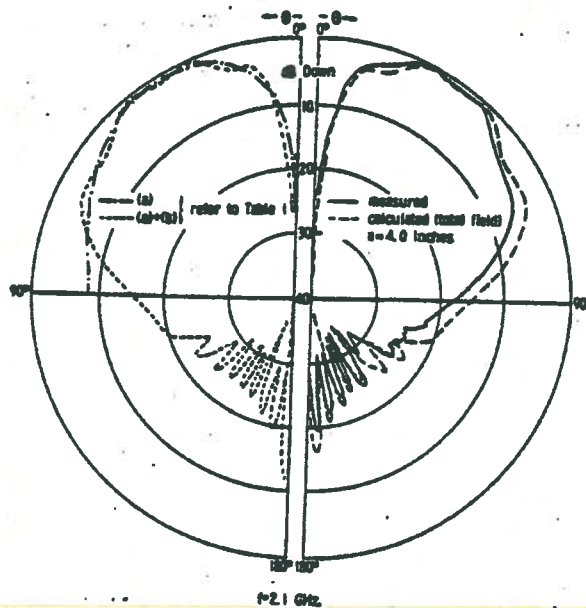
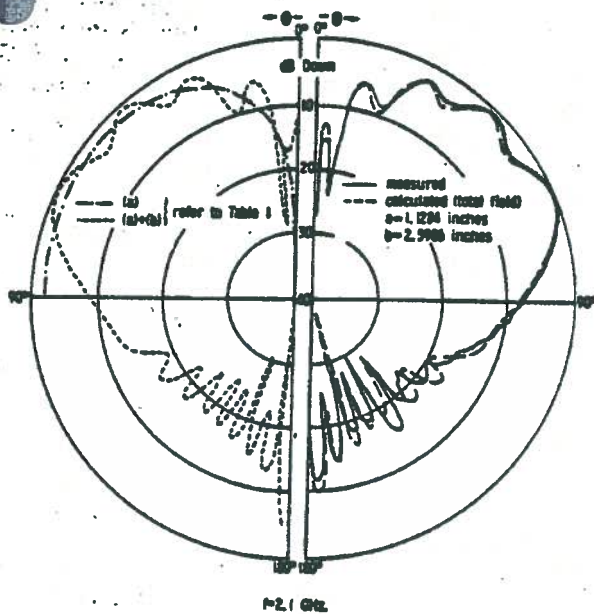


Fig. 3. Elevation plane pattern of coax in 48.0-in diameter ground plane.

Fig. 5. Elevation plane pattern of circular aperture in 48.0-in diameter ground plane.

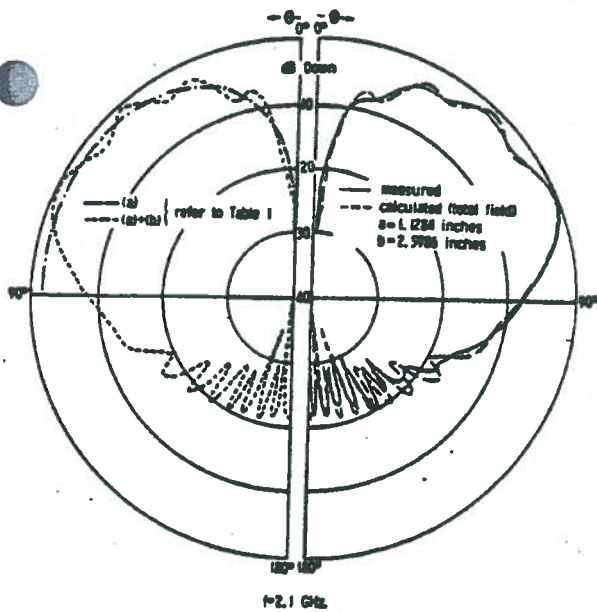
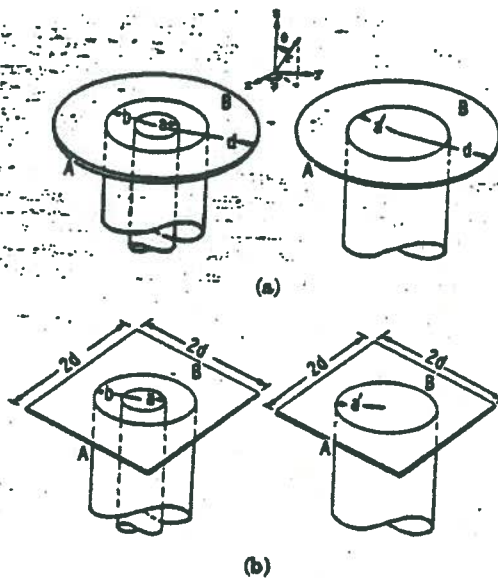


Fig. 4. Elevation plane pattern of coax in 48.0-in square ground plane.



Coax and circular apertures. (a) Circular ground plane. (b) Square ground plane.

# MODAL RAYS

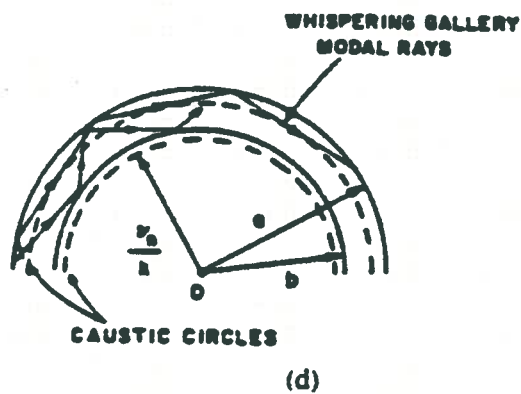
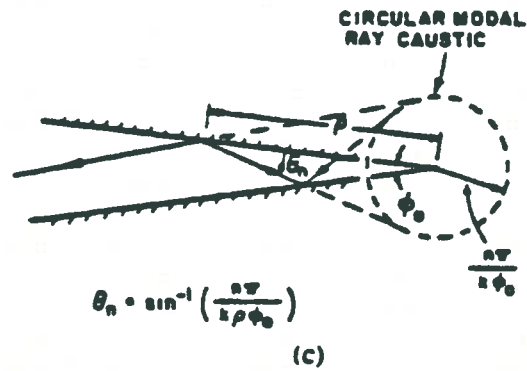
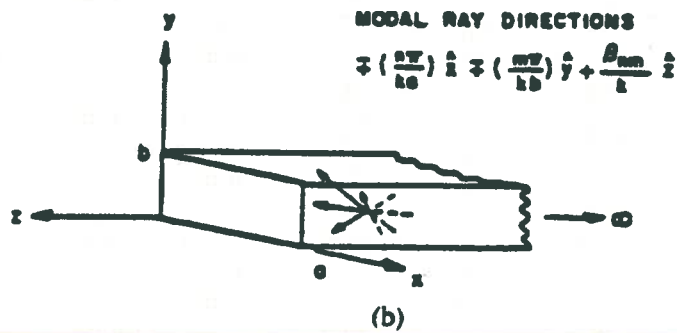
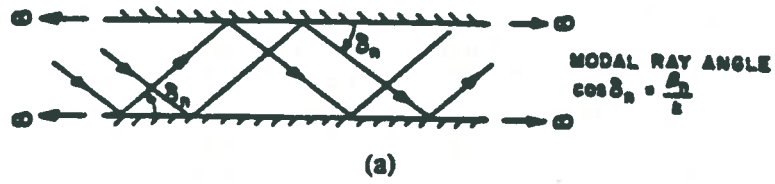


Fig. 6. Modal rays inside uniform waveguide geometries. (a) Parallel plate waveguide. (b) Rectangular waveguide. (c) Linearly tapered waveguide. (d) Annular waveguide region.

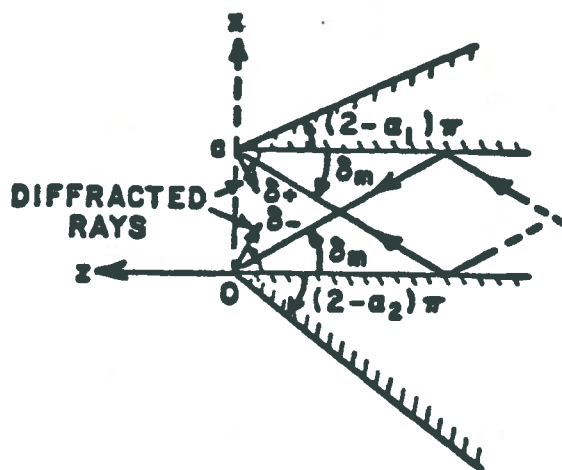
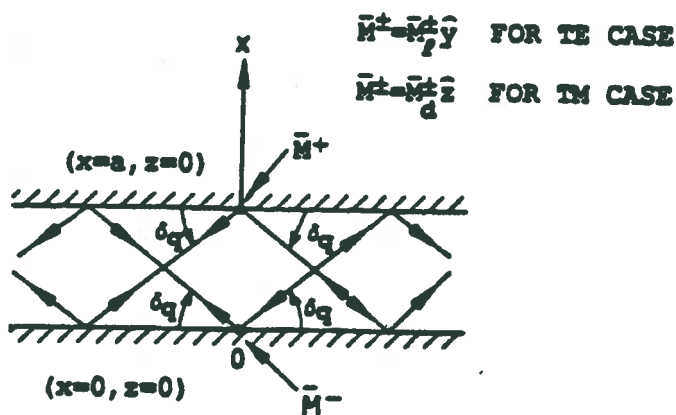


Fig. 6. Modal reflection from the open end of a parallel plate waveguide.

$$M_i^+(\delta_q) = \hat{y} \left[ -\frac{1}{Y_0} \left( \frac{8\pi}{jk} \right)^{1/2} \right] \frac{(-1)^m D_h(\delta_q, \delta_m, \alpha_1)}{2} \frac{D_h(\delta_q, \delta_m, \alpha_1)}{2}$$

$$M_i^-(\delta_q) = \hat{y} \left[ -\frac{1}{Y_0} \left( \frac{8\pi}{jk} \right)^{1/2} \right] \frac{1}{2} \frac{D_h(\delta_q, \delta_m, \alpha_2)}{2}$$



$$R_{qm} = - \left[ M_i^+(\delta_q) \cdot H_q^>(x=a, z=0) + M_i^-(\delta_q) \cdot H_q^>(x=0, z=0) \right] \cdot \left( 2 \int_C \vec{E}_q^< \times \vec{H}_q^> \cdot \hat{n} d\Gamma \right)^{-1}$$

PATHAK AND ALTINTAS: MODAL COEFFICIENTS FOR WAVEGUIDE DISCONTINUITIES

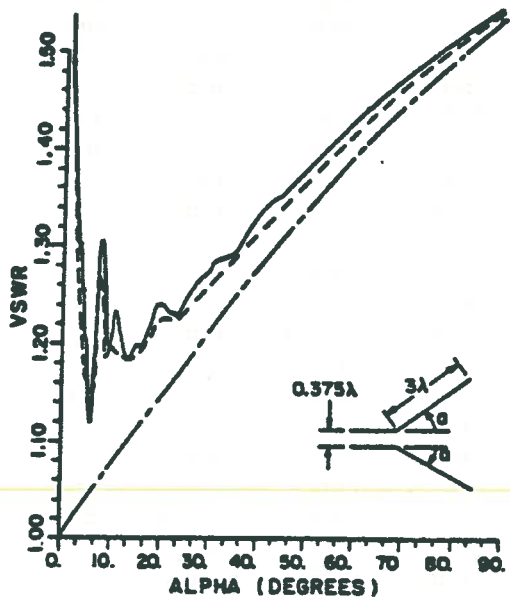


Fig. 11. The geometry and VSWR of a horn antenna. The dash-dotted curve denotes only throat contribution, the solid curve denotes throat and aperture contributions, and the dashed line denotes moment method calculation.

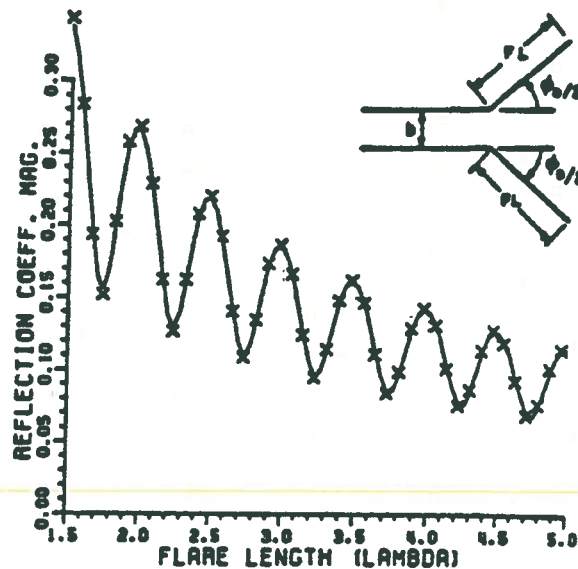


Fig. 12. Magnitude of the reflection from the two-dimensional *E* plane sectoral horn as a function of the wavelength. Here,  $b = 1.58$  cm, flare length (FL) = 31.92 cm, and  $\phi_0 = 33.5^\circ$ . The solid curve is from Jull [1972], and the crosses indicate results of the present analysis.

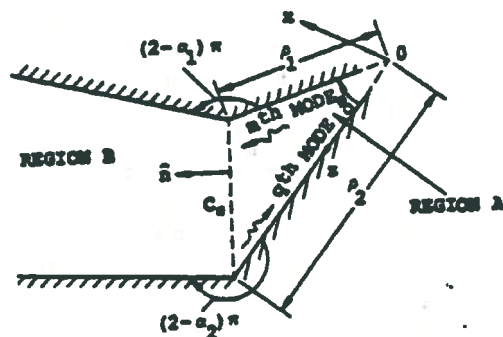
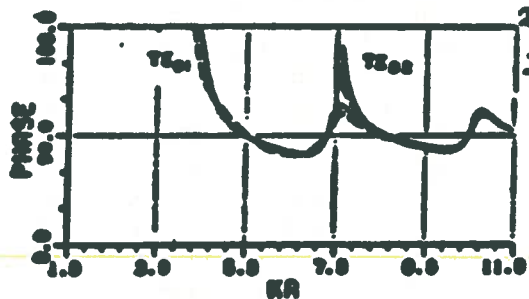
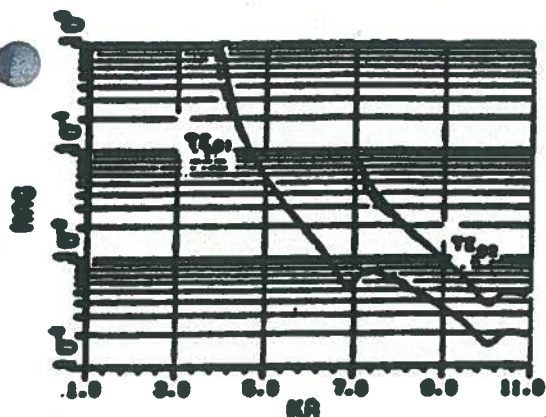


Fig. 9. Junction between two linearly tapered waveguides.

(FROM: Chuang & Pathak)

IEEE TRANSACTIONS ON ANTENNAS AND PROPAGATION, VOL. 37, NO. 3, MARCH 1989



2. Modal reflection coefficients due to an incident  $TE_{01}$  mode in an open-ended circular waveguide. — present solution; ---- Wisner-Hopf [12].

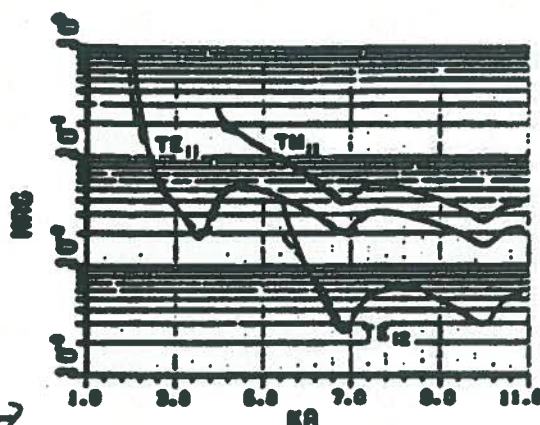


Fig. 3. Modal reflection coefficients due to an incident  $TE_{11}$  mode in an open-ended circular waveguide. — present solution; ---- Wisner-Hopf [12].

→ Pathak, P. H. & A. Altintas  
(Radio Science, Vol. 23, #6)  
Nov.-Dec. 1988

extended the use of non-rigorous ECM to interior regions.

Only M type equivalent currents remain if interior geom. is PEC.

→ Chuang, C. W. & P. H. Pathak  
(IEEE Trans. AP-37, Mar. '89)

used these interior equiv. currents to find modal reflection coeffs. for open-ended circular waveguides.

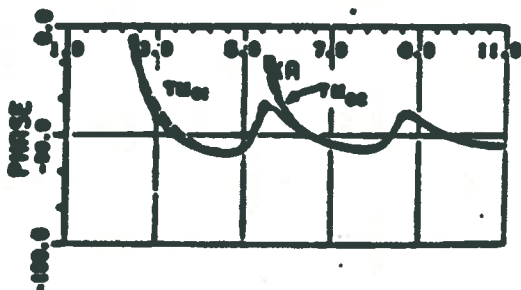
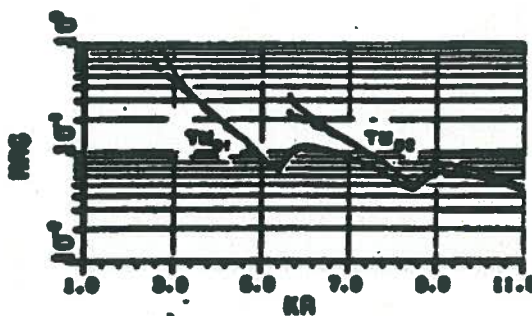
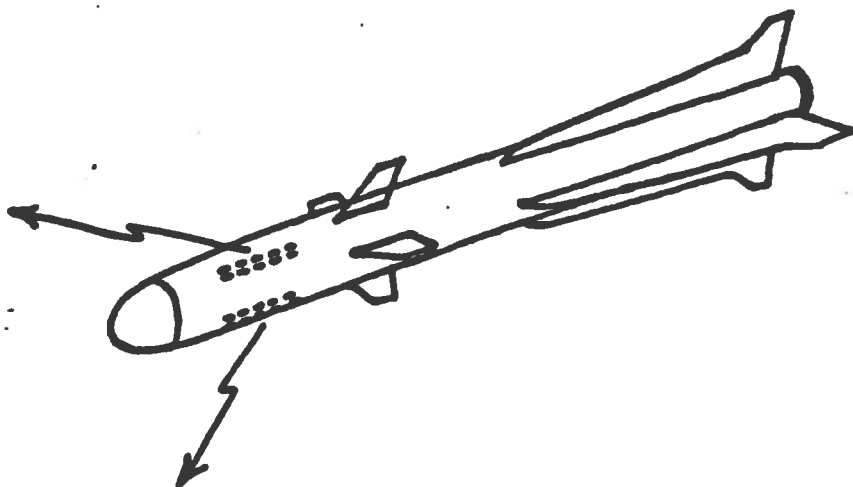
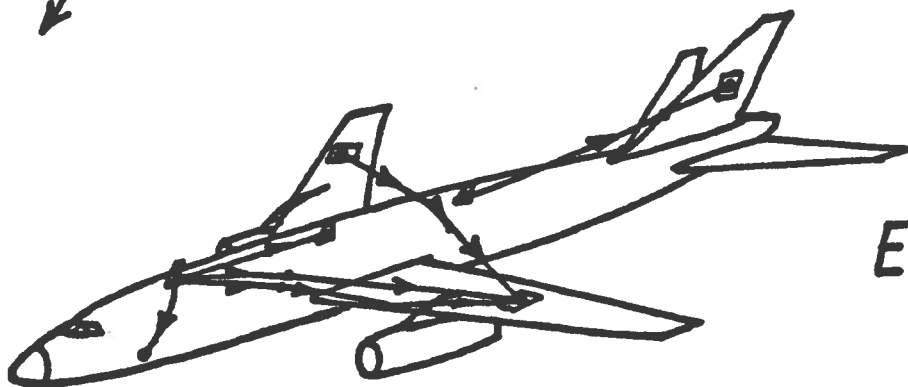


Fig. 4. Modal reflection coefficients due to an incident  $TM_{01}$  mode in an open-ended circular waveguide. — present solution; ---- Wisner-Hopf [12].



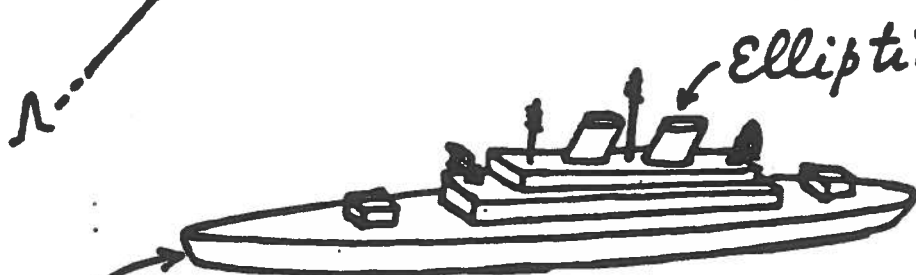
CONFORMAL  
ARRAYS



EMC



EMP

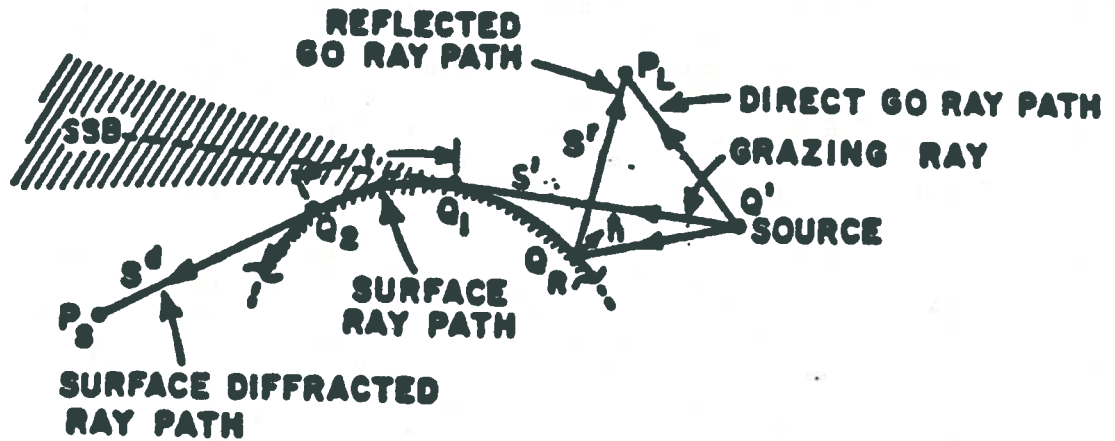


Elliptic Cone

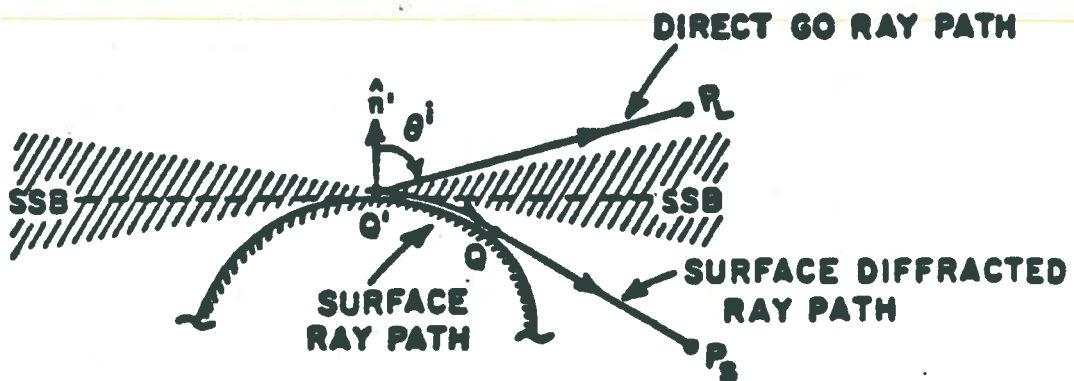
Elliptic Cylinder

EMC

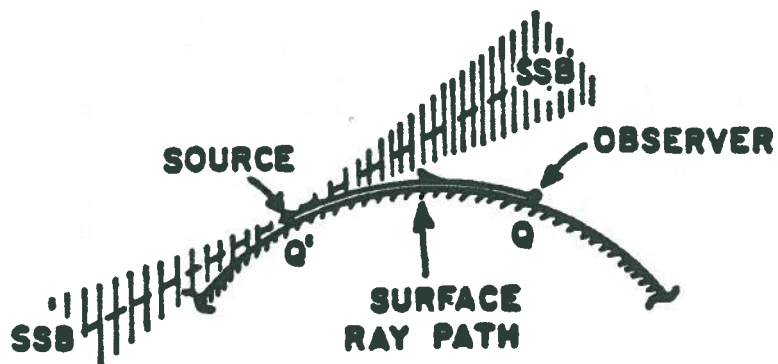
# Diffraction by a smooth convex surface



Geometry associated with the scattering problem.



Geometry associated with the radiation problem.



Geometry Associated with the Mutual Coupling Problem.

# GTD

## Surface Diffraction

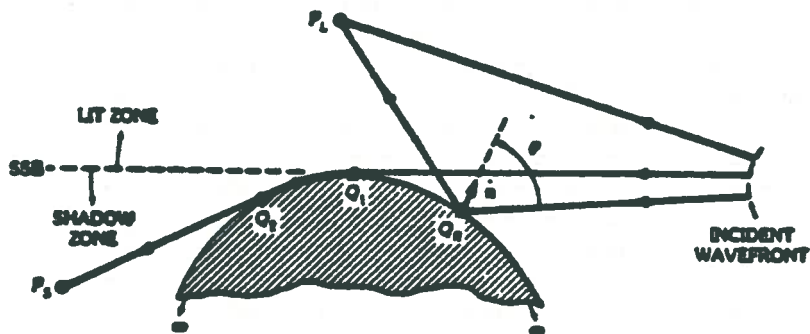
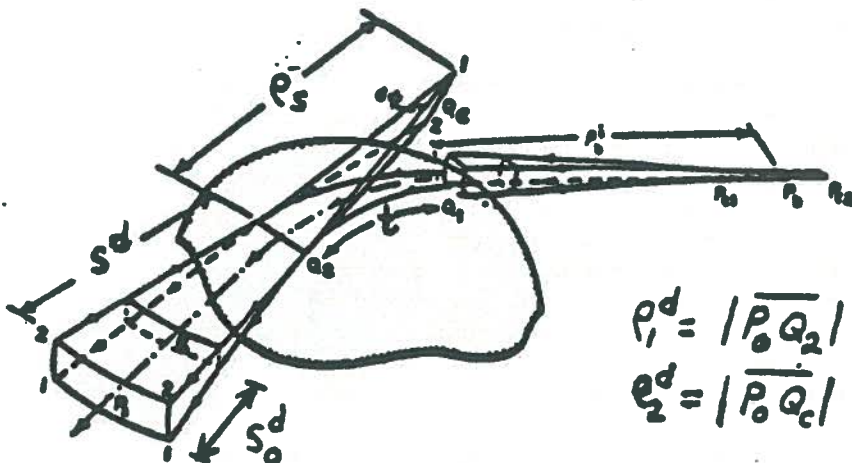


Fig. Rays associated with the scattering and diffraction by a convex surface.

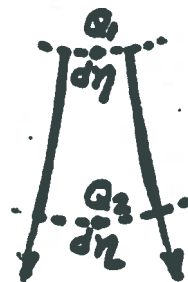
$$\bar{E}(P) = \begin{cases} \bar{E}^i(P_L) + \bar{E}^r(P_L), & \text{if } P = P_L \\ \bar{E}^d(P_S) & , \text{ if } P = P_S \end{cases}$$

$\bar{E}^i$  and  $\bar{E}^r$  at  $P_L$  are found as before using G.O.



$$p_1^d = |P_0 Q_1|$$

$$p_2^d = |P_0 Q_2|$$



$$\bar{E}^d(P_s) \sim \bar{E}^d(P_0) \sqrt{\frac{p_1^d p_2^d}{(p_1^d + s_0^d)(p_2^d + s_0^d)}} e^{-jks_0^d}$$

$$\bar{E}^d(P_s) = \lim_{p_1^d \rightarrow 0} [\sqrt{p_1^d} \cdot \bar{E}^d(P_0)] \sqrt{\frac{p_2^d}{(p_1^d + s_0^d)(p_2^d + s_0^d)}} e^{-jks_0^d}$$

$$\lim_{p_1^d \rightarrow 0} \sqrt{p_1^d} \bar{E}^d(P_0) \equiv \bar{E}^i(Q_1) \cdot \bar{T}^k(Q_1, Q_2) e^{-jkt} \sqrt{\frac{d\eta(Q_1)}{d\eta(Q_2)}}$$

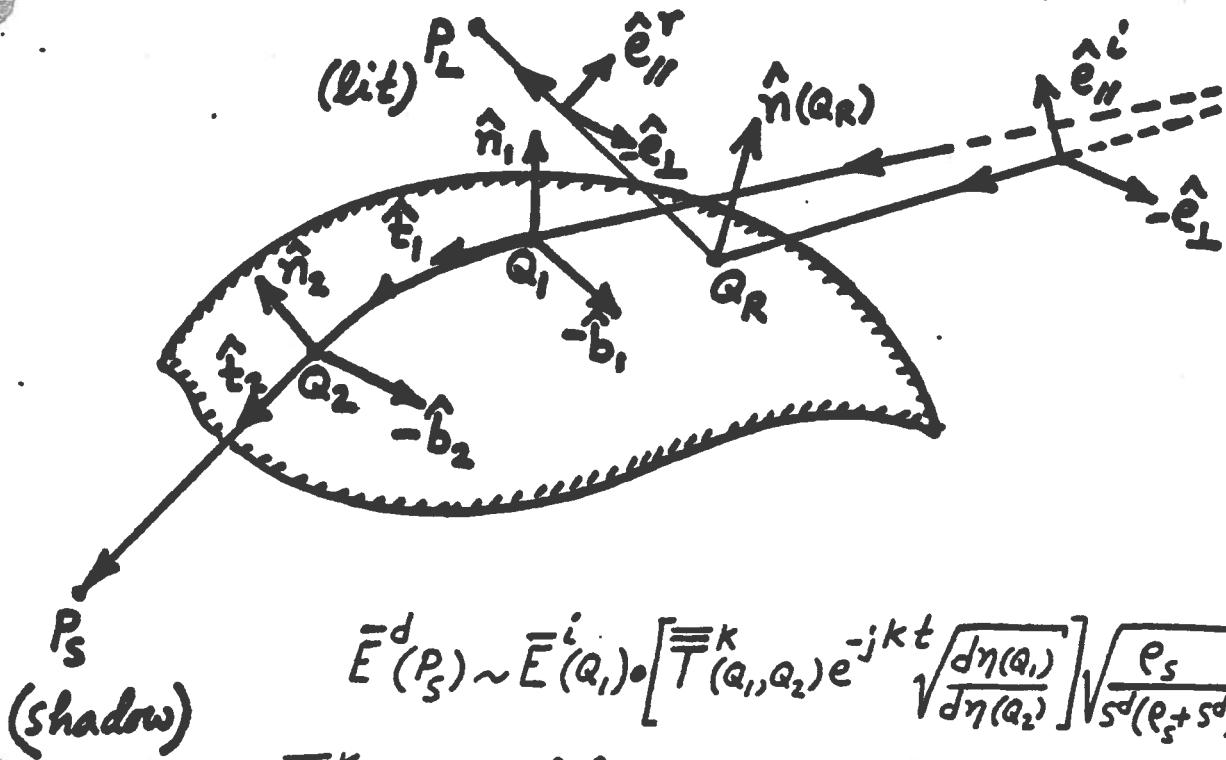
$\therefore$

$$\bar{E}^d(P_s) \sim \bar{E}^i(Q_1) \cdot \left[ \bar{T}^k(Q_1, Q_2) e^{-jkt} \sqrt{\frac{d\eta(Q_1)}{d\eta(Q_2)}} \right] \sqrt{\frac{p_s}{s^d(p_s + s^d)}} e^{jks^d}$$

since  $p_2^d \rightarrow p_s$  as  $P_0 \rightarrow Q_2$  (or  $p_1^d \rightarrow 0$ )

and  $s_0^d \rightarrow s^d$  as  $P_0 \rightarrow Q_2$  (or  $p_1^d \rightarrow 0$ )

# Scattering Problem (3-D case)



$$\bar{E}^d(P_S) \sim \bar{E}^i(Q_1) \cdot [\bar{T}^K(Q_1, Q_2) e^{-jkt} \sqrt{\frac{d\eta(Q_1)}{d\eta(Q_2)}}] \sqrt{\frac{\rho_s}{s^d(\rho_s + s^d)}} e^{-jks^d}$$

$$\bar{T}^K(Q_1, Q_2) = \hat{b}_1 \hat{b}_2 T_s + \hat{n}_1 \hat{n}_2 T_h$$

$$T_{s,h} = \sum_{n=1}^N D_n^{s,h}(Q_1) e^{-\int_{Q_1}^{Q_2} \alpha_n^{s,h}(t') dt'} D_n^{s,h}(Q_2)$$

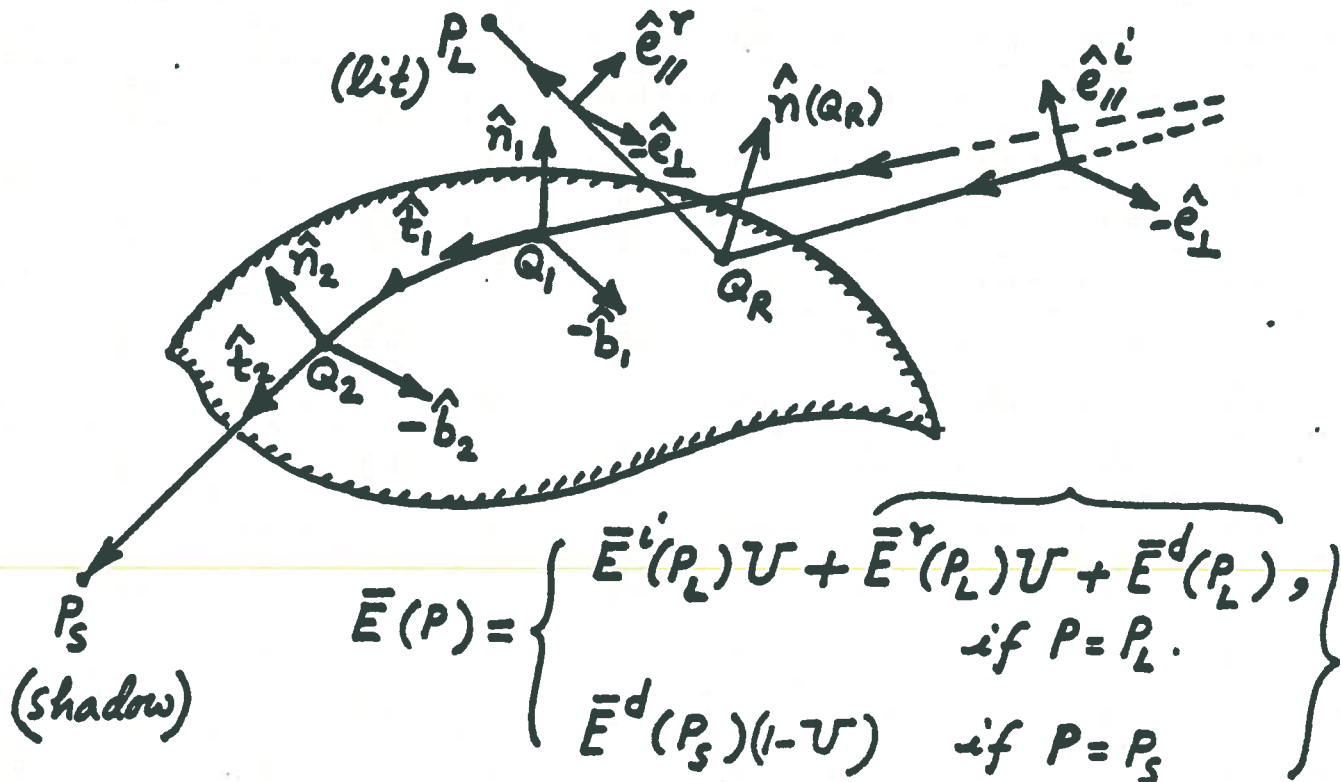
$$[D_n^s(Q)]^2 = \sqrt{\frac{1}{2\pi k}} m(Q) \frac{e^{-j\frac{\pi}{2}}}{[Ai'(-q_n)]^2} ; Ai(q_n) = 0 \quad n=1, 2, \dots, N$$

$$[D_n^h(Q)]^2 = \sqrt{\frac{1}{2\pi k}} m(Q) \frac{e^{j\frac{\pi}{2}}}{\tilde{q}_n [Ai'(-\tilde{q}_n)]^2} ; Ai'(-\tilde{q}_n) = 0 \quad n=1, 2, \dots, N$$

$$\alpha_n^s(Q) = \frac{q_n}{\rho_g(Q)} m(Q) e^{j\frac{\pi}{6}} ; \alpha_n^h(Q) = \frac{\tilde{q}_n}{\rho_g(Q)} m(Q) e^{j\frac{\pi}{6}}$$

$$m(Q) \equiv \left[ \frac{k \rho_g(Q)}{2} \right]^{1/3}$$

# UTD Analysis of Scattering Problem (3-D case)



$$\bar{E}(P) = \begin{cases} \bar{E}^i(P_L)U + \bar{E}^r(P_L)U + \bar{E}^d(P_L), & \text{if } P = P_L. \\ \bar{E}^d(P_S)(1-U) & \text{if } P = P_S \end{cases}$$

$$U = \begin{cases} 1, & \text{in lit region} \\ 0, & \text{in shadow region} \end{cases}$$

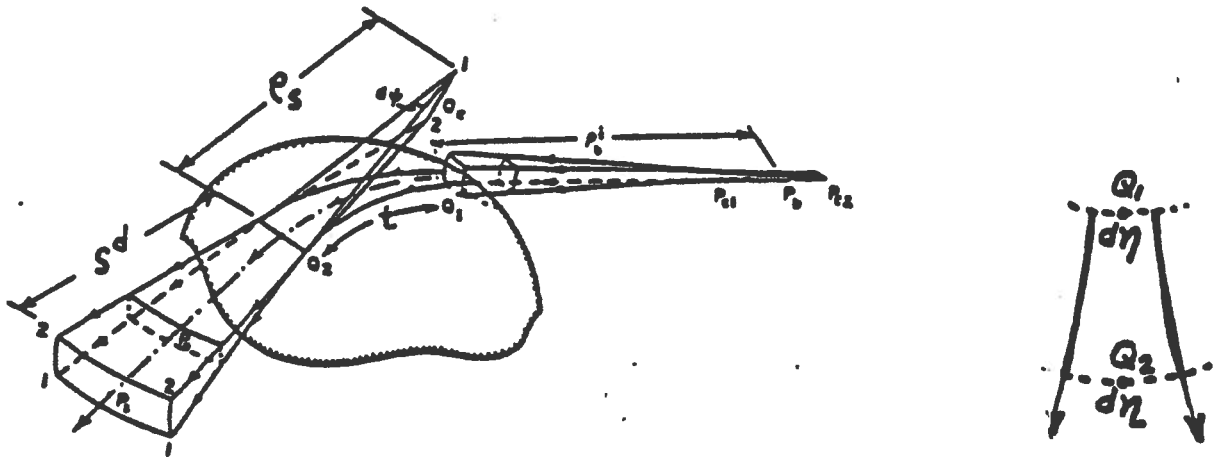
More conveniently:

$$\bar{E}(P) = \begin{cases} \bar{E}^i(P_L)U + \bar{E}^{gr}(P_L)U, & \text{if } P = P_L \\ \bar{E}^d(P_S)[1-U], & \text{if } P = P_S \end{cases}$$

$$\bar{E}^{gr}(P_L) \sim \bar{E}^i(Q_R) \cdot [\mathcal{R}_s \hat{e}_\perp \hat{e}_\perp + \mathcal{R}_h \hat{e}_\parallel \hat{e}_\parallel] \sqrt{\frac{\rho_r \rho_r'}{(\rho_r + s^r)(\rho_r' + s^r)}} e^{-jks^r}$$

$$\bar{E}^d(P_S) \sim \bar{E}^i(Q_1) \cdot [\mathcal{D}_s \hat{b}_1 \hat{b}_2 + \mathcal{D}_h \hat{n}_1 \hat{n}_2] \sqrt{\frac{\rho_s}{s^d(\rho_s + s^d)}} e^{-jks^d}$$

(P. H. Pathak et. al., IEEE Trans. AP-28, Sept. '80, pp 631-642)



Surface diffracted ray path

$$R_s = - \left[ \sqrt{\frac{-4}{\xi^L}} e^{-j(\xi^L)^3/12} \left( \frac{e^{-j\pi/4}}{2\sqrt{\pi} \xi^L} [1 - F(X^L)] + \tilde{P}_s(\xi^L) \right) \right]$$

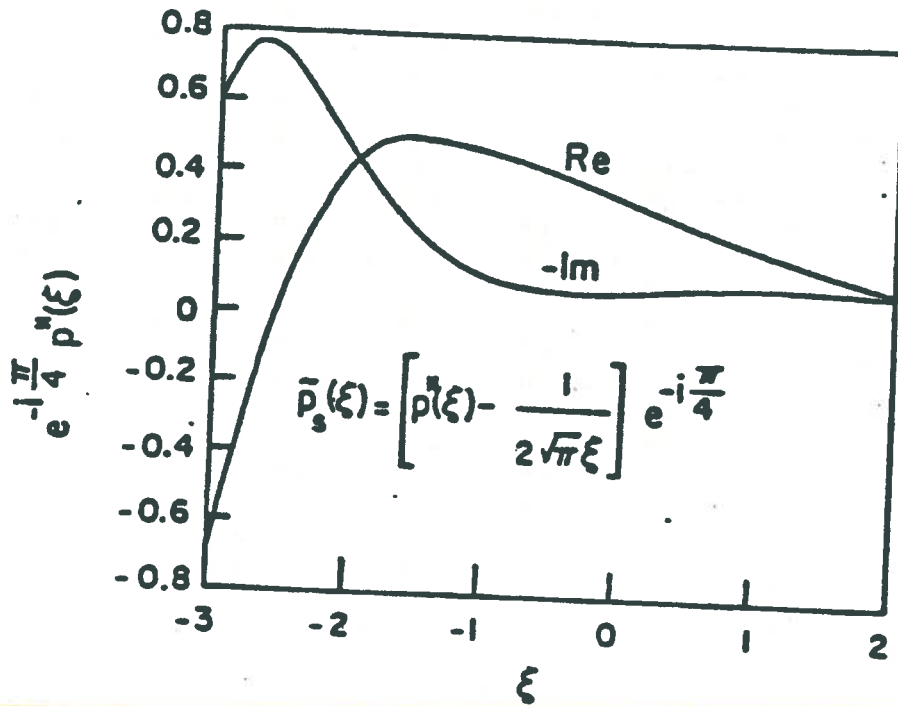
and

$$D_s = - \left[ \sqrt{m(Q_1)m(Q_2)} \cdot \sqrt{\frac{2}{k}} \frac{e^{-j\pi/4}}{2\sqrt{\pi} \xi} [1 - F(X^d)] + \tilde{P}_s(\xi) \right] \sqrt{\frac{d\eta(Q_1)}{d\eta(Q_2)}} e^{jk\ell}$$

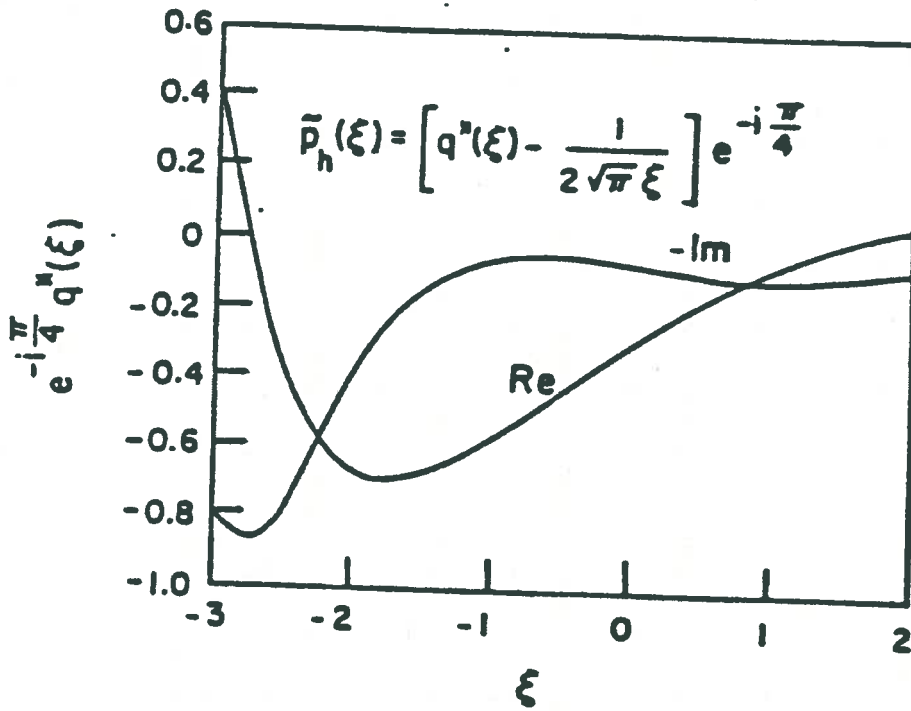
$$\xi^L = -2m(Q_R) \cos \theta^i ; \quad \xi = \int_{Q_1}^{Q_2} dt' \frac{m(t')}{c_g(t')} ; \quad m(\cdot) = \left[ \frac{k c_g(\cdot)}{2} \right]^{1/3}$$

$$t = \int_{Q_1}^{Q_2} dt' ; \quad X^L = 2kL \cos^2 \theta^i ; \quad X^d = \frac{kL \xi^2}{2m(Q_1)m(Q_2)}$$

**SURFACE  
GEODESIC  
PATH LENGTH**



Plot of  $e^{-i\pi/4} p^*(\xi)$  versus  $\xi$  based on tabulated data for  $p(\xi)$  by Logan (1959).



Plot of  $e^{-i\pi/4} q^*(\xi)$  versus  $\xi$  based on tabulated data for  $q(\xi)$  by Logan (1959).

$$L = \frac{e_1^i(Q_1) e_2^i(Q_1)}{(e_1^i(Q_1) + s)(e_2^i(Q_1) + s)} \cdot \frac{s(e_b^i(Q_1) + s)}{e_b^i(Q_1)}$$

where

$$s \equiv (s^r|_{SSB} = s^d|_{SSB}) ; e_b^i(Q_1) = \begin{cases} \text{incident} \\ \text{wavefront} \\ \text{radius in} \\ \hat{b}, \text{ dir. at } Q_1 \end{cases}$$

SPECIAL CASE:

(i) For a spherical wave illumination:

$$L = \frac{s' s}{s' + s}$$

with

$$s' \equiv (e_1^i(Q_1) = e_2^i(Q_1) = e_b^i(Q_1)) = \text{distance from point source to } Q_1.$$

(ii) For a plane wave illumination:

$$s' \rightarrow \infty \quad \text{and} \quad L = s$$

$$\tilde{P}_s(\delta) = \begin{Bmatrix} p^*(\delta) \\ q^*(\delta) \end{Bmatrix} e^{-j\frac{\pi}{4}} - \frac{e^{-j\frac{\pi}{4}}}{2\sqrt{\pi}\delta}, \quad (\text{Note: } \delta=0 \text{ at SSB})$$

$$\tilde{P}_s(\delta) = \frac{e^{-j\frac{\pi}{4}}}{\sqrt{\pi}} \int_{-\infty}^{\infty} d\tau \frac{\tilde{Q} V(\tau)}{\tilde{Q} W_2(\tau)} e^{-j\delta\tau}; \quad \tilde{Q} = \begin{cases} 1, & \text{for } \tilde{P}_s \\ \frac{\partial}{\partial \tau}, & \text{for } \tilde{P}_h \end{cases}$$

$$2j V(\tau) = W_1(\tau) - W_2(\tau)$$

$$W_1(\tau) = \frac{1}{\sqrt{\pi}} \int_{-\infty}^{\infty} dt e^{\tau t - t^3/3}$$

$$W_2(\tau) = \frac{1}{\sqrt{\pi}} \int_{\infty}^{\infty} dt e^{\tau t - t^3/3}$$

$$Ai(\tau) = V(\tau)/\sqrt{\pi}$$

It is easily verified that  $\left[ \bar{E}(P_L) = \bar{E}(P_S) \right]_{P_L=P_S=P}$  at SSB.

Note:  $\xi^L = \xi = 0$  at SSB.

$$\hat{P}_S(\delta) \Big|_{\delta \ll 0} \sim \pm \sqrt{\frac{-\delta}{4}} e^{j\delta^3/12}$$

in deep lit zone

$$\hat{P}_S(\delta) \Big|_{\delta \gg 0} = \left\{ \begin{array}{l} -\frac{e^{-j\pi/4}}{\sqrt{\pi}} \sum_{n=1}^N \frac{e^{j\pi/6} \delta q_n e^{-j5\pi/6}}{2[Ai'(-q_n)]^2} \\ -\frac{e^{-j\pi/4}}{\sqrt{\pi}} \sum_{n=1}^N \frac{e^{j\pi/6} \delta \bar{q}_n e^{-j5\pi/6}}{2[\bar{q}_n [Ai'(-\bar{q}_n)]^2]} \end{array} \right\} \begin{array}{l} \text{in deep shadow} \\ \text{zone.} \\ Ai(-q_n) = 0 \\ Ai'(-\bar{q}_n) = 0 \end{array}$$

$\therefore \bar{E}^y(P_L) \rightarrow \bar{E}^y(P_L)$ , in deep lit zone  
where  $X^L > 10$   
(and  $\xi^L \ll 0$ )

and

$\bar{E}^d(P_S) \rightarrow \bar{E}_K^d(P_S)$ , in deep shadow zone  
where  $X^d > 10$   
(and  $\xi \gg 0$ ).

$$\bar{E}_K^d(s) \sim \bar{E}^i(Q_1) \cdot \bar{T}^k(Q_1, Q_2) e^{-jkt} \sqrt{\frac{dn(Q_1)}{dn(Q_2)}} \sqrt{\frac{\rho_s}{s^d(\rho_s + s^d)}} e^{-jks^d}$$

$$\bar{T}^k(Q_1, Q_2) = \left[ \hat{b}_1 \hat{b}_2 T_s + \hat{n}_1 \hat{n}_2 T_h \right],$$

where

$$T_h = \sum_{n=1}^N D_n^h(Q_1) e^{-\int_{Q_1}^{Q_2} \hat{n}_n(t') dt'} D_n^h(Q_2)$$

## Keller's surface diffraction and attenuation coefficients:

$$\left\{ \begin{aligned} [D_n^s(Q)]^2 &= \sqrt{\frac{1}{2\pi k}} m(Q) \frac{e^{-j(\pi/12)}}{[Ai'(-q_n)]^2} \\ [D_n^h(Q)]^2 &= \sqrt{\frac{1}{2\pi k}} m(Q) \frac{e^{-j(\pi/12)}}{\bar{q}_n [Ai(-\bar{q}_n)]^2} \end{aligned} \right.$$

ZEROES OF THE AIRY FUNCTION	ZEROES OF THE DERIVATIVE OF THE AIRY FUNCTION
$Ai(-q_p) = 0$	$Ai'(-\bar{q}_p) = 0$
$q_1 = 2.33811$	$\bar{q}_1 = 1.01879$
$q_2 = 4.08795$	$\bar{q}_2 = 3.24820$
$Ai'(-q_1) = 0.70121$	$Ai(-\bar{q}_1) = 0.53566$
$Ai'(-q_2) = -0.90311$	$Ai(-\bar{q}_2) = -0.41902$

and

$$\left\{ \begin{aligned} r_n(Q) &= \frac{q_n}{\rho_g(Q)} m(Q) e^{j(\pi/6)} \\ h_n(Q) &= \frac{\bar{q}_n}{\rho_g(Q)} m(Q) e^{j(\pi/6)} \end{aligned} \right.$$

## 2-D case:

$$\rho_2^r \equiv \rho^r, \text{ if } \rho_1^r = + \text{ and } \rho_s = -$$

so that

$$E^{gr}(P_L) \sim E^i(Q_R). [R_s \hat{e}_\perp \hat{e}_\perp + R_h \hat{e}_{//} \hat{e}_{//}] \sqrt{\frac{\rho^r}{\rho^r + s^r}} e^{-jks^r}$$

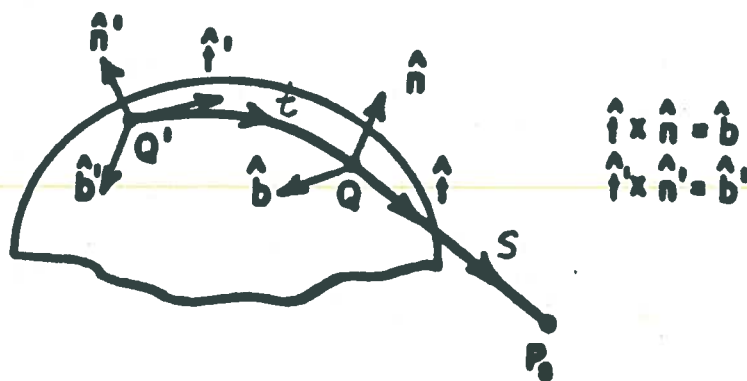
$$E^d(P_S) \sim E^i(Q_1). [D_s \hat{b} \hat{b} + D_h \hat{n}_1 \hat{n}_2] \frac{e^{-jks^d}}{\sqrt{s^d}}$$

$$\hat{b}_1 = \hat{b}_2 = \hat{b} = \hat{e}_\perp \text{ for 2-D case.}$$

$$L = \frac{s' s^d}{s' + s^d}$$

# Radiation Problem (3-D)

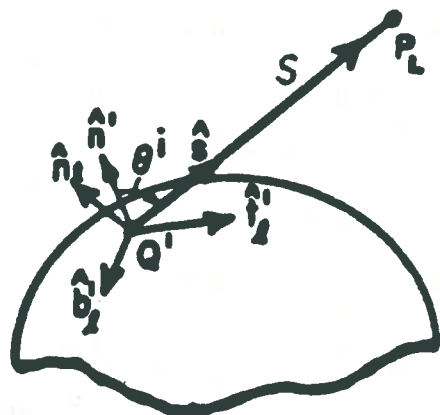
Pathak et. al.  
 IEEE Trans. AP-29, No.4  
 pp. 609-622, July 1981.



$$\begin{aligned} \hat{i} \times \hat{n} &= \hat{b} \\ \hat{i} \times \hat{n}' &= \hat{b}' \end{aligned}$$

FOR SHADOW REGION

$$\bar{E}_e(P_s) \sim d\bar{p}_e(Q') \cdot \bar{T}_e^s(Q, Q') \sqrt{\frac{\rho_s}{s(\rho_s + s)}} e^{-jks}$$

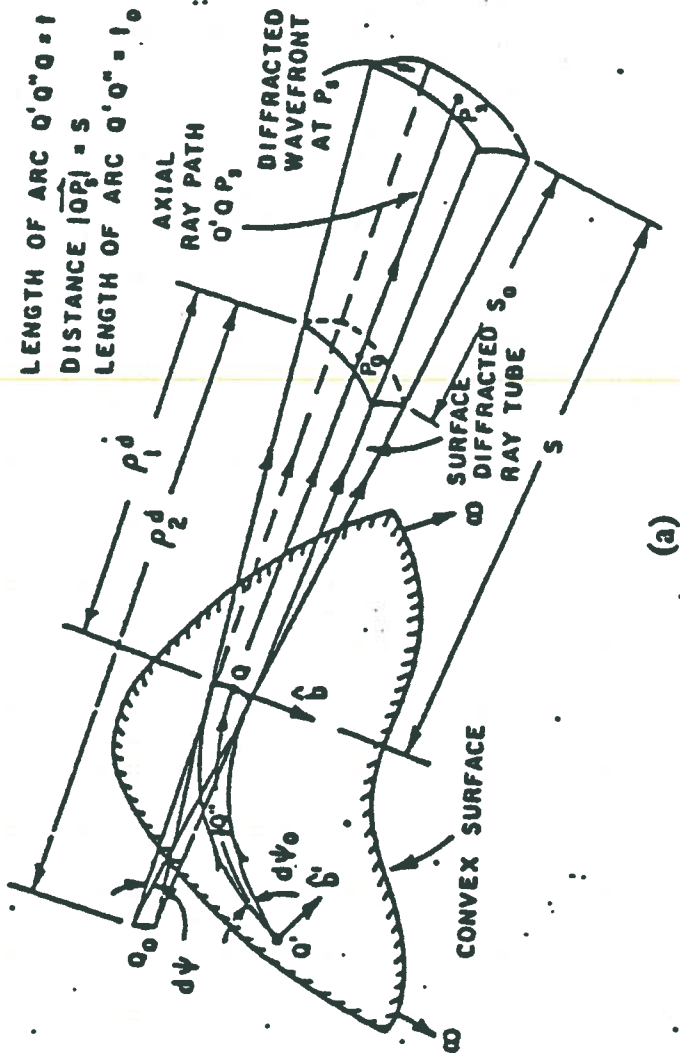


$$\begin{aligned} \hat{i}_1 \times \hat{n}' &= \hat{b}'_1 \\ \hat{s} \times \hat{n} &= \hat{b} \\ \hat{b} &= \hat{b}'_1 \end{aligned}$$

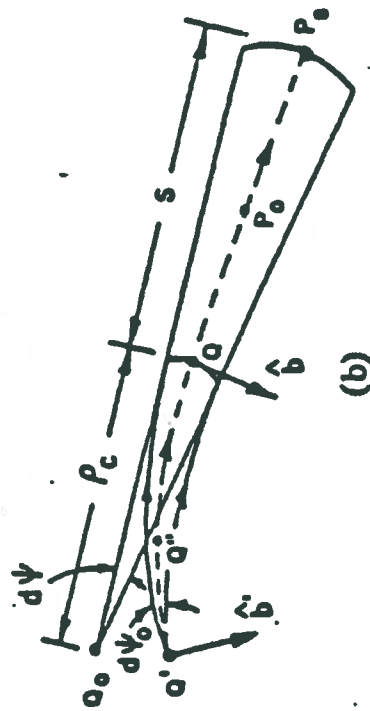
$$\bar{E}_e(P_L) \sim d\bar{p}_e(Q') \cdot \bar{T}_e^l(P_L, Q') \frac{e^{-jks}}{s}$$

FOR LIT REGION

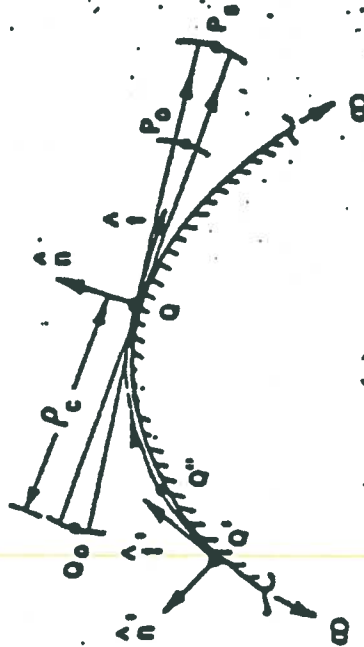
NOTE :  $\bar{T}^{l,s} = \bar{T}^{l,s}(G; \tilde{G})$



(a)



(b)

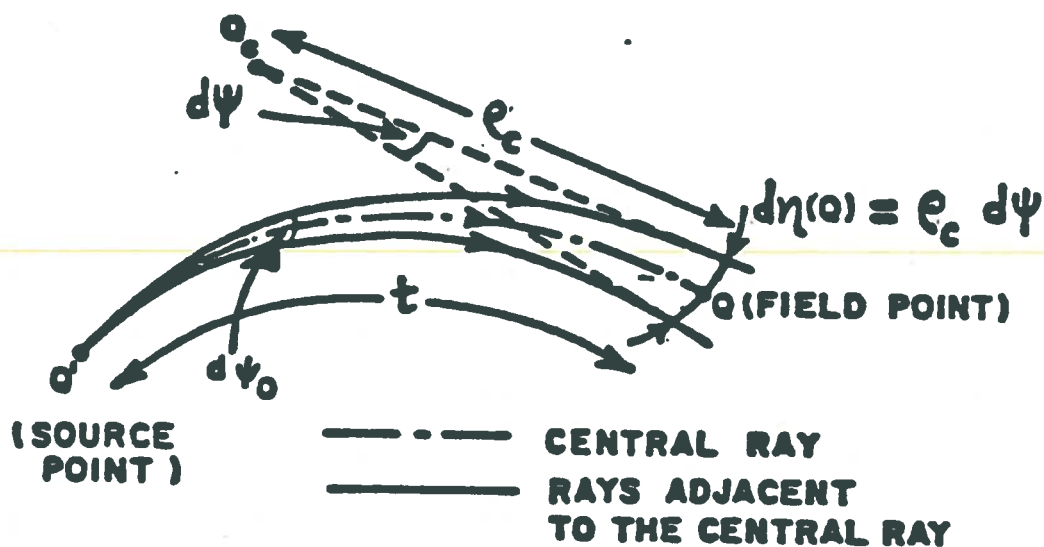


(c)

Surface diffracted ray tube and ray coordinates for the shadow region. (a) Perspective view of a surface diffracted ray tube. (b) Top view of a diffracted ray tube indicating the divergence of the rays and the unit binormal vectors at  $Q'$  and  $Q''$ . (c) Side view of a surface diffracted ray tube and the unit normal and tangent vectors at  $Q'$  and  $Q''$ .

Surface diffracted ray caustic distance:

$$\sqrt{\frac{d\psi_0}{d\eta(Q)}} = \sqrt{\frac{d\psi_0}{\rho_c d\psi}}$$



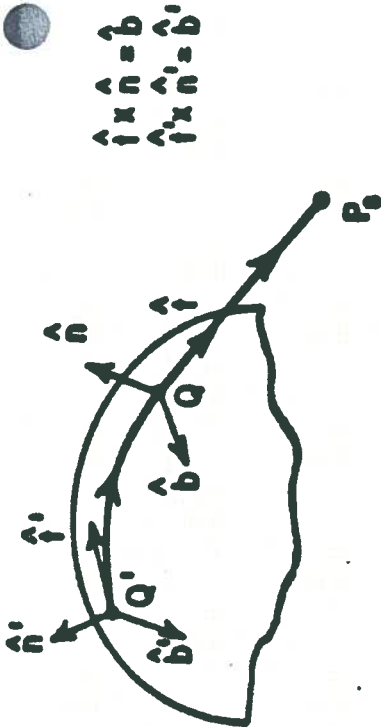
Surface Ray Strip

$$\rho_c = \frac{2\sqrt{\mathcal{E}} \mathcal{G}}{\partial \mathcal{G} / \partial t}$$

Here  $\mathcal{E}$  and  $\mathcal{G}$  denote two of the three "first fundamental coefficients"  $\mathcal{E}$ ,  $\mathcal{F}$  and  $\mathcal{G}$ , respectively which pertain to the differential arc length along a curve on a surface.

# Radiation Problem (3-D)

(P.H. Pathak et al., IEEE Trans. AP-29, July 1981, pp. 609-621.)



$$\hat{x} \hat{n} = \hat{b}$$

$$\hat{y} \hat{n} = \hat{a}$$

## FOR SHADOW REGION

TYPE OF CONVEX SURFACE	SLOT OR $d\vec{p}_m$ CASE			MONOPOLE OR $d\vec{p}_0$ CASE		SURFACE RAY TORSION $T(\theta')$	SURFACE RADIUS OF CURVATURE IN $\hat{y}$ DIRECTION $\rho_0(\theta')$	SURFACE RADIUS OF FRACTURE IN RAY CAUSTIC DIRECTION $\rho_c$
	$T_1(\theta')$	$T_2(\theta')$	$T_3(\theta')$	$T_4(\theta')$	$T_5(\theta')$			
SPHERE	1	1	0	0	1	0	0	$a \tan(\frac{1}{\rho})$
CIRCULAR CYLINDER	1	1	$\frac{\sin 2\theta'}{2a} \cdot \frac{a}{\sin^2 \theta'}$	0	1	$\frac{\sin 2\theta'}{2a}$	$\frac{a}{\sin^2 \theta'}$	1
ARBITRARY CONVEX SURFACE	1	1	$T_1(\theta') \rho_0(\theta')$	0	1	$T_1(\theta') \rho_0(\theta')$	$\frac{\sin 2\theta'}{2} \left( \frac{1}{R_2(\theta')} - \frac{1}{R_1(\theta')} \right)$ WITH $R_1(\theta') \geq R_2(\theta')$	$\left( \frac{\cos^2 \theta'}{R_1(\theta')} + \frac{\sin^2 \theta'}{R_2(\theta')} \right)^{-1}$
								$\frac{2\sqrt{a}}{2a/\rho}$

NOTE:  $d\vec{E}_m(\rho_0) = d\vec{p}_m(\theta') \cdot \vec{T}_m(\theta') \sqrt{\frac{\rho_c}{a(\rho_0 + a)}} e^{-jk\rho_0}$

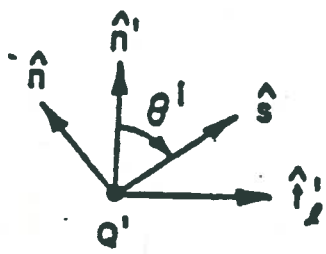
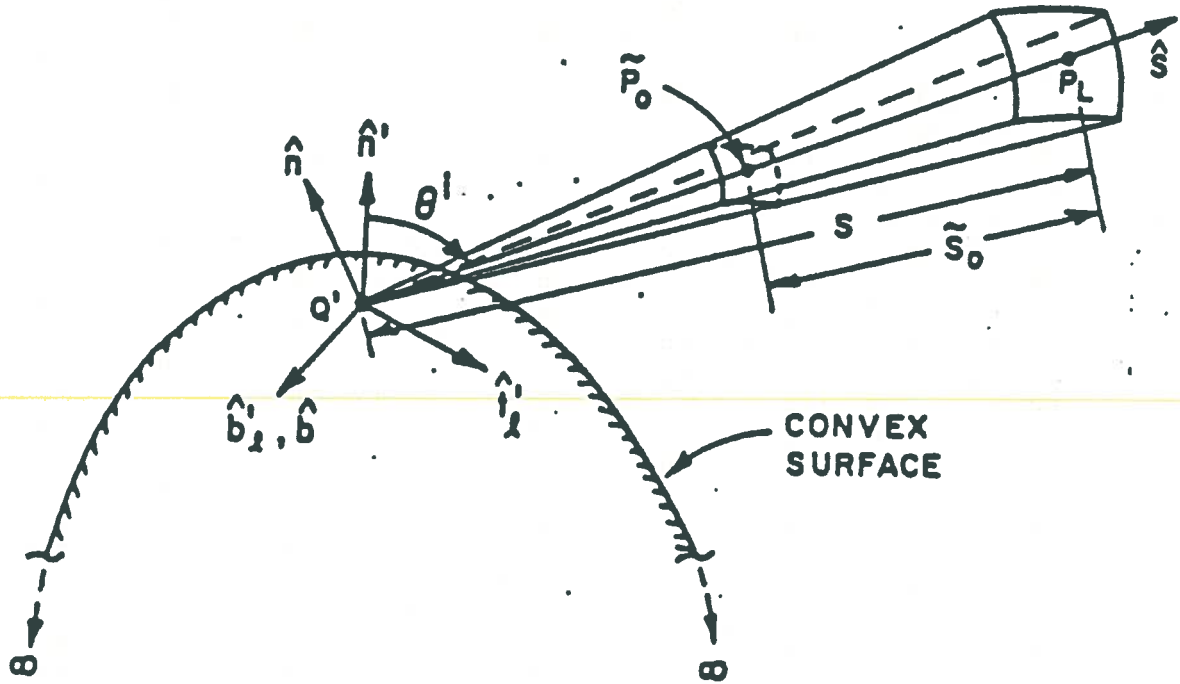
WITH

$$\vec{T}_m(\theta') = \frac{-jk}{4\pi} \left[ \hat{b} \hat{n} T_1(\theta') H + \hat{a} \hat{n} T_2(\theta') S + \hat{b} \hat{b} T_3(\theta') S + \hat{a} \hat{a} T_4(\theta') H \right] e^{-jk\rho_0} \sqrt{\frac{dV_0}{d\gamma(\theta')}} \left[ \frac{\rho_0(\theta')}{\rho_0(\theta')} \right]^{1/6}$$

FOR THE SLOT OR  $d\vec{p}_m$  CASE, AND

$$\vec{T}_0(\theta') = \frac{-jkz_0}{4\pi} \left[ \hat{a} \hat{n} T_5(\theta') H + \hat{a} \hat{n} \hat{b} T_6(\theta') S \right] e^{-jk\rho_0} \sqrt{\frac{dV_0}{d\gamma(\theta')}} \left[ \frac{\rho_0(\theta')}{\rho_0(\theta')} \right]^{1/6}$$

FOR THE MONOPOLE OR  $d\vec{p}_0$  CASE.

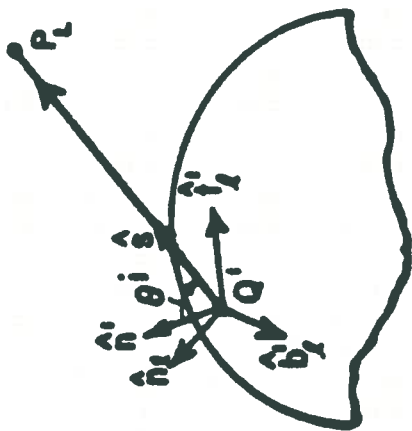


$$\hat{n}' \cdot \hat{s} = \cos \theta^i$$

$$\hat{s} = \hat{n}' \cos \theta^i + \hat{t}' \sin \theta^i$$

$$\hat{b}' = \hat{t}' \times \hat{n}' = \hat{b} = \hat{s} \times \hat{n}$$

Ray tube and ray coordinates for the lit region.



$$\begin{aligned} \hat{a}'_x \hat{a}'_y &= \hat{b}'_z \\ \hat{a}'_x \hat{a}'_z &= \hat{b}'_y \\ \hat{a}'_y \hat{a}'_z &= \hat{b}'_x \end{aligned}$$

FOR LIT REGION

SLOT OR $d\bar{p}_m$ CASE				MONOPOLE OR $d\bar{p}_0$ CASE			
A	B	C	D	M	N	$T_0$	T
$M^2 + T_0^2 T \cos \theta'$	$S^2 - T_0^2 T \cos^2 \theta'$	$T_0 T$	$T_0 T \cos \theta'$	$\sin \theta' [M^2 + T_0^2 T \cos \theta']$		$T_0 T$	$\frac{S^2 - M^2 \cos \theta'}{1 + T_0 \cos \theta'}$
						$T_0 T$	

NOTE:  $d\vec{E}_m(\vec{P}_L | Q') = d\vec{p}_m(Q') \cdot \vec{T}_m^A \frac{e^{-jkz}}{z}$

WITH  $\vec{T}_m^A = \frac{-jk}{4\pi} [ \hat{b}'_z \hat{a}'_x + \hat{a}'_y \hat{b}'_z + \hat{b}'_x \hat{a}'_z + \hat{a}'_x \hat{b}'_y ]$

AND  $\vec{T}_0^A = \frac{-jkZ_0}{4\pi} [ \hat{a}'_x \hat{a}'_y + \hat{a}'_y \hat{a}'_x ]$

FOR THE SLOT OR  $d\bar{p}_m$  CASE.

FOR THE MONOPOLE OR  $d\bar{p}_0$  CASE.

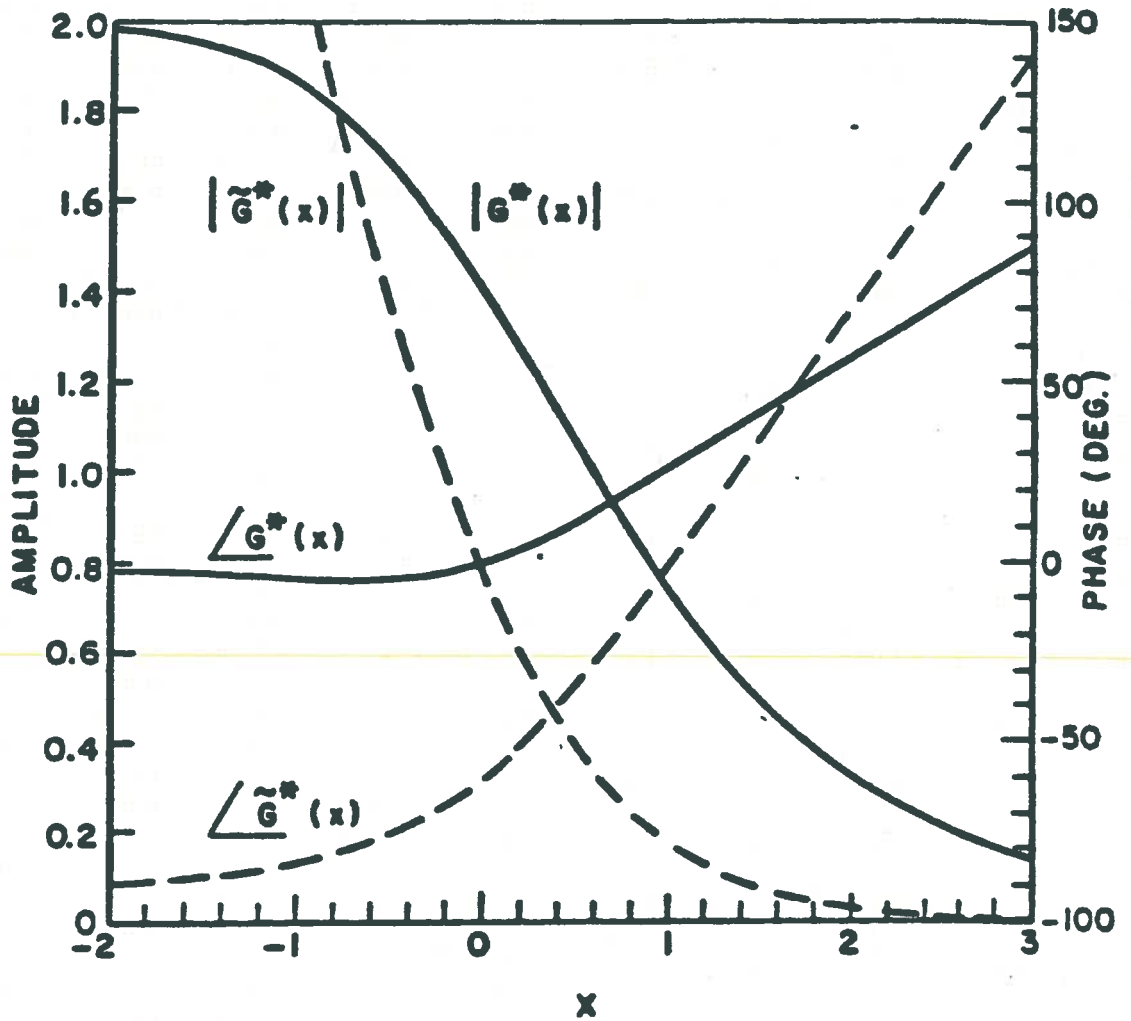
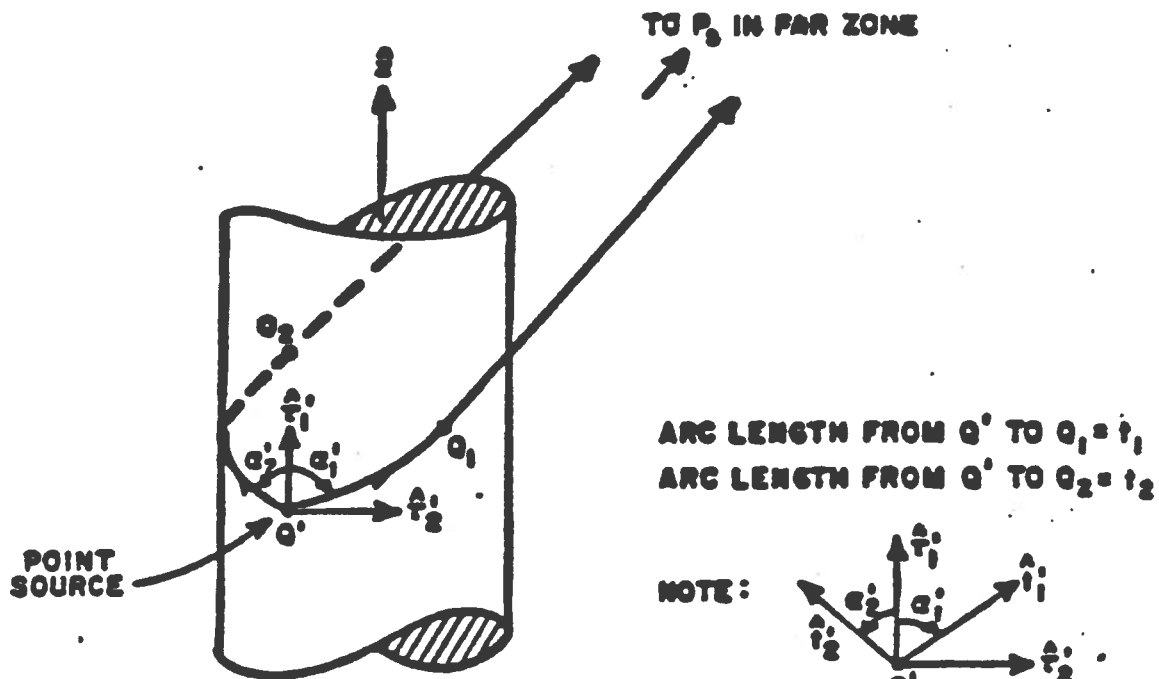


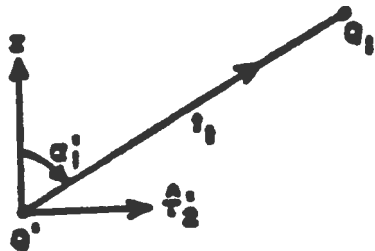
Figure . Fock functions  $G^*(x)$  and  $G^{\sim}(x)$ .

$$S^l(\xi^l) \equiv \frac{-j}{m(q')} \tilde{G}(\xi^l) \quad ; \quad S(\xi) \equiv \frac{-j}{m(q')} \tilde{G}(\xi)$$

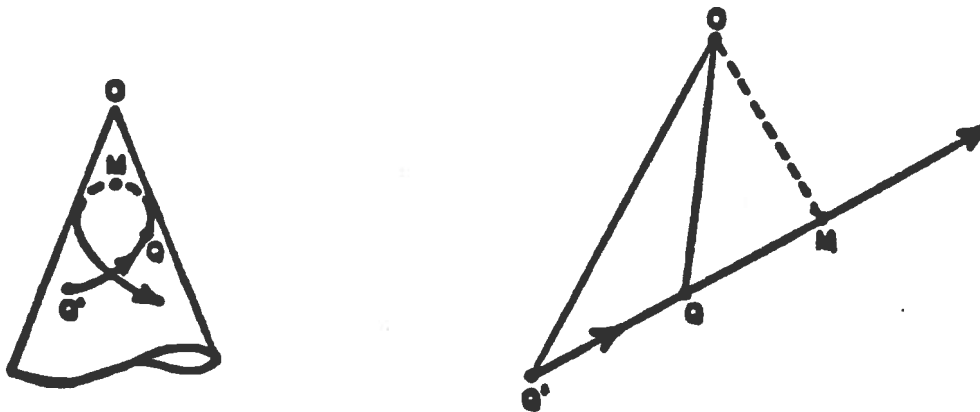
$$H^l(\xi^l) \equiv G(\xi^l) \quad ; \quad H(\xi) \equiv G(\xi) .$$



Dominant helical geodesic surface ray paths from source point at  $Q'$  to points of diffraction  $Q_1$  and  $Q_2$  on a convex cylinder. The angles  $\alpha_1'$  and  $\alpha_2'$  stay the same with respect to the generator (or the  $\hat{z}$  - direction) of the cylinder.



Helical geodesic surface ray path from  $Q'$  to  $Q_1$  of above Figure on a developed cylinder.



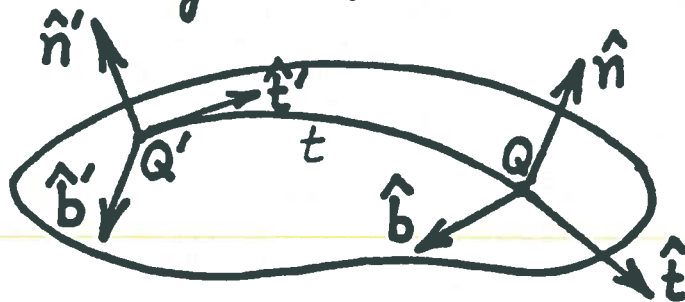
(a) Geodesic surface ray path on a cone

(b) Geodesic path on a developed cone

A typical surface ray path on a semi-infinite cone.

## 3-D Coupling Solution

Surface fields on an arbitrary convex conducting surface:



$$\xi = \int_{Q'}^Q ds' \frac{m(s')}{\rho_s(s')}$$

$$\bar{H}_m(Q) \sim \frac{-jk}{4\pi} d\bar{p}_m(Q') \cdot \bar{\bar{\tau}}_{h,m}(Q, Q') \mathcal{D} G_0(kt)$$

$$\bar{E}_m(Q) \sim \frac{-jk}{4\pi} d\bar{p}_m(Q') \cdot \bar{\bar{\tau}}_{e,m}(Q, Q') \mathcal{D} G_0(kt)$$

$$\bar{H}_e(Q) \sim \frac{-jk}{4\pi} d\bar{p}_e(Q') \cdot \bar{\bar{\tau}}_{h,e}(Q, Q') \mathcal{D} G_0(kt)$$

$$\bar{E}_e(Q) \sim \frac{-jk}{4\pi} d\bar{p}_e(Q') \cdot \bar{\bar{\tau}}_{e,e}(Q, Q') \mathcal{D} G_0(kt)$$

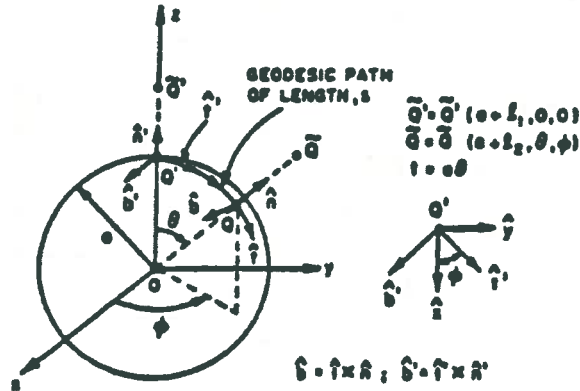
$$G_0(kt) = \frac{e^{-jkt}}{t}$$

$$\bar{\bar{\tau}} = \bar{\bar{\tau}}(U(\xi); V(\xi))$$

(P. H. Pathak & N. Wang, IEEE Trans. AP-29, Nov. '81, pp. 911-922)

## 3-D Coupling Solution

### A. Surface fields on a conducting sphere :



The  $d\bar{p}_m$  source at  $Q'$  generates the fields  $d\bar{H}_m$  and  $d\bar{E}_m$  on the surface at  $Q$ ; these fields are given by

$$d\bar{H}_m(Q|Q') = \frac{-jk}{4\pi} d\bar{p}_m \cdot \left\{ 2Y_0 \left( \hat{b}'\hat{b} \left[ \left( 1 - \frac{j}{kt} \right) V(\xi) + \mathcal{D}^2 \left( \frac{j}{kt} \right)^2 U(\xi) + \hat{i}'\hat{i} \left[ \mathcal{D}^2 \frac{j}{kt} V(\xi) + \frac{j}{kt} \left( 1 - \frac{2j}{kt} \right) U(\xi) \right] \right] \right\} \mathcal{D}G_0(kt),$$

and

$$d\bar{E}_m(Q|Q') = \frac{-jk}{4\pi} d\bar{p}_m(Q') \cdot \left\{ 2\hat{b}'\hat{n} \left[ 1 - \frac{j}{kt} \right] V(\xi) \right\} \mathcal{D}G_0(kt).$$

Similarly, the surface fields  $d\bar{E}_e$  and  $d\bar{H}_e$  due to the source  $d\bar{p}_e(Q')$  are given by

$$d\bar{E}_e(Q|Q') = \frac{-jk}{4\pi} d\bar{p}_e(Q') \cdot \left\{ 2Z_0 \hat{n}' \hat{n} \left[ 1 - \frac{j}{kr} \left( 1 - \frac{j}{kr} \right) \right] \right\} V(\xi) \mathcal{D} G_0(kr),$$

and

$$d\bar{H}_e(Q|Q') = \frac{-jk}{4\pi} d\bar{p}_e(Q') \cdot \left\{ 2\hat{n}' \hat{b} \left[ 1 - \frac{j}{kr} \right] V(\xi) \right\} \mathcal{D} G_0(kr).$$

where

$$r = a\theta,$$

$$\xi = \frac{mr}{a} = m\theta > 0,$$

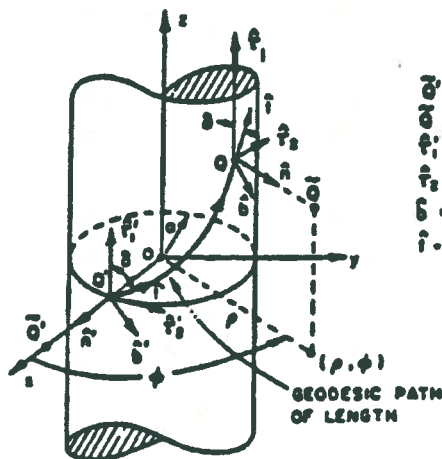
$$m = \left( \frac{ka}{2} \right)^{1/3}$$

$$\rho_c = a \tan \theta.$$

and

$$\mathcal{D} = \sqrt{\frac{\theta}{\sin \theta}}.$$

B. Surface fields on a conducting circular cylinder :



$$\begin{aligned} \vec{Q}' &= \vec{Q}(a+1, 0, 0) \\ \vec{Q} &= \vec{Q}(a+2, \phi, z) \\ \hat{r}'_1 &= \hat{z} \text{ AT } Q'; \hat{r}'_1 = \hat{z} \text{ AT } Q \\ \hat{r}'_2 &= \hat{\phi} \text{ AT } Q'; \hat{r}'_2 = \hat{\phi} \text{ AT } Q \\ \vec{b} &= \hat{i} \times \hat{n}; \vec{b}' = \hat{i}' \times \hat{n}' \\ \hat{i} \cdot \hat{z} &= \cos \theta = \hat{i}' \cdot \hat{z}' \end{aligned}$$

$$d\bar{H}_m(Q|Q') = \frac{-jk}{4\pi} d\bar{p}_m(Q')$$

$$\begin{aligned} & \cdot \left[ 2Y_0 \left( \vec{b}' \cdot \vec{b} \left\{ \left( 1 - \frac{j}{kt} \right) V(\xi) \right. \right. \right. \\ & + \mathcal{D}^2 \left( \frac{j}{kt} \right)^2 V(\xi) + T_0^2 \frac{j}{kt} [U(\xi) - V(\xi)] \left. \right\} \\ & + \ddot{z}' \dot{z}' \left\{ \mathcal{D}^2 \frac{j}{kt} V(\xi) + \frac{j}{kt} U(\xi) - 2 \left( \frac{j}{kt} \right)^2 V(\xi) \right\} \\ & + [\ddot{r}' \dot{b} + \dot{b}' \ddot{r}'] \left\{ T_0 \frac{j}{kt} [U(\xi) - V(\xi)] \right\} \left. \right] \\ & \cdot \mathcal{D}G_0(kt), \end{aligned}$$

$$d\bar{E}_m(Q|Q') = \frac{-jk}{4\pi} d\bar{p}_m(Q')$$

$$\cdot \left[ 2 \left( \delta' \dot{n} \left\{ \left( 1 - \frac{j}{kt} \right) V(\xi) \right. \right. \right.$$

$$\left. \left. + T_0^2 \frac{j}{kt} [U(\xi) - V(\xi)] \right\} \right.$$

$$\left. \left. + \dot{n}' \left\{ T_0 \frac{j}{kt} [U(\xi) - V(\xi)] \right\} \right) \right] \mathcal{D}G_0(kt).$$

$$d\bar{E}_e(Q|Q') = \frac{-jk}{4\pi} d\bar{p}_e(Q')$$

$$\cdot \left[ 2Z_0 \left( \dot{n}' \dot{n} \left\{ V(\xi) - \frac{j}{kt} V(\xi) + \left( \frac{j}{kt} \right)^2 U(\xi) \right. \right. \right.$$

$$\left. \left. + T_0^2 \frac{j}{kt} [U(\xi) - V(\xi)] \right\} \right) \right] \mathcal{D}G_0(kt),$$

and

$$d\bar{H}_e(Q|Q') = \frac{-jk}{4\pi} d\bar{p}_e(Q')$$

$$\cdot \left[ 2 \left( \dot{n}' \dot{\delta} \left\{ \left( 1 - \frac{j}{kt} \right) V(\xi) \right. \right. \right.$$

$$\left. \left. + T_0^2 \frac{j}{kt} [U(\xi) - V(\xi)] \right\} \right.$$

$$\left. \left. + \dot{n}' \dot{\delta}' \left\{ T_0 \frac{j}{kt} [U(\xi) - V(\xi)] \right\} \right) \right] \mathcal{D}G_0(kt).$$

where

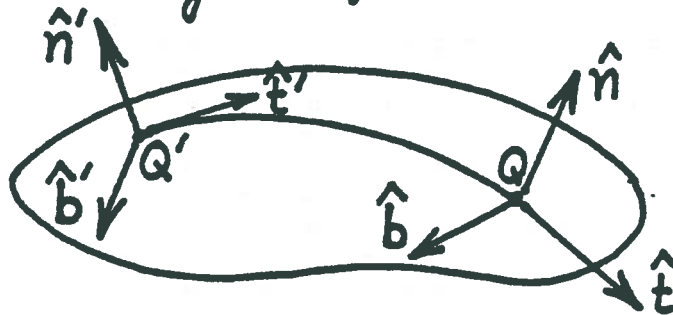
$$t = \sqrt{(a\phi)^2 + z^2}, \quad m = \left( \frac{k\rho_g}{2} \right)^{1/3}, \quad T\rho_g = \cot \delta.$$

$$\xi = \frac{mt}{\rho_g}, \quad \rho_g = \frac{a}{\sin^2 \delta}, \quad T_0 = \frac{\sin 2\delta}{2a} \cdot \frac{a}{\sin^2 \delta} = T\rho_g,$$

and

$$\mathcal{D} = 1.$$

c. Surface fields on an arbitrary convex conducting surface:



$$\xi = \int_{Q'}^Q dt' \frac{m(t')}{\rho_g(t')}$$

$$d\bar{H}_m(Q|Q') = \frac{-jk}{4\pi} d\bar{p}_m(Q')$$

$$\begin{aligned} & \cdot \left\{ 2Y_0 (\hat{b}'\hat{b}) \left[ \left(1 - \frac{j}{kr}\right) \bar{V}(\xi) \right. \right. \\ & + D^2 \left(\frac{j}{kr}\right)^2 (\Lambda_s \bar{U}(\xi) + \Lambda_c \bar{V}(\xi)) \\ & + \bar{T}_0^2 \frac{j}{kr} (\bar{U}(\xi) - \bar{V}(\xi)) \left. \right] \\ & + \hat{t}'\hat{t} \left[ D^2 \frac{j}{kr} \bar{V}(\xi) + \frac{j}{kr} \bar{U}(\xi) \right. \\ & - 2 \left(\frac{j}{kr}\right)^2 (\Lambda_s \bar{U}(\xi) + \Lambda_c \bar{V}(\xi)) \left. \right] \\ & + (\hat{t}'\hat{b} + \hat{b}'\hat{t}) \left[ \frac{j}{kr} \bar{T}_0 (\bar{U}(\xi) - \bar{V}(\xi)) \right] \left. \right\} \\ & \cdot DG_0(kr), \end{aligned}$$

NOTE :  $\bar{T}_0 = \text{sgn}[T_0(Q')] \cdot \text{sgn}[T_0(Q)] \cdot |\sqrt{T_0(Q')T_0(Q)}|$  ;  $D = \sqrt{\frac{td\psi_0}{d\eta(Q)}}$

$$d\bar{E}_m(Q|Q') = \frac{-jk}{4\pi} d\bar{p}_m(Q') \cdot \left\{ 2 \left( \hat{b}'\hat{n} \left[ \left( 1 - \frac{j}{kr} \right) \bar{V}(\xi) + \bar{T}_0^2 \frac{j}{kr} (\bar{U}(\xi) - \bar{V}(\xi)) \right] + \hat{i}'\hat{n} \left[ \bar{T}_0 \frac{j}{kr} (\bar{U}(\xi) - \bar{V}(\xi)) \right] \right) \right\} \mathcal{D}G_0(kr).$$

Similarly, the surface fields  $d\bar{H}_e$  and  $d\bar{E}_e$  due to  $d\bar{p}_e$  on an arbitrary convex surface are given by

$$d\bar{E}_e(Q|Q') = \frac{-jk}{4\pi} d\bar{p}_e(Q') \cdot \left\{ 2Z_0\hat{n}'\hat{n} \left[ \bar{V}(\xi) - \frac{j}{kr} \bar{V}(\xi) + \left( \frac{j}{kr} \right)^2 (\Lambda_s \bar{V}(\xi) + \Lambda_c \bar{U}(\xi)) + \bar{T}_0^2 \frac{j}{kr} (\bar{U}(\xi) - \bar{V}(\xi)) \right] \right\} \mathcal{D}G_0(kr),$$

and

$$d\bar{H}_e(Q|Q') = \frac{-jk}{4\pi} d\bar{p}_e(Q') \cdot \left\{ 2 \left( \hat{n}'\hat{b} \left[ \left( 1 - \frac{j}{kr} \right) \bar{V}(\xi) + \bar{T}_0^2 \frac{j}{kr} (\bar{U}(\xi) - \bar{V}(\xi)) \right] + \hat{n}'\hat{i} \left[ \bar{T}_0 \frac{j}{kr} (\bar{U}(\xi) - \bar{V}(\xi)) \right] \right) \right\} \mathcal{D}G_0(kr).$$

The generalized Fock integrals  $\bar{U}(\xi)$  and  $\bar{V}(\xi)$  for the arbitrary convex surface are given by

$$\bar{U}(\xi) = \left[ \frac{kr}{2m(Q')m(Q)\xi} \right]^{3/2} U(\xi)$$

$$\bar{V}(\xi) = \left[ \frac{kr}{2m(Q')m(Q)\xi} \right]^{1/2} V(\xi).$$

Also,  $\sqrt{\dots}$

$\xi \gg 0$  (DEEP SHADOW)

$$V(\xi) = e^{-j\frac{\pi}{4}} \sqrt{\pi} \xi^{1/2} \sum_{n=1}^N (\tau'_n)^{-1} e^{-j\xi \tau'_n}$$

$$U(\xi) = e^{j\frac{\pi}{4}} 2\sqrt{\pi} \xi^{3/2} \sum_{n=1}^N e^{-j\xi \tau_n}$$

$$\tau_n = |\tau_n| e^{-j\pi/3} \quad ; \quad \tau'_n = |\tau'_n| e^{-j\pi/3}$$

$n$	$ \tau_n $	$ \tau'_n $
1	2.33811	1.01879
2	4.08795	3.24819
3	5.52056	4.82010
4	6.78661	6.16331
$\vdots$	$\vdots$	$\vdots$

$\xi \rightarrow 0$  (NEAR SOURCE POINT)

$$V(\xi) \sim 1 - \frac{\sqrt{\pi}}{4} e^{j\frac{\pi}{4}} \xi^{3/2} + \frac{j7}{60} \xi^3 + \frac{7\sqrt{\pi}}{512} \xi^{9/2}$$

$$U(\xi) \sim 1 - \frac{\sqrt{\pi}}{2} e^{j\pi/4} \xi^{3/2} + \frac{j5}{12} \xi^3 + \frac{5\sqrt{\pi}}{64} e^{-j\frac{\pi}{4}} \xi^{9/2}$$

## Some UTD code developments in USA during 1980's – 1990's

The Ohio State Univ. (OSU) ElectroScience Lab. (ESL) UTD based codes:

- (a) OSU-ESL NEWAIR code
- (b) OSU-ESL BSC code

- Complex radiating and scattering objects modeled by simpler shapes consisting of ellipsoids, spheroids, cylinders, cone frustrums, flat plates, etc.



ElectroScience LABORATORY

7

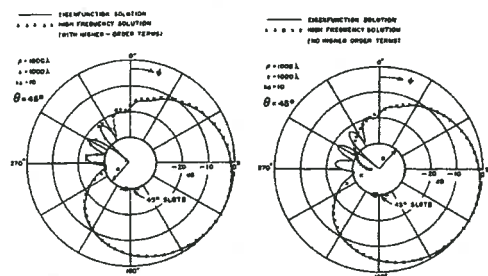


Fig. 8.  $|E_{\theta}|$  radiation pattern of a  $45^\circ$  (tilted) slot in a circular cylinder.

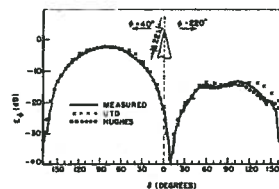


Fig. 9.  $|E_{\theta}|$  radiation pattern of a radial slot in a cone (see cone geometry in Fig. 10).

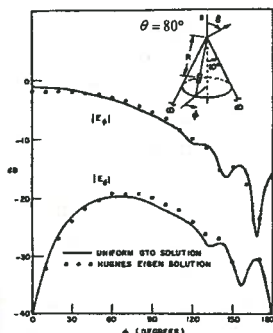


Fig. 10. Radiation patterns of a radial slot in a cone.

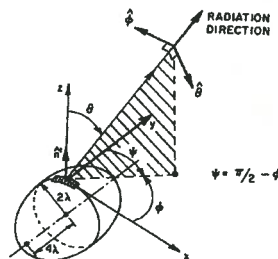
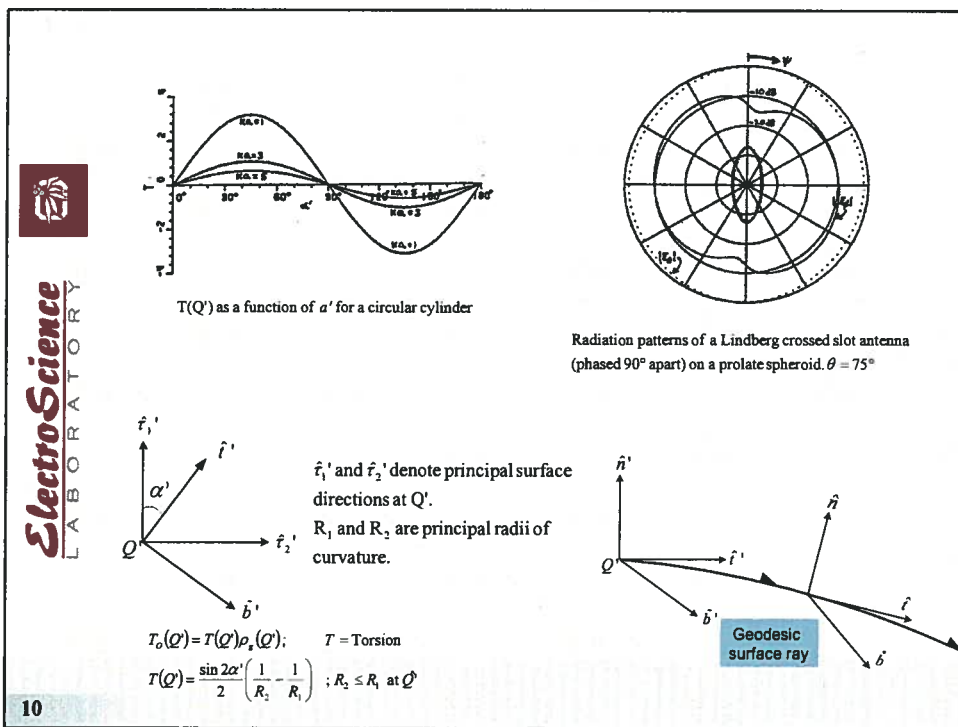
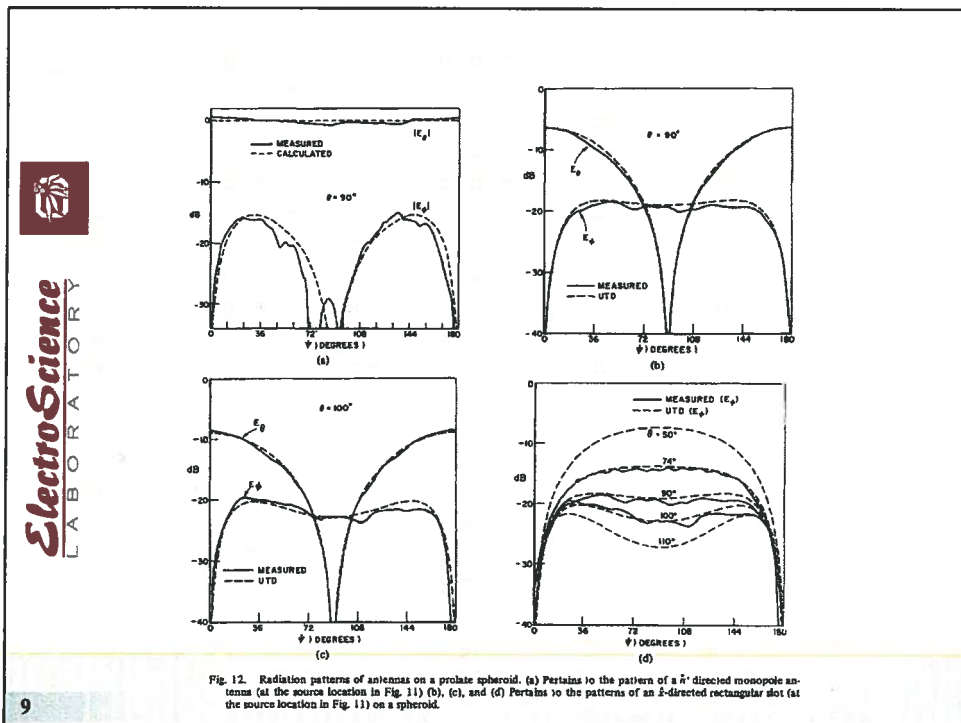


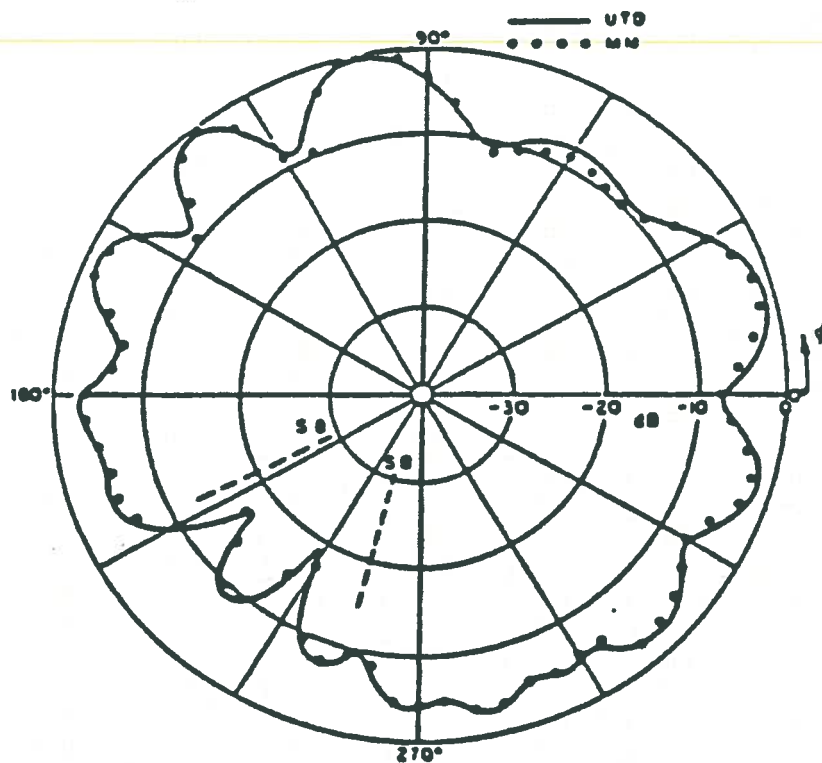
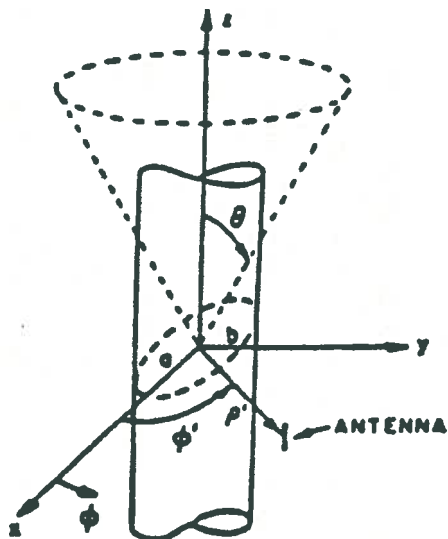
Fig. 11. Prolate spheroidal geometry.



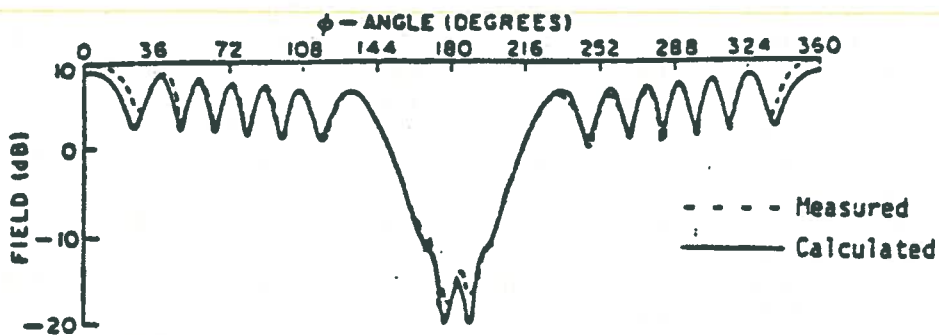
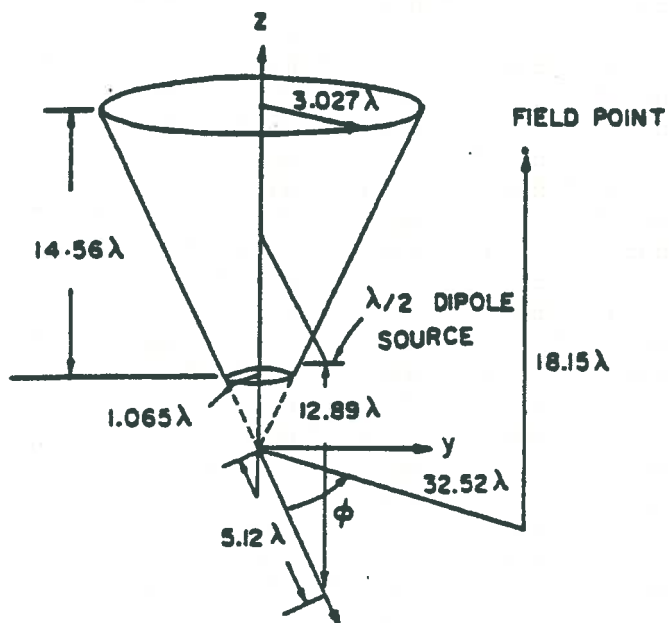
ElectroScience LABORATORY

8

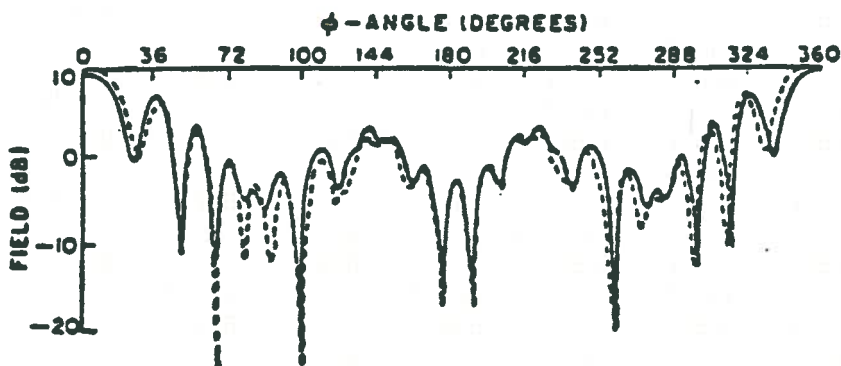




Radiation pattern of a magnetic dipole located parallel to axis of an elliptic cylinder.

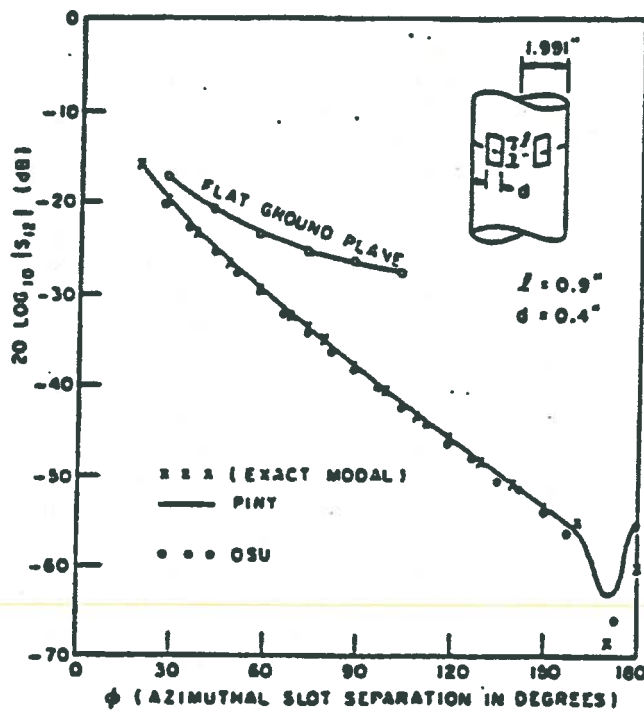


(b) VERTICAL POLARIZATION

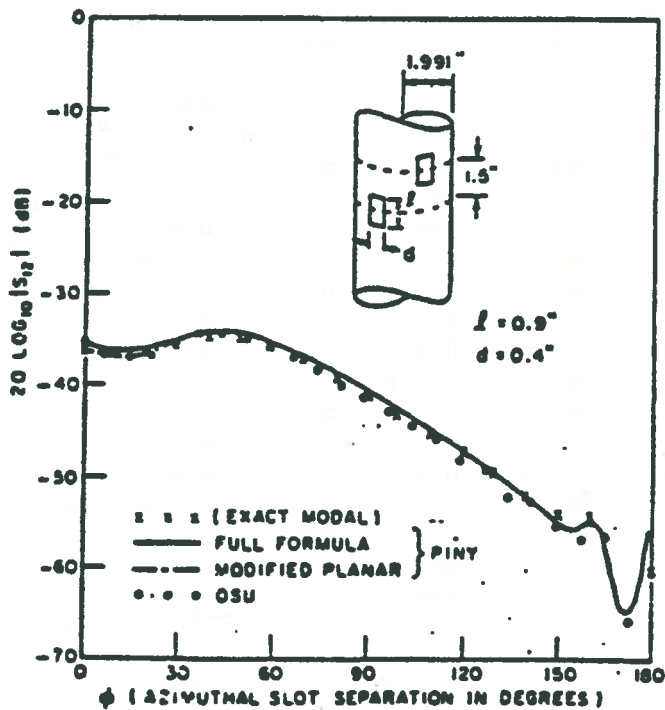


(c) HORIZONTAL POLARIZATION

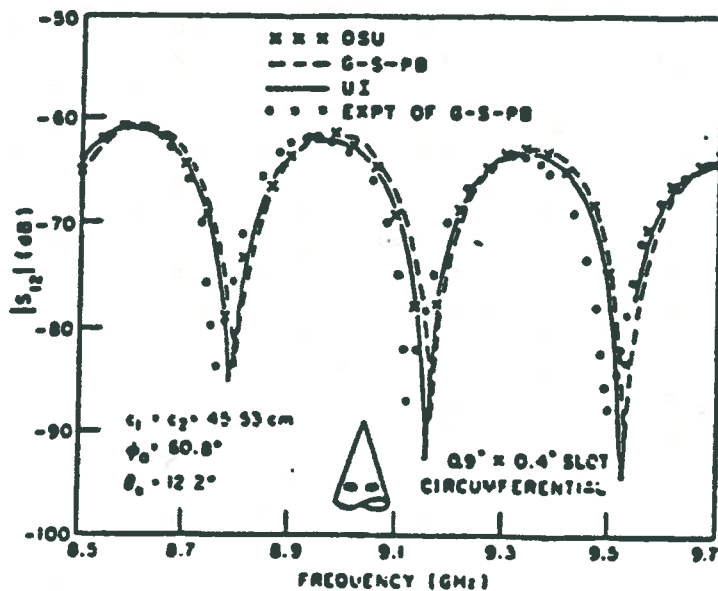
Radiation patterns of an electric dipole near the frustum of a cone.



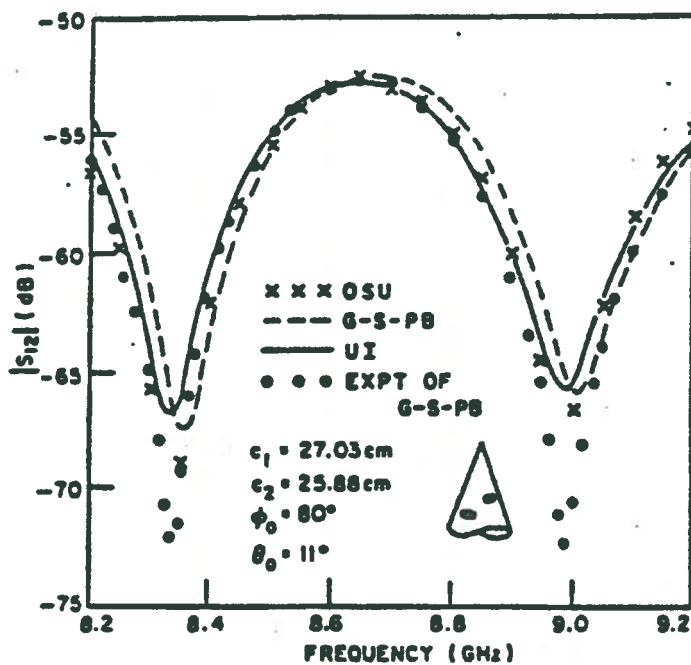
Isolation of axial slots on a conducting cylinder,  $a = 1.991$  inches;  
 $Z_0 = 0$ ; frequency = 9 GHz.



Isolation of axial slots on a conducting cylinder  $a = 1.991$  inches;  
 $Z_0 = 1.50$  inches; frequency = 9 GHz.



Coupling coefficient  $S_{12}$  between two circumferential slots on a cone versus frequency. The radial separation between the slots is  $|C_1 - C_2|$  and angular separation is  $\phi_0$ . The cone half angle is  $\theta_0$ .



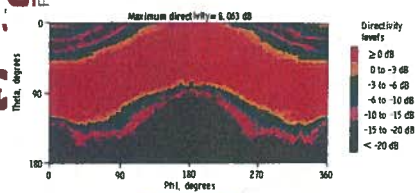
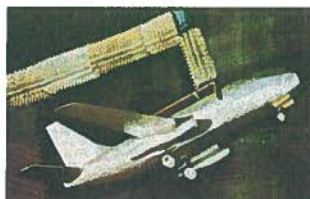
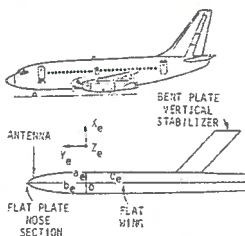
Coupling coefficient  $S_{12}$  between two circumferential slots on a cone versus frequency. The radial separation between the slots is  $|C_1 - C_2|$  and angular separation is  $\phi_0$ . The cone half angle is  $\theta_0$ .

C. L. Yu, W. D. Burnside, and M. C. Gilreath, "Volumetric pattern analysis of airborne antennas," *IEEE Trans. AP*, Sep. 1978.

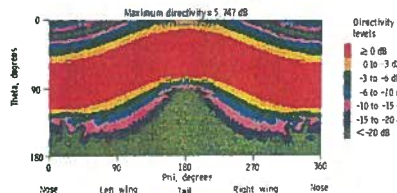


ElectroScience LABORATORY

Modeling of Boeing 737 aircraft



Measured

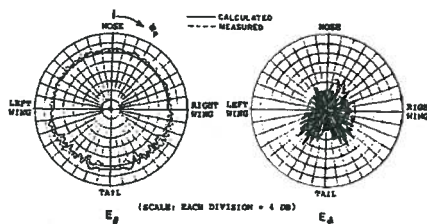
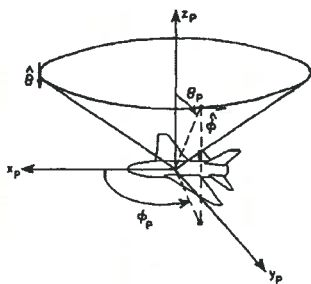
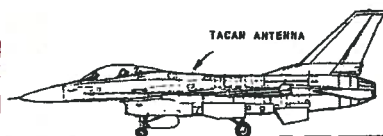


Calculated

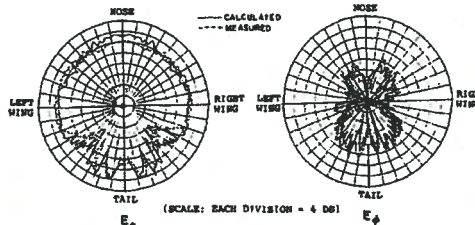
11



ElectroScience LABORATORY



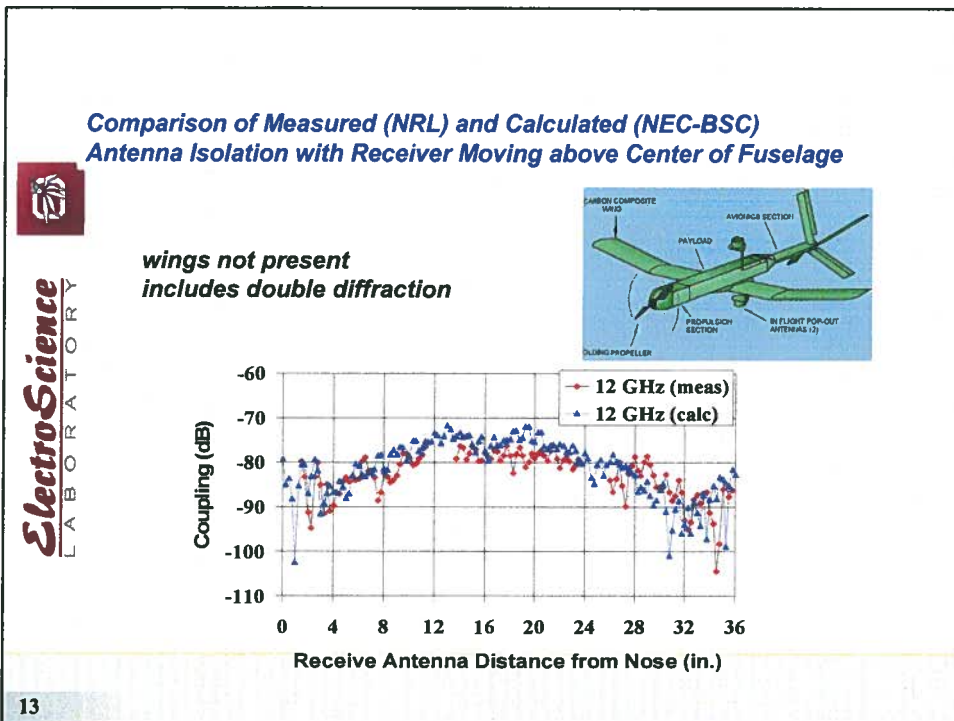
$\theta_p = 60^\circ$



$\theta_p = 80^\circ$

J. J. Kim and W. D. Burnside, "Simulation and Analysis of Antennas Radiating in a Complex Environment," *IEEE Trans. AP*, April 1986.

12



## Limitations of Existing UTD Codes

- Existing UTD codes such as NEC-BSC and NEW-AIR have proven to be successful over the past two decades.
- However, these codes are based on the approximation of the electrically large airborne platform in terms of canonical shapes, which is a complicated task.
- Moreover, a canonical shape representation may lead to inaccuracies.
- Very limited capability to analyze material coatings

Canonical representation for NEC-BSC

Canonical representation for NEW-AIR

14

## Previous Work on Thin Material Coated Metallic Wedge Structures

- Material coatings are generally replaced by approximate boundary conditions (e.g. Impedance Boundary Condition (IBC))
- Solutions to canonical problems with "approx." boundary conditions formulated exactly via Wiener-Hopf (W-H) or Maliuzhinets (MZ) methods for surfaces made up of planar structures. Ray solutions extracted analytically from them via asymptotic procedures.
- **W-H method:**
  - J. L. Volakis and T. B. A. Senior, "Diffraction by a Thin Dielectric Half-Plane", IEEE Trans. AP, Dec.1987
  - R. G. Rojas, "Wiener-Hopf Analysis of the EM Diffraction by an Impedance Discontinuity in a Planar Surface and by an Impedance Half-Plane", IEEE Trans. AP, Jan. 1988.
  - R. G. Rojas and P. H. Pathak, "Diffraction of EM Waves by a Dielectric/Ferrite Half-Plane and Related Configurations", IEEE Trans. AP, June 1989.
  - J. L. Volakis and T. B. A. Senior, "Application of a Class of Generalized Boundary Conditions to Scattering by a Metal-Backed Dielectric Half Plane", Proc. IEEE, May 1989.
  - V. G. Daniele and G. Lombardi, "Wiener-Hopf Solution for Impedance Wedges at Skew Incidence", IEEE Trans. AP, Sep. 2006 .
- **MZ method:**
  - G. D. Maliuzhinets, "Excitation, Reflection and Emission of Surface Waves from a Wedge with Given Face Impedance", Sov. Phys.-Dokl., 1958.
  - R. G. Rojas, "Electromagnetic Diffraction of an Obliquely Incident Plane Wave Field by a Wedge with Impedance Faces", IEEE AP, July 1988.
  - R. Tiberio and G. Pelosi and G. Manara and P. H. Pathak, "High-Frequency Scattering from a Wedge with Impedance Faces Illuminating by a Line Source, Part I: Diffraction", IEEE Trans. AP, Feb. 1989, see also IEEE Trans. AP, July 1993.
  - M. A. Lyalinov and N.Y. Zhu, "Diffraction of a Skew Incident Plane Electromagnetic Wave by an Impedance Wedge", Wave Motion, 2006.
- **Approx. skew incidence solution (MZ) for imp. wedges based on modifying the HP solution:**
  - H. Syed and J. L. Volakis, "Skew incidence diffraction by an impedance wedge with arbitrary face impedances", Electromagnetics, Vol. 15, No.3, 1995.

## An Approximate UTD Ray Solution for Skew Incidence Diffraction by Material Coated Wedges of Arbitrary Angle

**T Lertwiriayaprapa, P. H. Pathak and J. L. Volakis**

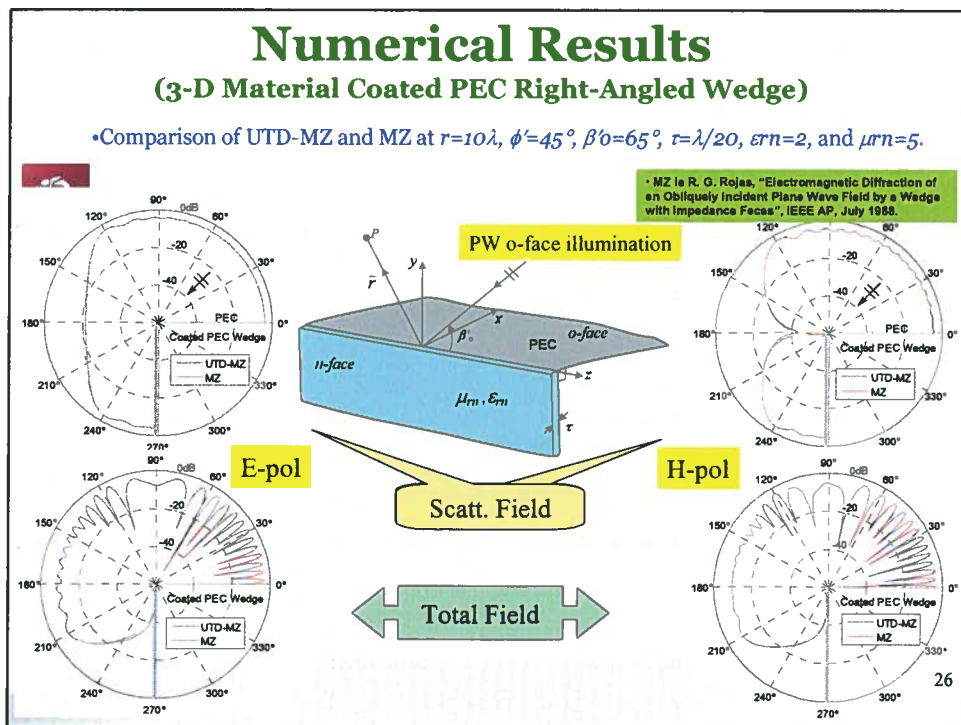
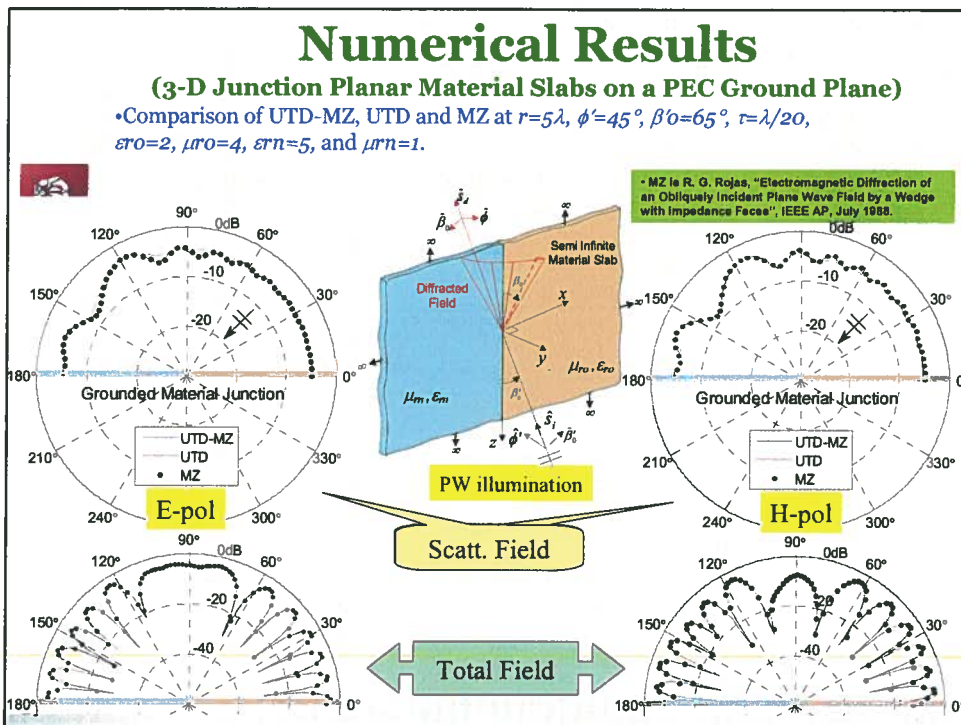
*ElectroScience Laboratory  
Department of Electrical and Computer Engineering  
The Ohio State University*

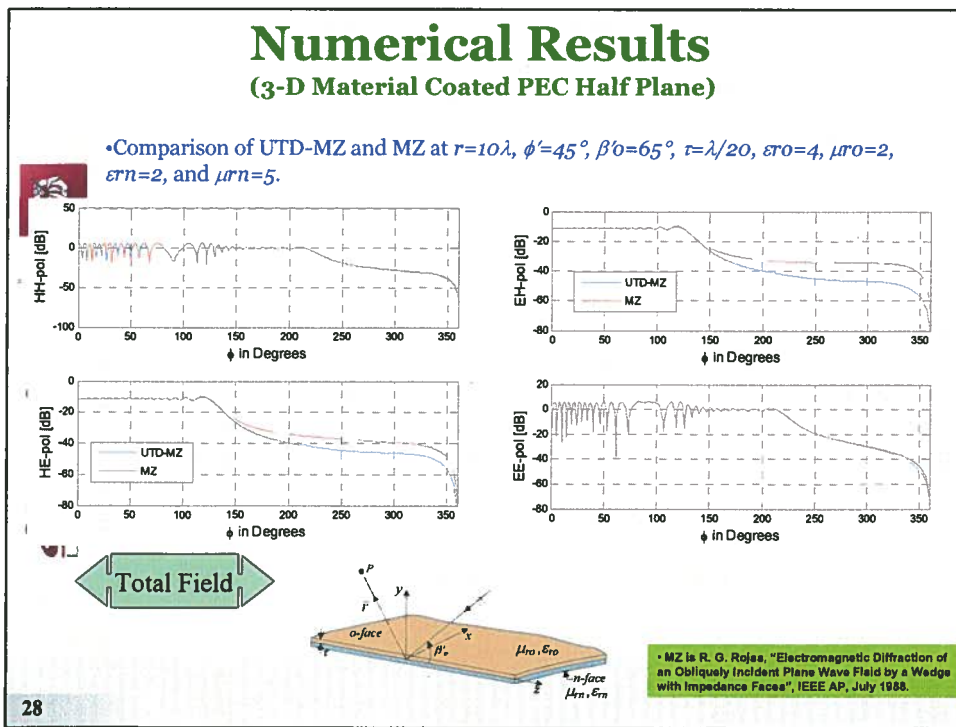
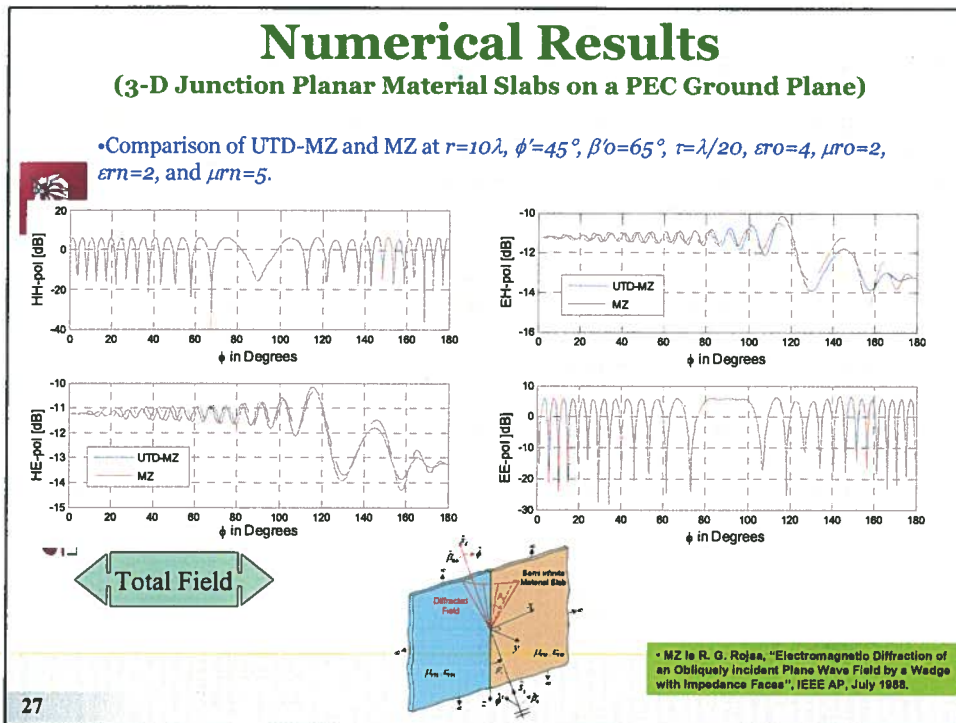
**URSI, Chicago 2008**

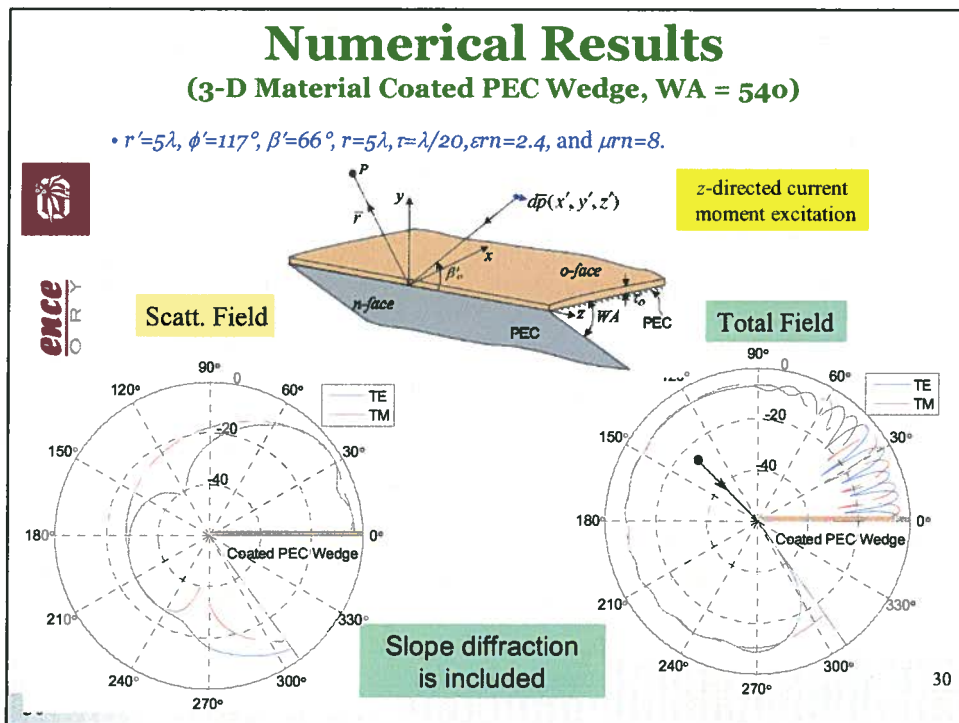
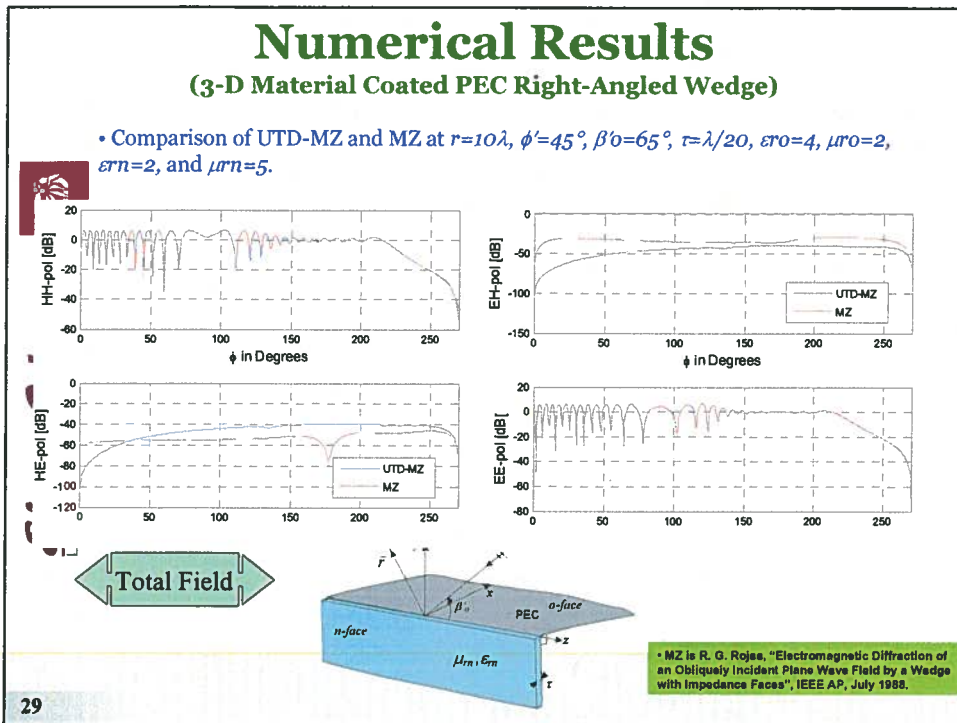
- Present solution based on spectral synthesis.
- Solution useful and accurate for engineering applications.

**ElectroScience**  
LABORATORY

**OHIO**  
STATE







## A UTD Diffraction Coefficient for a Corner Formed by Truncation of Edges in an Otherwise Smooth Curved Surface



ElectroScience  
LABORATORY

Giorgio Carluccio<sup>(1)</sup>, Matteo Albani<sup>(1)</sup>, and Prabhakar H. Pathak<sup>(2)</sup>

(1) Department of Information Engineering, University of Siena  
Via Roma 56, 53100 Siena, Italy, <http://www.dii.unisi.it>

(2) ElectroScience Laboratory, The Ohio State University  
1320 Kinnear Road, 43212 Columbus - OH, USA,  
<http://electroscience.osu.edu>

IEEE International Symposium on Antennas and Propagation  
and USNC/URSI National Radio Science Meeting

June 01-05, 2009



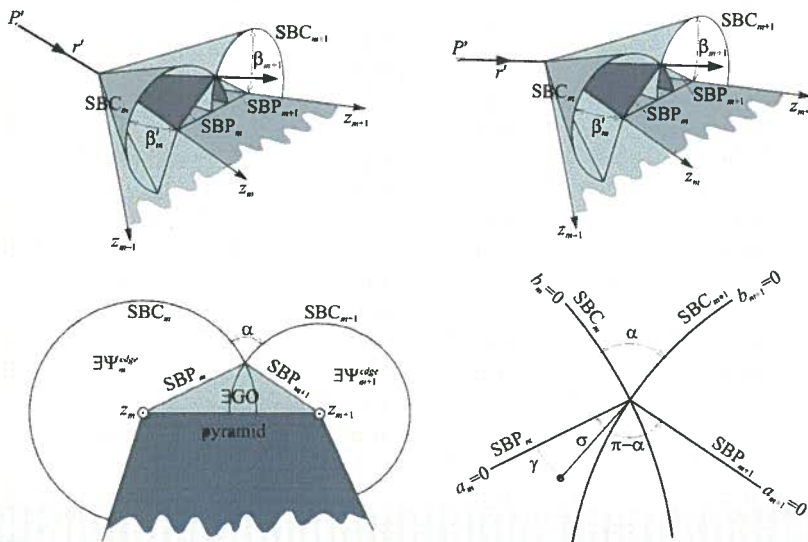
31

## UTD Vertex Diffraction Coefficient

Shadow Boundary Cones (SBCs) and Shadow Boundary Planes (SBPs):



ElectroScience  
LABORATORY



32

## UTD Vertex Diffraction Coefficient: Numerical Examples

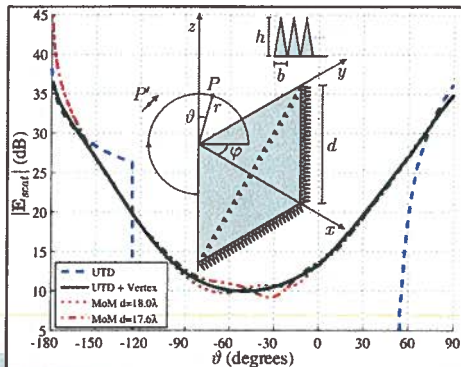
$P' = (-1, -1, 1)\lambda$        $\varphi = 45^\circ$

$\hat{p} = 0.5(1, 1, \sqrt{2})$        $r = 1.3\lambda$

$I\Delta\ell = 1\text{Am}$      $-180^\circ < \vartheta < 90^\circ$

$\hat{e}$

$b = 0.1\lambda$      $h = 0.25\lambda$



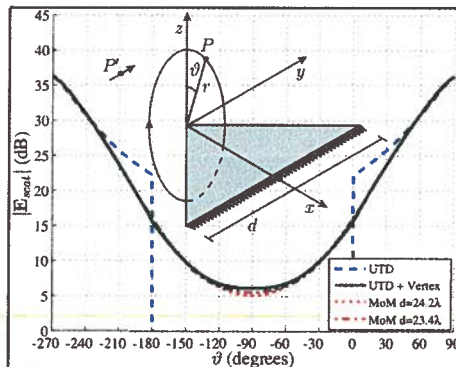
$P' = (-1, -1, 1)\lambda$        $xz$  plane scan

$\hat{p} = (0, 1, 0)$        $r = 1.3\lambda$

$I\Delta\ell = 1\text{Am}$

$\frac{1}{\sqrt{2}}(\hat{x}-\hat{y})$      $\frac{1}{\sqrt{2}}(\hat{x}+\hat{y})$  Edge Directions

$b = 0.1\lambda$      $h = 0.25\lambda$

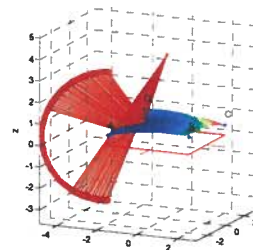


## I Example: Vertex Single Transition

We consider a smooth convex parabolic surface illuminated by an electric point source

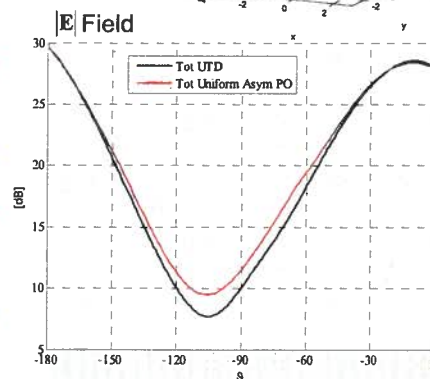
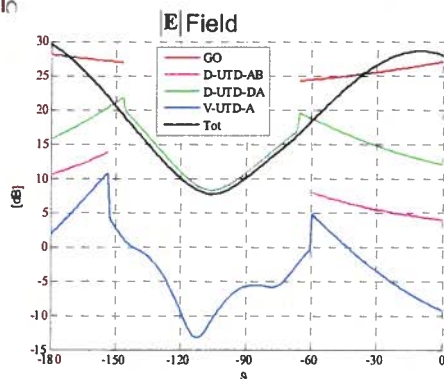
Scan Center on the Vertex A

$r = 3\lambda, \varphi = 25^\circ, -180^\circ < \vartheta < 0^\circ$



S. Inatan Science

34



# Remarks



ElectroScience  
LABORATORY

- A UTD diffraction coefficient for a corner formed by truncation of edges in a smooth curved surface was presented.
- A PO diffraction coefficient is derived by asymptotical evaluation of the PO integral, to understand how the surface curvature affects the diffracted field transitional behavior.
- The UTD diffraction coefficient was obtained by heuristically modifying the UTD diffraction coefficient for a corner in a flat surface, on the basis of the previous PO result.
- Numerical examples show how the proposed diffracted coefficient smoothly compensates for the abrupt discontinuity occurring when the GO field or the singly diffracted at edges abruptly vanish.
- Valid for astigmatic ray tube illumination.
- Can be extended to include thin material coating.

**A UTD Analysis of the Radiation and Mutual Coupling Associated with Antennas on a Smooth Perfectly Conducting Arbitrary Convex Surface with a Uniform Material Coating**

P. Mook and P.H. Pathak  
The Ohio State University ElectroScience Laboratory  
1320 Kinnear Road, Columbus, Ohio

**1 Introduction**

A uniform geometrical theory of diffraction (UTD) solution has been developed for predicting the radiation and mutual coupling associated with antenna and antenna placed anywhere within or on a uniform homogeneous material which covers a perfectly conducting convex surface of arbitrary shape. This work is of interest in the design of conformal antennas and arrays for aircraft, spacecraft, missiles and assemblies. The present solution is heuristically constructed, via locality of high frequency fields, from the asymptotic high frequency field solutions pertaining to the canonical problems of the radiation and coupling associated with sources located in or on a material coated circular conducting cylinder and a material coated conducting sphere, respectively. This solution employs the ray coordinates of the geometric theory of diffraction (UTD) illustrated in Figure 1. In the case of the coupling problem the surface field excited by the current source is associated with Keller's surface rays which traverse geodesic paths between the source point  $Q'$  and the surface field point  $Q$  as in Figure 1(a). In the radiation problem the field propagation along Keller's surface diffracted ray path, from the source at  $Q'$  to the observer at  $P$ , in the shadow region as in Figure 1(a), whereas in the lit region the incident field propagates along the geometric optics ray path from  $Q'$  to  $P$  as in Figure 1(b). The fields associated with each of the rays in Figure 1(a), 1(b), and 1(c) may be compactly expressed in terms of a dyadic  $\vec{T}_s(Q', Q)$  which behaves as a multipole function between the source located at  $Q'$  and field point. It is further noted that the components of the dyadic  $\vec{T}_s(Q', Q)$  are expressed in terms of generalized Fock type radiation, field and surface field integrals.

**2 The Form of the Field Solution**

In the case of the radiation field, the electric field  $\vec{E}(P)$  radiated by a source  $\vec{J}(Q' - r_{Q'})$  at  $Q'$  can be expressed asymptotically as

$$\vec{E}(P) = \vec{T}_s(P, Q') \cdot \vec{J} \quad \text{for } \beta \approx \beta_0 \text{ or } \infty \quad (1)$$

where  $\beta$  and  $\beta_0$  represent suit strength electric and magnetic point currents at  $Q'$  respectively. For the field point  $P = P_1$  in the lit region as in Figure 1(b), the dyadic  $\vec{T}_s(P, Q')$  is given as

$$\vec{T}_s(P, Q') \sim -\frac{j\beta_0}{4\pi} [\vec{A}A + \vec{C}B + \vec{D}C + \vec{E}AD] \frac{e^{-j\beta_0 R}}{R} \quad (2)$$

and for the field point  $P = P_2$  in the shadow region as in Figure 1(c)

$$\vec{T}_s(P, Q') \sim (-j\beta_0/4\pi) [\vec{V}A\vec{T} + \vec{T}B\vec{T} + \vec{V}C\vec{T} + \vec{T}D\vec{T}] e^{-j\beta_0 R} \sqrt{\frac{\beta_0}{4\pi(Q)} \frac{\beta_0 A(Q)}{\beta_0(Q)}} \sqrt{\frac{\beta_0}{4\pi(P)} \frac{\beta_0 B(P)}{\beta_0(P)}} e^{-j\beta_0 R} \quad (3)$$

where the components  $A, B, C, D, T_1, T_2, T_3$ , and  $T_4$  are deduced from the asymptotic solutions for the canonical problems and are expressed in terms of generalized Fock radiation type integrals developed here. The quantities  $\beta_0$  and  $\beta_0$  are the same as in [1]; also,  $\beta_0(Q)$  is the width of the surface ray at  $Q$ , and  $\beta_0(P)$  and  $\beta_0$  are the angles subtended by surface ray strip at  $Q'$  and  $Q$  respectively, also the same as in [1].

In the case of the mutual coupling, the UTD expressions for the EM fields  $\vec{E}(Q), \vec{H}(Q)$  at  $Q$  due to a point current element at  $Q'$  may be symbolically written as

$$\begin{Bmatrix} \vec{E}(Q) \\ \vec{H}(Q) \end{Bmatrix} = \begin{Bmatrix} \vec{T}_s(Q, Q') \\ \vec{T}_s(Q, Q') \end{Bmatrix} \cdot \vec{J} \quad (4)$$

Similar to [2] for the special case of the perfectly conducting convex surface without material coating,  $\vec{E}_s$  and  $\vec{H}_s$  can be expressed in terms of the unit vectors fixed in the surface ray coordinates as in (2). Thus  $\vec{E}_s$  and  $\vec{H}_s$  contain generalized surface type Fock integrals.

**3 Numerical Results**

An example of the numerical evaluation of a typical radiation type Fock integral is given below. Consider a dielectric coated conducting circular cylinder with inner radius  $a = 1.28\lambda_0$ , coating thickness  $t = .28\lambda_0$ , and with a dielectric constant  $\epsilon_r = 2.28$ . The radiation type of the Fock integral in the circular cross section plane for this geometry is given as

$$f^s(\beta) = \frac{1}{\sqrt{\beta}} \int_{-\beta}^{\beta} dt \frac{e^{-j\beta t}}{\sqrt{(\beta - t)^2 - \beta^2}} \omega(\beta, t) \quad (5)$$

where  $f^s(\beta)$  is a parameter dependent on the material coating, its thickness and material parameters, and  $\omega(\beta, t)$  is the Fock type Aky function [1, 2]. A numerically efficient, and accurate method has been developed based on the procedure prescribed by Pezanos [3], where this procedure has been extended to treat all classes of the Fock type integrals, namely the radiation and surface, including the U and V type of the latter. Figure 2 clearly illustrates the effectiveness of this newly developed method, a here the numerical evaluation of the radiation integral given in Equation (5) (represented by the solid line) agrees extremely well with its closed form asymptotic representation valid for large negative  $\beta'$  (corresponding to the lit region of the cylinder geometry) and with its residue series representation valid for large positive  $\beta'$  (corresponding to the deep shadow region).

**4 Conclusions**

The present UTD solution provides a relatively simple yet accurate solution which is ideally suited analyzing conformal antennas and antenna array problems whose electrical size or shape prohibits them from being solved by the standard numerical techniques. This solution which is valid for perfectly conducting convex surfaces with a material coating is valid uniformly within shadow boundary transition regions and is expressed in terms of a more general class of Fock functions that may be readily computed via a fast and efficient asymptotic procedure. In addition, this solution also explicitly shows the effect of surface ray tension on the radiated fields in the shadow and transition regions.

**References**

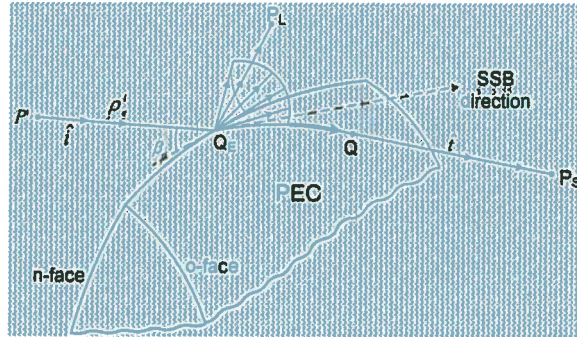
- (1) P.H. Pathak, N. Wang, W.D. Barabak, and R.G. Kocqranjian, "A Uniform GTD Solution for the Radiation from Sources on a Convex Surface," *IEEE Trans. on Antennas and Prop.*, Vol. AP-29, No. 1, July 1981.
- (2) P.H. Pathak and N. Wang, "An Analysis of the Mutual Coupling Between Antennas on a Smooth Convex Surface," Final Rep. 76483-7, Oct. 1978, The Ohio State University ElectroScience Lab., Dept. Electrical Engineering.
- (3) J.B. Keller, "Geometrical Theory of Diffraction," *J. Opt. Soc. Amer.*, Vol. 52, pp. 116-130, 1962.
- (4) V.A. Fock, *Electromagnetic Diffraction and Propagation Problems*, New York: Pergamon, 1968.
- (5) L.W. Pezanos, "A Scheme for Automatic Computation of Fock Type Integrals," *IEEE Trans. Antennas Propagat.*, Vol. AP-35, No. 10, pp. 1111-1118, Oct. 1987.

38

19

257

## Edge excited surface rays



ElectroScience  
LABORATORY

- Presently UTD solution has been obtained for ISB and SSB far apart.
- Work is in progress to obtain an asymptotic solution useful for engineering applications when ISB and SSB regions overlap.

39

## Conclusions

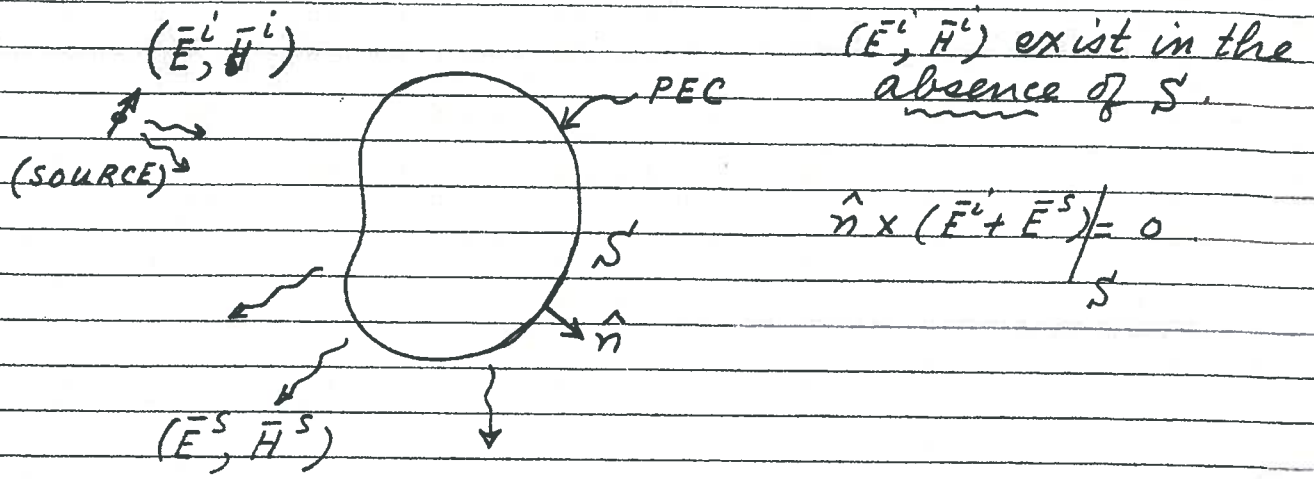


ElectroScience  
LABORATORY

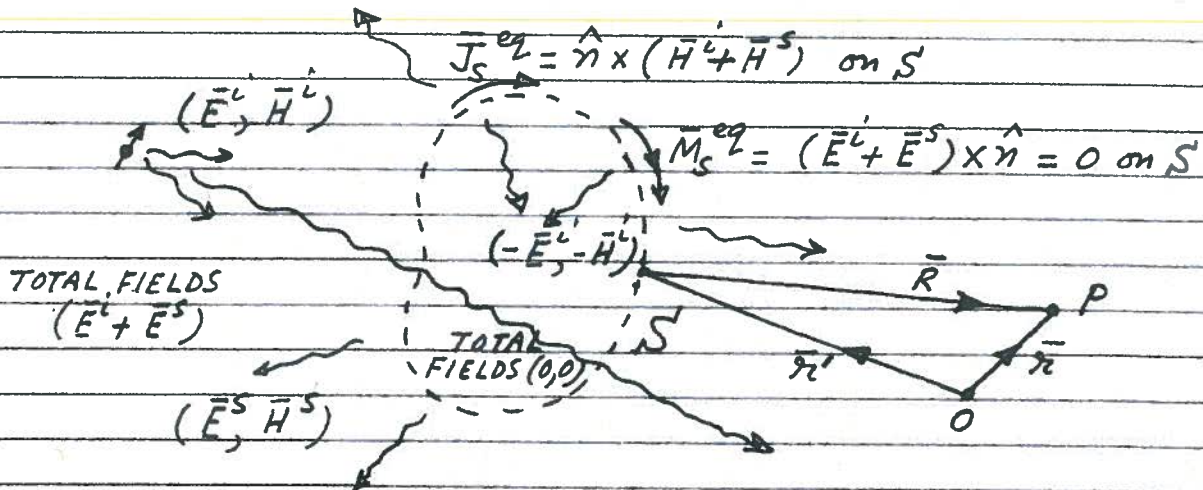
- Keller's original GTD is not valid at and near ISB, RSB, SSB (i.e. in SB transition regions).
- UTD developed to patch Keller's original theory within the SB transition regions.
- GTD corrects GO, and  $GTD = GO + \text{diffraction}$
- UTD corrects GTD, but usually  $UTD \rightarrow GTD$  outside SB transition regions.
- UTD ray paths remain independent of frequency.
- UTD offers an analytical (generally closed form) solution to many complex problems that can not otherwise be solved in an analytical fashion.

40

### Physical Optics Integral Technique:



### ORIGINAL CONFIGURATION

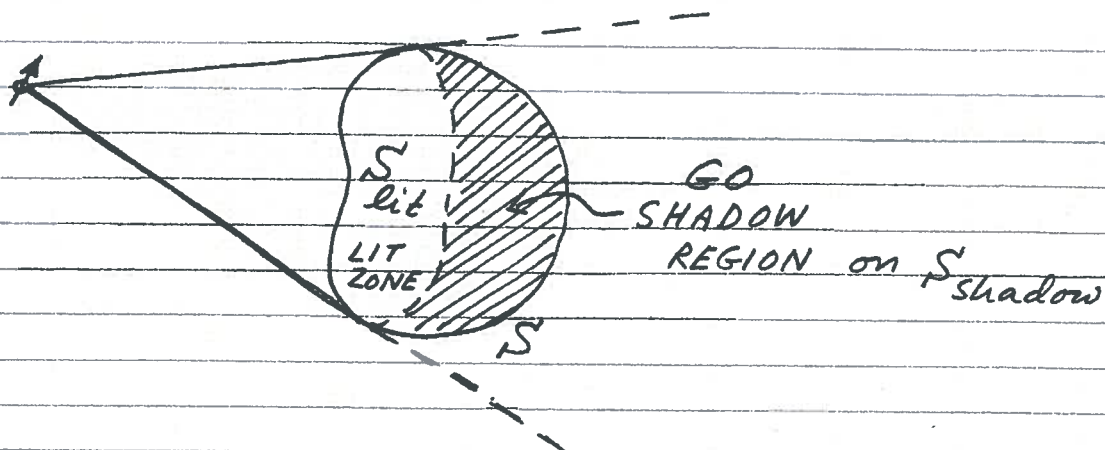


$$\vec{E}^s(O) = jkZ_0 \int_S \left( \vec{I} + \frac{\nabla \nabla}{k^2} \right) \frac{e^{-jkR}}{4\pi R} \cdot \vec{J}_s^{eq}(\vec{r}') ds'$$

$$\vec{E}^s(P) \approx \frac{jkZ_0}{4\pi} \int_S \left[ \hat{R} \times \hat{R} \times \vec{J}_s^{eq}(\vec{r}') \right] \frac{e^{-jkR}}{R} ds' ; \vec{R} = \vec{r} - \vec{r}'$$

$R = |\vec{R}|$

According to Physical Optics (PO), every point on  $S$  can be treated locally as if it has the same induced current  $\vec{J}_s$  as that which would exist on a tangent plane at that point.



In the PO approximation, which is valid when  $S$  or a large portion of it is well illuminated and when  $S$  is electrically large,  $\vec{J}_S = \vec{J}_S^{eq}$  is given by

$$\vec{J}_S^{eq} = \begin{cases} 2 \hat{n} \times \vec{H}^i & \text{on } S_{lit} \\ 0 & \text{on } S_{shadow} \end{cases}$$

Thus:

$$\vec{E}^S(P) \approx \frac{j k Z_0}{4\pi} \int_{S_{lit}} [\hat{R} \times \hat{R} \times (2 \hat{n} \times \vec{H}^i(\vec{r}'))] \frac{e^{-j k R}}{R} ds'$$

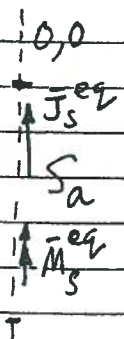
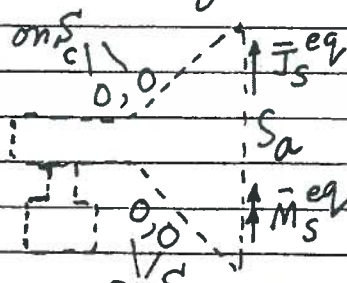
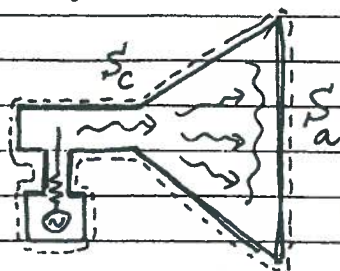
In 2-D:

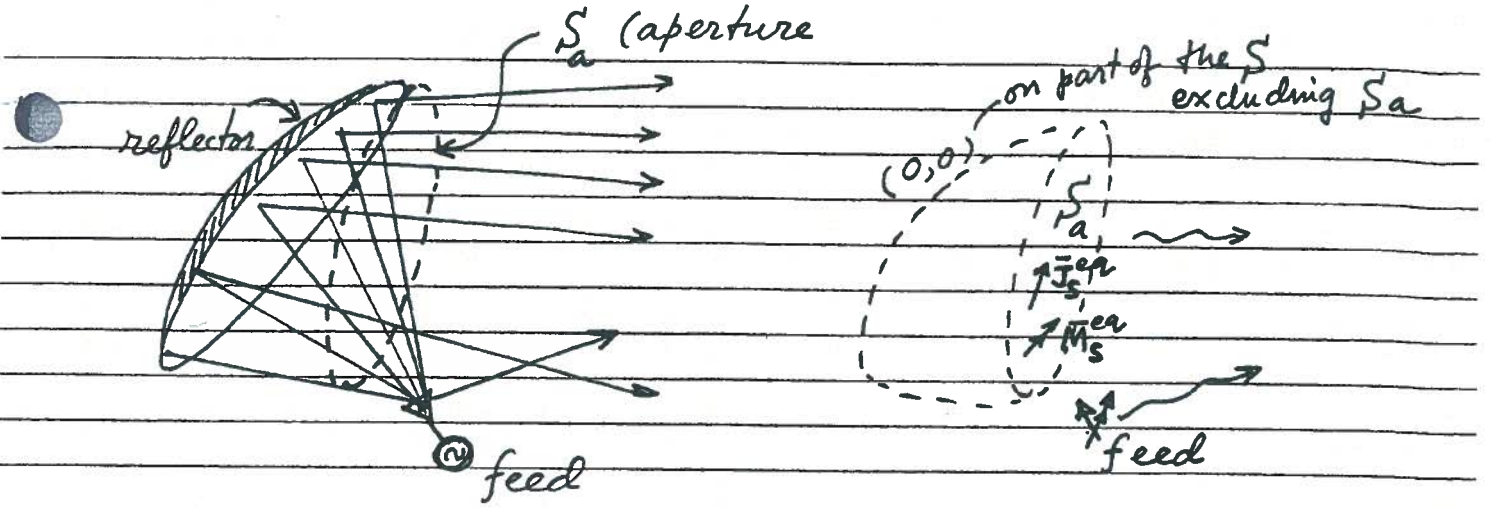
$$\vec{E}^S(P) \approx \frac{k Z_0}{4} \int_{S_{lit}} [\hat{R} \times \hat{R} \times (2 \hat{n} \times \vec{H}^i(\vec{p}'))] H_0^{(2)}(k|\vec{p}-\vec{p}'|) dl$$

## Aperture Field Integration Technique

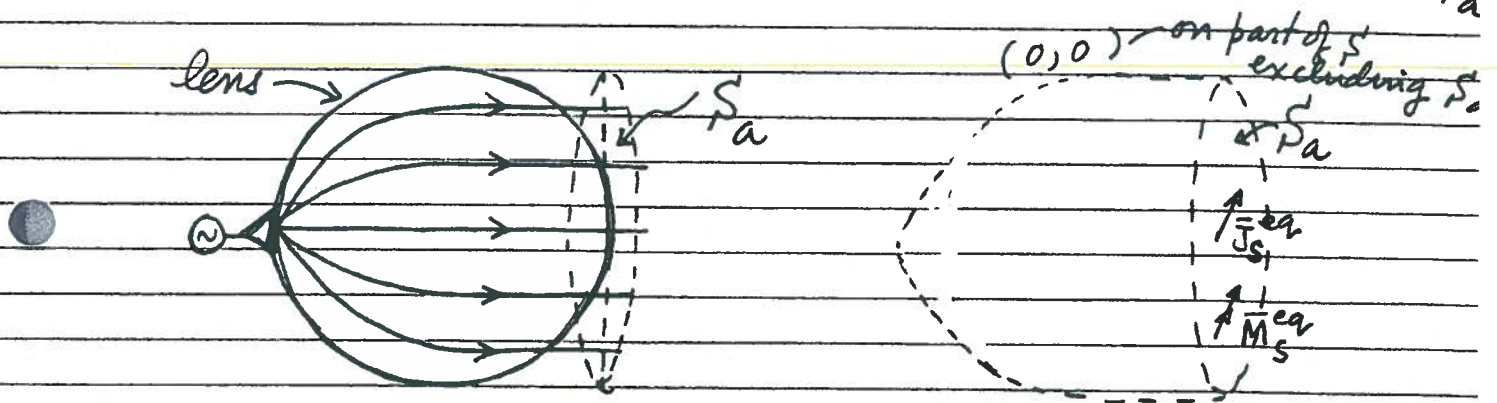
Just as in the PO integration technique, the aperture field (AF) integration technique is also based on the equivalence theorems which suggest the approximations to be utilized in calculating the equivalent sources over a conveniently chosen aperture. At high frequencies which are of interest here, the G.O. field is often employed to find the aperture field that then directly provides the equivalent sources. Note that in the PO method for PEC surfaces,  $\bar{J}_s^{eq}|_{\text{lit zone}} \approx 2\hat{n} \times \bar{H}_{GO}^i$  where  $\bar{H}^i \sim \bar{H}_{GO}^i$ ; i.e., GO is employed to find the equivalent source distribution in most cases at high frequencies.

Typically, the aperture, over which the equivalent sources are to be integrated to provide the radiated field, is chosen such that it captures the dominant part of the EM energy being radiated, and such that the aperture surface is also convenient for integration. Both, PO and AF when employing the GO approximation ignore the diffracted field contribution to the equivalent sources. Generally the diffracted component of the equivalent current contributes negligibly in the dominant regions (e.g. specular region in PO computations & main beam region for AF computations), but are usually important in predicting the fields away from such regions.





GO is used to find  $(\vec{J}_S^{eq}, \vec{M}_S^{eq})|_{S_a}$



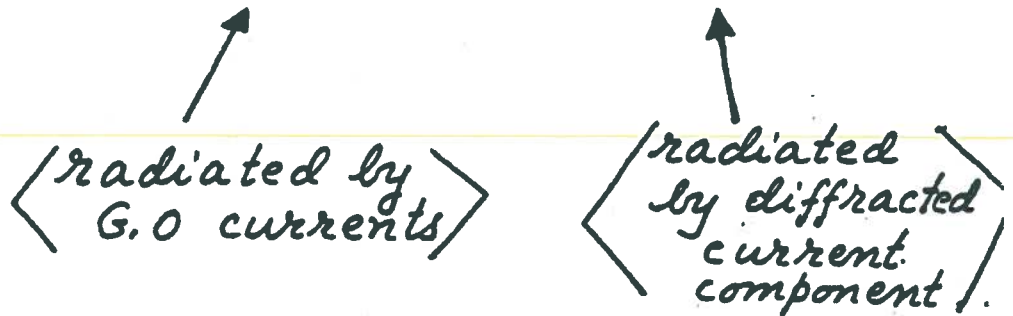
GO is used to find  $(\vec{J}_S^{eq}, \vec{M}_S^{eq})|_{S_a}$

## Physical Theory of Diffraction (PTD)

Ufimtsev (1957): extended Braunebek's approach to edge diffraction using the method of edge waves or PTD.

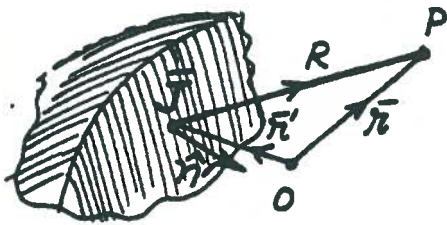
- PTD corrects P.O. just as GTD corrects G.O.

- $PTD \text{ field} = [P.O. \text{ field}] + [\text{edge wave field}]$



- PTD requires an integration over the surface currents.
- In retrospect, as might be expected, the PTD integrals reduce to the GTD if those integrals can be evaluated in closed form via asymptotic methods.
- In contrast to GTD, the PTD has been developed only for edged structures.

PTD



$$\bar{J} = \bar{J}_{G0} + \bar{J}_d$$

$$\therefore \text{in 3-D: } \bar{E}_{P0}^S(P) \approx \frac{jkZ_0}{4\pi} \iint_{S_{lit}} ds' [\hat{R} \times \hat{R} \times \bar{J}_{G0}] \frac{e^{-jkR}}{R}$$

$$\xi \text{ in 2-D: } \bar{E}_{P0}^S(P) \approx \frac{kZ_0}{4} \int_{C_{lit}} dl' [\hat{R} \times \hat{R} \times \bar{J}_{G0}] \frac{e^{-jkR}}{R}$$

$$\bar{J}_{G0} = \begin{cases} 2 \hat{n} \times \bar{H}^i, & \text{on lit side} \\ 0, & \text{shadow side} \end{cases}$$

$$\bullet \quad \bar{E}_{PTD}^S(P) \approx \bar{E}_{P0}^S(P) + \bar{E}_c^S(P)$$

where  $\bar{E}_c^S(P)$  represents a correction to P.O.

\* Ufimtsev did not find  $\bar{E}_c^S(P)$  directly via an integration of  $\bar{J}_d$ ; instead he found it indirectly in his original work.

## Connection between GTD & PTD :

$$\bar{E}_{PTD}^i(P) = \bar{E}^i(P) + \bar{E}_{PTD}^s(P)$$

If  $\bar{E}_{PTD}^s(P)$  can be approximated asymptotically in closed form, then

$$\begin{aligned} \bar{E}_{PTD}^s(P) &= \underbrace{\bar{E}_{PO}^s(P)} + \underbrace{\bar{E}_c^s(P)} \\ &\sim \underbrace{-\bar{E}^i(1-U^i) + \bar{E}^r U^r + \bar{E}^i(Q) \cdot \bar{D}_{PO} \sqrt{\frac{\rho_e}{s^d(e+s^d)}} e^{-jks^d}}_{\text{from } PO} \\ &\quad + \bar{E}^i(Q) \cdot \bar{D}_U \sqrt{\frac{\rho_e}{s^d(e+s^d)}} e^{-jks^d} \end{aligned}$$

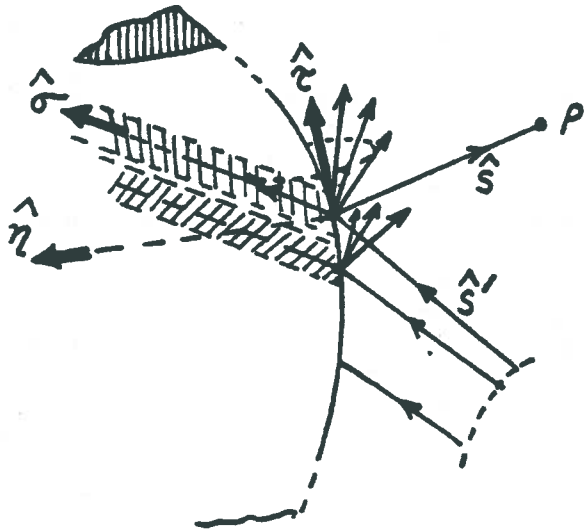
$$\text{or } \bar{E}_{PTD}^i(P) \sim \bar{E}^i U^i + \bar{E}^r U^r + \bar{E}^i(Q) \cdot [\bar{D}_{PO} + \bar{D}_U] \sqrt{\frac{\rho_e}{s^d(e+s^d)}} e^{-jks^d}$$

However:

$$\bar{E}_{GTD}(P) \sim \bar{E}^i U^i + \bar{E}^r U^r + \bar{E}^i(Q) \cdot \bar{D}_e \sqrt{\frac{\rho_e}{s^d(e+s^d)}} e^{-jks^d}$$

$$\therefore \bar{D}_e = \bar{D}_{PO} + \bar{D}_U \quad \Rightarrow \quad \bar{D}_U = \bar{D}_e - \bar{D}_{PO}$$

Edge Wave  
pattern.



$$\hat{s} = \frac{\overline{PQ}}{|\overline{PQ}|}$$

Instead of  $ds' = \frac{dzdn}{|J_A|}$   
as done earlier by  
Michaeli, let:

$$ds' = \frac{dzd\sigma}{|J_B|}$$

The latter transformation eliminates the singularities in  $I_m^f$  &  $M_m^f$  for the conditions  $\hat{s} \cdot \hat{\eta} = \hat{s}' \cdot \hat{\eta}$ ;  $\hat{s} \cdot \hat{\eta} = \hat{\sigma} \cdot \hat{\eta}$ .  
This development was presented by:

Butorin, D.I & P. Ya Ufimtsev (Sov. Phys. Acoust., 32(4), July-Aug. 1986; SUBMITTED MAR. 27, '85) for acoustic case,

and independently by:  
Michaeli (IEEE Trans. AP-34, July 1986; SUBMITTED JUNE 24, '85) for the EM case.

\* NOTE: PTD requires integration.

PTD cannot include multiple interactions easily; hence GTD/UTD could be employed to account for multiple interactions and added to PTD. In most situations GTD/UTD/UAT is to be preferred over PTD for efficiency & simplicity.

# Wide Angle Radiation from Reflector Antennas using UTD

2

(Ratnasiri, Kouyoumjian & Pathak, 1969).

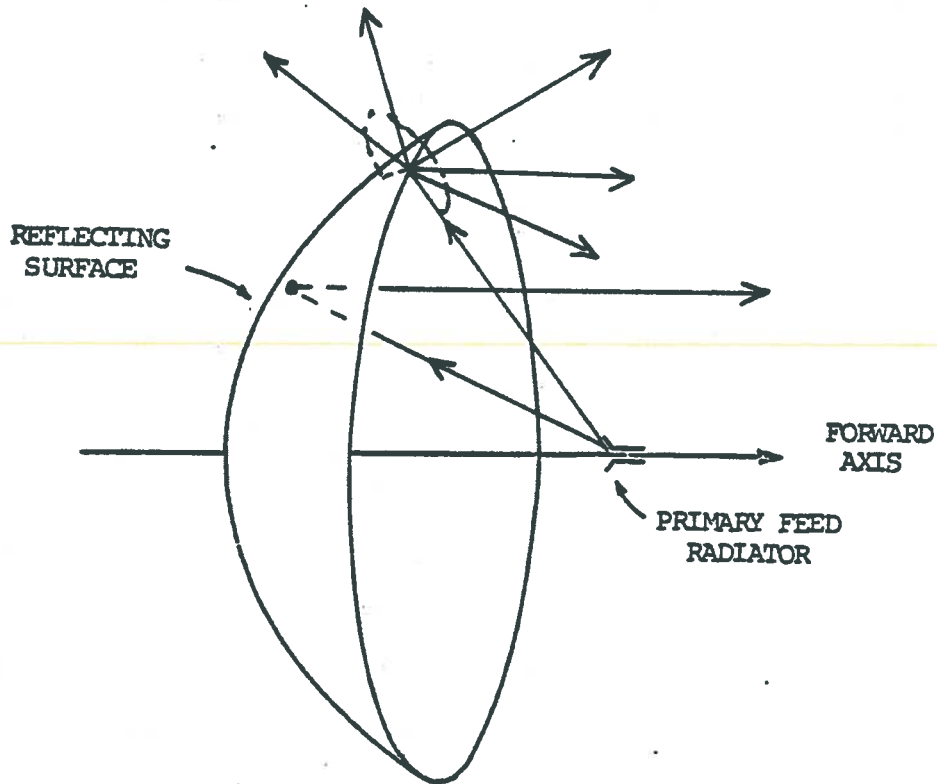
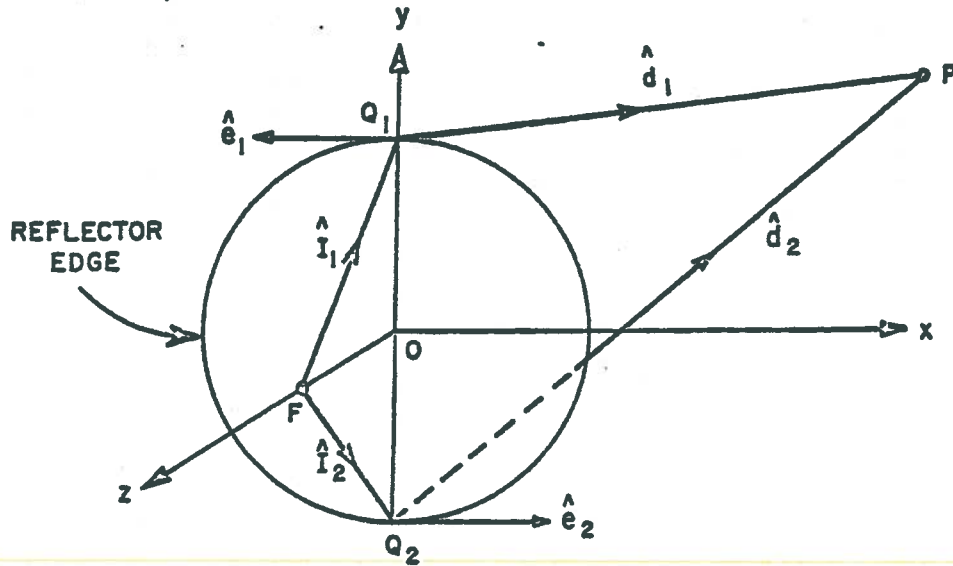
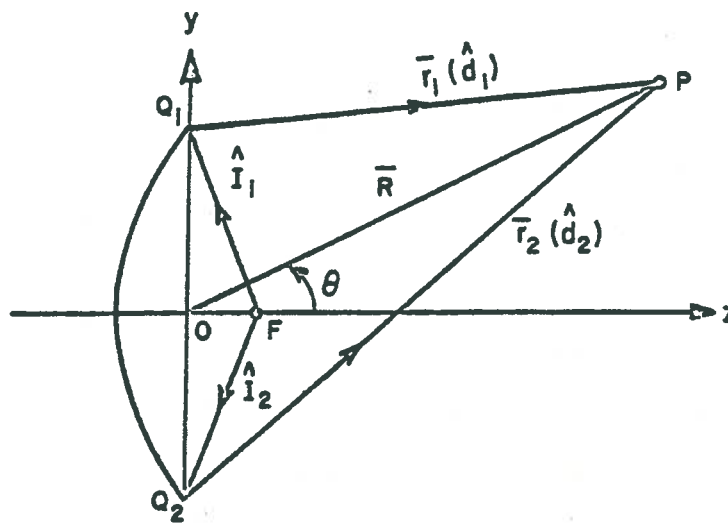


Figure 1. Reflector Antenna.

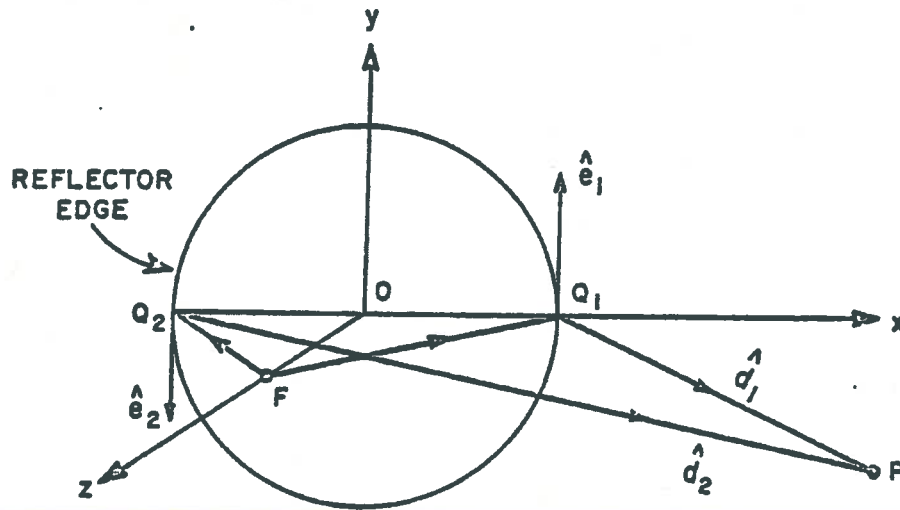


(a) FRONT VIEW

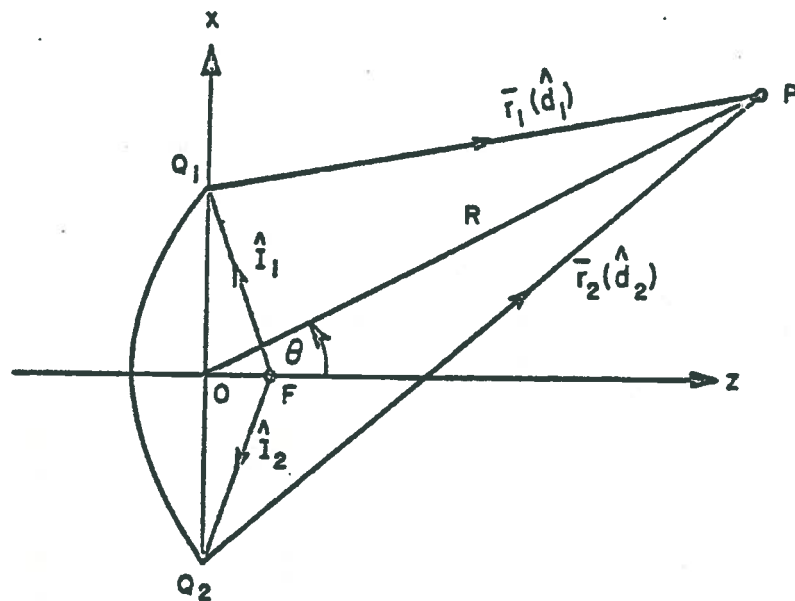


(b) SIDE VIEW

Figure 6. Geometry of the edge diffracted rays in the E-planes.

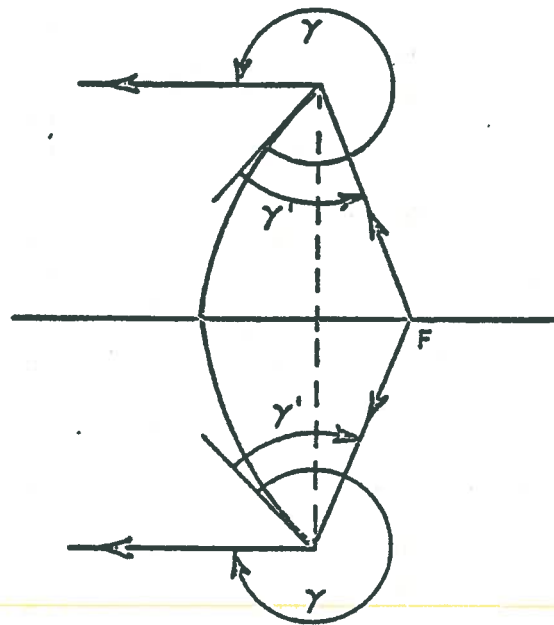


(a) FRONT VIEW



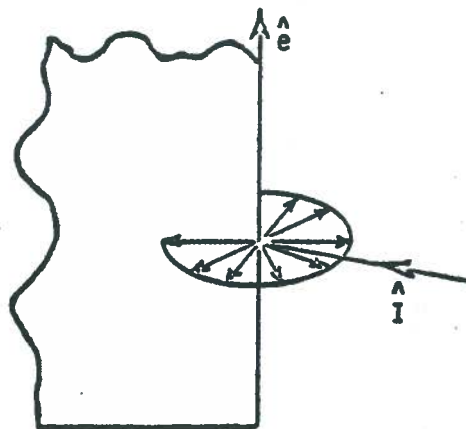
(b) TOP VIEW

Figure 7. Geometry of the edge diffracted rays in the H-plane.



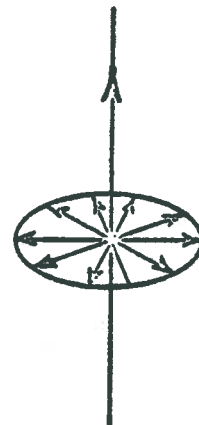
(a)

REFLECTOR ANTENNA AND RAYS FORMING REAR AXIAL CAUSTIC



(b)

DIFFRACTION AT HALF-PLANE



(c)

EQUIVALENT EDGE CURRENT

Figure 8.

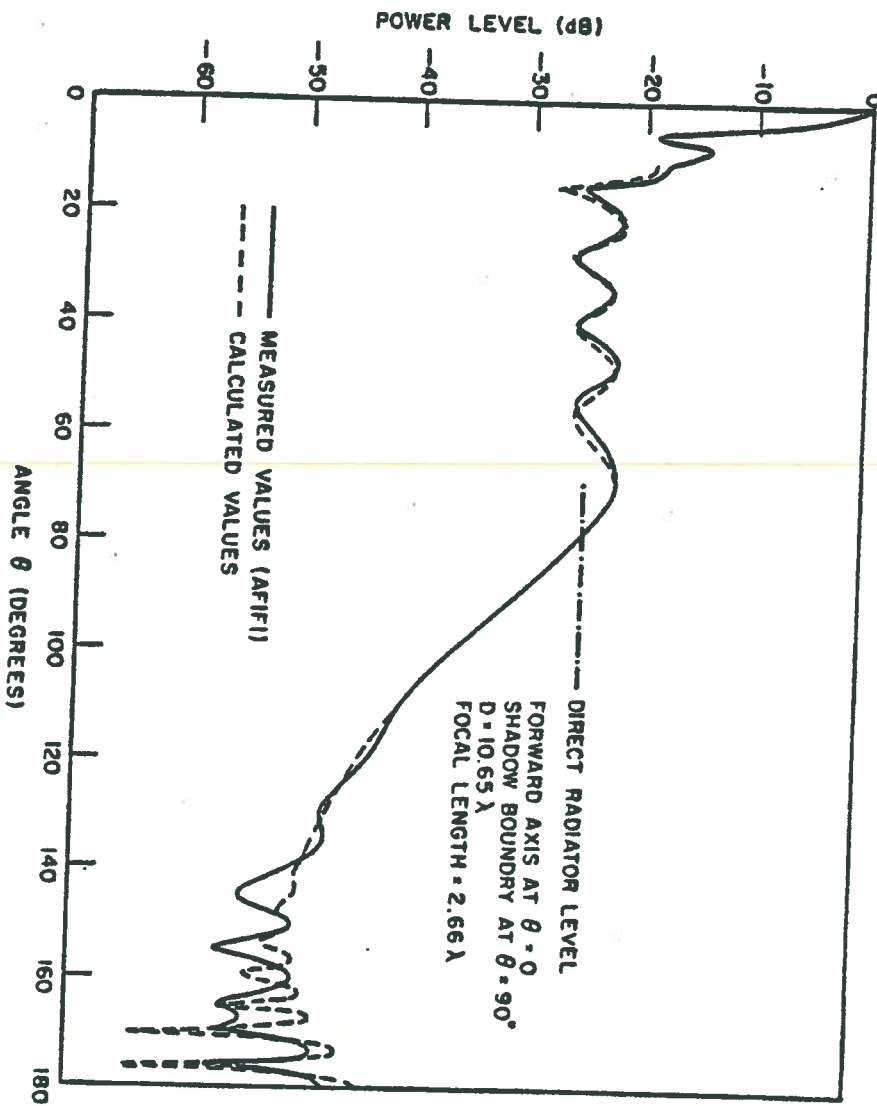


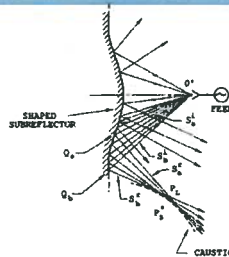
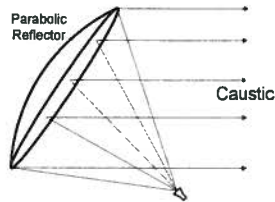
Figure 14. H-plane pattern of a parabolic reflector with a dipole feed.

## Beam Methods & Some Applications

- Beams provide useful basis functions for representing EM fields.
- Ray methods fail at caustics (foci) of ray systems. Caustics are formed by intersection or envelopes associated with the same class of rays. Beams remain valid in regions of real ray caustics



ElectroScience  
LABORATORY



- Beams can be used to treat large reflector systems and radome problems efficiently.
- Beams can be used to improve the speed of conventional Moment Method (MoM) solution of governing EM integral equation (IE) for the radiating object.
- Beams can also be used for Near Field → Far Field transformations required in near field measurements.

41

## Generation of a Complex Source Beam

- A beam type illumination is generated by a source positioned in complex space.\*
- The location of a complex source is obtained by analytically continuing the coordinates of a source in real space into complex space.\*



ElectroScience  
LABORATORY

$$\vec{r}' \Rightarrow \vec{r}' = \vec{r}' - j\vec{b}; \quad \vec{b} = b\hat{b}$$

- $\vec{r}' \rightarrow$  Position vector to the center of the beam waist.
- $b \rightarrow$  Beam parameter related to the size of the beam waist.
- $\hat{b} \rightarrow$  Direction of beam axis.

Let  $\vec{r}' = 0$ ;  $\vec{b} = b\hat{z} \Rightarrow \vec{r}' = (0, 0, -jb)$

Electric field radiated by a complex point source with a current that has the unit amplitude and the orientation of  $\hat{p}_e$  in real space

$$\vec{E}(\vec{r}) = \vec{G}(\vec{r} | \vec{r}') \cdot \hat{p}_e \quad \vec{G}(\vec{r} | \vec{r}') = -\frac{jkZ_0}{4\pi} \left[ \vec{I} + \frac{\nabla\nabla}{k^2} \right] \frac{e^{-jk\tilde{s}}}{\tilde{s}}$$

$$\tilde{s} = \sqrt{(\vec{r} - \vec{r}') \cdot (\vec{r} - \vec{r}')} = \sqrt{x^2 + y^2 + (z + jb)^2}, \quad \text{Re } \tilde{s} \geq 0$$

Within the paraxial region,  $\frac{b}{z} \ll 1$

$$\tilde{s} \approx \pm \left[ z + jb + \frac{x^2 + y^2}{2(z + jb)} \right] \Rightarrow \vec{G}(\vec{r} | \vec{r}') \propto \frac{e^{-jk\tilde{s}}}{\tilde{s}} \approx \pm \frac{e^{\pm kb}}{z + jb} e^{\mp jkz} \left( 1 + \frac{1}{2} \frac{x^2 + y^2}{z^2 + b^2} \right) e^{\mp \frac{1}{2} kb \frac{x^2 + y^2}{z^2 + b^2}} \quad \begin{matrix} z > 0 \\ z < 0 \end{matrix}$$

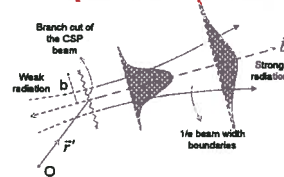
a CSB reduces to a rotationally symmetric Gaussian beam (GB) along the positive z direction.

- J. B. Keller and W. Streifer, "Complex rays with an application to Gaussian beam," *J. Opt. Soc. Amer.*, vol. 61, pp. 40.43, 1971.
- G. A. Deschamps, "Gaussian beam as a bundle of complex rays," *Electron. Lett.*, vol. 7, pp. 684.685, 1971.
- L. B. Felsen, "Complex source point solution of the field equations and their relation to the propagation and scattering of Gaussian Beams," *Symposia Mathematica*, 1976.

42



Spherical wave radiation



CSB radiation

## Previous work on CSP beam expansion



ElectroScience  
LABORATORY

- Some previous related work on CSP beam expansions for scalar fields:
  - I. T. Lu, L. B. Felsen, and Y. Z. Ruan, "Spectral aspects of the Gaussian beam method: reflection from homogenous half space," Geophys. J. R. Astron. Soc., vol. 89, pp. 915–922, 1987.
  - E. Heyman, "Complex source pulsed beam representation of transient radiation," Wave Motion, vol. 11, pp. 337–349, 1989.
  - A. N. Norris and T. B. Hansen, "Exact complex source representations of time harmonic radiation," Wave Motion, vol. 25, pp.127-141,1997.
  - T. B. Hansen and A. N. Norris, "Exact complex source representations of transient radiation," Wave Motion, vol. 26, pp. 101–115, 1997.
- The present work is different in that it is applicable to arbitrary EM source distributions ( $\mathbf{J}_v, \mathbf{M}_v$ ) in fully 3-D problems and unlike most previous work does not require a knowledge of spherical harmonic expansions for the fields of the sources to get the CSP beam coefficients.

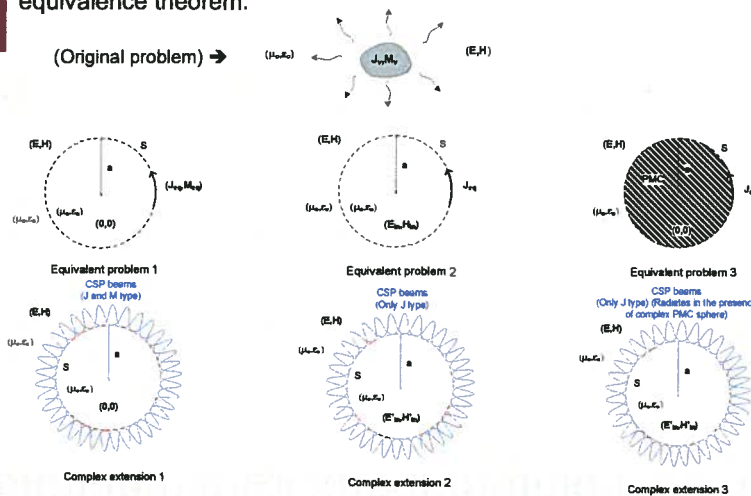
43

## Outline of present CSP Beam (CSB) Expansion Approach



ElectroScience  
LABORATORY

- A rigorous formulation is based on a complex extension of an EM surface equivalence theorem.



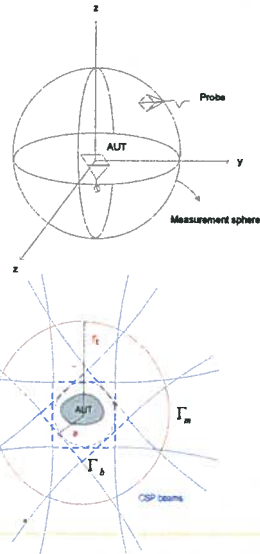
44

## Large Antenna Applications

### NF-FF Transformation with CSP beams (CSBs) for spherical scanning



Science  
LABORATORY



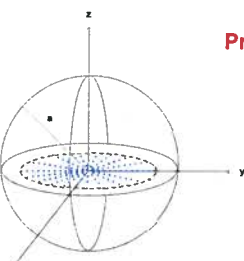
- The near field of AUT is measured over a spherical grid of test points.
- The far field pattern is computed by utilizing the near field measurement data on sphere  $\Gamma_m$ .
- CSP beams (CSBs) launched from complex sphere  $\Gamma_b$  are used to perform the NF-FF transformation.
- A numerical matching technique is applied to solve for the coefficients of the beams representing the AUT fields.
- A sparse matrix equation is formed by exploiting the local behavior of CSP beams.  $\mathbf{Z}\mathbf{I} = \mathbf{V}$
- The matrix equation can be solved by sparse matrix equation solution techniques.
- A preconditioner needs to be constructed for large problems.
- CSP beam approach can be potentially useful for other type of near field measurements, as well.

63

## Large Antenna Applications (cont.)

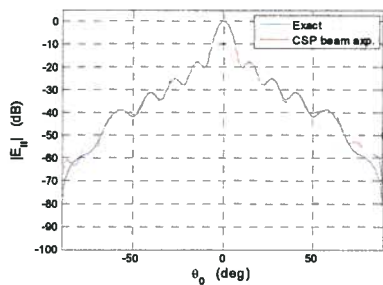


ence  
LABORATORY



### Preliminary numerical example for NF-FF Transformation

- Point sources are distributed over a disc of radius  $5\lambda$ .
  - $\tilde{\mathbf{a}} = 5.25\lambda - j15\lambda$  so the beams are launched from the sphere with radius  $a = 5.25\lambda$ .
  - The measurement sphere has the radius  $r_t = 15\lambda$ .
  - A total of 1388 beams (and test points) are used in the expansion. Size of  $\mathbf{Z}$  is  $2776 \times 2776$ .
  - Density of  $\mathbf{Z}$  matrix = 6 % with threshold  $= 10^{-4}$ . Zeros are assigned to the remaining 94 % of  $\mathbf{Z}$ . On average 50 out of the 1388 beams remained significant at a far field point.
- An incomplete LU (ILU) preconditioner is constructed to improve the convergence rate (with drop tolerance  $= 10^{-3}$ ).
- Density(L) + Density(U) = 22 %.



	CPU Time (s)
ILU factorization	67
Iterations	20

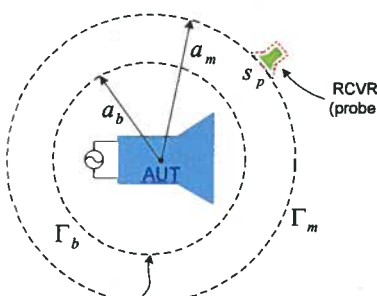
64

ElectroScience  
LABORATORY

• More generally,

$$V_{OC}^p = -\frac{1}{I_t^p} \int_{s_p} (\vec{E}^a \cdot \vec{J}_{sp} - \vec{H}^a \cdot \vec{M}_{sp}) ds_p$$

which includes probe compensation for finite probes.



Symbolic complex spherical surface of radius

$$\tilde{a}_b = a_b - jb \quad a_m > \sqrt{a_b^2 + b^2}$$

AUT generate  $(\vec{E}^a, \vec{H}^a)$   
 $\vec{J}_{s_p}, \vec{M}_{s_p}$  defined on  $s_p$  encapsulating probe.

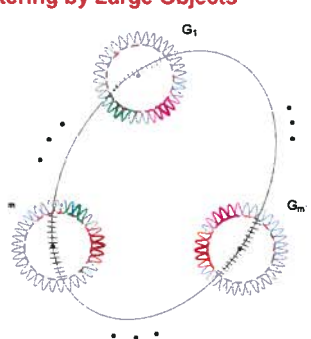
65

## Large Antenna Applications (cont.)

### CSP-MoM for Fast Solution to Radiation and Scattering by Large Objects

ElectroScience  
LABORATORY

- The subsectional basis elements are combined into groups of approximately equal size.
- Interactions of the near neighbor/self groups are performed in the conventional manner.
- For well separated groups:
  - The field radiated from each basis element is expanded into a set of CSPs radiated from the group of that element.
  - The field interactions between a pair of groups are performed by reacting their equivalent CSP sets.
  - Since CSP beams are localized wave objects, only a small portion of the CSP beams from each group contribute significantly to a group interaction. → Fast evaluation of group interactions.

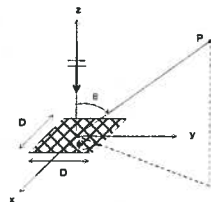


66

## Large Antenna Applications (cont.)



ElectroScience  
LABORATORY

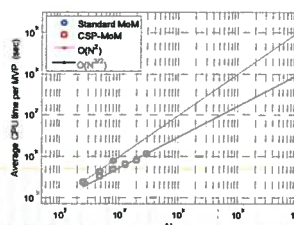
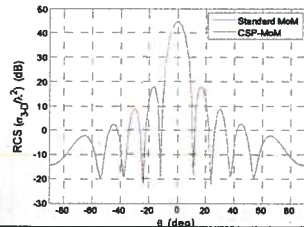


### Numerical example for CSP-MoM

- An x-polarized plane wave is normally incident on a PEC square plate of single dimension  $D=7\lambda$  ( $N=8064$ ).
- MoM formulation: Rooftop basis functions on a rectangular mesh ( $0.1\lambda \times 0.1\lambda$ ) with Galerkin testing.

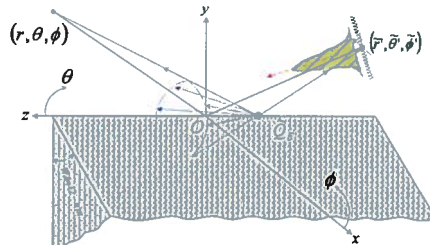
CSP-MoM		Standard MoM			
	CPU (s)		CPU (s)		Memory (MB)
Sol. for beam coeffs	3.8	Filling the matrix	1490	Standard MoM	992
Comp. sig. beam. inter.	2.48	Time per iteration	4.2	CSP-MoM	165
Filling for near/self	73				
Time per iteration	1.61				

Bistatic RCS comparison on the  $\phi=45^\circ$  plane.



67

## Complex Source Beam (CSB) Diffraction by a Wedge



- UTD for real source excitation of wedge developed via first order Pauli-Clemmow method (PCM) [1-4] for asymptotic solution of canonical wedge diffraction integral along a steepest descent path (SDP)
- First order PCM not strictly valid (for poles crossing the SDP away from saddle point); hence analytic continuation of UTD for complex source location without further study is questionable!
- First order Van der Waerden method (VWM) [1-4] is valid even where PCM fails.

ElectroScience  
LABORATORY

- However, one can show that the first order VWM method, upon using a key rearrangement (and combination) of terms, yields:

**Key Step**  $\rightarrow$   $VWM = PCM + \Delta \equiv EPCM$  (Extended PCM)

- Next, for the special wedge case of interest, it is shown analytically (and verified numerically) that  $\Delta \approx 0$ .

Note:  $PCM \rightarrow UTD$  for wedge  
 $VWM \equiv EPCM \rightarrow EUTD$  for wedge

Therefore, analytic continuation of UTD for a wedge is OK for complex waves

**For a wedge**  $\rightarrow$   $EUTD = UTD + \Delta \approx UTD$  (since  $\Delta$  is negligible)

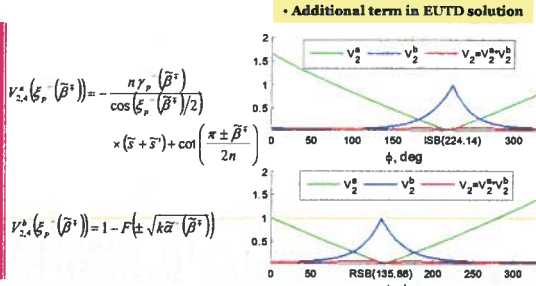
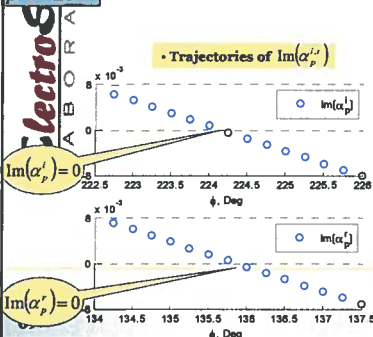
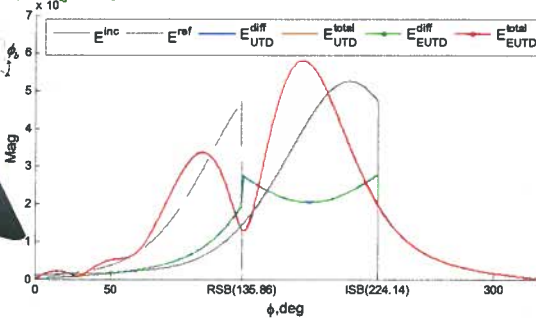
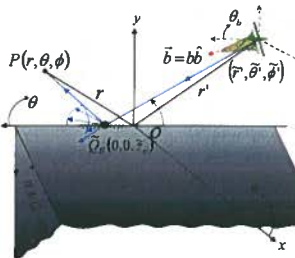
68

1. B. A. Spang and J. L. Volakis, "A rigorous Boundary Conditions in Electrodynamics," The Institute of Electrical Engineers, London, 1995.  
 2. I. B. Felsen and N. Marcuvitz, "Radiation and Scattering of Waves," Englewood Cliffs, N.J.: Prentice-Hall, 1972.  
 3. C. Christofilidis and C. Panayiotis, "A uniform asymptotic expansion of typical diffraction integrals with many coalescing simple poles singularities and a Riccati-Bessel function," *IEEE Trans. Antennas and Propagation*, vol. AP-32, pp. 1122-1134, Oct. 1984.  
 4. R. G. Rojas, "Comparison between two asymptotic methods," *IEEE Trans. Antennas and Propagation*, vol. 35, no. 12, pp. 1432-1433, Dec. 1987.

## Complex Source Beam (CSB) Diffraction by a Wedge (cont.)

### Numerical Result 1

$WA = 30^\circ$   
 $r' = 5\lambda$   
 $\theta' = 140^\circ$   
 $\phi' = 50^\circ$   
 $b = 10\lambda$   
 $\theta_b = 60.6^\circ$   
 $\phi_b = 217.4^\circ$   
 $r = 2\lambda$   
 $\theta = 45^\circ$   
 $\hat{p}^{i,r} = \pm \hat{z}$



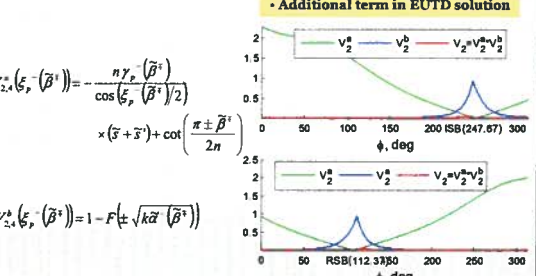
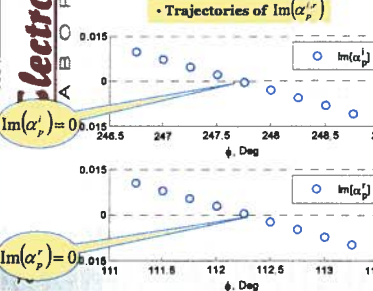
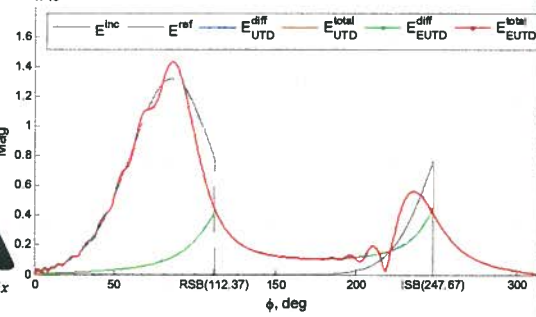
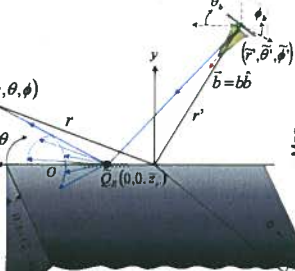
$$V_{2,a}^a(\xi_r, \beta^i) = -\frac{n\gamma_r(\beta^i)}{\cos(\xi_r(\beta^i)/2)} \times (\bar{s} + \bar{s}') + \cot\left(\frac{\pi \pm \beta^i}{2n}\right)$$

$$V_{2,a}^b(\xi_r, \beta^i) = 1 - F(\pm \sqrt{k\alpha}(\beta^i))$$

## Complex Source Beam (CSB) Diffraction by a Wedge (cont.)

### Numerical Result 2

$WA = 45^\circ$   
 $r' = 20\lambda$   
 $\theta' = 100^\circ$   
 $\phi' = 70^\circ$   
 $b = 10\lambda$   
 $\theta_b = 78.57^\circ$   
 $\phi_b = 258.57^\circ$   
 $r = 12\lambda$   
 $\theta = 40^\circ$   
 $\hat{p}^{i,r} = \pm \hat{z}$

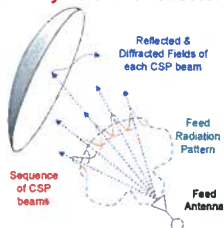


$$V_{2,a}^a(\xi_r, \beta^i) = -\frac{n\gamma_r(\beta^i)}{\cos(\xi_r(\beta^i)/2)} \times (\bar{s} + \bar{s}') + \cot\left(\frac{\pi \pm \beta^i}{2n}\right)$$

$$V_{2,a}^b(\xi_r, \beta^i) = 1 - F(\pm \sqrt{k\alpha}(\beta^i))$$

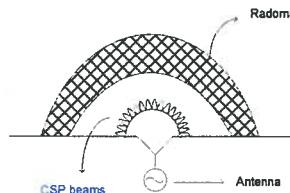
## Large Antenna Applications

### Fast analysis of the reflector antennas.



A GB-UTD (PO based) method was previously reported in [1].  
 With the CSP method, feed pattern is expanded into a set of **CSBs**.  
 Each CSP beam field is scattered from the reflector by using complex extension of UTD.  
 A 2-D case for a single beam illumination was reported in [2].  
 This new fully 3-D CSP-UTD approach (UTD for beams) is expected to be more accurate than [1].

### Antenna radiation in the presence of radomes.



- The field of the antenna is first expanded into a set of CSP beams.
- Each beam is next tracked through the radome.
- The transmitted beams are summed up at the observer location.
- Complex ray tracing can be employed for beam tracking through the radome [3,4].

[1] H. T. Chou, P. H. Pathak and R. J. Burkholder, "Novel Gaussian Beam Method for the Rapid Analysis of Large Reflector Antennas", IEEE Trans. Antennas Propagat., 2001  
 [2] G.A. Suedan and E.V. Jull, "Beam diffraction by planar and parabolic reflectors," IEEE Trans. Antennas Propagat., 1991.  
 [3] X. J. Gao and L. B. Felsen, "Complex ray analysis of beam transmission through two-dimensional radomes", IEEE Trans. Antennas Propagat., 1985  
 [4] J. J. Maciel and L. B. Felsen, "Gaussian beam analysis of propagation from an extended plane aperture distribution through dielectric layers, part I - plane layer," IEEE Trans. Antennas Propagat., 1990.

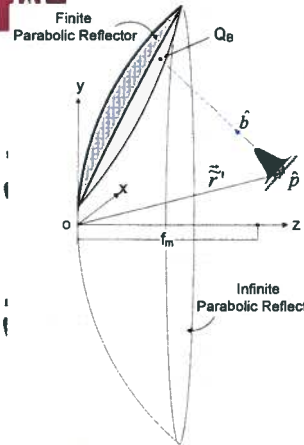


ELECTROSCIENCE LABORATORY

73

## CSB-UTD Diffraction by a Curved Wedge

$$z = \frac{x^2 + y^2}{4f_m}$$

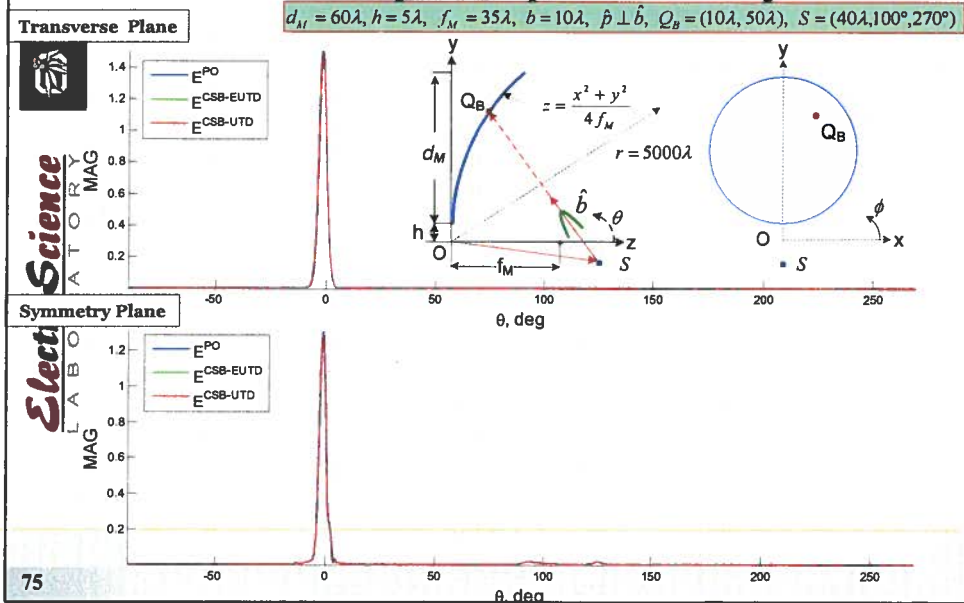


- The present CSB-UTD & CSB-EUTD solution for a CSB excited PEC curved wedge is obtained by analytically continuing the UTD solution for a PEC curved wedge excited by a real point source (or even real astigmatic ray) to deal with a CSB (or even more generally a complex astigmatic beam, i.e. CAB) illumination of a curved edge in a curved surface.
- The CSB reflected from doubly curved surface become an astigmatic Gaussian beam in paraxial region.
- The CSB-UTD solution is valid for analyzing CSB excited focus-fed parabolic reflector antennas since the caustics are now in complex space for the CSB excitation case.
- The PO analysis for a CSB excited parabolic reflector (a) loses its accuracy in the region of the main beam when a CSB axis hits near the edge. → can be improved by adding the additional edge diffraction term based on Physical Theory of Diffraction (PTD). (b) becomes more accurate when a CSB axis hits the actual reflector surface away from the edge.

74

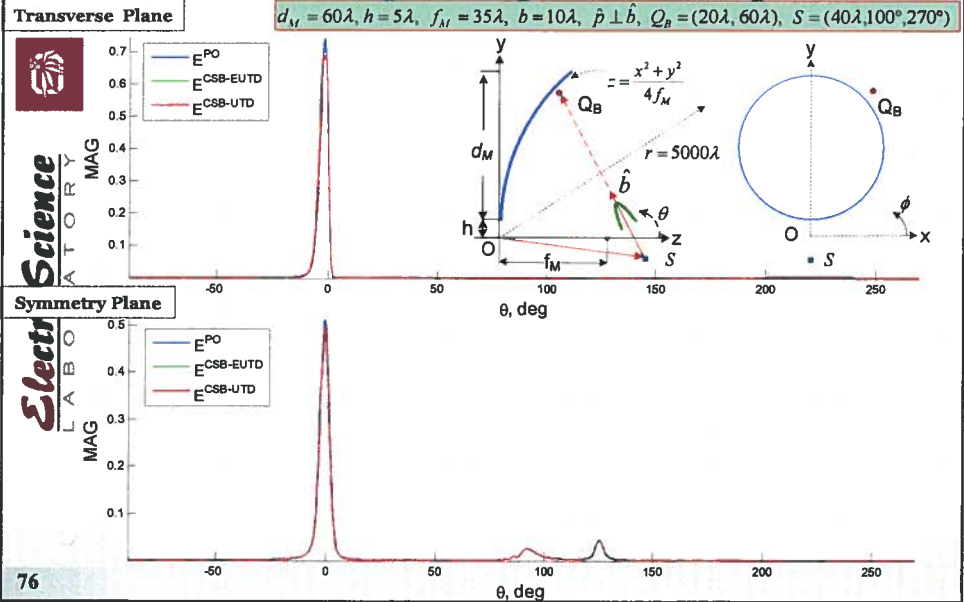
### CSB-UTD Diffraction by a Curved Wedge (cont.)

**Numerical Result : Finite parabolic reflector illuminated by a CSB**



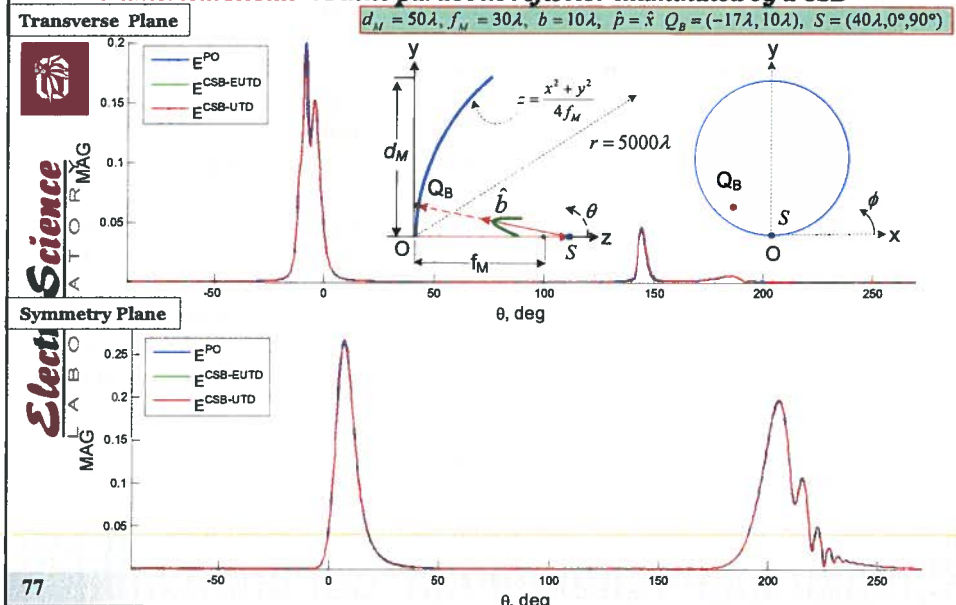
### CSB-UTD Diffraction by a Curved Wedge (cont.)

**Numerical Result : Finite parabolic reflector illuminated by a CSB**



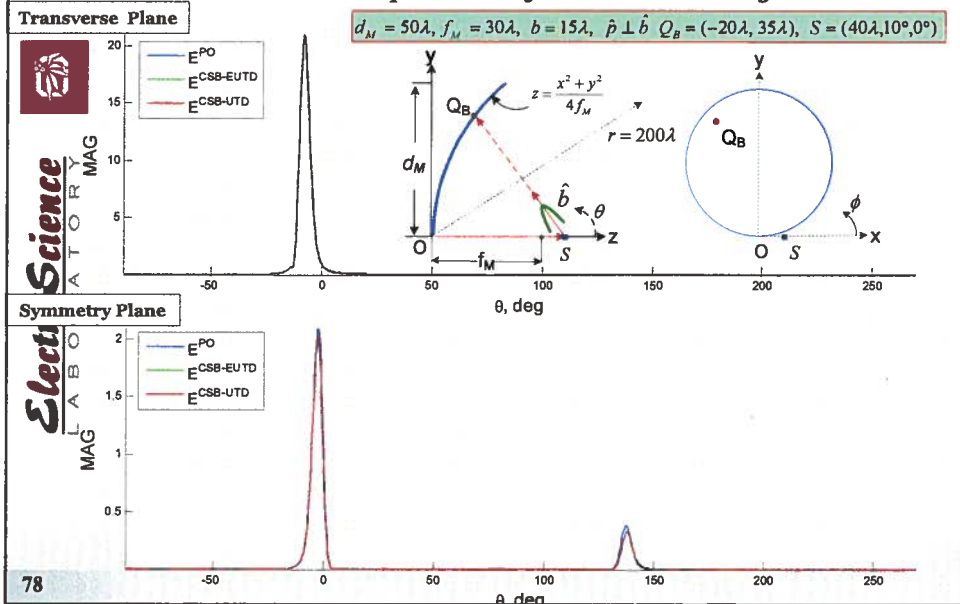
### CSB-UTD Diffraction by a Curved Wedge (cont.)

**Numerical Result : Finite parabolic reflector illuminated by a CSB**

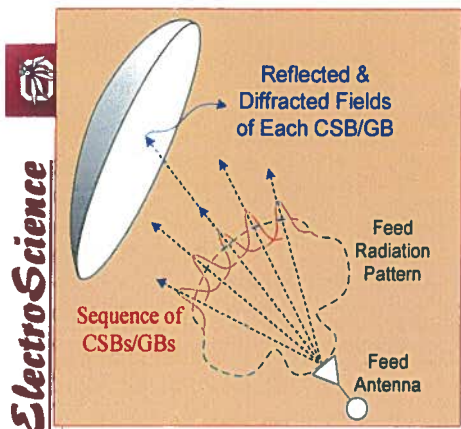


### CSB-UTD Diffraction by a Curved Wedge (cont.)

**Numerical Result : Finite parabolic reflector illuminated by a CSB**



## CSBs/GBs Illuminating a reflector



$$\vec{H}_f^i(\vec{r}_f) \sim \frac{e^{-jk r_f}}{r_f} [\hat{\theta}_f E_\theta(\vec{r}_f) + \hat{\phi}_f E_\phi(\vec{r}_f)]$$

$$\vec{E}_f^i(\vec{r}_f) \sim -Y_0 \hat{r}_f \times \vec{H}_f^i(\vec{r}_f)$$

Feed Radiation

$$\vec{H}_f^i(\vec{r}_f) \cong \sum_{n=1}^N \sum_{m=1}^M C_{nm} H_{nm}(\vec{r}_{f_{nm}}) e^{j\psi_{nm}}$$

GB Expansion

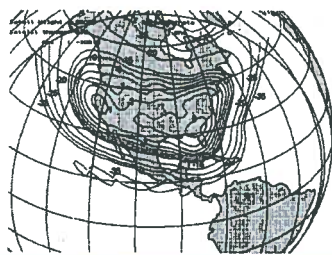
n = launching points in feed plane  
m = number of GBs from each n

79

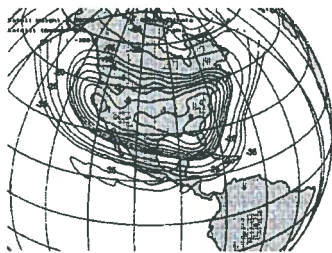
## Offset Shaped Reflector for CONUS Contour Beam Using GBs



ElectroScience  
LABORATORY



Normalized co-polarized contours based on the GB approach CONUS coverage by a shaped concave reflector with a feed pattern at 12 GHz with  $f = 18.51$ . Approximately 200GBs were used.



80

Normalized co-polarized gain contours based on the numerical PO integration approach for the same shaped reflector case as above.

$$D = 85\lambda$$

< 200 GBs

Time < 5 min/iter

NUM-PO

Time = 5 or 6 hrs/iter

Approx. 30 iter's\*

\* Rahmat-Samii's paper

?

## Conclusion



ElectroScience  
LABORATORY

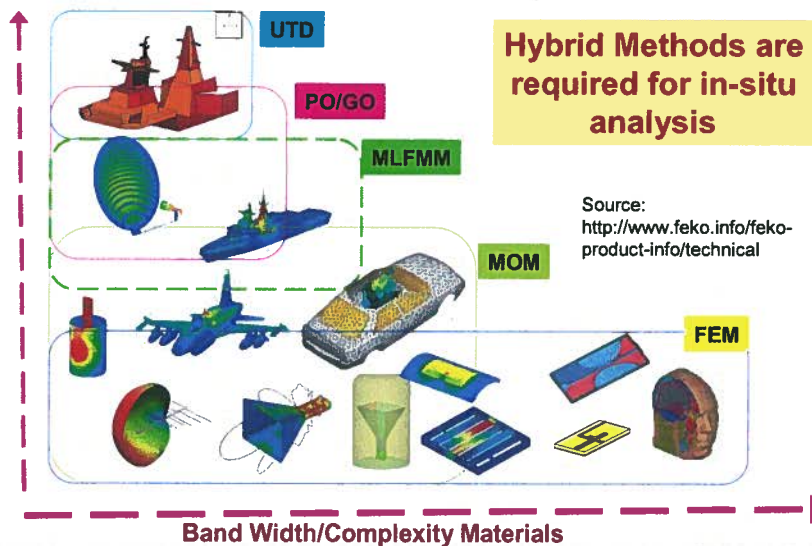
- CSP beam expansion methods for EM radiation are presented employing three different variants of the surface equivalence theorem.
- The analytical properties (validity region, truncation, etc.) of the approach are investigated.
- It is shown that accurate and efficient field representations can be obtained by conveniently truncating the beam expansion.
- It is demonstrated that the expansion idea is applicable to a class of EM radiation/scattering problems.

81

## Numerical Methods



ElectroScience  
LABORATORY  
Electrical Size



82

82

## Hybrid Method & Some Applications



**ElectroScience**  
LABORATORY

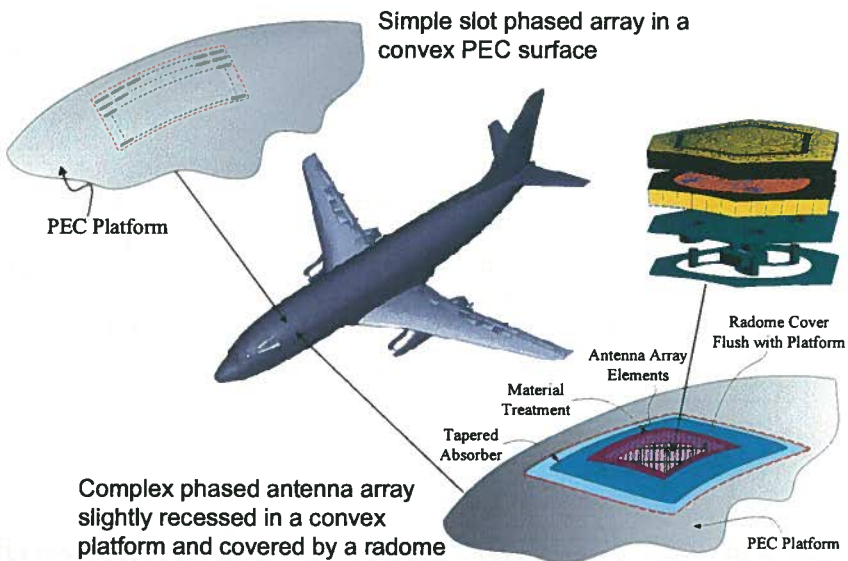
- In many applications, large antennas (arrays) and large antenna platforms contain both large and small features in terms of wavelength.
- For electrically large parts on radiating object, UTD ray method is useful but not valid for electrically small portions.
- For highly inhomogeneous and electrically small region (e.g. complex antenna elements/arrays) the FE-BI or numerical methods are useful, and UTD is not applicable here.
- A hybrid combination of FE-BI (or other suitable numerical methods) and UTD could handle the entire problem not otherwise tractable by each single approach by itself.

83

## Conformal Array Configurations



**ElectroScience**  
LABORATORY



84

## Proposed Hybrid Numerical-UTD Approach



ElectroScience  
LABORATORY

**Local Array Part**  
treated by full wave  
numerical methods.



**Present Collective  
UTD Solution**  
converts numerical  
array solution into  
rays launched from  
array aperture.

**External Platform Part**  
Collective UTD rays launched  
from aperture efficiently  
excite external platform which  
is analyzed by UTD.



85

## Local Array Part Treated by FEM, FE-BI



ElectroScience  
LABORATORY

Actual problem

Array+Radome  
Combination

Complex Array  
Platform (e.g. part of aircraft)

ABC

$M^*$

Local UTD Ray

PEC

Structure outside the local  
aperture region is ignored

A local array modeling  
for FEM

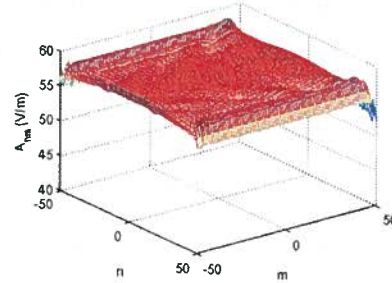
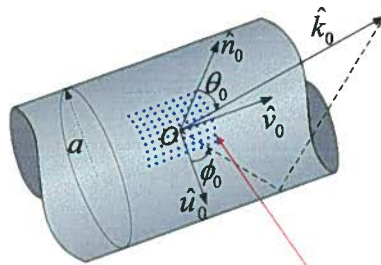
A local array modeling  
for FE-BI

86

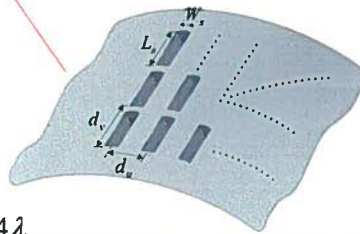
## Slot array on a PEC Circular Cylinder



**ElectroScience**  
LABORATORY



$f = 9.0 \text{ GHz}$   
 $a = 100.0\lambda$   
 $101 \times 101 \text{ elements}$   
 $d_u = d_v = 0.65\lambda$   
 $L_s = 0.55\lambda, W_s = 0.244\lambda$   
 Scan direction:  $\theta_0 = 30^\circ, \phi_0 = 90^\circ$



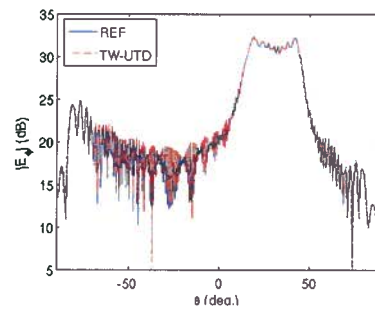
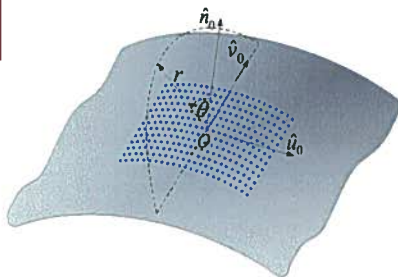
93 TWs ( $\approx 0.9\%$ ) were used !!

107

## Slot array on a PEC Circular Cylinder (cont.)



**ElectroScience**  
LABORATORY



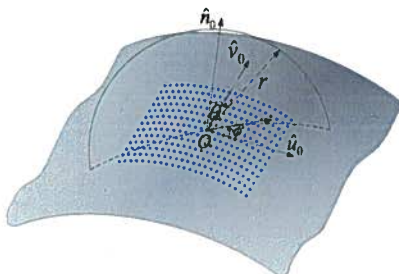
**Axial plane cut (scan plane)**  
 $r = 100 \lambda$  (near zone)  
 REF: 34.57 sec.  
 TW-UTD: 5.47 sec.

108

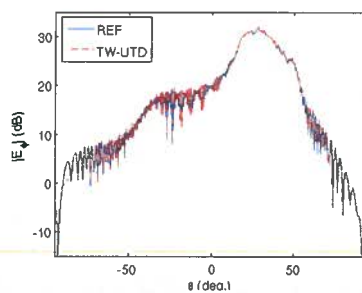
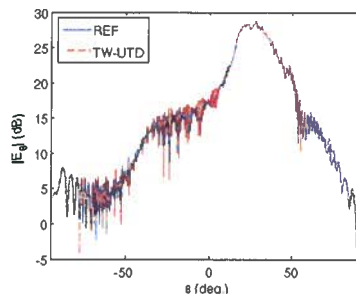
### Slot array on a PEC Circular Cylinder (cont.)



ElectroScience  
LABORATORY



Oblique plane cut:  $\phi = 60^\circ$   
 $r = 100 \lambda$  (near zone)  
 REF: 38.40 sec.  
 TW-UTD: 6.12 sec.

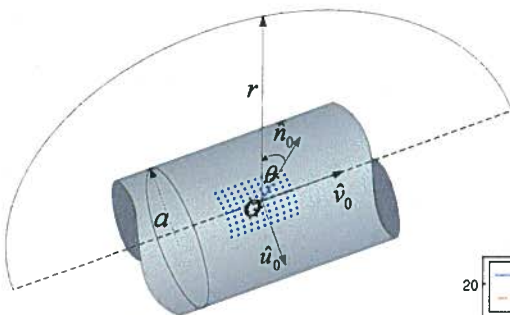


109

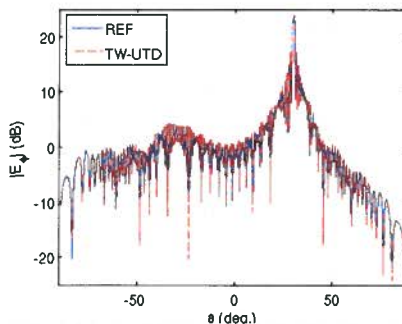
### Slot array on a PEC Circular Cylinder (cont.)



ElectroScience  
LABORATORY



Axial plane cut (scan plane)  
 far zone  
 REF: 33.48 sec.  
 TW-UTD: 4.39 sec.

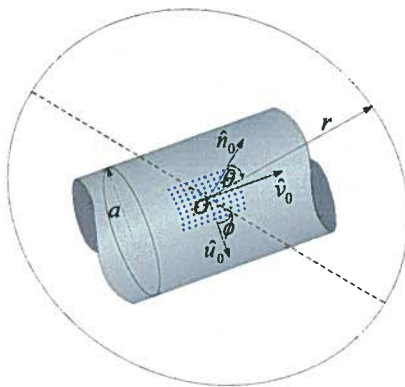


110

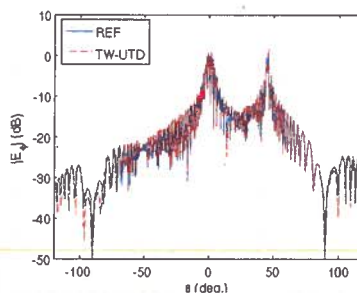
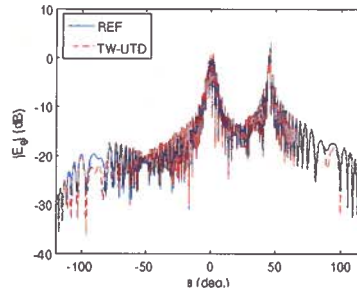
## Slot array on a PEC Circular Cylinder (cont.)



ElectroScience  
LABORATORY



Oblique plane cut:  $\phi = 45^\circ$   
**far zone**  
 REF: 51.39 sec.  
 TW-UTD: 6.08 sec.



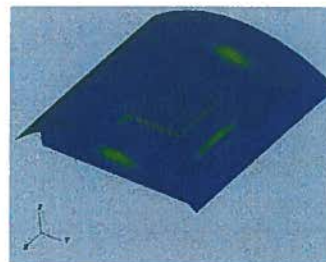
111

## Interface between Full-Wave solver and High Frequency method



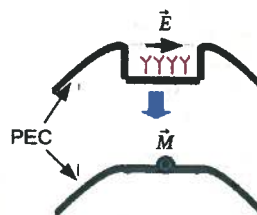
ElectroScience

- Simulate the antenna region with surrounding part of cavity.\*
- Take the tangential field on the aperture opening.
- Let  $\vec{M} = -\hat{n} \times \vec{E}$  to be the excitation source put on the surface of platform without aperture.
- UTD code NewAir is used to do the high frequency calculation for the sources on the smooth surface.\*\*



\* J-F. Lee's DD FEBI code.

\*\* P.H. Pathak, et al. A Uniform GTD Solution for the Radiation from Sources on a Convex Surface. TAP-29, No. 4, pp. 609-22.



112

## Conclusions

- An asymptotic **UTD** ray solution has been developed for describing, in a **collective** fashion, the fields radiated by large conformal antenna arrays on a doubly curved, smooth convex surface.
- The present solution will provide an **efficient link** between the local array part to be analyzed numerically and the full external platform part to be analyzed by UTD, in a **hybrid method** for analyzing large complex antenna phased arrays integrated into a realistic complex platform.
- The present collective UTD ray solution shows a good agreement with the conventional element-by-element UTD field summation solution.



ElectroScience  
LABORATORY

117

## The work presented is done in conjunction with the following researchers

### The Ohio State Univ. (OSU), ElectroScience Lab.(ESL), Columbus, Ohio, USA

- (1) Prof. Robert J. Burkholder
- (2) Dr. Youngchel Kim
- (3) Dr. His-Tseng Chou (now Prof. at Yuan-Ze Univ. Taiwan ROC)
- (4) Dr. Titipong Lertwiyaprapa
- (5) Dr. Pawuwat Janpugdee (Now member of research staff at TEMASEK Labs. NUS, Singapore)
- (6) Dr. Koray Tap (Now at ASELSAN, Ankara, Turkey)
- (7) Prof. W.D. Burnside
- (8) Dr. R.J. Marhefca
- (9) Dr. Nan Wang
- (10) Prof. Jin-Fa Lee

### Univ. of Siena, Italy

- (1) Giorgio Carluccio
- (2) Prof. Matteo Albani
- (3) Prof. Stefano Maci

### Applied EM

- (1) Dr. Cagatay Tokgoz
- (2) Dr. C. J. Reddy

118

# High-Frequency Techniques for Antenna Analysis

PRABHAKAR H. PATHAK, FELLOW, IEEE

*Invited Paper*

*A summary of various high-frequency techniques is presented for analyzing the electromagnetic (EM) radiation from antennas in the presence of their host environment. These techniques not only provide physical insight into antenna radiation mechanisms, but they are found to be highly efficient and accurate for treating a variety of practical antenna configurations. Examples to which these techniques have been applied include open-ended waveguide antennas, horn and reflector antennas, antennas on aircraft and spacecraft, etc. The accuracy of these techniques is established via numerical results which are compared with those based on other independent methods or with measurements. Furthermore, these high-frequency methods can be combined with other techniques, through a hybrid scheme, to solve an even greater class of problems than those which can be solved in an efficient and tractable manner by any one technique alone.*

## I. INTRODUCTION

A summary of some high-frequency techniques is presented for efficiently and accurately analyzing the electromagnetic (EM) radiation from antennas in the presence of their host environment. Such high-frequency techniques also provide a physical insight into the antenna radiation mechanisms involved; this property is useful for both analysis and design purposes.

At sufficiently high frequencies (or short wavelengths), EM wave radiation, propagation, scattering and diffraction, exhibit a highly localized behavior. Such a local description of high-frequency EM waves is given in terms of rays and their associated fields. Thus the total high-frequency field at an observation point is given by the superposition of the fields of all the rays that arrive there, such as via a direct (incident) ray path from the primary antenna excitation (source), and via rays which experience reflection and diffraction from generally different but highly localized regions or "flashpoints" on the antenna and its host structure, as shown for example in Fig. 1. In particular, the

Manuscript received January 5, 1991; revised June 15, 1991. This paper was supported in part by the Joint Services Electronics program under Contract N00014-88-K-004 with the Ohio State University during the preparation of this paper.

The author is with the Department of Electrical Engineering, Electro-Science Laboratory, Ohio State University, Columbus, OH 43212.  
IEEE Log Number 9105507.

incident and reflected rays obey Fermat's principle, and are associated with the usual geometrical optics (GO) incident and reflected fields. In the case of penetrable objects, there also exist GO transmitted rays. On the other hand, the diffracted rays are generally found to originate from geometrical and electrical discontinuities, and from points of grazing incidence on smooth convex portions of the radiating object. The existence of these types of diffracted rays has been postulated by Keller, via an extension of Fermat's principle, in his development of the geometrical theory of diffraction (GTD) [1]; this ray method will be summarized later in more detail. Such a rather simplified and physically appealing picture for the transport of high-frequency EM energy, locally along incident, reflected, and diffracted rays, is in sharp contrast to the description of EM wave radiation at low frequencies that is generally given in terms of the radiation integral on the currents induced globally over the antenna and its entire host structure by the primary antenna excitation. At lower frequencies, one can either employ numerical methods (e.g., moment method, conjugate gradient method, etc.) to solve integral equations for these induced currents, or numerically solve (using finite element or finite difference schemes) the partial differential equations governing the total field behavior. One could also employ a numerical modal (eigenfunction) matching technique for obtaining the relevant field solutions. However, at moderate to high frequencies all of these numerical techniques [64] become very poorly convergent and inefficient because numerical solutions are generally based on exact formulations that must satisfy field self-consistency in a global sense, i.e., over the entire radiating object, rather than requiring a knowledge of the fields in a local sense as done in the high-frequency approximations. It therefore becomes necessary to employ high-frequency techniques for analyzing electrically large radiating objects in a tractable fashion.

One could demonstrate the local nature of high-frequency radiation if one begins by considering the radiation integral over the spatial current distribution induced on a radiating object by the primary excitation. At high frequencies, the

0018-9219/92\$03.00 © 1992 IEEE

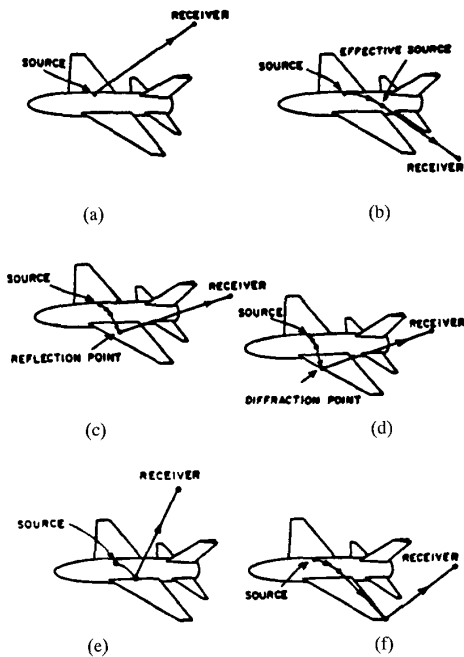


Fig. 1. Rays launched from an infinitesimal antenna element on an aircraft.

phase of the corresponding integrand oscillates rapidly and produces a destructive interference, or cancellation, between the various spherical wave contributions which arrive to a given observation point from the region of integration over the radiating object that excludes any stationary phase points in the integrand. The dominant contribution to the radiation integral then arises from the constructive interference between the spherical waves which emanate from the local neighborhood of any stationary phase points in the region of integration, and also from the end or boundary points of the integral, etc. A similar situation occurs when employing a spectral rather than the spatial representation of the radiation integral; in this case the dominant contribution to the spectral integral for the high-frequency case again arises from the local neighborhood of certain critical points in the spectral integrand, such as saddle points, poles, etc., while a destructive interference generally exists between contributions from the remaining portion of the spectrum. The critical points within the spatial representation of the radiation integral physically correspond to the “flashpoints” or points of reflection, transmission and diffraction on the radiating object. On the other hand, the critical points within the spectral representation for the radiation integral correspond to specific directions, or rays, along which the high-frequency field propagates to the observer. Furthermore, these rays originate from the flashpoints alluded to earlier; consequently, both the spatial and spectral forms of the radiation integral yield the same local picture for the radiation of high-frequency fields. Indeed, a critical point within the radiation integrand

of either the spatial or the spectral type leads to the description of a particular ray mechanism (e.g., ray reflection, ray diffraction, etc.) thereby analytically demonstrating the principal of localization of high-frequency fields. Such an evaluation of the radiation integrals in terms of a superposition of the contributions from just the isolated critical points in the integrand constitutes an asymptotic high-frequency approximation for the integrals. Typically, the asymptotic evaluation is performed with respect to a large parameter, e.g., the product of the wavenumber ( $2\pi/\lambda$ , where  $\lambda$  = wavelength) and some characteristic distance, and the asymptotic approximation becomes increasingly accurate with increase in the large parameter.

It can be verified from an asymptotic evaluation of the radiation integrals, as discussed above, that the ray fields exhibit a “local plane wave” behavior; i.e., the rays are perpendicular to the wavefront (or equiphase) surface in an isotropic medium as shown in Fig. 2; in particular, the wavefront is locally plane in this high-frequency approximation, and the ray field is polarized transverse to the ray. The rays are straight lines in a homogeneous medium. The concept of wavefronts and rays is not new; indeed, it has been central to the development of classical geometrical optics (GO). One recalls that GO includes only the incident, reflected and transmitted ray fields. Limiting the present discussion for the sake of convenience to antennas and their host structures that are impenetrable, it then follows that only the GO incident (or direct) ray from the primary excitation and the GO reflected rays can exist in this case. An example of this situation is shown in Fig. 3 where the line source excites an impenetrable structure; the GO incident and reflected rays exist only in certain portions of the space surrounding this structure. The incident rays (directly radiated from the line source) do not exist beyond the edge induced incident shadow boundary (ISB) and the smooth surface induced surface shadow boundary (SSB), respectively. Also, the reflected rays disappear beyond the edge induced reflection shadow boundary (RSB). Therefore, GO fails to predict a nonzero field within the shadow regions of the incident and reflected rays where such rays cease to exist, and consequently GO cannot describe the diffraction effects behind an impenetrable structure; this may be visualized in Fig. 3. The failure of GO in geometric shadow regions, where the source and its image are not directly visible, was overcome by Keller’s GTD [1]. The existence of these diffracted rays in the GTD can be readily verified via the asymptotic reduction of the radiation integrals pertaining to various canonical diffraction problems. Thus according to GTD, the field at the edge  $Q_E$ , which is incident from the line source at  $Q'$ , gives rise to edge diffracted rays emanating from  $Q_E$  as in Fig. 4. Likewise the incident ray from  $Q'$  which grazes the surface at  $Q_S$  launches a surface ray which propagates around the smooth convex boundary transporting energy into the shadow region. Surface diffracted rays are shed along the forward tangent to the surface rays as shown in Fig. 4. The field at  $P_1$  in Fig. 3 consists of simply the GO incident and reflected fields, whereas according to GTD

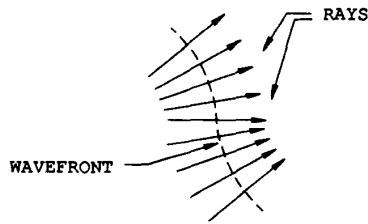


Fig. 2. Wavefront surface and associated family of rays.

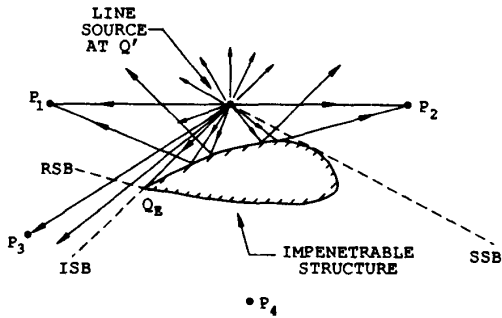


Fig. 3. Geometrical optics (GO) incident and reflected rays produced by a line source radiating in the presence of an impenetrable structure.

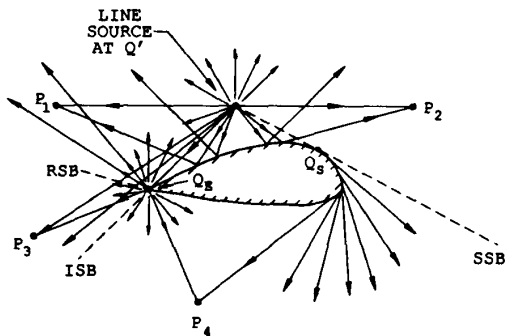


Fig. 4. Edge diffracted rays originating from the edge  $Q_E$  and rays diffracted tangentially from the surface ray excited at the point of grazing incidence  $Q_S$ .

the field at  $P_1$  in Fig. 4 also contains the additional edge diffracted ray field. The field at  $P_3$  in Fig. 3 is due only to the GO incident field, but GTD again requires that the edge diffracted field be included at  $P_3$  as in Fig. 4. The field at  $P_4$  in Fig. 3 vanishes as predicted by GO; in contrast, the GTD predicts a nonzero field at  $P_4$  which is a superposition of the edge and surface diffracted ray fields as in Fig. 4.

The GTD field is clearly a superposition of GO and diffracted ray fields. Just as the initial amplitudes of the GO reflected and transmitted ray fields are given in terms of the reflection and transmission coefficients, the initial value of a diffracted ray field is likewise given in terms of a diffraction coefficient. The relevant diffraction co-

efficients may be deduced from asymptotic solutions to simpler canonical problems that model the geometrical and electrical properties of the original problem in the local neighborhood of the point of diffraction. As a result of the extended Fermat's principle, the rays diffracted by an edge lie on a cone about the edge with the cone half angle equal to the angle that the incident ray makes with the edge tangent at the point of diffraction as in Fig. 9. In the case of a two-dimensional problem, the cone of diffracted rays collapses to a disk as in Fig. 4. Furthermore, the surface ray initiated at  $Q_S$  in Fig. 4 follows a geodesic path on the convex boundary; also once launched, the surface ray field attenuates as it propagates, because energy is continually shed via rays diffracted tangentially from the surface ray.

Away from the point of diffraction, the GTD diffracted ray field behaves just like a GO ray field. However, such a purely ray optical field description of the GTD fails within the transition regions adjacent to the shadow boundaries (e.g., ISB, RSB, and SSB in Fig. 3) where the GTD diffracted fields generally become singular. The angular extent of the transition region varies inversely with frequency and it also depends on some characteristic distances as will be discussed briefly in Section II. Such a transition region may be viewed as one through which the GTD field changes its ray optical behavior, e.g., as from an incident ray optical type to a diffracted ray optical type across an ISB. This failure of the GTD within the shadow boundary transition regions can be patched up via uniform versions of the GTD such as the uniform geometrical theory of diffraction (UTD) [2]-[4] and the uniform asymptotic theory (UAT) [5]. Additional references dealing with the GTD/UTD/UAT may be found in [6]-[11]. The UTD will be used in this paper as it has been developed for a variety of canonical shapes, whereas the UAT has been developed only for an edge at the present time.

It was indicated earlier that the asymptotic evaluation of radiation integrals gives rise to a total high-frequency field in terms of a superposition of the contributions from certain isolated or critical points in the integrand (which can be seen to correspond to the field of GTD rays). Some of these critical points can come close together when the observation point lies within the shadow boundary transition regions, and even coalesce for an observer on the shadow boundary itself. This leads to a "coupling between the critical points" and the asymptotics must then be modified; i.e., it must be performed via a uniform procedure which accounts for this coupling and thus forms the basis of the UTD. In the UTD, the GTD solution is modified through the use of uniform asymptotic procedures which systematically introduce additional factors, referred to as the UTD transition functions. These UTD transition functions compensate the GTD singularities at shadow boundaries and keep the total high-frequency field bounded, and continuous, across these boundaries, thus keeping the field valid within the transition regions. Furthermore, outside the shadow boundary transition layers, the UTD automatically reduces to the GTD. These transition functions are special functions characteristic of the diffraction process; e.g., in the case of

edge diffraction they involve Fresnel integrals, whereas in the case of convex surface diffraction they involve Fock functions [12] which contain integrals of Airy functions. The latter functions are named after V. A. Fock who contributed significantly to the analysis of wave diffraction by smooth convex boundaries.

It thus follows from the preceding paragraph that it is the UTD and not the GTD which must be used in practical applications to obtain continuous total (high-frequency) fields (around the radiating object). Besides the singularities of the GTD at the GO shadow boundaries discussed above, the GTD and its uniform versions such as the UTD, UAT, etc., exhibit singularities at the caustics of GO and diffracted rays. Ray caustics occur whenever a family of rays (i.e., ray congruences) merge or intersect; examples of ray caustics are shown in Figs. 5 and 6. In particular, the diffracted ray caustic at  $P$  in Fig. 5 is produced on the axis of a symmetric parabolic reflector illuminated by a feed at the focus. The smooth caustic of reflected rays in Fig. 6 is produced by a shaped subreflector which is a surface of revolution; it is illuminated by a feed antenna located on the subreflector axis. This subreflector surface exhibits an inflection point along its generator giving rise to the caustic. Such a smooth caustic can also be produced by a concave reflector surface. A curved edge can likewise generate a smooth caustic of diffracted rays. Ray caustics can become problematic in the GTD/UTD/UAT computations only if they occur in real space (exterior to the antenna and its host structure); otherwise, they are of little concern whenever they occur in virtual space e.g., within the scatterer or the antenna host structure, unless the transition region adjacent to the virtual caustic emerges into external space where a field or observation point may be located. The failure of the GTD/UTD at GO or diffracted ray caustics and their associated transition regions can be patched up through a uniformizing procedure which again introduces special functions (or caustic transition functions) to correct the pure ray solution. For a smooth caustic as in Fig. 6, the special transition function involves the Airy function and its derivative [13], [14]; if the caustic curve has a cusp then one obtains Pearcey functions (related to the parabolic cylinder functions) [15]. If either the smooth or the cusped caustic terminates, as might happen when the reflecting surface terminates at an edge, then one requires incomplete Airy functions or incomplete Pearcey functions, respectively [15], to evaluate fields near the caustic termination. These special functions (or transition functions) reflect the coupling of the pertinent critical points in the asymptotic evaluation of the radiation integral as discussed earlier.

A procedure which can treat more general diffracted ray caustic effects is based on the equivalent current method (ECM) [16], [17]. The ECM while primarily useful for handling caustics of diffracted rays can in some special cases also be employed to handle caustics of reflected rays. In general, the ECM, which corrects for the singularities of the fields at diffracted ray caustics that lie outside the ISB, RSB and SSB transition regions (where UTD

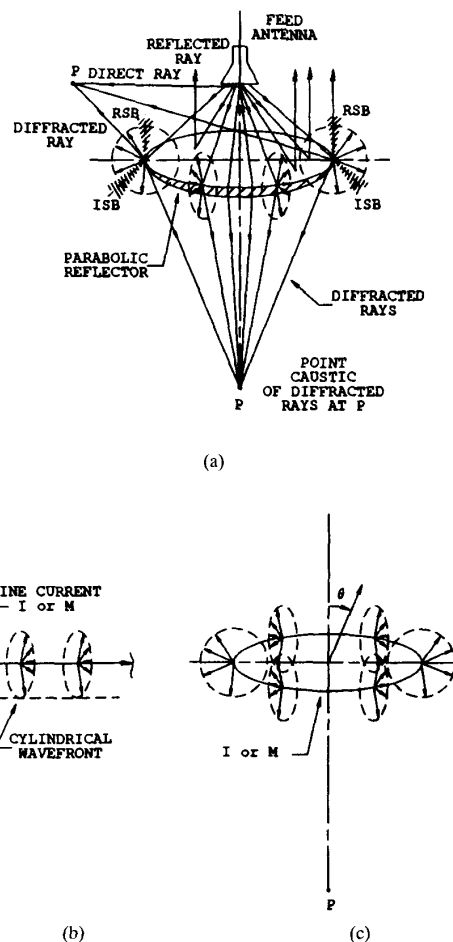


Fig. 5. Point caustic of edge diffracted rays on the axis of a symmetrically fed parabolic reflector.

reduces to GTD) describes the fields within such caustic transition regions in terms of a radiation integral over a set of equivalent *line* currents that replace the original geometry and its illumination; these equivalent currents are found from the GTD diffraction coefficients which are not singular in caustic directions even though the actual GTD ray field is singular there [4]. The fields in the diffracted ray caustic region of Fig. 5 can be treated by ECM. This ECM procedure, if formulated properly, is a uniform procedure in that away from the caustic transition region, the ECM radiation integral reduces asymptotically to the GTD. In a few cases, the ECM radiation integral reduces to a closed form result, or it can be expressed in terms of special functions (e.g., Airy or Pearcey functions) alluded to above; however, in general the integral must be evaluated numerically.

The diffraction effects within the GO shadow boundary transition regions are generally not localized to just the edges or points of diffraction because they are then coupled to the GO effects on the reflecting surface, and in order

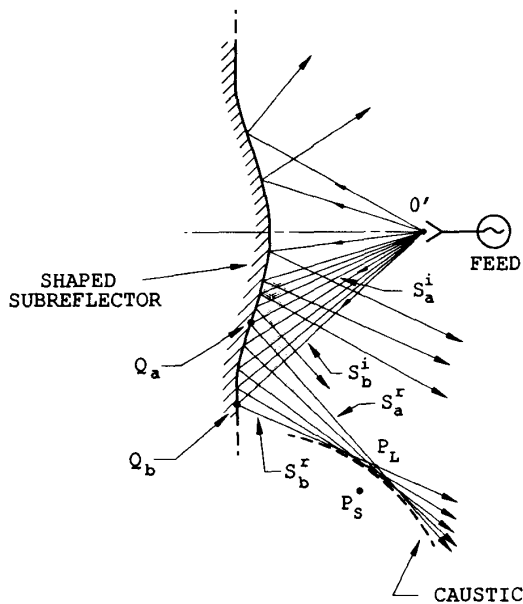


Fig. 6. Ray caustic generated by a shaped subreflector illuminated by a feed antenna.

to correct for the singularities of GTD ray caustics in directions where the associated caustic transition regions overlap with the GO shadow boundary transition regions, one must therefore resort to a *surface* integral representation and not the *line* integral approximations of ECM. The physical optics (PO) surface integral approach [18] and its modifications based on Ufimtsev's physical theory of diffraction (PTD) [19], [20] for edged bodies as discussed in Section II-C, and Fock's theory for curved bodies [12], become useful for treating the fields within the overlap of diffracted and/or GO ray caustic and GO ray shadow boundary transition regions. An example of the overlap of the caustic and GO shadow boundary transition regions is again provided by Fig. 5, where the RSB coincides with the forward axial caustic of the edge diffracted rays in the far zone of the reflector. Furthermore, there are also an infinite number of rays reflected from the parabolic surface which contribute to the far field in this forward axial direction. The forward axial direction of the parabolic reflector is therefore also a caustic of reflected rays in the far zone, in addition to being a caustic of the edge diffracted rays. While the PO method in itself gives quite accurate results for caustic fields in the region of the overlap of the GO shadow boundary and caustic transition regions, the PTD which provides a correction to PO can yield more accurate results outside the caustic region. *It is noted that the PTD is a superposition of PO and the correction to PO as specified by Ufimtsev.*

In general, the integrals in the PTD approach must be evaluated numerically; only in special cases can they be evaluated in closed form. In situations where the integrals

in the PTD can be evaluated asymptotically, they recover the leading terms of the GTD fields. Furthermore, if these PTD integrals can be evaluated asymptotically in a uniform fashion, then PTD can be shown to recover the UTD. The intimate connection between the PTD and the GTD/UTD indicated above allows one to view PTD as an integral version of the GTD/UTD which is valid even in regions of ray caustics, and also in regions of overlap of caustic and GO shadow boundary transition regions where GTD/UTD fails. However, PTD requires an integration whereas UTD does not. Therefore, it appears to be far more efficient to employ UTD everywhere except at ray caustics, and in the overlap of caustic and GO shadow boundary transition regions, where the more general PTD integrals may be used to patch up the UTD. While the PTD is a high-frequency technique in its own right like the GTD/UTD, it has been developed only for edges as indicated previously, whereas the UTD can also handle surface diffraction and other types of diffraction mechanisms. Furthermore, the PTD cannot account for multiple diffraction effects as easily as the GTD/UTD; such higher order multiple wave interactions can become important if the scattering/diffraction centers come close together on a radiating object (e.g., if a pair of interacting edges come close together). Nevertheless, the PTD has been often used for predicting the dominant contribution to the radar cross section (RCS) of complex targets (e.g., aircraft, missiles, etc.).

The above-mentioned high-frequency techniques based on the GTD/UTD, ECM, and PTD will be applied to some illustrative antenna examples in the next section. An  $e^{+j\omega t}$  time convention for the sources and fields will be assumed and suppressed in the following work. Also,  $k$  is assumed to be the wavenumber in the isotropic homogeneous medium external to the antenna and its host structure ( $k = 2\pi/\lambda$ ;  $\lambda =$  wavelength in the external medium).

## II. SUMMARY OF HIGH FREQUENCY TECHNIQUES WITH SPECIFIC ANTENNA APPLICATIONS

The high-frequency techniques such as the GTD/UTD, ECM, and PTD, which have been briefly discussed above in Section I, are reviewed in slightly more detail in this section and results based on these techniques are illustrated for dealing with some antenna geometries of interest. The main focus will be on GTD/UTD-based applications; these will be discussed first. The applications based on the ECM and the PTD will be illustrated next only from the perspective of patching up GTD/UTD in those few special situations where the latter fails as discussed previously, such as in regions of ray caustics, and where there is a confluence of caustic and GO shadow boundary transition regions.

### A. GTD and Its Uniform Version, UTD

As discussed in Section I, the GTD/UTD is a ray technique. Therefore, it would be worthwhile to firstly develop a general expression for the ray optical field. While there are several procedures, involving either the relevant asymptotic approximations of radiation integrals pertaining to

certain canonical radiation problems, or the asymptotic (Luneberg–Kline) series expansion of the wave equation, to arrive at a ray optical field expression, the simpler and less rigorous approach based on geometrical considerations is employed here. In particular, since energy in the high-frequency EM field is assumed to be transported along rays, it follows from geometrical considerations that power must be conserved in each narrow tube of rays (or a ray pencil) in a lossless medium. Thus consider any given (central or axial) ray  $OP$  in a ray tube as shown in Fig. 7. Let the principal wavefront radii of curvature at  $O$  be  $\rho_1$  and  $\rho_2$ , respectively; the corresponding principal wavefront radii of curvature of that ray at  $P$  are  $(\rho_1 + s)$  and  $(\rho_2 + s)$ , where  $|\overline{OP}| = s$ . Let the electric field intensity at  $O$  and  $P$  be  $\overline{E}(O)$  and  $\overline{E}(P)$ , respectively; thus, the power crossing the area  $dA_o$  is given by  $(1/Z_o)|\overline{E}(O)|^2 dA_o$  where  $dA_o \approx |(\rho_1 d\psi_1)(\rho_2 d\psi_2)|$  and where  $Z_o$  is the plane wave impedance in the medium; likewise, the power crossing  $dA_p$  is  $(1/Z_o)|\overline{E}(P)|^2 dA_p$  where  $dA_p \approx |[(\rho_1 + s)d\psi_1][(\rho_2 + s)d\psi_2]|$ . Conservation of power in the ray tube requires  $(1/Z_o)|\overline{E}(P)|^2 dA_p = (1/Z_o)|\overline{E}(O)|^2 dA_o$ ; i.e.,

$$|\overline{E}(P)| = |\overline{E}(O)| \sqrt{\frac{\rho_1 \rho_2}{(\rho_1 + s)(\rho_2 + s)}}. \quad (1a)$$

Incorporating the local plane wave polarization and phase heuristically into (1a) yields the rule for continuation of the field  $\overline{E}(O)$  at  $O$  to the field  $\overline{E}(P)$  at  $P$  along the ray  $\overline{OP}$  as

$$\overline{E}(P) \sim \overline{E}(O) \sqrt{\frac{\rho_1 \rho_2}{(\rho_1 + s)(\rho_2 + s)}} e^{-jks}. \quad (1b)$$

The field in (1b), which is referred to as an arbitrary ray optical field (where  $\rho_1$  and  $\rho_2$  are arbitrary), can be shown to reduce to a plane wave (if  $[\rho_1, \rho_2] \rightarrow \infty$ ), cylindrical or conical wave (if  $\rho_1$  or  $\rho_2 \rightarrow \infty$ ), and a spherical wave (if  $\rho_1 = \rho_2 = \text{finite value}$ ), respectively. Thus the latter more familiar wave types are all special cases of a ray optical field whose general form is (1b). One notes that the ray congruences at 1–2 and 3–4 form a ray caustic (or centers of radii of curvature  $\rho_1$  and  $\rho_2$ , respectively of the wavefront) in Fig. 7. The  $\rho_1$  and  $\rho_2$  are positive if the ray caustics at 1–2 and 3–4 occur before reaching the reference point  $O$  along the ray direction  $\hat{s}$  in Fig. 7; otherwise, they are negative. The positive branch of the square root is chosen in (1b); hence, if  $\rho_{1,2} < 0$  and  $s > -|\rho_2|$  or  $s > -|\rho_1|$ , then a caustic is crossed at 1–2 or 3–4, respectively, and  $(\rho_2 + s)$  or  $(\rho_1 + s)$  changes sign so that a phase jump of  $\pi/2$  due to caustic traversal needs to be included in (1b), because

$$\sqrt{\frac{\rho_i}{\rho_i + s}} = \left| \sqrt{\frac{\rho_i}{\rho_i + s}} \right| e^{j\pi/2},$$

if  $\rho_i = -|\rho_i|$  and  $s > -|\rho_i|$ , for  $i = 1, 2$ .

Furthermore, the magnetic field  $\overline{H}(P)$  at  $P$  is found from  $\overline{E}(P)$  in (1b) via the local plane wave condition along a ray; namely,

$$\overline{H}(P) = Y_o \hat{s} \times \overline{E}(P) \quad (2)$$

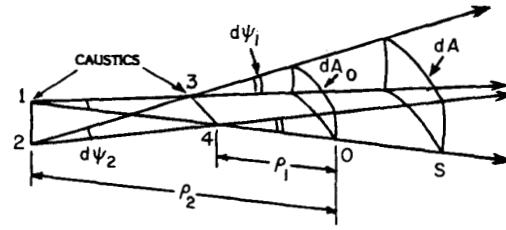


Fig. 7. Ray tube (ray pencil).

where  $Y_o = 1/Z_o$ , and  $Z_o$  as before is the local plane wave impedance of the medium in which the ray propagates.

The quantity  $\overline{E}(P)$  in (1b) may represent a field which is associated with either an incident ray, or with rays that are reflected or transmitted at an interface between two media, or with diffracted rays. The initial ray amplitudes at the points of reflection and transmission can be found by enforcing the EM boundary conditions at the interface; these conditions also lead to Snell's laws of reflection and transmission which are consistent with Fermat's principle and which could in fact have been derived from it. The initial value of the diffracted ray field is given in terms of the diffraction coefficient and the diffracted ray path obeys the extended Fermat's principle. Thus in general, (1b) can be written as

$$\overline{E}^p(P) \sim \overline{E}^p(O_p) \sqrt{\frac{\rho_1^p}{\rho_1^p + s^p} \cdot \frac{\rho_2^p}{\rho_2^p + s^p}} e^{-jks^p} \quad (3a)$$

$$\text{with } p \rightarrow i, r \text{ or } d \quad (3b)$$

where the superscript or subscript,  $p$ , refers to the incident ( $i$ ), reflected ( $r$ ) or diffracted ( $d$ ) ray fields.

1) *Incident GO Ray Field:* Letting  $p = i$  in (3a) and (3b) allows one to write the GO incident ray field as

$$\overline{E}^i(P) = \overline{E}^i(O_i) \sqrt{\frac{\rho_1^i}{\rho_1^i + s^i} \cdot \frac{\rho_2^i}{\rho_2^i + s^i}} e^{-jks^i} U_i \quad (4a)$$

where  $U_i$  is unity in the region where the GO incident ray field exists and is zero otherwise. The incident principal wavefront radii of curvature  $\rho_1^i$  and  $\rho_2^i$  are measured from the reference point  $O_i$  along the incident ray to  $P$ . It is noted that  $s^i = |\overline{O_i P}|$ . In the two-dimensional case  $\rho_2^i \rightarrow \infty$  and (4a) becomes

$$\overline{E}^i(P) = \overline{E}^i(O_i) \sqrt{\frac{\rho_1^i}{\rho_1^i + s^i}} e^{-jks^i} U_i. \quad (4b)$$

2) *Reflected GO Ray Field:* An expression for the reflected ray field can be obtained by letting  $p = r$  in (3a) and (3b), and by letting the point  $O_p = O_r$  move to the point of reflection  $Q_R$ , then (3a) and (3b) become

$$\overline{E}^r(P) \sim \overline{E}^r(Q_R) \sqrt{\frac{\rho_1^r}{\rho_1^r + s^r} \cdot \frac{\rho_2^r}{\rho_2^r + s^r}} e^{-jks^r} U_r. \quad (5a)$$

where the step function  $U_r$  is unity in the region where the reflected ray field exists and is zero otherwise. The reflected

field  $\overline{E}^r(Q_R)$  at the point of reflection  $Q_R$  can be related to the incident field  $\overline{E}^i(Q_R)$  at  $Q_R$  by the dyadic surface reflection coefficient  $\overline{R}$  as follows:

$$\overline{E}^r(Q_R) = \overline{E}^i(Q_R) \cdot \overline{R}. \quad (5b)$$

Incorporating (5b) into (5a) yields the required expression for the reflected field at  $P$  due to the field incident on the surface at the point of reflection  $Q_R$  as

$$\overline{E}^r(P) \sim \overline{E}^i(Q_R) \cdot \overline{R} \sqrt{\frac{\rho_1^r}{\rho_1^r + s^r} \cdot \frac{\rho_2^r}{\rho_2^r + s^r}} e^{-jks^r} U_r. \quad (5c)$$

The reflected wavefront radii of curvature  $\rho_{1,2}^r$  are shown in Fig. 8 and they may be calculated via the expressions given in [2]. The dyadic reflection coefficient  $\overline{R}$  may be found by approximating the original surface locally by a plane tangent to that surface at the point of reflection  $Q_R$  when it is illuminated by an EM plane wave, and by enforcing the EM boundary conditions at  $Q_R$ . It is convenient to express the incident and reflected fields in terms of the unit vectors fixed in the incident and reflected rays as in Fig. 8. Let  $\hat{e}_{\parallel}^i$  and  $\hat{e}_{\parallel}^r$  be unit vectors fixed in the plane of incidence containing the unit normal vector  $\hat{n}$  to the surface at  $Q_R$  and the incident ray direction  $\hat{s}^i$  at  $Q_R$ , and let these vectors also be perpendicular to the incident and reflected ray directions  $\hat{s}^i$  and  $\hat{s}^r$ , respectively. Likewise, let  $\hat{e}_{\perp}$  be a unit vector perpendicular to the plane of incidence at  $Q_R$ . In these ray fixed unit vectors,  $\overline{R}$  becomes

$$\overline{R} = \hat{e}_{\parallel}^i \hat{e}_{\parallel}^r R_h + \hat{e}_{\perp} \hat{e}_{\perp} R_s. \quad (6)$$

For a perfectly conducting surface,  $R_s = -1$  and  $R_h = 1$ . If the reflecting boundary and illumination becomes two-dimensional, then  $\rho_2^r \rightarrow \infty$  and (5a) becomes

$$\overline{E}^r(P) \sim \overline{E}^i(Q_r) \cdot \overline{R} \sqrt{\frac{\rho_1^r}{\rho_1^r + s^r}} e^{-jks^r} \quad (\text{two-dimensional case}) \quad (7)$$

3) *Edge Diffracted Ray Field*: Consider an edge diffracted ray field produced by an incident wave which strikes a wedge at  $Q_E$  as in Fig. 9. One can obtain the general expression for the edge diffracted ray field once again from (3a) and (3b) by letting  $p = d$  so that

$$\overline{E}^d(P) \sim \overline{E}^d(O_d) \sqrt{\frac{\rho_1^d}{\rho_1^d + s^d} \cdot \frac{\rho_2^d}{\rho_2^d + s^d}} e^{-jks^d}. \quad (8a)$$

It is useful to move the reference point  $O_d$  along the edge diffracted ray at  $P$  to the point  $Q_E$  at the point of diffraction on the edge; thus  $\rho_1^d \rightarrow 0$  as can be seen from Fig. 9. Even though  $\rho_1^d \rightarrow 0$  in (8a) one can show that:

$$\lim_{\substack{\rho_1^d \rightarrow 0 \\ O_d \rightarrow Q_E}} \left[ \overline{E}^d(O_d) \sqrt{\rho_1^d} \right] = \overline{E}^i(Q_E) \cdot \overline{D}_e. \quad (8b)$$

where  $\overline{E}^i(Q_E)$  is the field of the ray incident at  $Q_E$  and  $\overline{D}_e$  is the dyadic edge diffraction coefficient. Incorporating

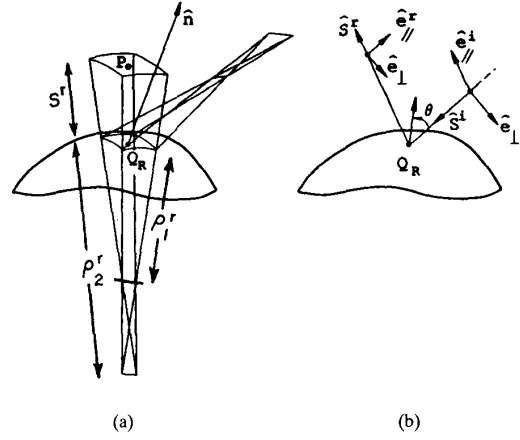


Fig. 8. Reflected wavefront curvatures and unit vectors associated with the reflection problem.

(8b) into (8a) with  $\rho_1^d \rightarrow \rho^d$  as  $O_d \rightarrow Q_E$  gives

$$\overline{E}^d(P) \sim \overline{E}^i(Q_E) \cdot \overline{D}_e \sqrt{\frac{1}{s^d} \cdot \frac{\rho^d}{\rho^d + s^d}} e^{-jks^d}. \quad (8c)$$

It is convenient to express the incident field  $\overline{E}^i(Q_E)$  and the diffracted field  $\overline{E}^d(P)$  in terms of unit vectors fixed in the incident and diffracted rays as shown in Fig. 9. The edge tangent  $\hat{e}$  at  $Q_E$  and the incident ray direction  $\hat{s}^i$  form the edge fixed plane of incidence. The unit vectors  $\hat{\beta}'_o$  and  $\hat{\phi}'$  are parallel and perpendicular, respectively, to the edge fixed plane of incidence. Likewise  $\hat{\beta}_o$  and  $\hat{\phi}$  are parallel and perpendicular, respectively, to the edge fixed plane of diffraction formed by  $\hat{e}$  and the diffracted ray direction  $\hat{s}^d$ . Furthermore,  $\hat{\beta}'_o = \hat{s}^i \times \hat{\phi}'$  and  $\hat{\beta}_o = \hat{s}^d \times \hat{\phi}$ . Thus  $\overline{E}^i = \hat{\beta}'_o (\hat{\beta}'_o \cdot \overline{E}^i) + \hat{\phi}' (\hat{\phi}' \cdot \overline{E}^i)$  and  $\overline{E}^d = \hat{\beta}_o (\hat{\beta}_o \cdot \overline{E}^d) + \hat{\phi} (\hat{\phi} \cdot \overline{E}^d)$ , so that  $\overline{D}_e$  is given by [2]:

$$\overline{D}_e = -\hat{\beta}'_o \hat{\beta}_o D_{es}(\phi, \phi'; \beta_o) - \hat{\phi}' \hat{\phi} D_{eh}(\phi, \phi'; \beta_o). \quad (9)$$

The scalar UTD edge diffraction coefficients  $D_{es}$  and  $D_{eh}$  contained in the dyadic UTD edge diffraction coefficient  $\overline{D}_e$  are obtained from a uniform asymptotic solution to the canonical problem of the diffraction of plane, cylindrical, conical and spherical incident waves by a perfectly conducting wedge [2] and they contain a sum of four simple terms, each of which is a product of a cotangent function (involving  $\phi$ ,  $\phi'$ , and  $\beta_o$ ) and a transition function  $F$  containing a Fresnel integral, where

$$F(x) = 2j\sqrt{x} e^{jx} \int_{\sqrt{x}}^{\infty} d\tau e^{-j\tau^2}. \quad (10)$$

The argument of the  $F$  functions depend on the incident, reflected and diffracted wavefront curvatures, and they are defined in [2]; the  $F$  function, which is well tabulated, is responsible for keeping the  $\overline{E}^d$  bounded at the GO shadow boundaries where GTD predicts a singularity. Outside the GO shadow boundary transition regions, the  $F$  function

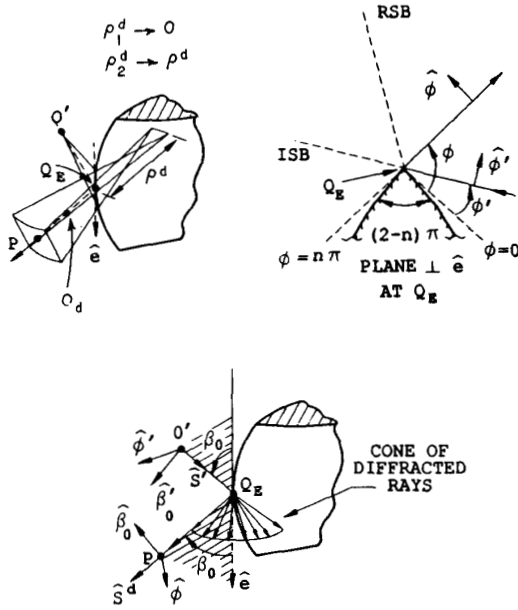


Fig. 9. Wedge diffraction geometry.

becomes unity and the UTD result then reduces automatically to GTD. In the two-dimensional case,  $\rho^d \rightarrow \infty$  in (8c) so that  $\bar{E}^d(P) = \bar{E}^i(Q_E) \cdot \bar{D}_e \sqrt{(1/s^d)} e^{-jks^d}$  for two-dimensional edge configurations. Some examples which can be analyzed using these UTD edge diffraction concepts are indicated below.

Consider the symmetric parabolic reflector antenna with a feed whose phase center is at the focus of the parabola as shown in Fig. 10. The UTD electric field at  $P_{01}$  in the near zone of this reflector as shown in Fig. 10 is then given by

$$\bar{E}(P_{01}) \sim \bar{E}^i(P_{01}) + \bar{E}_1^d(P_{01}) + \bar{E}_2^d(P_{01}) \quad (11)$$

where the field  $\bar{E}^i$  directly radiated by the feed to  $P_{01}$  has the form

$$\bar{E}^i(P_{01}) \sim c \bar{f}(\theta, \phi) \frac{e^{-jks^i}}{s^i} U_i \quad (12)$$

with

$$U_i = \begin{cases} 1, & \text{in region where the feed is directly visible,} \\ 0, & \text{behind the reflector (within } ISB_1 \text{ and } ISB_2 \text{)} \\ & \text{where the feed is shadowed.} \end{cases}$$

The quantity  $c$  in (12) is a known complex constant, and  $\bar{f}(\theta, \phi)$  is the vector radiation pattern of the feed with  $\theta$  measured with respect to the  $z$  axis while  $\phi$  is the azimuthal angle about this axis of symmetry of the paraboloidal reflector antenna; the quantity  $\bar{f}$  is also assumed to be known. The field in (12) constitutes a spherical wave from the feed. The fields  $\bar{E}_1^d$  and  $\bar{E}_2^d$  are diffracted from two distinct points on the edge of the reflector, where the plane containing  $P_{01}$  and the reflector axis intersects the edge at  $Q_1$  and  $Q_2$  in accordance with the extended Fermat's

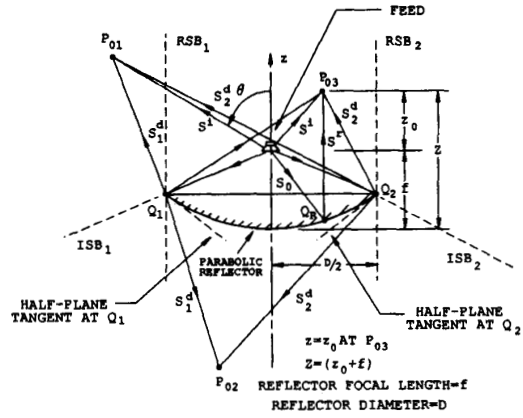


Fig. 10. Rays contributing to the near field of a symmetric parabolic reflector antenna.

principle; these will be described in (16). Next, the field  $\bar{E}(P_{02})$  at  $P_{02}$  also in the near zone behind the reflector is:

$$\bar{E}(P_{02}) \sim \bar{E}_1^d(P_{02}) + \bar{E}_2^d(P_{02}) \quad (13)$$

Likewise, the field  $\bar{E}(P_{03})$  at  $P_{03}$  in the near zone becomes

$$\bar{E}(P_{03}) \sim \bar{E}^i(P_{03}) + \bar{E}^r(P_{03}) + \bar{E}_1^d(P_{03}) + \bar{E}_2^d(P_{03}) \quad (14)$$

in which  $\bar{E}^r$  is the field at  $P_{03}$  that is reflected from  $Q_R$  as in Fig. 10; it is given via (5c) by

$$\bar{E}^r(P_{03}) \sim \bar{E}^i(Q_R) \cdot \bar{R} \sqrt{\frac{\rho_1^d \rho_2^d}{(\rho_1^d + s^r)(\rho_2^d + s^r)}} e^{-jks^r} U_r \quad (15)$$

with,

$$U_r = \begin{cases} 1, & \text{within the region containing the } z\text{-axis} \\ & \text{and bounded by } RSB_1 \text{ and } RSB_2 \\ 0, & \text{otherwise.} \end{cases}$$

Also,  $\bar{E}^i(Q_R) \sim c \bar{f}(\theta_o, \phi_o) (e^{-jks_o}/s_o)$  in (15) where  $(\theta_o, \phi_o)$  are the values of  $(\theta, \phi)$  along the direction  $\hat{s}_o = (\overline{OQ_R})/(|\overline{OQ_R}|)$ . Finally, the two edge diffracted ray fields  $\bar{E}_1^d$  and  $\bar{E}_2^d$  in (11), (13), and (14) have the general form:

$$\begin{aligned} \bar{E}_j^d(P_o) \sim & \left[ \bar{E}^i(Q_j) \cdot \bar{D}_e(Q_j) + \frac{\partial \bar{E}^i}{\partial n_j^i} \right]_{Q_j} \\ & \cdot \left[ \bar{d}_e^i(Q_j) + \frac{\partial \bar{E}^r}{\partial n_j^r} \right]_{Q_j} \cdot \bar{d}_e^r(Q_j) \\ & \cdot \sqrt{\frac{\rho_j^d}{s_j^d(\rho_j^d + s_j^d)}} e^{-jks_j^d} \end{aligned} \quad (16)$$

with  $j = 1, 2$  corresponding to  $Q_1$  and  $Q_2$ . While the term involving  $\bar{E}^i(Q_E) \cdot \bar{D}_e$  in (16) has been introduced in the discussion on the UTD for edge diffraction leading to (8c), the term containing  $\bar{d}_e^{i,r}$  in (16) is an additional contribution to the UTD edge diffracted field, and it is termed as the slope diffraction contribution [3], [4]. The

slope diffraction contribution becomes important if the incident field  $\bar{E}^i$  and/or the reflected field  $\bar{E}^r$  exhibits a rapid spatial variation near the point of diffraction  $Q_E$  on the edge. For example, if the field  $\bar{E}^i$  vanishes at the point of diffraction  $Q_E$ , then the field diffracted from  $Q_E$  calculated via  $\bar{E}^i(Q_E) \cdot \bar{D}_e$  would also vanish; however, if  $\bar{E}^i(Q_E)$  tends to vanish rapidly at  $Q_E$  so that its spatial derivative symbolized here by  $\partial \bar{E}^i / \partial n^i$  may be significant, then it could give rise to the slope edge diffraction contribution which must therefore be included for accuracy. In the present application, if the feed pattern  $\bar{f}(\theta, \phi)$  is rapidly varying at the edges  $Q_{1,2}$  then the slope diffraction term in (20) will be important; otherwise, the slope effects are generally negligible. The results in (11)–(16) have been employed in [21] to obtain the near field radiation from a parabolic reflector antenna in the plane  $Z = z_o + f$  in Fig. 11. However, the results in (11) and (13) can also be used in the far zone of the reflector outside the paraxial region. The numerical results in Fig. 11 based on the UTD as obtained in [21] are compared with those based on GO ( $\bar{E}^i + \bar{E}^r \approx \bar{E}^r$  in the forward direction since  $|\bar{E}^i| \ll |\bar{E}^r|$  for the feed employed in this example), and with the commonly used but far less efficient aperture integration (AI) technique. It is noted that the GO reflected field  $\bar{E}^r$  is discontinuous in Fig. 11 as required by  $U_r$  in (15). Also, the agreement between UTD and the reference solution based on AI is quite good in that figure. Finally, it is noted that, for a small range of angles near the plane of the reflector, one of the edges is always shadowed by the reflector geometry, and this shadow zone is filled by surface rays which are excited on the back (convex) side of the reflector surface via edge diffraction, and these rays then shed energy tangentially as surface diffracted rays. A whispering gallery type field can also be excited on the concave front side of the reflector via edge diffraction. Such edge excited surface diffracted rays [22]–[25], and the diffraction of whispering gallery fields [26] occur in a small angular region and may generally be neglected to first order without incurring serious errors.

4) *UTD Corner (Vertex) Diffracted Field:* Corners or vertices can occur if an edge is truncated, e.g., as in the case of a plane angular sector, or a finite plate structure for which the edge tangent is discontinuous (to form the corner), or as in the case of a pyramidal structure with planar facets whose edges converge to a point; these specific examples are illustrated in Figs. 12(a) and (b). In addition, corners or tips can also occur in a smooth conical geometry, as shown in Fig. 12(c). When a corner in an impenetrable surface is illuminated by a source, then the incident ray is diffracted in all radial directions from the corner as shown in Fig. 12. The UTD field of these corner diffracted rays illustrated in Fig. 12(a) and (b) keeps the total high-frequency field bounded and continuous across the corner induced shadow boundaries of rays diffracted by the edges, just as the UTD edge diffracted fields keep the total high-frequency field bounded and continuous across the edge induced shadow boundaries of the GO incident and reflected

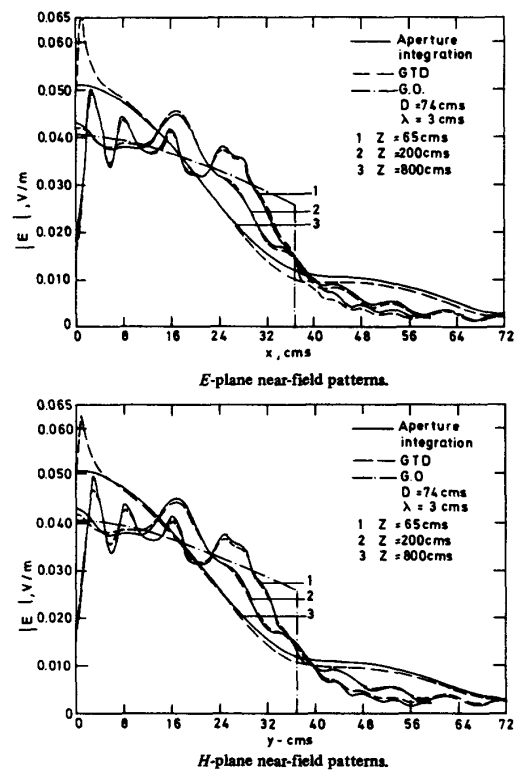


Fig. 11. Near field radiation patterns of a parabolic reflector antenna (from [21]).

rays. The corner induced shadow boundaries of the edge diffracted rays of course occur because such rays cease to exist whenever the edges terminate (at the corner). The general UTD form of the corner diffracted field is given by

$$\bar{E}_c^d(P) \sim \bar{E}^i(Q_C) \cdot \bar{D}_c \frac{e^{-jks_c^d}}{s_c^d} \quad (17)$$

$$\bar{H}_c^d(P) = Y_o \hat{s}_c^d \times \bar{E}_c^d(P). \quad (18)$$

Recently, an approximate but useful UTD result for  $\bar{D}_c$  has been obtained for the case of the diffraction by a corner in a perfectly conducting plane angular sector as shown in Fig. 12(a). The UTD transition function present in  $\bar{D}_c$ , which compensates for the corner induced discontinuity in the edge diffracted fields may be viewed as an integral of a Fresnel integral that can be calculated quite efficiently. The present more rigorously obtained UTD corner diffraction coefficient in [27], [28] constitutes an improvement over a previous one which was constructed heuristically [29]. Figure 13 indicates the far zone radiation pattern of a dipole antenna located near a perfectly conducting rectangular plate, which has been calculated via the new  $\bar{D}_c$  in [27], [28]; this pattern is seen to compare very well with an independent moment method (MM) solution of an integral equation for the problem.

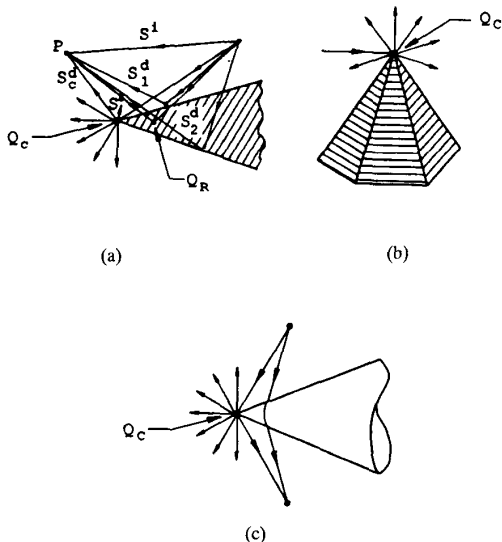


Fig. 12. Examples of corner diffracted rays.

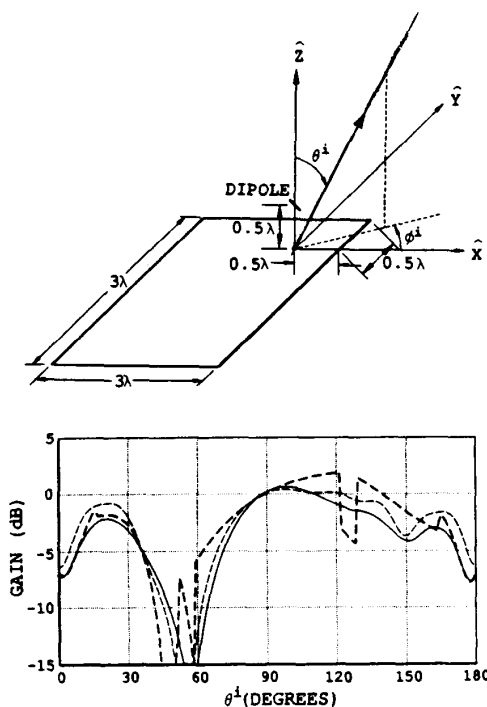


Fig. 13. Radiation pattern of a dipole near a perfectly conducting rectangular plate. (— UTD; - - - MM; · · · UTD without corner diffraction term). Note:  $\phi^i = 47.5^\circ$ .

For the case in Fig. 12(c), there are no edge diffracted rays because the cone geometry is smooth (except at the tip) and contains no edges; however, there are surface diffracted rays that are launched from the smooth portion of the conical surface. The nature of the surface diffracted rays changes rapidly as the surface rays on the cone approach the cone tip because of the rapid decrease in the surface

radius of curvature (except along the cone generator) as the tip is approached. The UTD cone tip diffracted field must then contain information on this change in the nature of the surface ray field near the tip; such a general UTD solution has not yet been developed although some initial attempts have been made [30]. On the other hand, an approximate UTD-type diffraction coefficient based on the PO approximation has been developed for the problem of EM plane wave diffraction by a fully illuminated semi-infinite perfectly conducting cone [31], as illustrated in Fig. 14(a); thus, the incident angle  $\theta$  measured from the axial direction must remain less than the half cone angle  $\theta_c$  (see Fig. 14(a)). This plane wave diffraction solution also provides the tip diffracted ray field which propagates along the generator of the cone to any point  $Q$  on the surface. Let an electric current point source  $\hat{p}_t \delta(\bar{r} - \bar{r}_p)$  at a distant point  $P$  produce this locally plane wave set of fields  $(\bar{E}_t^i, \bar{H}_t^i)$  which are incident at  $Q_C$  and  $Q$ . For convenience,  $\hat{p}_t$  is directed perpendicular to the ray (or local plane wave) incident at an angle  $\theta$ ; i.e.,  $\hat{p}_t = \hat{\theta}$  or  $\hat{p}_t = \hat{\phi}$ , where  $\hat{\theta}$  is shown in Fig. 14(a). Also, let  $\hat{p}_t$  produce the total field  $(\bar{E}_t, \bar{H}_t)$  at  $Q$ , where in the UTD sense,

$$\bar{E}_t(Q) = \bar{E}_t^i(Q) + \bar{E}_t^r(Q) + \bar{E}_t^d(Q) \quad (19)$$

$$\bar{H}_t(Q) = \bar{H}_t^i(Q) + \bar{H}_t^r(Q) + \bar{H}_t^d(Q) \quad (20)$$

with  $(\bar{E}_t^d, \bar{H}_t^d)$  representing the cone tip diffracted fields as given in [31]. The  $(\bar{E}_t(Q), \bar{H}_t(Q))$  at  $Q$  also directly provides, via the reciprocity theorem, a knowledge of the fields  $(\bar{E}(P); \bar{H}(P))$  radiated to the far-zone point  $P$  by a point current source  $\hat{p} \delta(\bar{r} - \bar{r}_Q)$  at  $Q$  as in Fig. 14(b); thus,

$$\hat{p} \cdot \bar{E}(P) = \begin{cases} \hat{j} \cdot \bar{E}_t(Q), & \text{if } \hat{p} = \hat{j} \text{ where } \hat{j} \text{ is the} \\ & \text{strength of an electric} \\ & \text{current point source at } Q \\ -\hat{m} \cdot \bar{H}_t(Q), & \text{if } \hat{p} = \hat{m} \text{ where } \hat{m} \text{ is the} \\ & \text{strength of a magnetic} \\ & \text{current point source at } Q. \end{cases} \quad (21)$$

Generally, the contribution from the cone tip diffraction to the far field radiation by antennas on cones becomes negligible outside the paraxial region; this point will be clarified later when dealing with radiation from antennas on a smooth convex surface.

5) *UTD Ray Fields Associated with the Diffraction by Smooth Convex Surfaces*: UTD solutions for the problems of diffraction by smooth, perfectly conducting convex surfaces are useful, for example, for predicting the EM scattering from aircraft fuselage shapes or ship masts when they are illuminated by airborne or shipboard antennas, respectively, and also for predicting the EM radiation and mutual coupling associated with antennas placed conformally on smooth convex portions of an aircraft, missile or spacecraft, etc. Three separate cases are considered below.

a) *Source and observation points off the smooth convex surface*: The UTD solution for the case when the source (antenna) and observation points are both off the convex surface is obtained from a uniform asymptotic solution to

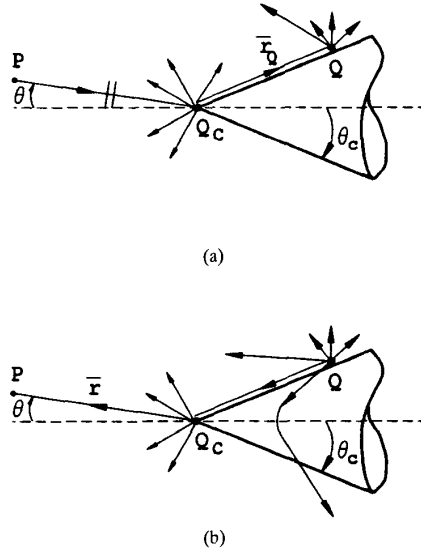


Fig. 14. Cone tip diffraction within the paraxial region ( $\theta < \theta_c$ ).

the problem of EM scattering by a circular conducting cylinder [32], and it is given separately for the lit and the shadow regions. The field at  $P_L$  in the lit region is associated with the incident and reflected ray paths as shown in Fig. 15(b) and it is given by

$$\bar{E}(P_L) \sim \bar{E}^i(P_L)U + \bar{E}^{gr}(P_L)U \quad (22)$$

where  $\bar{E}^i$  is the GO incident field and  $\bar{E}^{gr}$  is the generalized reflected field which contains surface diffraction effects (in addition to the GO reflected field  $\bar{E}^r U$ ). The latter effects become significant only within the transition region near the SSB shown in Fig. 3. The step function  $U$  in (22) serves as an SSB indicator:

$$U = \begin{cases} 1, & \text{in the lit region which lies above the SSB} \\ 0, & \text{in the shadow region which lies below the SSB} \end{cases} \quad (23)$$

The extent of the transition region around the SSB is of order  $1/(m(Q_1))$ , where

$$m(\bullet) = \left[ \frac{k\rho_g(\bullet)}{2} \right]^{1/3} \quad (24)$$

and  $\rho_g(\bullet)$  is the radius of curvature at any point ( $\bullet$ ) along the surface ray. The field  $\bar{E}^{gr}$  is expressed as [32], [33]:

$$\bar{E}^{gr}(P_L) \sim \bar{E}^i(Q_R) \cdot \bar{\mathcal{R}} \sqrt{\frac{\rho_1^r}{\rho_1^r + s^r} \frac{\rho_2^r}{\rho_2^r + s^r}} e^{-jk_s r} \quad (25)$$

with

$$\bar{\mathcal{R}} = \mathcal{R}_s \hat{e}_\perp \hat{e}_\perp + \mathcal{R}_h \hat{e}_\parallel^i \hat{e}_\parallel^r \quad (26)$$

The unit vectors contained in (26), and the quantities  $\rho_{1,2}^r$  and  $s^r$  are the same as those given previously in (5c). The UTD functions  $\mathcal{R}_s$  and  $\mathcal{R}_h$  in (26) are defined in [32], [33] and they contain two transition functions, namely the  $F$  function introduced in (10) as well as the Pekeris

function  $\tilde{P}_{s,h}(\xi_l)$  which is well tabulated [34], in which  $\xi^l = -2m(Q_R) \cos \theta$ . Here  $\theta$  represents the incident angle defined in Fig. 8, and  $m(Q_R)$  contains  $\rho_g(Q_R)$  which is the surface radius of curvature in the plane of incidence at  $Q_R$ . It is noted that  $\tilde{P}_{s,h}$  contains an integral of the Airy functions [32], namely:

$$\tilde{P}_s(\delta) = \frac{e^{-j\pi/4}}{\sqrt{\pi}} \int_{-\infty}^{\infty} \frac{V(\tau)}{W_2(\tau)} e^{-j\delta\tau} d\tau \quad (27a)$$

$$\tilde{P}_h(\delta) = \frac{e^{-j\pi/4}}{\sqrt{\pi}} \int_{-\infty}^{\infty} \frac{V'(\tau)}{W_2'(\tau)} e^{-j\delta\tau} d\tau \quad (27b)$$

where

$$2jV(\tau) = W_1(\tau) - W_2(\tau) \quad (28a)$$

$$W_2(\tau) = \frac{1}{\sqrt{\pi}} \int_{-\infty}^{\infty} \frac{e^{\tau t - t^3/3}}{e^{\tau + j2\pi/3}} dt. \quad (28b)$$

Next, the field at  $P_S$  in the shadow region is given by [32], [33]

$$\bar{E}(P_S) \sim \bar{E}^d(P_S)[1 - U] \quad (29)$$

where

$$\bar{E}^d(P_S) \sim \bar{E}^i(Q_1) \cdot \bar{T}(Q_1, Q_2) \sqrt{\frac{\rho^d}{s^d(\rho^d + s^d)}} e^{-jks^d} \quad (30)$$

with one of the diffracted ray wavefront surface radii of curvatures,  $\rho^d$ , shown in Fig. 15; likewise, the diffracted ray distance  $s^d$  from  $Q_2$  to  $P_S$  is also shown in that figure. The dyadic transfer coefficient  $\bar{T}$  is given as [32], [33]:

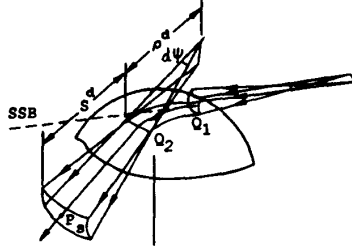
$$\bar{T}(Q_1, Q_2) = [\hat{b}_1 \hat{b}_2 \mathcal{D}_s + \hat{n}_1 \hat{n}_2 \mathcal{D}_h] \cdot \sqrt{\frac{d\eta(Q_1)}{d\eta(Q_2)}} e^{-jkt} \quad (31)$$

in which  $d\eta(\bullet)$  is the width of the surface ray tube (or strip) at any point ( $\bullet$ ) along the surface ray path, and  $t$  equals the arc length of the surface ray path from  $Q_1$  to  $Q_2$ . It is noted that the surface rays constitute geodesic paths on the convex surface. It is seen from (31) that  $\bar{T}$  is expressed compactly in terms of orthogonal unit vectors ( $\hat{t}, \hat{n}, \hat{b}$ ) fixed in the surface ray with  $\hat{t}$  being a unit tangent to the surface ray and  $\hat{n}$  is a unit normal to the surface along the surface ray, while  $\hat{b}$  is the binormal vector ( $\hat{b} = \hat{t} \times \hat{n}$ ). Again,  $\mathcal{D}_s$  and  $\mathcal{D}_h$  both contain  $F$  as in (10) as well as  $\tilde{P}_{s,h}(\xi)$ . The quantity  $\xi$  is sometimes referred to as the shadow Fock parameter given by

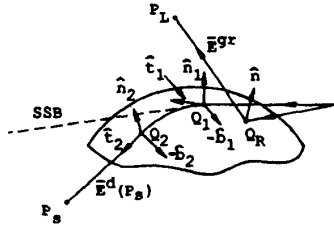
$$\xi = \int_{Q_1}^{Q_2} \frac{m(t')}{\rho_g(t')} dt'. \quad (32)$$

The parameters  $\xi^l$ ,  $\xi$ ,  $X^l$  and  $X^d$  present in (26) and (31), which are defined elsewhere in detail [32], [33], ensure that the total UTD field is continuous across the SSB; i.e.,  $\bar{E}(P_L)$  in (22) and  $\bar{E}(P_S)$  in (29) are equal at the SSB.

It is noted that in the lit zone outside the SSB transition region,  $\bar{E}^{gr} \rightarrow \bar{E}^r$  which is the usual GO reflected field (i.e.  $\bar{\mathcal{R}} \rightarrow \bar{\mathcal{R}}$  as in (5)). Likewise, in the shadow zone outside the



(a)



(b)

Fig. 15. Ray paths for scattering by a smooth convex surface.

SSB transition region,  $D_{s,h} \rightarrow T_{s,h}$ , where  $T_{s,h}$  is defined as

$$T_{s,h} \equiv \left[ \sum_{n=1}^N D_n^{s,h}(Q_1) \cdot \exp\left(-\int_{Q_1}^{Q_2} \alpha_n^{s,h}(t') dt'\right) D_n^{s,h}(Q_2) \right] \quad (33)$$

in which  $D_n^{s,h}(Q)$  is the Keller's (or GTD type) diffraction coefficient for the  $n$ th surface ray mode which indicates how the surface modes are launched at  $Q_1$  by the incident ray which grazes the surface [35]; by reciprocity,  $D_n^{s,h}$  at  $Q_2$  indicates how the surface ray modes detach from the surface into the external medium. Similarly,  $\alpha_n^{s,h}$  indicates the rate of attenuation of the surface ray modes [35] due to the continual tangential shedding of energy along the surface ray. Thus the UTD result automatically recovers the GTD result outside the SSB transition layer.

b) *Radiation by sources on a smooth convex surface:* Consider the radiation by a slot or a short thin wire antenna on a smooth, perfectly conducting surface. A UTD analysis of the radiation from these antennas can be constructed in terms of a uniformly asymptotic high-frequency approximation to the dyadic Green's function,  $\bar{\Gamma}_{i,m}$ , which provides the radiation from a point electric ( $i$ ) or magnetic ( $m$ ) current source  $\bar{p}\delta(\bar{r} - \bar{r}_{Q'})$  at  $Q'$  on the convex boundary.

$$\hat{p} = \begin{cases} \hat{i} & \text{for an electric point current source at } Q' \\ \hat{m} & \text{for a magnetic point current source at } Q' \end{cases} \quad (34)$$

The electric field  $\bar{E}(P)$  radiated by  $\hat{p}$  at  $Q'$  can then be expressed as

$$\bar{E}(P) = \begin{cases} \bar{\Gamma}_i(P|Q') \cdot \hat{p}, & \text{if } \hat{p} = \hat{i} \\ \bar{\Gamma}_m(P|Q') \cdot \hat{p}, & \text{if } \hat{p} = \hat{m} \end{cases} \quad (35)$$

in which  $\bar{\Gamma}_{i,m}$  is obtained from uniform asymptotic solutions to problems of radiation by  $\hat{p}$  on conducting cylinders and spheres [36].

$$\bar{\Gamma}_m \sim \begin{cases} (-jk/4\pi) (\hat{b}'\hat{n}A + \hat{t}'\hat{b}B + \hat{b}'\hat{b}C + \hat{t}'\hat{n}D) (e^{-jks}/s), & \text{for } P = P_L \\ (-jk/4\pi) (\hat{b}'\hat{n}T_1H + \hat{t}'\hat{b}T_2S + \hat{b}'\hat{b}T_3S + \hat{t}'\hat{n}T_4H) \\ \cdot e^{-jkt} \sqrt{(d\psi_o/d\eta(Q))} [\rho_g(Q)/\rho_g(Q')]^{1/6} \\ \cdot \sqrt{\rho^d/(s^d(\rho^d + s^d))} \exp(-jks^d), & \text{for } P = P_S \end{cases} \quad (36)$$

and

$$\bar{\Gamma}_i \sim \begin{cases} (-jkZ_o/4\pi) (\hat{n}'\hat{n}M + \hat{n}'\hat{b}N) (e^{-jks}/s), & \text{for } P = P_L \\ (-jkZ_o/4\pi) (\hat{n}'\hat{n}T_5H + \hat{n}'\hat{b}T_6S) \\ \cdot e^{-jkt} \sqrt{(d\psi_o/d\eta(Q))} [\rho_g(Q)/\rho_g(Q')]^{1/6} \\ \cdot \sqrt{\rho^d/(s^d(\rho^d + s^d))} \exp(-jks^d), & \text{for } P = P_S. \end{cases} \quad (37)$$

The field point  $P = P_L$  in the lit region (where the source at  $Q'$  is directly visible), and  $P = P_S$  in the shadow region. Although the fields in (36) and (37) are given separately for  $P = P_L$  and  $P = P_S$ , respectively, they join smoothly at the shadow boundary SSB which is defined by a plane tangent to the surface at  $Q'$ . The quantities  $\rho^d$  and  $s^d$  are shown in Fig. 15; also,  $d\eta(Q)$  is the width of the surface ray strip at  $Q$ . The  $d\eta$  was defined earlier in (31); furthermore,  $d\psi_o$  and  $d\psi$  are the angles subtended by the surface ray strip at  $Q'$  and at  $Q$ , respectively (e.g.,  $d\psi$  is shown in Fig. 15) [36]. The unit vectors  $(\hat{t}', \hat{b}', \hat{n}')$  at  $Q'$  and  $(\hat{t}, \hat{n}, \hat{b})$  at  $Q$  are fixed in the surface ray from  $Q'$  to  $Q$  as in Fig. 16, and they have the same meaning as in Fig. 15. Similarly, the unit vectors  $(\hat{t}'_l, \hat{n}_l, \hat{b}'_l)$  are fixed in the ray from  $Q'$  to  $P_L$  such that  $\hat{t}'_l, \hat{n}_l, \hat{t}'$  and  $\hat{n}'$  all lie in the plane of incidence (defined by  $\hat{s} = (\overline{Q'P_L})/|\overline{Q'P_L}|$ ) and  $\hat{n} \cdot \hat{s} = 0 = \hat{b}'_l \cdot \hat{s}$  as shown in Fig. 16. The usual angle of incidence  $\theta = \cos^{-1}(\hat{n}' \cdot \hat{s})$  defines the radiation angle measured from the  $\hat{n}'$  direction.

The quantities  $A, B, C, D, M$  and  $N$  in (36) and (37) for  $P = P_L$ , and the quantities  $T_1$  through  $T_6$  in those equations for  $P = P_S$  are all defined in [36]; they contain the special UTD transition functions  $g(\bullet)$  and  $\tilde{g}(\bullet)$  corresponding to the well tabulated radiation Fock functions [34], [36] that are expressed in terms of an integral of Airy functions.

$$g(\delta) = \frac{1}{\sqrt{\pi}} \int_{-\infty}^{\infty} d\tau e^{-j\delta\tau} [W_2'(\tau)]^{-1} \quad (38a)$$

$$\tilde{g}(\delta) = \frac{1}{\sqrt{\pi}} \int_{-\infty}^{\infty} d\tau e^{-j\delta\tau} [W_2(\tau)]^{-1}. \quad (38b)$$

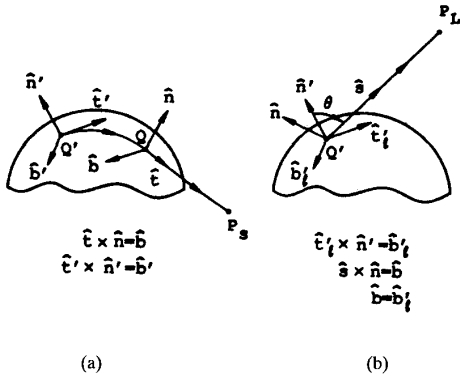


Fig. 16. Unit vectors fixed in rays to  $P_L$  and  $P_S$  from a source on a convex surface.

The argument  $\delta$  of the Fock functions is given by  $\xi_l = -m(Q') \cos \theta$  for  $P = P_L$ , while it is given by the shadow Fock parameter  $\xi = \int_{Q'}^Q (m(t')/\rho_g(t')) dt'$  when  $P = P_S$  as defined previously in (32).

Outside the SSB transition region, where  $\xi_l \ll 0$  and  $\xi \gg 0$  the UTD results in (36) and (37) automatically reduce to the GTD form; namely,  $A \rightarrow 2$ ,  $B \rightarrow 2 \cos \theta$ ,  $M \rightarrow 2 \sin \theta$  and  $(C, D, N) \rightarrow 0$  in (36) and (37) for  $P = P_L$  and  $\xi_l \ll 0$ , and similarly, the results for  $P = P_S$  and for  $\xi \gg 0$  reduce to terms involving

$$\sum_{n=1}^N L_n^{s,h}(Q') \exp\left(-\int_{Q'}^Q \alpha_n^{s,h}(t') dt'\right) D_n^{s,h}(Q).$$

In the latter sum, the  $L_n^{s,h}(Q')$  (which is proportional to  $D_n^{s,h}(Q')$ ) is the launching coefficient at  $Q'$  of the  $n$ th surface ray mode, and  $D_n^{s,h}(Q)$  is the  $n$ th surface ray mode diffraction coefficient introduced earlier in (33). Within the SSB transition region, the GTD launching and diffraction mechanisms are no longer distinct; indeed, such a coupling between the launching and diffraction effects within the transition region is naturally contained in the UTD results of (36) and (37) due to the presence of  $g(\delta)$  and  $\tilde{g}(\delta)$  in those equations.

The geodesic surface ray path from  $Q'$  to  $Q$  may be torsional. A torsional path, is one for which  $\hat{b} \neq \hat{b}'$ ; i.e., a torsional path is a nonplanar curve. It is noted that the geodesic surface ray paths are helices on convex cylinders, and they are great circles on spheres; they can be found easily for developable surfaces, but they must be found numerically for more general surfaces such as spheroids, etc. [36]. Furthermore, for closed surfaces, rays that creep around or encircle such surfaces can also diffract (shed) tangentially into the lit region. Generally, for electrically large closed surfaces the contribution from such encircling rays is weak because of the continuous tangential shedding of energy along such rays.

The result in (35) can be readily generalized to deal with the radiation from a slot antenna on a convex surface [36]; thus, the field radiated by a slot antenna becomes (via a

direct generalization of (21) with  $\hat{p} = \hat{m}$ ):

$$\bar{E}(P) = \int \int_{S_a} \bar{\Gamma}_m(P|Q') \cdot [\bar{M}_S(Q')] ds' \quad (39)$$

where  $\bar{M}_S(Q') = \bar{E}_a(Q') \times \hat{n}'$  is the equivalent magnetic current in terms of the transmitting electric field  $\bar{E}_a(Q')$  in the slot aperture of area  $S_a$ ; this  $\bar{M}_S$  replaces the aperture  $S_a$  which is now short circuited. Likewise, the radiation from a short thin monopole of height  $h$  and transmitting current  $I(l')$  fed at the base  $Q'$  on a convex surface can be found as [36]:

$$\bar{E}(P) \approx \begin{cases} \bar{\Gamma}_i(P|Q') \cdot \hat{n}' \int_0^h I(l') \cdot \cos(kl' \cos \theta) dl', & \text{if } P = P_L \\ \bar{\Gamma}_i(P|Q') \cdot \hat{n}' \int_0^h I(l') dl', & \text{if } P = P_S. \end{cases} \quad (40)$$

Figure 17(a) indicates the far zone radiation pattern of a short, thin monopole antenna on a spheroid, which is calculated in the SSB plane (i.e. in the plane tangent to the spheroid at the base of the monopole) via UTD, and is shown to compare very well with measurements. Besides the constant  $|\bar{E}_\theta|$  pattern which is the only component that would exist in the SSB plane for a monopole on a sphere, or on a finite or infinite flat ground plane, there is an additional (cross-polarized)  $|\bar{E}_\phi|$  component of the pattern that is present for the spheroid because it has two different principal surface curvatures  $K_1$  and  $K_2$ ; i.e.,  $\bar{E}_\phi$  in the SSB plane of the spheroid results from the “launching” of torsional surface rays by the monopole since torsion is proportional to  $|K_1 - K_2|$ . The present UTD solution thus predicts the complex, surface dependent field and polarization effects in the SSB transition region through the explicit presence of torsion factors and the radiation Fock functions in (36) and (37). It is noted that, even though Fock functions are utilized here, Fock’s original work did not contain effects of torsional surface rays. The far zone UTD radiation pattern of a radial slot on a semi-infinite cone is seen to compare very well with an exact modal (eigenfunction) solution in Fig. 17(b). The effect of the tip is ignored in Fig. 17(b); however, as pointed out earlier, this effect is generally negligible outside the paraxial region.

c) *Mutual coupling between antennas on a convex surface:* The UTD expressions for the EM fields  $(\bar{E}(Q), \bar{H}(Q))$  at  $Q$  on a convex surface that are produced by a slot antenna, or a short and thin monopole antenna on the same surface, respectively, are given in detail in [37]; those analytical expressions have been obtained from the high-frequency solutions to the same canonical problems as for the radiation problem in part (b) above, and are presented only symbolically in (41) and (42), shown on the next page. Expressions alternative to those in [34] for the slot case are presented in [38].

The UTD expressions for  $\bar{\Gamma}_{ee,eh,he,hh}$  which occur in (41) and (42) contain special transition functions  $\bar{U}(\xi)$  and  $\bar{V}(\xi)$  [37], [38]; these transition functions are expressed in terms of an integral containing a ratio of Airy functions, and they keep the above solutions valid in their SSB transition

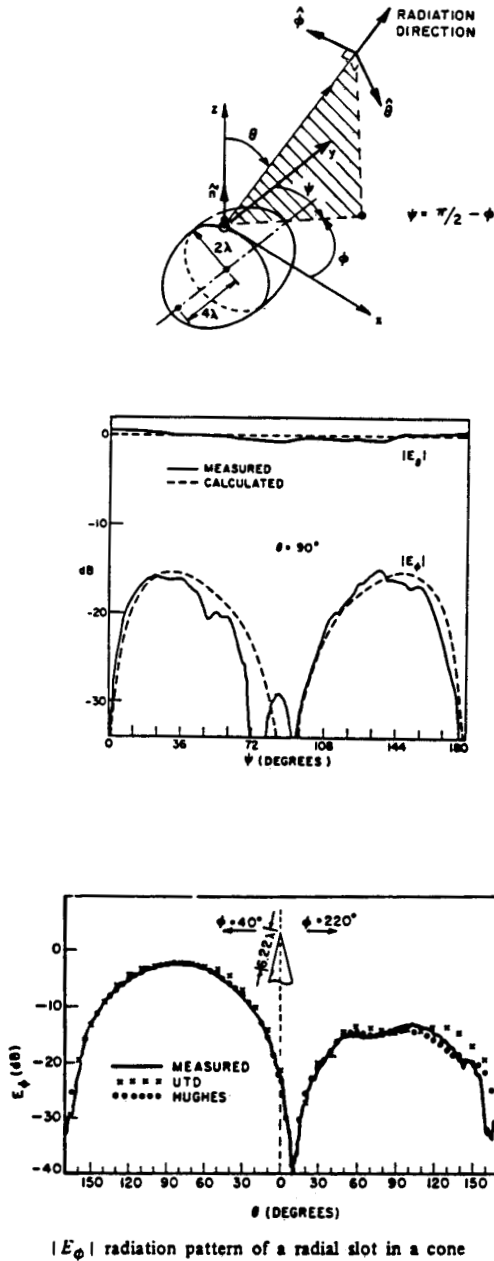


Fig. 17. Radiation patterns of antennas on perfectly conducting spheroids and cones (cone half angle = 10°).

$$\left\{ \begin{array}{l} \bar{E}(Q) \\ \bar{H}(Q) \end{array} \right\} \sim \left\{ \begin{array}{l} \bar{\Gamma}_{ee}(Q|Q') \\ \bar{\Gamma}_{he}(Q|Q') \end{array} \right\} \cdot \hat{n}' \int_0^h I(l') dl', \quad \text{for a monopole antenna as in (40)} \quad (41)$$

and

$$\left\{ \begin{array}{l} \bar{E}(Q) \\ \bar{H}(Q) \end{array} \right\} \sim \iint_{S_a} \left\{ \begin{array}{l} \bar{\Gamma}_{eh}(Q|Q') \\ \bar{\Gamma}_{hh}(Q|Q') \end{array} \right\} \cdot [\bar{E}_a(Q') \times \hat{n}'] ds', \quad \text{for a slot antenna as in (39)} \quad (42)$$

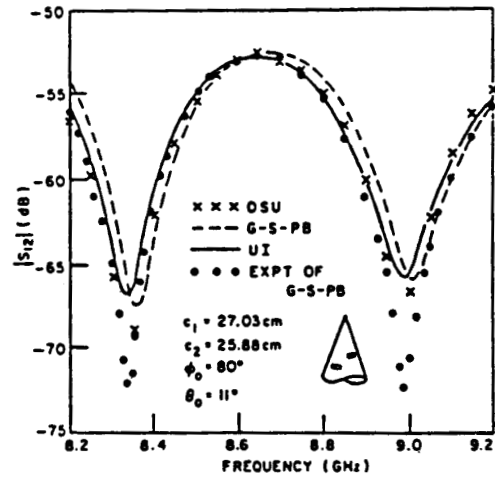


Fig. 18. Mutual coupling between a pair of slots on a perfectly conducting cone.

region on the surface.

$$\begin{aligned} \tilde{U}(\xi) &= \left[ \frac{kt}{2m(Q')m(Q)\xi} \right]^{3/2} \cdot \frac{\xi^{3/2} e^{j(3\pi/4)}}{2\sqrt{\pi}} \\ &\quad \cdot \int_{-\infty}^{\infty} d\tau e^{-j\xi\tau} \frac{W_2'(\tau)}{W_2(\tau)} \quad (43) \\ \tilde{V}(\xi) &= \left[ \frac{kt}{2m(Q')m(Q)\xi} \right]^{1/2} \\ &\quad \cdot \frac{\xi^{1/2} e^{j\pi/4}}{2\sqrt{\pi}} \int_{-\infty}^{\infty} d\tau e^{-j\xi\tau} \frac{W_2(\tau)}{W_2'(\tau)}. \quad (44) \end{aligned}$$

Expressions for the mutual coupling between a pair of antennas on a convex surface can be found using (43) and (44) as described in [37], [38]. Figure 18 indicates the mutual coupling between a pair of slot antennas on a cone calculated via UTD [37]; it is seen to compare very well with an exact eigenfunction solution. The pattern in Fig. 18 results from the interference between the dominant surface rays and the tip diffracted ray. The tip diffracted ray field is calculated as described in [38].

The UTD edge and convex surface diffraction solutions discussed above are employed to predict the radiation patterns of a TACAN monopole antenna mounted behind the canopy on the top side of an F-16 aircraft fuselage; the

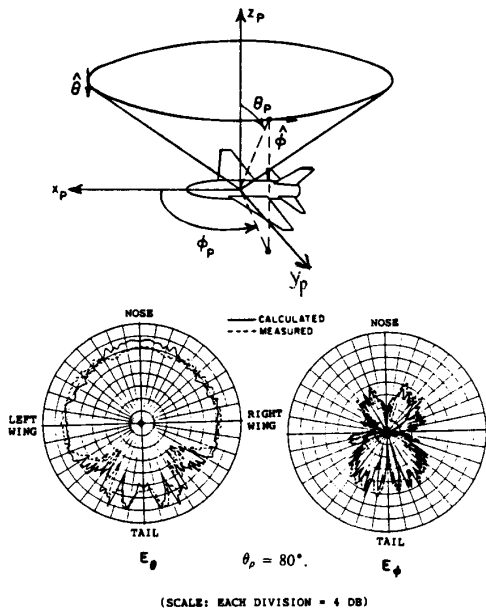


Fig. 19. Radiation pattern of monopole antenna on an F-16 fighter aircraft (see [39]).

results are shown in Fig. 19 [39]. The UTD model of the F-16 is built up from connecting spheroidal and flat plate surfaces. The excellent comparison of these UTD results with measurements is also shown in that figure.

An application of the UTD solution for radiation and mutual coupling associated with antennas on a convex surface is shown in Fig. 20 for predicting the radiation from a  $9 \times 9$  element dominant mode rectangular waveguide-fed axial slot antenna phased array in a perfectly conducting cylinder; this array exhibits a cosine tapered distribution along both the axial and circumferential directions. The cosine taper is realized incorporating the effects of mutual coupling. Figure 20 shows the radiation pattern of this array when it is phased to radiate in the  $\theta = 45^\circ$ ,  $\phi = 45^\circ$  direction [40].

6) *Uniform Analysis of Reflection within Caustic Regions:* Figure 6 illustrates a concave-convex surface of revolution which contains an inflection point along its generator; such a surface can occur in the design of shaped subreflectors in dual reflector antenna systems. The feed, which is a source of a spherical wave, illuminates the subreflector which is assumed to be in the far zone of the feed. The rays reflected from the subreflector form a smooth caustic surface of revolution. It is usually of interest to find the fields scattered by the subreflector which then illuminate the main reflector.

One can employ GO to find the rays reflected from the subreflector as shown in Fig. 6. On the lit side of the caustic there are two real GO reflected rays that contribute to the field at  $P_L$ . However, conventional GO fails to predict a field at  $P_S$  on the shadow side of the caustic where no real

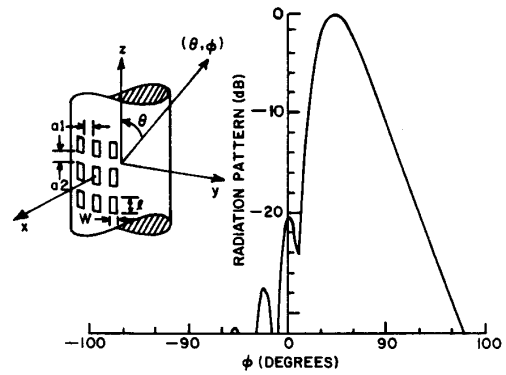


Fig. 20. Radiation from a  $9 \times 9$  axial slot phased array on a perfectly conducting circular cylinder.  $a = 5\lambda$ ;  $a_1 = 0.114\lambda$ ;  $a_2 = 0.095\lambda$ . Slot length =  $0.686\lambda$ ; slot width =  $0.305\lambda$ .

reflected rays exist, and it also fails at the caustic where it predicts a field singularity. Therefore, conventional GO must be patched up by a uniform GO solution which not only provides a bounded and smooth variation of the field across the caustic, but which also automatically recovers the real ray fields of GO on the lit region outside the caustic transition layer, and which likewise recovers the “complex” ray field [41] outside the transition layer on the shadow side of the caustic (since “real” ray fields cannot exist there). Such a uniform GO solution for the scattered fields ( $\vec{E}^s, \vec{H}^s$ ) is described in [14]; it is summarized below:

$$\vec{E}^s(P_L) \sim 2\pi j e^{-jk\delta_l} \left[ \bar{P}_l k^{-1/3} Ai(-k^{2/3}\zeta_l) + j^{1/2}\zeta_l \bar{Q}_l k^{-2/3} Ai'(-k^{2/3}\zeta_l) \right] \quad (45)$$

where  $Ai$  is an Airy function [13]–[15] given by

$$Ai(\delta) = \frac{1}{2\pi} \int_{-\infty}^{\infty} dt \exp(-j(t^3/3 + \delta t))$$

and  $Ai'$  is its derivative. Furthermore,

$$\begin{aligned} & \left\{ \begin{array}{l} \bar{P}_l \\ \bar{Q}_l \end{array} \right\} \\ &= \zeta_l^{1/4} \sqrt{\frac{k}{\pi}} \left[ \frac{\bar{A}(Q_a) \cdot \bar{R}(Q_a)}{s_a^i} \right. \\ & \quad \cdot \sqrt{\frac{\rho_{1a}^r}{\rho_{1a}^r + s_a^r}} \sqrt{\frac{\rho_{2a}^r}{\rho_{2a}^r + s_a^r}} e^{-j\pi/4} \\ & \quad \mp \frac{\bar{A}(Q_b) \cdot \bar{R}(Q_b)}{s_b^i} \sqrt{\frac{\rho_{1b}^r}{\rho_{1b}^r + s_b^r}} \sqrt{\frac{\rho_{2b}^r}{\rho_{2b}^r + s_b^r}} e^{+j\pi/4} \left. \right] \quad (46a) \end{aligned}$$

in which

$$\delta_l = \frac{1}{2} [(s_b^i + s_b^r) + (s_a^i + s_a^r)] \quad (46b)$$

$$\zeta_l^{3/2} = \frac{3}{4} [(s_b^i + s_b^r) + (s_a^i + s_a^r)] \quad (46c)$$

and

$$\bar{E}^i(Q_{a,b}) = \bar{A}(Q_{a,b}) \frac{\exp(-jks_{a,b}^i)}{s_{a,b}^i} \begin{pmatrix} \text{field incident at} \\ Q_{a,b} \text{ from the feed} \end{pmatrix} \quad (46d)$$

It is noted that  $\bar{R}$  in (46a) is the dyadic reflection coefficient as in (5). While (45) is given for the lit side, a similar expression exists for the shadow side, namely,

$$\bar{E}^s(P_s) \sim 2\pi j e^{-jk\delta_s} \left[ \bar{P}_s k^{-1/3} Ai(+k^{2/3}\zeta_s) + \zeta_s^{-1/2} \bar{Q}_s k^{-2/3} Ai'(+k^{2/3}\zeta_s) \right] \quad (47)$$

In (46d), the  $Q_a$  and  $Q_b$  correspond to the two “real” points of reflection on the surface as in Fig. 6; the parameters in (46b) and (46c) are defined in terms of  $Q_a$  and  $Q_b$ . The parameters in (47), for the shadow side, are defined in terms of “complex” points of reflection  $Q_{ac}$  and  $Q_{bc}$ ; these complex points are determined by an analytical continuation of the original surface into complex coordinate space [14], [41]. In practice, the subreflector in Fig. 6 is bounded by an edge which then truncates the caustic surface in question. The results in (45) and (47) are valid for observation points near the smooth portion of the caustic away from the caustic truncation and away from the second (or the other) caustic surface which also exists. Outside the given caustic transition region, (45) automatically recovers the GO result.

7) *Multiple Ray Interactions:* A diffracted ray which is incident on a discontinuity undergoes a second diffraction to create a doubly diffracted ray. Likewise, doubly diffracted rays can produce triply and higher order multiply diffracted rays. The effect of multiply diffracted rays is generally quite weak and may be ignored in that case. However, one can easily assess the importance of the latter, because leaving these out generally creates a discontinuity in the field (much like GO exhibits discontinuities along GO ray shadow boundaries); if this discontinuity is significant then it is clear that the multiple interactions must be included to some order until the discontinuity becomes sufficiently small. Finally, rays reflected and then diffracted (or vice versa) are of the same order as singly diffracted rays; thus they must be generally included to keep all significant interactions to the same order of asymptotic approximation (in terms of inverse powers of  $k$ ) [3]. Multiple interactions within ray transition regions need to be treated with care [63].

#### B. ECM

An expression for the GTD/UTD edge diffracted field has been presented in (8c) above, namely,

$$\bar{E}^d(P) \sim \bar{E}^i(Q_E) \cdot \bar{D}_e \sqrt{\frac{\rho^d}{s^d(\rho^d + s^d)}} e^{-jks^d}.$$

This expression reveals that the edge diffracted field has a singularity at the edge where  $s^d = 0$ ; such a singularity results from the fact that the edge is a caustic of the edge diffraction rays, and this caustic at  $Q_E$  is evident

from the edge diffracted ray tube illustrated in Fig. 9. The GTD/UTD expression for the asymptotic high-frequency ray field is valid away from the edge (i.e., it is valid outside the so-called edge boundary layer), and the proper behavior near the edge must be obtained from separate considerations. On the other hand, if  $\rho^d < 0$  then the other diffracted ray caustic can occur in the external space surrounding the wedge whenever the observation point at  $P$  is such that  $s^d = |\rho^d|$ , and the expression for  $\bar{E}^d(P)$  of (8c) thus becomes singular and consequently fails at and near this caustic; such a caustic can generally occur along the diffracted ray if the edge is curved or if the incident wavefront is concave. For smooth caustics of diffracted rays one could use the expressions in (45) and (47) directly within the diffracted ray caustic region except that the reflected ray parameters present in (45) and (47) must now be replaced by the corresponding diffracted ray parameters. However, the use of the ECM in this case will yield the same result as in (45) and (47) if the integrals present in the ECM, which are defined later on, are evaluated using a uniform asymptotic procedure. Furthermore, the ECM is very useful for treating a point caustic of diffracted rays (as in Fig. 5 for a symmetric parabolic reflector with the feed at the focus); the uniform approximation of (45) and (47) is not valid in regions at and near the intersection or proximity of the two smooth caustic surfaces, nor where these two caustic surfaces degenerate to form a single point caustic.

The basic idea behind ECM may be understood as follows. If  $ks^d \gg 1$  but  $s^d \ll |\rho^d|$ , then in the near zone of the edge but sufficiently far from  $Q_E$ , the expression for  $\bar{E}^d(P)$  in (8c) becomes:

$$\bar{E}^d(P) \sim \bar{E}^i(Q_E) \cdot \bar{D}_e \frac{e^{-jks^d}}{\sqrt{s^d}} \quad \left( \begin{array}{l} \text{with} \\ s^d \ll |\rho^d| \\ ks^d \gg 1 \end{array} \right) \quad (48)$$

Clearly the field at  $P$  in (48) may be viewed as being produced by an appropriate equivalent line source tangent to the curved edge at  $Q_E$ , because a line source field also exhibits an asymptotic behavior of the type  $e^{-jks^d}(s^d)^{-1/2}$  as in (48) when  $ks^d \gg 1$ , to describe a cylindrical wave as illustrated in Fig. 5(b). Thus one can find the strengths of equivalent electric ( $I$ ) and magnetic ( $M$ ) line currents locally tangent to the edge (i.e., along  $\hat{e}$ ) at  $Q_E$ , which generate the desired fields ( $\bar{E}^d(P)$ ,  $\bar{H}^d(P)$ ). For a perfectly conducting edge, the equivalent line currents  $I$  and  $M$  are given by [16]

$$\left\{ \begin{array}{l} I(Q_E) \\ M(Q_E) \end{array} \right\} = \frac{-e^{-j\pi/4}}{\sin \beta_0} \sqrt{\frac{8\pi}{k}} \left\{ \begin{array}{l} Y_0 \\ Z_0 \end{array} \right\} \hat{e} \cdot \left\{ \begin{array}{l} \bar{E}^i(Q_E) D_{es} \\ \bar{H}^i(Q_E) D_{eh} \end{array} \right\} \quad (49)$$

in which  $D_{es,eh}$  have been indicated previously in (9) and are evaluated in (49) for a diffracted ray which lies on the Keller cone and in the caustic direction. Only if the phase of  $\bar{E}^i(Q_E)$  in (48) is uniform then does (48) describe a “locally” cylindrical wave emanating from the

edge as in Fig. 5(b). On the other hand, if the incident rays strike the edge obliquely (so  $\beta_o \neq \pi/2$ ) then the phase of  $\bar{E}^i(Q_E)$  is not uniform, and neither does the phase of  $I$  and  $M$  remain constant but instead contains a traveling wave factor automatically through the presence of  $\bar{E}^i(Q_E)$  in (49). In the latter case the diffracted field behavior in (48), and likewise the corresponding asymptotic line source field behavior,  $e^{jks^d}(s^d)^{-1/2}$ , now describes a more general conical rather than a cylindrical wave. In the ECM, these conical waves thus locally simulate the Keller cones of edge diffracted rays. Even though (8c) becomes singular at diffracted ray caustics, the currents in (49) are defined and well behaved at every point along the curved edge, and hence they can be incorporated within the radiation integral to yield a bounded result for the total diffracted field  $\bar{E}_{\text{total}}^d$  at and near the caustic. Thus

$$\bar{E}_{\text{total}}^d(P) \sim \frac{jkZ_o}{4\pi} \oint \left[ \hat{R} \times \hat{R} \times I\hat{e} + Y_o\hat{R} \times M\hat{e} \right] \frac{e^{-jKR}}{R} dl' \quad (50)$$

where  $\bar{R}$  is the vector from  $Q_E$  to  $P$ , and the integration is around the edge contour which produces the caustic of diffracted rays.

It is noted that an edge diffracted ray exhibits the local line source field variation of the type  $e^{jks^d}(s^d)^{-1/2}$  in (48) only when  $\bar{D}_e$  is not range dependent; i.e., only when one observes the edge diffracted field outside the edge boundary layer and external to the incident and reflection boundary (ISB and RSB) transition regions where the UTD reduces to GTD. This is true because the special range dependent Fresnel type UTD transition function  $F$  in  $\bar{D}_e$ , which is different from unity within the ISB and RSB transition regions, modifies the  $e^{jks^d}(s^d)^{-1/2}$  type cylindrical or conical wave behavior within these transition layers. Consequently, the GTD-based ECM remains valid only if the edge diffracted ray caustic transition layer does not overlap with the ISB and RSB transition layers.

The ECM is an outgrowth of some early work in [42] which was later formulated in terms of the GTD in [16] to yield (49). A heuristic modification to extend the use of  $D_{es,eh}$  in (49), which are defined only on the Keller cone, so that they can be approximately generalized to be defined along radiation directions lying outside the Keller cone is provided in [17] by splitting the  $(\sin \beta_o)^{-1}$  factor in (49) as well as the one present in the  $D_{es,eh}$  of (49), symmetrically into  $\sqrt{\sin \beta'_o \sin \beta_o}$ , where  $\beta'_o$  is the angle between the incident ray and  $\hat{e}$  at  $Q_E$ , and  $\beta_o$  is the angle between the observation direction and  $\hat{e}$  at  $Q_E$ . If  $\beta_o = \beta'_o$ , only then does the direction of radiation from  $I$  or  $M$  at  $Q_E$  coincide with the diffracted ray from  $Q_E$  that lies on the Keller cone. Such a generalization involving a symmetric split is useful in that away from the caustic transition layer, where the GTD is valid, it allows the integral in (50) to reduce asymptotically (i.e., for large radius of curvature of the edge) to the expected GTD description [4,17] in terms of a superposition of isolated edge diffracted ray contributions

$\sum_{j=1}^J \bar{E}_j^d(P)$ , where each term  $\bar{E}_j^d(P)$  is of the type in (8c). The effect of truncating the limits of integration to the portion of the edge which is directly illuminated may create spurious contributions; this aspect and possible remedies are discussed in [4]. It is noted that unlike true currents, the  $I$  and  $M$  in (49), together with the modification of  $\sin \beta_o$  to  $\sqrt{\sin \beta'_o \sin \beta_o}$ , depend on the radiation or observation direction.

The GTD-based ECM discussed above provides the diffracted field contribution without having to find the diffracted ray paths as in the GTD. However, the ECM requires an integration, which only in some special cases can be evaluated in closed form, and which in general must be evaluated numerically. This ECM can be used to find the fields diffracted within the rear axial caustic region of the symmetric parabolic reflector of Fig. 5(a) as shown in Fig. 11. An analogous ECM application is to calculate the fields in the rear axial caustic direction of a coaxial waveguide fed aperture in a finite circular ground plane [43]. An ECM analysis of the radiation by an axial monopole on a circular ground plane, and on a flat-backed cone may be found in [9], and [44], respectively.

The GTD-based ECM can also be employed to describe the fields diffracted by an offset fed parabolic reflector for those observation directions in which isolated points of edge diffraction which move on the elliptic rim can coalesce and thereby create a singularity in the conventional GTD calculation. In this case, the ECM integral could asymptotically be expressed in terms of a parabolic cylinder function, thus providing an analytical result if desired.

In addition, the ECM can be employed in special cases to evaluate the fields at caustics of reflected rays, and of surface diffracted rays. Furthermore, it can be extended to treat the scattering by a class of interior waveguide discontinuities. The equivalent currents for interior waveguide regions are defined via the concept of modal ray fields which are found either exactly or asymptotically from the interior waveguide modes [45], [46]. The equivalent currents  $I$  and  $M$ , which "replace" the interior structure, and asymptotically produce the same interior modal fields as those created by the discontinuity via not only  $I$  and  $M$ , but also their images due to the effect of the waveguide walls, have been developed in [46] to find the modal reflection coefficients and the radiation by an incident modal field associated with an open-ended semi-infinite parallel plate waveguide antenna geometry. Other related work may be found in [47]–[49]. An alternative approach in which only equivalent magnetic currents  $M$  are impressed at the discontinuity and which radiate the desired fields within interior (or exterior) regions in the "presence" of the interior waveguide geometry have been developed in [50], [51]; such an ECM-based approach, which does not require one to explicitly find the images of the equivalent sources and their fields, can treat a somewhat more general class of waveguide discontinuities. Examples of the use of the latter ECM for interior regions are illustrated for finding the modal reflection coefficients of a waveguide fed horn antenna in [50], and for an open-ended circular waveguide

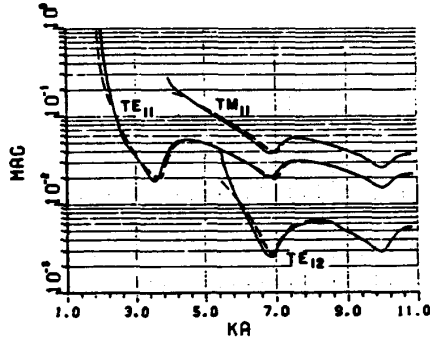


Fig. 21. Application of ECM to find the modal reflection coefficient of open-ended circular waveguide and horn antennas. (Exact Wiener-Hopf solution in: Weinstein, *The Theory of Diffraction and the Factorization Method*, Golem Press, 1968.)

aperture antenna in [51] as presented in Fig. 21. The ECM based results in Fig. 21 are seen to compare extremely well with exact Wiener-Hopf calculations.

More recently, the GTD-based ECM for edged bodies has been formulated in [52] directly from the asymptotic treatment of the integral representation for the canonical wedge diffraction problem, from which a set of slightly improved equivalent currents  $I$  and  $M$  can be identified. It may be remarked that the ECM concept is closely related to the incremental length diffraction coefficient (ILDC) concept developed by Mitzner [53]; a comparison of ILDC and ECM is available in [54], [55].

### C. PTD

As indicated in Section I, the PTD was developed by Ufimtsev [19] at about the same time Keller developed the GTD. The PTD serves to correct PO, while GTD provides a correction to GO. Thus the PTD field is a superposition of the PO field and its correction which is the so-called "edge wave field." The PO field is produced by the GO approximation for the currents induced on the radiating object, whereas the edge wave field is produced by the diffracted component of the current on the radiating object. Since GTD/UTD is the sum of the GO and diffracted ray fields, it is not surprising that if the PTD radiation integrals (i.e., the PO integral plus the integral over the diffracted current component) are evaluated using high-frequency asymptotics then the PTD reduces to the GTD. Furthermore, when the asymptotics is performed in a uniform fashion, the PTD can recover the UTD. Clearly, therefore, the PTD can be employed to patch up GTD/UTD in regions where GTD/UTD and even the GTD-based ECM fails. Elsewhere, the GTD/UTD and the GTD-ECM become applicable and are expected to be far more efficient than the PTD which generally requires the evaluation of PO integrals over an electrically large radiating object. Furthermore, multiple wave interactions can generally be accounted for in a straightforward fashion using the GTD ray technique, which is not true for the PTD. Also, the PTD has been developed only for an edge at the present time;

consequently, the GO current discontinuity at the geometric shadow boundary on the smooth portion of a scatterer can induce a spurious diffraction contribution to the PO integral. Ways to remove such spurious effects are discussed in [56]. Nevertheless, the PTD becomes particularly useful for patching up the GTD/UTD in regions where there is a confluence of reflected and/or diffracted ray caustic transition regions with the GO (incident or reflected) ray shadow boundary transitions regions. It is recalled that the GTD-ECM-based approach also fails there. The PTD electric field at an observation point  $P$  can be written as

$$\bar{E}(P) \sim \bar{E}^i + \bar{E}_{PTD}^S \quad (51a)$$

$$\bar{E}_{PTD}^S = \bar{E}_{PO}^S + \bar{E}_U^S \quad (51b)$$

where  $\bar{E}^i$  is the classical incident field from the primary source radiating in the absence of any scattering structure, and  $\bar{E}_{PTD}^S$  is the PTD based asymptotic approximation to the field scattered by the presence of the structure when excited by the primary source. Unlike the incident GO field  $\bar{E}^i U_i$  which is discontinuous (see (4a)), the  $\bar{E}^i$  in (51a) is continuous everywhere. The  $\bar{E}_{PTD}^S$  is calculated by superposing the physical optics contribution,  $\bar{E}_{PO}^S$  and the Ufimtsev correction,  $\bar{E}_U^S$  as in (51b), where

$$\bar{E}_{PO}^S(P) = \frac{-jkZ_0}{4\pi} \int \int_{S_{lit}} \bar{J}_S^{GO}(\bar{r}') \cdot \left[ \bar{I} + \frac{\nabla \nabla}{k^2} \right] \frac{e^{-jk|\bar{r}-\bar{r}'|}}{|\bar{r}-\bar{r}'|} ds' \quad (52)$$

in which  $\bar{J}_S^{GO}(\bar{r}')$  is the GO approximation to the current induced at any point  $\bar{r}'$  on a perfectly conducting boundary excited by a primary source (the source of  $\bar{E}^i$ ). The boundary may be a host structure for an antenna which serves as a primary source, or, the primary source could be a feed antenna for a reflecting boundary (e.g., a parabolic reflector). Thus  $\bar{J}_S^{GO}(\bar{r}') = \hat{n}' \times [\bar{H}^i(\bar{r}')U_i + \bar{H}^r(\bar{r}')U_r]$  on the part of the boundary surface  $S_{lit}$  which is directly illuminated by the primary source, and  $\bar{J}_S^{GO} = 0$  elsewhere (i.e., in the shadow region) on the boundary. Here,  $\bar{H}^i(\bar{r}')U_i$  and  $\bar{H}^r(\bar{r}')U_r$  are the incident and reflected GO components of the magnetic field at  $\bar{r}'$ . The position vector to the observation point is  $\bar{r}$ , and  $\hat{n}'$  is the unit outward normal vector to the boundary at  $\bar{r}'$ . It appears that Ufimtsev found  $\bar{E}_U^S$  indirectly in his original work [19]. If the PTD integrals in (51), (52) are approximated asymptotically, then

$$\bar{E}_{PO}^S \sim -\bar{E}^i(1 - U_i) + \bar{E}^r U_r + \bar{E}^i(Q_E) \cdot \bar{D}_e^{PO} \sqrt{\frac{\rho^d}{s^d(\rho^d + s^d)}} e^{-jks^d} \quad (53)$$

and  $\bar{E}_U^S(P)$  can be expressed as

$$\bar{E}_U^S(P) \sim \bar{E}^i(Q_E) \cdot \bar{D}_e^U \sqrt{\frac{\rho^d}{s^d(\rho^d + s^d)}} e^{-jks^d} \quad (54)$$



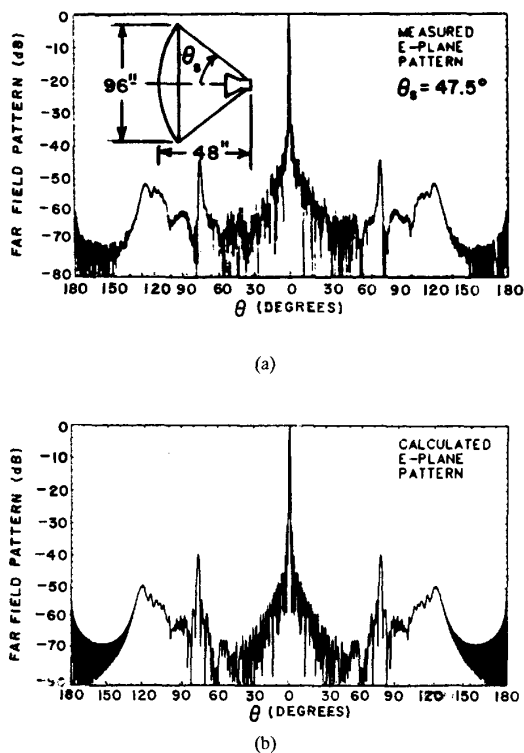


Fig. 23 Measured and calculated  $E$  plane patterns of a symmetric parabolic reflector antenna at 11 GHz. (a) Measured. (b) Calculated (see [58]).

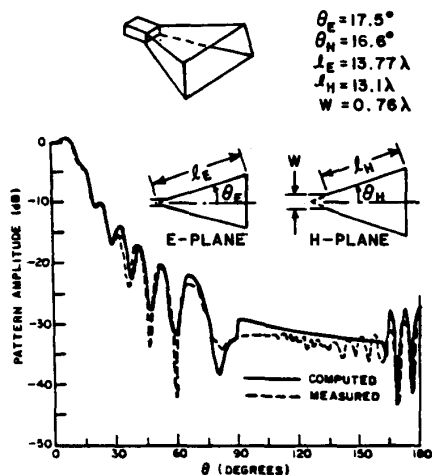


Fig. 24 Measured and calculated  $E$  plane patterns of a pyramidal horn antenna (see [59]).

AI becomes important if one employs AI not just to calculate the antenna main beam and the first few sidelobes, but to also calculate the wide angle sidelobes and back lobes.

### III. CONCLUSIONS

It is seen that high-frequency techniques are conceptually

simple as well as versatile in being able to predict the radiation patterns, mutual coupling and other effects associated with a large variety of practical antenna configurations. However, as also seen from Section II, the use of GTD/UTD technique requires a knowledge of the relevant diffraction coefficients; therefore, while several diffraction mechanisms can presently be characterized by UTD coefficients, more UTD coefficients need to be developed to solve a greater variety of antenna problems which are relevant to present and future EM technology. Some UTD coefficients which are known only approximately at present need to be refined in some cases; others need to be found for additional perfectly conducting as well as nonconducting (and even penetrable) canonical structures. Some work in the latter case which is available in [60], [61] needs to be developed further; such work would be useful, for example, to predict the reduction in coupling between antennas on a metal surface by introducing a lossy (absorbing) material patch placed between the pair of antennas, or to predict the effects of the canopy of private aircraft, or helicopters, on the antennas located on such structures, etc. The PTD likewise needs to be formally extended to deal with nonconducting surfaces and to smooth surfaces without edges, etc. Not discussed in this paper are spectral techniques which can be used in conjunction with high-frequency approximations to deal with complex (nonray optical) illumination of the host structure by the primary source (antenna) [62], [63]. Finally, hybrid procedures which combine high and low frequency techniques [66], and the Gaussian beam techniques have also not been discussed here due to space limitations. Different aspects of ray and Gaussian beam methods have appeared previously as a collection of papers in [65]; the latter also contains a paper by Borovikov and Kinber, which in turn provides a large bibliography of Soviet papers on high-frequency techniques. The hybrid procedures as well as the Gaussian beam techniques appear to hold promise to solve some high-frequency EM antenna and scattering problems which may otherwise become intractable.

### REFERENCES

- [1] J. B. Keller, "Geometrical theory of diffraction," *J. Opt. Soc. Amer.*, vol. 52, pp. 116–130, 1962.
- [2] R. G. Kouyoumjian and P. H. Pathak, "A uniform geometrical theory of diffraction for an edge in a perfectly conducting surface," *Proc. IEEE*, vol. 62, pp. 1448–1461, Nov. 1974.
- [3] —, "A uniform GTD approach to EM scattering and radiation," in *Acoustic, Electromagnetic and Elastic Wave Scattering—High and Low Frequency Asymptotics*, vol. II, Varadan and Varadan, Eds. Amsterdam, The Netherlands: North Holland, 1986.
- [4] P. H. Pathak, "Techniques for high frequency problems," in *Antenna Handbook, Theory Application and Design*, Y. T. Lo and S. W. Lee, Eds. New York: Van Nostrand Reinhold, 1988.
- [5] S. W. Lee and G. A. Deschamps, "A Uniform Asymptotic theory of EM diffraction by a curved wedge," *IEEE Trans. Antennas Propagat.*, vol. AP-24, pp. 25–34, Jan. 1976.
- [6] R.C. Hansen, Ed., *Geometrical Theory of Diffraction*. New York: IEEE Press, 1981.
- [7] G. L. James, *Geometrical Theory of Diffraction for Electromagnetic Waves*. IEE EM Wave Series 1, (Peter Peregrinus), 1976.
- [8] D. A. McNamara, C. W. I. Pistorius, and J. A. G. Malherbe, *Introduction to the Uniform Geometrical Theory of Diffraction*. New York: Artech House, 1990.

- [9] C. A. Balanis, *Advanced Engineering Electromagnetics*, IEE EM Wave Series 10, (Peter Peregrinus), 19.
- [10] E. V. Jull, *Aperture Antennas and Diffraction Theory*, IEE EM Wave Series 10, (Peter Peregrinus), 1981.
- [11] A. Ishimaru, *Electromagnetic Wave Propagation, Radiation and Scattering*. Englewood Cliffs, NJ: Prentice-Hall, 1991.
- [12] V. A. Fock, *Electromagnetic Diffraction and Propagation Problems*. New York: Pergamon, 1965.
- [13] L. B. Felsen and N. Marcuvitz, *Radiation and Scattering of Waves*. Englewood Cliffs, NJ: Prentice-Hall, 1973.
- [14] P. H. Pathak and M. C. Liang, "On a uniform asymptotic solution valid across smooth caustics of rays reflected by smoothly indented boundaries," *IEEE Trans. Antennas Propagat.*, vol. AP-38, pp. 1192–1203, Aug. 1990.
- [15] J. J. Stamnes, *Waves in Focal Regions*. Bristol and Boston, MA: Adam Higler 1986.
- [16] C. E. Ryan Jr. and L. Peters Jr., "Evaluation of edge diffracted fields including equivalent currents for caustic regions," *IEEE Trans. Antennas Propagat.*, vol. AP-7, pp. 292–299, May 1969; also, see correction, *IEEE Trans. Antennas Propagat.*, vol. AP-8, p. 275, Mar. 1970.
- [17] E. F. Knott and T. B. A. Senior, "Comparison of three high-frequency diffraction techniques," *Proc. IEEE*, vol. 62, pp. 1468–1478, Nov. 1974.
- [18] R. F. Harrington, *Time Harmonic Electromagnetic Fields*. New York: McGraw-Hill, 1961.
- [19] P. Ya Ufimtsev, "Method of edge waves in the physical theory of diffraction," (from the Russian "Method Krayevykh Voin V Fizicheskoy Teorii Difraktsii," *Izd-Vo Sov. Radio*, pp. 1–243, 1962), Translation prepared by the U. S. Air Force Foreign Technology Division, Wright-Patterson AFB, OH; released for public distribution Sept. 7, 1971.
- [20] D. I. Butorin and P. Ya Ufimtsev, *Sov. Phys. Acoust.*, vol. 32, no. 4, July–Aug. 1986.
- [21] M. S. Narasimhan and K. M. Prasad, "GTD analysis of near field patterns of a prime focus symmetric parabolic reflector antenna," *IEEE Trans. Antennas Propagat.*, vol. AP-29, pp. 959–961, Nov. 1981.
- [22] A. Michaeli, "Transition functions for high frequency diffraction by a curved perfectly conducting wedge—parts I, II and III," *IEEE Trans. Antennas Propagat.*, vol. 37, pp. 1073–1092, Sept. 1989.
- [23] M. C. Liang, C. W. Chuang, and P. H. Pathak, Paper on edge diffracted surface rays, in preparation.
- [24] M. C. Liang, P. H. Pathak, and C. W. Chuang, "A generalized UTD analysis for the diffraction by a wedge with convex faces to include surface ray effects and grazing angles of incidence/diffraction," presented at the 1988 Int. IEEE APS/Radio Science Meeting, Syracuse Univ., Syracuse, NY, June 6–10, 1988.
- [25] M. C. Liang, "A generalized uniform GTD ray solution for the diffraction by a perfectly-conducting wedge with convex faces," Ph.D. dissertation, The Ohio State Univ., 1988.
- [26] M. Idemen and L. B. Felsen, "Diffraction of a whispering gallery mode by the edge of a thin concave cylindrically curved surface," *IEEE Trans. Antennas Propagat.*, vol. AP-29, pp. 571–579, July 1981.
- [27] K. C. Hill and P. H. Pathak, "On the computation of the transition function occurring in a new approximate UTD corner diffraction coefficient," in preparation.
- [28] K. C. Hill, "A UTD solution to the EM scattering by the vertex of a perfectly-conducting plane angular sector," Ph.D. dissertation, The Ohio State Univ., 1990.
- [29] F. A. Sitka, W. D. Burnside, T. T. Chu, and L. Peters Jr., "First order equivalent current and corner diffraction scattering from flat plate structures," *IEEE Trans. Antennas Propagat.*, vol. AP-31, pp. 584–589, July 1983.
- [30] K. E. Golden, G. E. Stewart, and D. C. Pridmore-Brown, "Approximation techniques for the mutual admittance of slot antennas on metallic cones," *IEEE Trans. Antennas Propagat.*, vol. AP-22, pp. 43–48, 1974.
- [31] K. D. Trott, P. H. Pathak, and F. A. Molinet, "A UTD type analysis of the plane wave scattering by a fully illuminated perfectly conducting cone," *IEEE Trans. Antennas Propagat.*, vol. AP-38, pp. 1150–1160, Aug. 1990.
- [32] P. H. Pathak, "An asymptotic analysis of the scattering of plane waves by a smooth convex cylinder," *Radio Sci.*, Vol. 14, pp. 419–435, May–June 1979.
- [33] P. H. Pathak, W. D. Burnside, and R. J. Marhefka, "A uniform UTD analysis of the diffraction of electromagnetic waves by a smooth convex surface," *IEEE Trans. Antennas Propagat.*, vol. AP-28, pp. 609–622, Sept. 1980.
- [34] N. A. Logan and K. S. Yee, "A mathematical model for diffraction by convex surfaces," in *Electromagnetic Waves*, R. Langer, Ed., Madison, WI: Univ. Wisconsin Press, 1962.
- [35] B. R. Levy and J. B. Keller, "Diffraction by a smooth object," *Comm. Pure Appl. Math.*, vol. 12, pp. 159–209, Feb. 1959.
- [36] P. H. Pathak, N. Wang, W. D. Burnside and R. G. Kouyoumjian, "A uniform GTD solution for the radiation from sources on a convex surface," *IEEE Trans. Antennas Propagat.*, vol. AP-29, pp. 609–621, July 1981.
- [37] P. H. Pathak and N. Wang, "Ray analysis of mutual coupling between antennas on a convex surface," *IEEE Trans. Antennas Propagat.*, vol. AP-29, Nov. 1981.
- [38] S. W. Lee, "Mutual admittance of slots on a cone: Solution by ray technique," *IEEE Trans. Antennas Propagat.*, vol. AP-26, pp. 768–773, Nov. 1978.
- [39] J. J. Kim and W. D. Burnside, "Simulation and analysis of antennas radiating in a complex environment," *IEEE Trans. Antennas Propagat.*, vol. AP-34, pp. 554–562, Apr. 1986.
- [40] P. H. Pathak, A. Ghantous, C. W. Chuang, and O. M. Buyukdura, "A preliminary investigation of conformal antenna phased arrays on perfectly-conducting convex surfaces," The Ohio State Univ. ElectroScience Lab., Tech. Rep. 717060–2, (prepared under Contract L5XM-379206–947, for Rockwell International, Los Angeles, CA,) Nov. 1985.
- [41] H. Ikuno and L. B. Felsen, "Complex ray interpretation of reflection from concave–convex surfaces," *IEEE Trans. Antennas Propagat.*, vol. 36, pp. 1206–1271, Sept. 1988.
- [42] R. F. Millar, "An approximate theory of the diffraction of an electromagnetic wave by an aperture in a plane screen," *Proc. Inst. Elect. Eng.*, vol. 103C, pp. 177–185, 1956.
- [43] C. R. Cockrell and P. H. Pathak, "Diffraction theory techniques applied to aperture antennas on finite circular and square ground planes," *IEEE Trans. Antennas Propagat.*, vol. AP-22, pp. 443–448, May 1974.
- [44] C. A. Balanis, "Radiation from conical surfaces used for high speed aircraft," *Radio Sci.*, vol. 7, pp. 339–343, Feb. 1972.
- [45] H. Y. Yee and L. B. Felsen, "Ray optical techniques for waveguide discontinuities," Rep. PIBEP-68–005, Polytechnic Inst. of Brooklyn, NY, 1968.
- [46] H. Y. Yee, L. B. Felsen, and J. B. Keller, "Ray theory of reflection from the open end of a waveguide," *SIAM J. Appl. Math.*, vol. 16, pp. 268–300, 1968.
- [47] S. W. Lee, "Ray theory of diffraction by open-ended waveguides: Applications," *J. Math. Phys.*, vol. 13, pp. 656–664, 1972.
- [48] J. Boersma, "Ray-optical Analysis of Reflections in an open ended parallel plane Waveguide: TM case," *SIAM J. Appl. Math.*, vol. 29, pp. 164–195, 1975.
- [49] R. C. Rudduck and L. L. Tsai, "Aperture reflection coefficients for TEM and TE<sub>10</sub> mode parallel-plate waveguides," *IEEE Trans. Antennas Propagat.*, vol. AP-16, pp. 83–89, 1968.
- [50] P. H. Pathak and A. Altintas, "An efficient high-frequency analysis of modal reflection and transmission coefficients for a class of waveguide discontinuities," *Radio Sci.*, vol. 23, no. 6, pp. 1107–1119, Nov.–Dec. 1988.
- [51] C. W. Chuang and P. H. Pathak, "Ray analysis of modal reflection for three-dimensional open-ended waveguides," *IEEE Trans. Antennas and Propagat.*, vol. 37, pp. 339–346, Mar. 1989.
- [52] A. Michaeli, "Elimination of infinities in equivalent edge currents, parts I and II," *IEEE Trans. Antennas Propagat.*, vol. AP-34, pp. 912–918, July 1986 and pp. 1034–1037, Aug. 1986.
- [53] K.M. Mitzner, "Incremental length diffraction coefficients," Aircraft Div., Northrop Corp., Tech. Rep. AFAL-TR-73–296, Apr. 1974.
- [54] E.F. Knott, "The relationship between Mitzner's ILDC and Michaeli's equivalent currents," *IEEE Trans. Antennas Propagat.*, vol. AP-33, pp. 112–114, Jan. 1985.
- [55] R. A. Shore and A. D. Yaghjian, "Incremental diffraction coefficients for planar surfaces," *IEEE Trans. Antennas Propagat.*, vol. 36, pp. 55–70, Jan. 1988.
- [56] I. J. Gupta, C. W. I. Pistorius, and W. D. Burnside, "An efficient method to compute spurious endpoint contributions in PO solutions," *IEEE Trans. Antennas Propagat.*, vol. AP-35, Dec. 1987.

- [57] S. W. Lee, "Comparison of uniform asymptotic theory and Ufimtsev's theory of electromagnetic edge diffraction," *IEEE Trans. Antennas Propagat.*, vol. AP-25, pp. 162-170, Mar. 1977.
- [58] T. H. Lee, R. C. Rudduck, and K. M. Lambert, "Pattern measurements of Reflector Antennas in the compact range and validation with computer code simulation," *IEEE Trans. Antennas Propagat.*, vol. AP-23, pp. 889-895, June 1990.
- [59] C. A. Mentzer, L. Peters Jr., and R. C. Rudduck, "Slope diffraction and its application to horns," *IEEE Trans. Antennas Propagat.*, vol. AP-23, pp. 153-159, Mar. 1975.
- [60] R. G. Rojas and P. H. Pathak, "Diffraction of EM waves by a dielectric/ferrite half-plane and related configurations," *IEEE Trans. Antennas Propagat.*, vol. AP-35, pp. 1483-1487, Dec. 1987.
- [61] J. L. Volakis and T. B. A. Senior, "Diffraction by a thin dielectric half plane," *IEEE Trans. Antennas Propagat.*, vol. AP-35, pp. 1483-1487, Dec. 1987.
- [62] Y. Rahmat-Samii and R. Mittra, "A spectral domain interpretation of high frequency phenomena," *IEEE Trans. Antennas Propagat.*, vol. AP-25, pp. 676-687, Sept. 1977.
- [63] R. Tiberio, G. Manara, G. Pelosi, and R.G. Kouyoumjian, "High-frequency electromagnetic scattering of plane waves from double wedges," *IEEE Trans. Antennas Propagat.*, vol. AP-37, pp. 1172-1180, Sept. 1989.
- [64] E. K. Miller and G. J. Burke, "Low frequency computational electromagnetics for antenna analysis," *Proc. IEEE*, vol. 80, this issue.
- [65] G. A. Thiele, "Overview of selected hybrid methods in radiating system analysis," *Proc. IEEE*, vol. 80, this issue.
- [66] Special Issue on Rays and Beams, *Proc. IEEE*, vol. 62, Nov. 1974.



**Prabhakar H. Pathak** (Fellow, IEEE) received the B.Sc. degree in physics from the University of Bombay, India, in 1952, the B.S. degree in electrical engineering from the Louisiana State University, Baton Rouge, in 1965, and the M.S. and Ph.D. degrees from The Ohio State University (OSU), Columbus, in 1970 and 1973, respectively.

From 1965 to 1966 he was an Instructor in the Department of Electrical Engineering at the University of Mississippi, Oxford. During the summer of 1966 he worked as an electronics engineer with Boeing Company, Renton, WA. Since 1963 he has been with the OSU Electro-Science Laboratory. His research interests are in mathematical methods, electromagnetics, and uniform ray techniques. In 1983, he joined the faculty of the Department of Electrical Engineering, The Ohio State University, where he is currently a Professor. He has contributed to the development of the uniform geometrical theory of diffraction (UTD), which can be applied to analyze a variety of practical electromagnetics antenna and scattering problems. His work continues to be in the UTD and other high-frequency techniques, as well in the analysis of guided waves, and microstrip and reflector antennas using high-frequency asymptotic procedures. He has presented invited lectures, and several short courses on the UTD, both in the U.S. and abroad. He has also authored and coauthored chapters on ray methods for five books. He has served as Associate Editor for the IEEE TRANSACTIONS ON ANTENNAS AND PROPAGATION for about five years.

Dr. Pathak is a member of Commission B of the International Scientific Radio Union (URSI) and Sigma Xi.